An investigation into the behaviour of pressed-in piles

David John White

Churchill College
University of Cambridge

April 2002

A dissertation submitted for the
degree of Doctor of Philosophy
at the University of Cambridge

ERRATA

1) Page 5-57, Figure 5.20

The labels ‘Transition from vertical compression to extension’ and ‘Transition from horizontal extension to compession’ should be reversed.

2) Page 3-18, Equation 3.4

Corrected version of Equation 3.4: $R_n(\underline{s}) = \frac{R(\underline{s})}{\sqrt{N(\underline{s})}}$

D. J. White

February 2003

DECLARATION

I hereby declare that, except where specific reference is made to the work of others, the contents of this dissertation are original and have not been submitted in whole or in part for consideration for any other degree or qualification a this, or any other, university. This dissertation is entirely the result of my own work and includes nothing which is the outcome of work done in collaboration.

Permission to exceed the recommended limits of 65,000 words and 150 figures was granted by the Board of Graduate Studies in their letter dated 16 April 2002, ref. kjw/193031038/disswd. This dissertation is presented in less than the revised limits of 75,000 words and 165 figures.

D. J. White

April 2002

ABSTRACT

An investigation into the behaviour of pressed-in piles has been conducted. The press-in method of pile installation allows large pre-formed foundation piles to be constructed without the noise and vibration associated with conventional dynamic techniques, and with minimal requirement for temporary works. This investigation is divided into two parts; a fundamental study of the mechanics of press-in pile installation in sand and a sequence of field tests to examine the behaviour of pressed-in piles at full scale.

The mechanics of pile installation have been studied using a plane strain calibration chamber. A new system for deformation measurement in plane strain modelling and other forms of geotechnical testing has been developed. This system combines techniques of digital photography, Particle Image Velocimetry (PIV) and close range photogrammetry. A series of validation experiments demonstrated that the system offers greater accuracy and precision than existing measurement techniques. This improved performance is achieved concurrent with an order-of-magnitude increase in the number of measurement points that can be established within the observed soil.

A series of 8 calibration chamber tests is reported. The pattern of soil displacement during pile installation was measured. These measurements were of sufficient quality to allow soil strain paths during installation to be calculated. The influence of soil type and initial density was examined, and the post-installation strain distribution was found. The concentration of shear and volumetric strain close to the pile tip was quantified, and a reversal of strain direction as the soil passes around the pile shoulder was observed.

A zone of highly compacted soil was observed immediately below the pile tip and along the pile shaft. Contraction of this sleeve of broken soil grains was observed with continued penetration of the pile. A mechanism is proposed to link this kinematic observation to the distribution of shaft friction close to the tip of displacement piles.

A further mechanism is proposed to predict the distribution of external shaft friction along the upper part of a pile shaft. This mechanism is based on vertical arching theory, and is an extension of a previous approach for the prediction of internal shaft friction.

Four series of field tests using pressed-in piles were conducted. The first series demonstrated that internal shaft friction is well predicted by vertical arching theory. Since vertical arching evolves according to an exponential function, pile performance can be dramatically influenced by only small changes to the governing parameters. The improvement of driveability using an internal driving shoe was investigated.

The final series of load tests demonstrated a novel foundation solution in which the high shaft friction created by vertical arching can be ‘switched on’ after installation. This is achieved using a construction sequence involving H-section piles. During press-in installation of each pile, the geometry does not create vertical arching. During loading of the entire structure, arching occurs. This leads to a high positive group effect, and an efficient foundation structure.

Keywords: pile, sand, foundation, press-in, particle image velocimetry, photogrammetry, geotechnical.

ACKNOWLEDGEMENTS

First and foremost I wish to acknowledge the supervision provided by Prof. Malcolm Bolton. Malcolm has always been generous with his time and has constantly been on hand to provide guidance and inspiration when needed. In addition, he gave me the freedom to choose my own direction by spending most of the 1st year of this research 10,000 miles away in Perth, Australia.

Secondly, without the enthusiastic technical input provided by Chris Collison and his team, I could not have completed the laboratory testing. Chris, Jason, Chrissie, Alan and John's skills and support make the Schofield Centre an excellent laboratory in which to conduct research. Back in the Department of Engineering, Alistair Ross, Dave Pittock, Alan Bevin and John Wallis all played a part in constructing the experimental apparatus. Danny Slater made a great job of welding the calibration chamber together. Dr. Adrian Hyde of the University of Sheffield kindly provided the Dog's Bay sand.

I am grateful to Giken Seisakusho for the opportunity to conduct field testing in Japan. A large number of staff were involved in these tests and particular thanks are due to Masaaki Katami, Takahiko Ikeda, Teruo Nagayama, Kazuo Wako, Kayoko Yamamoto and Yuichi Matsuoka. Grant Bearss of Giken America has been a very useful source of practical advice.

The geotechnical research student community in Cambridge has grown in size considerably during the past 4 years. I have benefited from this community spirit, and thank all of my colleagues, past and present. I am particularly grateful to Lis Bowman, Stuart Haigh and Andy Take- my neighbours on The Shelf. Thank you for the many drinks and discussions during the past 4 years.

Also, Dr. Kenichi Soga, Dr. Chris Martin and Dr. Aleksander Spasojevic provided useful advice during the development of the ideas in this dissertation.

Johnny Cheuk, SW Jacobsz and Xavier Borghi, when proof reading this thesis, demonstrated to me that English is best written by foreigners. Thank you, gentlemen.

I am grateful to the EPSRC for funding my extended stay in Cambridge. Churchill College contributed to the cost of attending conferences, and St John's College elected me to a Research Fellowship during the closing months of this work. I am now checked in for a further three years of Cambridge treatment.

Part of the reason for staying so long in Cambridge is that it remains so enjoyable. Many people- too many to name all- have brought good times, especially you, Katharine.

Finally, my parents. Thank you for your love and support through the past years.

CONTENTS

NOTATION

Related to geotechnical engineering

Roman

e	Voids ratio
f_s	Shear stress on CPT friction sleeve
h	Distance above pile tip
h_{plug}	Length of soil column (or plug) within tubular pile
p	Mean pressure
q_b	Base resistance
q_c	Cone tip resistance
q_s	Mean local shaft friction along pile length
r_p	Pile radius
s	Pile settlement
t	Wall thickness
v	Specific volume
x	Horizontal coordinate
y	Vertical coordinate
z	Depth

A	Area
B	Pile breadth
D	Pile diameter
D_{10}	10% passing particle diameter
D_{50}	Mean (50% passing) particle diameter
E	Young's Modulus
F	Flexibility ratio
G	Shear stiffness
G_s	Specific gravity
I_D	Relative density
I_R	Rigidity ratio
I_{RR}	Reduced rigidity ratio (Vesic, 1972)
K	Horizontal earth pressure coefficient
L	Pile length
N_q	Bearing capacity factor
P_a	Atmospheric pressure (101.6 kPa)
Q	Capacity
R	Radius
R_{cla}	Centreline average roughness
R_{max}	Peak-to-trough roughness
R_n	Normalised roughness, R_{max}/D_{50}

Subscripts

I, II	Indicate principal directions and quantities
a	Active
av	Average
eng	Engineering
f	At failure, final
h	Horizontal
i	Intenal
log	Logarithmic
max	Maximum
min	Minimum
o	Initial, in situ conditions
o	One-dimensional
o	Outside (external)
p	Plug
p	Pile
r	Radial
s	Shaft
v	Vertical
w	Wall

Greek

α_{cone}	Reduction factor on cone tip resistance
β	Shaft friction parameter, $K \tan \delta$
β_{init}	Anti-clockwise inclination of bedding plane from horizontal
δ	Interface friction angle
δh	Small change in cavity radius
ε	Direct strain
ϕ	Angle of friction
ψ	Angle of dilation
γ	Shear strain
γ	Bulk density
η	Vertical shear transfer factor
κ	Unloading stiffness (in log stress- volume space)
μ	Friction fatigue decay rate (Randolph *et al.*, 1994)
σ	Direct stress
τ	Shear stress
τ_s	Local shaft friction
ζ	Group efficiency
Δ	Change in value
Δ	Volumetric compression
Ψ	Volume state parameter (Been & Jefferies, 1985)

Related to image analysis and photogrammetry

Roman

f	Focal length
k_1, k_2	Coefficients of radial lens distortion
n	Refractive index
p_1, p_2	Coefficients of tangential lens distortion
$\underline{s}$	Search zone coordinate vector
s_{max}	Maximum component of $\underline{s}$
t	Time
t	Window thickness
t_1, t_2, t_3	Translation components of P_R
u_0, v_0	Pixel coordinates of principal point
$\underline{x}$	Image-space coordinate vector (x,y), (x,y,z)
D	Difference matrix
D_v, D_h	CCD pixel height and width
F	Deformation gradient matrix
H	Distance from projective centre to object plane in Z-direction
I	Digital image matrix
L	Patch width
L	Displacement gradient matrix
M	Mask vector or matrix (unity)
N	Normalisation matrix
P_C	CCD calibration matrix
P_P	Perspective projection matrix
P_R	Rotation-translation matrix
R	Autocorrelation matrix
R_n	Normalised autocorrelation matrix
U	Stretch matrix
$\underline{U}$	Image coordinate vector (u,v)
$\underline{X}$	Object-space coordinate vector (X,Y), (X,Y,Z)
W	Width

Subscripts

CTRL	Control point

Greek

α	CCD pixel aspect ratio
λ	Refraction scaling component
ρ	Standard error
θ, ϕ, φ	Euler angles of rotation

ABBREVIATIONS

API	American Petroleum Institute
CAF	Cell action factor
CCD	Charge coupled device
CNS	Constant normal stiffness
COV	Coefficient of variation
CPT	Cone penetration test
CPU	Central processing unit
CSL	Critical state line
DBS	Dog's Bay sand
EURIPIDES	European initiative on piles in dense sands
FEM	Finite element method
FFT	Fast Fourier transform
FMM	Film measurement machine
IC	Imperial College
LBS	Leighton Buzzard sand (Fraction B)
NCL	Normal compression line
OCR	Over-consolidation ratio
PIV	Particle image velocimetry
PTFE	Polytetrafluoroethylene
SPM	Strain path method
SPT	Standard penetration test
TX	Triaxial
USB	Universal serial bus

CHAPTER 1

INTRODUCTION

1.1 PREFACE

For many thousands of years, piles have been used to support heavy structures by transferring loads to deeper and more competent soil strata (Kerisel, 1985). The construction of heavier, taller structures at increasingly marginal sites, and the technological improvements of the equipment used to install piles, make the economics of deep foundations ever more attractive (Salgado, 1995).

These technological improvements have led to a proliferation of pile types and installation methods. Displacement piles, driven into the ground by hammering or vibration, remain widely used for offshore and nearshore foundations. For onshore foundations, non-displacement piles have increased in popularity during the late 20th century since these can be installed without the noise and vibration associated with conventional methods of pile driving. Increasingly stringent noise and vibration legislation virtually precludes the installation of displacement piles by dynamic methods in urban Europe and Japan.

This is a study into the behaviour of displacement piles in sand. Particular attention is given to one novel pile installation technique: the press-in method. This is a recently-developed pile installation technique which allows displacement piles to be installed without creating the noise and vibration associated with dynamic methods.

1.2 PRESSED-IN PILES

Pre-formed displacement piles can be installed by static jacking force alone if sufficient reaction force is available. Small rigs capable of forcing micro-piles into the ground for underpinning have been widely used for many years. Reaction is often provided by the weight of the structure being underpinned.

A refinement of this approach is the 'press-in method', in which large capacity pre-formed displacement piles are installed by static force, with reaction being provided by adjacent previously installed piles. The static force is applied by a press-in piling machine that stands on the advancing pile wall, 'walking' forward after the installation of each pile (Figure 1.1). This technique is widely used in Japan for the installation of sheet piles. The recent development of stronger press-in pilers has provided a new alternative to dynamic methods for the installation of large high-capacity displacement piles for axially loaded foundations or retaining structures.

The most obvious difference between the press-in method and conventional dynamic methods of displacement pile installation is the reduced noise and vibration. White *et al.* (2002) demonstrated that ground vibrations during press-in pile installation are more than an order of magnitude lower than those created by dynamic methods. Also, noise emissions from press-in pilers are below current legislative limits.

1.3 PREDICTION….

Although piles are well established as a foundation solution, their behaviour remains one of the largest sources of uncertainty in geotechnical engineering. In spite of the >6500 papers which have been published on this subject[1], current design methods offer low reliability (Chow, 1997) and are not based on the physical processes which govern pile capacity (Randolph *et al.*, 1994). As a result, large factors of safety are required in

[1] Within the database of soil mechanics publications held by the Swedish Geotechnical Institute (http://public.swedgeo.se/index-e.html)

design. Alternatively, costly field trials must be conducted to deduce site-specific design parameters.

This dissertation tackles *prediction* by examining the mechanisms that govern pile installation, and subsequent loading. The physical processes underlying this behaviour are examined using controlled laboratory testing. A novel technique for quantifying the deformation and strain induced during installation of a displacement pile is developed, and applied to a programme of plane strain calibration chamber testing. By revealing the life-cycle of soil elements close to a displacement pile, this testing demonstrates the regime of soil behaviour operative during pile installation and loading. Aspects of pile behaviour in which pressed-in piles differ from those installed by conventional methods are highlighted.

Further investigations are carried out using field-scale test piles to examine the *prediction* of plugging and installation force of pressed-in tubular displacement piles. A comparison is made with current design methods, which are derived primarily from experience of dynamically-installed piles.

1.4 ….AND PERFORMANCE

Recent advances in construction technology have led to a variety of novel pile types and installation techniques, including the press-in method. The study of pile behaviour has historically concentrated on relating the in situ soil condition to the behaviour of the completed foundation. This is the domain of *prediction*. A relatively small amount of attention has been devoted to the influence of the installation method, or construction process, on the behaviour, or *performance* of the foundation. In this dissertation, *performance* is used to describe the influence of the installation procedure, since this construction process can be altered and optimised, whereas the in situ soil conditions can not.

The *performance* of the press-in method is examined in two respects. Firstly, driveability is examined. The maximum size of pile that can be installed by the press-in method is limited by the soil resistance encountered during installation, and the static

force capacity of the piler. Techniques for reducing this soil resistance are examined through field testing of instrumented piles.

Secondly, the *performance* of a completed pressed-in pile foundation is studied. A novel foundation for large onshore structures is considered, in which the installation procedure and foundation geometry are optimised to gain maximum capacity. Field load tests demonstrate that this solution is extremely efficient. A very high capacity foundation can be constructed using only a relatively weak piling machine, and causing minimal environmental impact. This is high *performance*.

1.5 DISSERTATION STRUCTURE

Chapter 2 reviews the literature relating to axially-loaded piles in sand. The review is divided into two parts. Firstly, previous research into the mechanics of pile behaviour is highlighted. Secondly, current design methods for axial pile capacity are examined. Links are drawn between the complex and often contradictory behavioural observations, and the relative unreliability of current design methods.

Chapter 3 describes the development of a new technique for the measurement of displacements in geotechnical physical modelling. This technique is based on digital imaging technology, Particle Image Velocimetry (PIV) and close range photogrammetry. The operation and validation of the technique are described, and the resulting performance is compared to previous experimental techniques.

Chapter 4 explains the methodology of the calibration chamber testing programme. The design of the chamber and instrumentation is described, and the details of the test programme are outlined.

Chapter 5 presents the results from the calibration chamber testing. A series of tests in silica and carbonate soil are reported. The penetration mechanism is quantified, throwing light on the origin of both base resistance and shaft friction. The pattern of soil flow around an advancing pile is examined, and the resulting distribution of strain is found. The influence of the installation method on this regime is discussed.

Chapter 6 describes the three programmes of field testing conducted in Japan during the course of this research. The first test programme prompts an examination of shaft friction, leading to a re-examination of the origin of this component of pile capacity. The distribution of shaft friction inside and outside of pressed-in tubular piles is examined within the framework of vertical arching. This leads to a study into the optimisation of this installation method. Techniques for improving the driveability of individual piles and the efficiency of the completed foundation are demonstrated.

Chapter 7 summarises the key conclusions from this work, and makes suggestions for future research.

a) A 300 tonne press-in piler for installing 1000-1200 mm diameter steel tubular piles

b) The installation of a wall of interlocking steel tubular piles near New York

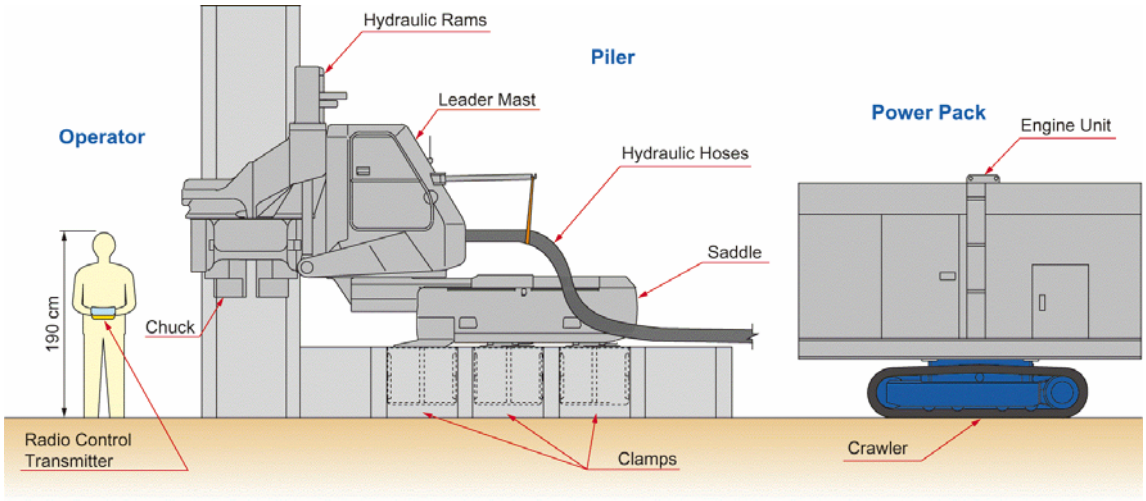

Diagram courtesy of Giken Seisakusho

c) A schematic diagram of a press-in piler for installing steel tubular piles

Figure 1.1 The press-in method of pile installation

CHAPTER 2

LITERATURE REVIEW

2.1 INTRODUCTION

2.1.1 Previous piling research

The literature on piles is extensive. The largest database of soil mechanics publications is held by the Swedish Geotechnical Institute (http://public.swedgeo.se/index-e.html), and contains over 50,000 references catalogued by keyword. 'Pile' is the fourth most popular keyword, after the generic terms 'soil', 'clay' and 'test', and features on over 6500 papers at the time of writing. Such prolific research is in contrast to the advice of Terzaghi & Peck (1967), who stated that:

> "…theoretical refinements in dealing with pile problems … are completely out of place and can be safely ignored."

In spite of this pessimism, pile capacity in sand represents one of the most widely discussed topics in geotechnics, partly due to the rapidly advancing technology of pile construction methods and partly since it remains, despite so much debate, "arguably the area of greatest uncertainty in foundation design" (Randolph *et al.*, 1994).

This uncertainty led the recent draft Eurocode 7 (1997), when discussing the design of onshore piles, to insist that any design calculations must be related back to the results of static load tests (Eurocode 7, C7.4.1). This implies that any design based purely on a

Class A prediction from site investigation data is considered by the Eurocode panel to be unsafe. This Chapter examines the origin of this mistrust of pile design methods by reviewing the current understanding of pile behaviour.

2.1.2 Reliability of current prediction methods

The lack of confidence in pile design methods derives from the wide range of predictions for ultimate capacity that are produced by current methods. A prediction contest was recently held as part of the "Geotechnics in the New Millenium" Symposium at Imperial College, London (Jardine *et al.*, 2001). Contestants were asked to predict the ultimate capacity of a single 457 mm diameter tubular pile driven into dense sand at Dunkirk, France. The design problem was well defined, without the complications of group effects or unusual ground conditions, and the contestants were provided with the results of an extremely thorough site investigation. However, the scatter of predictions was wide (Figure 2.1a). This scatter is comparable with a reliability assessment of pile design methods carried out 13 years previously by Briaud & Tucker (1988) (Figure 2.1b). Little improvement in reliability is evident. Subsequent publication of the winning design procedure revealed that the base capacity had been predicted using a limit equilibrium solution first published by Berezantzev *et al.* in 1961 (Ground Engineering, November 1999).

To elucidate this disparity between the quantity of research output concerned with piles and the continuing uncertainty surrounding the prediction of pile capacity, this literature review aims to:

- outline the fundamental differences between pile behaviour and other better-understood geotechnical processes,
- examine previous experiments that have aimed to observe the processes underlying pile installation, and shed light on the governing variables,
- examine the assumptions and input parameters required by current pile design methods, and
- contrast the observed governing variables with those used in current design methods.

Reflecting the particular interest of this dissertation in the press-in method of pile installation in sand, the review concentrates solely on displacement piles, and in particular those installed by jacking into granular soil.

2.1.3 Performance, in addition to prediction

A second particular concern of this dissertation is performance. Reliable *prediction* can lead to cost savings through reduced safety factors. Similarly, improved *performance* through optimised construction procedures and novel installation techniques can lead to more economic design. However, prediction methods that are wholly empirical (category 1 in the classification system of Poulos, 1989) offer no cues for improving performance. Instead, improvements in performance can only be derived from an understanding of the underlying physical processes, and the influence of the installation procedure on these processes.

Therefore, this review concentrates on studies of the ground behaviour and governing soil parameters during pile installation, and less regard is given to research which, although perhaps offering reliable prediction, does not provide insight into the underlying mechanics of pile behaviour.

2.2 THE COMPLEXITY OF PILE BEHAVIOUR

The strength and stiffness of soil have a non-linear dependency on stress and strain level and history. During the installation of a displacement pile in sand, the stress and strain within the deforming soil vary from the in situ stress level and zero strain to tens of MPa stress and of the order of 100% strain. The strain levels, and hence operative stiffness ranges, experienced in other geotechnical processes are considerably lower (Figure 2.2).

Coop (1999) highlighted the lack of understanding of the behaviour of sands at high stress levels, as encountered during pile installation. He noted that few triaxial apparatus operate at the stress level of interest. As a result, existing soil models often do not correctly capture the relevant behaviour. For example, relative density is a widely-

used reference state, since a more reliable stress state linked to the critical state line or normal compression line cannot be identified without high pressure testing.

Furthermore, whereas conventional soil constructions typically consist of a single event, pile installation and subsequent loading is better considered as a process. This process begins with the gross deformation during installation. The nature of this deformation depends not only on the in situ soil properties and the geometry of the completed foundation, but also the installation technique. Jacking is characterised by monotonic loading and soil deformation. Hammering and vibro-installation methods are both characterised by cyclic loading, but can yield differing capacities (e.g. Mansur & Hunter, 1970).

The process continues with a period during which the pile head is unloaded prior to construction of the supported building, or load testing of the completed pile. During this period, pore pressure dissipation (e.g. Randolph & Wroth, 1979), soil ageing (Schmertmann, 1991) and creep of locked in stresses (Åstedt *et al.*, 1992) may occur, with a resulting change in pile stiffness and strength. Figure 2.3 links each stage of this process with the deformation experienced by a typical soil element.

The complex history of a soil element close to a displacement pile shown in Figure 2.3 encompasses most facets of soil behaviour. Noting the constitutive complexity of geo-materials, and the near-impossibility of sampling and characterising each aspect, Hight (1999) emphasised that progress is best made by determining which features of soil behaviour control performance. This point is particularly relevant to the analysis of piles in sand. Simplification of processes shown in Figure 2.3 by identifying the controlling aspects is essential if pile behaviour is to be rationalised. Thereafter, only the relevant characterisation and appropriate analysis need be conducted.

A number of experimental studies have been conducted with the aim of observing the soil behaviour during pile installation. These are reviewed below.

2.3 PREVIOUS OBSERVATIONS OF PILE INSTALLATION

2.3.1 Experiments to observe ground movements during installation

2.3.1.1 Berezantzev *et al.*, 1961; Mikasa & Takada, 1973

Berezantzev *et al.* (1961) report a series of model pile tests conducted at the Leningrad Institute of Railway Engineers. By installing a model pile into layered sand, the pattern of ground movement was revealed as a series of distinct slip surfaces on alternate sides of the pile (Figure 2.4a). This observed deformation pattern motivated a limit equilibrium solution for pile base capacity governed by angle of friction that remains widely quoted today (e.g. Craig, 1997, Simons & Menzies, 2000).

It should be noted that the experiments of Berezantzev *et al.* were conducted without surcharging the soil. With an overburden of 1 m, the in situ vertical stresses were less than 20 kPa.

These experiments of Berezantzev *et al.* can be contrasted with those of Mikasa & Takada (1973), which are geometrically similar, but are conducted both at 1-g and in a centrifuge (Figure 2.4b). No quantitative measurement of the displacement pattern is possible, but stereoscopic photography offers an indication of the penetration mechanism. At 1-g the observed behaviour matches that of Berezantzev *et al.*, with slip surfaces extending to the ground surface. However, when the field stress level is replicated under centrifuge conditions, a confined penetration mechanism is evident, involving compression close to the pile tip. Mikasa & Takada attribute this to the influence of stress level on dilatancy.

2.3.1.2 Robinsky & Morrison, 1964

A series of model pile tests are reported by Robinsky & Morrison (1964). These followed the general format of the Berezantzev *et al.* tests, using dry silica sand, with installation by jacking. An X-ray method was used to track the movement of lead shot embedded in the soil model. The resulting displacement vectors were used to deduce contours of volumetric strain. An erratic variation in density close to the pile is

observed (Figure 2.5a), with compressive volumetric strain of up to 11% in loose sand (initial relative density= 17%).

2.3.1.3 Chong, 1988

Chong (1988) used a penetrometer equipped with thermal probes to measure density variations close to and at the surface of a model pile. An 18 mm diameter probe was installed to a depth of up to 360 mm in a tank of silica sand on the laboratory floor. No quantitative measurements of density change are reported, but four general zones of behaviour were identified (Figure 2.5b).

2.3.1.4 Davidson *et al.*, 1981

Davidson *et al.* (1981) installed a model penetrometer, cut longitudinally, against the window of a glass-sided tank of dry sand. A stereo-photogrammetric method was used to record sand movement and deduce volumetric strain. Once again, a seemingly erratic variation in compression was observed, with the authors stating that their study is *"primarily qualitative"* (Figure 2.5c).

2.3.1.5 Allersma, 1988a, 1988b

Allersma (1988a, 1988b) studied the penetration of a plane strain penetrometer into crushed glass using a photoelastic method to observe the principal stress directions. The crushed glass was observed to flow around the soil tip at constant volume, with failure occurring by a wedge-type Prandtl mechanism creating heave at the top surface. This led to the proposition that base capacity is governed by the angle of friction, according to conventional bearing capacity theory (Figure 2.6).

It should be noted that the Allersma probe was not installed from the ground surface, but partially "wished in place". The stress within the soil adjacent to the probe shaft would be different had the pile been installed from the ground surface. Furthermore, the constitutive behaviour of crushed glass at the stress levels experienced during the reported testing is significantly different to that of sand during pile installation. Although Allersma reports a similar friction angle to sand of 38º, the maximum stress level measured close to the pile tip is 150 kPa. This value is significantly lower than typical values for field piles.

To reach the correct constitutive regime, a comparable state relative to the CSL or NCL is desirable. Joer *et al.* (1999) note that the normal compression line of glass particles is reached at a stress level of around 10 MPa, which is comparable to that of silica sand, and an order of magnitude higher than that of carbonate sand. This suggests that the stresses in experiments using crushed glass should be comparable or higher than in sand if similitude is to be maintained.

2.3.1.6 Summary

In summary, previously conducted experiments to observe ground movements during pile installation, with the exception of Mikasa & Takada (1973), have all taken place at a low stress level, at which more dilatant behaviour is expected than in the field. This is partly due to the difficulty of constructing apparatus that allows ground movement to be observed, and which is sufficiently strong to resist the loads associated with penetration at a realistic stress level.

Small but scattered variations in density were recorded, usually accompanied by heave. It is not clear whether the scatter is evidence of random variations in density or random errors in the displacement measurements. The observation of heave and shear planes at low stress has lead to the general conclusion that pile behaviour is governed by frictional strength, with relative density influencing the arrangement of shear planes and the angle of friction. However, it is unlikely that the penetration mechanisms observed in these experiments match that around field-scale piles.

2.3.2 Experiments to observe the stress distribution in and near a pile

The measurement of stress distribution in or near a pile is more straightforward than the measurement of ground movement. Instrumented piles and buried total stress cells have been used in a large number of research projects. In particular, the measurement of stress rather than ground movement has previously been the *only* source of insight into shaft friction. The kinematics of shaft friction are of very small magnitude; no soil movements at the pile-soil interface have previously been measured in either the

laboratory or the field. Instead, sophisticated load cells to measure normal and shear stress acting on the pile interface have been developed.

This literature review does not aim to cover every reported use of instrumented piles. Instead, the research that provides some insight into the penetration mechanism, and the resulting development of base resistance and shaft friction will be discussed.

2.3.2.1 De Nicola, 1996; Bruno, 1999

The measurement of the shaft friction distribution on piles installed in the centrifuge is reported by De Nicola (1996) and Bruno (1999). A model pile driving actuator was used to install piles in-flight by hammering. Scaling similitude laws for dynamic installation were satisfied by either reducing particle size or by using a viscous pore fluid.

The distribution of shaft friction measured during load testing reported by De Nicola and Bruno features a sharp decrease in local shear stress away from the pile tip. This is coupled with a decrease in shear stress at a given soil horizon as the pile tip penetrates further (Figure 2.7).

This characteristic behaviour is referred to as *'friction fatigue'* (Heerema, 1980) or the *'h/R effect'* (Bond & Jardine, 1991). De Nicola and Bruno compared their measured profiles of shaft friction with the design approach proposed by Randolph *et al.* (1994). This approach attributes the decay in local shaft friction at a given soil horizon to a progressive reduction in horizontal earth pressure coefficient, K, with continued shearing at the pile-soil interface. The value of K at a given soil horizon varies with h, the vertical distance from that soil horizon to the pile tip.

The resulting design equation is shown below (Equation 2.1). The variables in this formulation are the maximum and minimum values of horizontal earth pressure coefficient, K_{max}, K_{min}, and the decay rate, μ. Randolph *et al.* (1994) proposed that the rate of decay is governed by:

- compressibility and/or crushability of the surrounding soil
- roughness of the pile surface
- incremental driving energy required to advance the pile, and
- the effective displacement ratio at the pile tip

$$K(h) = K_{\min} + (K_{\max} - K_{\min})e^{-(\mu h / D)} \quad (2.1)$$

2.3.2.2 Klotz, 2000; Klotz & Coop, 2001

Klotz (2000) designed an instrumented model pile capable of measuring radial stress in addition to shaft friction distribution, allowing the separate influences of K and interface friction angle, δ, on local shaft friction to be detected. The model pile was jacked into dry carbonate and silica sands in the centrifuge.

The measured profiles of shaft friction differ sharply from those observed by De Nicola (1996) and Bruno (1999). The maximum radial stress occurs some distance behind the pile tip, and decays gently towards the ground surface (Figure 2.8). Klotz & Coop (2001) note that this profile compares well with that reported by Vesic (1970), although no mechanism to explain the observed behaviour is proposed. However, the Vesic data was shown by Fellenius & Altaee (1995) to be polluted by residual stresses, with the true profile likely to fall closer to the form observed by De Nicola and Bruno (Figure 2.9). The Klotz (2000) data is not influenced by residual stress since continuous measurement of load was made throughout installation and loading, and so these contrasting observations are unresolved.

2.3.2.3 Wersching, 1987

Earlier measurements of radial stress acting on a model pile are reported by Wersching (1987). An instrumented model pile equipped with a “Cambridge-type” load cell, capable of measuring both shear and normal load, was jacked into Leighton Buzzard sand. Although hampered by the unrealistically low ambient stress level, these tests provide an insight into the mobilisation of shaft friction during loading. Figure 2.10 shows the variation in radial stress and shear stress at a single location on the pile during a load test. Initially, a small reduction in radial stress is evident. Thereafter, an

increase in radial stress of typically 80% is evident. This variation in radial stress is attributed to contraction followed by dilation of the soil adjacent to the pile.

2.3.2.4 Chow, 1997; Lehane, 1992

A major programme of field testing in sand using a heavily instrumented 7 m pile is reported by Chow (1997) and Lehane (1992). The instrumented pile featured measurement of local shaft friction and radial stress at three locations along the shaft. Two key observations relating to the mechanism of shaft friction were made.

Firstly, 'friction fatigue', or the '*h/R* effect', was quantified. Figure 2.11a demonstrates the reduction in radial effective stress at a given soil horizon as the pile tip penetrates further. Secondly, the stress path during loading was quantified. A sharp increase in radial effective stress during loading was observed, corroborating Wersching's (1987) observation of an increase in σ'_r as failure is approached (Figure 2.10). This increase is attributed to dilation at the pile-soil interface (Figure 2.11b). The resulting design equations are shown below (Equations 2.2-2.4). The notation is as follows:

τ_f	Local shear stress at failure
σ'_{rf}	Local radial effective stress at failure
δ_f	Interface friction angle at failure
σ'_{rc}	Local radial effective stress after installation and equalisation
$\Delta\sigma'_r$	Dilatant increase in local radial effective stress during loading
q_c	Cone tip resistance
P_a	Atmospheric pressure
h	Distance above the pile tip
R	Pile radius
G	Shear stiffness, estimated using Baldi *et al.*'s (1989) correlation with q_c
δh	Pile roughness, equal to 2 R_{cla} (twice the centreline average roughness)

$$\tau_f = \sigma'_{rf} \tan\delta_f = \left(\sigma'_{rc} + \Delta\sigma'_r\right)\tan\delta_f \qquad (2.2)$$

$$\sigma'_{rc} = 0.029 q_c \left(\sigma'_{v0} / P_a\right)^{0.13} \left(h/R\right)^{-0.38} \qquad (2.3)$$

$$\Delta\sigma'_r = 2G\delta h / R \qquad (2.4)$$

Lehane (1992) and Chow (1997) propose that the following factors govern the 'h/R effect' (Figure 2.12):

- Free surface effects: heave of soil away from the pile shaft reduces the radial stress- i.e. a geometric effect
- Lateral pile movements during driving: 'whipping' or 'gapping' after each impact at the pile head- i.e. a function of the installation method
- Soil's stress history: the relative location of the soil adjacent the shaft, and the region of high stress close to the pile tip- i.e. a geometric effect, also influenced by the magnitude of base resistance and shape of the pressure bulb
- Cyclic stress decay: the tendency for soil elements adjacent to the pile to collapse under the cyclic loading induced by a series of jacking strokes, or more significantly a series of hammer blows- i.e. a function of the installation method and the cyclic compressibility of the soil.

The governing variables, primarily installation method and soil compressibility, are in broad agreement with those hypothesised by Randolph *et al.* (1994).

The change in radial stress during loading, $\Delta\sigma'_r$, is attributed by Chow (1997) to the following factors:

- An initial reduction in σ'_r due to contraction of the soil as the applied shear stress creates a rotation of the principal stress direction, following laboratory observations by Symes *et al.* (1988). This factor is small and variable and can be ignored during compression loading.
- A subsequent increase in σ'_r due to dilation of a thin band of soil at the interface. This is attributed to the rolling of sand particles out from roughness troughs on the pile (Figure 2.13a). It is implicit in this statement that sliding at the interface causes particles to roll outwards by a distance equal to the

roughness asperity height, yet no particles are allowed to roll back into the troughs (Figure 2.13b). The effect is for the interface layer to expand a cylindrical cavity by a change in radius equal to the peak-to-trough asperity height.

These observations on interface dilation contrast with the observations of Dietz (2000). In Dietz's interface direct shear box tests, interface dilation was measured during cyclic loading analogous to that experienced by a soil element adjacent to a pile. On each change in the direction of shear, an initial contraction is followed by gentle dilation (Figure 2.14). This dilation accumulates over an interface slip displacement of 20 particle sizes, rather than the single particle diameter hypothesised in Figure 2.13. The magnitude of dilation only exceeds the contraction during the first two cycles, suggesting that in constant volume or constant normal stiffness conditions around a pile, the net effect would be a reduction in radial stress.

De Nicola & Randolph (1993) add a further contribution to the increase in radial stress on loading, by noting that Poisson strains cause radial expansion and contraction of a pile during compressive and tensile loading respectively.

2.3.2.5 Bruno, 1999; Tomlinson, 2001: recent field data

Two final examples of shaft friction distribution are from load testing of 762 mm diameter open-ended tubular steel piles. The first load test is reported by Bruno (1999), and forms part of the EURIPEDES project (Zuidberg & Vergobbi, 1996). This pile is equipped with instrumentation to measure shaft friction at 12 locations along the 49 m length. The measured distribution of shaft friction features a sharp decay away from the pile tip (Figure 2.15a). This decay rate is comparable to Bruno's (1999) centrifuge modelling of driven piles, and larger than that exhibited by the shallower jacked piles of Lehane (1992) and Chow (1997).

Tomlinson (2001) presents data from load testing of a 762 mm diameter open-ended tubular pile embedded in loose to medium dense micaceous silt at the site of the Jamuna

River Bridge in Bangladesh (Figure 2.15b). Once again, the shaft friction is concentrated very close to the pile tip, decaying rapidly along the shaft.

2.3.2.6 Summary

The recent development of highly-instrumented model and field-scale piles has shed light on the distribution of load within a pile. 'Friction fatigue' and changes in radial stress during loading have been identified as key factors governing the magnitude of shaft friction.

However, attempts to improve prediction and performance are hampered because:

- the underlying physical mechanisms are not clear
- different behaviour is observed at model and field scale
- the influence of installation method is not quantifiable

These points can be demonstrated by attempting to normalise the profiles of local shaft friction reported above. The design approaches of Randolph *et al.* (1994) and Jardine & Chow (1996) describe the variation in local shaft friction with depth using an exponential or power law. For the purposes of this example, the Randolph *et al.* approach will be used since it has a convenient variable, μ, to describe this rate of decay.

The design framework described by Randolph *et al.* (1994) captures the 'h/R effect' by predicting the horizontal earth pressure coefficient, K, to decay exponentially with distance from the pile tip (Equation 2.1). Design values for μ have been deduced from four of the sources referenced above (Table 2.1). Figure 2.16 shows normalized curves of local shaft friction for each decay rate shown in Table 2.1, assuming $K_{min} = 0.2$, $K_{max} = 1$ and $L/D = 20$. These curves predict significantly different profiles of local shaft friction.

This raises the question; why does each dataset reported in Table 2.1 display a different decay rate? It should be possible to normalise the measured rates of decay using some

similitude condition. The different scales and embedment ratios of the pile tests shown in Table 2.1 should offer some insight into which of the factors listed in Sections 2.3.2.1 and 2.3.2.4 govern μ.

If the initial ('unfatigued') local shaft friction is defined as the shear stress acting one diameter behind the pile tip, a reference length, $h_{50\%}$, can be defined as the distance over which the shearing process reduces local shaft friction by a factor of 2 (Figure 2.16b). This definition neglects any change in τ_{max} over the short distance $h_{50\%}$. This reference length has been extracted from the original data reported in Table 2.1, and has been normalised by three local length scales; pile diameter, original D_{50} grain size, and pile length. No clear trend is evident.

Author	Description	Pile size	Decay rate, μ
Randolph *et al.* 1994)	Best fit to database of field tests	Database of various L/D=15–60	0.05
De Nicola (1996)	Best fit to database of centrifuge tests.	L= 150 mm D= 16 mm	0.25 – 0.35
Bruno (1999)	Best fit to database of centrifuge tests.	L= 200 mm D=11.5 mm	0.65
Bruno (1999)	Best fit to field test.	L= 45 m D= 0.76 m	0.2

Author	Distance from pile tip to $\tau_s = \tau_{max}/2$ ($h_{50\%}$)				
	Actual $h_{50\%}$	Prototype $h_{50\%}$	$h_{50\%}/D$	$h_{50\%}/D_{50}$	$h_{50\%}/L$
Randolph *et al.* (1994)	20 m*	20 m*	13*	≈200000* (D_{50} ≈ 0.1mm)	0.4
De Nicola (1996)	66 mm	6.6 m	3.7	1300 (D_{50} = 45 μm)	0.44
Bruno (1999)	24 mm	2.4 m	2.1	500 (D_{50} = 45 μm)	0.12
Bruno (1999)	4 m	4 m	5.2	≈40000 (D_{50} ≈ 0.1 mm)	0.09

* Data from worked example in original reference for L= 50m, D= 1.5m.

Table 2.1: Friction fatigue parameters deduced from field and laboratory testing

The scatter of data in the lower part of Table 2.1 shows that the decay in normal effective stress is not a direct function of absolute distance sheared (prototype or centrifuge scale), or distance sheared normalised by pile diameter, pile length or original D_{50} grain size. Therefore the geometric effects listed in Section 2.3.2.4 based on a continuum stress distribution around the pile tip do not alone govern the decay rate.

Alternative governing factors could derive from the installation method. All the pile tests listed in Table 2.1 involve dynamic installation, and demonstrate higher decay rates than measured during the jacked field tests of Chow (1997), indicating the possible influence of cyclic loading during installation.

The sharply differing profiles of shaft friction distribution presented above indicate that further research is required to understand the properties which govern friction fatigue and the increase in radial stress during loading. This uncertainty is highlighted by Thompson (1997), who applied the Jardine & Chow (1996) method of shaft friction prediction to carbonate sands. Jardine & Chow's decay rate is independent of soil type and installation method and offers excellent prediction in silica sands ($Q_{calculated}/Q_{measured}$ = 1.00, COV = 0.20). However, when applied to carbonate sands, shaft friction is dramatically overpredicted ($Q_{calculated}/Q_{measured}$ = 7.3) and a new set of empirical factors is required (Thompson & Jardine, 1997).

It is concluded that although current empirical prediction methods accounting for friction fatigue can offer good reliability in the soil conditions from which they were derived (Randolph *et al.*, 1994; Jardine & Chow, 1996), the apparent strong influence of installation method indicates that there is scope for improving performance. Also, a unified understanding which encompasses both silica and carbonate sand remains to be found.

2.3.3 Measurements of stress close to a pile

A small number of experiments have been conducted to measure the stress distribution close to an advancing pile using total stress cells embedded in the soil.

2.3.3.1 Nauroy & Le Tirant, 1983

Nauroy & Le Tirant (1983) carried out calibration chamber tests in which open- and closed-ended piles were hammered or jacked past a buried total stress cell (Figure 2.17). Two key observations can be drawn from this data:

- The zone of high stress surrounding the advancing pile has an approximate extent of 10 pile diameters
- The stress level measured during jacking is approximately one third higher than during hammering
- The stress level measured in a carbonate soil is approximately four times lower than in a silica soil

Thus, installation method and soil type have a strong influence on the mechanism of penetration.

2.3.3.2 Leung *et al.*, 1996; Leung *et al.*, 2001

Leung *et al.* (1996) report a series of centrifuge tests in which a model pile is jacked past an array of buried vertical and horizontal total stress cells. The results follow the general pattern observed by Nauroy & Le Tirant (1983) (Figure 2.18). 'Locked in' horizontal stresses are apparent after the pile tip has passed. Close to the ground surface the vertical stress reduces to below the geostatic level after the pile has passed. At depth, vertical stress appears to be 'locked in'. These results may have been influenced by cell action factor effects due to the relative movement of the load cell and the surrounding soil.

After installation of the test pile, Leung *et al.* conducted a 12.5 hour maintained load test without stopping the centrifuge. This revealed creep of the pile head, which plotted as a straight line on settlement-log time axes (Figure 2.19a). During a subsequent maintained load test, an instrumented pile allowed the applied load to be divided into base resistance and shaft friction along the upper and lower parts of the shaft. A steady decrease in base resistance was recorded, compensated for by a corresponding increase

in shaft friction (Figure 2.19b). This reduction in base load over time matches with observations by Chow (1997) during maintained load testing in the field.

Measurements from the buried load cells matched the progressive load transfer within the pile during the maintained load test. The vertical and horizontal stress adjacent to the shaft increased during the load test as shaft friction increased. In contrast, the buried cell measuring horizontal stress 15 mm (1.1 diameters) above the pile tip recorded a reduction in stress (Figure 2.19c), indicating stress relaxation within this region. Leung *et al.* also recorded the movement of the ground surface, and found that the maintained load tests were accompanied by settlement of the ground surface. This indicates that the creep process was associated with volume contraction within the ground, rather than heave.

Oedometer tests were carried out to replicate the creep associated with the high locked-in stresses close to the pile tip (Leung *et al.*, 1996, 2001). Tests conducted at constant stress revealed progressive settlement and particle breakage over time (Figure 2.20a). Tests conducted with initial compression followed by creep at constant volume revealed a stress relaxation (Figure 2.20b).

The tests of Leung *et al.* (1996, 2001) link the development and time-induced variation of base capacity with volume change in the surrounding soil, through particle breakage. Both oedometer compression data and pile load test settlement show a linear variation against log-time.

2.3.4 Measurements of the factors affecting base resistance

The difficulty in achieving repeatability in pile tests due to the conflicting influences of installation method, soil type, and pile geometry means that little insight into the parameters which govern base resistance can be gained from a single test. This review will only cover research in which the same pile has been installed in different ground, or multiple piles (or penetrometers) have been installed in the same ground.

2.3.4.1 Chow, 1997; Lehane, 1992

The sophisticated relationship for predicting shaft friction proposed by Jardine & Chow (1996) is in contrast to the simple relationship they propose for base resistance (Equation 2.5). This approach links CPT cone resistance, q_c, to base resistance, q_b, via pile diameter, D, and CPT diameter, D_{CPT}, which is equal to 35.7 mm.

$$q_b = q_c\left[1 - 0.5\log\left(D / D_{CPT}\right)\right] \tag{2.5}$$

This curve was fitted to the database of pile load tests shown in Figure 2.21, and comprises of a reduction factor on CPT resistance depending on pile diameter. This scale effect is attributed to the influence of shear banding, although no variable relating to shear band formation is included in the scaling factor. A qualitative explanation for this scale effect is that a dilating shear band will impede the penetration of a small CPT more than that of a large pile.

This hypothesis is plausible for a dense dilatant soil at low stresses, but breaks down when extended to a loose or contractile soil. Either no scale effect will exist (if it is assumed that shear banding will not occur in a strain-hardening material) or the opposite scale effect will exist (because a contracting shear band will ease the penetration of a small CPT more than that of a large pile).

However, the curve provides a good fit to the database, which includes the instrumented pile tests at Dunkirk referred to in Section 2.3.2.4 (marked DK on Figure 2.21). These data points are derived from 2 load tests carried out on separate installations of the instrumented pile, 13.3 and 15 hours after installation. During installation of the pile, the base resistance was equal to the CPT resistance (Figure 2.22a). A maximum change in pore water pressure of ±5 kPa from hydrostatic was recorded, with equalisation taking place in less than a minute. These results match those of Lehane (1992), who recorded matching profiles of q_b and q_c during installation of the same pile in dune sand at Labenne, France (Figure 2.22b).

During the 13.3 and 15 hour equalisation periods at Dunkirk, 16% and 20% increases in radial effective stress close to the pile tip were recorded respectively.

During subsequent load tests the mobilised base resistance was lower than during installation. At the pile head displacement required to mobilise peak shaft capacity, a base resistance equalling 72% of the q_b measured at the end of installation was recorded. This base load increased slightly with increased settlement, reaching a plateau after ≈6 mm head displacement, but did not exceed 90% of the installation values. The load tests were drained, with measured pore pressures never exceeding the hydrostatic values by more than 10 kPa.

This disparity between installation force and load test capacity reported by Chow (1997) during these two heavily-instrumented pile tests at Dunkirk cannot be attributed to consolidation, but must instead be a time effect due to creep, or a change in strength due to the partial unload-reload cycle during equalisation. This observation matches with those of Leung *et al.* (1996).

If time effects are removed from Figure 2.21 by using the measurements of base resistance recorded during installation for the Labenne (LB) and Dunkirk (DK) data, no scale effect would be evident from these data points.

Even if the relaxation permitted is permitted before measuring a definitive base capacity, the evidence for a scale effect on diameter is unclear. The first-time compression load test conducted at Labenne after installation of pile LB1 revealed a maximum base load of 4.7 MPa (Lehane, 1992; Figure 2.23). This load was reached at a head displacement of 7 mm. This value is 10% greater than the CPT resistance at that depth, and 8% greater than the average CPT resistance over 1.5 diameters above and below the pile tip (Figure 2.22b).

What insight do these results offer to the origin of base resistance? Clearly some correlation is to be expected between CPT data and pile base resistance. However, a scale effect arising from diameter is not clear from the experiments carried out at

Dunkirk and Labenne, and any effect may be hidden by the influence of creep and stress relaxation. Further discussion of the correlation between CPT resistance and pile base capacity is contained in Section 2.4.1.2.

2.3.4.2 De Nicola & Randolph, 1999; Foray *et al.*, 1996

An alternative link between CPT and base resistance was proposed by De Nicola & Randolph (1999). A series of centrifuge tests was conducted in which model CPT tests were followed by the installation of open and closed-ended model piles. Base resistance, q_b, was defined as the base capacity at a head displacement of $D/10$. Figure 2.24a shows design curves for the variation of q_b/q_c with overburden stress derived from the results of 26 compression load tests. A general trend of decreasing q_b/q_c with increasing overburden is evident. A similar relationship between CPT and base resistance was proposed by Foray *et al* (1996), who suggest that q_b/q_c decreases with both increasing overburden stress and increasing density (Figure 2.24b).

2.3.4.3 The influence of soil properties on base resistance

The previous two Sections have examined the use of CPT data to predict base capacity, and similar empirical correlations have been proposed by Bustamante & Gianaselli (1982), De Ruiter & Beringen (1979), Kraft (1990), Robertson & Campanella (1983). However, by definition, such correlations offer little insight into the governing soil properties. The following selected references have attempted to link measurements of base resistance with soil properties, by conducting tests in multiple soils in a controlled laboratory environment.

2.3.4.4 Relative density

A large number of authors have conducted laboratory tests to examine the influence of relative density on pile base (and CPT) resistance (eg. Houlsby & Hitchman, 1988; Jamiolkowski *et al.*, 1988; Schmertmann, 1976). Unsurprisingly, a general trend of increasing resistance with increasing density is observed, and this is mechanistically attributed to either the reduction in compressibility or the increase in friction angle associated with increasing relative density. No reliable direct correlation between base capacity and relative density exists, as exhibited by the wide number of unfavourable

reviews of the API design method which links relative density (and grain size) to base resistance (Hossain & Briaud, 1993; Coyle & Castello, 1981; Malhotra, 2000).

2.3.4.5 Stress state

Why is there no reliable correlation between relative density and base resistance? Either the governing mechanism involves other factors, or relative density is an inappropriate reference state. Klotz & Coop (2001) suggest that a stress state parameter (eg. Jovocic & Coop, 1997) offers a better reference state and demonstrate that for a given soil, a good correlation between bearing capacity factor and stress state can be found (Figure 2.25a). Tentative design lines can be drawn through their centrifuge test data to link stress state to both bearing capacity factor and mean shaft friction. However, different soils require different design lines (Figure 2.25b). For a mechanistic understanding of the behaviour, which would allow the design method to be applied to soils for which a calibrating series of centrifuge model tests have not been conducted, a further material parameter appears necessary.

2.3.4.6 Compressibility

Measurements of relative density to determine angle of friction and bearing capacity factors for design are widely used, and have mostly evolved from experience with silica sands, which have low compressibility. The extension of conventional design methods from silica to carbonate sands can lead to unconservative predictions (Angemeer *et al.*, 1973; Thompson & Jardine, 1997; Randolph, 1988). This is due to the high but brittle angles of friction and low volumetric stiffness of carbonate sands. Figure 2.26 illustrates the dangers of applying conventional bearing capacity theory, which links friction angle to bearing capacity factor, to the design of piles in carbonate soils.

The significantly lower base resistance of piles in carbonate soils indicates the strong influence of compressibility. Yasufuku & Hyde (1995) and Yasufuku *et al.* (2001) conducted model pile tests in compressible sands with coloured layering. Sharply differing base resistances in carbonate and silica sand were measured. Post-test excavation of the soil revealed a zone of high compression close to the pile tip.

The authors used Vesic's 1972 cavity expansion method to capture the effect of compressibility on pile base resistance, in order to back analyse their model pile tests. Vesic's method extends the rigid elastic-plastic cavity expansion solution of Gibson & Anderson (1961) to include compressibility. This is achieved by reducing the rigidity ratio, I_R, by a factor of $(1+\Delta_{av})$ to compute the reduced rigidity ratio, I_{RR}. Rigidity ratio is defined as the ratio of shear modulus to shear strength. Δ_{av} is the mean volumetric compression in the plastic zone. Two approaches are proposed to deduce Δ_{av}.

The first approach uses a triaxial test along a general stress path representative of cavity expansion to produce an experimental stress-volume relationship. This allows an incrementally updated version of the rigid-plastic solution to be numerically evaluated. The second approach, if such data is unavailable, is to use an empirical relationship between volumetric strain and a low power of current stress divided by in situ stress, which can be solved analytically. Baligh (1976) extended this analytical solution to include a curved Mohr-Coulomb failure envelope, thus accounting for the reduction of friction angle with increasing mean stress.

A key assumption within Vesic's cavity expansion approach is that plastic volume change arises only within a plastic zone defined by a Mohr-Coulomb failure surface. In other words, irrecoverable volume change is initiated by shear failure. This is in contrast to concepts of Critical State Soil Mechanics, in which the yield surface reaches round to the isotropic plane, allowing an increase in mean stress to create volumetric strain.

Yasufuku *et al.* (2001) used the refined versions of Vesic's equations published by Yasufuku & Hyde (1995) to evaluate Δ_{av} for a variety of soils. It was found that an almost unique relationship exists between Δ_{av} and I_R for a variety of compressible sands, (Figure 2.27a) although no comparable relationship for a silica sand has been presented. Therefore, the tortuous routine for deducing volume strain in the plastic zone can be circumvented, since I_{RR} can be found directly from I_R. Thus only shear modulus and friction angle are required for the calculation procedure. Yasufuku's design approach

can be presented as base resistance, q_b, against mean volume strain in the plastic zone, Δ_{av}, for various values of overburden stress (Figure 2.27b).

This relationship provides a mechanistic link between the volume change during penetration and the resulting base resistance. Yasufuku *et al.* do not quote the plastic radius derived in the calculation used to produce Figure 2.27b, although Vesic (1972) records plastic radii equal to 2-3 times the pile radius in (compressible) micaceous silt, increasing to 4-6 times the pile radius in loose or dense sand respectively.

Previous experimental measurements of volume change close to the pile tip are shown in Figure 2.5. Measurement of the volumetric strain around Robinsky & Morrison's (1964) pile in loose sand reveals a mean volumetric strain of 7.5% if the plastic radius is assumed to equal 4 pile radii. The same exercise on Davidson *et al.*'s (1981) results in loose sand reveals a mean volumetric strain of 3.5%. These results are plotted on Figure 2.27b, but since they are from 1-g model tests without any surcharge stress, the datapoints lie well outside the range of in situ vertical stresses for which Yasufuku *et al.*'s relationship has been evaluated. Model tests conducted at more realistic stress levels with measurement of volume change close to the pile tip would offer a better opportunity to validate the mechanistic realism of Yasufuku *et al.*'s approach.

Yasufuku *et al.*'s design approach is compared to a database of 19 pile load tests in both silica sands and crushable carbonate sands. Good correlation is observed, and it is notable that this is the only design approach that has been tested against a database of both silica and carbonate soils (Figure 2.28).

2.3.4.7 Time effects: creep and ageing

The changes in pile capacity noted by Leung *et al.* (1996) during the relatively short holding period of their centrifuge tests plot as a straight line against log time. Chow (1997) noted creep behaviour during the equalisation period following installation, and during the maintained load tests conducted at Dunkirk.

An increase in radial stress was observed after installation during the short equalisation period, unaccompanied by any changes in pore water pressure. Base capacity was observed to gradually reduce, with shaft friction increasing to compensate. This continued until sudden failure of the shaft, which re-established the base capacity.

These observations can be extended to the long term. Large databases of changing pile capacity with time are presented by Chow *et al.* (1998) and Axelsson (2002). Although wide scatter exists, there is a clear trend for capacity to increase, with the additional capacity deriving primarily from shaft resistance. This increase in capacity with time is referred to as 'set-up'. Three possible hypotheses for this increase are explored in the above publications:

- The effect of corrosion or chemical action
- The effect of age on soil properties
- A change in the stress regime around the pile

Chow *et al.* (1998) studied the corrosion observed on aged field piles and found that zones of high set-up do not correlate with zones of high corrosive action. Therefore, the second two hypotheses are most favoured.

Chow *et al.* (1998) examine the possible influence of age on soil properties using the cavity expansion framework of Equation 2.4. It is argued that some increase in δ and G could be expected over time. However, the likely increase in $\Delta\sigma'_r$ is not sufficient to fully account for the observed set-up, and the implied influence of pile diameter indicated by Equation 2.4 is not evident in the field data.

Instead, Chow *et al.* (1998) suggest that set-up is primarily due to a change in the stress regime close to the pile. Following Åstedt *et al.* (1992), it is proposed that the pile is surrounded by a sleeve of loose soil, which promotes arching of radial stresses. This arching breaks down over time due to fluctuations in pore pressure (climactic or tide-related), or sand creep. The authors note that further research is required to quantify the possible effect of sand creep. The creep behaviour of the sand around the shaft during

ageing is likely to depend on the stress and strain path taken during installation, in addition to the current stress state. Since the penetration-induced stress and strain paths are unknown, it remains difficult to replicate the possibility of arching, and subsequent set-up, using element testing.

In contrast to Chow *et al.* (1998), Axelsson (2002) attributes set-up primarily to constrained dilation. Field tests over a period of two years and laboratory simulations using a rod shear device are reported. The key observation is that whilst some stress relaxation is observed, the majority of set-up is due to a larger $\Delta\sigma'_r$ on reloading after a period of set-up (Figure 2.29). This is associated with constrained dilation. It is argued that ageing of the soil around the shaft leads to an increase in dilatancy. On loading, this dilatancy is constrained, leading instead to an increase in stress.

2.3.5 Measurements of the influence of installation method

2.3.5.1 Driven, bored and jacked piles

Although this research is concerned only with displacement piles, some insight into the mechanisms of pile behaviour can be gained from instances where a combination of bored (non-displacement), driven and jacked piles have been installed at the same site or in the same experiment. Key examples are reviewed below.

2.3.5.2 Driven piles: impact hammer vs. vibrating hammer

Mosher (1987) examined field data from 5 sites and concluded that in the majority of cases, the ultimate capacity of a pile installed using an impact hammer is greater than that installed using a vibratory hammer. Mansur & Hunter (1970) found that vibrodriving in dense sand reduced base resistance by one third compared to hammering at the same site.

O'Neill & Vipulanandan (1989) concur with these observations for loose sands, noting a 20% greater strength for hammered piles compared to vibrated. However, in contrast to Mansur & Hunter, they note that in dense sands the reverse is true.

2.3.5.3 Driven vs. jacked piles

Meyerhof (1976) summarised a number of pile tests in sand, and suggested that the shaft capacity of a jacked pile is only one third of that of a driven pile. Chow (1997) suggested that there is little evidence for this installation effect, and recorded similar behaviour when testing jacked and driven piles at Dunkirk. The BCP Committee (1971) concur with this observation, after installing a number of test piles into dense sand at Akasaka. A jacked pile exhibited a stiffer load-settlement response than the driven piles, although comparable ultimate capacities were recorded.

Foray *et al.* (1989) conducted model testing using the downward hydraulic gradient method to obtain stress-level similitude (Zelikson, 1969). It was found that jacked piles mobilised 20% greater base resistance than driven piles, but 40% less shaft friction.

De Nicola & Randolph (1997) conducted centrifuge model tests of jacked and driven pipe piles. Static load tests after a period of pore pressure dissipation revealed comparable base and shaft capacities, although the jacked piles revealed a stiffer base resistance response on the soil plug.

2.3.5.4 Jacked vs. bored piles

Fioravante *et al.* (1994) conducted a series of model pile tests in the centrifuge. Bored piles were simulated by pouring sand around the pre-formed pile prior to testing. Jacked piles were installed in-flight. The shaft capacity of the bored piles was significantly lower than that of the jacked piles. The base resistance of both pile types was comparable, although a large settlement (>1 diameter) was required to mobilise the base capacity of the bored pile, whereas the base capacity of the jacked pile was mobilised at a head displacement of $D/5$.

The Foray *et al.* (1989) study also included a bored pile. This pile exhibited a much more compliant base response compared to driven or jacked piles, with 20-40% lower ultimate base and shaft capacity than a jacked pile.

2.4 PILE DESIGN AND ANALYSIS

The above review has examined experimental data of the behaviour of piles. In order to compare these observations with current design practice, a brief review of the wide variety of current design techniques is presented below.

2.4.1 Prediction of base capacity

2.4.1.1 Methods based on soil properties

Bearing capacity theory remains a widely used technique for the prediction of pile base capacity, which is related to in situ vertical effective stress via a factor, N_q (Equation 2.6). A wide number of correlations propose a link between angle of friction and bearing capacity factor (Figure 2.26). However, these correlations show a significant variation in predicted capacity, and conflict with field observations of an apparent limiting base resistance with depth.

$$q_b = N_q \sigma'_{vo} \quad (2.6)$$

Bond *et al.* (1997) note that the widely-used API pile design method (API RP2A, 1993) adapted bearing capacity theory by applying different factors to different pile and soil types. Also, the imposition of maximum values on N_q provided a better fit to field data for deep piles.

Bolton (1984, 1986) examined the influence of stress level and relative density on friction angle. He noted that the friction angle used to deduce a bearing capacity factor should decrease with increasing ambient stress, or depth. This lead to Randolph's (1985) relationships for the variation of bearing capacity factor with relative density, critical state friction angle, and ambient stress. These curves are found by iterating Bolton's correlations through Berezantzev *et al.*'s (1961) original bearing capacity factors, and are reproduced in the widely-used design handbook by Fleming *et al.* (1992).

Zeitlin & Paikowsky (1982) use a similar approach in which friction angle is allowed to vary only with stress level, and in a more exaggerated fashion than laboratory data suggests, in order for base resistance to approach a limiting value with depth.

Cavity expansion theory offers an alternative design approach for base capacity. The assumption of a confined mechanism instead of the shear planes of bearing capacity theory removes the strong dependency of base resistance on depth. This matches more closely with trends observed in the field. Vesic's 1972 cavity expansion approach incorporates some dependency on the average plastic volume compression close to the expanding cavity, Δ_{av}. Although this approach captures the behaviour of sand more closely than the rigid plasticity of bearing capacity theory, the calculation of Δ_{av} remains problematic, as discussed in Section 2.3.4.6.

The design approach proposed by Randolph *et al.* (1994) uses spherical cavity expansion theory to predict base resistance. It is proposed that the cavity expansion analysis of Carter *et al.* (1986) or Yu & Houlsby (1991) be used to evaluate cavity limit pressure. These solutions model an elastic-perfectly plastic soil with a Mohr-Coulomb failure criterion and a constant rate of dilation.

Randolph *et al.* (1994) note that this cavity expansion approach matches well with the previous Fleming *et al.* (1992) design curves. Furthermore, the influence of shear stiffness can be captured by varying the input value of G.

In design, the use of a cavity expansion method has the disadvantage of requiring a relatively large number of input parameters. Also, from a theoretical approach, the soil model can be criticised for not capturing changes in volume in a rigorous manner. Firstly, the predicted cavity pressure is strongly dependent on the angle of dilation (Yu, 1990). Therefore, it is important to evaluate this parameter precisely. Precise evaluation of dilation angle is difficult since it varies significantly with stress and strain level; some suitable averaging procedure is required. Secondly, plastic volume compression is not included in the soil model. This discounts the significant volume change associated with compressible soils, which is demonstrated by Yasufuku *et al.* (2001) to be critical

to the reliable prediction of base resistance in both compressible and non-compressible soils.

2.4.1.2 Methods based on in situ testing

The uncertainty surrounding the soil properties which govern base resistance, coupled with the difficulties in sampling and characterising sand, have lead to the development of design methods based on the results of in situ testing. SPT correlations remain widely used, although methods based on the cone penetration test (CPT) are considered more reliable due to the similarity between the test procedure and the installation of a displacement pile.

This similarity suggests that a direct match between pile base resistance and cone resistance is likely, with the coefficient α_{cone} in Equation 2.7 equalling unity.

$$q_b = \alpha_{cone} q_c \quad (2.7)$$

This relationship is implicit in cavity expansion models for base and cone resistance since these are scale-independent. Based on a database of field load tests, Biddle (1996, 1997) recommends that Equation 2.7 would offer reliable prediction of base resistance with α_{cone} equal to unity. In contrast, the larger database assembled by Chow (1997) shows that the assumption of base resistance equalling cone resistance leads to an over-prediction of the base capacity of closed-ended piles by 113% on average.

A number of authors have proposed that α_{cone} is less than unity, with a modified value of q_c being appropriate for design. These modifications are summarised below, and illustrated schematically in Figure 2.30:

- A reduction factor due to embedment (depth/diameter) ratio, *L/D*

Tejchman & Gwizdala (1979) report a series of model pile tests in which the unit base resistance decreases with increasing pile diameter. This observation is attributed to the

differing patterns of failure surface at different embedment ratios, (Figure 2.30a). Reduction factors related to *L/D* are proposed by Kraft (1990) and Meyerhof (1983).

A second influence of the *L/D* ratio on base resistance arises from consideration of the stress interaction between the base and shaft. Shaft friction has the effect of exerting downward shear stress on the soil surrounding the pile, which in turn elevates the vertical stress on the horizontal plane of the pile base to above the in situ value. This effect is likely to increase with increasing embedment ratio (Figure 2.30b). A calculation procedure for evaluating the corresponding change in base resistance is outlined by Winterkorn & Fang (1975). The Author, working in collaboration with Mr X Borghi, has demonstrated the existence of such an interaction mechanism (Borghi *et al.*, 2001). Further discussion of the downdrag created by the downward shear stresses exerted by the pile on the surrounding soil is presented in Chapter 6.

De Nicola & Randolph (1999) and Foray *et al.* (1996) present reduction factors on cone resistance based on laboratory test data (Figure 2.24). They observe a reduction in q_b/q_c with stress level, which could equally be interpreted as a reduction with embedment depth.

- A reduction factor due to local inhomogeneity

Kraft (1990) also proposes that α_{cone} should be less than unity to account for local inhomogeneities (Figure 2.30c). The probability of the base resistance of a pile being reduced due to a local variation in density is higher than that of a CPT due to the larger volume of soil under consideration. Values of α_{cone} varying from 0.5-0.6 are recommended.

Other authors propose that local inhomogeneities can be accounted for simply by taking either the geometric or average of the cone resistance over a zone of soil above and below the pile tip (Meyerhof, 1983; Eslami & Fellenius, 1997; Jardine & Chow, 1996).

- A reduction factor due to pile diameter

As discussed in Section 2.3.4.1, Jardine & Chow (1996) recommend a reduction factor on diameter to convert cone resistance to pile base resistance (Figure 2.30d, Equation 2.5). This correction factor predicts a sharp reduction in capacity with increasing pile diameter. A 1 m diameter closed-ended pile is predicted to mobilise less than 30% of the local cone resistance. This method provides an excellent match with a large database of pile load tests.

Interestingly, no scale effect on diameter was revealed within Chow's (1997) database of load tests on piles in *clay*, suggesting that the scale effect is due to a material property of sand rather than a geometric property of piles.

- A reduction factor due to partial mobilisation

Lee & Salgado (1999) introduce a further reduction factor by noting that the definition of pile capacity by a displacement criterion (e.g. settlement of pile head equal to 10% of diameter) may lead to an apparent scale effect (Figure 2.30e). They predict that if a pile were pushed down to a condition of continued penetration at constant load, the base resistance would equal the CPT resistance. By comparing finite element analyses of 'wished-in-place' piles with predicted cone resistance based on a cavity expansion method (Salgado *et al.*, 1997), curves of q_b/q_c with pile base displacement are produced (Figure 2.31). These curves are for non-displacement piles, in which the stiffness of the soil close to the pile base is unchanged from the in situ value. Lee & Salgado (1999) note that the installation process for a displacement pile has the effect of pre-loading and hence stiffening the soil close to the tip. This explains the observations of De Beer (1984) and Ghionna *et al.* (1993) that the ratio q_b/q_c for a displacement pile at a settlement ratio of 10% is typically double that of a non-displacement pile.

This mobilisation effect could shed light on the Chow (1997) scale effect in which increasing diameter leads to reduced base resistance (Figure 2.21). In practice, longer piles also tend to have a greater diameter. Elastic compression of the pile during static loading has the effect of reducing the movement of the pile tip compared to the head.

Therefore, a failure criterion is defined as $D/10$ settlement of the pile *head*, translates as a ($D/10$ - Δ_{pile}) movement of the pile tip, where Δ_{pile} is the elastic shortening of the pile, which increases with pile length, for a given load.

Therefore, it is likely that piles on the left hand side of Figure 2.21 have reached Lee & Salgado's "steady-state penetration mechanism", in which no further increase in base resistance with pile head displacement will occur. In contrast, piles towards the right hand side of Figure 2.21 have a base resistance defined at a lower *base* settlement ratio, and are less likely to have reached "steady-state penetration".

For design, this mobilisation scale effect is very difficult to quantify since a suitable value of soil stiffness below the pile must be estimated. The stiffness of the soil surrounding the pile tip depends on the installation process. Furthermore, the load distribution and hence elastic compression of the pile must be considered, in order that the failure criterion of a pile head displacement can be converted to a displacement of the pile tip.

2.4.2 Prediction of shaft capacity

2.4.2.1 Methods based on soil properties

Design methods for shaft capacity based on soil properties use the Coulomb equation to predict local shaft friction, τ_s, which is integrated over the pile length (Equation 2.8).

$$Q_s = \int \tau_s \, dA_s = \int K\sigma'_{vo} \tan\delta \, dA_s \qquad (2.8)$$

Design procedures require the selection of K and δ, and in some cases limiting values of τ_s. The API RP2a (1993) design method proposes values of δ which increase with particle size and relative density. This is in contrast to the recommendations of Jardine *et al.* (1992) who suggest values of δ which decrease with increasing particle size.

This anomaly could derive from the assumption in the API (1993) method that K remains roughly constant, and δ is the dominant variable. A value of K= 0.8 is

recommended for open-ended piles, with K increased to 1.0 for closed-ended piles. Chow (1997) notes that the IC instrumented pile tests at Dunkirk and Labenne saw a tenfold variation in K, and only a 2.6 times variation in tan δ.

Limiting values of local shaft friction are included in the API method, although their existence is a subject of debate. Early pile load tests contained little information on the distribution of shaft friction, only the total value. A good fit to this limited data could be achieved by back-analysis which assumed that a limiting value of shaft friction existed. However, whilst Meyerhof (1976) expressed the critical depth in terms of an embedment ratio, the API guidelines express it in terms of a stress level.

An alternative explanation for the apparent limiting value of mean shaft friction is linked to friction fatigue. The decay of local shaft friction at a given soil horizon with continued pile penetration leads to a quasi-constant mean shaft friction. This mechanism is demonstrated by the Dunkirk instrumented pile data presented by Chow (1997) (Figure 2.32).

Since the existence of friction fatigue was recognised, new design methods have been proposed to capture the influence of pile tip depth on earth pressure coefficient K. Toolan *et al.* (1990) present equations in which the profile of shaft friction along the pile length is idealised as a triangle. The maximum shaft friction at the tip is related to relative density, reducing linearly towards the surface with a minimum value of $K \tan \delta = 0.24$ imposed. Randolph *et al.* (1994) present a more sophisticated approach in which an exponential decay in local shaft friction away from the tip is proposed. This method is discussed in detail in Section 2.3.2.

2.4.2.2 Methods based on in situ testing

SPT and CPT data can be converted to shaft resistance using a variety of empirical correlations. Meigh (1987) recommends values of mean shaft friction, q_s, from 0.0033 to 0.018 q_c depending on pile type, following Te Kamp (1977), Schmertmann (1978) and Thorburn & McVicar (1970). No account is made for pile length or diameter.

Measurements of the shear stress, f_s, acting on a CPT friction sleeve can be correlated with shaft friction. Fleming *et al.* (1992) recommend a direct correlation between f_s and q_s. Te Kamp (1977) recommends values of q_s that vary from 0.6 to 1.6 times f_s depending on pile type, and Begemann (1977) suggests $q_s = 0.7f_s$. Once again, no account is made for pile length or diameter.

The above design approaches ignore any influence of pile geometry or friction fatigue on the mobilised shaft friction. Jardine & Chow (1996) present a more sophisticated approach for shaft friction based on CPT data. This approach matches more closely the distribution of shaft friction observed during instrumented pile tests, as discussed in Section 2.3.2.

2.5 CONCLUSIONS

This review of previous piling research can be summarised as follows:

- Previous laboratory testing has given some insight into the mechanisms by which base and shaft resistance are mobilised, but has been influenced by unrepresentative ambient stress levels, or inaccurate measurement of soil displacement and strains.
- Recent field testing has revealed a number of features of pile behaviour which were previously unknown, particularly in relation to the distribution of shaft friction, and the mobilisation of shaft friction during loading. In particular, the IC method (Jardine & Chow, 1996) offers significantly improved prediction of shaft friction in silica sands at field scale, based on CPT data.
- The prediction of base resistance remains highly empirical. CPT data often forms the starting point for prediction of pile capacity since the cone penetrometer is geometrically similar to a pile. However, reduction factors are usually applied to CPT data to find base resistance, and a variety of conflicting hypotheses exist to justify these reduction factors (Figure 2.30).
- The prediction of base resistance from soil properties is subject to even greater uncertainty. Most design methods are based on shearing resistance

(friction angle), although some laboratory observations suggest that the penetration mechanism consists of compression close to the pile tip. No design methods rigorously account for both aspects of soil behaviour.

- Additional uncertainty in the prediction and measurement of pile capacity arises from the influence of time effects. Laboratory and field tests have revealed changes in stress distribution within and around displacement piles in both the short and long term. These effects are independent of pore pressure changes and are therefore associated with the creep and ageing of sand.
- This uncertainty associated with the ground movements during pile installation has implication beyond the capacity of the pile itself. The interaction between piles within a group or between piles and existing structures depends on the penetration mechanism associated with pile installation. Reliable modelling of these interactions requires reliable prediction of the free-field ground movements during pile installation.
- The transfer of recent design methods from field scale tests in silica sands to either model scale tests in silica sands or field scale tests in carbonate sands leads to inaccurate prediction, particularly with respect to friction fatigue.
- Finally, from the point of view of improving foundation performance, there is scope for selecting and improving the optimum installation technique in order to gain maximum capacity at a given site. Field and laboratory test data reveals that a jacked, hammered and vibrated piles can exhibit significantly different capacity, although the optimum installation method appears to vary from site to site. This may be because subtle changes in the installation procedure have a large influence on performance.
- The unreliability associated with prediction methods, and the apparent influence of installation method on performance are complimentary effects. Unknown installation effects prevent the improvement of prediction methods. Improved performance may be achievable through the optimisation of installation effects.

In summary, the mechanism by which a pile penetrates sand is not well understood. The influence of the installation method on this process is not well quantified. An

understanding of the mechanism, and the governing soil properties, could lead to improved prediction and performance.

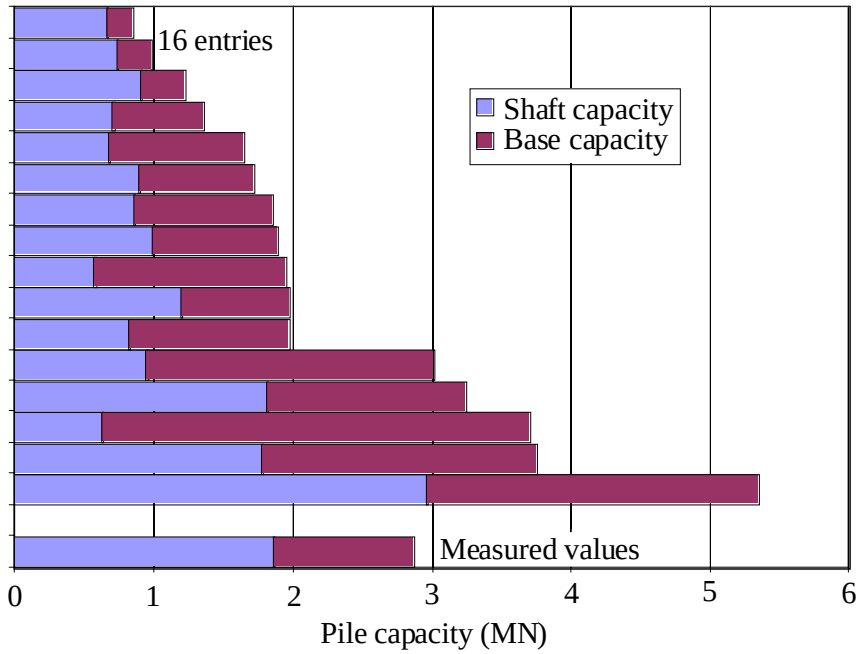

a) Entries to the IC50 pile capacity prediction contest (after Jardine *et al.* 2001)

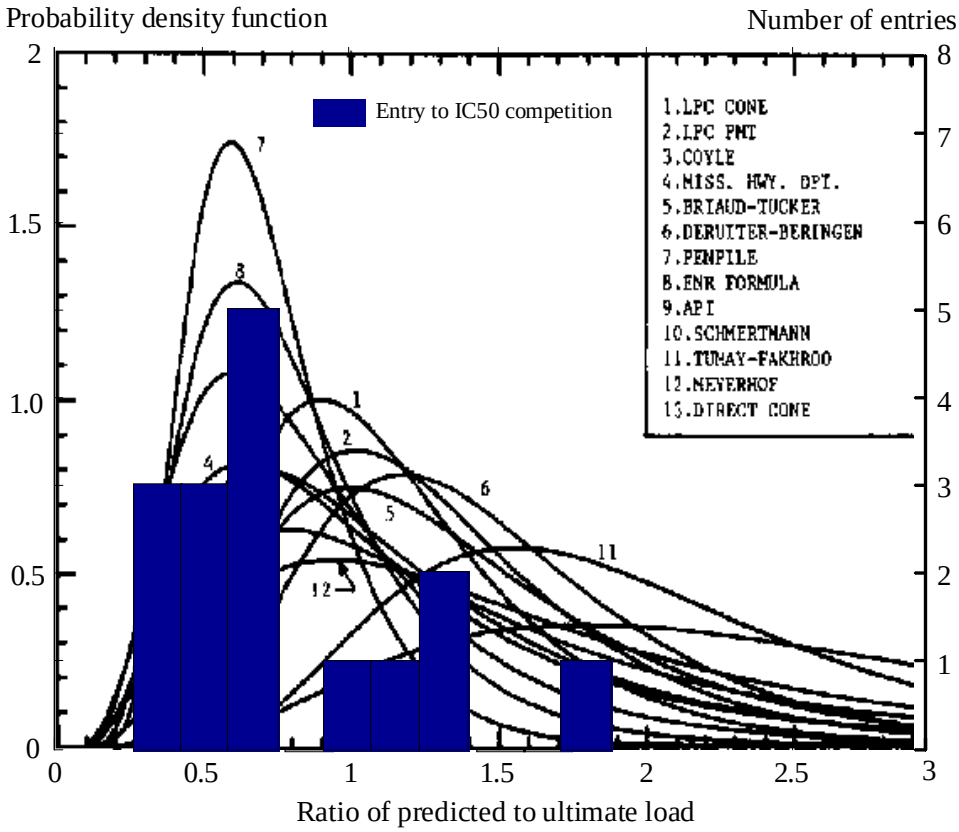

b) Reliability of pile design methods (after Briaud & Tucker, 1988 and Jardine *et al.*, 2001)

Figure 2.1 Recent observations on the reliability of pile design methods

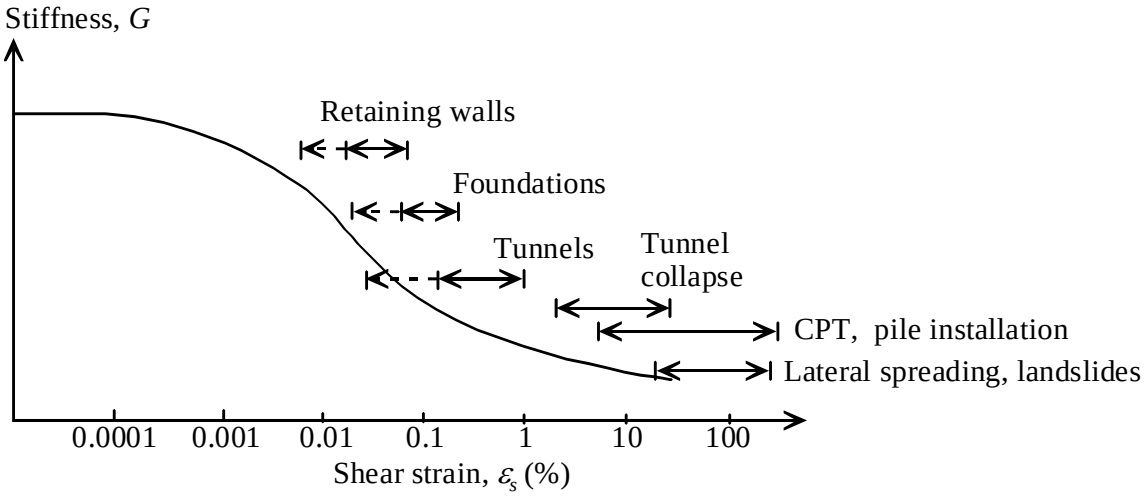

Figure 2.2 Strain levels in the geotechnical world (after Mair, 1993)

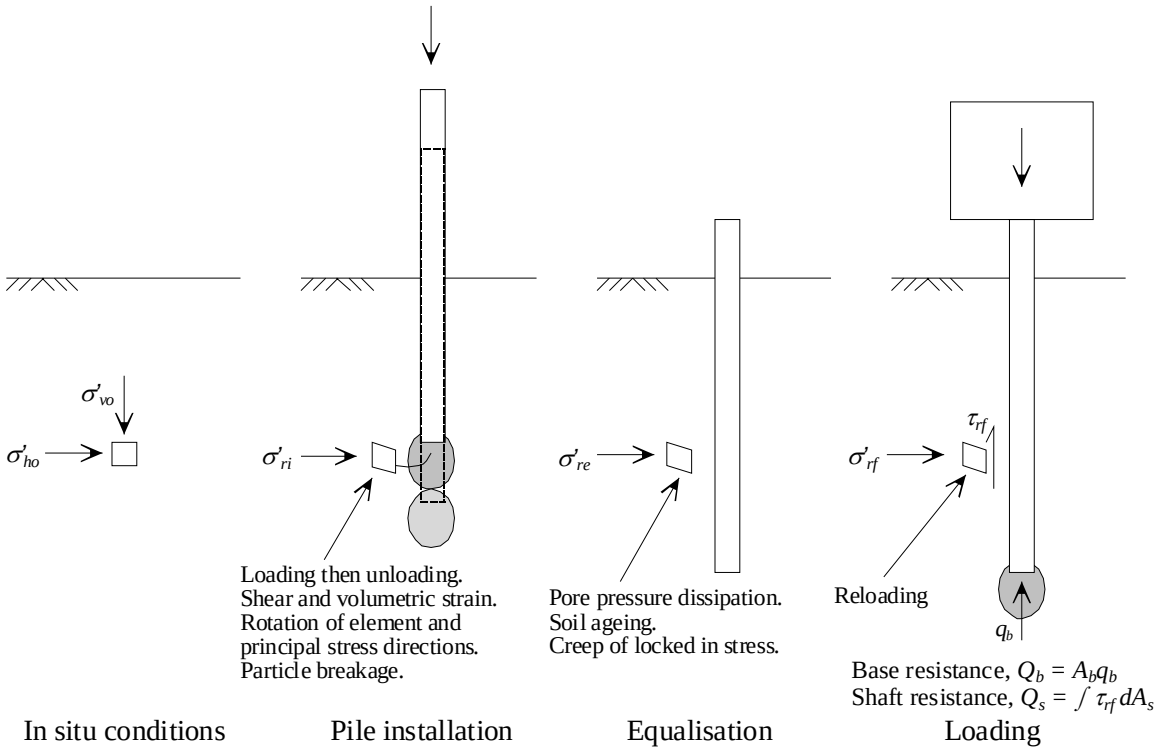

Figure 2.3 The life of an axially loaded pile and a nearby soil element

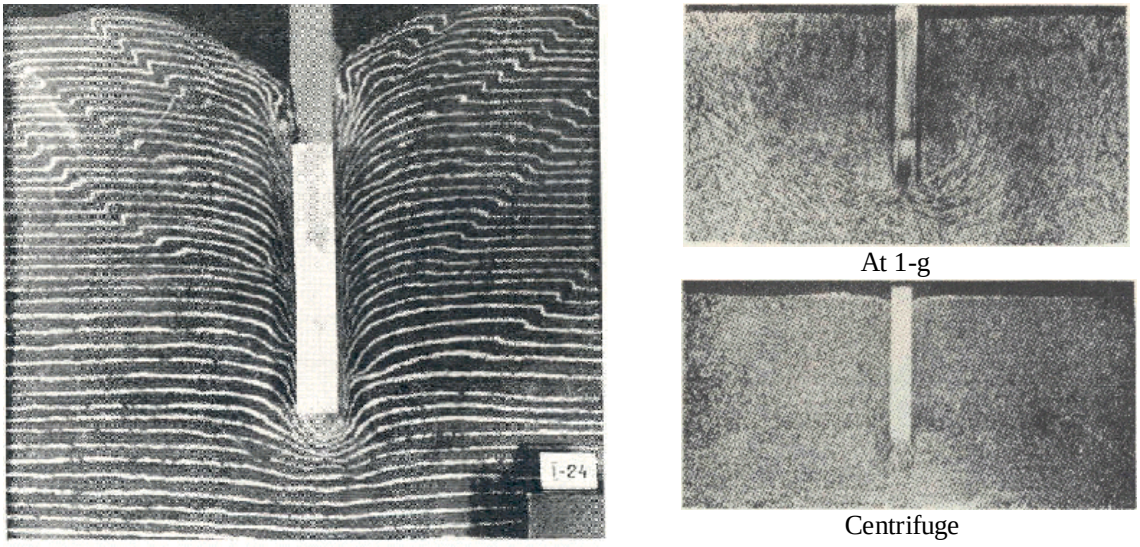

a) Berezantzev et al, 1961 b) Mikasa & Takada, 1973

Figure 2.4 Comparison of failure mechanisms at low and high stress

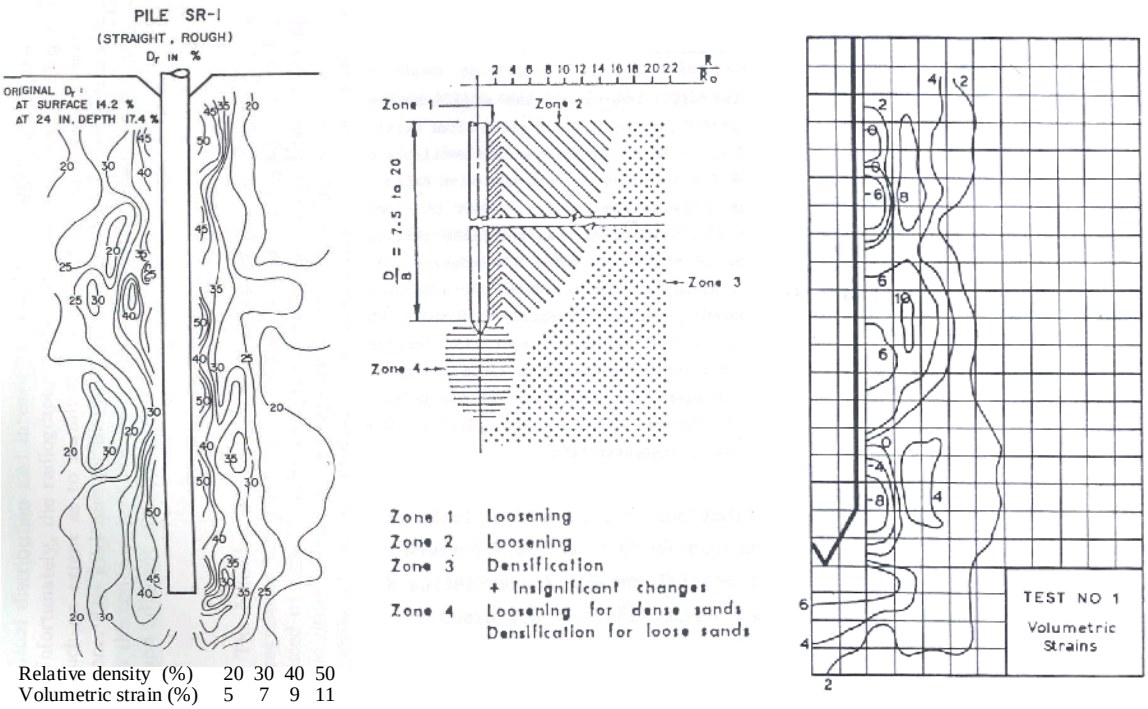

a) Robinsky & Morrison (1964) b) Chong (1988) c) Davidson et al (1981)

Figure 2.5 Observed changes in density during model pile installation

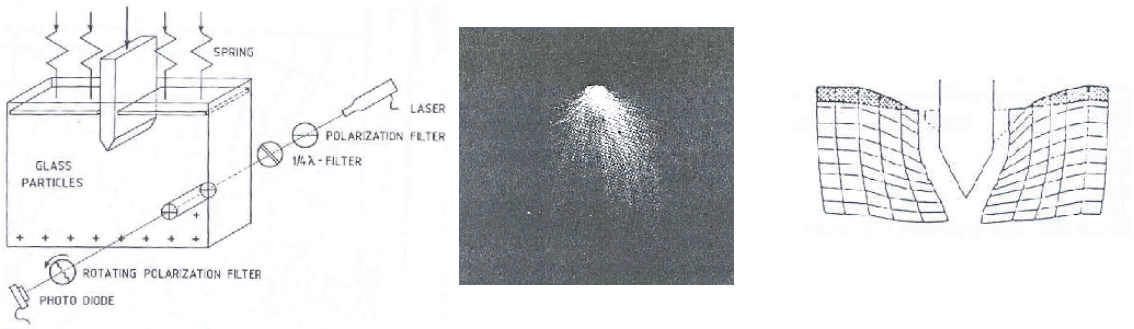

Apparatus Principal stresses from photoelasticity Observed failure mechanism

Figure 2.6 Observation of penetration in crushed glass (Allersma, 1988a, 1988b)

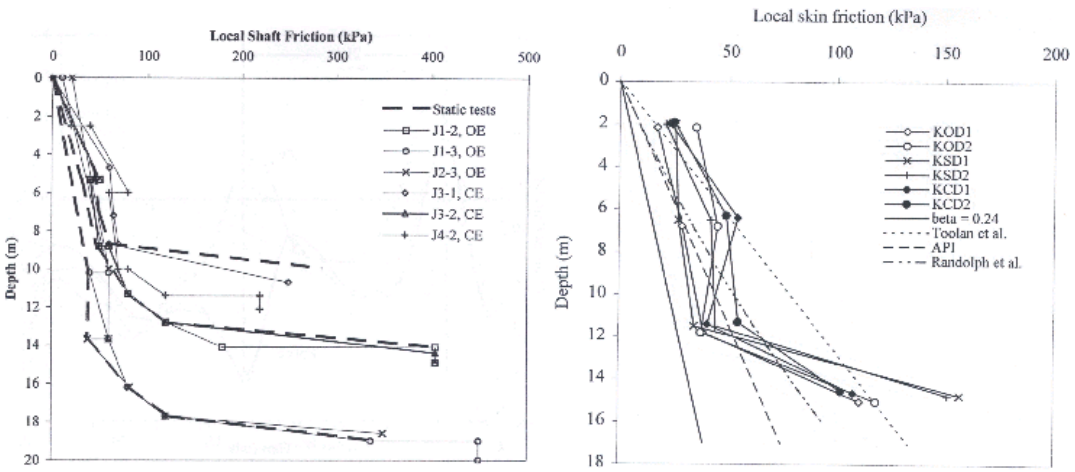

Bruno (1999) De Nicola (1996)

Figure 2.7 Measurements of shaft friction distribution on centrifuge model piles (De Nicola, 1996; Bruno, 1999)

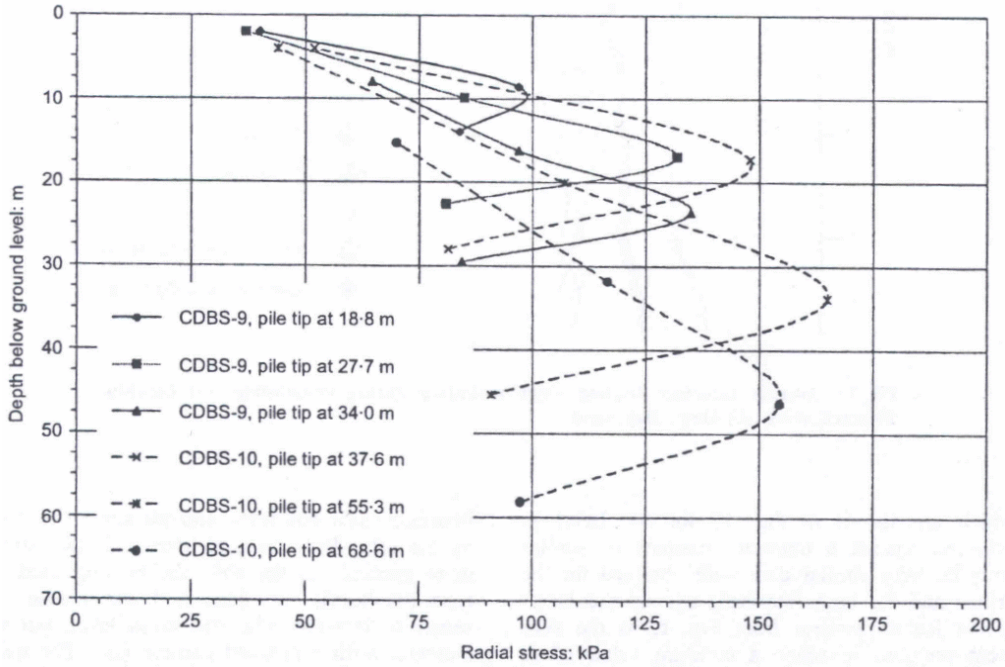

Klotz & Coop, 2001

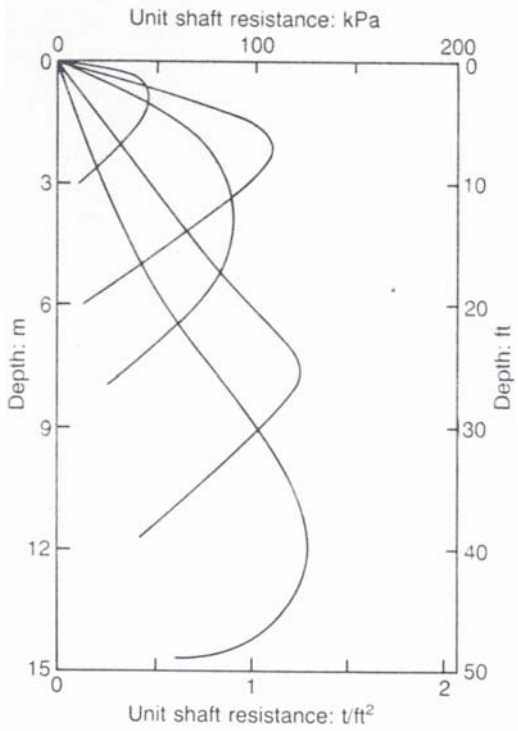

Vesic, 1970

Figure 2.8 Measurements of shaft friction distribution on model and field-scale piles (Klotz & Coop, 2001, Vesic, 1970)

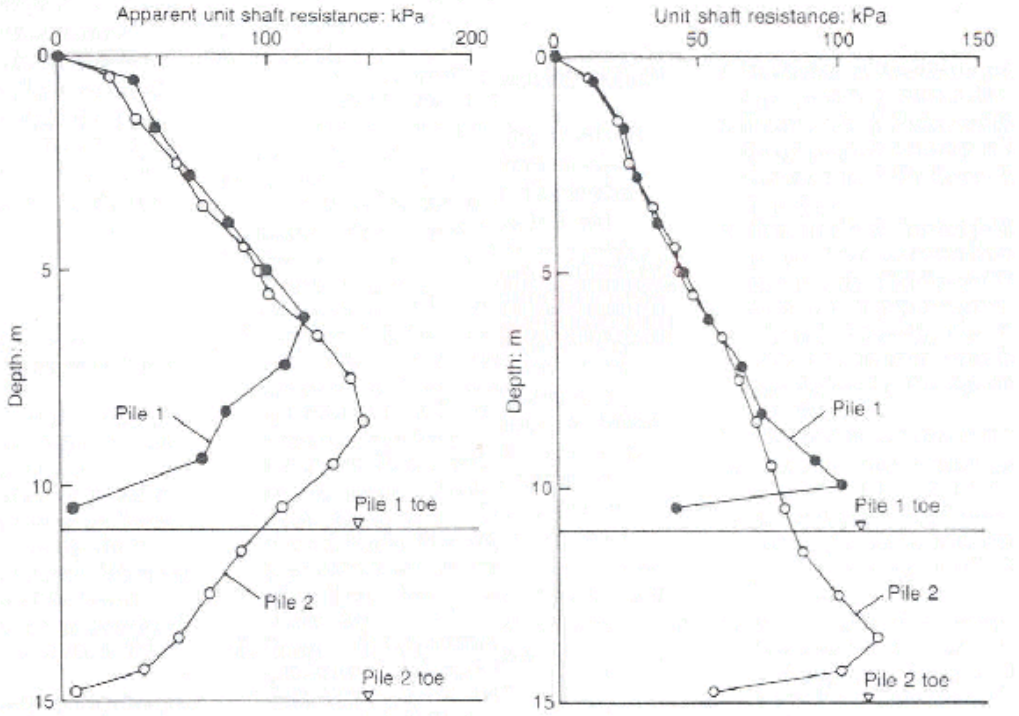

Measurements ignoring residual stresses Measurements accounting for residual stresses

Figure 2.9 Residual stresses create misleading profiles of local shaft friction (Fellenius & Altaee, 1995)

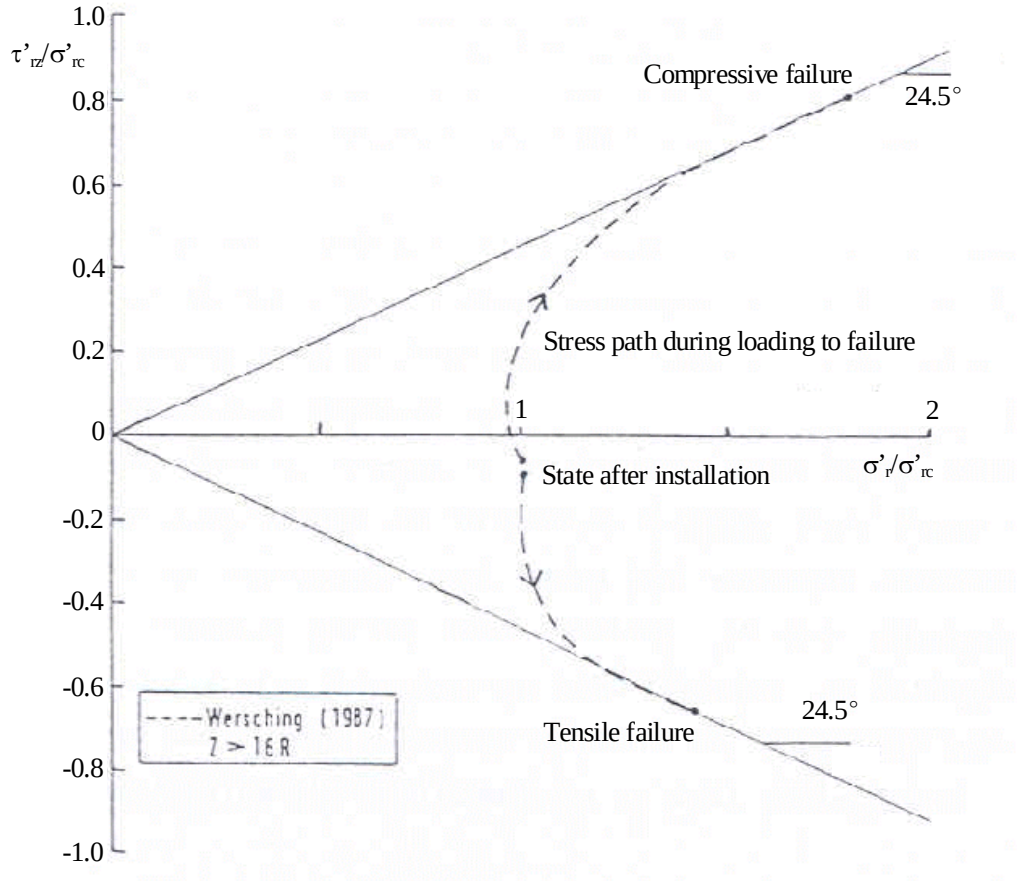

Figure 2.10 Shaft friction 'stress paths' during loading (Wersching, 1987)

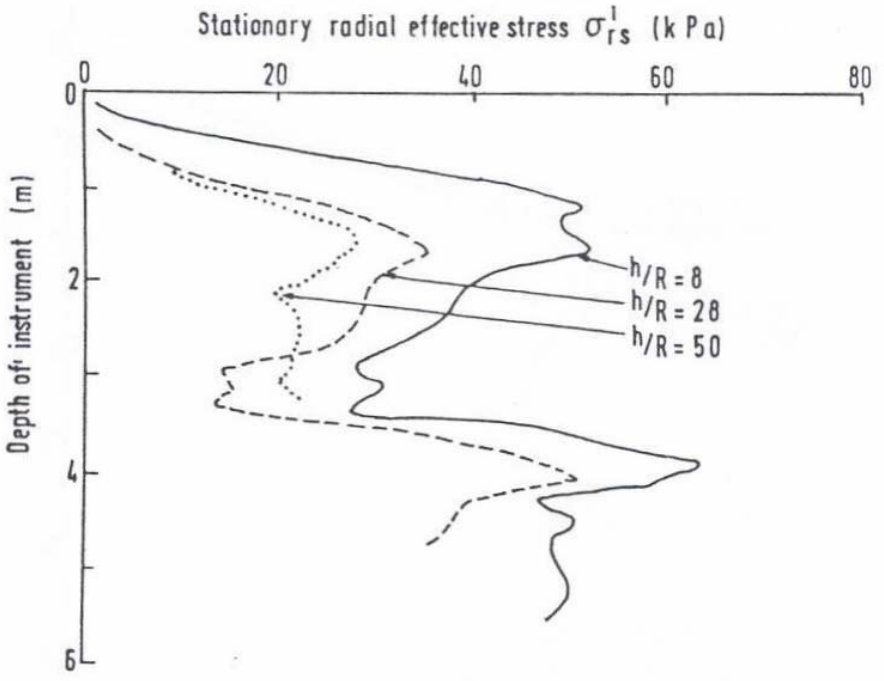

a) Shaft friction degradation (Lehane *et al.*, 1993)

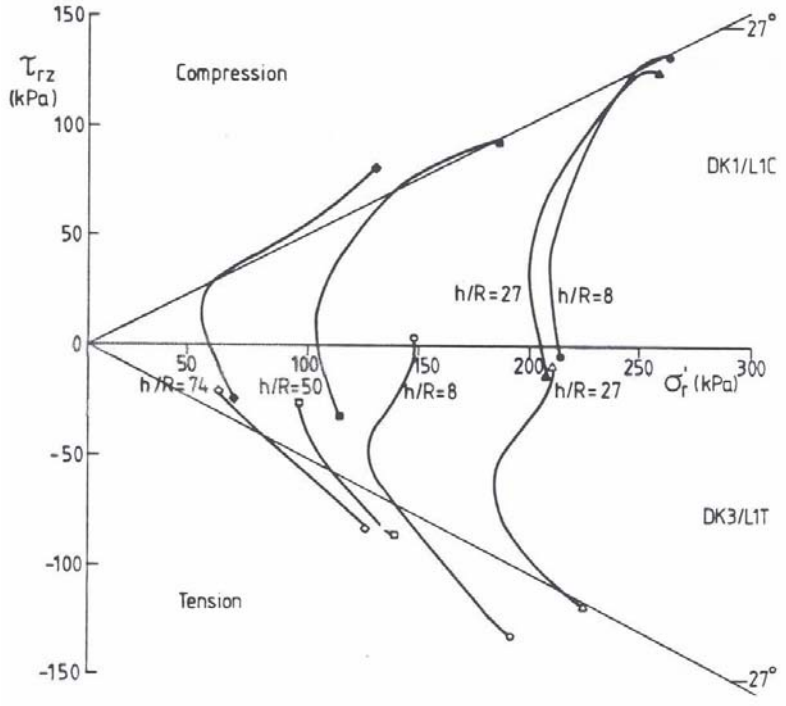

b) Changes in local radial and shear stress on loading (Chow, 1997)

Figure 2.11 Measurements of shaft friction degradation and change on loading

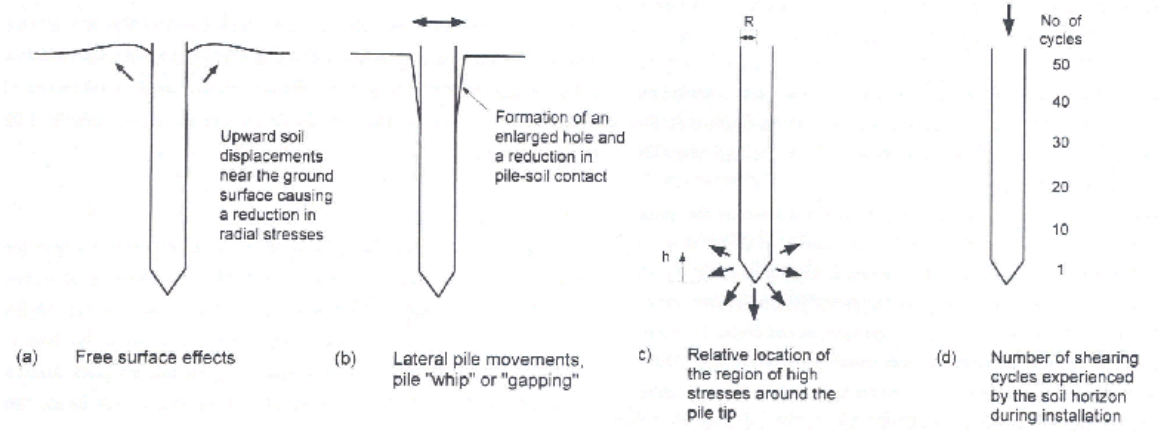

Figure 2.12 Possible reasons for 'friction fatigue' (the 'h/R effect') (Chow, 1997)

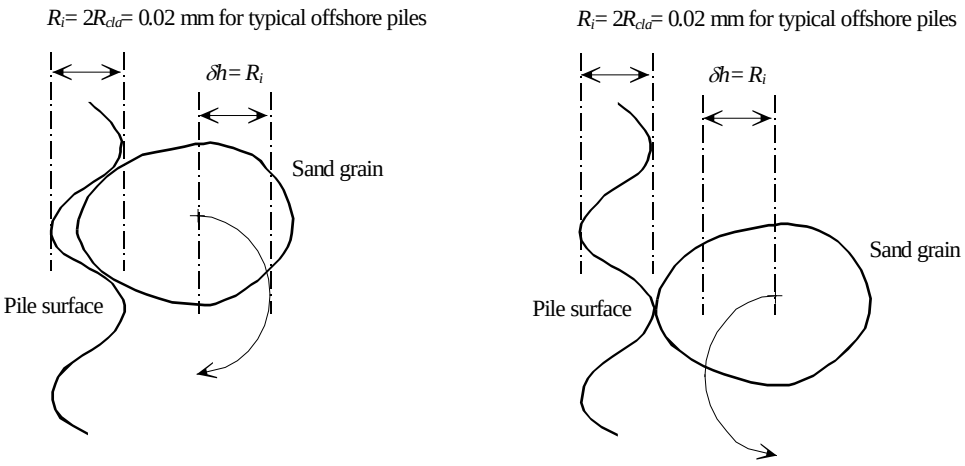

a) Interface dilation (after Chow, 1997) b) A similar mechanism, offering interface contraction

Figure 2.13 Simplified mechanisms for dilation or contraction at a pile wall

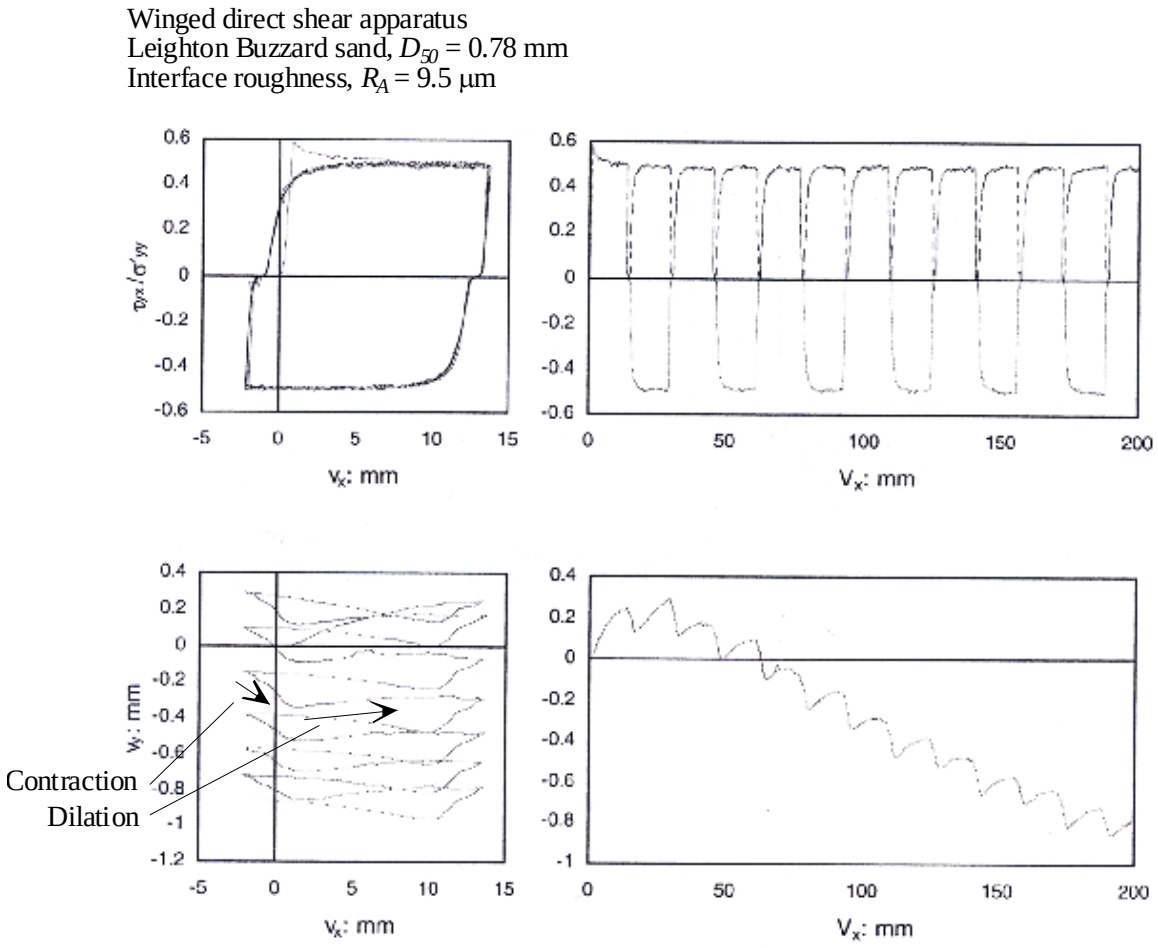

Figure 2.14 Interface dilation measurements in the direct shear apparatus (Dietz, 2000)

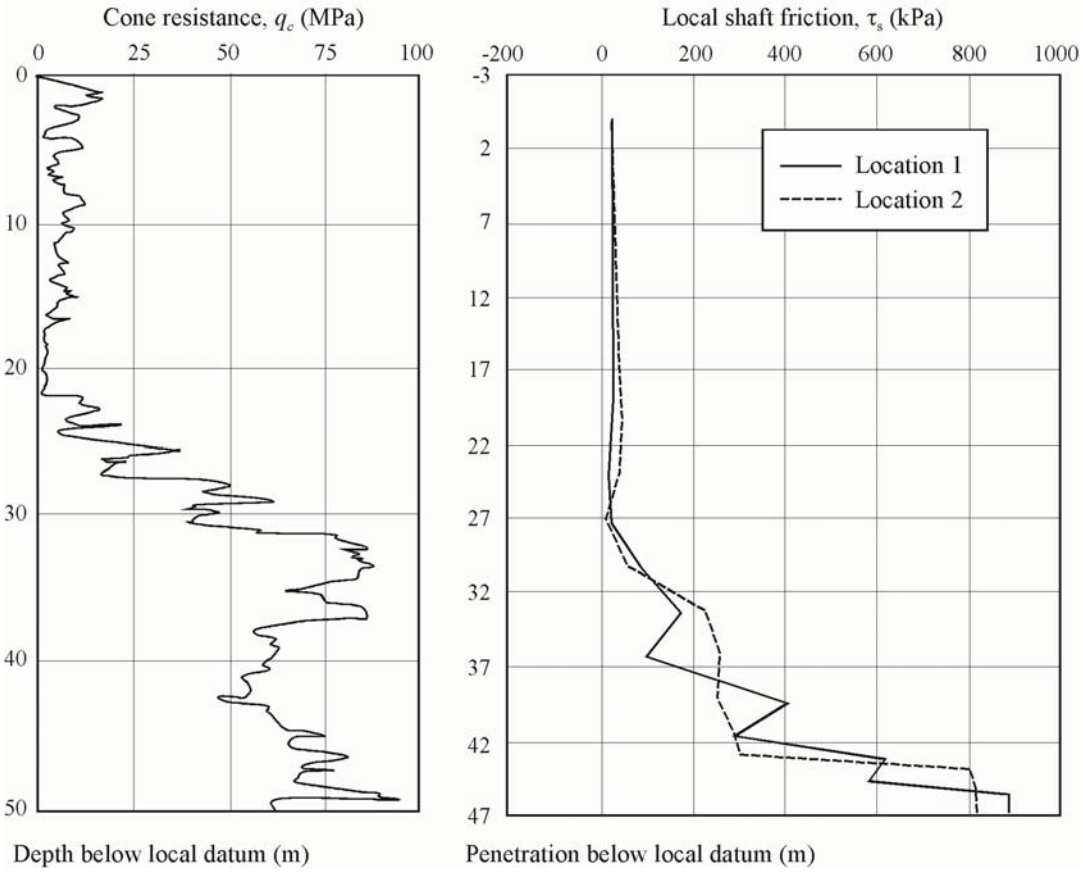

a) EURIPEDES compression load test
(CPT data: Zuidberg & Vergobbi, 1996. Load test data: Bruno, 1999)

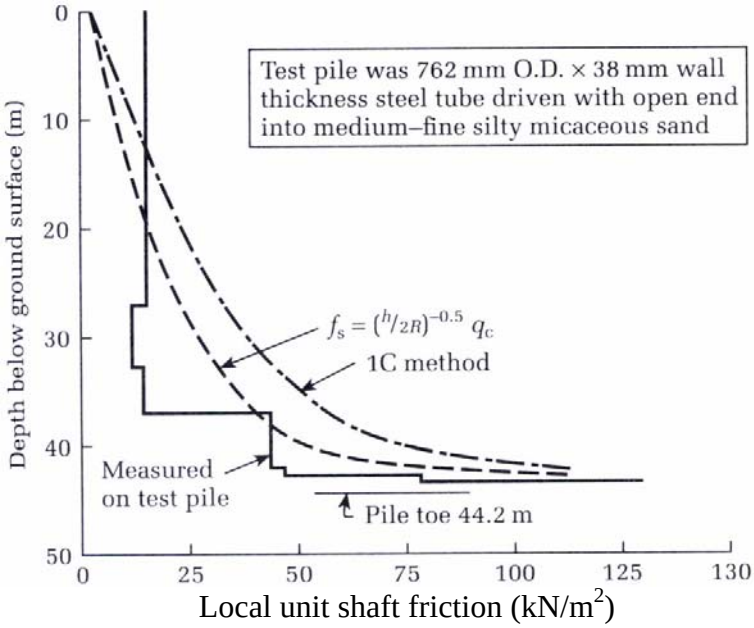

b) Jamuna River Bridge instrumented pile test (Tomlinson, 2001)

Figure 2.15 Field measurements of shaft friction distribution

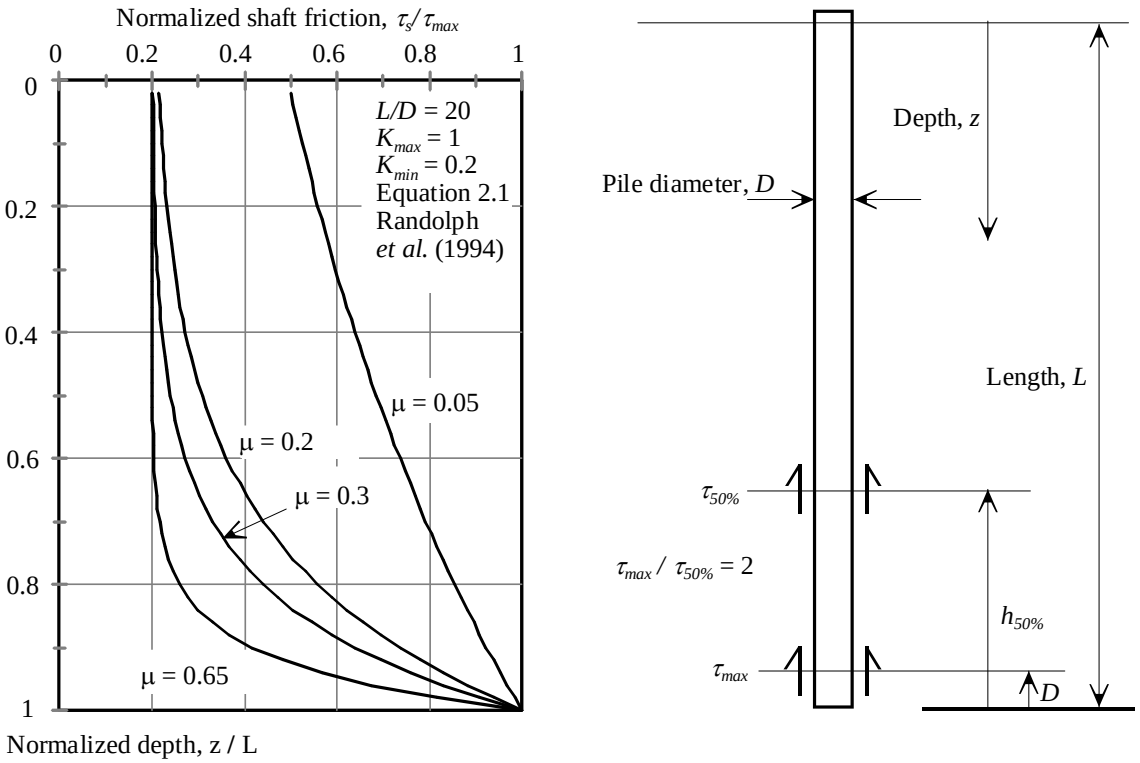

Figure 2.16 The influence of friction fatigue rate on shaft friction distribution

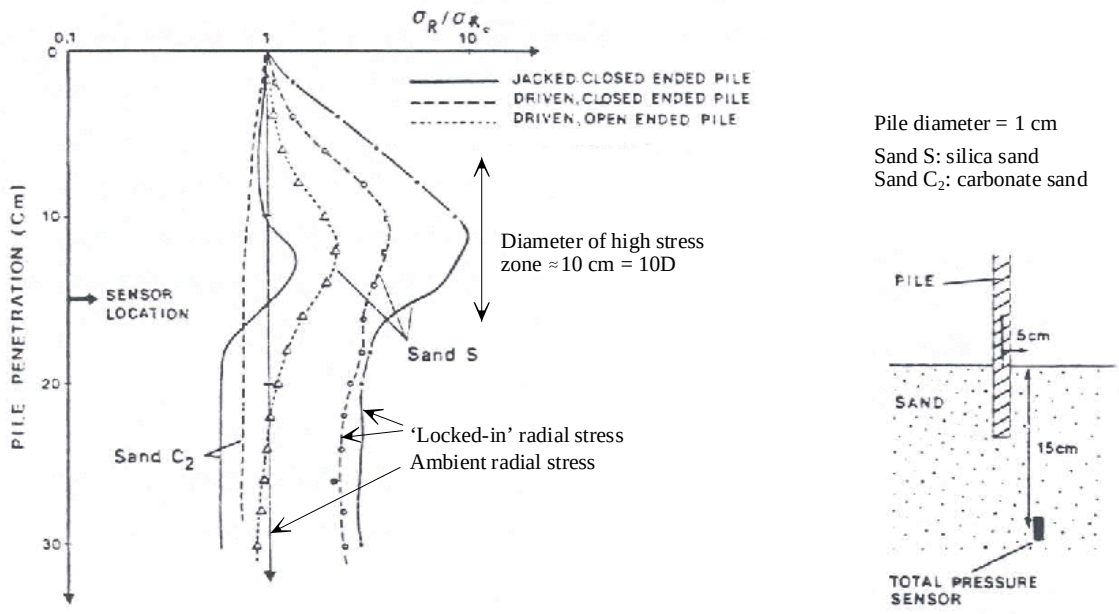

Figure 2.17 Measurement of horizontal stress close to an advancing pile (Nauroy & Le Tirant, 1983)

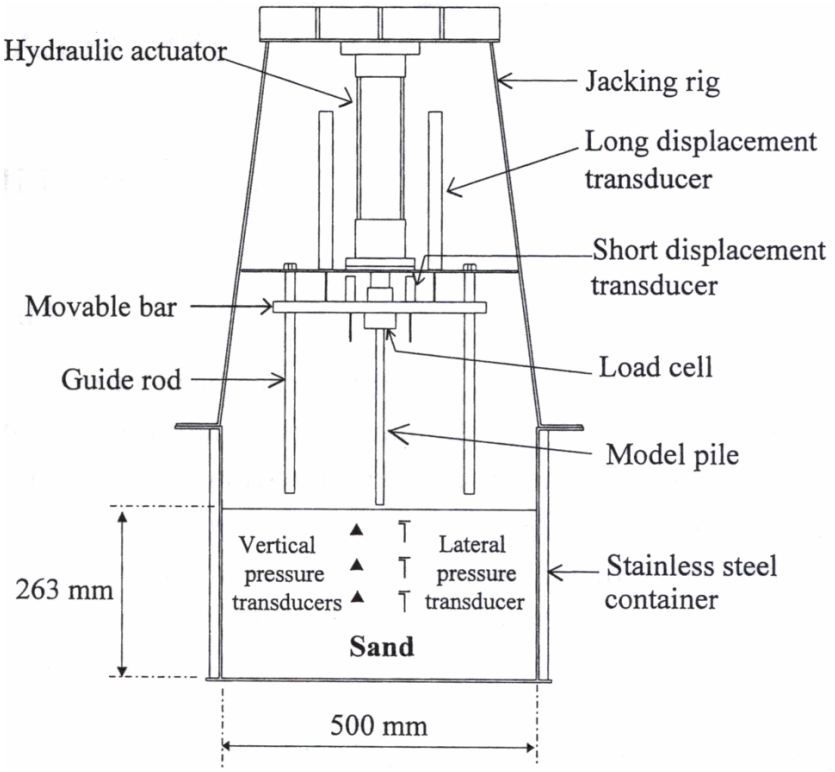

Experimental apparatus

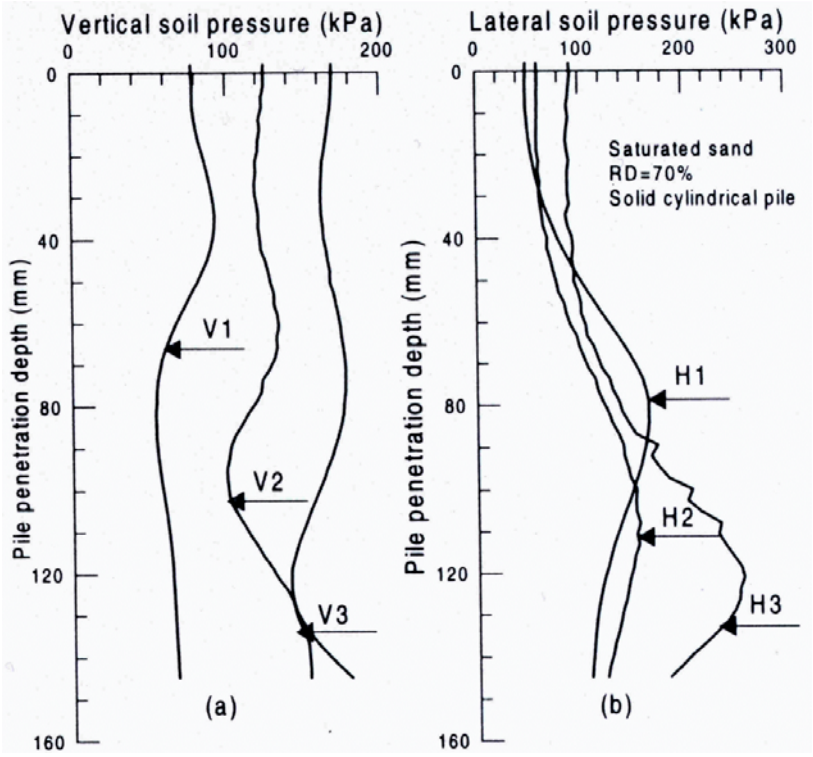

Measurements of stress (arrows indicate elevation of pressure transducers)

Figure 2.18 Measurements of horizontal and vertical stress close to an advancing pile (Leung *et al*., 1996)

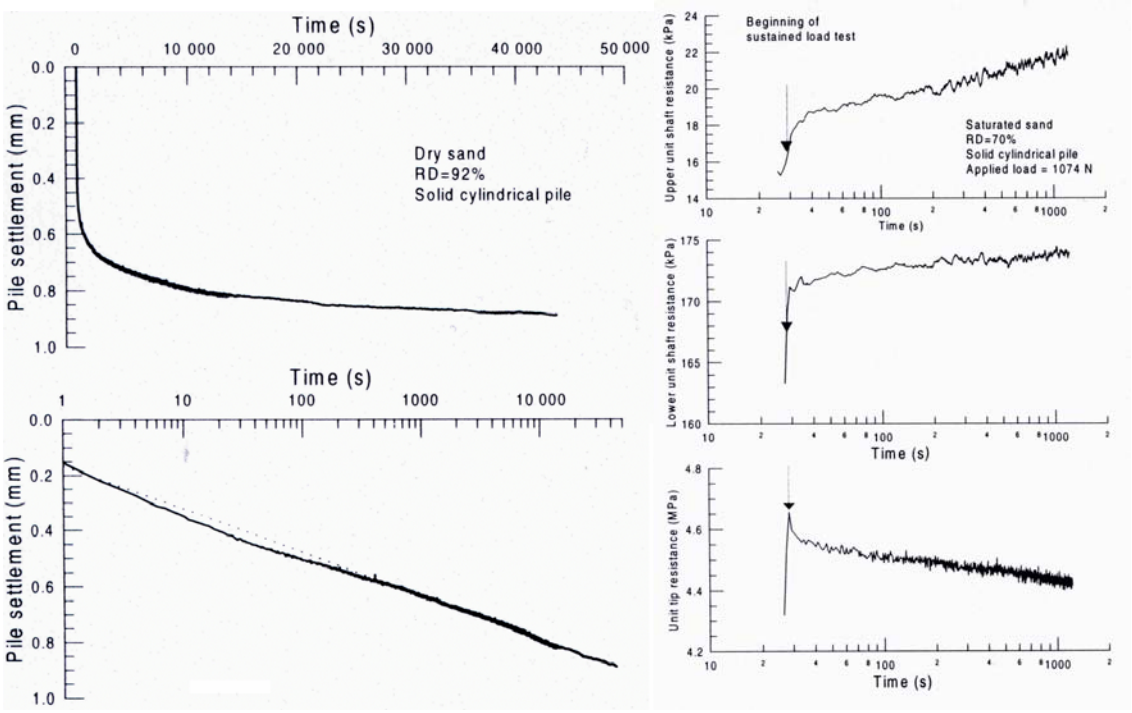

a) Settlement during maintained load test b) Load redistribution during load test

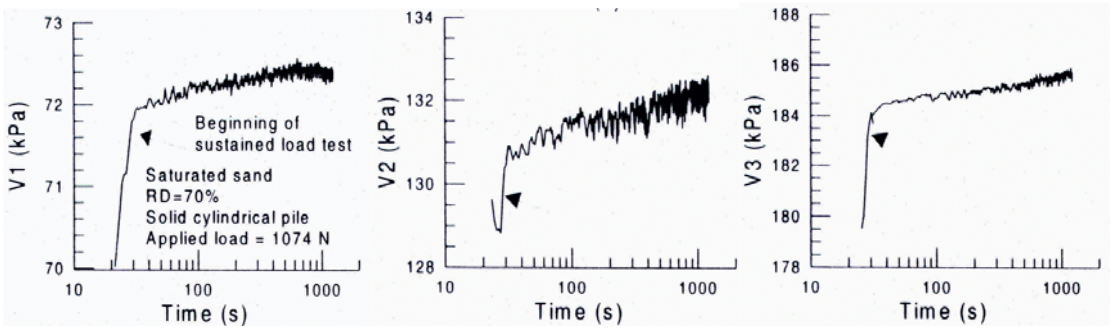

Vertical stress variation during load test

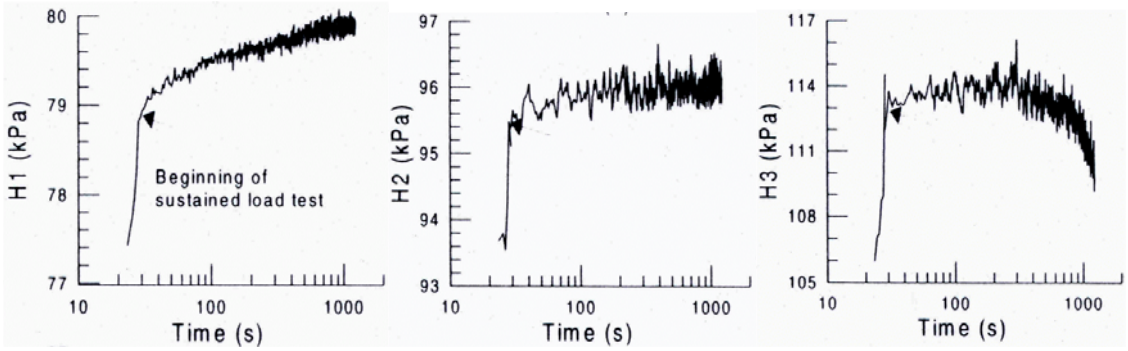

Horizontal stress variation during load test

c) Stress relaxation during maintained load test

Figure 2.19 Creep and stress relaxation during a maintained load test on a centrifuge model pile (Leung *et al.*, 1996)

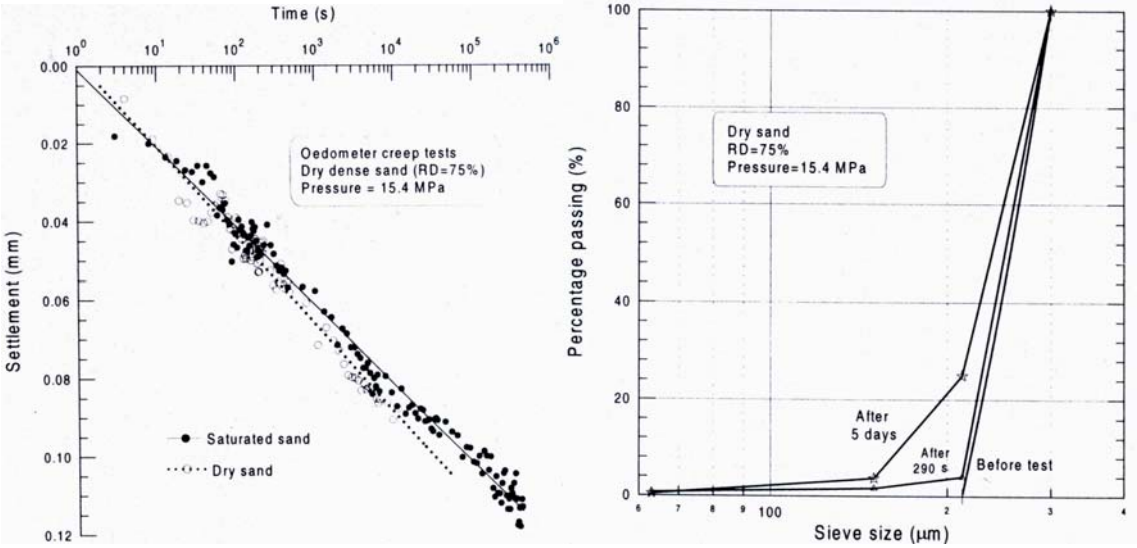

a) Maintained load oedometer test: observation of settlement and particle breakage

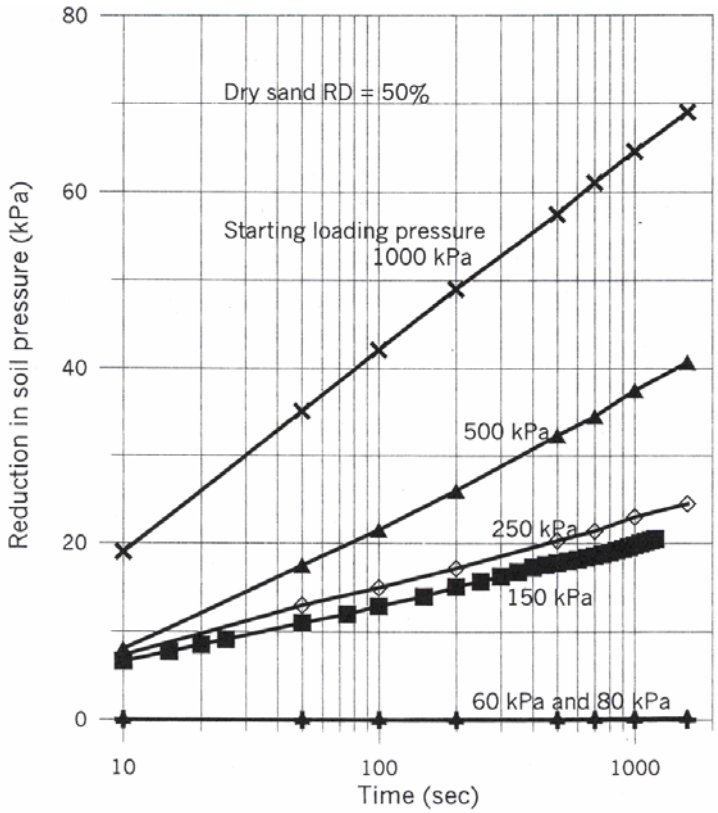

b) Maintained volume oedometer test: observation of stress relaxation

Figure 2.20 Creep and stress relaxation in an oedometer (Leung *et al.*, 1996, 2001)

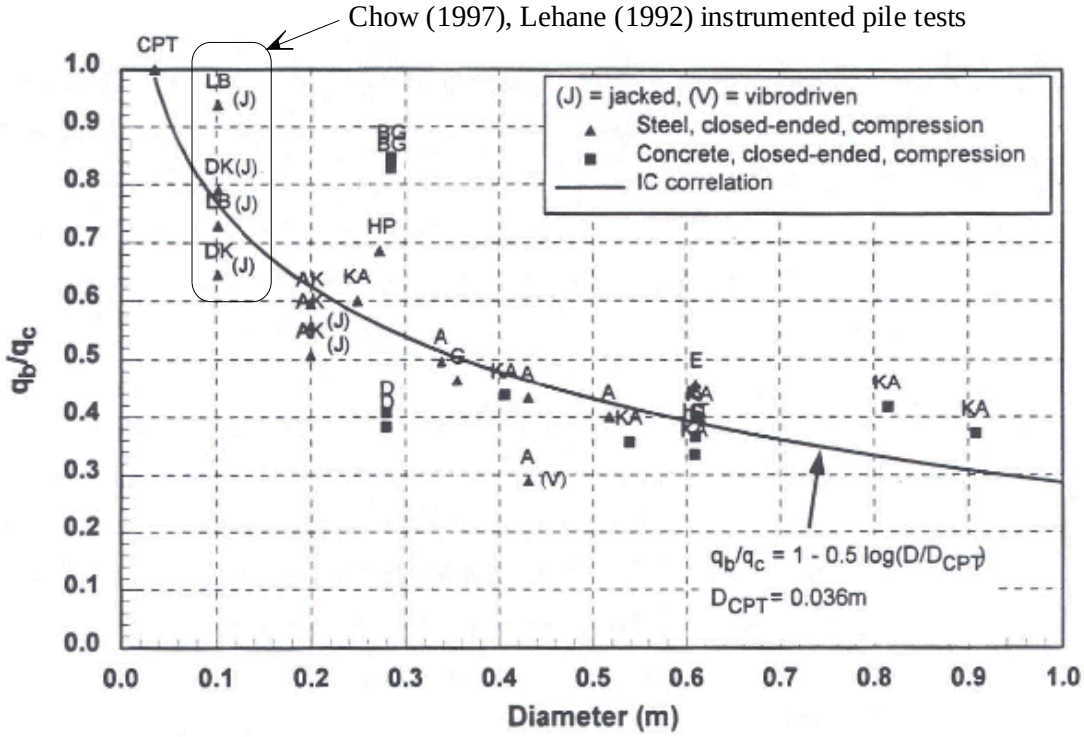

Figure 2.21 A base resistance scale effect on diameter (Chow, 1997)

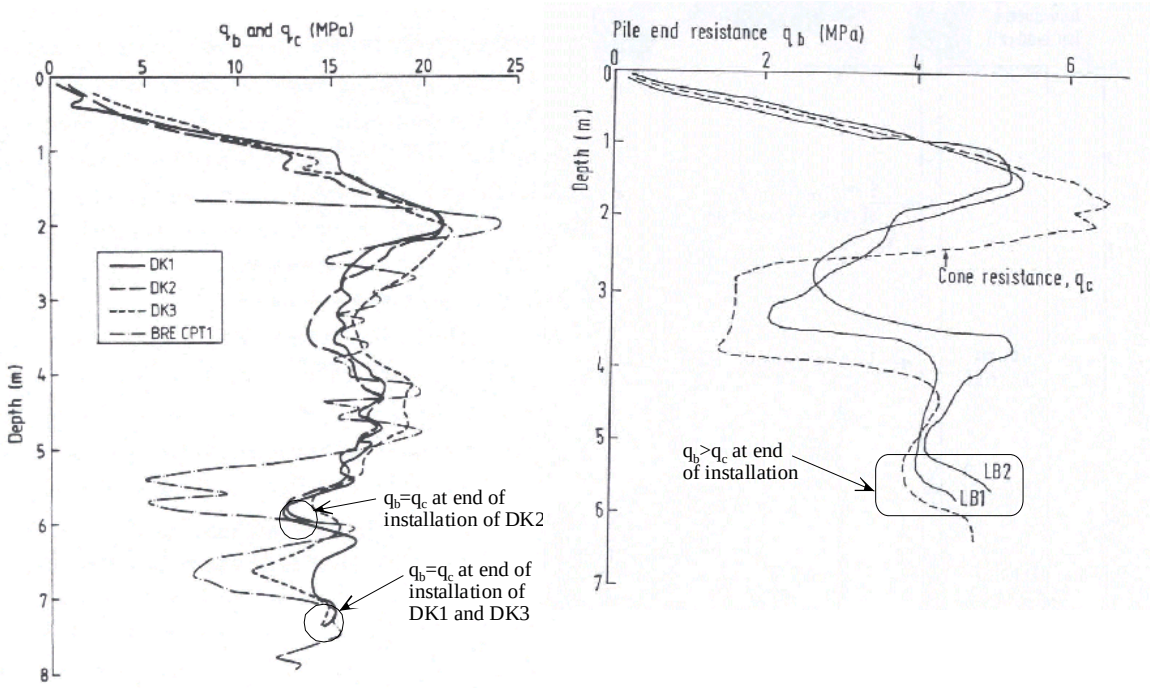

Dense marine sand, Dunkirk
a) Chow (1997)

Loose to medium dense sand, Labenne
b)Lehane (1992)

Figure 2.22 Base resistance during installation of IC test pile at Labenne and Dunkirk

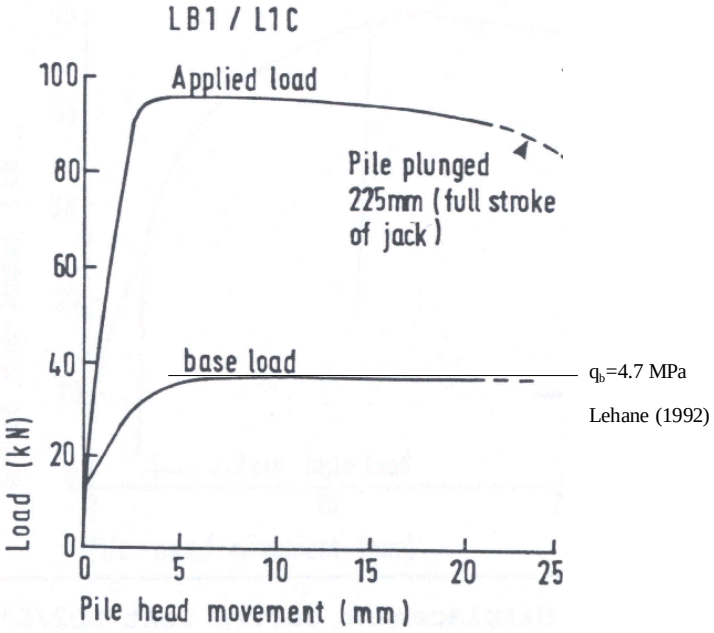

Figure 2.23 Base capacity during first compression test of IC test pile at Labenne (Lehane, 1992)

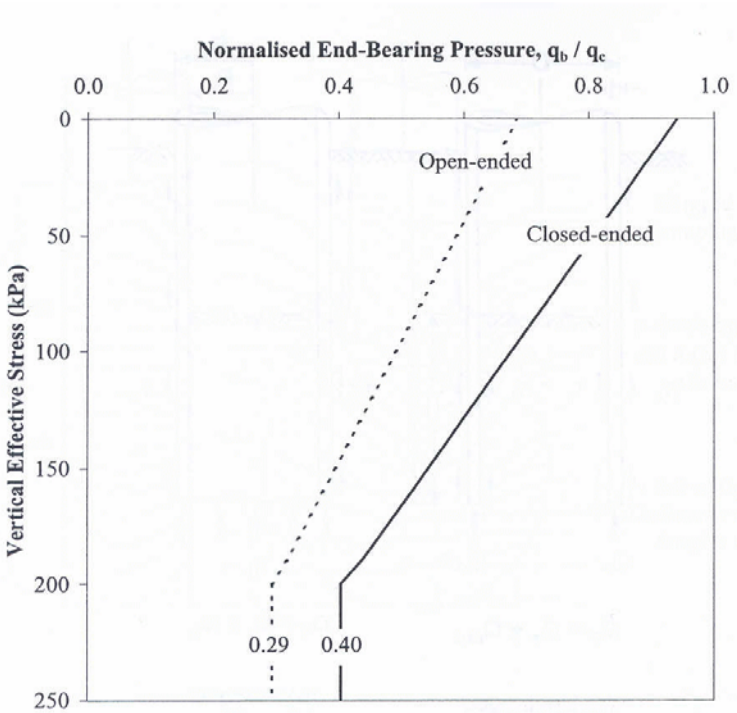

a) De Nicola & Randolph, 1999

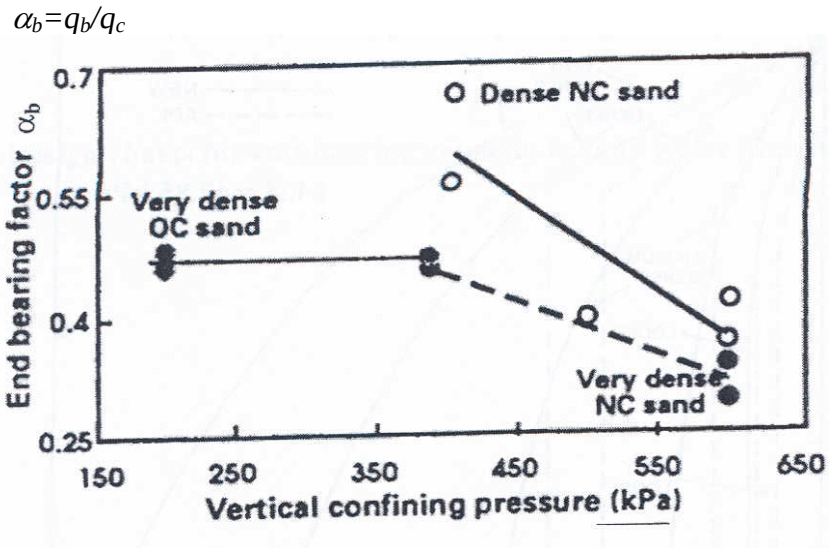

b) Foray *et al.* (1996)

Figure 2.24 A base resistance scale effect on overburden stress

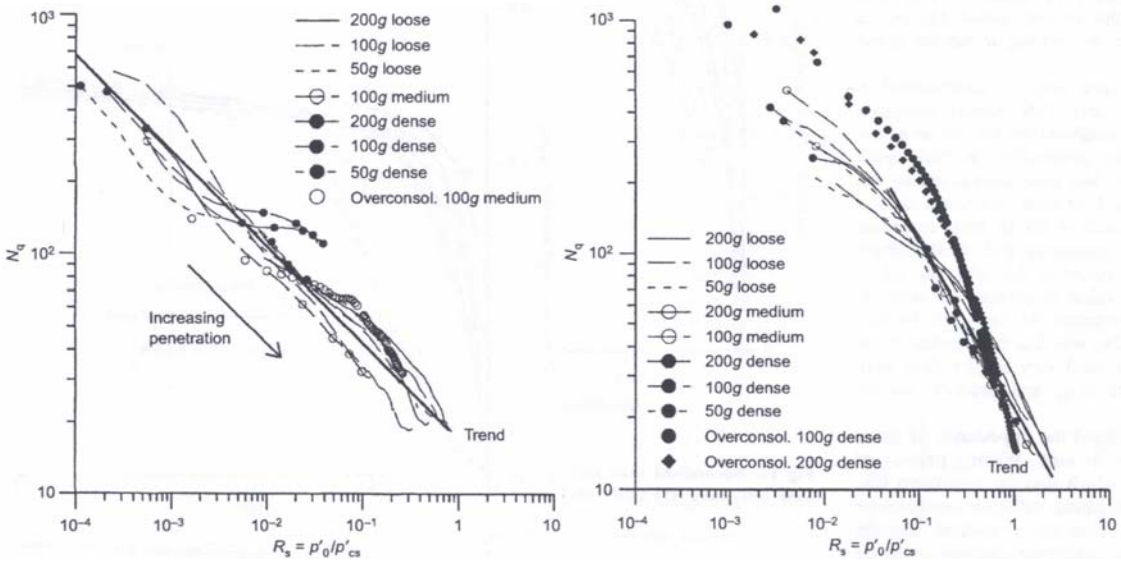

Leighton Buzzard silica sand Dog's Bay carbonate sand

a) Bearing capacity factor vs. stress state

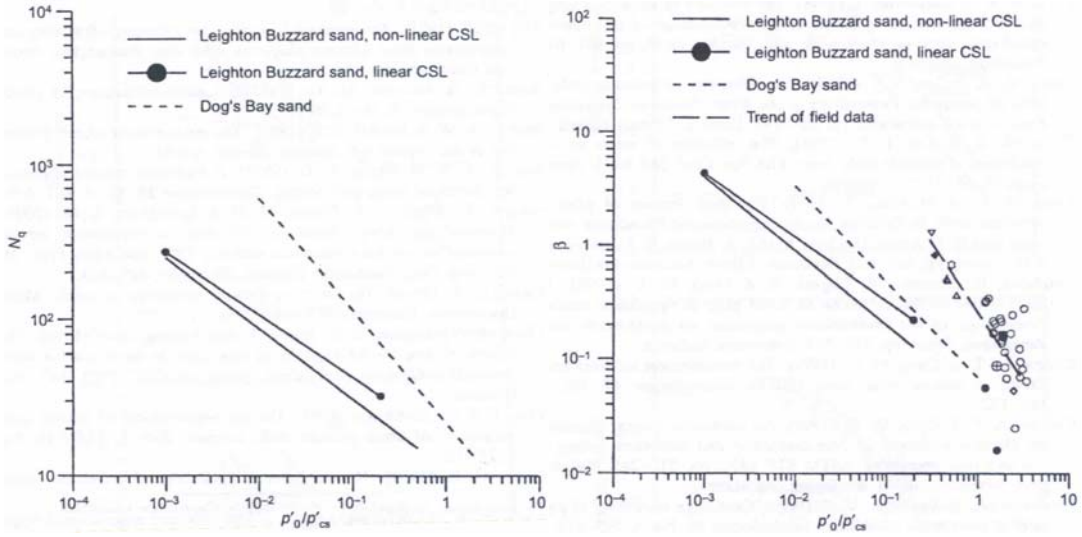

Base resistance Shaft friction

b) Design lines based on stress state

Figure 2.25 The influence of soil state on pile capacity
Klotz (2000), Klotz & Coop (2001)

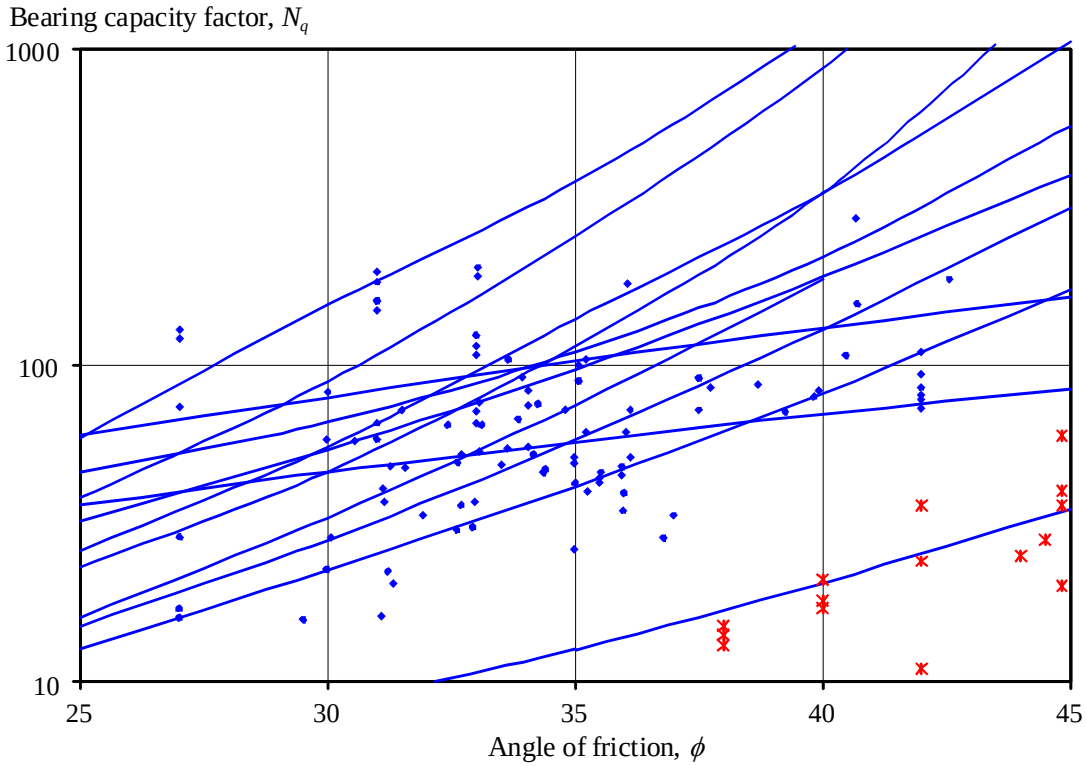

Key

Pile load test result from sand with calcareous content (Murff, 1992; Yasufuku & Hyde, 1995)

Pile load test result for silica sand.
References: Beringen et al, 1979; Briaud et al, 1989; Brucy et al, 1991; Chow, 1997; Gurtowski & Wu, 1984; Lehane, 1992; Mey et al, 1985; Vesic, 1970; Yen et al, 1989; Randolph et al, 1994; BCP Committee, 1971.

Design curves based on bearing capacity theory (collated by Coyle & Castello, 1981).
References: Berezantzev, 1961; Brinch Hansen, 1951; Brinch Hansen, 1961; Caquot-Kerisel, 1956; De Beer, 1945; Meyerhof, 1953; Skempton et al., 1953; Terzaghi (general & local), 1943; Vesic, 1963 ;Vesic, 1972.

Figure 2.26 Unconservative predictions of base resistance in carbonate soils from bearing capacity theory

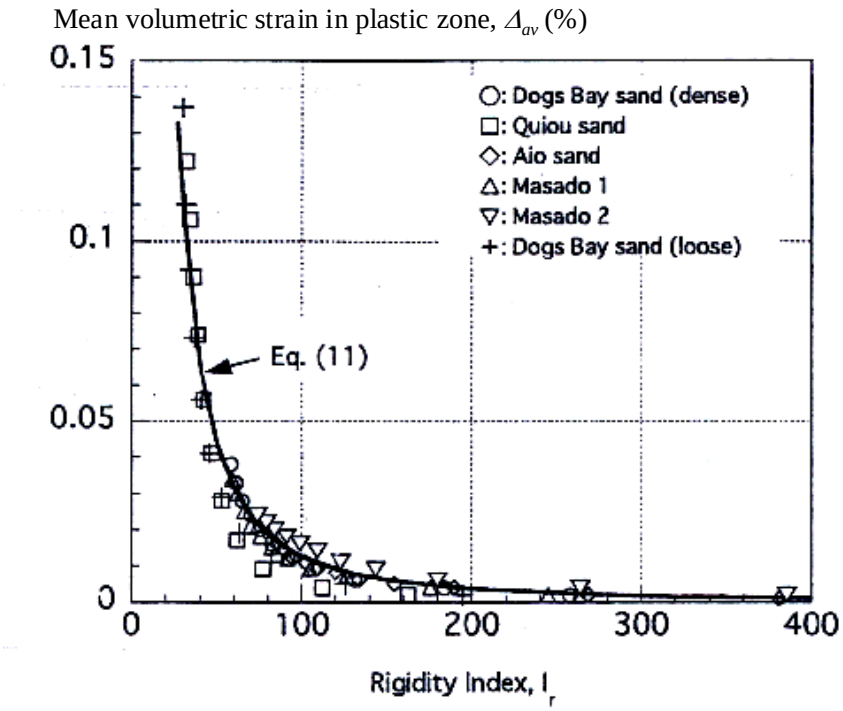

a) Unique relationship between Δ_{av} and I_R

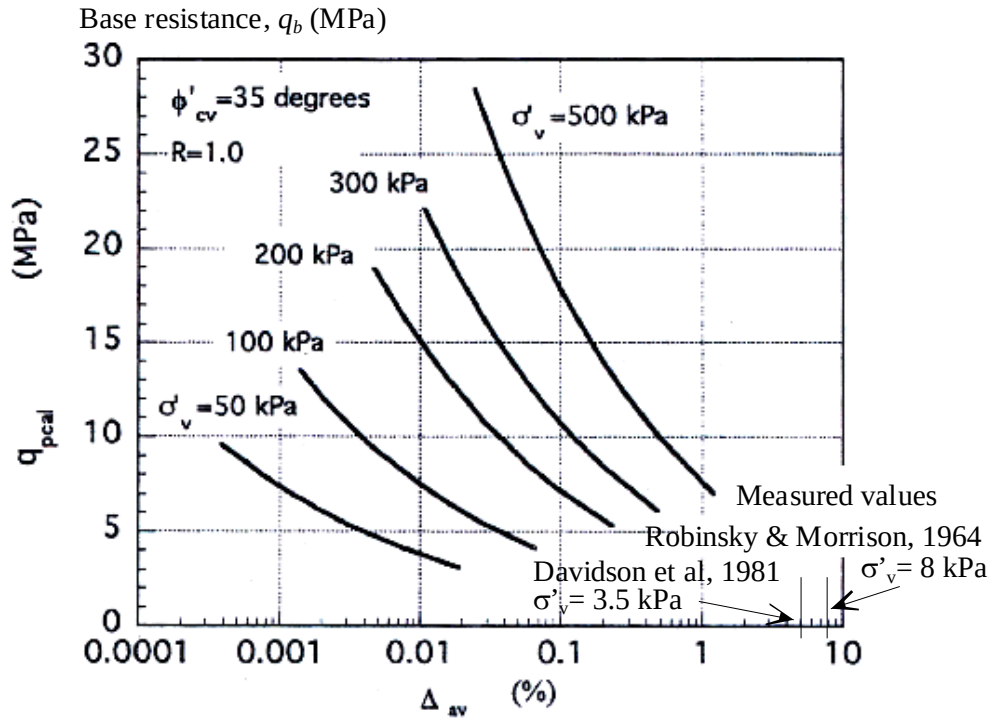

b) Relationship between plastic volume change, in situ vertical stress, and base resistance

Figure 2.27 Scheme for base capacity prediction using cavity expansion analysis with volumetric compressibility (Yasufuku *et al*., 2001)

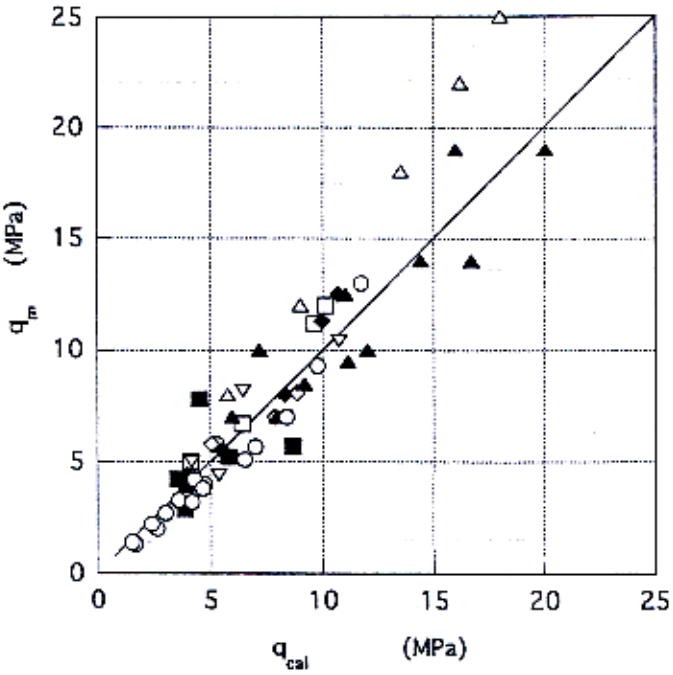

Calculated vs. measured pile capacity

Figure 2.28 Reliability of base capacity prediction using cavity expansion analysis with volumetric compressibility (Yasufuku *et al.*, 2001)

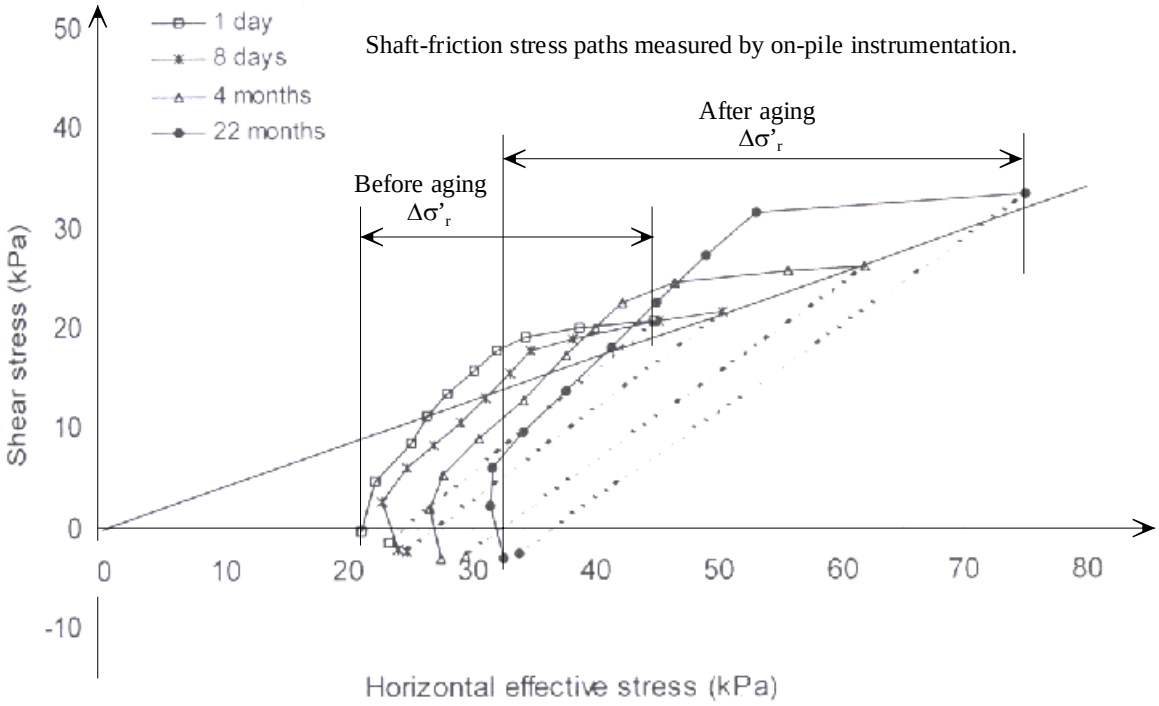

Figure 2.29 Stress paths during pile load tests after set-up (Axelsson, 2002)

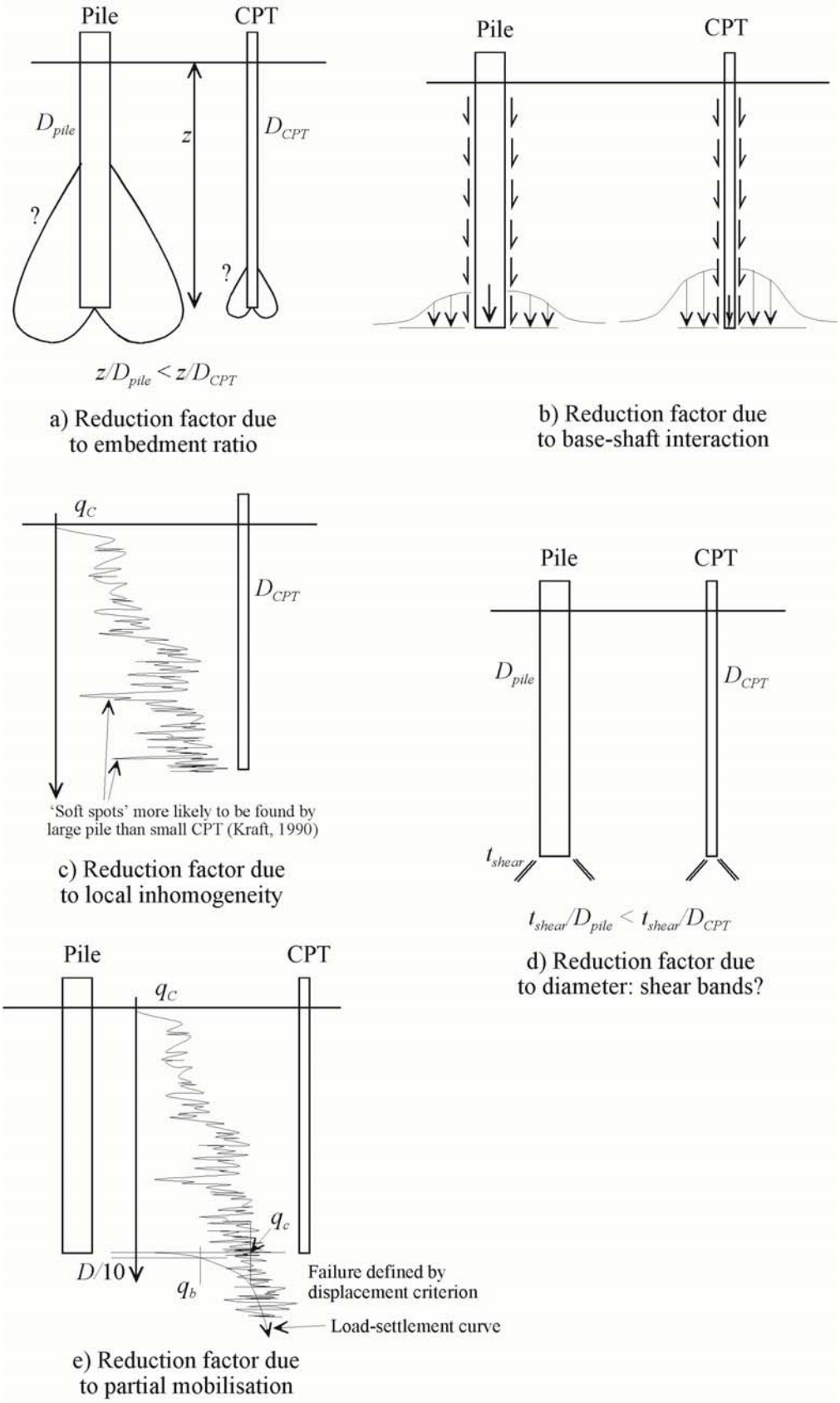

Figure 2.30 Factors influencing the reduction factor between CPT and base resistance

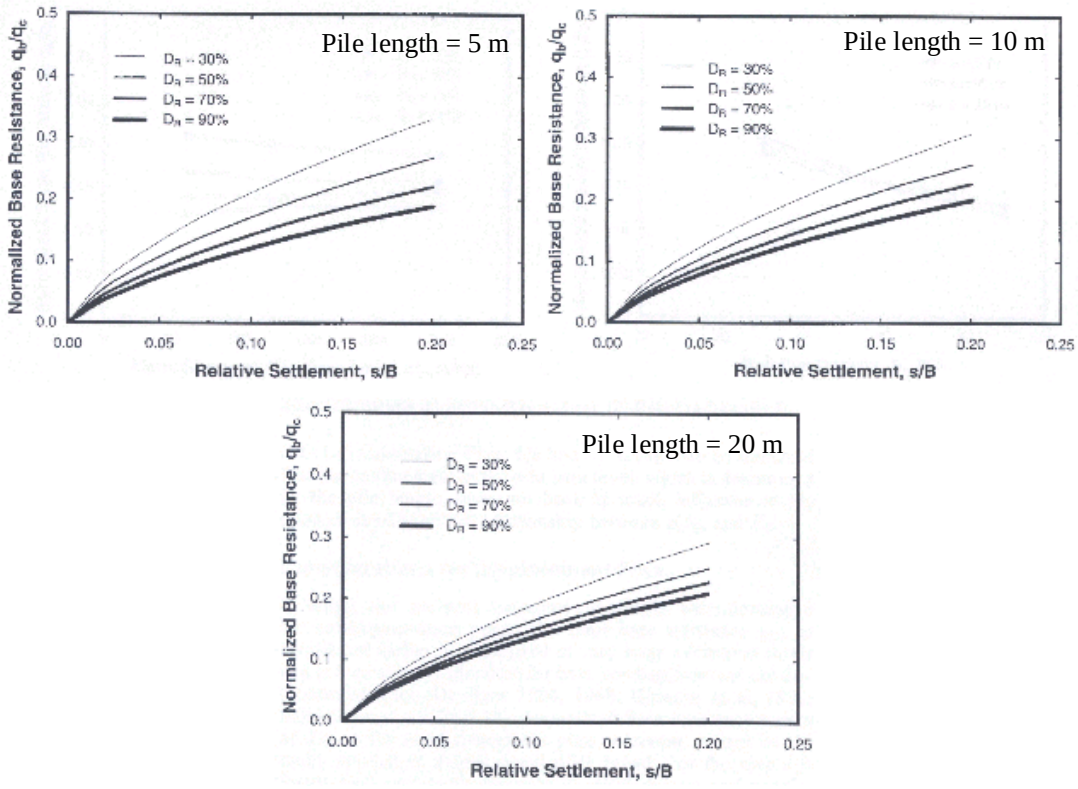

Figure 2.31 Mobilisation curves of q_b/q_c (Salgado & Lee, 1999)

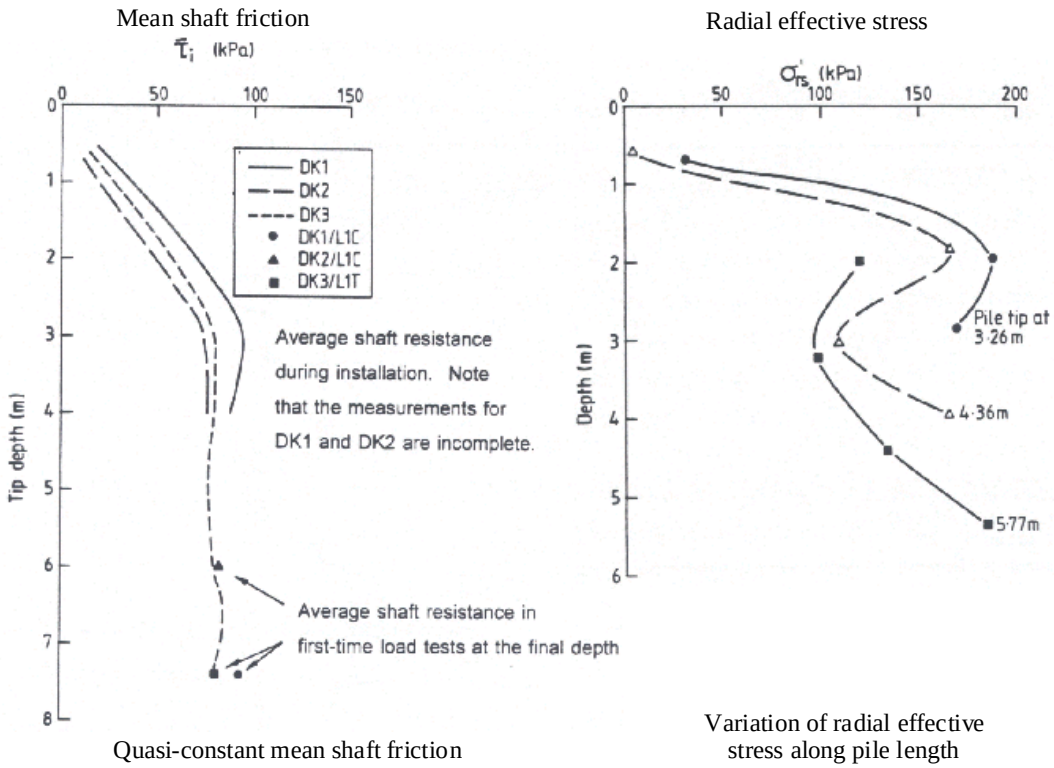

Figure 2.32 A quasi-constant mean shaft friction due to friction fatigue (Chow, 1997)

CHAPTER 3

DISPLACEMENT MEASUREMENT TECHNOLOGY

3.1 INTRODUCTION

Chapter 2 established the precise measurement of soil deformation around a jacked pile as a key goal of this research. In order to gather this data, a suitable displacement measurement system is required. A review of the available measurement methods concluded that a new technique was desirable. This chapter describes the development of a new system, and compares its performance to previous methods of displacement measurement in geotechnical modelling.

Although developed primarily for this project, the new system is widely applicable throughout geotechnical testing and offers a flexible technique for non-contact measurement of soil deformation at pre-failure strain levels without recourse to target markers. The system combines three technologies: digital still photography, Particle Image Velocimetry (PIV) and close-range photogrammetry.

3.2 MEASURING DISPLACEMENT IN GEOTECHNICAL MODELS

3.2.1 A desired specification

The programme of physical modelling outlined in Chapter 2 requires the measurement of displacements that are typical of any geotechnical modelling exercise in which ground movements as well as displacements at the boundary are of interest. A system

for measuring ground movements within a geotechnical model should be designed with the following considerations:

- to maximise the measurement resolution,
- to maximise the area over which measurements are made,
- to maximise the number of points at which measurements are made,
- to minimise the influence of the measurement system on the model behaviour, and
- to minimise the (time or displacement) interval between which measurements can be made (i.e. maximise the sampling rate).

Other considerations may exist for particular applications. For example, all components of a measurement system for use in centrifuge modelling must operate under elevated self-weight.

3.2.2 Desired measurement precision: is current technology satisfactory?

The measurement system described in this chapter has been developed not only for this project, but with the requirements of the wider field of geotechnical modelling in mind. It is argued below that an improvement in the precision of deformation measurements gathered from geotechnical models is desirable.

The measurement of gross deformations is key to understanding the *ultimate* failure mechanism of a geotechnical structure. It is through the observation of failure mechanisms that design solutions for ultimate load are verified. Gross, or ultimate, displacements can usually be observed through post-test excavation of a geotechnical model. Such measurements form ‘before' and ‘after' snapshots of the model, allowing the failure mode to be inferred. However, the origin of a progressive failure may not be evident from observation of the final state alone.

In contrast to the gross deformations present at the ultimate limit state, *serviceability* limit state design requires an understanding of settlements and ground movements at much lower strains. To achieve this aim, measurement resolution must be reduced by at

least an order of magnitude. Coupled with the reduced scale of geotechnical models, and hence a corresponding reduction in the size of the relevant movements, the measurement of pre-failure deformations remains a difficult task.
Figure 2.2 presents the strain ranges experienced during various geotechnical processes. The range 0.01% - 1% strain encompasses serviceability and pre-failure deformations. It is the measurement of these movements that is a challenge in small-scale geotechnical modelling. Larger deformations, which can also be of interest to geotechnical modellers, are also shown. Some are associated with catastrophic events (eg. landslides, lateral spreading and tunnel collapse) and others with construction processes (eg. CPT/pile penetration).

A useful deformation measurement technique must have sufficient precision to capture the lowest relevant strain throughout the field of interest. If element tests and physical models are to capture the relevant behaviour, they must be equipped with a deformation measurement system that can detect pre-failure strains of the order of 0.01%. The strain levels presented in Figure 2.2 can be converted into a corresponding required measurement precision.

For example, on a 100 mm high triaxial sample, a strain of 0.01% corresponds to a platen displacement of 10 μm. A typical geotechnical physical model might have a 300 mm × 200 mm area of interest. To measure a pre-failure strain of 0.01% in a zone of 10% of the model would require the detection of a movement of 3 μm. This precision of 3 μm can be non-dimensionalised by dividing by the field of view (300 mm in this case), giving a normalised precision of $1/100{,}000^{th}$. The following literature review highlights the disparity between this desired precision and the precision currently available to physical modellers.

3.3 PREVIOUS MEASUREMENT TECHNIQUES

A review of the techniques previously used to measure displacements (and deduce strains) within geotechnical modelling is presented. Each technique is assessed with

respect to the specification outlined in Section 3.2.1, and the optimum normalised precision as defined in Section 3.2.2.

3.3.1 X-ray film measurement

3.3.1.1 Typical system overview

The first measurements of displacements within a soil mass were carried out by Gerber (1929) using an X-ray method. A typical X-ray-based measurement system uses lead shot embedded in the soil model. As the test proceeds, successive radiographs are exposed to follow the movement of these markers. If the model is sand, changes in sample density associated with shear band formation can also be observed. However, these changes in density cannot be easily quantified since the level of exposure is a function not only of the sand density but also the model depth, and the absorption properties of the sides of the model container. X-ray systems have been widely used to detect strain patterns in large sand models and shear apparatus (eg. Roscoe *et al.*, 1963; James, 1965).

3.3.1.2 Precision and area of interest

The precision of measurements deduced by X-ray methods is influenced by the following sources of error (Bransby, 1968; James, 1965):

- repositioning of the cassette and X-ray tube between exposures,
- estimation of the position (of the centroid) of the lead shot,
- shrinkage and swelling of the X-ray film, and
- non-planar movement of the lead shot.

Two approaches can be used to assess these errors. The first method involves statistical summation of the errors incurred at each stage of the process. A second approach is to measure the apparent deformations recorded between successive radiographs when no soil movement has occurred. James (1965) used this second approach to reveal a precision (defined as the standard deviation of the random error) of 16 μm (6.25×10^{-4}

inches) when measuring the position of lead shot exposed onto a 14" × 17" sheet of X-ray film.

This technique was successfully used to produce contours of shear and volumetric strain at intervals of 0.5% through large (2.0 m × 0.5 m) models (James, 1965). However, the procedure used by James to locate and measure each marker restricted the rate of analysis to 4 minutes per measurement point. This limited the number of frames that could be practically analysed.

To reduce the tedium of James' film measurement technique, Bransby (1968) photographed his radiographs down to a size that could be used on a small automatic film measurement table (2 μm precision). However, the process of photographic reproduction added to the random errors, and he reports a precision of 78 μm in object space.

An automatic film measurement machine (FMM) was subsequently developed by James to measure full-size (17" x 14") radiographs and is described by Tennekoon (1970). The standard deviation of random error in displacement measurements obtained using this method is reported as 25 μm (Tennekoon, 1970) and strain contours have been presented at intervals of 1% (Bransby & Milligan, 1975).

The most precise reported displacement data using the X-ray technique remain James' 1965 measurements. His standard error of 16 μm when measuring an X-ray film of length 432 mm (17 inches) represents a normalised precision of $1/27000^{th}$ of the field of view (considering only a single sheet of X-ray film). The finest contours of strain produced using this approach are 0.5% (James, 1965) (Figure 3.1a). Since the 1960's, limited further research has been conducted using radiographic measurements, and no methods of achieving increased precision have been reported.

3.3.1.3 Number of measurement points

The number of measurement points permitted within the deforming soil is limited by the following considerations:

- closely-spaced markers may reinforce the soil body and act as stiff inclusions,
- widely-spaced markers 'smear' areas of high strain gradient, and
- large numbers of markers are time-consuming to install and measure.

The use of small lead shot and a patient research worker typically allows a grid of 400-600 markers to be installed and tracked within the model (eg. Smith, 1972; Milligan, 1974).

3.3.1.4 Measurement interval

The minimum interval between the capture of successive X-ray images is governed by the exposure period (typically 3-15 minutes depending on soil density) plus the time required to change the film.

3.3.1.5 Influence of measurement system on observed behaviour

As noted in Section 3.3.1.3, the dense grid of stiff inclusions created by the use of lead markers may alter the behaviour of the model.

3.3.1.6 Other comments

The bulky equipment and heavy screening required by the X-ray method plus the need to change film between exposures precludes its use in centrifuge modelling.

3.3.2 Photographic film measurement

3.3.2.1 Typical system overview

To avoid the difficulties associated with the safe use of radiation, centrifuge modellers adapted the X-ray technique by using standard film and exposing a plane of the model by adding a transparent window. Measurement points are either determined by a grid of target markers (eg. Potts, 1976; Mair, 1979) or individual grains are identified and recorded manually (Butterfield *et al.*, 1970).

3.3.2.2 Precision and area of interest

The reduced size of centrifuge models compared to the previous large-scale testing coupled with the reduction in scale from model-space to film-space lead to a decrease in precision. Potts (1976) and Mair (1979) present in-flight strain data to a resolution of 1%, from a quoted measurement precision of ± 85-100 μm (Figure 3.1b). Considering their ≈ 450 mm × 360 mm field of view this data represents a normalised precision of 1 part in 5000.

The reduction in scale from model to film can be avoided by using a large format camera. Butterfield *et al.* (1970) report a system based on stereo-photogrammetry which allows the relative position of an identifiable feature, for example a soil grain, in two successive photographs to be manually traced and measured. This technique is an adaptation of stereo-photogrammetry in which the two photographs differ by a small increment of displacement of the subject rather than camera position. The random error within a dataset gathered using this method suggests a precision of 5 μm (Andrawes & Butterfield, 1973) (Figure 3.1c). Normalisation by the longest dimension of the field of view (54 mm) indicates a precision of 1 part in 11000.

3.3.2.3 Number of measurement points

When using target markers, the number of measurement points is limited by the considerations listed in Section 3.3.1.3. The difficulties associated with model preparation are less for target markers behind a window compared to lead shot within a model since the targets can be installed after preparation of the soil. The targets do not need to be in position whilst the model is poured or consolidated. 400-600 target markers are typically used to fill a ≈ 0.2 m^2 exposed plane of centrifuge model with the largest reported grid featuring 900 targets covering the surface of a 550 mm x 200 mm model (Taylor *et al.*, 1998).

3.3.2.4 Measurement interval

High speed photography allows a high frame rate to be achieved. Whilst X-ray methods are unsuitable for dynamic processes, high speed photography allows the movement of target markers during and soon after earthquake events (eg Kutter, 1982). The

maximum frame rate is limited by the winding-on period of the camera and, if a stationary camera is being used to view a centrifuge model, the angular velocity of the centrifuge.

3.3.2.5 Influence of measurement system on observed behaviour

When deducing strain and displacement fields from the exposed plane of a model, it is assumed that the displacement field adjacent to the exposed boundary is equal to the displacement field at mid-plane. Arthur & Roscoe (1965) performed a direct comparison of mid-plane X-rays and photography of the exposed plane of the soil behind a model retaining wall, and found excellent correlation. This lead them to note that since photography of an exposed plane is easier, quicker and cheaper than X-ray methods, its use is preferable in model testing.

3.3.3 Video photography of target markers

3.3.3.1 Typical system overview

The development of video photography in the 1980s increased the available frame rate and eliminated the need for time-consuming measurement of conventional film. The image processing technique of ‘blob tracking’ or centroiding allows the location of an array of target markers to be automatically found.

A typical system consists of a PAL resolution video camera feeding an analogue signal into video tape, or for improved image quality, directly into a PC frame grabber. The images are digitised by the frame grabber, and analysed by a centroiding method. The use of centroiding requires the soil plane to contain a grid of discrete target markers.

3.3.3.2 Precision and area of interest

The resolution of any measurement taken from a digital image is proportional to the object-space pixel size. Video capture in the European PAL format produces a nominal resolution of around 730 × 550 pixels, although the number of photo-sensitive elements

within a typical camera CCD[1] is often considerably less. 'Line jitter' and the transmission of the analogue video signal through centrifuge sliprings can further reduce image quality.

The captured images can be analysed by centroiding (Garnier *et al.*, 1991; Taylor *et al.*, 1998). Various algorithms can be used to identify the location of the intensity peak created by a coloured target on a contrasting background. The location is often defined as the centroid of the peak, although this position is dependent on the threshold used to separate the target from the background.

Chen *et al.* (1996) found that under the test conditions of a typical centrifuge model, the random error when repeatedly locating a stationary target marker using centroiding can be up to 0.3 pixels. Taylor *et al.* (1998) report a centroiding-based measurement system that can track movements of 3 mm diameter target markers embedded in clay to a precision of 60-105 μm over a 300 × 200 mm field of view. This represents a maximum normalised precision of 1 part in 5000. Grant (1998) analysed the displacement of *clay* using the system and presented the data as contours of strain with a resolution of 1% (Figure 3.1d). Grant's data from *sand* models was not analysed since large errors were present. The markers became obscured by the surrounding sand grains and the precision of the centroiding method was reduced since sand does not offer a suitably uniform contrasting background to the target markers.

If target markers are not desirable, features within a video image can be manually digitised (e.g. Saada *et al.*, 1999). Manual measurement can only be used to track easily identifiable features, and is subject to user errors. Manual digitising limits precision to a single pixel. Using PAL standard video images, this represents a normalised precision of approximately 1/700th of the field of view.

[1] CCD: Charge Coupled Device. This is the flat element within the camera on which the image is formed. In digital photography a CCD is used to capture the image, instead of photographic film.

An alternative technique for the analysis of target markers is video extensometry. Gill (1999) and Gill & Lehane (2001) report the use of a video extensometer to capture the movement of 25 beads embedded in transparent clay around a model penetrometer. Video extensometry is an advancement on centroiding, and operates by evaluating the position of a target marker by measuring the centroid of many lines drawn across the marker and using interpolation and time-averaging to reduce random errors. Multiple line measurements are made at many incremental angles, and from a time-averaged sequence of images. The drawbacks associated with the use of target markers apply.

3.3.3.3 Number of measurement points

Digital analysis of video images eliminates the drawbacks associated with time-consuming manual film measurement. As a result, the number of measurement points is limited by the minimum size and spacing of the target markers. Each target marker must occupy a minimum area of 3-5 pixels in diameter for the centroiding algorithm to operate, although larger markers are preferable since the precision of centroiding is improved (Chen *et al.* 1996). Placing target markers at 5 diameter centres to avoid excessive reinforcement of the soil allows a grid of 600-1000 target markers to be placed within the soil model.

3.3.3.4 Measurement interval

If desired, all frames in the video stream can be captured and digitised for subsequent analysis. The frame rate of video photography is 25 Hz; far higher than is needed for conventional non-dynamic geotechnical modelling.

3.3.3.5 Influence of measurement system on observed behaviour

The comments in Section 3.3.2.5 for film measurements of an exposed plane of soil apply equally to video analysis.

3.3.4 Review summary: the state-of-the-art

The technology of the systems described in this brief literature review has evolved considerably in the previous 70 years. The state-of-the art is currently represented by video capture of the movement of discrete target markers followed by analysis of these

images using centroiding. The resulting data has been plotted as contours of strain data at intervals of 1%. Two drawbacks are immediately evident in this state-of-the-art.

Firstly, the best achievable strain measurement is two orders of magnitude above the required level set out in Section 3.2.2 and depicted in Figure 2.2. This strain precision in geotechnical model testing can be set against recent improvements in the precision of strain measurement in geotechnical element testing. Measurements of the high pre-failure stiffness of soil at strain levels of the order of 0.001-0.1% have significantly improved the understanding of serviceability behaviour. New constitutive models have emerged (e.g. Simpson *et al.*, 1979; Gunn, 1993), and field predictions have improved (e.g. Jardine *et al.*, 1986).

Small-scale modelling has long represented a valuable tool for the prediction of ultimate limit state behaviour, and the validation of numerical predictions of medium to large strain behaviour. However, until the strain resolution of small-scale modelling approaches that of element testing, validation of predictions of serviceability behaviour will remain difficult.

Secondly, the continuing reliance on discrete target markers or manual feature measurement is a significant drawback. Target markers suffer the following limitations:

- the reinforcing effect of a dense grid of inclusions is not easily quantified,
- the detail in areas of high strain gradient is unsatisfactory,
- measurement reliability reduces if targets become partially obscured by soil, and
- the points at which measurements are made must be chosen prior to the modelling event.

A new system based on the three technologies of digital photography, PIV analysis and close range photogrammetry has been developed during the course of this research. This system eliminates the reliance on target markers, and provides displacement measurements to a precision higher than described above. The implementation of each of these three technologies is described below.

3.4 DIGITAL PHOTOGRAPHY

The first step in a video-based analysis system is to digitise the video image, using a PC frame-grabbing card. In digitised form, a monochrome image consists of a two dimensional integer matrix containing the intensity (brightness) recorded at each CCD pixel. A typical 8-bit frame-grabbing card records brightness on an integer scale from 0 to 255. Colour images consist of three matrices; one for each colour channel. Image analysis techniques for displacement measurement such as centroiding operate on these integer matrices (Figure 3.2).

Techniques used to measure displacement from a digitised image have a precision determined in image-space as some fraction of a pixel. For example, centroiding techniques typically offer a precision of 0.1-0.3 pixel (Chen *et al.*, 1996). Manual digitisation of identifiable features can have a precision of only a single pixel. Noting that precision is defined in image-space as some fraction of a pixel, if the field of view can be covered with an increased number of pixels, a corresponding increase in precision is achieved. In other words, a twofold increase in pixel resolution leads to a doubling of the measurement precision.

Image frames acquired from a European standard (PAL) video signal have a nominal resolution of around 730 × 550 pixels. In contrast, digital still cameras offer significantly higher pixel resolution. Throughout this research, a Kodak DC280 digital still camera was used to capture images (Figure 3.3). This camera has a pixel resolution of 1760 x 1168. Compared to PAL video, this resolution represents a 2.4 times reduction in object-space pixel size, with a corresponding increase in precision. Digital still cameras offer other benefits over video. As well as having better resolution, the resulting images are more stable since they are converted to a digital signal within the camera rather than in a frame-grabbing card. This avoids line-jitter and the additional noise associated with analogue transmission.

Most digital cameras can be controlled via a PC link using native control software, allowing remote adjustment of camera settings and downloading of images. This feature

reduces the likelihood of accidental camera movement during operation, leading to an apparent displacement. The DC280 camera can interface with a PC using a Universal Serial Bus (USB) connection, allowing faster image download than a conventional RS232 serial link. In-house Windows software for the adjustment of camera settings and downloading of images, written by Mr W.A. Take, was used throughout this research.

A drawback of digital still photography is the low frame rate. A full cycle of image capture, digital conversion, JPEG image compression, and transmission through USB link to hard disk must be completed before a subsequent image can be captured. A capture rate of 30 seconds per frame can be achieved by the DC280 in maximum resolution mode, although slower performance results if more than one camera is connected to the PC.

3.5 PARTICLE IMAGE VELOCIMETRY (PIV)

3.5.1 PIV in fluid mechanics

Particle Image Velocimetry (PIV) is a velocity-measuring technique that was originally developed in the field of experimental fluid mechanics. Although PIV is widely established, the Author is unaware of any previously published use of this technique in geotechnical modelling. Since PIV is not discussed in previous soil mechanics literature, a brief introduction to the basic theory behind the technique is presented, followed by a description of the algorithms used by the software written during the course of this research.

The flow field of a fluid can be examined by seeding the flow with marker particles. If the seeding density is low, the particles can be tracked individually. This method of tracking forms a subset of PIV, known as Particle Tracking Velocimetry (PTV). If the seeding density is high, small patches within the image that contain a number of particles are tracked; this subset is known as High Image Density PIV (Adrian, 1991), and is the technique which has been used in this research.

Experimental fluid mechanics is usually concerned with relatively high flow velocities. The flow field is typically illuminated by multiple pulses of a sheet of laser light or a photographic flash and captured on a single photograph. The procedure for analysis of the recorded image is shown in Figure 3.4. The image is divided into a grid of interrogation patches for which velocity vectors are to be evaluated. The auto-correlation, $R(\underline{s})$, of each patch is evaluated (Equation 3.1). The domain of the vector $\underline{s}$ is the area over which the degree of correlation is evaluated, with each component of the vector varying between $\pm s_{max}$. The domain of $\underline{s}$ represents the zone in which the displaced fluid element is searched for. If the element has displaced a distance greater than the maximum magnitude of $\underline{s}$, the search will be unsuccessful.

The auto-correlation process reveals a pair of maxima in $R(\underline{s})$ where the successive exposures of each marker overlap, representing plus/minus the displacement vector of that patch, and a central self-correlation peak. Since the direction of fluid flow is usually known, the correct sign of the displacement vector can be assumed.

$$R(\underline{s}) = \sum_{U} I(\underline{U}) \cdot I(\underline{U} + \underline{s}) \tag{3.1}$$

The auto-correlation function is a convolution of the interrogation patch with itself. A convolution of two variables can be evaluated directly in the space domain or via a double Fourier transform in the (spatial) frequency domain. This is following the convolution theorem, which shows that the Fourier transform of the convolution of two variables is equal to the product of the Fourier transforms of each variable (eg. Kreyszig, 1999, p. 574). The Fourier transform approach has historically been favoured for two reasons:

- The first Fourier transform can be found using an optical method in which the image is projected through a lens to create a pattern of Young's fringes (Goodman, 1968). The second Fourier transform can be derived in one dimension optically (Kaufman *et al.*, 1980; Meynart, 1983), or digitally using a Fast Fourier Transform (FFT) (Cooley & Tukey, 1965).

- The particle seeding density used in multiple-exposure techniques is low. Consequently, interrogation patches digitised from photographic film require a large number of pixels to capture sufficient particles (typically 256 x 256, Adrian (1991), e.g. Figure 3.4). Convolution of such large matrices is more efficiently carried out by an FFT rather than by being evaluated directly.

Using modern high-speed photographic techniques and digital Fourier analysis, Keane *et al.* (1990) were able to conduct single-exposure multiple-frame PIV. Instead of auto-correlation of a single interrogation patch, cross-correlation of an interrogation patch with a second interrogation patch from the same location in a subsequent image was performed. This resulted in reduced noise, and removed the uncertainty associated with multiple auto- and self- correlation peaks.

3.5.2 PIV in soil mechanics

3.5.2.1 Natural texture

The deformation of soil can be considered as a low-velocity flow process. Image sequences suitable for single-exposure multiple-frame PIV can be gathered without the use of high-speed photography. Whilst fluid requires seeding with particles to create features upon which image processing can operate, natural sand has its own texture in the form of different coloured grains, and the light and shadow formed between adjacent grains when illuminated. Texture can be added to an exposed plane of clay by the addition of coloured ‘flock’ material or fine sand.

3.5.2.2 Reduced patch size

The minimum allowable patch size in PIV derives from the requirement that the patch contains sufficient texture to be identifiable in the subsequent image by producing a sharp correlation peak. An example of a 6 x 6 pixel patch taken from a digital image of silica sand is shown in Figure 3.5. The continuous spatial variation of pixel brightness, or intensity, is in contrast to the sharp isolated peaks created by flash-illuminated fluid markers on an unlit background (Figure 3.4).

Since images of soil contain a continuous variation in texture, without unlit featureless zones, the size of an interrogation patch can be significantly reduced compared to the analysis of seeded fluid flow. This reduced patch size allows more measurement points to be contained within a single image. Also, it will be shown later that the reduced patch size can influence the choice of matching algorithm.

3.5.2.3 Strain paths, not velocity fields

The aim of PIV in fluid mechanics is usually to obtain an instantaneous velocity field. Analysis of a single image pair is sufficient since most phenomena occur at a steady state. In geotechnical modelling, the full soil movement throughout the entire modelling event is required. Consequently, the multiple-flash method, followed by analysis of a single image is not appropriate. Instead, a full series of images must be captured, and compared in sequence to allow a sequence of strain increments to be deduced. The image manipulation steps for calculating a single displacement vector following this procedure are shown in Figure 3.6a. The flowchart for evaluating the displacement field of an entire image pair is shown in Figure 3.6b.

3.5.3 Matching algorithm

3.5.3.1 Cross-correlation

Image processing algorithms have been written under MatLab[2] to implement PIV through a sequence of digitally-captured images of soil. The kernel of multiple-frame PIV analysis is the matching algorithm used to compare interrogation patches taken from successive images. A close relation to the auto-correlation matching method described in Section 3.5.1 is cross-correlation (Equation 3.2), as used by Keane *et al.* (1990). Whilst auto-correlation methods operate on only one interrogation patch, the use of cross-correlation introduces two interrogation patches, hereafter referred to as the test patch, I_{test} from image 1, and the search patch, I_{search}, from image 2.

$$R(\underline{s}) = \sum_{U} I_{test}(\underline{U}) \cdot I_{search}(\underline{U} + \underline{s}) \tag{3.2}$$

[2] Software distributed by The MathWorks Ltd, Cambridge. http://www.mathworks.co.uk

However, Equation 3.2 alone is not sufficient for robust detection of the patch displacement for the following reasons. The maxima of $R(s)$ generated by Equation 3.2 may not represent a definite 'best match' since the interrogation matrices I_{test} and I_{search} can be a different size and I_{search} may feature a general variation in brightness across the patch; a one-dimensional demonstration of this lack of correlation is shown in Figure 3.7a-c. This is often not a consideration in fluid mechanics PIV. When analysing typical images of seeded fluid flow, the highest correlation peak in $R(s)$ usually corresponds to the 'best match' between the test patch and search patch. This is because the two patches are spatially overlapping in consecutive images (i.e. s_{max} is less than patch width, L), are extracted from the full image matrix before analysis (i.e. the null padding shown in Figure 3.6c is carried out), and have a flat background intensity (as shown in the flash photography of seeded flow) (Figure 3.4).

When analysing film photographs by a digital Fourier transform method, this extraction is carried out by digitising only the area of the second image that overlaps the interrogation patch from the first image. In the case of this research, in which the images are initially in a digital format, the equivalent operation would be to assign null values to the search patch, $\underline{I}_{search}$, for values of $(\underline{U} + \underline{s})$ which lie outside the range of $\underline{U}$ (Figure 3.6c).

The disadvantage of this extraction process is that particle images that move out of the zone covered by the test patch between exposures are lost from the matching process, and cannot contribute to the correlation peaks. This approach reduces the reliability of the matching process at high displacements, and requires that s_{max} remains less than $L/2$.

These disadvantages can be overcome by extending the correlation process as follows. The matching process is improved to allow the search patch to extend beyond the zone covered by the test patch using an extension of the cross-correlation method. A normalisation matrix, $N(\underline{s})$ is created by computing the cross-correlation of the square of the search zone matrix with a dummy mask test patch, $M(\underline{U})$, of uniform amplitude

(Figure 3.7d, Equations 3.3, 3.4). This normalisation process is presented for the case of a one-dimensional intensity matrix in Figure 3.7d-f.

$$N(\underline{s}) = \sum_{U} \left[I_{search}(\underline{U} + \underline{s}) \cdot I_{search}(\underline{U} + \underline{s}) \right] \cdot M(\underline{U}) \tag{3.3}$$

$$R_n(\underline{s}) = \frac{R(\underline{s})}{N(\underline{s})} \tag{3.4}$$

The matrix $R_n(\underline{s})$ represents a map of 'degree of match' of the test patch I_{test} over each part of the search zone, I_{search} (Figure 3.6a), and features a single correlation peak located at $\underline{s}_{peak}$ denoting the displacement vector between t_1 and t_2 of the soil element represented by matrix I_{test}.

The cross-correlation functions shown in Equations 3.2 and 3.3 are a form of convolution. Two alternative algorithms were written to carry out this convolution in the space domain and in the frequency domain by FFT (Equations 3.5, 3.6). Within the space domain, the correlation matrices $R(\underline{s})$ and $N(\underline{s})$ are evaluated directly by multiplying the overlapping coefficients of the test and search matrices. The computational requirement of this process scales with the square of the patch size (L^2). Furthermore, since the correlation must be evaluated for each location at which a match is evaluated, the computational requirement also scales with the square of the maximum search distance, s_{max}.

$$R(\underline{s}) = \Im_{inv} \left[\Im I_{test}(\underline{U}) \cdot \Im I_{search}(\underline{U} + \underline{s}) \right] \tag{3.5}$$

$$N(\underline{s}) = \Im_{inv} \left[\Im \left(I_{search}(\underline{U} + \underline{s}) \cdot I_{search}(\underline{U} + \underline{s}) \right) \cdot \Im M(\underline{U}) \right] \tag{3.6}$$

The computational requirement of correlation within the frequency domain using an FFT scales with (L log L), where L is the patch size, if L is a power of 2 (Cooley & Tukey, 1965). If L is not a power of two, the patch must first be interpolated to side length 2^n or padded with null cells in order for the FFT algorithm to operate. This results in a reduction in computational efficiency. The actual processing requirement for an FFT depends strongly on the initial interpolation stage, which offsets the theoretical

($\log L$ / L) speed advantage over convolution in the space domain. The relative performance of each algorithm is compared in Section 3.5.3.3.

3.5.3.2 Difference minimisation

It is noted in Section 3.5.2.2 that the patch size appropriate for PIV on soil images is significantly smaller than is typically used in fluid mechanics. Consequently, during development of this software, it was considered that direct calculation of the absolute difference between the test and search patches may provide a computationally more efficient matching process than the correlation methods described in Section 3.5.3.1. Summation of the absolute difference of each pixel intensity over the test and search patches leads to a difference matrix, $D(\underline{s})$, the minimum of which identifies the best match (Equation 3.7). No normalisation is required, and the preparation of each intensity matrix for a digital Fourier transformation is avoided.

$$D(\underline{s}) = \sum_{U} \left| I_{test}(\underline{U}) - I_{search}(\underline{U} + \underline{s}) \right| \tag{3.7}$$

3.5.3.3 Computation time

The computational efficiency of the three matching techniques described above (Equations 3.2, 3.5, 3.6, 3.7) was compared for various values of patch size (L) and maximum search distance, s_{max}. A MatLab script was used to generate random intensity matrices to represent test and search patches. The CPU time required to evaluate the normalised correlation matrices, $R_n(\underline{s})$, using both direct and FFT methods, and the difference matrix, $D(\underline{s})$ was recorded. The test was run on a Pentium III (700 MHz) PC with 256 MB of RAM.

Patch size, L, was varied from 6 to 50 pixels. The difference in size between the test and search patches, $2s_{max}$, was varied from 1 to 25 pixels. Odd values of $2s_{max}$ are permitted since the random patches used in this test do not represent real test patches centred in a search with an equal search distance to either side. Surface plots of the CPU time required to evaluate 100 correlation matrices using each method are shown in Figure 3.8. Direct calculation of the absolute minimum difference is the slowest of the three algorithms (Figure 3.8a). The increase in calculation time with L^2 and s_{max}^2 when using

spatial convolution is evident in Figure 3.8b. The use of an FFT reduces computation time significantly (Figure 3.8c). The spiky variation with both patch and search zone size indicates the significant influence of the null-padding process. The algorithm is quickest for values of L and $L+s_{max}$ that are multiples of 2, and slowest when these dimensions are prime, or have high prime factors.

Figure 3.9 shows cross-sections through the surface plots of Figure 3.8 for values of L equal to 10, 20, 30, 40 and 50 pixels, allowing the speed of each algorithm to be compared directly. The FFT method is never slower than the other techniques. However, when analysing a very small test patch (e.g. 10 x 10 pixels), spatial cross-correlation is comparably fast. As the patch size increases to 50 x 50 pixels, the FFT method becomes an order of magnitude quicker. Also, when analysing a test patch of any size over a very small search range, s_{max}, (<2 pixels), the direct difference method is comparable to the FFT approach. As the search range increases to a more realistic 16 pixels (i.e. 8 pixels in either direction) the FFT method is an order of magnitude faster than direct difference calculation.

3.5.3.4 Sub-pixel interpolation

The matching algorithms described above provide a map of ‘degree of match’ over the chosen search zone, defined by the domain of $\underline{s}$. The highest peak of the map, i.e. the maximum value of $R_n(\underline{s})$ gives the displacement vector to single-pixel precision. Spline interpolation around this point of best match is used to assess the displacement to sub-pixel precision.

Cubic spline interpolation in one dimension corresponds to the fitting of a third-order polynomial to the interval *(i)* to *(i + 1)* in a discrete series. The coordinates at the nodes *(i - 1)* and *(i + 2)* are used to solve for the polynomial coefficients. Four nodes are required to solve for a unique third order polynomial. When applied to PIV, the spline must be fitted in two dimensions *(i, j)*, and five nodes are required in each dimension *((i - 2)* to *(i + 2))*. The extra node is necessary since the matrix $R_n(s)$ provides no indication of whether the sub-pixel maximum lies within the range *(i)* to *(i + 1)* or *(i)* to *(i - 1)*.

The peak of a typical normalised correlation matrix is shown in Figure 3.10, before and after sub-pixel interpolation. The spline is evaluated intervals of $1/100^{th}$ of a pixel. This interval is chosen to be smaller than the measured random errors in the PIV matching process, which are evaluated below (see Section 3.6.5).

3.6 PIV VALIDATION

3.6.1 Apparatus and procedure

A series of bench-scale experiments were conducted to assess the precision and reliability of the PIV algorithms written by the Author when measuring the displacement of small elements of soil. The experimental apparatus consists of a rigid brass container that translates along a track in an aluminium base plate. The brass container runs on PTFE guides, allowing smooth translation when pushed by a manual micrometer (Figure 3.11). This apparatus allows a non-deforming plane of soil to be translated horizontally beneath a rigidly fixed camera. Small known increments of movement are applied to the soil container via the micrometer and the resulting sequence of photos are analysed using PIV. The precision of PIV is evaluated by comparing the displacement vectors deduced from a grid of patches overlying the soil. Since the soil is translating as a rigid body, the displacement vectors should be identical. The entire apparatus was mounted on a vertically-translating calibration frame to allow the camera-object distance to be varied. The camera was mounted in a protective aluminium box and bolted to the translating plane of the frame.

All digital images were acquired using a Kodak DC280 camera. The field of view of the entire 1760 × 1168 pixel image was 176 mm × 117 mm which corresponds to a nominal object-space pixel size of 0.10 mm (Figure 3.12). This field of view was chosen to be similar to that used during the calibration chamber tests described in chapter 4. Three tests were conducted, each with a different subject in (or on) the translating container; sand, textured clay, and a calibrated photogrammetric target. The photogrammetric target consisted of a grid of black dots, which were used to represent typical markers used in target-based displacement measurement techniques.

3.6.2 PIV validation with sand

3.6.2.1 Procedure and analysis

Dog's Bay carbonate sand was used to test the precision of PIV for tracking the displacement of sand (Figure 3.12). Successive images were captured at nominal displacement increments of 20 μm (1/50th mm). These displacements are nominal since subsequent analysis of the images revealed that the increments were not equal in size. This discrepancy arose because the tip of the micrometer was slightly offset from the axis of rotation, and the contact point on the translating box was not perfectly normal to the axis of rotation. Hence, the changing point of contact created unequal displacement increments over part-rotations of the micrometer.

PIV analysis of image pairs separated by three different displacement increments is presented below. The influence of patch size on the measured displacements is examined. The three chosen displacement increments are 0-40 μm, 0-100 μm and 0-1 mm. These correspond to nominal image-space displacements of 0.4, 1 and 10 pixels, allowing the precision for both integer and sub-pixel increments to be assessed. The influence of patch size is examined by using square patches of side length 6, 8, 10, 16, 24, 32 and 50 pixels.

3.6.2.2 PIV results: small displacement increments

Figure 3.12 shows the extremes of patch size used in this analysis. In the case of 6 × 6 pixel patches, a grid of 88 × 30 patches overlie the tray of sand, each of object-space size of 0.6 mm × 0.6 mm. Using this patch size, an entire image from the DC280 camera can contain a total of 57,000 patches (grid size 293 × 194). The largest patch size (50 × 50 pixels) covers the soil with a grid of only 32 patches, and would fill the entire image using only 805 patches (grid size 35 × 23). Although this coarse grid contains two orders of magnitude less measurement points compared to 6 × 6 patches, the total number of measurement points is comparable to the maximum achievable using target markers (see Section 3.3.3.3). Comparison of Figures 3.13 and 3.5 reveals the differing texture present in small and large PIV patches.

The displacement vectors generated from PIV analysis over the 0–100 μm displacement increment of the patches shown in Figures 3.12 are shown in Figure 3.14, with a typical normalised correlation matrix. By collating the displacement vectors as histograms, the magnitude of random error can be seen. Figures 3.15 and 3.16 show the histograms of measured displacement for PIV analysis over a nominal 100 μm displacement (1 pixel) and 40 μm displacement (0.4 pixel) respectively.

It can be seen that the standard deviation of measured displacement decreases with increasing patch size. A comparison of the standard error for the 1 pixel and 0.4 pixel displacement increments reveals that the precision is reduced slightly by sub-pixel interpolation to a peak which is far from an integer value. White *et al.* (2001a) quote a standard error of 0.043 pixels for 10 × 10 pixel patches, based on early analysis of this data. Figure 3.15 indicates that this precision can be improved five-fold by increasing the patch size to 50 × 50 pixels. The variation of precision with patch size is shown in Figure 3.17. The selection of an optimum patch size is affected by two conflicting interests. Large patches offer improved precision. Small patches allow the image to contain a greater number of measurement points.

The selection of the most appropriate matching procedure is revisited at this point. Section 3.5.3.3 compared the relative computational demand of matching routines based on three different correlation techniques, concluding that a FFT method was the most economical. However, it was considered that different correlation procedures may produce different shaped correlation peaks, influencing the precision of the sub-pixel interpolation. The analyses presented in Figure 3.15 and 3.16 were repeated using the two slower matching algorithms. It was found that the mean and standard deviations in measured displacement were unchanged to two significant figures (<1% difference, <0.01 pixel). The results from spatial cross-correlation (Equation 3.2) were identical to the faster FFT method (to the precision of the CPU), indicating that the Fourier algorithm is exact.

3.6.2.3 PIV results: larger displacement increments

Analysis of the measured displacement vectors over the 0-1 mm (10 pixels) displacement increment using 32 × 32 pixel patches revealed a standard error of 0.0530 pixels. This compares unfavourably with the standard error of 0.0109 measured using identically-sized patches over a 1 pixel increment (Figure 3.15). What is the origin of this reduction in precision?

The measured displacement vectors from the 0-1 mm (10 pixel) increment are shown in Figure 3.18. Over this larger displacement increment a systematic variation in measured displacement from around 9.8 on the left side of the image to 9.95 pixels on the right side is evident. This is not a random error, and so is not associated with the PIV process. Instead it is a systematic ‘error’, and is associated with a variation in image scale (mm/pixel) across the image. If left uncorrected and differentiated, the displacement field shown in Figure 3.18 represents a tensile strain of (9.95-9.8)/500 = 0.03%.

Manual measurement of the image reveals that the marker dots on the right side of the image (labelled C and D in Figure 3.12) appear to be 1-2% further apart than those on the left side of the image (labelled A and B in Figure 3.12). By approximating this distortion as a linear variation across the image, an apparent difference in displacement measurement of 0.1-0.2 pixels over a 10 pixel increment would be expected, as is evident in Figure 3.18. Since the standard error for a data set evenly distributed between +/- x is 0.58 x, this image distortion contributes a standard error of 0.029-0.058 pixels to the distribution of displacements recorded over a 10 pixel increment. This range of systematic error, when added to the random PIV error of 0.0109, matches well with the measured standard deviation of 0.0530.

This systematic error due to distortion can be neglected when analysing the displacement measurements recorded over the single pixel increment since the corresponding systematic error of 0.0029-0.0058 pixels is small compared to the random PIV error shown in Figures 3.15 and 3.16.

3.6.2.4 Image distortion: spatial variation in image scale

The change in the image scale factor that relates distances within the image (measured in pixels) and actual distances on the object (measured in mm) is an important consideration. The object plane (containing the observed soil) and the image plane (the CCD within the camera) are not related by a linear scaling factor. For example, any non-coplanarity of the soil and the CCD creates a constantly varying scale across the image. This spatial variation in image scale is referred to as image distortion.

Could this non-coplanarity be avoided? The distortion discussed in Section 3.6.2.3 could be due to misalignment of the camera by around 1°. In the case of these simple validation tests, the calibration frame could have been rebuilt with adjustable 'yaw' of the translating table, allowing precise adjustment of the axis of the camera lens. This would allow the misalignment to be removed, with resulting images being free from distortion due to non-coplanarity. However, precise alignment to a tolerance of better than 1° cannot be relied upon when capturing images during an experiment. The flexible optics of consumer digital still cameras exhibit significant distortion under the influence of enhanced self-weight during centrifuge modelling. When tested under 100g, the Kodak DC215 camera exhibits an apparent CCD rotation of 3° (Take, 2002).

Furthermore, non-coplanarity is not the only source of image distortion. A number of other sources of distortion influence the scaling factor between the image and object planes. Image-based displacement measurement systems in geotechnical modelling usually overlook image distortion by assuming that the image scale factor is constant throughout the image. These PIV validation tests indicate that the improved precision over small displacement increments offered by PIV must be accompanied by some correction for image distortion if the measurements are to be extended to large displacements. The sources of image distortion are explored and analysed in Section 3.7, within the framework of close-range photogrammetry.

3.6.3 PIV validation with clay

3.6.3.1 Adding image texture to clay

Unlike images of sand, which have an inherent texture due to the light and darkness caused by shadows between grains the differing colour of the grains themselves, clay has no discernable texture. Histograms of the pixel intensity of 36 × 36 pixel patches of sand and clay are shown in Figure 3.19. A patch of kaolin clay contains negligible spatial variation in intensity (Figure 3.19a), preventing reliable correlation; the random variation in intensity recorded in consecutive digital images at a given pixel is of the same magnitude as the spatial variation in intensity. Hence, reliable correlation peaks cannot be obtained. In comparison, Figure 3.19b indicates that well-lit images of many grains of sand contain an intensity variation spanning around two-thirds of the pixel intensity range, with an apparently random spatial distribution. These image conditions lead to sharp correlation peaks, and the high precision reported in Section 3.6.2.

In order to create comparable texture within images of clay, the clay surface can be coated with coloured particles. Experiments were conducted using two marker materials: dyed sand and coloured 'flock', obtained from a model shop. The flock material can be dusted onto the wet clay surface and adheres easily. Figure 3.19c shows a 36 × 36 pixel patch of clay material including some pieces of coloured 'flock' material. The resulting intensity histogram covers a similar range of the spectrum as sand.

3.6.3.2 Validation data: thresholding to define texture (White *et al.*, 2001a)

The Author conducted a series of validation experiments using clay and flock material in collaboration with Mr W.A. Take, which are reported in White *et al.* (2001a). These experiments examine the ability of 'flock' material to provide sufficient texture to analyse images of clay using PIV. A light dusting of flock was applied to a sample of kaolin clay before translating the sample using the procedure described in Section 3.6.1. The density of the flock dusting was purposefully made lower than that required for each patch to contain texture. The comparison of displacement vectors recorded for patches with and without texture is shown in Figure 3.20. A patch was declared to

contain ‘texture’ if at least 10% of the pixels were significantly darker (i.e. 30 units of intensity) than the background (i.e. the mode of intensity).

Figure 3.20a shows the sample of kaolin with the textured patches highlighted; 124 of the 420 10 × 10 pixel patches contain texture. The measured displacement vectors for the textured patches are shown in Figure 3.20b. However, the histogram of measured displacement including all patches indicates that a significant number of ‘wild’ vectors were recorded (Figure 3.20c). These ‘wild’ vectors derive from patches being incorrectly identified in the subsequent image due to insufficient image texture. Removal of the untextured patches from this distribution leads to the sharper histogram shown in Figure 3.20d, which has a standard deviation of 0.076 pixels. This error is 0.03 pixels higher than for identically sized patches of sand, and indicates that a simple threshold criterion can be used to discard untextured patches, preventing the measurement of ‘wild’ vectors.

3.6.3.3 Subsequent analysis: larger patches

Subsequent analysis of the same images using 50 × 50 pixel patches has been conducted by the Author. A texture criterion is not necessary since all patches contain flock material. The standard deviation in measured displacement was 0.027 pixels, compared to 0.0088 for sand (Figure 3.15). It can be concluded that whilst flock material allows texture-based PIV analysis to be conducted on clay as well as sand, this particular validation test indicates that the precision is 2-3 hundredths of a pixel lower than in sand.

3.6.4 PIV validation with target markers

3.6.4.1 Photogrammetric target

Although the use of PIV eliminates the need for target markers to be placed within the deforming soil, the image should contain some stationary reference markers to allow soil movement to be isolated from movement of the camera. These reference markers can also be tracked by PIV.

A validation experiment was conducted to assess the relative precision of centroiding and PIV for detecting the movement of stationary reference targets. A 150 mm × 150 mm calibrated photogrammetric target consisting of three grids of 1.5 mm, 3 mm and 6 mm diameter reference dots was obtained from Edmund Industrial Optics, USA (Figure 3.21). These reference dots have a similar appearance to typical markers used in target-based displacement measurement techniques. Figure 3.19d shows the pixel intensity histogram of a 50 x 50 pixel patch containing a single reference dot.

3.6.4.2 PIV measurement of sub-pixel displacement

The target was attached to the translating table apparatus shown in Figure 3.11. A pair of images was obtained between which the table was translated by 0.45 pixels (≈ 45 μm). The performance of the PIV method in measuring the small displacement of each reference dot was compared with an area-based centroiding algorithm written by Mr W. A. Take. Figure 3.22 shows the distribution of displacement measurements for various different patch sizes. The trend of increasing precision with increasing patch size is once again evident, with the precision matching closely that obtained for sand (Section 3.6.2). There is no difference in measured displacement or precision when tracking the smaller reference dots in the centre of Figure 3.21. The only requirement for successful PIV measurement is that the patch size is greater than the diameter of the reference dot, to ensure that the patch contains some variation in intensity.

3.6.4.3 Centroid-based displacement measurement: sources of errors

In contrast to PIV, the precision of centroid-based measurement techniques is highly dependent on the size of the target marker. If the target marker contains only a few pixels, the location of the centroid is strongly influenced by the inclusion or exclusion of a single pixel close to the periphery of the marker. This can lead to a loss of precision as follows. Consider a stationary target marker of diameter 5 pixels. A small random change in the intensity recorded at a pixel close to the edge of a marker could take that pixel across the intensity threshold, leading to its inclusion or exclusion from the centroiding calculation. If the target marker has a diameter of 5 pixels, and hence

contains around 20 pixels, the loss of a peripheral pixel leads to a movement of the centroid by $1/20^{th}$ of the target radius, or 0.125 pixels.

Centre-weighted centroiding algorithms allow the influence of peripheral pixels to be reduced. The use of photo-reflective targets also reduces this source of error. By increasing the contrast in intensity between pixels that are 'in' the target marker and those that form the background, the likelihood of a pixel straying across the threshold between consecutive images is reduced. Chen *et al.* (1996) report a centre-weighted algorithm which exhibits a precision of 0.01 pixels when locating stationary photo-reflective target markers captured in consecutive video images under optimum lighting conditions. Photo-reflective target markers produce a bright white target on a black background. However, Chen *et al.* (1996) note that when locating black targets on a white background under the lighting conditions achievable during geotechnical modelling, the target location error is typically 0.3 pixels.

The errors described above, and quantified by Chen *et al.* (1996) arise even before any displacement of the target marker is considered. It should be clarified that the precision quoted by Chen *et al.* refers to the apparent displacement of a target marker that is actually stationary. This is different to the error in displacement measured for a marker that is in motion. Measurement of a moving marker will lead to a larger error since any sub-pixel movement of the target marker will change the intensity that will theoretically be recorded at each pixel location. In simple terms, a marker which neatly illuminates a 3 x 3 zone of pixels to the required threshold intensity must illuminate a 4 x 3 zone of pixels when translated horizontally by 0.5 pixels in order to record the correct displacement. Whether this occurs depends on the intensity of the background, and the location of the threshold.

3.6.4.4 Centroid-based displacement measurement: measured precision

Three sets of centroiding analysis were conducted on images of the photogrammetric target before and after a displacement of 0.45 pixels; one set of analysis for each size of reference dot. Figure 3.23 shows histograms of the measured displacement deduced by an area-based centroiding algorithm. A clear trend of increasing precision with

increasing target size is evident, although the measured standard deviation of 0.15-0.22 pixels lies above the error found using PIV.

3.6.4.5 Comparison of PIV and centroiding

The results for PIV and centroiding of target markers are combined in Figure 3.24. In order to compare the two methods, a common size axis has been chosen by equating PIV patch size with target marker size plus a border of 3 pixels on either side. This Figure demonstrates that PIV can be successfully used to measure target movement to a precision of almost an order of magnitude better than is achieved by the area-based centroiding algorithm. The use of large 50 x 50 pixel patches leads to a precision better than $1/60^{th}$ of a pixel, which represents $1/100{,}000^{th}$ of the field of view of a DC280 camera.

3.6.5 Summary: PIV precision

A series of validation tests has established the precision of PIV when observing sand, clay and target markers. The key conclusion is that precision is a strong function of PIV patch size, and a weak function of object texture. Smaller random errors are present over integer-pixel displacement steps compared to sub-pixel steps. The results are summarised in Figure 3.17. In addition to the ability to track soil elements without the requirement to add markers, a comparison with an area-based centroiding method shows that PIV offers improved precision over centroiding when tracking discrete target markers.

To obtain an estimate of the precision of PIV prior to conducting an analysis, a simple relationship between patch size and precision can be deduced from Figure 3.17. By combining this relationship with the width of the field of view in image and object space (pixels and mm) the precision of PIV analysis can be predicted using Equations 3.8 and 3.9. Equation 3.8 represents an upper bound estimate of the standard error in image space, ρ_{pixels}, from the chosen patch size, L (pixels), and is shown on Figure 3.17. Equation 3.8 can be extended to an estimate of the standard error in object space, ρ_{mm} by introducing the field of view width in pixels, W_{pixels}, and millimetres, W_{mm} (Equation 3.9). This approximation ignores any change in scale across the image. It should be

noted that Equations 3.8 and 3.9 are merely fitted to Figure 3.24 and are therefore only valid over the range L = 6-50 pixels.

$$\rho_{pixel} = \left(\frac{0.6}{L}\right) + \left(\frac{150000}{L^8}\right) \tag{3.8}$$

$$\rho_{mm} = \frac{\rho_{pixel} \times W_{mm}}{W_{pixel}} = \left(\frac{W_{mm}}{W_{pixel}}\right) \times \left[\left(\frac{0.6}{L}\right) + \left(\frac{150000}{L^8}\right)\right] \tag{3.9}$$

Equation 3.9 indicates that the normalised precision, ρ_{mm}/W_{mm}, of small-displacement image-space movement data gathered using PIV and images from the DC280 camera (W_{pixel} = 1768) with 50 x 50 pixel patches is 1/150000th. Using this size of patch, an image can contain over 800 data points. This precision is a 30 times improvement over the state-of-the-art described in Section 3.3.4. If the goal is to obtain displacement data at the maximum number of locations within the image, 8 x 8 pixel patches could be used. The corresponding precision is 1/21000th, using a grid of 220 x 144 = 31000 patches. This arrangement offers a 30 times increase in the number of measurement points, and a fourfold increase in precision, compared to the state-of-the-art.

It should be noted that the above precision refers to a single increment of displacement. If patches are tracked through a sequence of images, with the displaced coordinates of one increment forming the initial coordinates of the next increment, the precision error of each step must be summed to find the total error in the displaced coordinates in the final image. Since this error is a random walk, the precision quoted in Equation 3.9 must be multiplied by $\sqrt{n}$ where n is the number of displacement increments (Appendix 3).

3.6.6 Application to element testing

Although the PIV software described above was developed primarily for model testing, the technique can equally be applied to element testing. Working with Dr S Munachen, the Author examined the feasibility of measuring the deformation of a triaxial sample during testing using PIV.

Figure 3.25 shows a typical image of a 40 mm ‘gauge length’ of triaxial sample within a textured membrane, obtained during a compression test on a dry sample under vacuum. The vector field in Figure 3.25 shows 1100 displacement vectors and was obtained during a top platen movement of 50 mm. This boundary displacement matches closely with the vertical component of the displacement vectors at sample mid-height, which measure a nominal 24 mm. Measurement noise of around 3 μm is evident, which corresponds to a strain of 0.01%, and is in agreement with the system precision given in Section 3.6.5.

This use of PIV in element testing allows local strain measurement without requiring on-sample instrumentation. Since the system can obtain displacement measurements at multiple locations, it can be used to examine the onset and evolution of non-homogenous deformations.

3.7 CLOSE RANGE PHOTOGRAMMETRY

3.7.1 Image distortion

3.7.1.1 Is camera calibration necessary?

Section 3.6.2.3 noted that a spatial variation in image scale is revealed over large displacement steps. This spatial variation in image scale leads to errors if the displacement vectors measured by PIV are converted from image-space (pixels) into object-space (mm) using a single scaling factor. Most previous geotechnical researchers, with the notable exceptions of Taylor *et al.* (1998) and Ethrog (1994), have overlooked image distortion, assuming that the image scale factor is constant throughout the image. This approach is perhaps justified given that the image-scale displacement data is typically plotted to a strain precision of 1%. The image distortion reported in Section 3.6.2.3 created an apparent strain of less than 0.1%.

However, noting that the validation tests reported in Section 3.6 demonstrate an order-of-magnitude increase in image-space measurement precision, PIV must be accompanied by some correction for image distortion if the improved precision is to be

exploited. The process of correcting for image distortion is known as camera calibration. Instead of the straightforward single scaling factor to link pixel *(u,v)* and object-space *(X)* coordinates, a mathematical framework is used to describe the transformation $(u,v) \Rightarrow \underline{x} \Rightarrow \underline{X}$ (Figure 3.26a).

This mathematical framework is based on the principles of close-range photogrammetry, and accounts for a number of sources of image distortion. These sources are described below.

3.7.1.2 Non-coplanarity

The non-coplanarity noted in Section 3.6.2.3 is illustrated schematically in Figure 3.26b. The coordinate systems of the CCD and the object plane are rotated relative to each other by the Euler angles θ, ϕ and φ, such that the normals to the image and object planes are not parallel. Take (2002) reports that the enhanced self weight of a typical digital still camera during centrifuge testing at 100g leads to an apparent 3° rotation of the CCD. Even without centrifuge acceleration, precise alignment of the CCD and object plane is difficult, perhaps leading to the 1-2% spatial variation in image scale observed in Section 3.6.2.3.

3.7.1.3 Radial and tangential lens distortion

The pinhole camera model, signified in Figure 3.26a by the bundle of light rays passing straight through a single point to form a perspective projection of the object on the camera CCD, is an approximation. Radial lens distortion causes the light ray to be deflected radially from the normal to the lens (Slama, 1980). This distortion is depicted in Figure 3.26c, and is commonly known as fisheye.

A second error arises since the centres of curvature of the lens surfaces through which the light is refracted are not always perfectly collinear. This is particularly the case for cameras with optical systems that contain multiple lenses. This creates decentring distortion, which has both a radial and a tangential distortion component (Slama, 1980). The tangential component is commonly known as barrelling (Figure 3.26c).

3.7.1.4 CCD non-squareness

A further source of variation in image scale is the non-squareness of CCD pixels (Figure 3.26d). Although small, this error is a linear scaling factor, and so can be easily incorporated into the transformation from pixel coordinates to image space coordinates. The aspect ratio, α, is defined as the height of a pixel divided by the width, and is typically in the range 1 ± 0.004 (Heikkila & Silven, 1998; Ahmad & Chandler, 1999), and is considered to be constant over the CCD.

3.7.1.5 Refraction through a viewing window

A further variation in image scale arises when the object is behind a viewing window, causing the light rays to be refracted. An apparent change in object size arises, as shown in Figure 3.26e. This apparent scaling depends on the thickness and refractive index of the window, which do not vary across the image, and the inclination of the rays to the normal of the window, which does vary across the image. Snell's Law is used to model refraction.

3.7.2 Camera calibration: the image- to object-space transformation

3.7.2.1 Perspective projection

A pinhole camera model is used to convert between the object-space $(\underline{X})$ and image-space $(\underline{x})$ reference frames and model the reduction in scale through perspective projection, allowing variations in image scale due to non-coplanarity to be accounted for. The location and orientation of these reference frames are shown in Figure 3.27a. The pinhole model is based on the principle of collinearity, in which each point in object-space is projected by a straight line through the projection centre into the image plane. The image-space coordinate system has its origin at the projective centre, the *z*-axis is aligned with the optical axis, and the *x* and *y* directions coincide with the CCD array axes.

The transformation between reference frames is described by a 6 degree of freedom rigid-body rotation and translation (Figure 3.27a). The rotation is defined by the three Euler angles of rotation θ, ϕ and φ, but can be expressed as a 3 x 3 matrix to allow

multiplicative transformation between reference frames. The translation between the origin of the two reference frames is defined by the vector $\underline{t}$ in the image space coordinate system.

Homogenous coordinates are created by adding a fourth cell equal to unity to the object space position vector, $\underline{X}$. The use of homogenous coordinates allows the transformation to image-space to be carried out purely by matrix multiplication. The alternative is to use multiplication to carry out the rotation, then add the translation component. The 6 degree-of-freedom rotation and translation is described by the matrix P_R (Equation 3.10). The nine elements which comprise the rotation portion of matrix P_R are not independent, but can be reduced to the three Euler angles of rotation.

$$\underline{x} = P_R \underline{X} = \begin{bmatrix} 3x3 rotation & \underline{t} \end{bmatrix} \underline{X} = \begin{bmatrix} r_{11} & r_{12} & r_{13} & t_x \\ r_{21} & r_{22} & r_{23} & t_y \\ r_{31} & r_{32} & r_{33} & t_z \end{bmatrix} \begin{bmatrix} X \\ Y \\ Z \\ 1 \end{bmatrix} \tag{3.10}$$

Since the image-space coordinate system is centred on the projective centre, the scaling transformation from the object to image plane is represented by the ratio f / z. In other words, using the pinhole model and comparing similar triangles, an object point located at (x, y, z) will be projected onto the point in the CCD plane with the coordinates $(fx / z, fy / z, -f)$ (Figure 3.27a).

Hence, the projection of an image point, (x, y, z) onto the image plane (x_{CCD}, y_{CCD}) can be found using Equation 3.11 (Figure 3.27b). A further transformation is required to convert these space coordinates into pixel coordinates, taking account of the offset of the principal point from the origin of the CCD array (Equation 3.12, Figure 3.27b). This transformation uses the pixel height and width, D_v and D_u, which are related by the pixel aspect ratio α (Figure 3.26d). Also required are the coordinates of the principal point, (u_o, v_o) defined as shown in Figure 3.27b.

$$\begin{bmatrix} x_{CCD} \\ y_{CCD} \end{bmatrix} = \frac{f}{z}\begin{bmatrix} x \\ y \end{bmatrix} \tag{3.11}$$

$$\begin{bmatrix} u \\ v \end{bmatrix} = \begin{bmatrix} \frac{1}{D_u} & 0 & u_0 \\ 0 & \frac{1}{D_v} & v_0 \end{bmatrix}\begin{bmatrix} x_{CCD} \\ y_{CCD} \\ 1 \end{bmatrix} \tag{3.12}$$

Equations 3.11 and 3.12 can be combined to link image-space coordinates, $\underline{x}$, with scaled pixel coordinates, $\underline{w}$ by defining the perspective projection matrix, P_P, and the CCD calibration matrix, P_C (Equation 3.13). Note that the pixel coordinate scale factor, μ, is equal to the z coordinate of the object point. This scaling factor exists because there is not a single solution to convert from two-dimensional pixel-coordinates *(u,v)* to three-dimensional space coordinates *(x, y, z)*. Similar but scaled objects located at different ranges along the optical axis appear identical.

$$\underline{w} = \begin{bmatrix} \mu u \\ \mu v \\ \mu \end{bmatrix} = P_C P_P \underline{x} = \begin{bmatrix} \frac{1}{D_u} & 0 & u_0 \\ 0 & \frac{1}{D_v} & v_0 \\ 0 & 0 & 1 \end{bmatrix}\begin{bmatrix} f & 0 & 0 \\ 0 & f & 0 \\ 0 & 0 & 1 \end{bmatrix}\underline{x} \tag{3.13}$$

Equation 3.13 introduces a further five parameters, although D_u and D_v are linked by aspect ratio, α. However, these parameters are not wholly independent since the perspective projection can be scaled arbitrarily. A doubling of f is equivalent to a halving of the pixel dimensions, D_u, D_v. Also, if the object and image planes are approximately collinear, any scaling in f has the same effect as a scaling of t_z. Hence, although the matrices P_R, P_P and P_C contain a total of 11 physical parameters, only 10 are independent. Multiple solutions of the 11 parameters can define the same image- to object-space transformation, with only an arbitrary scaling difference in the pinhole model.

3.7.2.2 Non-linear lens distortion

The pinhole camera model described above is not adequate when high accuracy is required. The lens systems of short focal length cameras suffer from radial lens distortion, which has the effect of deflecting the light ray radially from the principal point. The resulting additional component of the image plane position vector *(x_{CCD}, y_{CCD})* can be calculated using Equations 3.14 and 3.15, by introducing radial distortion coefficients k_1 and k_2 (Slama, 1980).

$$r = \sqrt{{x_{CCD}}^2 + {y_{CCD}}^2} \tag{3.14}$$

$$\begin{bmatrix} \delta x_{CCD}^{\ radial} \\ \delta y_{CCD}^{\ radial} \end{bmatrix} = \begin{bmatrix} x_{CCD}(k_1 r^2 + k_2 r^4) \\ y_{CCD}(k_1 r^2 + k_2 r^4) \end{bmatrix} \tag{3.15}$$

Tangential lens distortion, which leads to barrelling, can be modelled in a similar fashion, by introducing tangential distortion coefficients p_1 and p_2 (Slama, 1980; Equation 3.16).

$$\begin{bmatrix} \delta x_{CCD}^{\ \tan gential} \\ \delta y_{CCD}^{\ \tan gential} \end{bmatrix} = \begin{bmatrix} 2p_1 x_{CCD} y_{CCD} + p_2(r^2 + 2x_{CCD} r^2) \\ p_1(r^2 + 2y_{CCD} r^2) + 2p_2 x_{CCD} y_{CCD} \end{bmatrix} \tag{3.16}$$

These models for lens distortion introduce a further four independent parameters, and make the image- to object-space transformation non-linear. As a result, direct solution is not possible, and an iterative method is required.

3.7.2.3 Refraction

The calibration chamber described in chapter 4 features a double-layer viewing window consisting of a thick Perspex window in front of a thin sheet of glass. The effect of refraction is to make an object point appear radially further from the point in the window defined as the source of the normal that intersects the projection centre (point A in Figure 3.27c). This refractive distortion is accounted for by defining an additional radial displacement vector in object space coordinates (Equation 3.17), which is added to the object-space coordinates. This has the effect of moving the object point radially

between its actual position to the position at which it appears to be, to account for the influence of refraction on the object-space to image-space transformation.

Snell's Law is used to model refraction (Equation 3.18). For the case of a single-layer window, the scaling component λ is can be found by combining the geometry shown in Figure 3.27c with Snell's Law (Equation 3.19). A more complex expression has been derived in the same manner for two-layer windows (Figure 3.27, Equations 3.20, 3.21). This correction vector introduces two new independent parameters; thickness, *t* and refractive index, *n* (four parameters are used in the case of a double-layer window).

Equations 3.17-3.21 describe the construction of $\delta R^{refraction}$ for the conversion of an object point (i.e. a measured PIV patch location) from its apparent position, to the actual position; in this case $\underline{R}_{apparent}$ is known and $\underline{R}_{actual}$ is required (see Figure 3.27 for notation). A similar geometric construction is used for the reverse step, in which $\underline{R}_{actual}$ is known and $\underline{R}_{apparent}$ is required. This reverse construction is used when translating a control point from its known actual location, to its apparent position.

$$\delta \underline{R}^{refraction} = \begin{bmatrix} \delta X^{refraction} \\ \delta Y^{refraction} \end{bmatrix} = \lambda \begin{bmatrix} X_{apparent} - X_A \\ Y_{apparent} - Y_A \end{bmatrix} \tag{3.17}$$

$$\sin\alpha = n \sin\beta \tag{3.18}$$

$$\lambda = -\frac{t}{H} + \frac{t}{\sqrt{n^2\left(H^2 + \left|\underline{R}_{apparent} - \underline{R}_A\right|^2\right) - \left|\underline{R}_{apparent} - \underline{R}_A\right|^2}} \tag{3.19}$$

$$\lambda = -\frac{t_1 + t_2}{H} + \frac{t_1}{\left|\underline{R}_{apparent} - \underline{R}_A\right| \cot\beta_1} + \frac{t_2}{\left|\underline{R}_{apparent} - \underline{R}_A\right| \sqrt{n_2^2\left(\cot^2\beta_1 + 1\right) - 1}} \tag{3.20}$$

$$\cot\beta_1 = \sqrt{n_1^2\left(\frac{H^2}{\left|\underline{R}_{apparent} - \underline{R}_A\right|^2} + 1\right) - 1} \tag{3.21}$$

3.7.2.4 Stability of transformation parameters

Sections 3.7.2.1-3.7.2.3 introduce a mathematical framework in which a total of 16 independent parameters are used to describe the transformation from object-space to pixel coordinates. This transformation can be used to:

1) deduce the 16 independent transformation parameters if both the object-space and pixel coordinates of a set of image points are known.
2) deduce the object-space coordinates of a set of image points if the pixel coordinates and transformation parameters are known.
3) deduce the pixel coordinates of a set of image points if the object-space coordinates and transformation parameters are known.

In the case of geotechnical modelling, the task is to convert pixel coordinates (in this case, measured using PIV) into object space coordinates; task 2. However, this can only be carried out if the transformation parameters are known. Hence, task 1 must first be carried out, using a set of control points whose object-space coordinates are precisely known, to solve for the transformation parameters. Task 3 is what a camera does.

Transformation parameters which do not vary over time, or when the camera is moved between viewing positions, can be found during a single calibration experiment, and held constant. Taylor *et al.* (1998) report that the intrinsic parameters $(u_0, v_0, \alpha, f, k_1, k_2, p_1, p_2)$ of an analogue video camera do not vary during centrifuge testing to 100g. However, Take (2002) reports that significant changes in the internal geometry of the Kodak DC280 occur during centrifuge testing. Whilst the analogue video cameras used by Taylor *et al.* have no moving lens parts, the flexible lens system of a digital still camera leads to changes in the intrinsic parameters. Furthermore, the 6 extrinsic parameters relating to the camera pose (contained in the matrix P_R) will also change if the camera distorts and rotates during a centrifuge test.

During 1-g testing the extrinsic parameters may change if the camera is accidentally disturbed during testing, and both the intrinsic and extrinsic parameters may change during long tests under hot lighting conditions due to contraction and expansion of the

apparatus. Hence, throughout this research, all transformation parameters are deduced from images captured during model testing. The only parameters that are held fixed are those relating to refraction.

The procedure used to convert a fine mesh of pixel coordinate points found from PIV analysis into object-space coordinates is as follows:

1) The pixel coordinates of a small number of control points, whose object-space coordinates (relative only to each other) have been deduced prior to the experiment, are identified.
2) These coordinates are used to solve for the transformation parameters.
3) The deduced transformation parameters are used to convert the pixel coordinates of the PIV measurement points into object-space coordinates.

3.7.2.5 Control points

An array of 15-20 control points was installed in each window of the calibration chamber to allow the transformation parameters to be deduced from each image. The control points consisted of 1.8 mm diameter black dots laser printed onto an overhead transparency. After adding a square patch of white correction fluid, the resulting control point had dimensions of approximately 3 mm square, occupying a nominal 25 x 25 pixel zone in image space. The overhead transparency was installed between the Perspex and glass layers of the window. The control points are distributed throughout the field of view, to ensure that the deduced parameters represent a good fit for the entire image.

The dimensional accuracy of laser printing is lower than required for satisfactory calibration. The as-printed dimensions of each overhead transparency were found by photographing the transparency whilst overlain on the calibrated photogrammetric target (Figure 3.21). By calibrating this photograph using the calibrated target to provide control points, the location of each laser printed control point was found to the accuracy of the target.

Since all the control points are coplanar, accurate depth information cannot be obtained. The perspective distance cannot be deduced, and hence multiple solutions to the pinhole model with arbitrary image scaling are possible. This does not affect the precision of the image- to object-space transformation. However, precise determination of the physically-significant camera parameters is prevented; an incorrectly estimated perspective projection will influence the corresponding non-linear distortion parameters.

3.7.2.6 Matrix solution method and iterative procedure

Since the refraction and lens distortion models contain non-linear components, an iterative solution procedure is necessary. The iterative process of deducing the transformation parameters is shown on the left hand side of Figure 3.29. The input data consists of the known object-space and measured image-space coordinates of the control points.

The optimisation stage uses algorithms described by Heikkila & Silven (1996) and published electronically by Heikkila (1998). A first estimate of the linear parameters is made using a Direct Linear Transformation (Abdel-Aziz & Karara, 1971). These parameters are used as initial values for a non-linear optimisation using the Levenberg-Marquardt method. After a first optimisation of the transformation, refraction is considered. The first-estimate parameters allow the correction vector $\delta R^{refraction}$ to be evaluated, and the object-space control points shifted from their actual location to their apparent location. This method of 'hiding' the refractive effect allows the optimisation to be repeated, using data that is unpolluted by refraction. Improved transformation parameters are found, and the iteration is repeated sufficient for steady values to be achieved.

Having deduced the transformation parameters, the image-space data points produced from PIV analysis are converted into object-space following the steps shown on the right hand side of Figure 3.29. The non-linear distortion is back-calculated using the reconstruction algorithm published electronically by Heikkila (1998).

3.8 CAMERA CALIBRATION: VALIDATION

3.8.1 Validation methodology

3.8.1.1 Conventional methods of assessing accuracy and precision

The camera calibration scheme described in Section 3.7 has been validated as follows. Validation considers two aspects of performance: *accuracy* and *precision*. Accuracy is defined as the systematic difference between the coordinates of an object as predicted through camera calibration, and the true coordinates of that object. Precision, or repeatability, is defined as the random difference between multiple measurements of the same object.

The accuracy and precision of a photogrammetric camera calibration system is often assessed using self-calibrating bundle adjustment (eg. Ahmad & Chandler, 1999; Taylor *et al.*, 1998). This procedure involves the photography of a 3-dimensional array of targets, whose true coordinates are known, from many angles. After extraction of the image coordinates of each target, the camera calibration parameters are deduced by combining this image-space information from each photograph. The known true object-space coordinates of the target array are not used during the calibration process.

On completing the calibration, the precision of the calibration procedure is found from the variation in object-space target coordinates predicted from each image. Accuracy is assessed by comparing the true and the mean predicted object-space coordinates. Both precision and accuracy are expressed as a fraction of the field of view.

3.8.1.2 Accuracy in geotechnical modelling

In this application, a different validation approach has been used for the following reasons. Self-calibrating bundle adjustment measures the accuracy of the camera calibration transformation only at the location of each target. The fit of the image-space to object-space transformation is only assessed at the measurement points from which the fit was deduced. A more arduous test of a camera calibration routine is to compare the true and predicted coordinates of targets that were *not* used to generate the

transformation. This test is particularly relevant for this application, since the camera calibration routine is used to convert PIV coordinates from image-space to object-space. These PIV coordinates are spread throughout the entire image. In contrast, most photogrammetric applications are designed to extract the object-space coordinates of targets that have been observed in multiple images.

Geotechnical modellers usually have only a single image of the object of interest. Even if multiple images were available, a multiple-image calibration procedure could not be used in combination with PIV data since this consists of a grid of patches that are defined in image-space, rather than being tied to a particular target in object-space.

Hence a single-image approach is used in this validation exercise. Accuracy, defined as the difference between predicted and true coordinates, is evaluated as the difference between the true and reconstructed coordinates of a grid of simulated 'PIV data points'. These are not actual PIV data points, but a grid of dots on a calibrated target. This procedure is described in Section 3.8.2.1.

3.8.1.3 Precision in geotechnical modelling

In conventional photogrammetric applications, the random errors from which precision is determined arise from multiple predictions of object-space target coordinates derived from multiple images of the same target. However, such a measurement is not relevant to the type of geotechnical modelling under consideration here since each target is observed from only one viewpoint. Multiple predictions of target coordinates arise from images taken at different points in time, rather than different points in space. It is therefore this variation in target location over time, i.e. through a sequence of images taken from the same location, that offers a relevant measurement of camera calibration precision.

These twin definitions of accuracy and precision can be expressed simply as follows. During an experiment, the task is to measure the displacement of a point of interest in a plane of soil. Accuracy indicates the possible error in the recorded location of that point

of interest at the start of the experiment. Precision indicates the possible error in the recorded movement of that point during the experiment.

3.8.2 Evaluation of accuracy

3.8.2.1 Methodology: reconstruction of unknown points

During a typical experiment, the field of view contains a number of target markers sufficient to deduce the transformation (see Section 3.7.2.5). The resulting transformation is then used to convert the image-space coordinates of a grid of PIV points into object-space. The accuracy of the camera calibration routine is equal to the difference between these predicted object-space coordinates and their true values.

To measure this difference, the calibrated photogrammetric target described in Section 3.6.4.1 was used. This target was mounted on the test frame shown in Figure 3.11 and photographed with and without a 50 mm thick block of Perspex on top. The image-space location of each 3 mm x 3 mm dot was found using an area-based centroiding method. A subset of 14 of these dots spread throughout the image was used to deduce the camera calibration parameters. These parameters were used to reconstruct the object-space coordinates of the remaining 362 dots. The discrepancy between these predicted coordinates and the true coordinates indicates the accuracy of the calibration routine.

3.8.2.2 Results: camera calibration

Figure 3.30a shows the grid of measured dots, and the discrepancy vectors between the predicted and true object-space coordinates. The mean of these discrepancy vectors is 0.0 μm, with a standard deviation of 13.3 μm, representing a normalised STD error of $1/18000^{th}$ of the field of view (Figure 3.31a).

It is surprising that the magnitude and direction of these discrepancy vectors are randomly distributed. Since the true image-space to object-space transformation is a smooth continuous function, any error in the deduced transformation parameters would be revealed by systematic spatial variation in discrepancy vector.

The random distribution of discrepancy vectors is evidence that these vectors are governed by the precision of either the image-space or object-space target coordinates used this validation, rather than the accuracy of the transformation between these measurements. So, perhaps the precision of the target coordinates used to generate the transformation is worse than the transformation itself?

The object-space target locations are certified to an *accuracy* of 0.2 mm over the 212 mm corner-to-corner dimension of the target grid (calibration certificate SN0000-0038, Max Levy Autograph Inc, Philadelphia). No value for the *precision* of each dot location within the target grid is given. Whilst this accuracy is much worse than the measured STD error, the likely source of a reduction in accuracy is shrinkage or swelling of the entire target grid, which would lead to a systematic error distribution, rather than the random error shown in Figure 3.30a.

The image-space target locations were derived by an area-based centroiding method with a precision of around 0.1 pixels. When normalised, this precision represents $1/17600^{th}$ of the field of view. This value is remarkably similar to the STD error of the reconstructed dots.

The above analysis was repeated for the grid of smaller dots in the centre of the calibration target. Centroiding methods offer a lower precision when locating smaller dots (Chen *et al.*, 1998). An increase in the magnitude of discrepancy vectors was found, indicating that the performance of the calibration routine is dependent on the precision of the image-space target coordinates.

It is clear that the accuracy of the calibration routine itself is higher than can be assessed using this method. Instead, the accuracy of any object-space measurements deduced from PIV image-space data depends on the precision of the method used to find the image-space coordinates of the target markers from which the transformation parameters are solved.

3.8.2.3 Results: camera calibration with refraction

The reconstruction described above was repeated for an image of the target viewed through a 50mm thick block of Perspex (Figure 3.31c). The discrepancy vectors again had a random spatial distribution, with a slightly increased standard error of 14.5 μm, which corresponds to a normalised error of 1/16500th of the field of view.

3.8.2.4 Results: linear scaling

To quantify the accuracy of linear scaling, a similar reconstruction exercise was carried out using a single scale factor for the image-space to object-space transformation, as is conventionally used in geotechnical modelling. The performance of linear scaling in this validation is likely to be better than during an actual experiment for the following reasons.

Firstly, the linear scaling factor was optimised by selecting the value for which the sum of the discrepancy vectors is equal to zero. All 376 dots were measured in image-space, with the origin of the image-space and object-space coordinate systems located at the centroid of the same dot. An optimisation that varied both the linear scaling factor, and the relative rotation of the two coordinate systems was carried out.

Secondly, every effort was made to ensure that the CCD and target were coplanar, removing one source of image distortion. In a real experiment this coplanarity is more difficult to ensure, particularly under centrifuge conditions.

The resulting discrepancy vectors are shown in Figure 3.30b. The continuous spatial variation in direction and magnitude of these vectors is indicative of a systematic error. The standard deviation of these discrepancy vectors is 107.6 μm (1/2230th of the field of view). This error is almost an order of magnitude higher than that obtained using camera calibration (Figure 3.31b) and is systematic, and hence due to the accuracy of the transformation rather than the precision of the target location method.

The true spatial variation in image scale over the image of the photogrammetric target has been found by using the transformation parameters to reconstruct a fine mesh of

equally-spaced image-space points spread throughout the entire image. The image scale at a given point in the image is found by comparing the image- and object- space coordinates of this mesh. The resulting spatial variation in horizontal and vertical image scale is shown in Figure 3.32. The optimum linear scale factor of 7.374 is exceeded by ±1% at the extremities of the dot array.

3.8.3 Evaluation of precision

The experimental methodology for the use of control markers to deduce camera calibration parameters on an image-by-image basis is as follows. At the start of the experiment, the image-space location of each control marker is found by performing centroiding analysis on the first image of the experimental sequence. In subsequent images, the location of each control marker is found by comparing that image with the initial image using PIV. Therefore, the magnitude of any random changes in the image-space location of the control markers, and therefore the camera calibration transformation parameters, is governed by the precision of PIV (Equations 3.8, 3.9). The precision of PIV when tracking markers is assessed in Section 3.6.4.

In fact, the magnitude of a random error in the location of a control point represents the *maximum* erroneous apparent movement of a reconstructed PIV data point. This can be illustrated by considering the effect of randomly moving the image-space location of a single control point (Figure 3.33). This random movement will be accounted for in the camera calibration routine by a change in the non-linear transformation, illustrated by the red and green networks in Figure 3.33. This change in transformation will cause the apparent movement of an otherwise stationary PIV datapoint. This movement will be equal to, or less than, the random movement of the control point.

3.8.4 Summary: Camera calibration

In conclusion, it has been found that a rigorous calibration procedure for the pixel coordinate to object-space transformation is essential if the high precision available from PIV measurement is to be exploited over large displacement increments. The non-coplanarity of the CCD and the soil plane, coupled with the radial and tangential lens

distortion present in short focal-length optics, leads to a variation in image scale across the image.

If the parameters governing the non-linear image-space to object-space transformation are likely to vary during the course of an experiment it is necessary to calibrate every image. This is particularly the case for experiments that have a long duration during which camera temperature or pose may change, or which take place under centrifuge conditions. Calibration of each image can be carried out if the field of view contains a number of control points whose object-space coordinates are accurately known.

By measuring the image-space positions of these control points, the parameters which describe the image-space to object-space transformation can be deduced, and a fine mesh of PIV data points reconstructed. The calibration routine developed in this research uses a total of 14 parameters to describe the object-space to image-space transformation, with two further parameters introduced for each refractive layer between object and camera.

The accuracy and precision of the calibration routine was evaluated through the reconstruction of an array of dots on a calibrated photogrammetric target. The accuracy of the calibration routine was shown to be greater than the precision of the centroiding procedure used to determine the image-space coordinates of the control points. Hence, the weakest link in the calibration procedure is the precision of the method used to locate the control points. Therefore, a conservative estimate of the accuracy of the pixel coordinate to object-space transformation is the random error found during target reconstruction, which was $1/18000^{th}$ of the field of view.

The precision of the calibration procedure was evaluated by considering the random error introduced when calibrating a sequence of images. Since the control points are tracked using PIV, it is argued that the precision of the calibration routine derives from random errors in the location of the control points when tracked using PIV. The control points used in this validation exercise are covered by PIV patches of dimensions 25 x

25 pixels, leading to a normalised precision of 1/73000th of the field of view (Equation 3.8).

It should be noted that this validation data applies only to the particular geometric conditions under which these tests were carried out. The performance of the calibration routine may be different if the camera is oblique to the target, if a different type of camera is used, or if the field of view or lighting conditions are significantly changed. The camera type, camera-object distance and lighting conditions during this validation were chosen to be similar to the calibration chamber testing reported in chapter 4.

3.9 OVERALL SYSTEM PERFORMANCE

The overall precision of the system can been found by combining the errors, expressed as a fraction of the field of view, accrued during the image measurement and calibration stages. The PIV measurement precision is a strong function of the PIV patch size. This relationship is indicated on Figure 3.17 and can be conservatively predicted using Equation 3.8. The precision of the camera calibration procedure is equal to the precision of the PIV method used to follow the control points. Geometric summation of precision errors of the PIV and camera calibration stages is required to find the overall system precision, $\rho_{system,mm}$. Since the precision of the camera calibration stage is equal to the precision of the PIV tracking of the control points, an extended version of Equation 3.9 can be used to predict $\rho_{system,mm}$ by including the control point patch size, L_{CTRL} (Equation 3.22).

$$\rho_{system,mm} = \left(\frac{W_{mm}}{W_{pixel}}\right) \times \sqrt{\left[\left(\frac{0.6}{L}\right) + \left(\frac{150000}{L^8}\right)\right]^2 + \left[\left(\frac{0.6}{L_{CTRL}}\right) + \left(\frac{150000}{L_{CTRL}{}^8}\right)\right]^2} \qquad (3.22)$$

Table 3.1 compares the accuracy and precision of this system with various other published techniques. Two levels of PIV patch size have been quoted. It should be noted that most previous authors have not drawn a distinction between accuracy and precision. In this case, the performance has been described in Table 3.1 as ‘resolution’. Also, those systems that use linear scaling suffer from a systematic loss of accuracy of

the kind demonstrated in Section 3.8.2.4. No Authors who use linear scaling have reported any investigation into this possibility.

Reference	*Capture method*	*Analysis method*	*Calibration method*
This work. 10 x 10 patches	Digital still	PIV	Close range Photogrammetry
Taylor *et al.* 1998	Video	Auto centroiding	Close range Photogrammetry
Allersma *et al.*, 1994	Video	Manual target digitising	Linear scaling
Phillips, 1991	Film	Auto target recognition	Linear scaling
Obaidat *et al.*, 1998	Video	Manual digitising	Close range photogrammetry
Saada *et al.*, 1999	Video	Manual digitising	Linear scaling
Andrawes *et al.* 1973	Film	Manual measurement	Linear scaling

Reference	*Measurements per image*	*Quoted performance*	*Normalised Performance*
This work. Patch size, L= 8 L_{CTRL} = 25	31000	Accuracy[1] = 16.7 μm Precision[1] = 14.9 μm	<1/18000 1/20000
Patch size, L= 50 L_{CTRL} = 25	805	Accuracy[1] = 16.7 μm Precision[1] = 4.6 μm	<1/18000 1/65000
Taylor *et al.* 1998	≈ 625	Accuracy = 60 μm Precision[2] = 50-80 μm	1/5600 1/6720-1/4200
Allersma *et al.*, 1994	≈ 300	Resolution = 200 μm	1/500
Phillips, 1991	≈ 1000	Precision = 5 μm	1/10000
Obaidat *et al.*, 1998	Limited by number of identifiable features	Resolution = 150-230 μm	1/2000-1/1300
Saada *et al.*, 1999		Precision = 130 μm	1/1400
Andrawes *et al.* 1973		Precision = 5 μm	1/11000

[1] Over field of view of 300 mm x 200 mm.
[2] Quoted by Grant (1998) for same experimental system described by Taylor *et al.* (1998)

Table 3.1. Image-based displacement measurement methods: comparative performance

To allow each system to be compared, the performance originally quoted by each Author has been normalised by the field of view used in the original reference. The normalised performance of each system is compared in Figure 3.34.

Table 3.1 shows that the system described in this thesis offers an order-of-magnitude increase in measurement precision compared to the state-of-the-art, and a significant increase in accuracy. This is accompanied by a massive increase in the number of measurement points that can be fitted in an image.

3.10 STRAIN FORMULATION

3.10.1 Previous strain calculation techniques

The PIV and camera calibration analysis produces a grid of displacement vectors. These are differentiated to produce strain. The most straightforward method of evaluating direct strain, ε, and engineering shear strain, γ, from displacement vectors uses a single line element constructed from two measurement points (Figure 3.35a, Equations 3.23-3.25).

$$\varepsilon_{xx} = \frac{\Delta x}{x} \tag{3.23}$$

$$\varepsilon_{yy} = \frac{\Delta y}{y} \tag{3.24}$$

$$\gamma_{xy} = \frac{\Delta x}{y} + \frac{\Delta y}{x} \tag{3.25}$$

Although theoretically valid and elegantly concise, Equations 3.23-3.25 are not suited to numerical evaluation since two of the equations will have a denominator close to zero if the line element is oriented close to a reference axis. Small errors due to the precision of each displacement measurement will represent a large fraction of this small denominator, producing large errors in the deduced strain. If the line element is exactly parallel to a reference axis, a division by zero is required.

Roscoe *et al.* (1963) circumvented this numerical difficulty by evaluating strain at measurement points defined by a grid of four markers which form two initially perpendicular line elements. These line elements are used to calculate direct strains in the direction to which they are initially perpendicular, with shear strain calculated according to a modification of Equation 3.25 (Equation 3.26, Figure 3.35b).

$$\gamma_{xx} = \frac{\Delta x_{\gamma}}{y} + \frac{\Delta y_{\gamma}}{x} \tag{3.26}$$

This approach is numerically more precise in its initial orientation since all denominators are equal to the gauge length of the strain measurement. However, it is inefficient that four target markers are required to create a single strain measurement point. Also, numerical precision is reduced as line elements rotate away from their original reference direction. If the two elements experience a 90° rigid body rotation, the division-by-zero difficulty of the single line element method is reached.

3.10.2 Improved strain calculation technique

3.10.2.1 Rotating reference frames

Since the displacement path around an advancing pile involves a large component of rigid body rotation, the strain calculation technique described in Section 3.10.1 was considered unreliable. Instead, a more advanced strain calculation procedure has been adopted. This procedure uses a co-rotational deformation formulation that allows rotation, translation and distortion to be separated. This approach eliminates the numerical instabilities associated with small gauge lengths, and separates rigid body rotation from deformation.

Three reference frames are considered in the strain analysis (Appendix 1, Figure A1.1). The first reference frame, *XY*, is the non-rotating frame of the control points. The displacement data from the calibrated PIV analysis refers to this frame. The second and third reference frames provide two methods of illustrating the strain within the deforming soil model. These two frames are initially both aligned with the bedding, and

potential anisotropy, of the soil. This plane is initially inclined at an angle β_{init} anti-clockwise from the non-rotating *XY* plane. In the case of the calibration chamber testing described in chapter 4, the control point *X* axis is approximately horizontal, and the soil has been poured in horizontal layers so β_{init} is approximately zero. The second frame, $XY_{betainit}$ is non-rotating, remaining inclined at β_{init} to the control axes, and is used as a frame in which the spatial variation of incremental strains, and their principal directions, can be described. The third frame, *xy*, rotates with each soil element, and is used to evaluate total strains.

This approach of using a non-rotating frame to illustrate the spatial variation in incremental strains and a rotating frame to cumulate total strains is used for the following reasons. At any moment during an experiment, different soil elements will have deformed such that their bedding planes, and hence their *xy* reference frames, are oriented in different directions.

The spatial variation of incremental strains indicates the current mechanism of deformation of the soil model. It would be meaningless to plot the spatial variation in, for example, incremental direct strain aligned in the *x*-direction, since the *x*-direction in each soil element is oriented differently. Instead, incremental strains and their principal directions should be referred to a non-rotating reference frame. The most appropriate non-rotating reference frame is one that refers to the original plane of bedding, β_{init}.

In contrast, total strains should be cumulated from the reference frame of the soil element, which eliminates the influence of rigid body rotation. Consider a soil element that undergoes a deformation described in the reference frame of the apparatus *(XY)* as vertical compression followed by 90° rotation and further vertical compression. If meaningful back-analysis of the strain path is to be carried out, the *xy* reference axes should be used, ensuring that the total strain at the end of this loading path is correctly evaluated as a combination of vertical and horizontal compression.

3.10.2.2 Decomposition of deformation

The grid of displacement measurement points is divided into a network of constant strain triangles. The centroid of each triangle defines a strain measurement point. The measured displacement of the three vertices of the triangle over a single increment of deformation is used to construct the displacement gradient matrix. Appendix 1 describes how the displacement gradient matrix is converted to the deformation gradient matrix of the total or incremental deformation, and how the corresponding strain components extracted.

3.11 CONCLUSIONS

Conventional techniques of measuring soil deformation in geotechnical models rely on intrusive target markers and video image capture. The reported accuracy and precision of such systems when viewing a typical (300 mm × 200 mm) soil model is approximately 100 μm. Differentiation of the resulting displacement vectors has allowed contours of 1% strain to be produced. The use of target markers has a number of drawbacks, and video image capture is unstable and of low resolution.

A new system of displacement measurement based on digital image capture, PIV image analysis, and close range photogrammetry has been developed. A rigorous series of experiments has been carried out to validate the PIV analysis and close range photogrammetric framework. The precision and accuracy of the resulting displacement measurements has been found to significantly exceed the current state-of-the-art. An accuracy of $1/18000^{th}$ of the field of view has been proven. The precision is even higher, and depends on the PIV patch size.

This improved performance is achieved alongside an increase in the number of measurement points of more than an order of magnitude, whilst removing the need for target markers within the soil model. The resulting displacement vectors are analysed within a more rigorous deformation algorithm than has been previously used in geotechnical modelling, allowing finite deformations to be analysed by decomposition of strain and rotation.

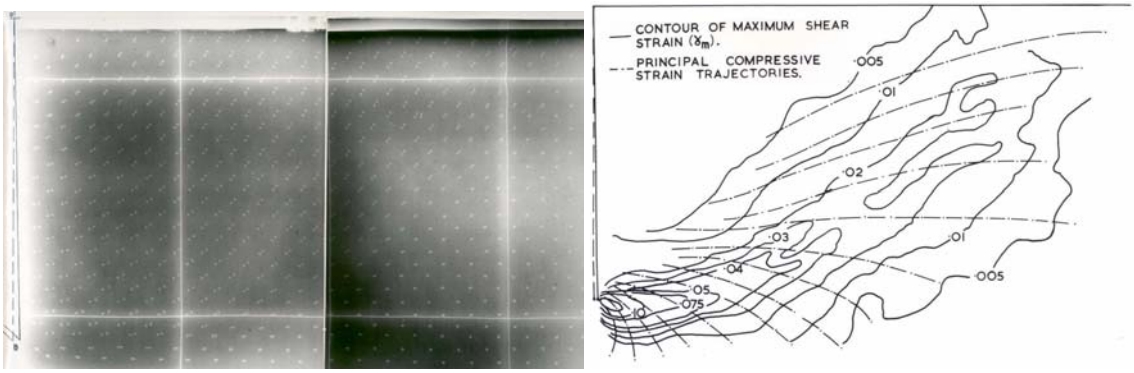

a) Target markers and radiography: James, 1965

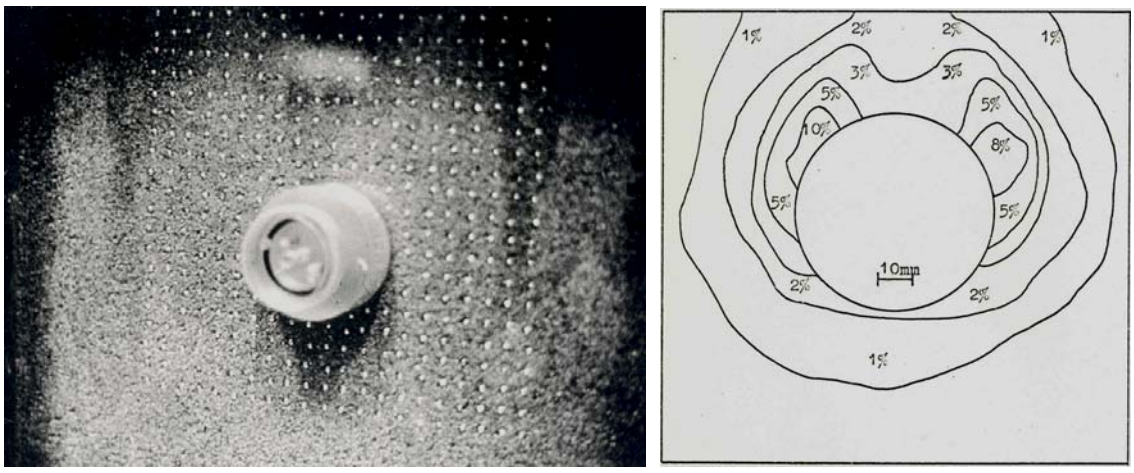

b) Target markers and conventional film: Potts, 1976

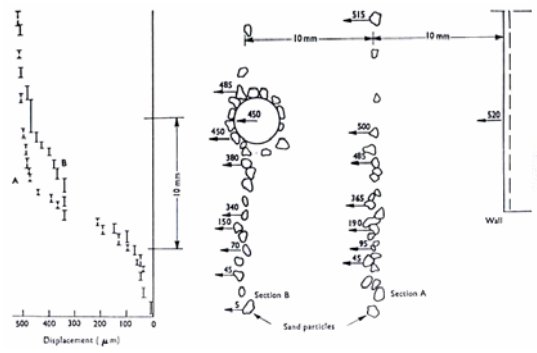

c) Stereophotogrammetry: Andrawes *et al*., 1973

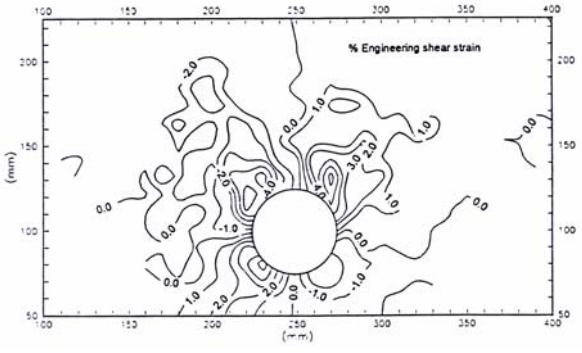

d) Target markers and video capture Grant, 1998

Figure 3.1 Previous displacement measurement methods in geotechnical modelling

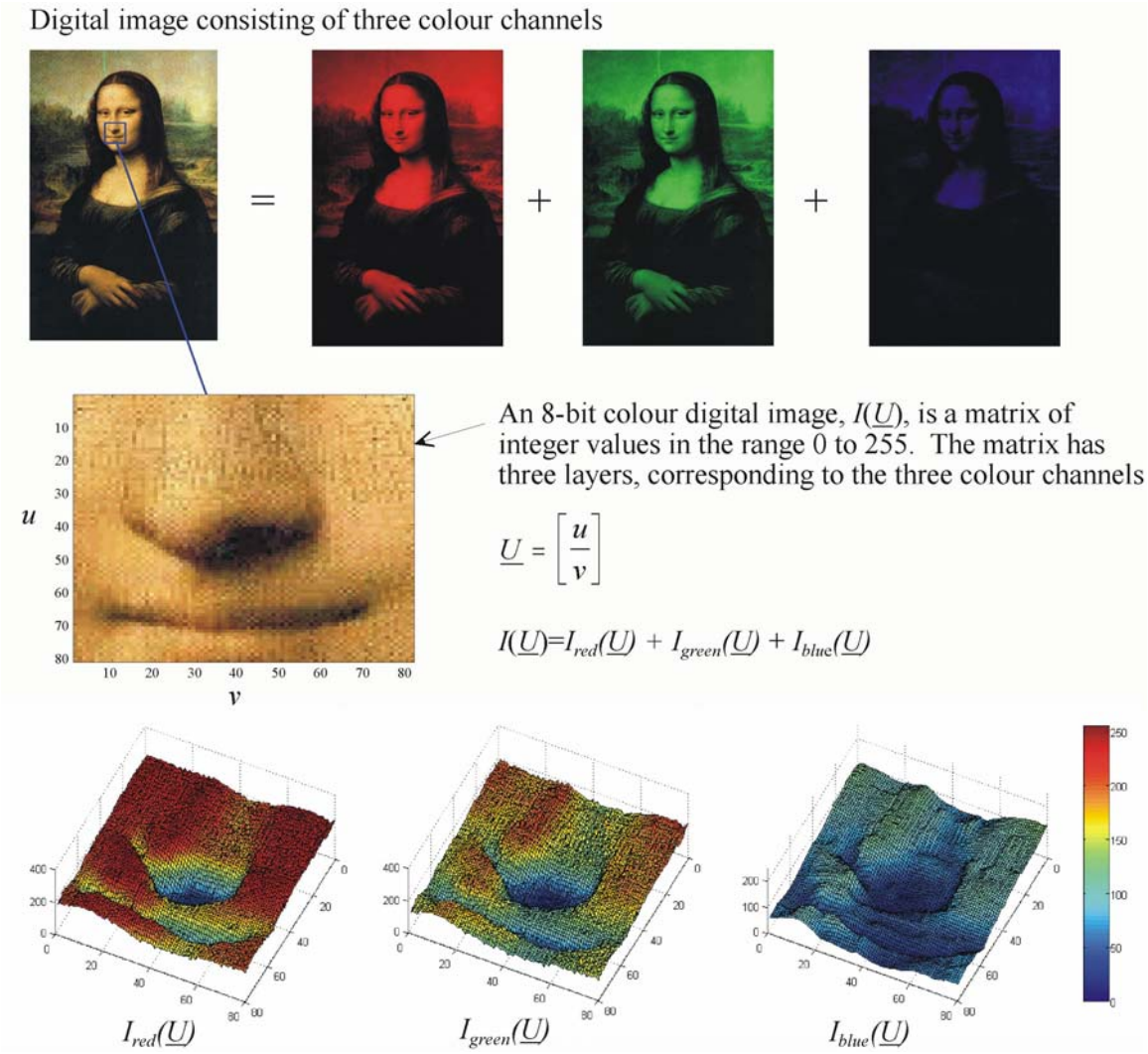

Figure 3.2 Colour digital images: matrix form

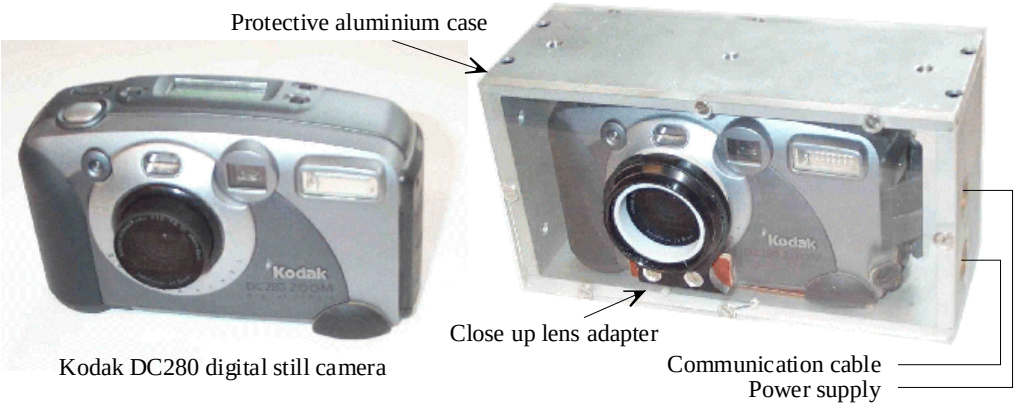

Figure 3.3 Digital photography

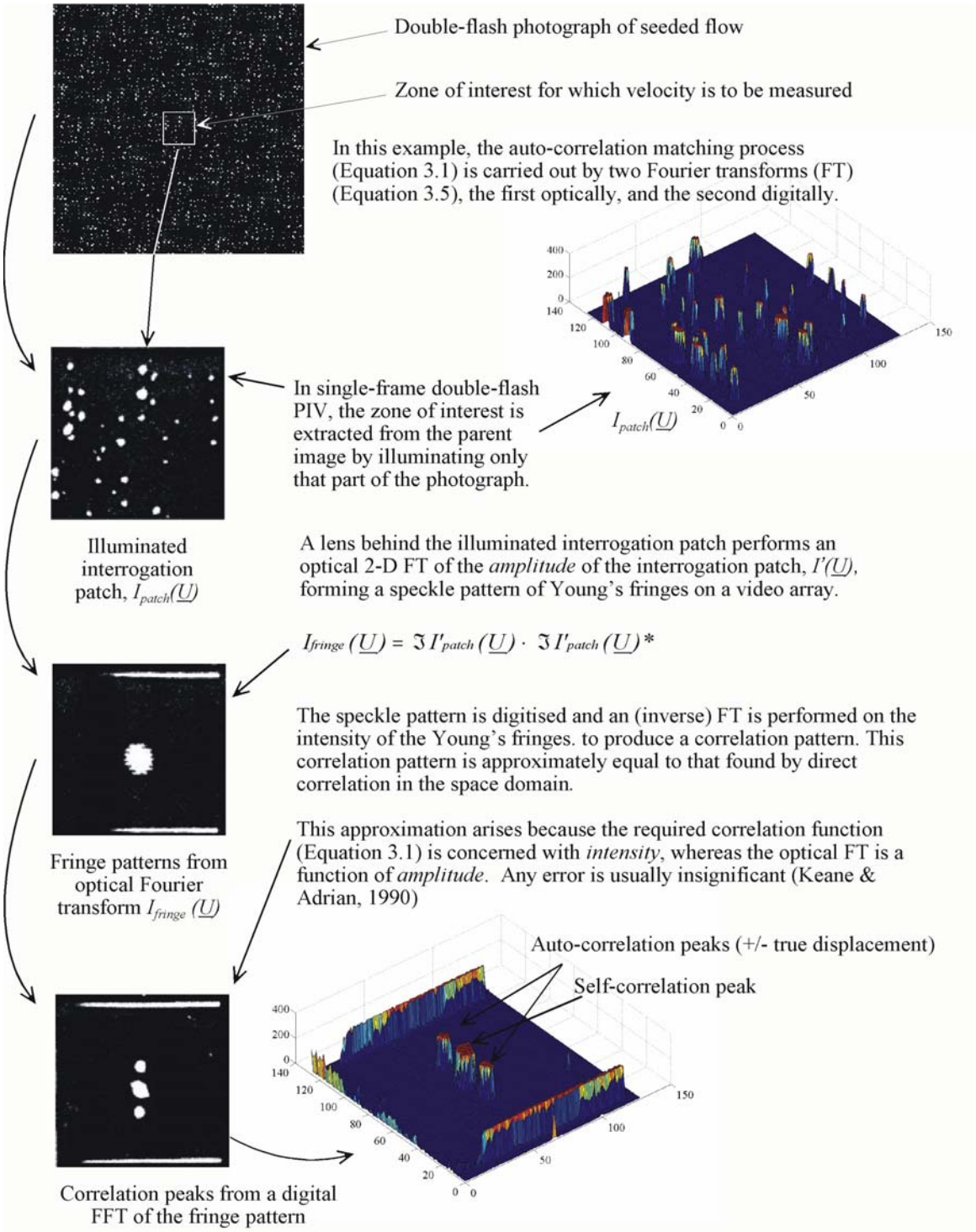

Figure 3.4 Particle Image Velocimetry using auto-correlation (data from Landreth & Adrian, 1989).

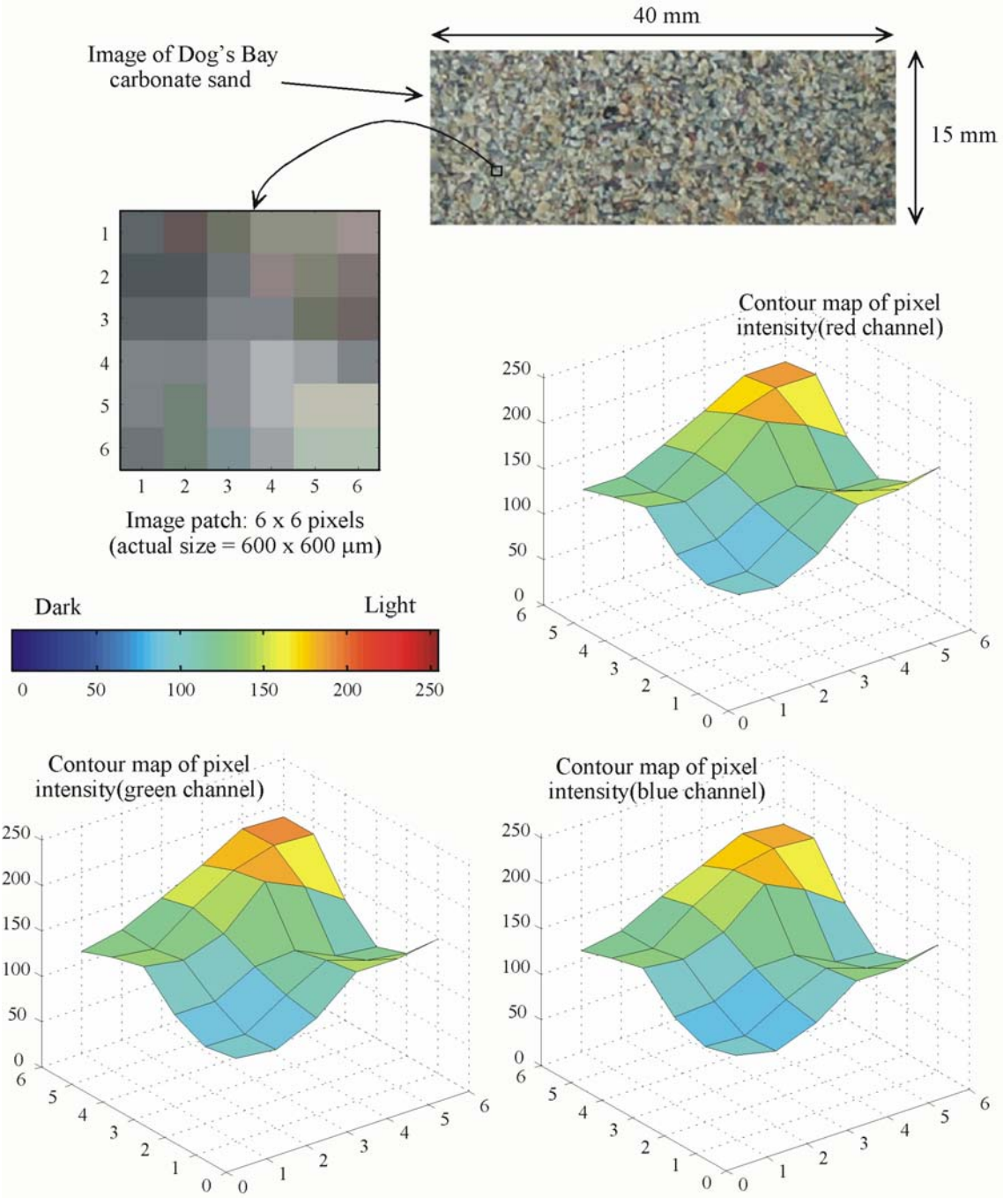

Figure 3.5 Raw image and intensity matrices of a 6 x 6 pixel patch of soil

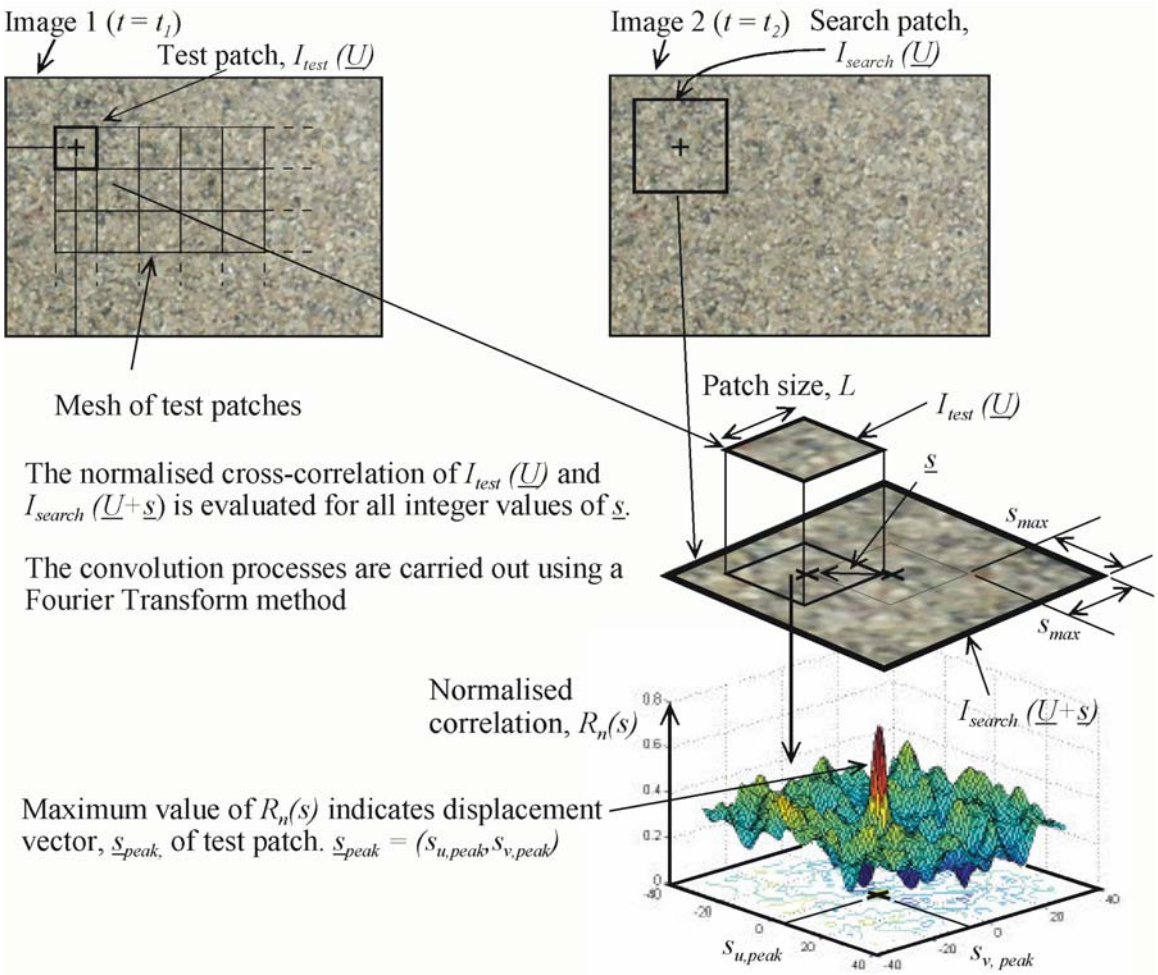

a) Image manipulation during PIV analysis

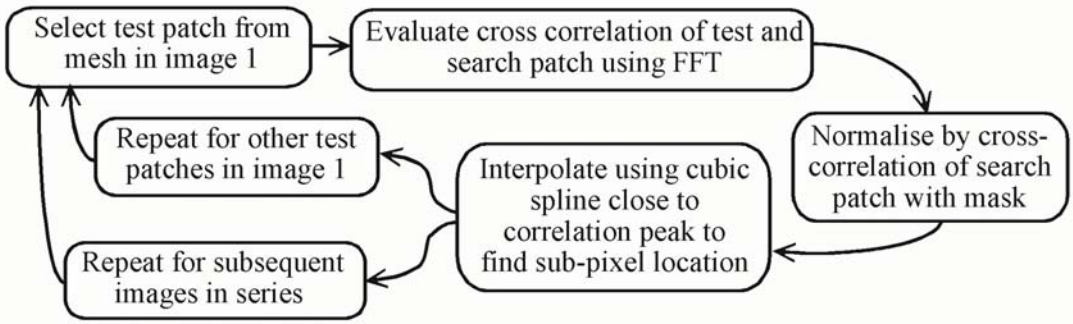

b) Flowchart of PIV analysis

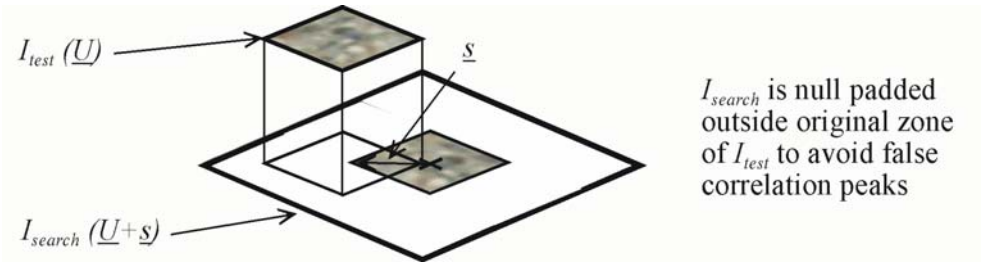

c) Null padding of search patch to prevent false correlation peaks

Figure 3.6 Multiple-frame Particle Image Velocimetry (PIV) in geotechnical modelling

a) The test patch, I_{test}, is extracted from image 1, and null-padded.

b) In this simple example, I_{test} is present in I_{search} at an offset, s, of 2 pixels. However, I_{search} contains regions of greater intensity than are present in the test patch.

c) Cross-correlation of the test and search patches reveals a small maximum at the correct offset, but a larger maximum is created by the high-intensity region of the search patch.

d) The mask function, $M(x)$ has intensity unity over a region equal to I_{test}.

e) The normalising function, $N(s)$, is created by correlating the mask function with the square of I_{search}.

f) The normalised correlation function, $R_n(s)$ reveals the correct correlation peak.

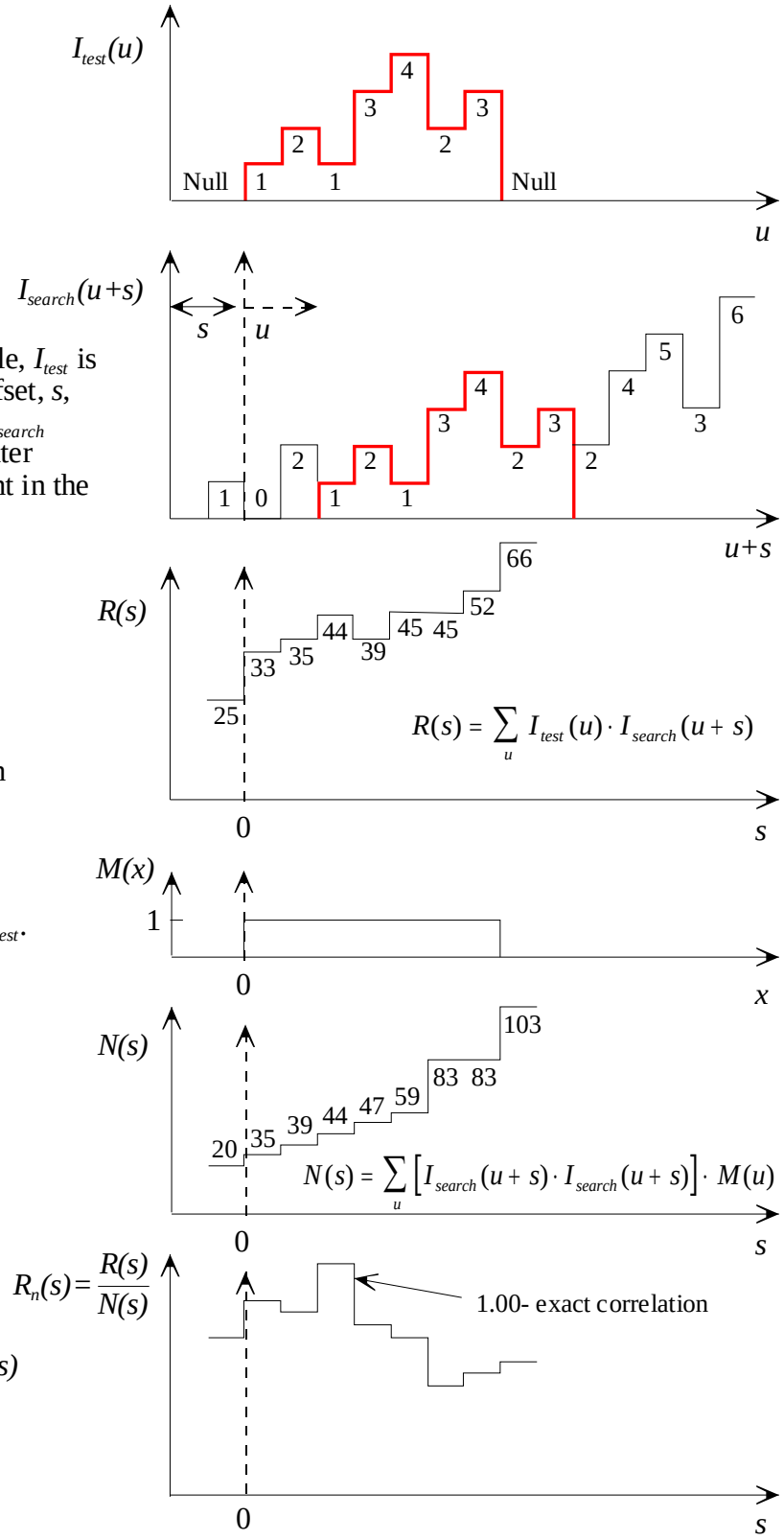

Figure 3.7 One-dimensional cross-correlation: the need for normalisation

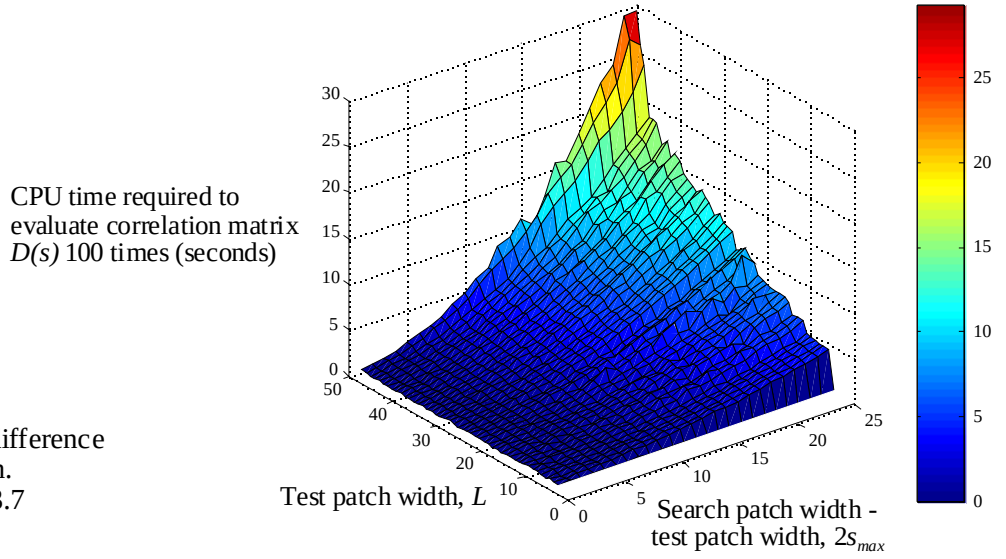

a) Direct difference calculation. Equation 3.7

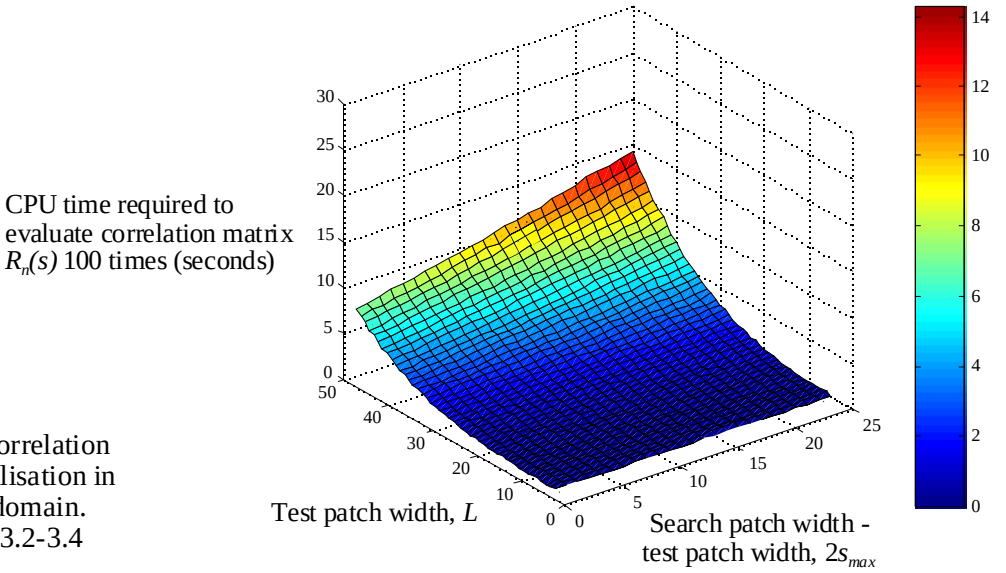

b) Cross-correlation and normalisation in the space domain. Equations 3.2-3.4

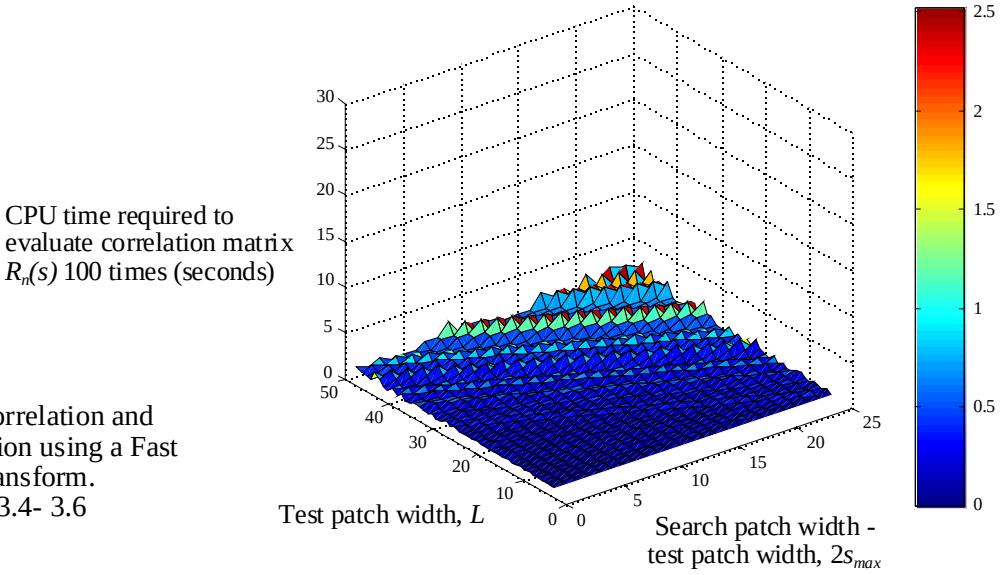

c) Cross-correlation and normalisation using a Fast Fourier Transform. Equations 3.4- 3.6

Figure 3.8 Surface plots of CPU time required to calculate PIV correlation matrices

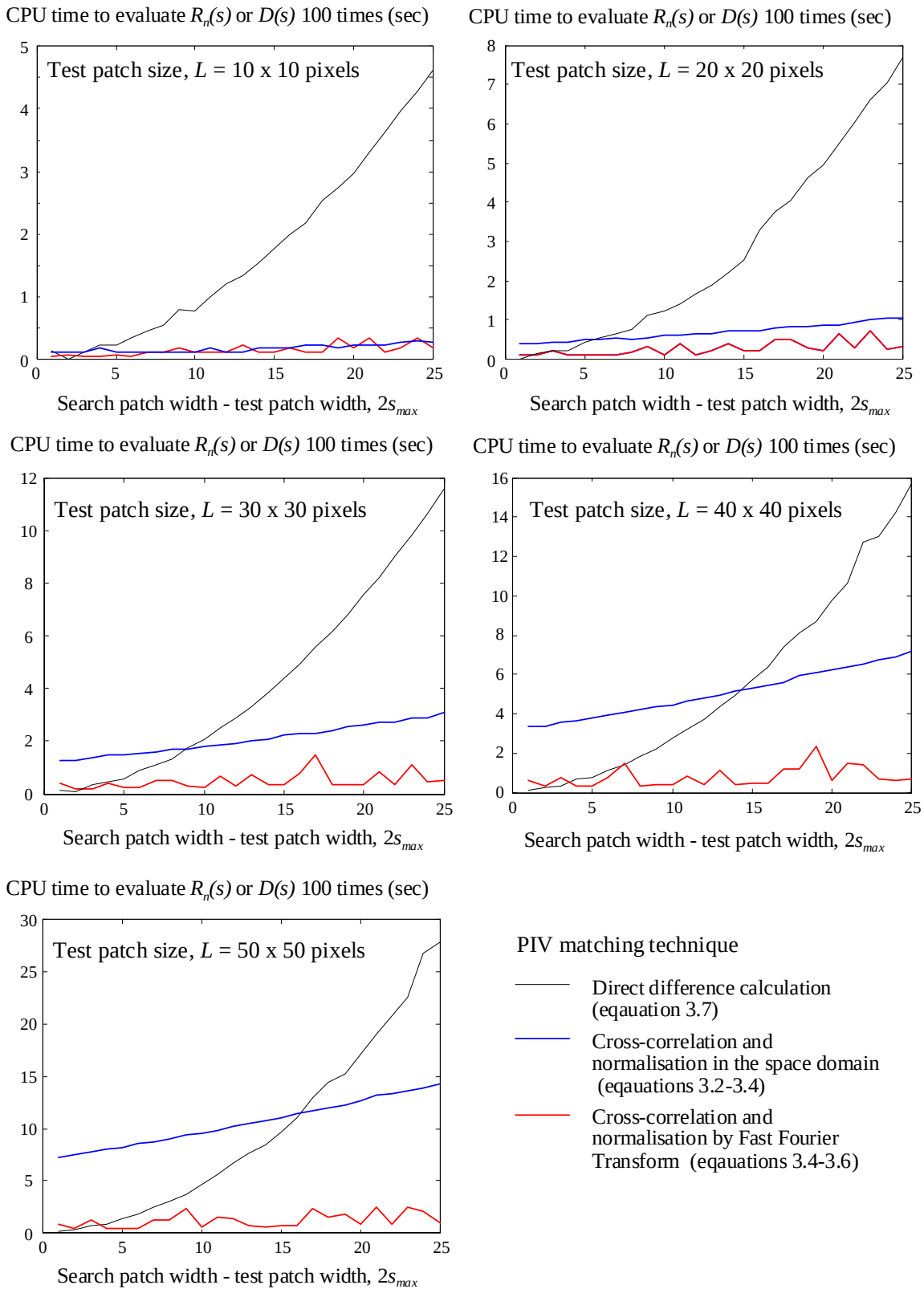

Figure 3.9 Line plots of CPU time to calculate PIV correlation matrices

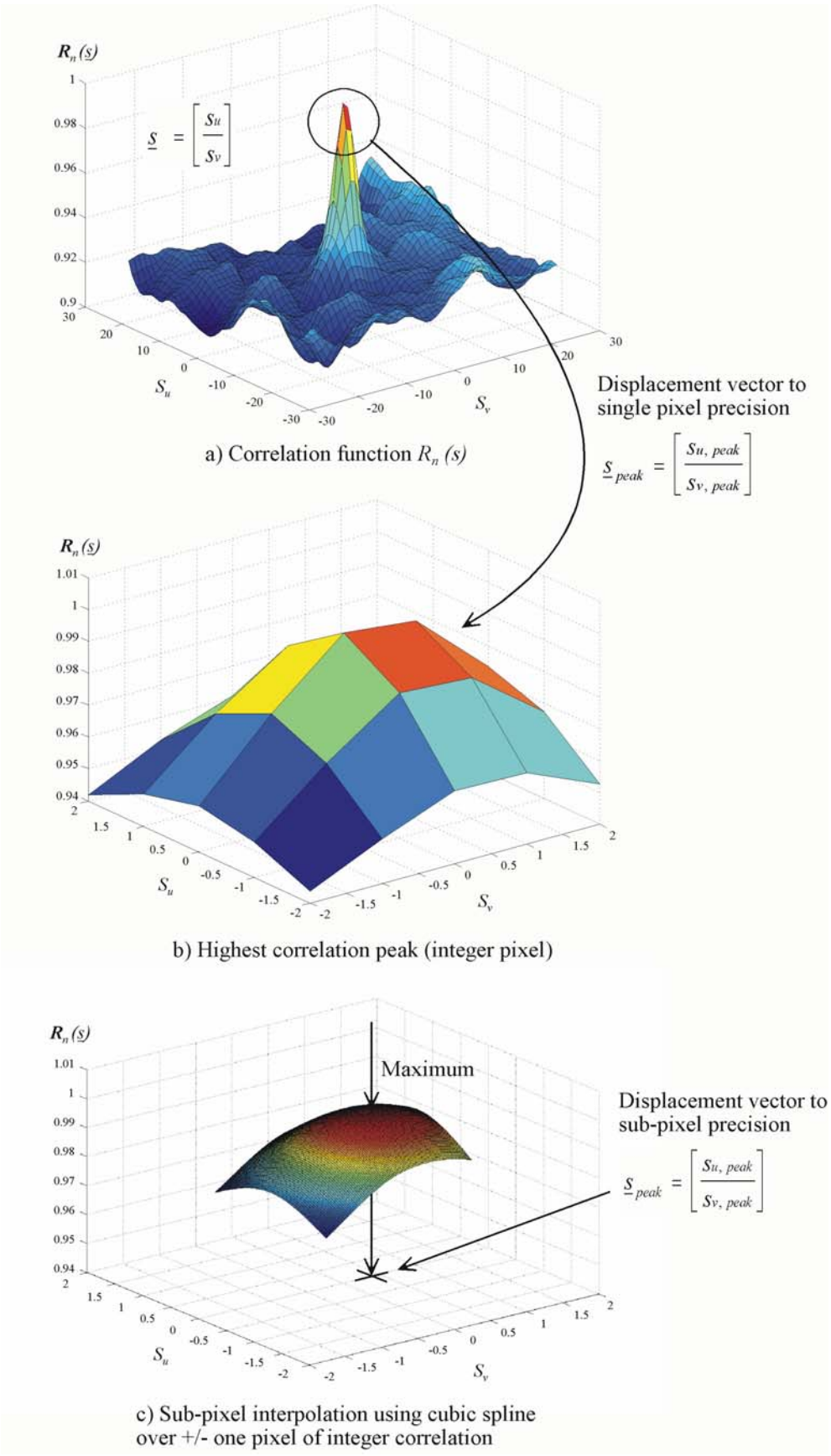

Figure 3.10 Spline interpolation to locate correlation peaks to sub-pixel precision

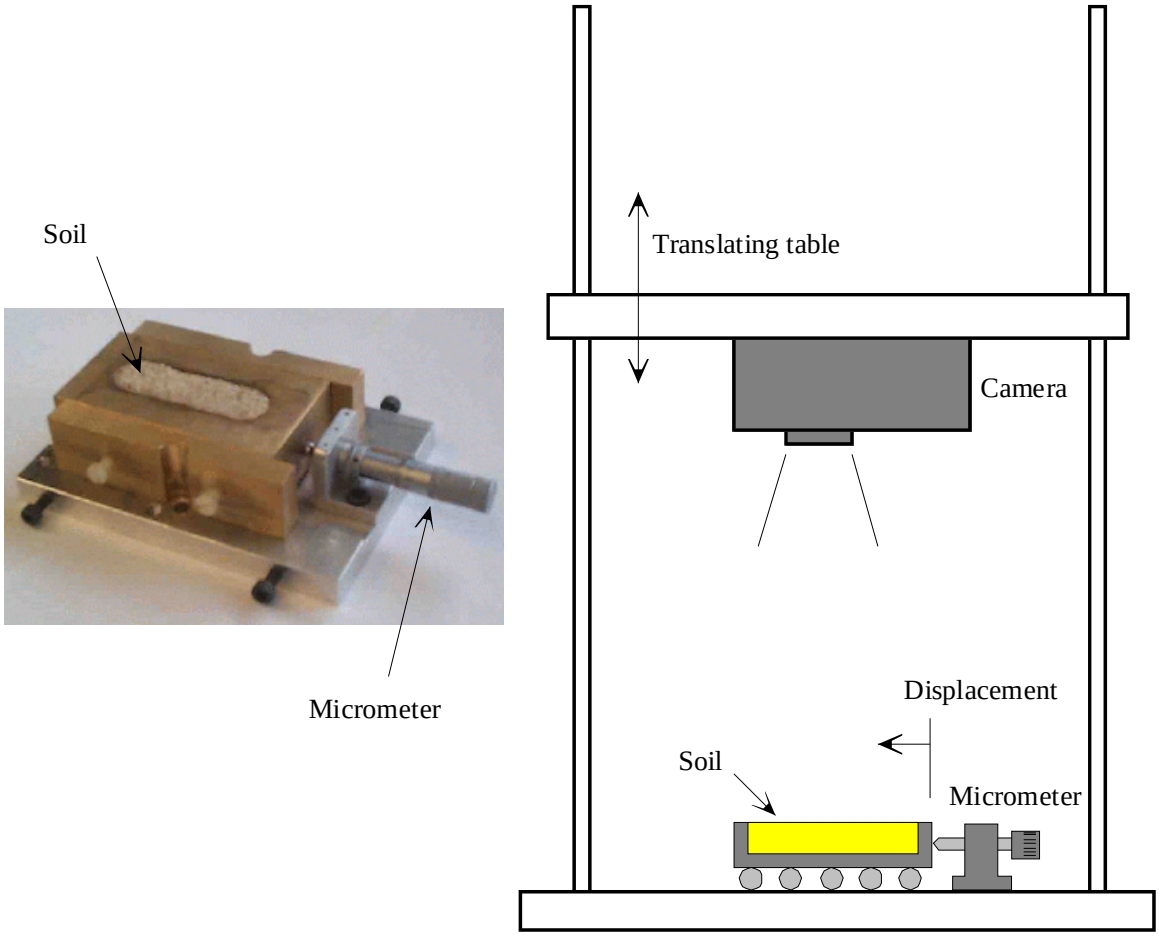

Figure 3.11 Apparatus for PIV validation tests

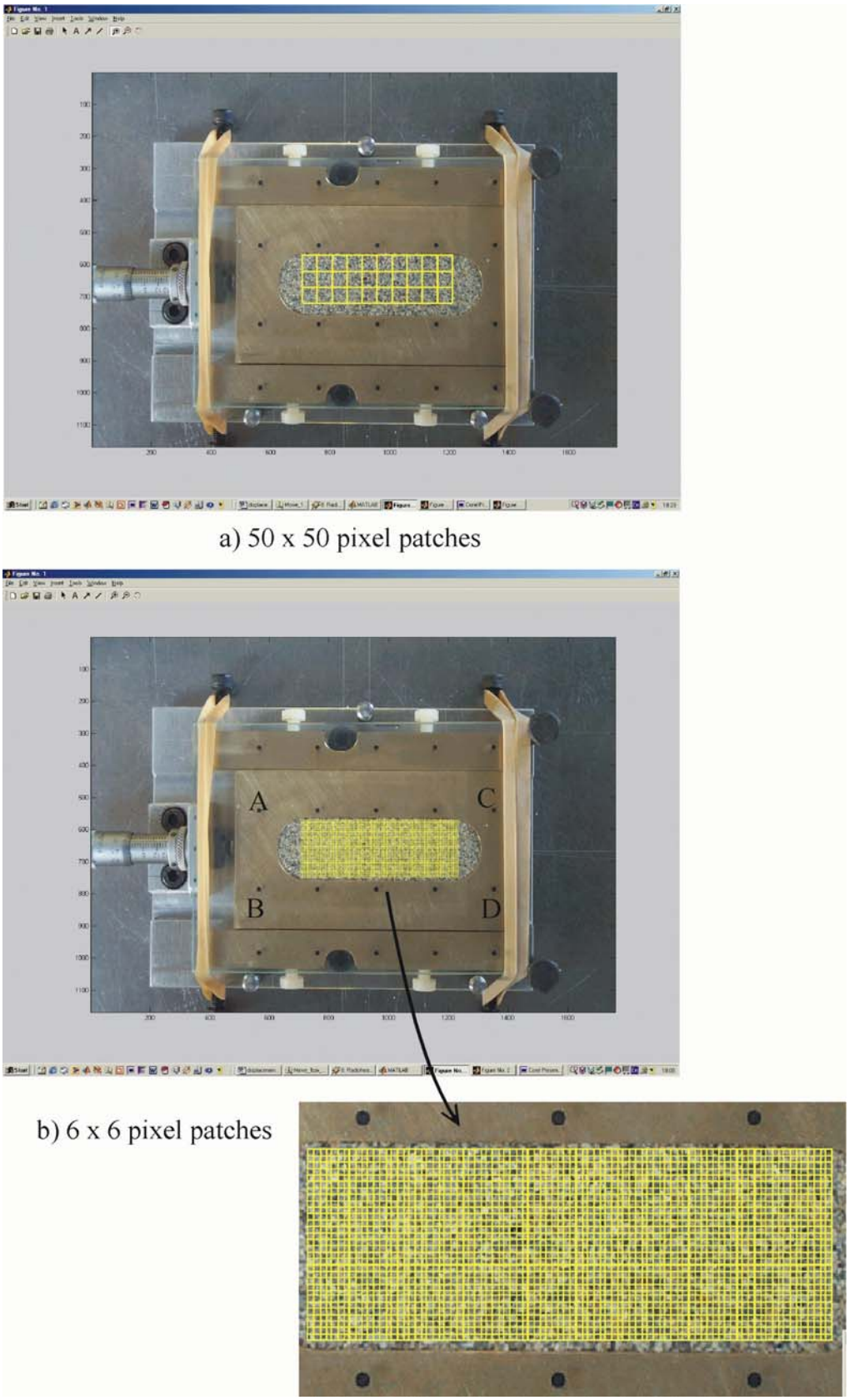

Figure 3.12 PIV validation tests

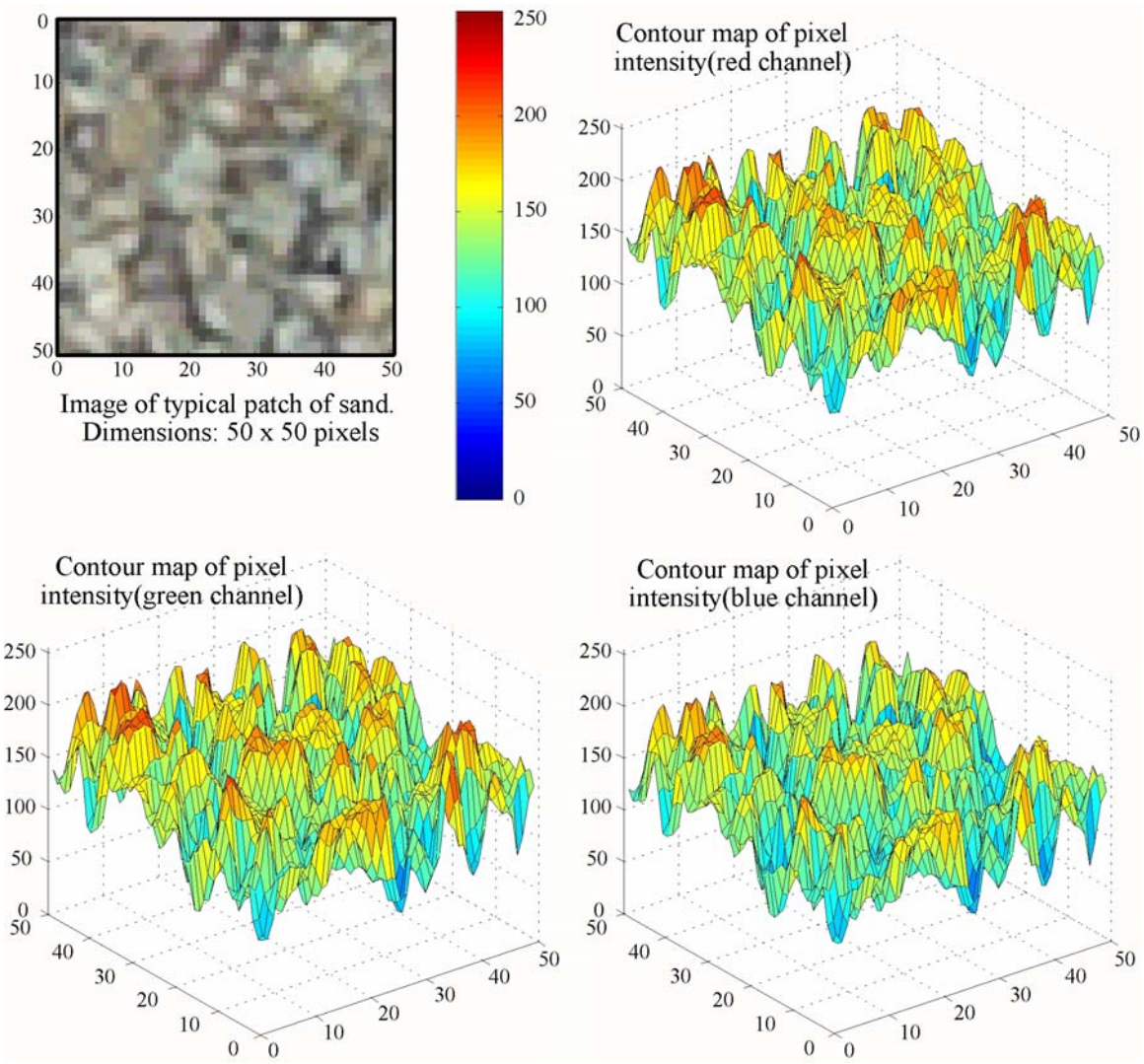

Figure 3.13 50 x 50 pixel PIV patch: raw image and intensity distribution

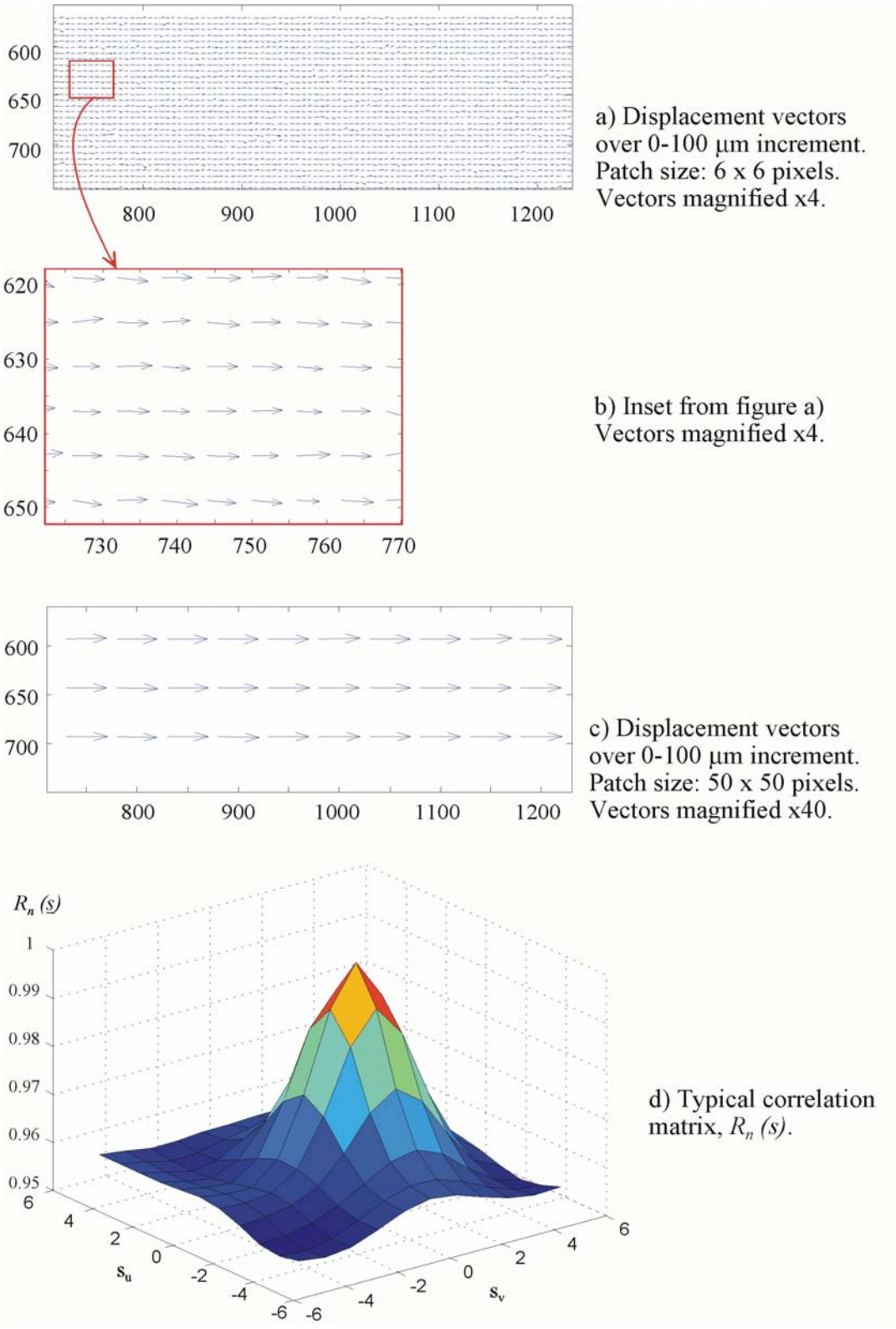

Figure 3.14 Displacement vectors from PIV analysis of integer pixel movement of sand.

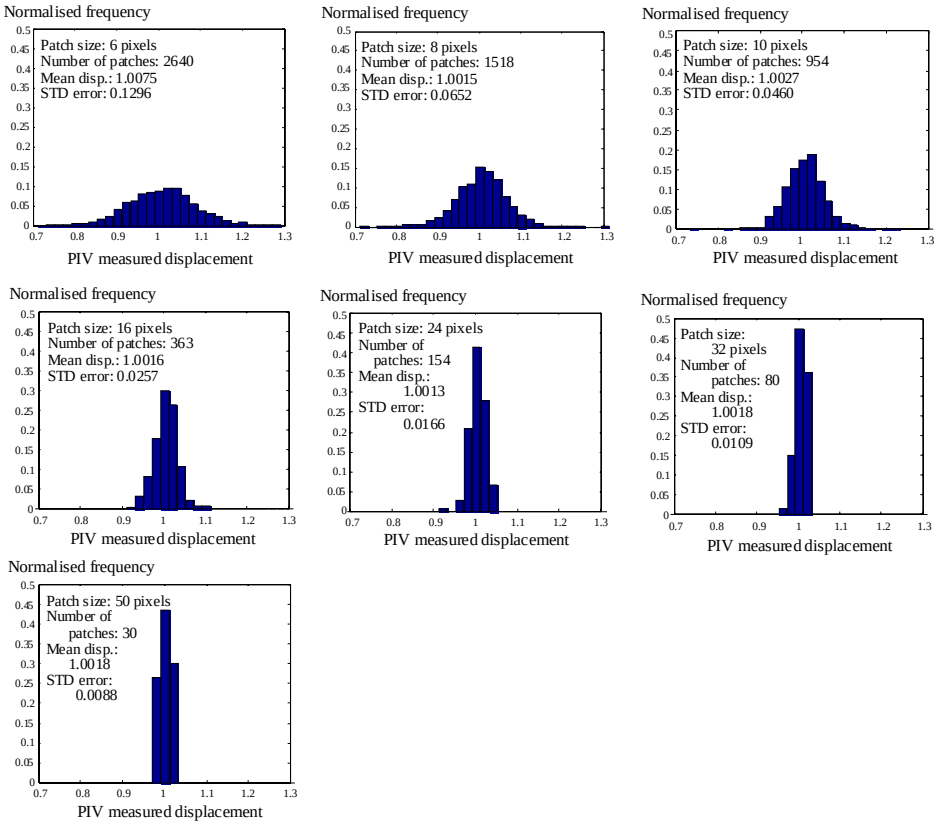

Figure 3.15 PIV precision for integer pixel displacement measurement of sand

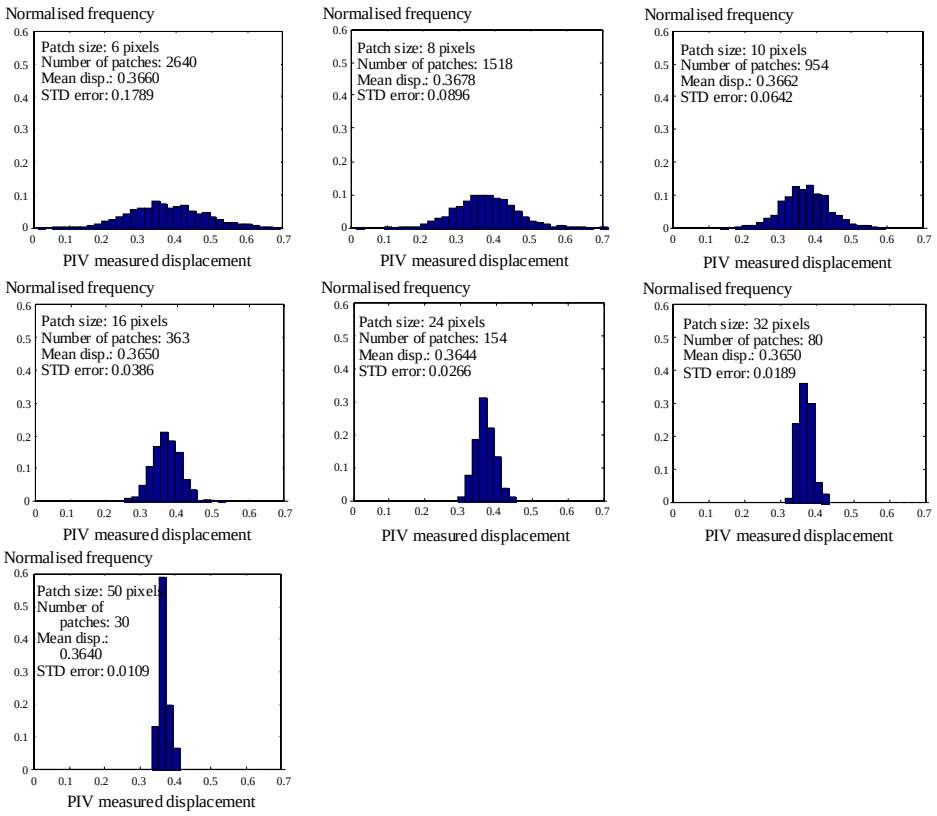

Figure 3.16 PIV precision for sub-pixel displacement measurement of sand

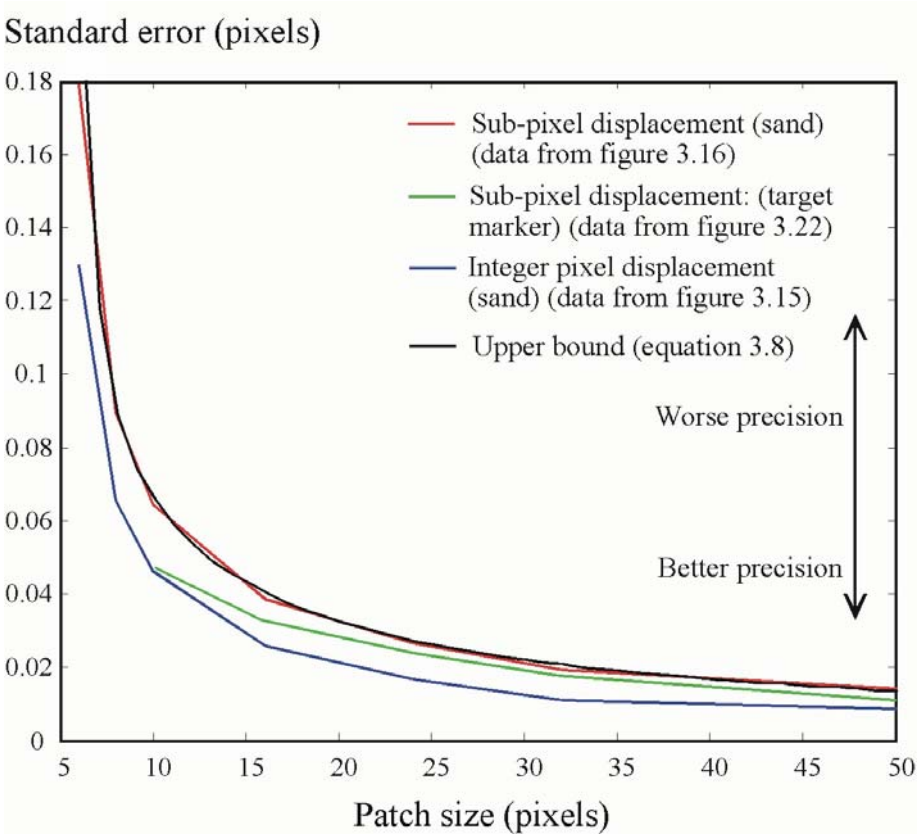

Figure 3.17 The variation of PIV precision with patch size

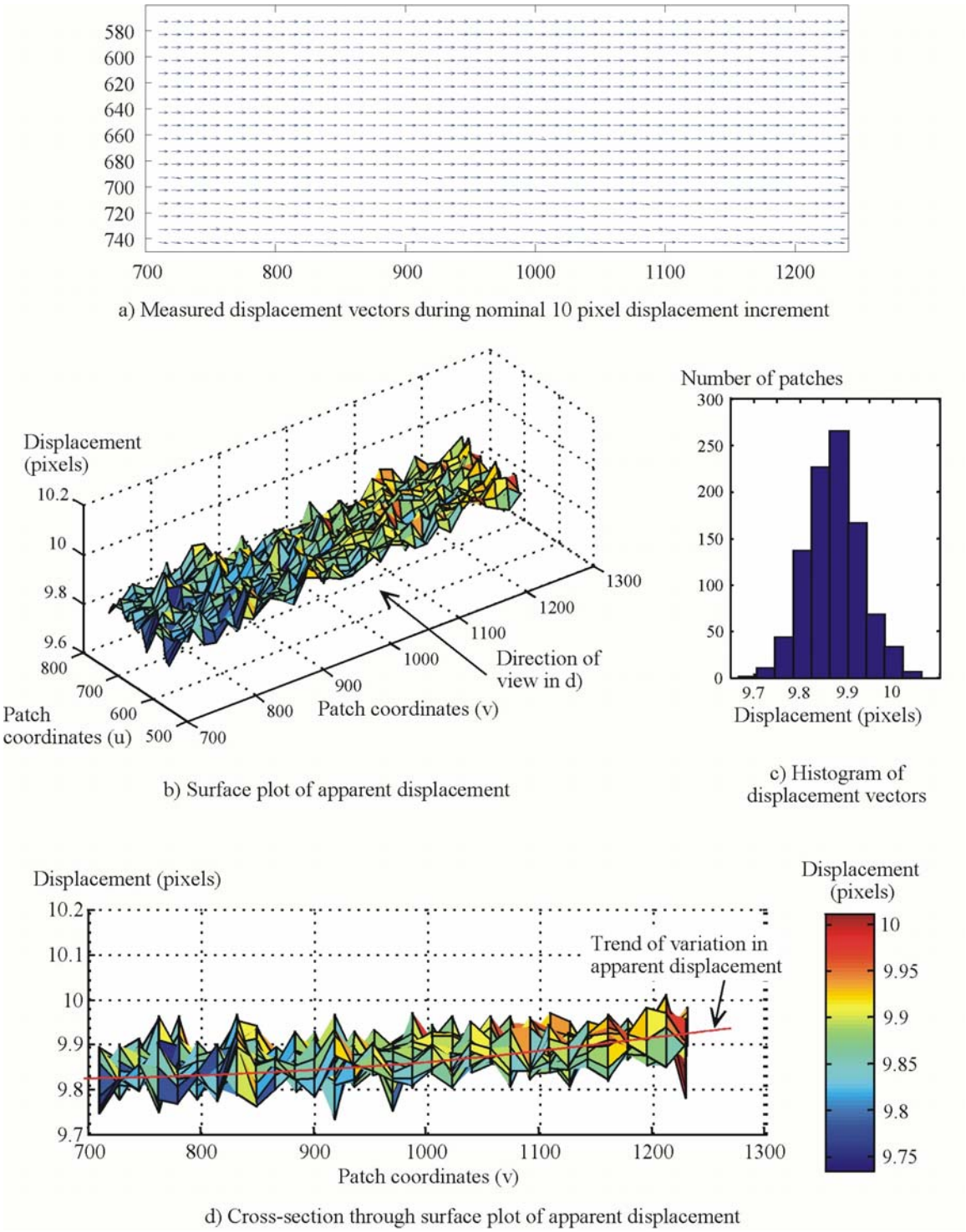

Figure 3.18 PIV data for 10 pixel (1 mm) displacement increment: a systematic error?

a) Kaolin clay

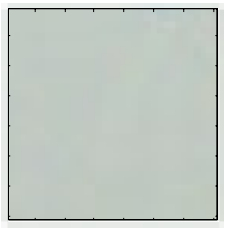

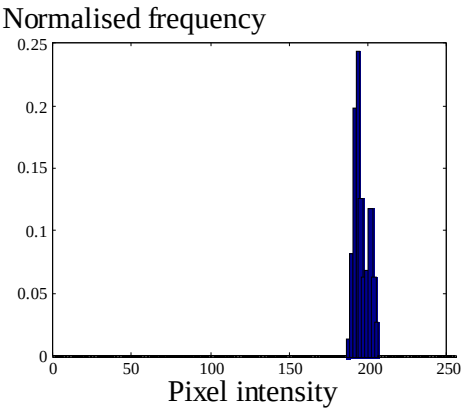

b) Sand

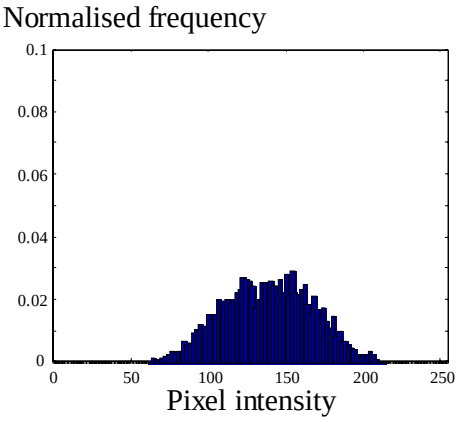

c) Kaolin clay with flock texture

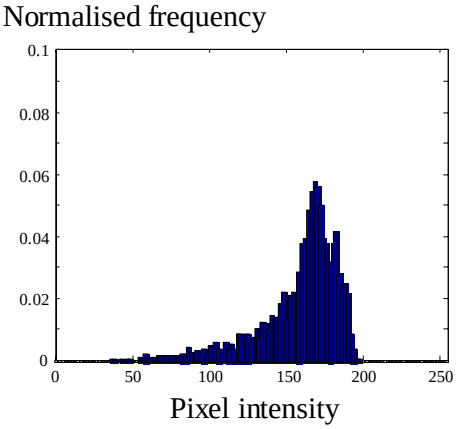

d) Target marker

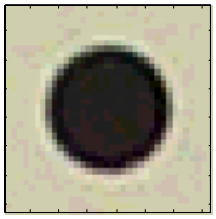

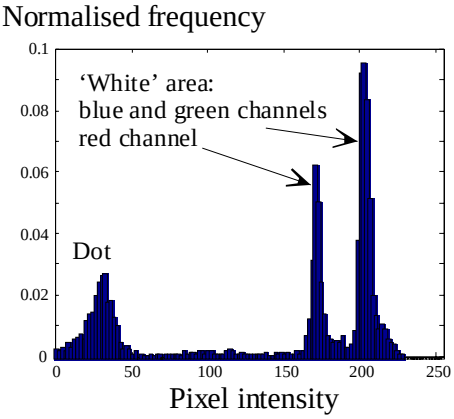

Figure 3.19 Histograms of pixel intensity for sand, clay and target markers

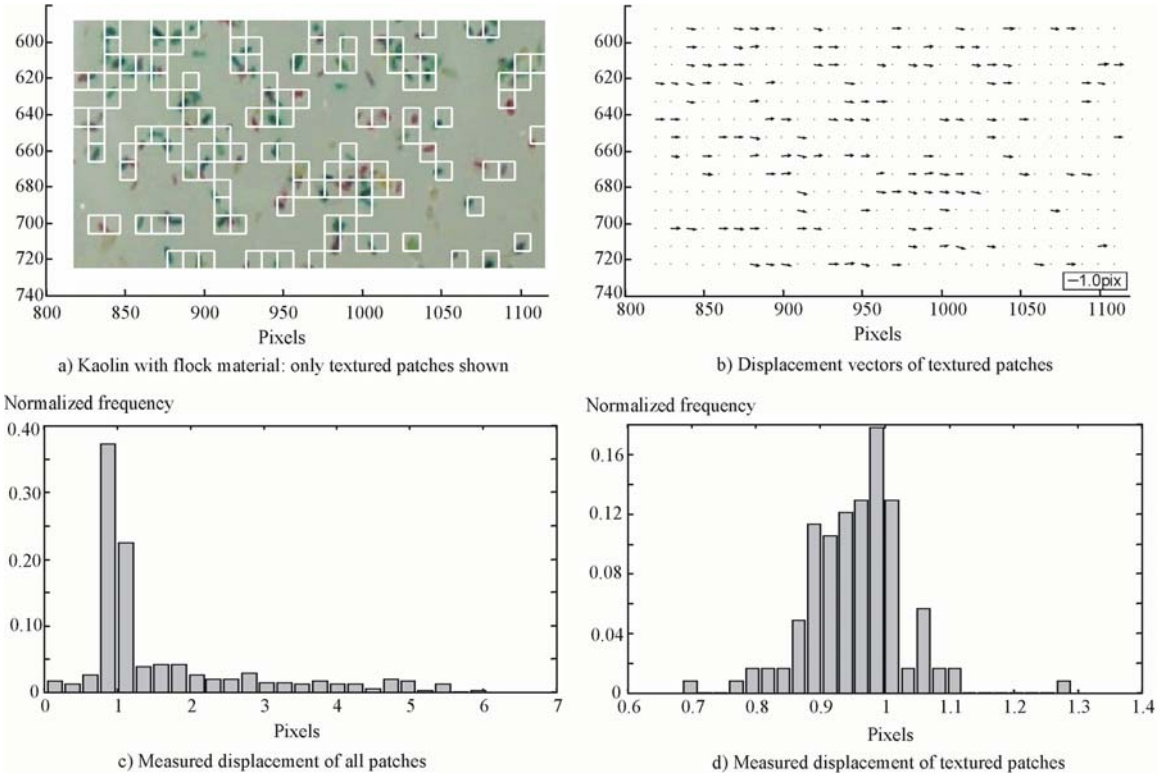

Figure 3.20 The use of flock material to add texture to kaolin (after White *et al.*, 2001a)

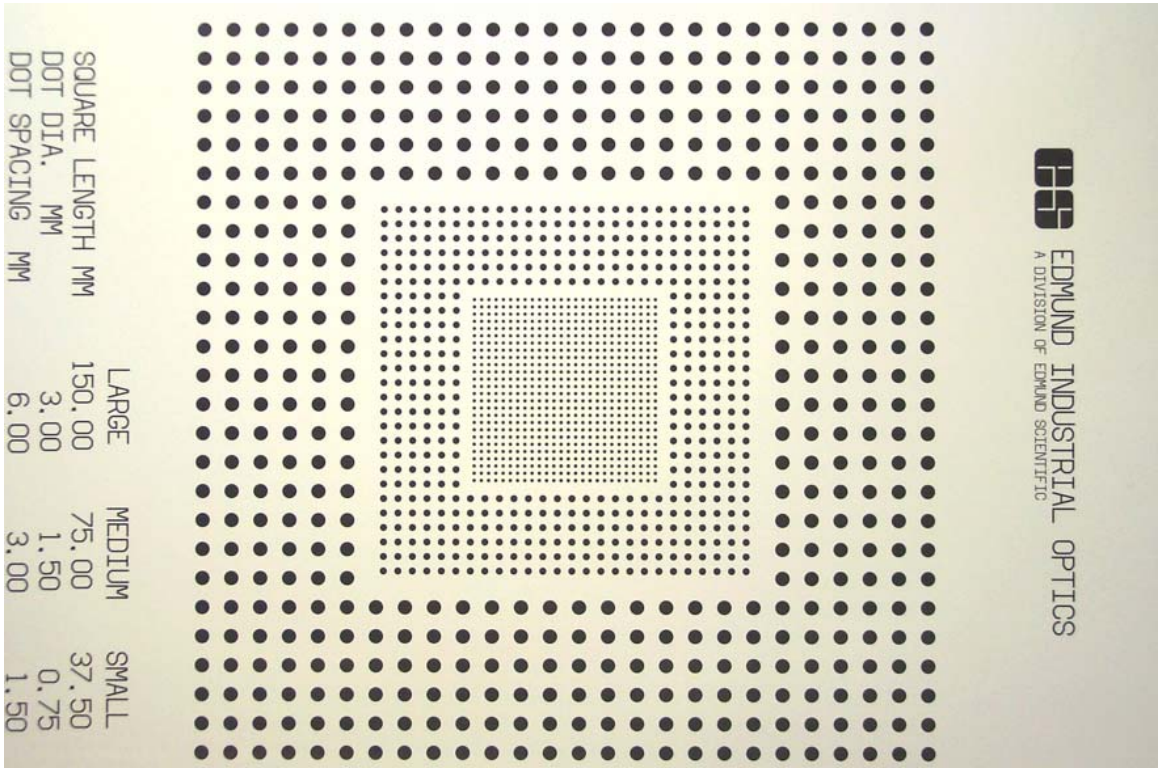

Figure 3.21 Image of calibrated photogrammetric target

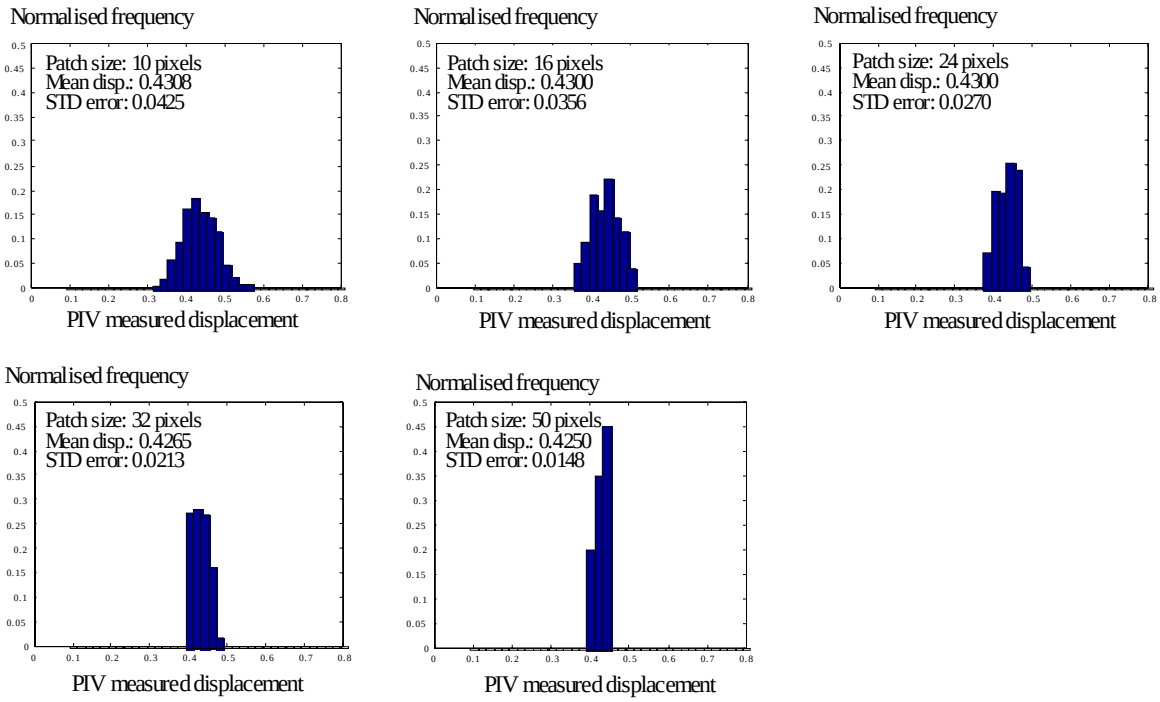

Figure 3.22 PIV precision for sub-pixel displacement measurement of target markers

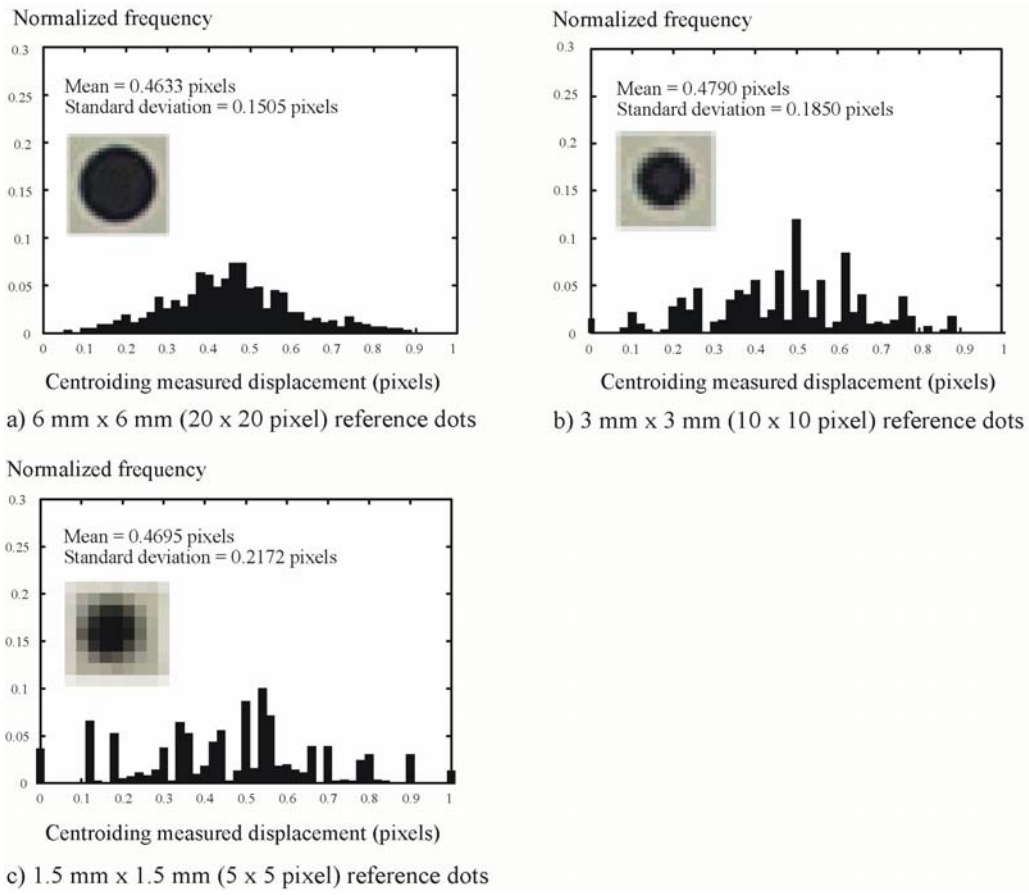

Figure 3.23 Centroiding precision for sub-pixel displacement measurement of target markers (after White *et al.*, 2001b)

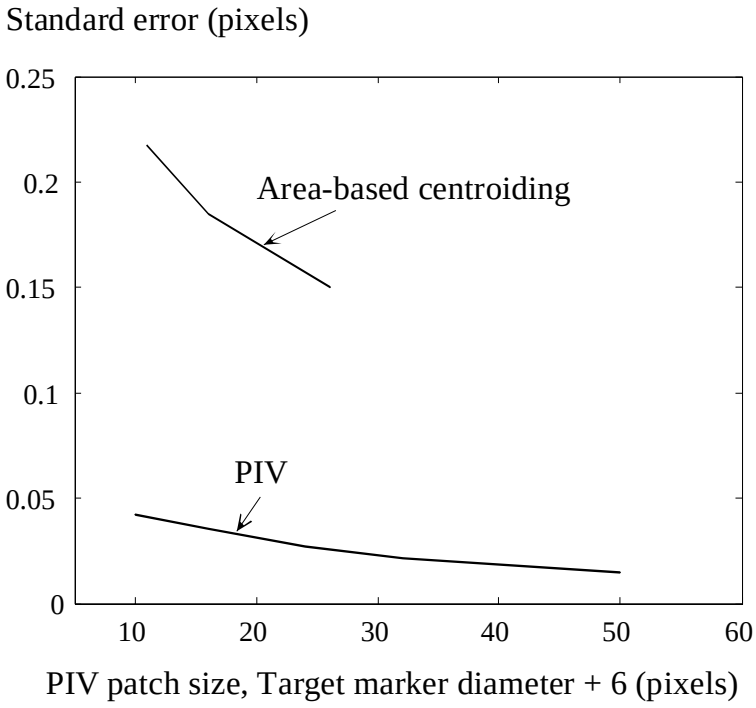

Figure 3.24 Relative precision of PIV and centroiding methods

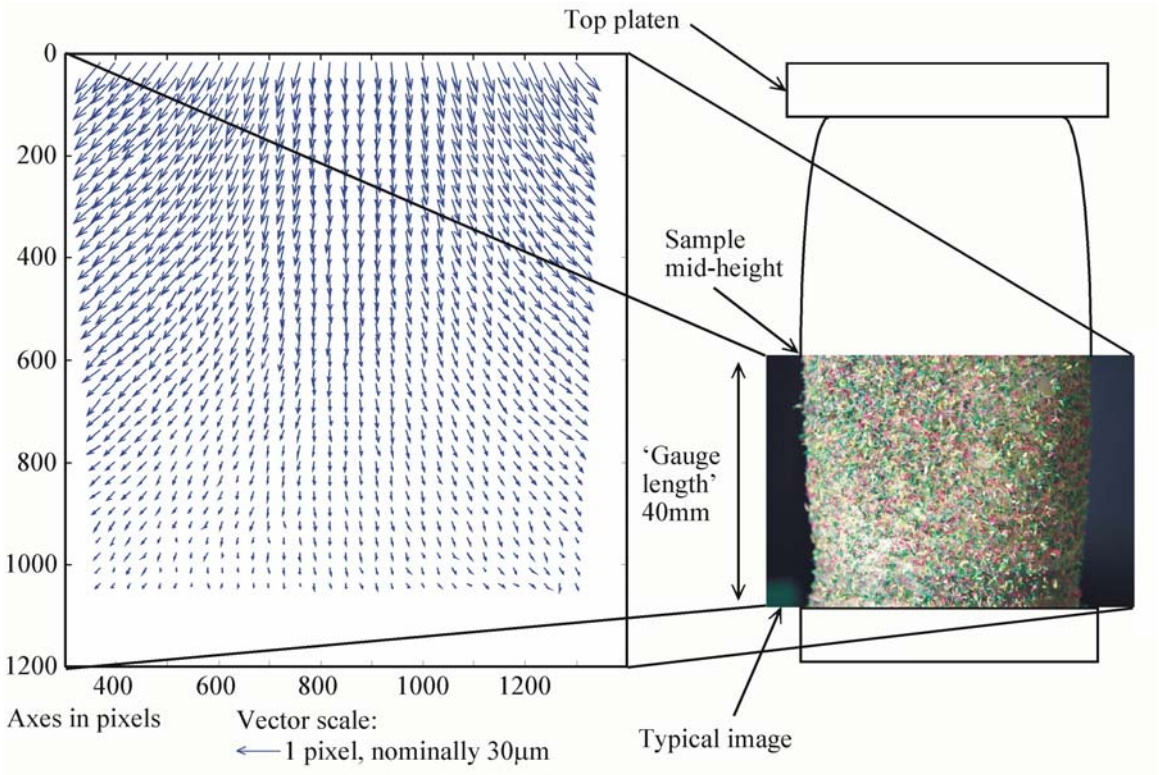

Figure 3.25 Measurement of the surface deformation of a triaxial sample using PIV

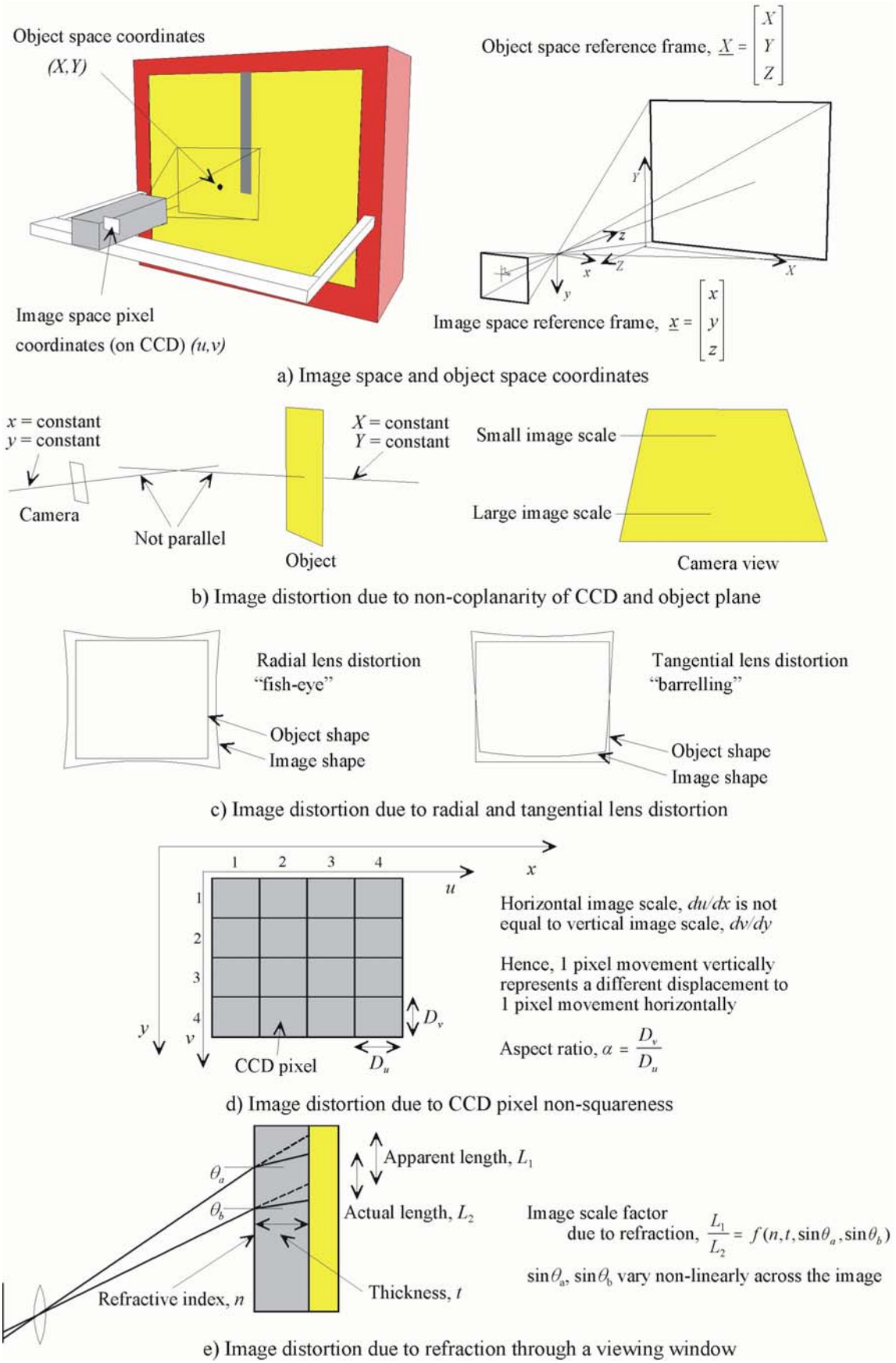

Figure 3.26 Sources of image distortion

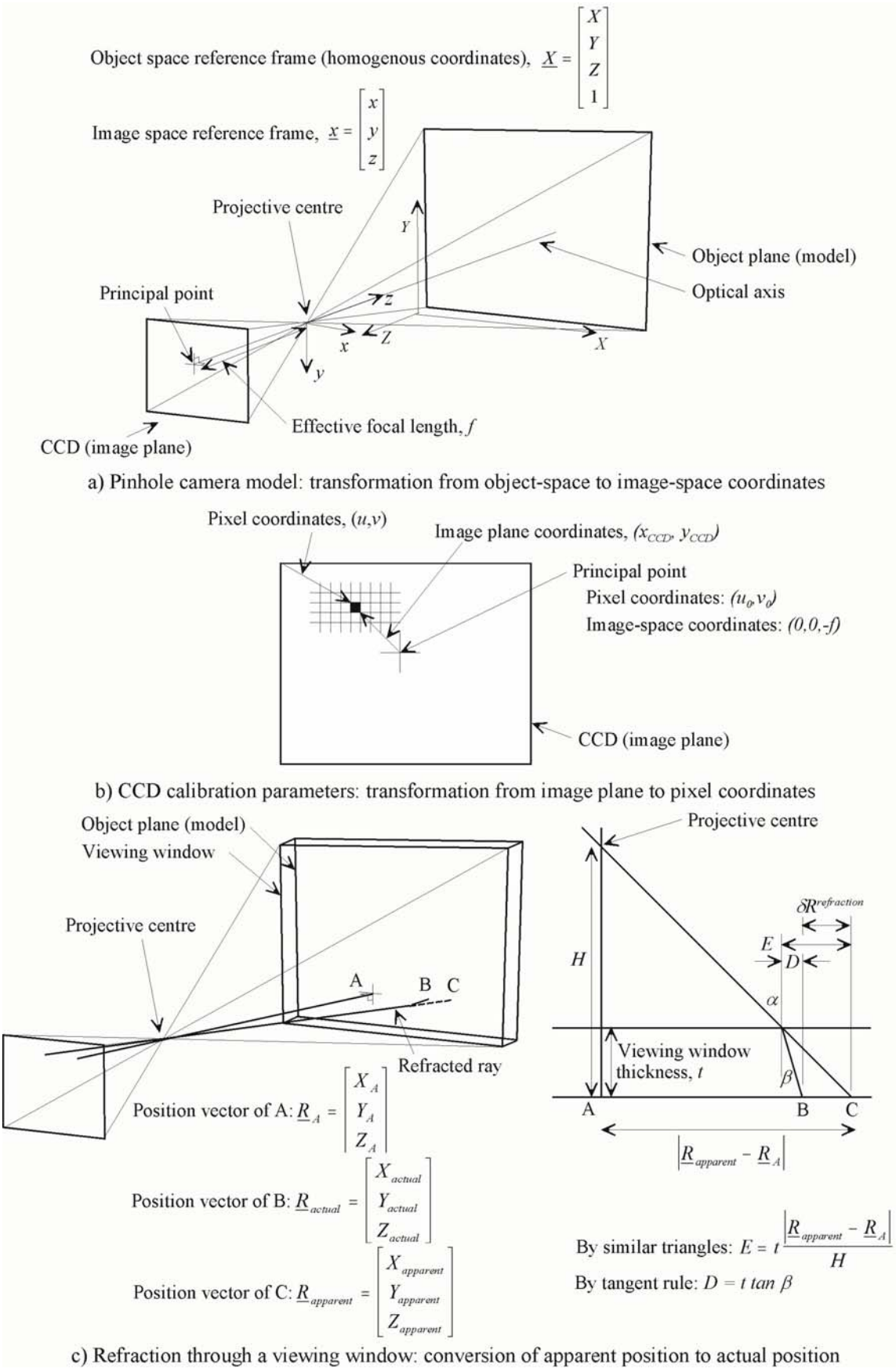

Figure 3.27 Mathematical framework for camera calibration

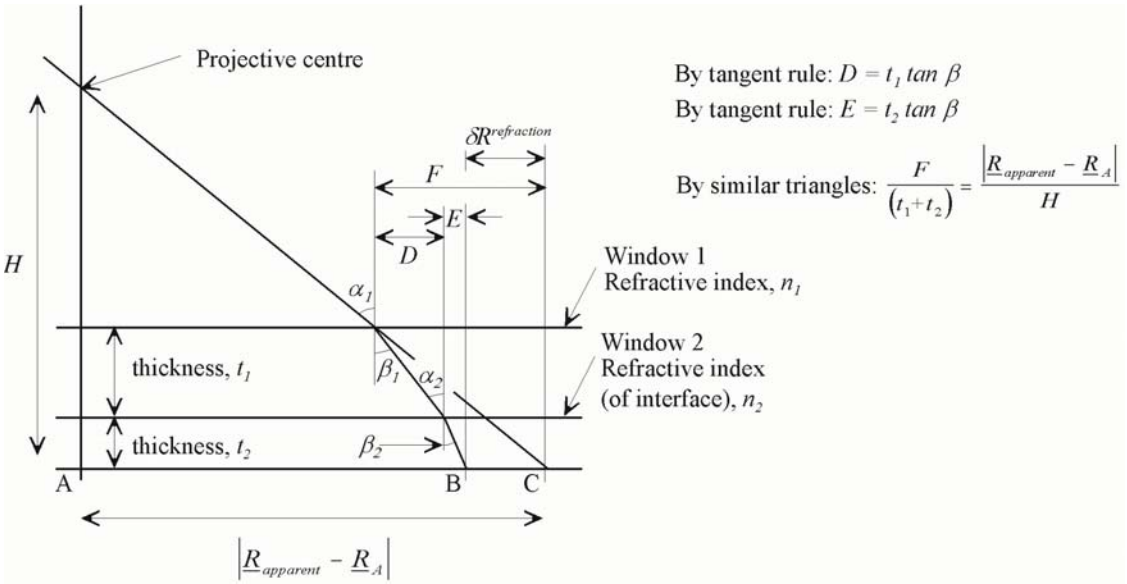

Figure 3.28 Refraction through a two-layer window

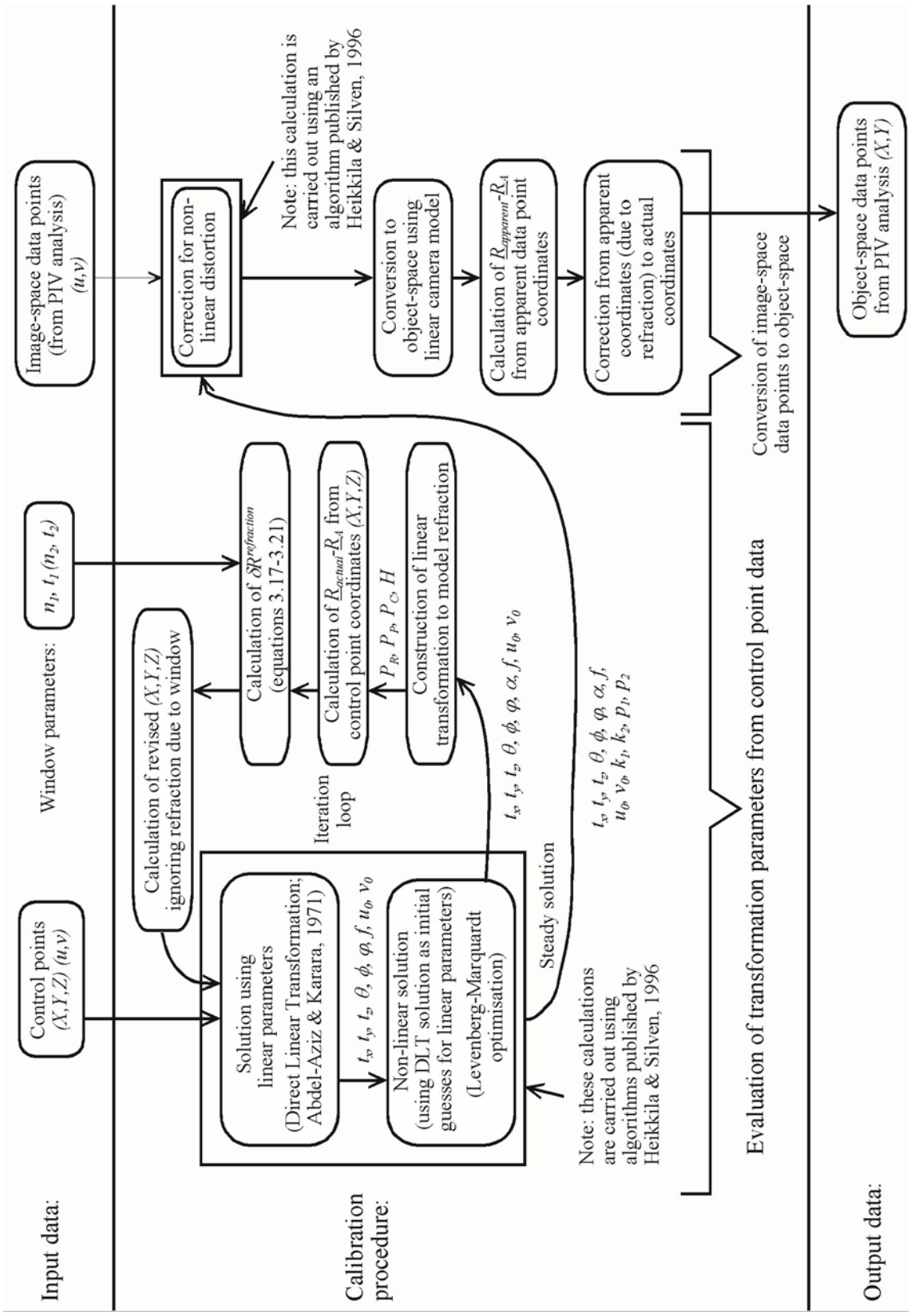

Figure 3.29 Calibration procedure

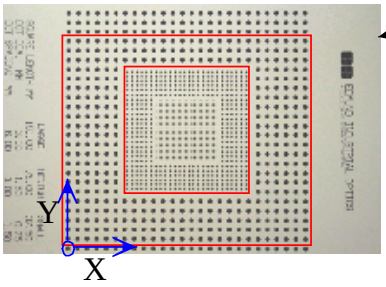

Photogrammetric target

The image-space coordinates of 376 dots within the outlined zone were located by centroiding. Since the target is precisely calibrated, the object-space locations of all dots are known.

A subset of 14 dots were used to deduce the transformation parameters

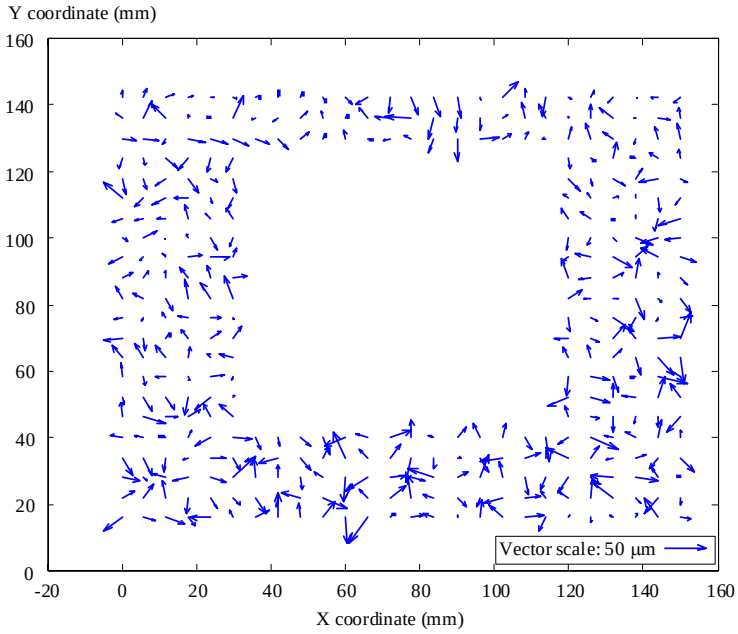

The deduced transformation parameters were used to calculate the object-space location of all 376 dots.

The discrepancy vectors between the calculated and actual locations are randomly directed.

The distribution of the magnitude of these discrepancy vectors is shown in Figure 3.31

a) Discrepancy between actual positions of dot array and positions calculated using camera calibration

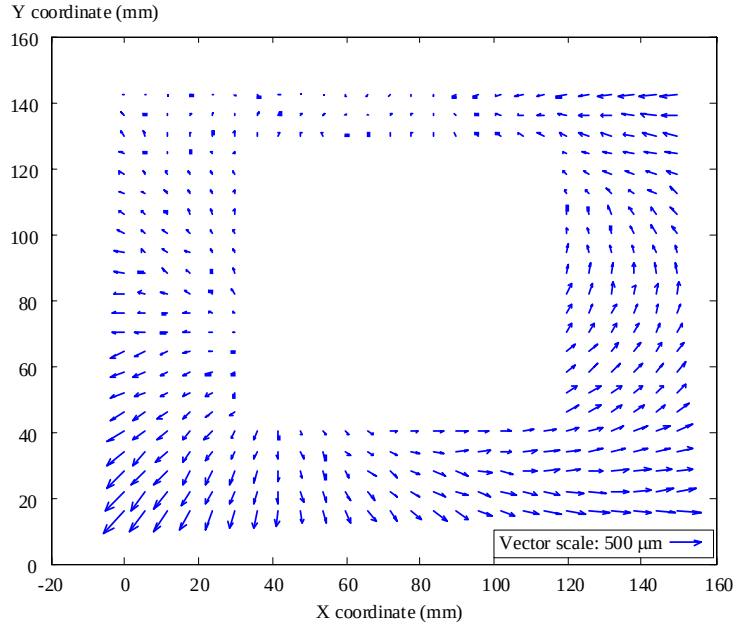

A constant image scale factor of 7.374 has been used to relate the measured image-space coordinates to the actual coordinates.

The accuracy of this scale factor is maximised by ensuring that the sum of the discrepancy vectors is equal to zero.

These discrepancy vectors show a smooth variation in magnitude and direction indicating a systematic error.

The distribution of the magnitude of these discrepancy vectors is shown in Figure 3.31

b) Discrepancy between actual positions of dot array and positions calculated using linear scaling

Figure 3.30 Reconstruction of dot array on photogrammetric target

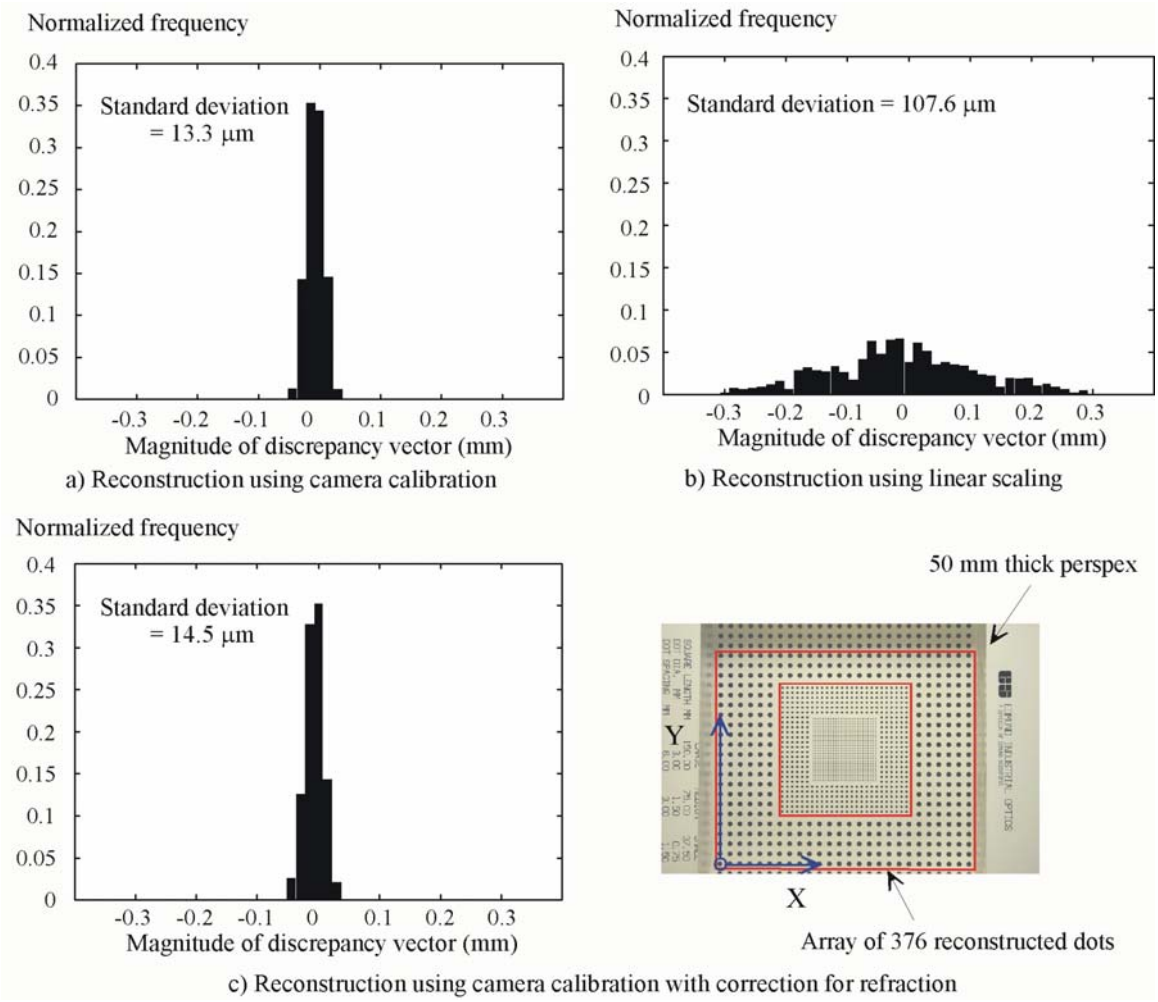

Figure 3.31 Distribution of discrepancy vectors after dot array reconstruction (after White *et al.*, 2001b)

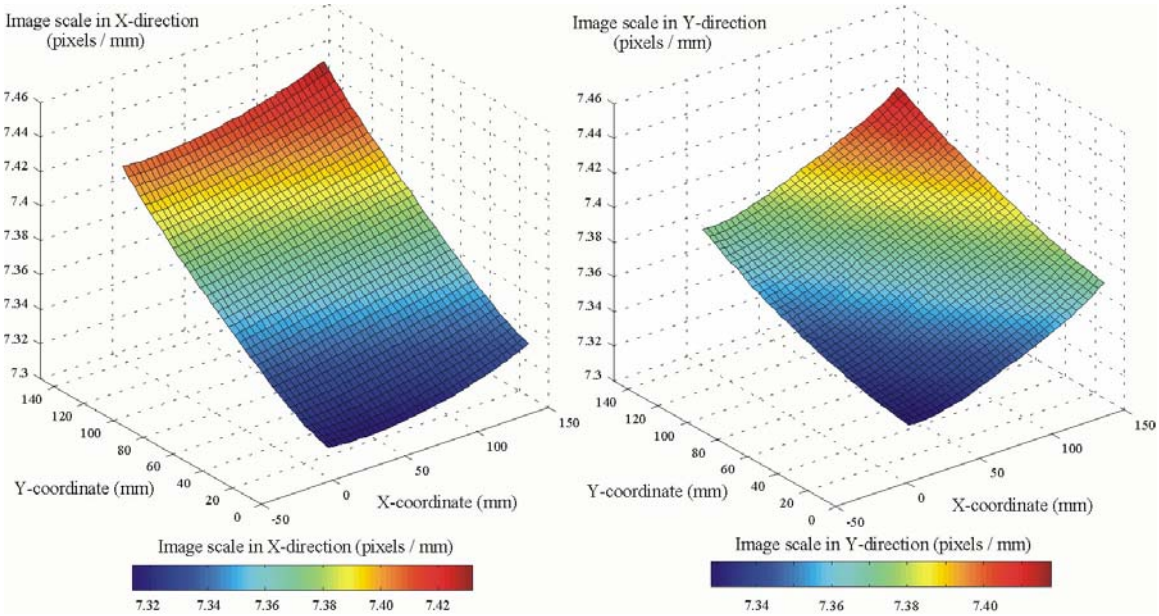

Figure 3.32 Spatial variation in image scale deduced from camera calibration (original image shown in Figure 3.34a)

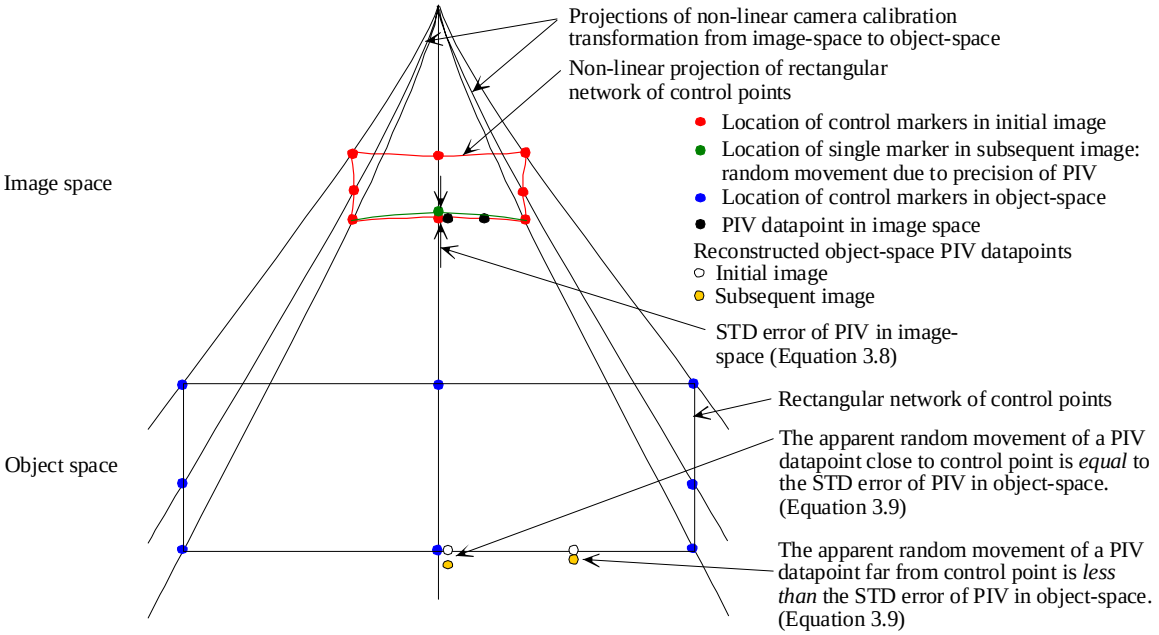

Figure 3.33 Error in PIV datapoint reconstruction due to error in control point location

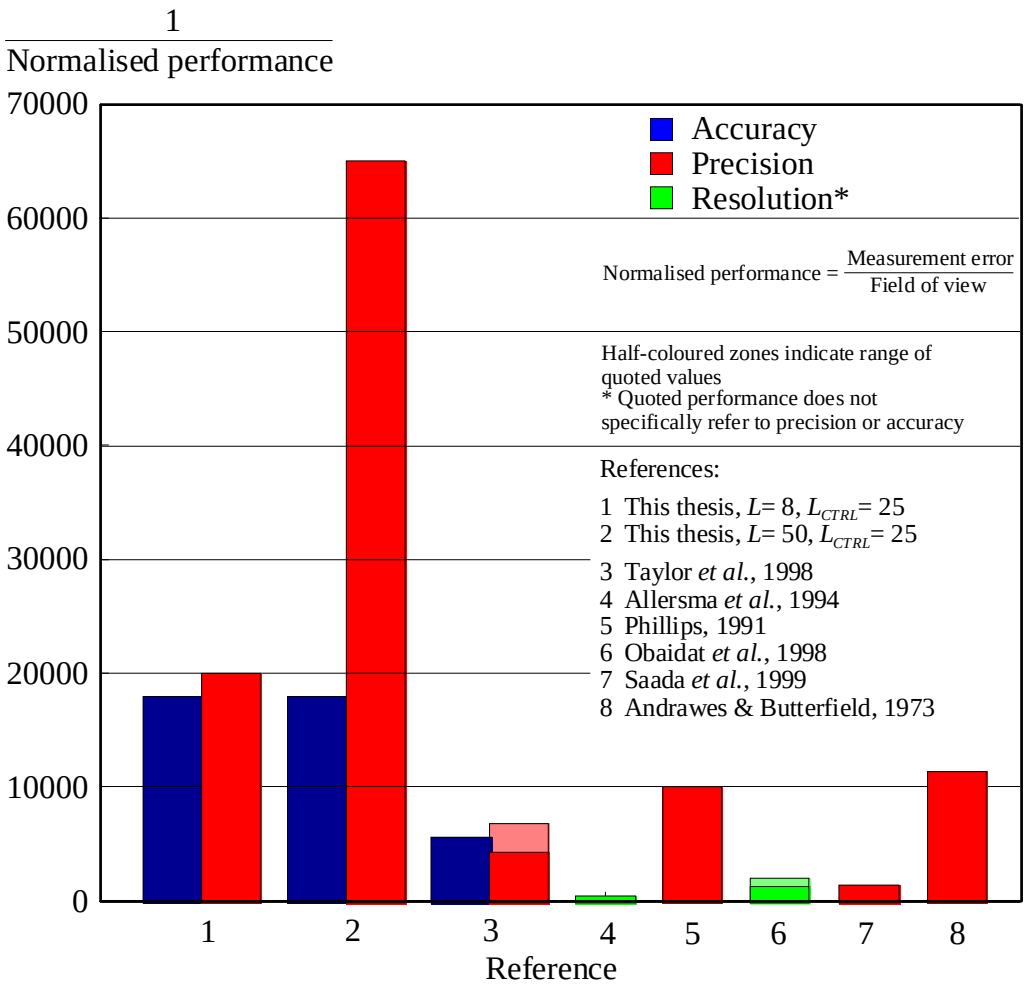

Figure 3.34 Relative performance of image-based displacement measurement systems,

or,

“Accuracy is telling the truth, precision is telling the same story over and over again” (Yiding Wang)

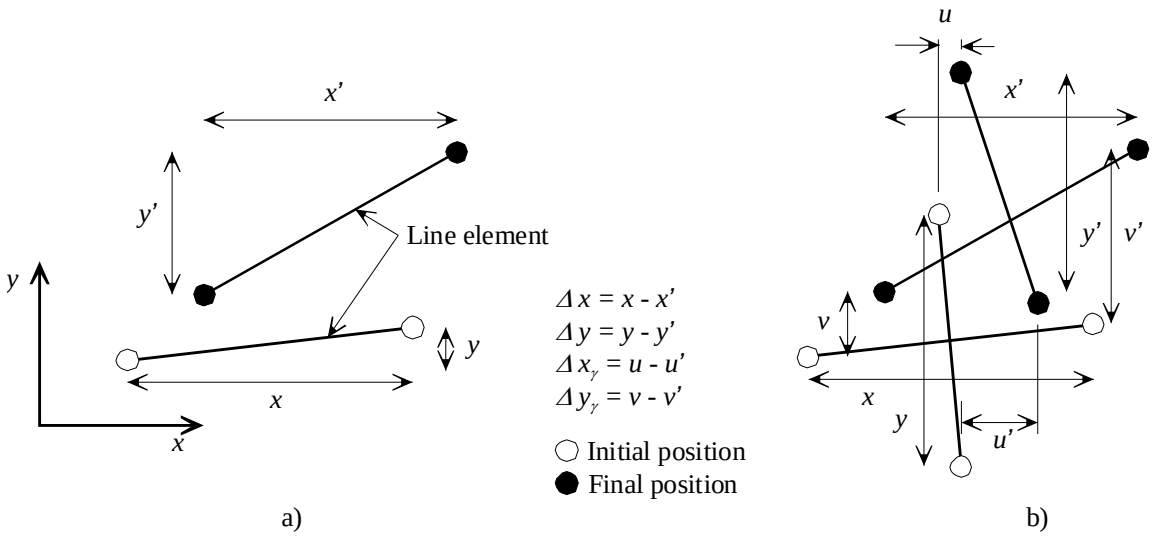

Figure 3.35 The use of line elements to deduce strains

CHAPTER 4

MODEL TESTING METHODOLOGY

4.1 INTRODUCTION

The literature review presented in chapter 2 demonstrated that the current understanding of pile behaviour is limited by the lack of knowledge of the penetration mechanism around the base of the pile. The primary goal of the model testing presented in this dissertation is to observe the ground movements associated with the installation of a pile in sand. Previous attempts to quantify these movements have been hampered by poor measurement resolution, the need to use artificial 'soil' material and the inability of the apparatus to replicate field stress levels around the pile tip. This chapter describes the design and construction of a calibration chamber that allowed pile installation to be observed without these drawbacks.

4.2 EXPERIMENTAL CONCEPT

4.2.1 Centrifuge or 1-g?

Many researchers have conducted small-scale modelling of piles using centrifuge modelling (eg. Klotz & Coop, 2001; Fioravante *et al.*, 1994; Bruno & Randolph, 1999; De Nicola & Randolph, 1997), and conventional 1-g modelling (e.g. Robinsky & Morrison, 1964; Golightly & Nauroy, 1990; Chin & Poulos, 1996; Yasufuku & Hyde, 1995; Leung *et al.*, 1996).

Mikasa & Takada (1973) demonstrated the difference in penetration mechanism between geometrically identical pile models in the centrifuge and at 1-g using stereoscopic photography (Figure 4.1). Under centrifuge conditions the penetration mechanism involves compression close to the pile tip, whereas at 1-g slip surfaces extending to the ground surface are evident. Mikasa & Takada note that this difference is due to the stress level at the pile tip. At high stress the soil is contractile, whereas at low stress the soil is dilatant. For correct replication of the penetration mechanism present in the field, the stress level at the pile tip must be replicated.

But is a centrifuge necessary? Previous researchers have used calibration chambers with surcharges applied at the boundaries to model pile behaviour at small-scale. Indeed the term ‘calibration’ was coined to describe this type of chamber during the development of correlations between the properties of soil samples prepared under carefully controlled laboratory conditions, and the resistance measured when installing field-scale CPT probes into the chamber (e.g. Houlsby & Hitchman, 1988; Jamiolkowski *et al.*, 1988; Been *et al.*, 1987; Yu *et al.*, 1996; Parkin, 1988; Baldi *et al.*, 1983). This form of research relies on the penetration resistance and hence stress regime surrounding the tip of the CPT (which can be considered as a miniature pile) being equal to conditions in the same soil and at the same ambient stress level in the field.

The fundamental difference in stress regime between a surcharged calibration chamber and a centrifuge model is not the absolute stress level that is present, but the stress gradient with depth. Replication of this stress gradient is essential for the modelling of boundary value problems in which the geo-structural mechanism involves elements which span a large ambient stress range; e.g. embankments or retaining walls. In contrast, Figure 4.1 demonstrates that the mechanism of deep penetration has a smaller zone of influence. The difference in ambient stress level within the zone of deforming soil is low in comparison to the stress level itself. Thus, it is argued that the replication of the ambient stress gradient is not essential to replication of the penetration mechanism.

Although many researchers have found success when studying penetration mechanisms through the use of calibration chambers in order to develop correlations between CPT tip resistance and soil properties, it should be noted that shaft resistance on a pile is more difficult to replicate in a chamber. The aspect ratio of a field pile cannot easily be maintained in a calibration chamber. Also, the ambient stress level along the shaft of a typical pile varies from zero at the ground surface to a few hundred kPa close to the base. This variation is not replicated in a surcharged calibration chamber. However, a comparison of recent field and centrifuge data of shaft friction distribution suggests that conventional scaling laws do not apply to shaft friction. The analysis presented in Section 2.3.2 demonstrates that 'friction fatigue' cannot be normalised by the usual scaling laws. The resulting variation in shaft friction along the length of a centrifuge model pile differs significantly from field observations. Therefore it is not necessarily true that observation of ground movement adjacent to a small-scale pile in the centrifuge would provide a significantly greater insight into the mechanisms of shaft friction than a small-scale pile in a surcharged calibration chamber.

The improved measurement precision offered by the image-based technique described in Chapter 3 requires the pile installation to take place behind a viewing window. This style of small-scale modelling is widely established for geotechnical processes in which the stress levels are close to geostatic (multiplied by the relevant scaling factor on the centrifuge); e.g. embankments, retaining walls, shallow foundations and tunnels. Windows made from Perspex or glass typically of dimensions 0.5 m × 0.5 m offer sufficient strength and stiffness.

However, penetration processes (i.e. pile and CPT installation) create stress levels that are at least an order of magnitude higher than geostatic conditions. To the Author's knowledge, the only published research in which penetration has been modelled behind a viewing window under centrifuge conditions is that of Mikasa & Tanaka (1973). Subsequent testing of this kind has been discouraged due to the difficulty of constructing a sufficiently strong and stiff window to resist the unknown stress field around the pile, noting that the consequences of failure of the window and loss of containment during a test are serious.

After considering the relevant merits of centrifuge and 1-g modelling, it was concluded that a surcharged calibration chamber was the most appropriate modelling technique for the purposes of this research.

4.2.2 Plane strain or axisymmetry?

4.2.2.1 Selection process

Two possible chamber configurations allow a model plane to be viewed: half-cylinder axisymmetry and plane strain. The choice between these two configurations was made by considering the following:

1. What is the influence of the each imposed boundary condition on the observed behaviour and what type of pile does that boundary condition represent?
2. Can each boundary condition be practically achieved within a simple experimental apparatus?

4.2.2.2 Field-scale equivalence

A model-scale axisymmetric probe is geometrically identical to a field-scale CPT, a reduced-scale close-ended tubular pile, or an open-ended tubular pile that is penetrating in a plugged manner. If similitude of stresses and strains is assumed, then a model-scale axisymmetric probe is the ideal representation of these field-scale problems.

A model-scale plane strain probe is geometrically similar, but not identical, to a section of sheet or H-section pile, or a segment of an open-ended tubular pile that is penetrating in an unplugged manner. A sheet pile does not quite represent plane strain conditions, since it is not of infinite length. However, in the terminology of strip foundations, a sheet pile typically has a length to width ratio of 15-30. For this length to width ratio, the shape factor adjustment to correct for a plane strain approximation is less than 1% (Brinch Hansen, 1970; Meyerhof, 1963).

A segment of tubular pile does not quite represent plane strain conditions due to the curvature over the segment length. An estimate of this deviation from plane strain conditions can be made by considering an extremely idealised estimate of the radial

variation in stress as follows. A simple elastic model predicts radial stress to decrease away from the surface of a tubular pile with $(r_{pile}/r)^2$. If the zone of significant deformation is around 5 wall thicknesses (eg. Chin, 1986), the drop in stress over this zone of deformation adjacent to a pile of aspect ratio, r/t, equal to 40 is only 20%. In contrast, if side friction is ignored, in plane strain conditions this stress should remain constant with distance from the pile.

4.2.2.3 Practicality of achieving the assumed boundary conditions

In practice the boundary condition of half-cylinder axisymmetry against a window is difficult to achieve during deep penetration. Any ingress of sand between the probe and the window will cause the probe to deviate from the vertical, losing contact with the window. The penetration mechanism can then no longer be observed. Furthermore, any sand ingress between the viewing window and the probe will create point loads on the window, increasing the chances of failure. These problems can be overcome in plane strain by maintaining a tight fit between the front and rear faces of the box.

After considering the relative merits of axisymmetry and plane strain, and noting that the timescale of this research would not permit the construction of more than one box, it was concluded that a plane strain box offered the best chance of successfully observing the penetration mechanism.

4.3 CHAMBER DESIGN AND CONSTRUCTION

4.3.1 Required specification

4.3.1.1 Boundary distance

A number of researchers have examined the minimum separation of a model probe and the wall of the test chamber to avoid boundary effects (e.g. Last, 1979; Parkin & Lunne, 1982; Mayne & Kulhawy, 1991). Most recently, Bolton *et al.* (1999) conducted a series of centrifuge cone penetration tests in dense Fontainebleau silica sand, with various ratios of cone to container diameter. They propose that a minimum diameter ratio of 30 is required to avoid boundary effects, although the influence of the mechanical

properties of the sand is not considered. Klotz (2000) reports a series of centrifuge model pile tests carried out with a container to pile diameter ratio of 19 in carbonate and silica sands. Although this ratio is significantly lower than that proposed by Bolton *et al.*, there is no evidence of boundary effects except in the case of dense silica sand (Klotz & Coop, 2001).

The boundary effects examined above apply to the case of axisymmetric geometry. In plane strain, the boundary should be further from the penetrometer since the stress level and displacement field decrease less sharply with distance. However, no investigation of this difference has been reported.

4.3.1.2 Displacement measurement resolution

Although a large container to pile breadth ratio is desirable to reduce the possibility of boundary effects, any reduction in pile breadth decreases the number of displacement measurement points which can be placed within the zone of interest. For optimum measurement of ground movement, a large pile breadth is desirable.

4.3.1.3 Instrumentation of the model pile

In order to measure the base resistance acting on the model pile, instrumentation is required. Typical model CPT probes and piles measure base resistance using strain gauges positioned slightly behind the tip of the penetrometer. However, this data is polluted by the influence of high shaft friction close to the tip of the probe (Bruno, 1999; Cohen & Frydman, 2002). In the case of a plane strain model, this uncertainty is increased due to the unknown friction between the probe and the viewing window.

An alternative instrumentation scheme was adopted, in which the force acting on the base of the model pile was measured directly by a button load cell embedded in the tip. This required the pile breadth to be greater than the smallest available load cell capable of carrying the expected load.

4.3.1.4 Selected chamber size

Considering the geometric constraints described above, a chamber of dimensions 1000 × 850 × 85 mm was adopted. Two pile breadths were used. The model pile in tests

DJW-01 to DJW-07 was of breadth 32.2 mm (container width to pile breadth ratio = 31). A smaller pile of breadth 16.1 mm was used in test DJW-08, increasing the container width to pile breadth ratio to 62.

The breadth of the chamber was selected as 85 mm as a compromise between minimising the influence of side friction and reducing the structural load on the actuator and reaction frame. The design maximum base resistance of 50 MPa acting on the base of the pile, plus a further 10% allowance for friction on the probe, leads to a jacking force of 125 kN, which must be reacted through the structure of the chamber.

4.3.2 General arrangement

The structural design of the chamber was carried out by the Author. Compared to cylindrical calibration chambers, the structural design of a plane strain chamber is more arduous. The penetration-induced stress field acts directly on the structure of the chamber and must be resisted in bending. In a cylindrical chamber the penetration-induced stress is dissipated before reaching the structure and can be resisted by tensile hoop stresses. CAD drawings of the completed design were produced by Mr S Lesley.

The general arrangement of the chamber is shown in Figures 4.2 and 4.3. The chamber is designed against failure at a maximum load of 50 MPa on the pile tip, and against a maximum outwards deflection of the chamber at midspan of 50 μm to prevent loss of K_0 conditions. An outwards deflection of 50 μm corresponds to a lateral strain of 0.06%.

The deflection criteria proved most demanding, and required the viewing area to consist of a thick window, divided into a grid of 6 portholes by deep I-section reinforcing straps. Since the penetration mechanism is symmetrical, the viewing window is off-centre to allow a larger part of the mechanism to be viewed. The front and rear panels are designed to be 2-way spanning using Hillerborg's strip method, with the chamber lid carrying tension. The stress field created by the penetrometer was approximated using elastic cylindrical cavity expansion theory.

The structural element of the viewing window is a 72.8 mm thick piece of Perspex. The inside of the box is lined with non-structural 4.4mm laminated glass. Perspex is used for the structural component since it has a higher allowable stress than glass, and is more safely ductile in failure. Glass is used for the inner faces of the box to reduce wall friction and to provide a hard interface to prevent scratching.

4.3.3 Manufacture

The chamber was manufactured from black mild steel. In order to allow easy handling and future modification of the completed chamber most components are bolted together. However, to provide sufficient strength, the front and rear panels of the chamber are welded assemblies. The front and rear plates were fabricated from material with a nominal thickness 10 mm greater than their finished thickness. After welding of the stiffening ribs, this allowed the inevitable bowing to be removed by machining the inner faces. The total mass of the assembled chamber excluding the actuator is 987 kg. Two lifting rods are attached to the sides of the chamber, 100 mm above the centre of gravity, to allow easy lifting and rotation to the horizontal for the purposes of assembly and post-mortem examination.

4.3.4 Actuator

The actuator consists of a machine screw driven by a stepper motor through a reduction gearbox. The machine screw is a Duff-Norton KME1819, supplied by Powerjacks Ltd of Fraserburgh, Aberdeenshire, and is equipped with a keyed thread to prevent rotation of the screw. A Parker-Hannifin SX186 Compumotor is connected via flexible couplings and a 40:1 David Brown Radicon reduction gearbox to the machine screw. A further 24:1 reduction is provided within the worm drive of the machine screw.

The stepper motor allows the displacement of the pile head to be found from feedback of the motor position, removing the need for a displacement transducer. This measurement is influenced by the stiffness of the loading system. Any deflection of the loading system leads to ‘false’ measurement of pile head displacement. A simple elastic analysis of the reaction frame was carried out to estimate deflection under maximum design load. A jacking force of 125 kN was calculated to cause an upwards deflection of

125 μm of the machine screw. The maximum deflection of the flexible couplings is estimated to be 4 degrees. Summation of the deflection of both couplings, and reduction through the gearboxes leads to a further false displacement at the pile head of 7 μm. The final component of false deflection arises from compression of the leadscrew. This was calculated from the manufacturer's data as 150 μm under maximum load. After installation of the model pile to a depth of 500 mm, assuming the maximum base resistance of 50 MPa is encountered, the total deflection of the loading system represents a displacement error of less than 0.05%.

4.3.5 Surcharge system

A vertical stress boundary condition was applied by a pair of rubber surcharge bags placed on the surface of the sand on either side of the model pile. The lid of the chamber provided reaction against these bags. The lid also acted in tension, holding together the front and rear faces of the chamber. The bags were pressurised by compressed air. A relief vent close to the inlet of each bag ensured a continuous flow through the supply line, smoothing the performance of the regulator. The pressure within the bags was monitored by a Druck PDCR810 pressure transducer.

4.3.6 Instrumentation

The total stress acting on the chamber base below the pile tip was measured using an Entran ELW-D2-2.5kN washer load cell (Figure 4.4). This was mounted within a circular surround before machining to ensure a flush fit. The successful measurement of total stress in soil requires that the stiffness of the load cell be matched with the stiffness of the surrounding material. Any differential settlement of the load cell and the surrounding material will change the measured force. This effect is widely overlooked by experimentalists, and is often the source of unexpected results when using total stress cells.

Clayton & Bica (1993) examined the influence of diaphragm stiffness on the response of total pressure cells. The Cell Action Factor (CAF) is defined as the ratio of measured stress to the value that would have applied in the absence of the pressure cell. Ideally, this value should be close to unity. Askegaard (1961) relates the CAF of diaphragm

load cells to the flexibility ratio, F, of the cell-soil system. The flexibility ratio is a function of the stiffnesses of the soil, E_{soil} and the diaphragm material, E_{cell}, the radius of the diaphragm, R, and the thickness of the diaphragm, t (Equation 4.1).

$$F = \frac{E_{soil} R^3}{E_{cell} t^3} \tag{4.1}$$

The relationship between CAF and flexibility ratio found by Clayton & Bica (1993) applies to diaphragm-type load cells. For estimation of the CAF of a piston-type load cell arrangement, as used in this research, it is suggested in subsequent discussion that the deflection of a piston-type cell should be doubled for equivalence with the midspan deflection of a diaphragm load cell (Clayton & Bica, 1995). This approach has been used to estimate the CAF of the Entran washer load cell. Using values of sand stiffness at low and high stress levels from Baldi *et al.* (1987) and Coop (1990), the predicted CAF varies from 0.87-0.92 and 0.90-0.96 in silica and carbonate sand respectively.

4.3.7 Influence of boundaries

The influence of friction between the sand and the front and rear faces of the chamber on the idealised plane strain conditions is considered as follows. Glass sheets are used on both inside faces of the box to reduce the angle of interface friction. The mean glass-sand friction angle, δ_{sg}, for Fraction B Leighton Buzzard silica sand was measured as 11° in a series of three direct shear box interface tests. This value matches well with Dietz's (2000) measurements of interface friction angle between sand and polished steel (which has a comparable relative roughness), and is slightly lower than the value of 14° reported by Cousens (1975) for a finer fraction of Leighton Buzzard sand.

Since the interface friction angle is significantly lower than the soil friction angle, failure will occur at the interface rather than within the soil body. This, coupled with the tight fit of the model pile between the front and rear faces of the chamber, ensures that the ground movement observed at the window is equal to that present through the soil model.

However, although the deformation is constant through the plane of the model, the stress field is influenced by wall friction. The magnitude of this effect is examined by considering the transmission of the surcharge load through the soil mass to the chamber base. In the absence of wall friction, the stress on the chamber base would be equal to the applied surcharge pressure plus the weight of the soil. However, during application of the surcharge load, upwards wall friction acts on the soil, creating arching. Equilibrium analysis allows the resulting profile of vertical stress with depth to be deduced (Appendix 3). The influence of wall friction is strongly dependent on β ($=K_0 \tan \delta$), which can only be estimated from measured values of δ and predicted values of K_0.

Figures 4.6 shows profiles of vertical stress with depth for various values of β. Arching is clearly evident, even for low values of β. This sharply varying profile of vertical stress with depth was partly overcome during this research by reducing the surcharge to 50 kPa after loading to 100 kPa prior to each test. The profiles of vertical stress with depth predicted using the vertical arching analysis described in Appendix 3 are shown in Figure 4.7. Whilst the variation in stress is now reduced, the OCR varies with depth. However, these low values of OCR at such low stress levels are not considered to have a major influence on the resulting behaviour. The loading and re-loading stiffness of sand in one-dimensional compression at stresses of less than 100 kPa are almost identical. At this low stress level, the ‘knee’ in the normal compression line, and hence the onset of significant irrecoverable volume change, has not been reached.

This influence of pre-compression can be quantified by considering the variation of sand state with depth after pre-compression. Stress state (Coop & Lee, 1993; Jovocic & Coop, 1997) and volume state (Been & Jefferies, 1985) parameters are widely used to interpret soil behaviour and derive correlations with soil properties. For satisfactory initial conditions a minimal variation in state parameter with depth is desired. In stress-volume space, this implies that the soil at all depths should be similarly distant from the normalising reference states of the critical state line (CSL) and normal compression line (NCL).

This variation in state is examined as follows for the two sands used in this research: Dog's Bay carbonate sand and Leighton Buzzard Fraction B sand. Figure 4.8 uses the non-linear critical state line for Dog's Bay sand presented by Klotz (2000) to estimate the soil state after pre-compression along a typical K_0 compression curve (from Coop, 1990). The volume state parameter, ψ, is shown to be virtually unaffected by pre-compression, whilst the stress state parameter, p'/p'_e, is changed slightly. Over the range of vertical stress present after pre-compression (from the predictions shown in Figure 4.7), the stress state parameter varies by ± 15% from the mean throughout the depth of the calibration chamber.

This variation in state predicted for Dog's Bay sand (DBS) is significantly greater than the influence of pre-compression on the state of Leighton Buzzard sand (LBS). No published NCL is available for fraction B LBS due to the high stress required to reach this line, preventing identification of the stress state parameter. However, the CSL presented by Klotz (2000) for fine LBS lies approximately one log cycle to the right of that for DBS at the same relative density. Therefore, the small changes in stress due to pre-compression of LBS are even more remote from the NCL and CSL than in DBS.

Further analysis of the measured variation in vertical stress with depth is presented in Chapter 5, using data from the load cell in the base of the chamber.

4.4 MODEL PILES

4.4.1 Design and manufacture

The model piles were machined from Duraluminium, and fitted with 3 mm thick stainless steel base plates. Piles of two breadths were used: 32.2 mm and 16.1 mm. A narrow hole was drilled longitudinally through the pile to carry the load cell wiring. After assembly of the chamber using fresh glass plates, the pile was machined to provide a tight fit across the width, to allow for the slight variation in thickness of different batches of glass (typically ±40 μm).

The surface of each pile was machined in a vertical direction. The resulting roughness was measured using a Scanning White Light Interferometer (SWLI) manufactured by the Zygo Corporation, Middlefield, Connecticut, USA. This machine was used to determine average roughness, R_A, at ten locations parallel and perpendicular to the direction of machining. Parallel to machining, i.e. in the vertical direction during installation, the average value of R_A found from 10 measurements was 0.326 μm. Perpendicular to machining, in the horizontal direction, R_A was equal to 1.424 μm. These values compare closely with other reported model pile tests, which typically use piles of roughness 1-2 μm (Bruno, 1999; Klotz, 2000).

The tip of the pile was fitted with a driving shoe for test DJW-07. The driving shoe consisted of the standard load cell cover plate shown in Figure 4.5, extended to overhang on either side of the pile by 4 mm.

4.4.2 Instrumentation

Load cells were used to measure the force on the base of the pile and the base of the chamber directly below the pile. To ease construction and improve reliability a commercial load cell inset within the pile base was preferred to an arrangement of strain gauging close to the pile tip. The pile base load cell for tests DJW-01 to DJW-07 is shown in Figure 4.5. During initial design of the model pile, the smallest load cell capable of withstanding the expected load without unacceptable deflection was the ELHM-B4-50kN compact load cell manufactured by Entran, Watford, UK.

To fit this load cell within the pile base, a breadth of 32.2 mm was required. Subsequently, an XFC-100 miniature load cell manufactured by GS Sensors, Ephrata, Pennsylvania, was used to fabricate a second, narrower, model pile for use in test DJW-08. The load cells were mounted within the model pile before the base was machined, ensuring a flush fit between the load cell cap and the base of the pile. The CAF of this load cell was calculated as varying from 0.85 to 0.91 in loose carbonate and dense silica sand respectively, following the procedure described in Section 4.3.6.

4.5 EXPERIMENTAL PROGRAMME

4.5.1 Sand properties

4.5.1.1 Crushable and uncrushable sands

The mechanical behaviour of sands is usually considered to depend on whether or not the particles are crushable, with existing literature making a sharp distinction between the two. This has derived from the historic tendency for sands to be tested at stresses which are too low for the clearly defined common reference states of a linear CSL and NCL to be reached (e.g. Airey *et al.*, 1988).

Instead, in very general terms, crushable sands have been characterised by high peak angles of friction which decrease with stress level and decay sharply with shear strain (Yasufuku & Hyde, 1995). Compression of crushable sands leads to significant volume change due to particle breakage, which offsets the influence of dilation due to rearrangement. Uncrushable sands are characterised by a smaller variation in angle of friction with stress level and very high volumetric stiffness. Significant dilation occurs during shearing of loose samples.

However, when taken to higher stresses such as those induced by pile installation, sands which are considered crushable, as well as those not normally thought so, reveal similar patterns of behaviour. These patterns have much in common with Critical State Soil Mechanics, and are often related to particle breakage (Coop, 1999).

Two sands were selected for this research project, representing two extremes of mineralogy and particle strength; Dog's Bay carbonate sand and Leighton Buzzard Fraction B silica sand.

4.5.1.2 Dog's Bay carbonate sand

Dog's Bay sand is of biogenic origin with 88-94% carbonate content (Houlsby *et al.*, 1988) and consists of broken shell fragments. The open structure created by these angular particles allows high voids ratios to be achieved. However, the low number of

contact points between adjacent angular particles, combined with the low Moh hardness of calcite compared to quartz, means that the onset of particle breakage in carbonate sands occurs at significantly lower stress levels than in silica sands (Airey *et al.*, 1988). The mechanical properties of Dog's Bay sand have been reported by Golightly & Hyde (1988), Coop (1990), Yasufuku & Hyde (1995) and Jovocic & Coop (1997).

It should be noted that previous research has been conducted using different gradings of Dog's Bay sand. Firstly, two distinct gradings have been obtained from Dog's Bay near Roundstone, Connemara, Ireland. Working at the University of Oxford, Evans (1987) identified this site as a suitable source of carbonate sand with similar properties to the problematic Australian Rankin field deposits and collected sand from a dune environment with a D_{50} size of 0.2 mm (Houlsby *et al.*, 1988); this sand is subsequently referred to as the Oxford batch. Further sand was obtained from Dog's Bay as part of wider study of carbonate sands by Golightly (1989) at the University of Bradford. The early batches of sand used by Golightly were collected from the dune and have a D_{50} of 0.44 mm. Later batches used during the Bradford research were dug from below the high water mark and are coarser. This sand is referred to as the Bradford batch.

Secondly, researchers have often chosen to test only a selected grading of the natural soil. Golightly (1989) removed the gravel fraction and fines smaller than 60 microns from the Bradford batch. Coop (1990), Coop & Lee (1993) and Klotz (2000) used only a narrow band of the original Oxford batch, typically between the 150-212 μm sieve sizes. The resulting PSD curves are shown in Figure 4.9. During previous triaxial studies (Coop, 1990; Coop & Lee, 1993), the sand has not been reused between tests, to avoid errors due to different initial gradings. This was not possible during the centrifuge test series reported by Klotz (2000) due to the volume of sand required. Instead the original grading curve was reconstructed between tests. Although this process of resieving restores the grading curve, the shape distribution is not restored since particle breakage increases roundness (Festag & Katzenbach, 2001).

The research described in this dissertation was carried out using the natural grading of the Bradford batch of Dog's Bay sand having been passed through a 1.18 mm sieve to

remove the gravel fraction. This sand was provided by Dr A.F.L. Hyde of the University of Sheffield, and formerly of the University of Bradford. The PSD curve found by sieving is shown in Figure 4.9. Index properties are shown in Table 4.1, and a photograph of typical grains is shown in Figure 4.10a.

4.5.1.3 Leighton Buzzard Fraction B silica sand

Leighton Buzzard sand has been widely used in research for the past 50 years, and is a rounded silica sand (Figure 4.10b). Although no longer quarried from Leighton Buzzard, the material originates from the same geological deposit, the Lower Greensand. The original name has been kept for continuity. Fraction B is the 0.6-1.18 mm sieve fraction, and is often referred to as 14/25. The mechanical behaviour of this fraction has been investigated by Stroud (1971), Budhu (1979), Lee (1989) and Schnaid (1990). Index properties of the sand used in this research are shown in Table 4.1.

For both sands, the maximum voids ratio was found using the procedure described in BS1377 (1990). To avoid grain crushing, the minimum voids ratio was found by vibrating a 1 kg sample without the use of a surcharge weight. The resulting values match closely with those previously published (eg. Stroud, 1971; Golightly & Hyde, 1988).

Sand	*Mineralogy*	G_s	D_{50} *(mm)*	e_{max}	e_{min}
Dog's Bay sand	Calcium carbonate	2.75[1]	0.44	1.87	0.98
Leighton Buzzard fraction B	Silica	2.65[2]	0.84	0.80	0.51

[1] From Golightly (1989). [2] From Tan (1990).

Table 4.1 Index properties of test sands

4.5.2 Test details

A series of 8 tests were carried out (Table 4.2). Sample density, sand type, pile breadth and pile tip geometry were varied during the test series. Tests DJW-01 – DJW03 and DJW-06 were conducted using DBS at different initial states. Tests DJW-04 and DJW-05 were conducted using LBS at two different initial states. Test DJW-07 featured a pile shoe and test DJW-08 used a narrower pile. In each case the surcharge pressure

was 50 kPa, following pre-compression to 100 kPa. All models were poured and tested dry.

Test identity	*Date*	*Sand type*	*Initial voids ratio, e_0*	*Relative density (%)*	*Pile breadth (mm)*	*Pile tip configuration*
DJW-01	8/6/00	DBS	1.30	64	32.2	Flat-ended
DJW-02	16/8/00	DBS	1.48	44	32.2	Flat-ended
DJW-03	28/9/00	DBS	1.24	71	32.2	Flat-ended
DJW-04	26/02/01	LBS	0.70	34	32.2	Flat-ended
DJW-05	4/4/01	LBS	0.64	55	32.2	Flat-ended
DJW-06	27/6/01	DBS	1.12	84	32.2	Flat-ended
DJW-07	25/9/01	DBS	1.47	45	32.2	Driving shoe
DJW-08	29/10/01	DBS	1.46	46	16.1	Flat-ended

Table 4.2 Calibration chamber test series

4.5.3 Model preparation

Each sand model was prepared by dry pluviation using an automated sand pourer. This device allows drop height and volume flow rate to be varied in order that the desired sample density can be achieved. Each model was poured in lifts of approximately 50 mm with density checks carried out after each lift. The relative density of lifts within a single model fell within a range of ±2%.

4.5.4 Control points

A set of control points was installed within each porthole in the viewing window. These control points were printed onto overhead transparency sheets and measured using the procedure described in Section 3.7.2.5 prior to installation between the glass sheets and the Perspex window.

4.5.5 Lighting

The viewing window was illuminated using a set of halogen floodlights. These provided very bright coverage of the exposed plane of soil, but also strongly heated the nearby cameras. This heating resulted in a loss of colour quality if the cameras were allowed to overheat and may also be the source of a small apparent camera motion as the camera mounting plates heated up. The close range photogrammetric correction procedure allowed this camera movement to be isolated from the soil movement.

4.5.6 Test procedure

The procedure followed during a typical test is described in Appendix 4.

4.5.7 Post-mortem analysis

After completion of each test the chamber was rotated to the horizontal and the front assembly removed to reveal the entire front plane of soil. During this operation, although some slumping of the soil close to the deflated surcharge bag occurred, the remaining soil appeared undisturbed. A mosaic of close-up photographs of the soil fabric in the disturbed zone close to the pile was taken. Finally, small samples of sand were taken from a grid of points close to the pile for future analysis.

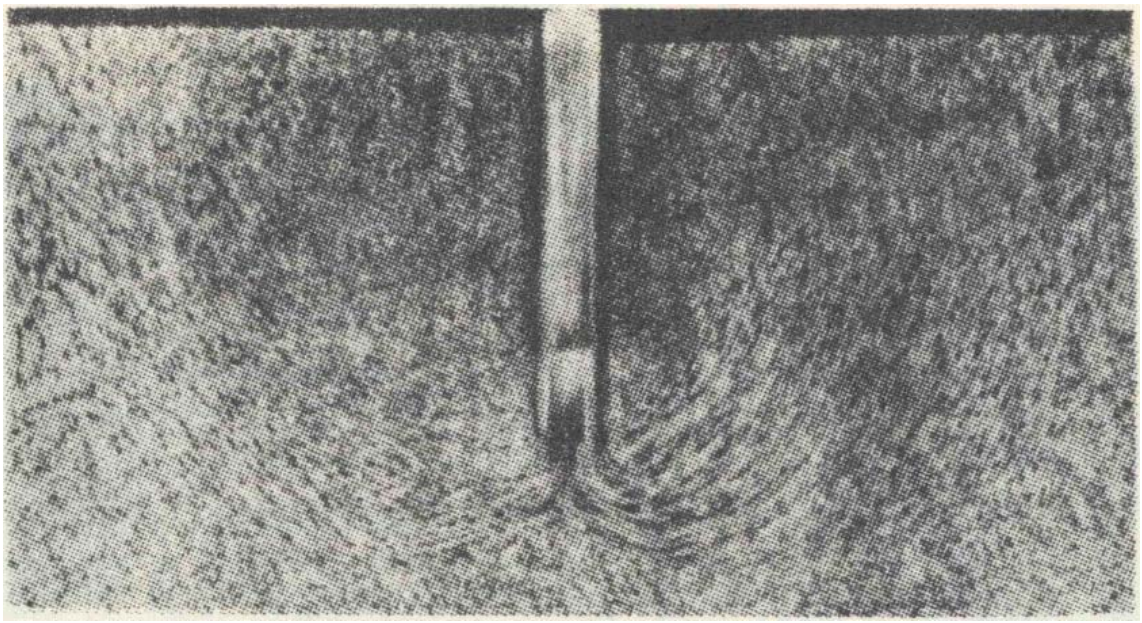

Pile installation at 1-g without surcharge

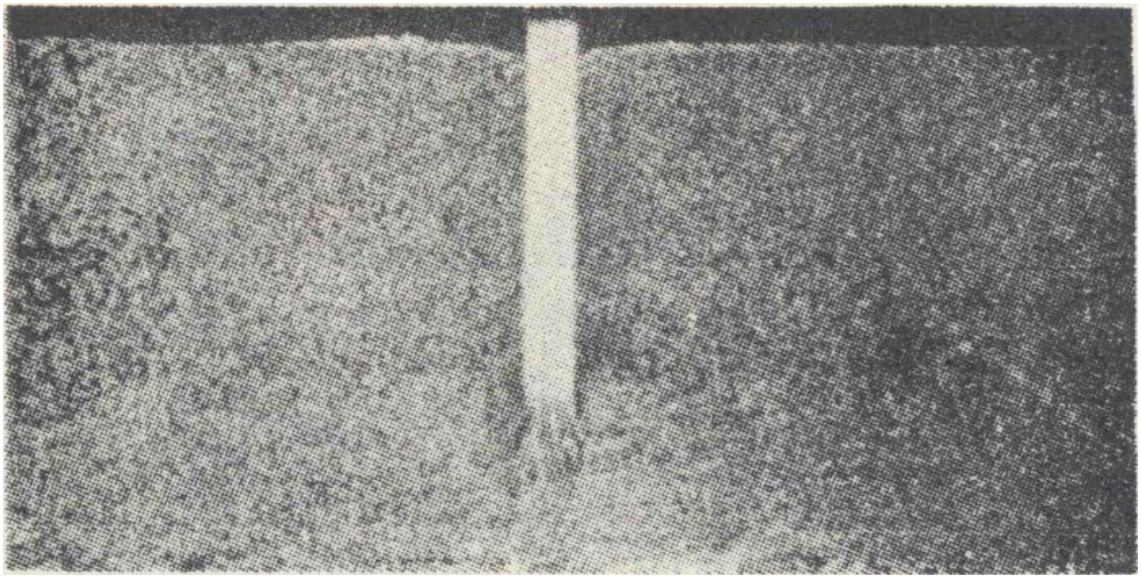

Pile installation at 40-g

Figure 4.1 Particle movements during pile installation at 1-g and in a centrifuge (Mikasa & Tanaka, 1973)

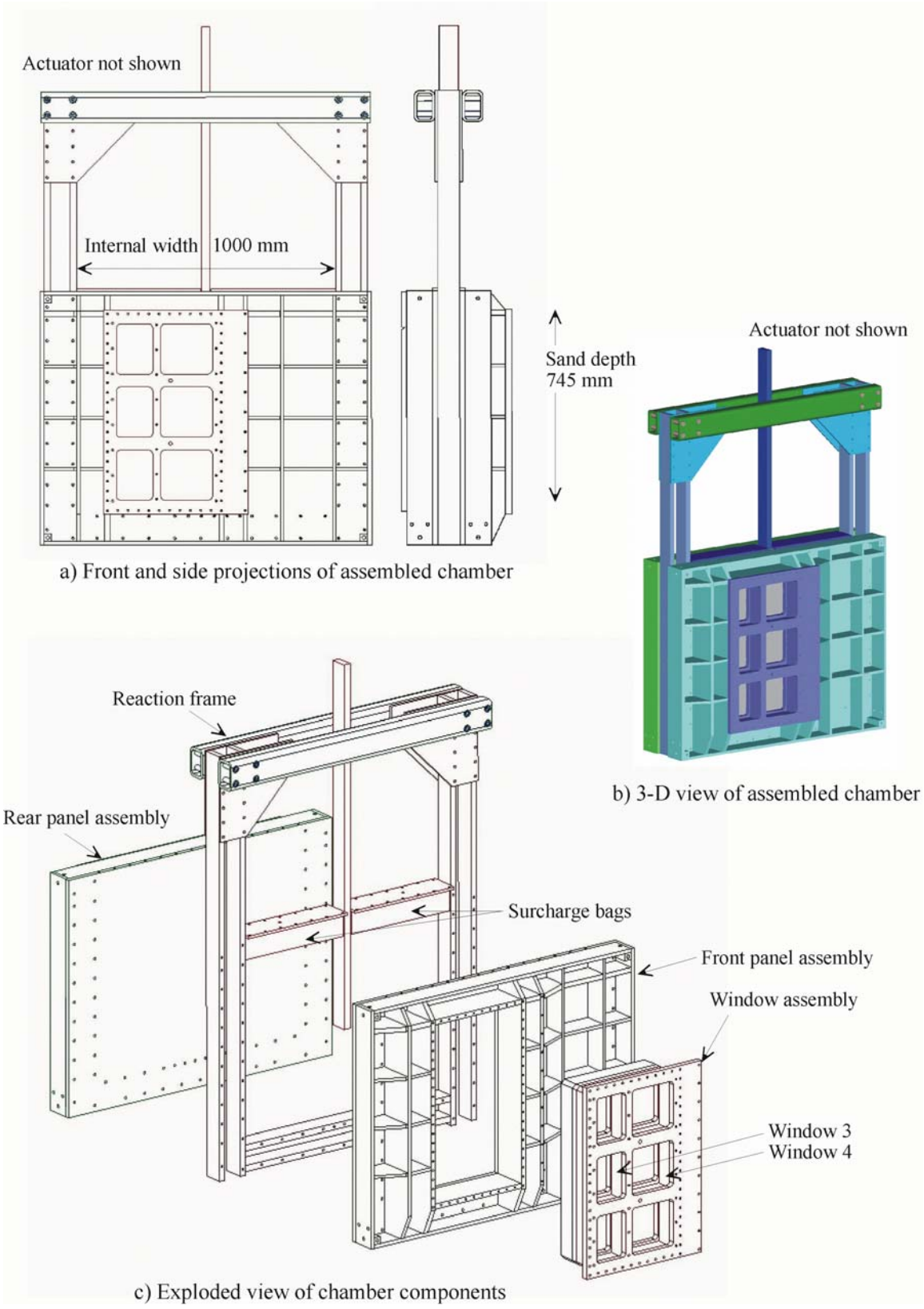

Figure 4.2 Schematic arrangement of calibration chamber

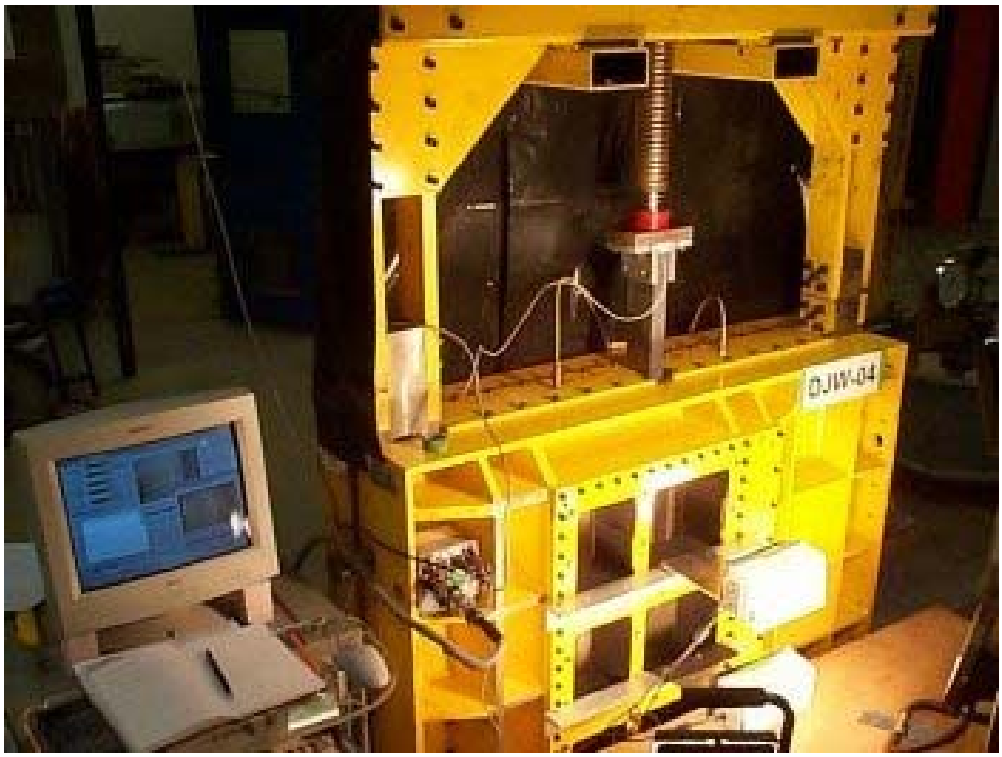

Figure 4.3 Assembled calibration chamber

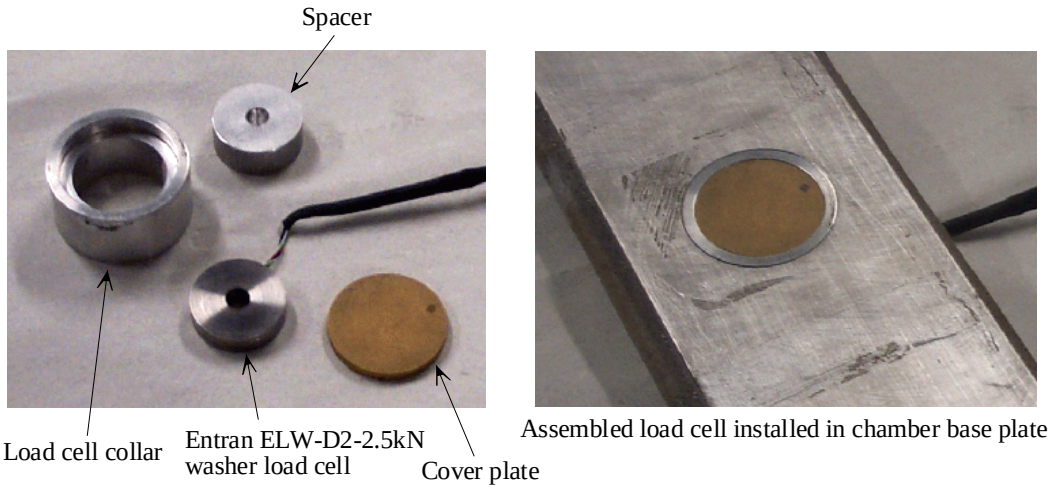

Figure 4.4 Load cell to measure stress acting on chamber base below pile tip

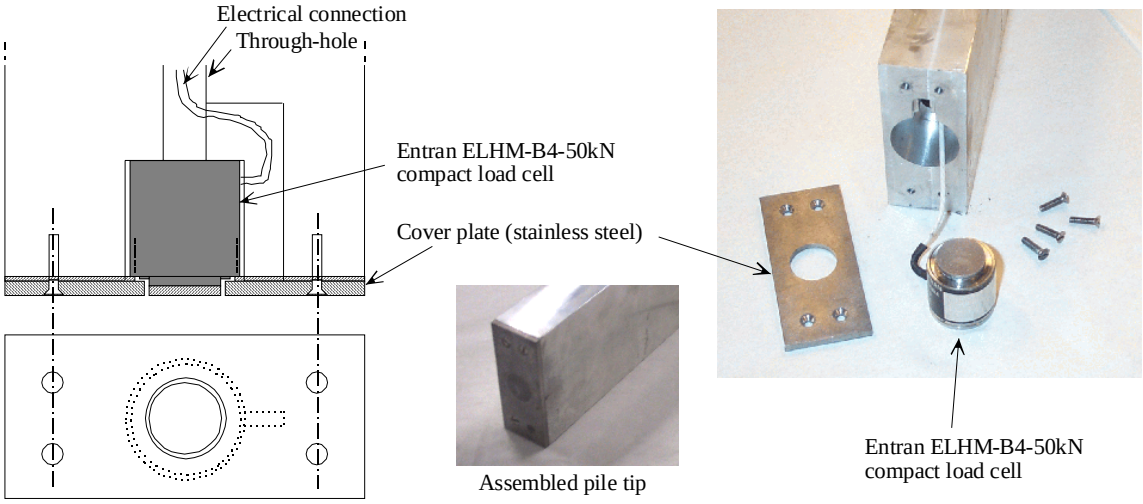

Figure 4.5 Load cell to measure base resistance acting on pile tip

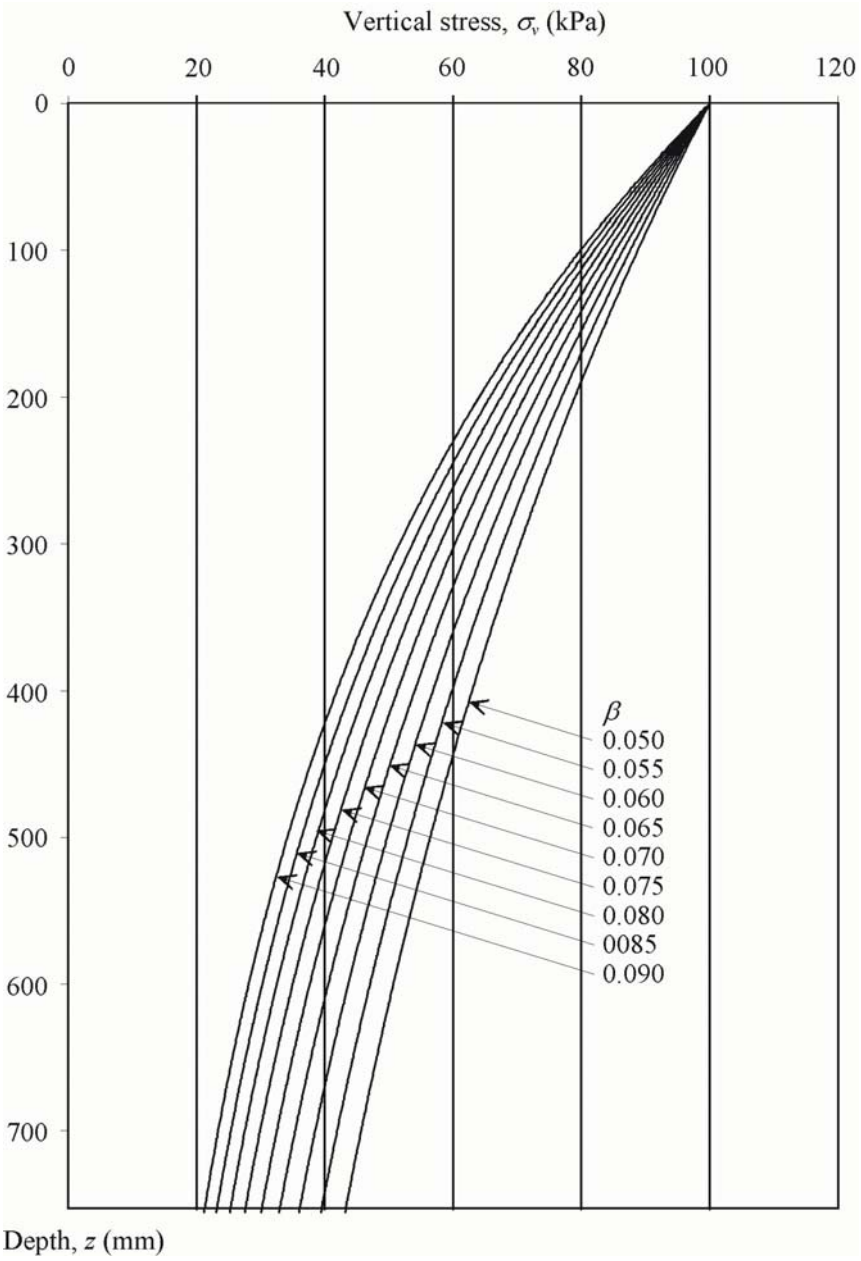

Figure 4.6 Predicted profile of vertical effective stress after compression to 100 kPa

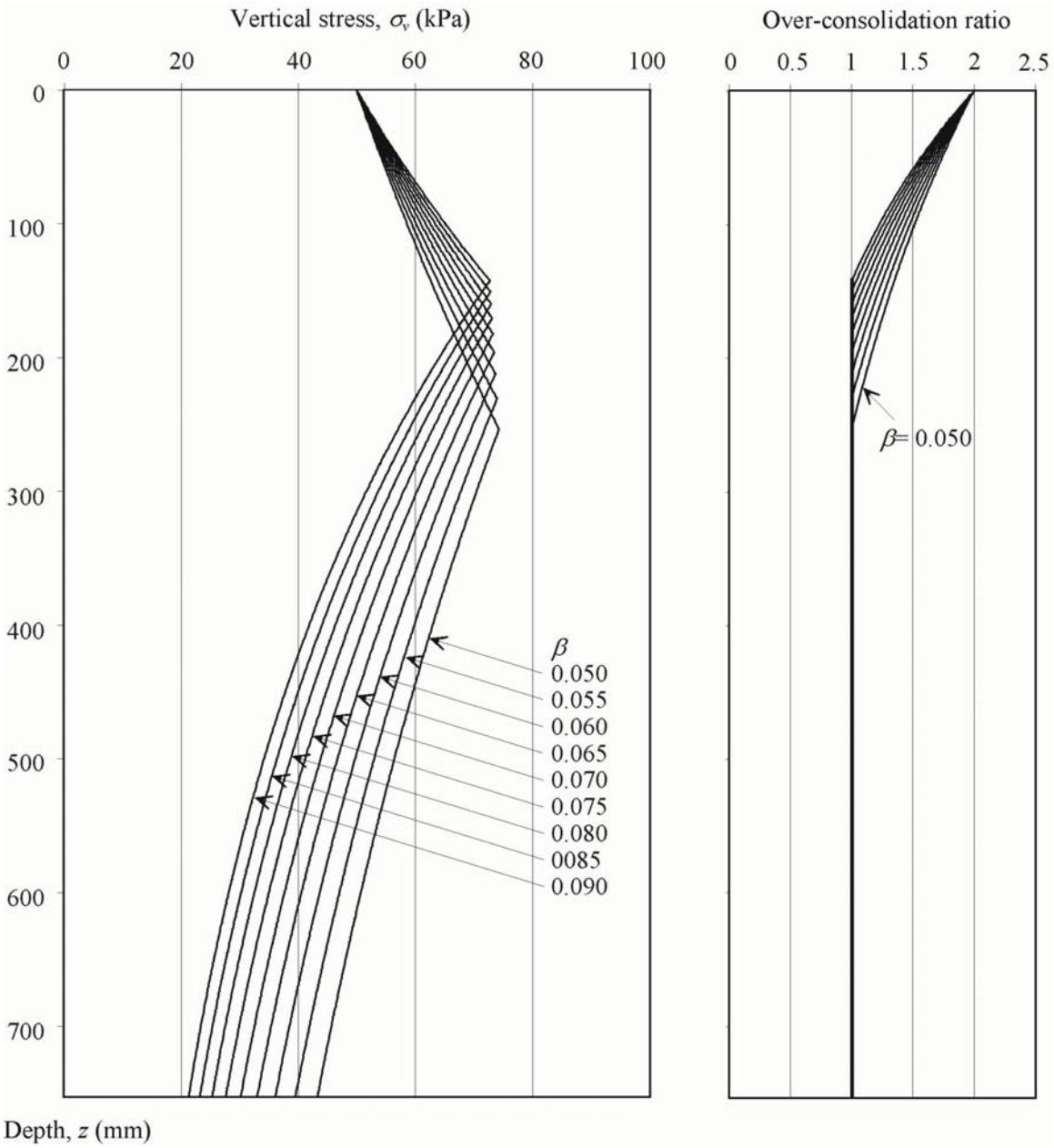

Figure 4.7 Predicted profile of vertical effective stress after pre-compression to 100 kPa and unloading to 50 kPa

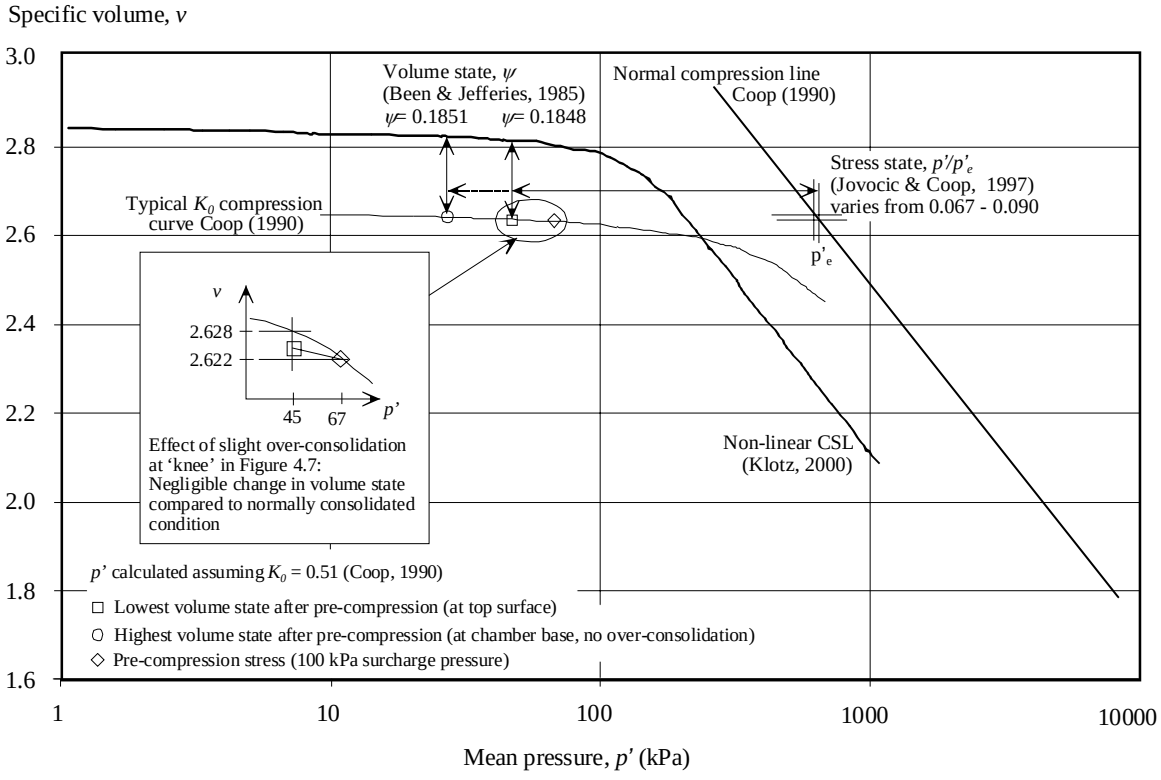

Figure 4.8 Influence of pre-compression on soil state

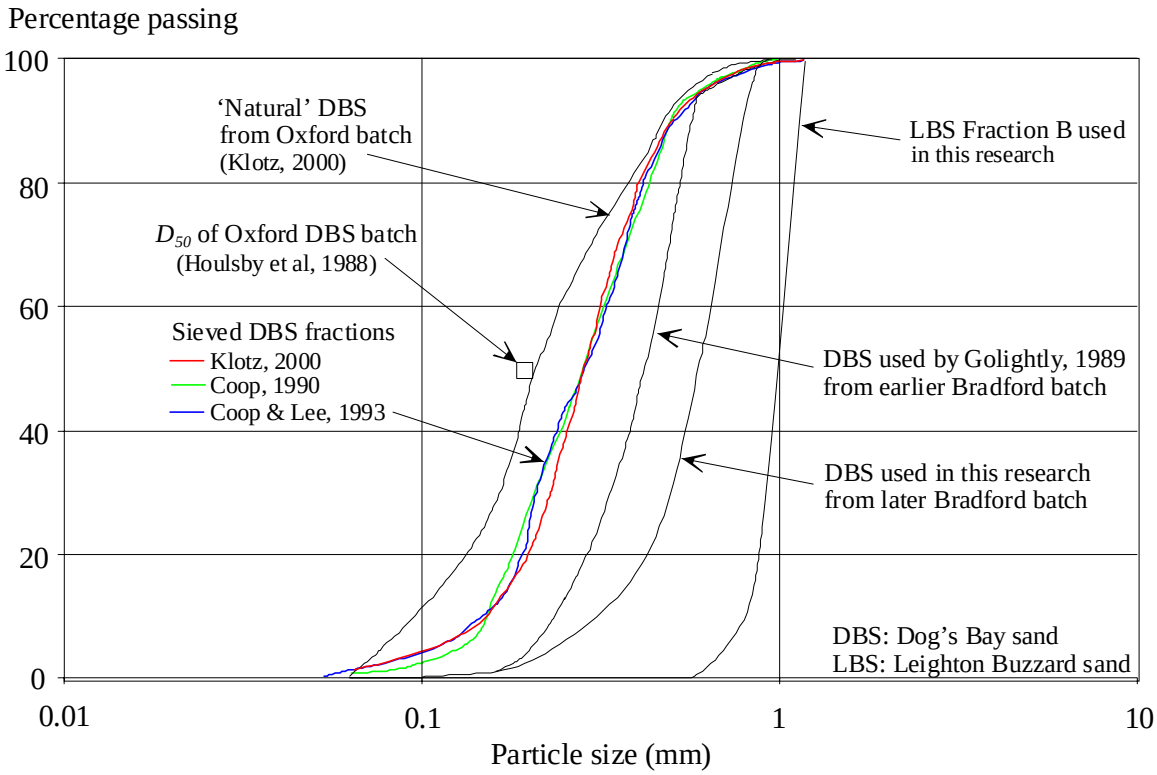

Figure 4.9 Grading curves of test sands

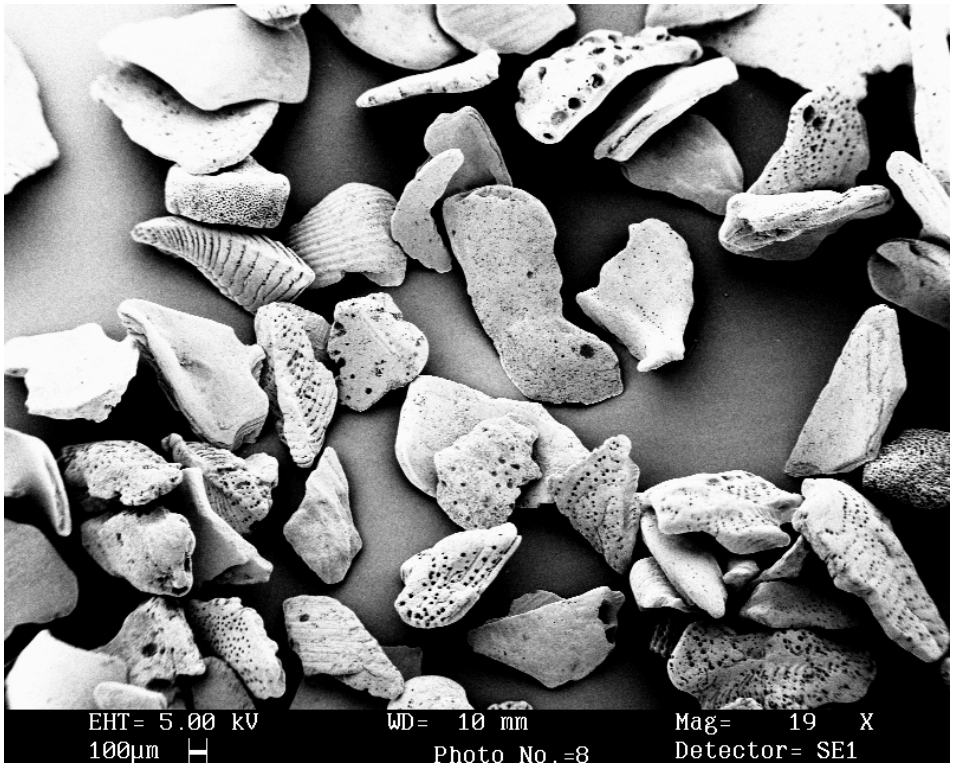

a) Dog's Bay carbonate sand (SEM image from Bowman *et al.*, 2001)

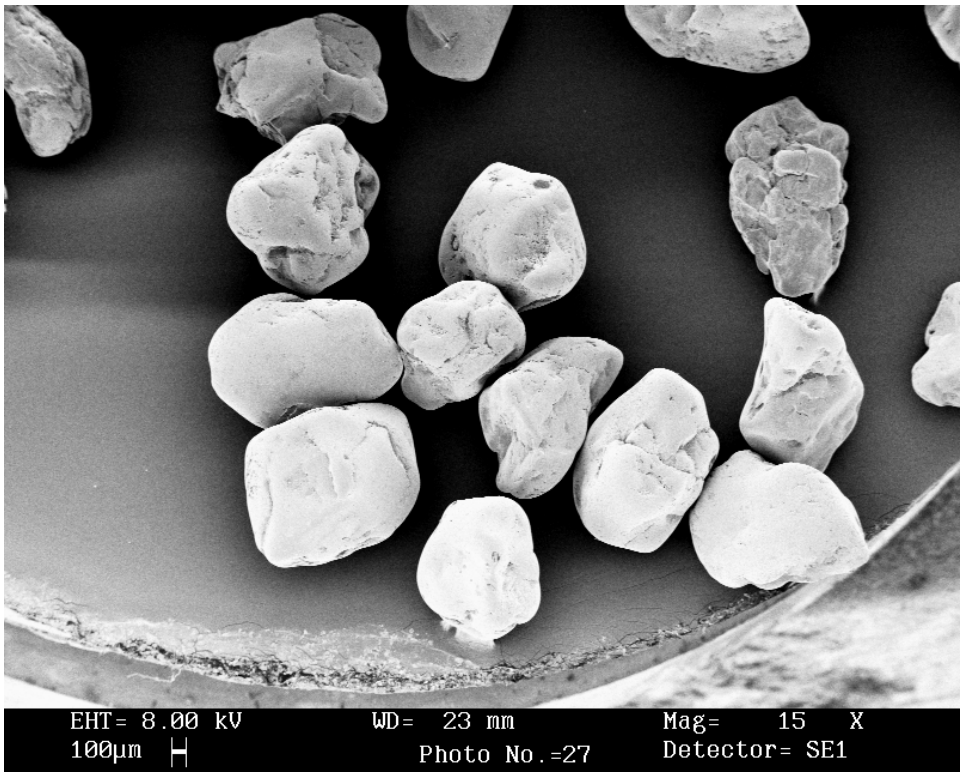

b) Leighton Buzzard Fraction B silica sand (SEM image from Sentenac *et al.*, 2001)

Figure 4.10 Typical grains of each test sand

CHAPTER 5

MODEL TESTING RESULTS

5.1 INTRODUCTION

This chapter presents results and analysis of the calibration chamber test programme. The results are divided into two parts. Firstly, data from the conventional instrumentation is discussed. This includes load-depth profiles for each pile installation, and the vertical stress measured at the bottom boundary of the chamber. Secondly, the soil displacement and strain data from the digital photography and PIV analysis is analysed.

Table 4.2 in Chapter 4 shows details of each test, including soil type and initial density. The different pile types are also listed.

5.2 PILE BASE RESISTANCE

5.2.1 Variation with pile tip depth

The load cell shown in Figure 4.5 provided measurement of the pile base resistance, q_b, thoughout each installation. Figure 5.1 shows the variation of q_b with pile tip depth for each test. Within each test there is a general trend of sharply increasing base resistance during the first 30-50 mm of penetration, followed by more steady response.

During the DBS tests, q_b increased by only 0-20% between depths of 100 mm and the final installation depth. An approximate steady state penetration resistance is reached in each case. This suggests that any small variation in initial ambient stress level due to

side friction has a negligible influence on the penetration mechanism, and that the bottom boundary of the chamber has no effect on the penetration mechanism.

However, the possibility that these factors do have an influence, albeit opposite, cannot be ruled out. It could be argued that the unavoidable decrease in ambient stress level with depth due to side friction (Figure 4.7) would ease penetration at depth. In contrast, the approach of the chamber base as penetration deepens would impede the pile. These effects could have been present, partly cancelling each other. This possibility is unlikely, judging from the steadiness of each q_b- depth profile.

During the LBS tests, a steady value of q_b was not reached. During the loose test (DJW-04) an increase in q_b of 32% was recorded between depths of 100 mm and 440 mm. The concave shape of the q_b-depth curves for the LBS tests suggests that a steady state is not being approached. Instead, this trend could derive from an increasing influence of the chamber base with pile tip depth. This contrast with the DBS tests is as expected, since the influence of a remote rigid boundary would be larger in stiff silica sand than the compressible carbonate sand. Klotz & Coop (2001) also observed boundary effects when installing model piles in LBS, whilst tests in DBS using the same chamber appear unaffected.

Test DJW-05 was halted at a depth of 301 mm since the base resistance was approaching the maximum design load of the chamber.

5.2.2 Variation with soil density

The steady state values of base resistance achieved during the DBS tests allow the influence of relative density to be examined. A trend of increasing q_b with initial relative density is evident from Figure 5.2. If it is assumed that the ambient vertical stress in the region of steady state penetration is 50 kPa, the bearing capacity factor, N_q, varies in the range 36 – 116 between relative densities of 44% (DJW-08, q_b= 1.82 MPa) and 84% (DJW-06, q_b= 5.8 MPa). This relative density corresponds to the soil state prior to application of the surcharge pressure. The influence of surcharging on soil state is discussed in Section 5.5.

These values of N_q are typically 20-30% higher than those measured by Yasufuku & Hyde (1995) in DBS at comparable initial stress and density during their axisymmetric calibration chamber testing. The observation of these higher values is likely to be associated with the geometric difference between the test series.

At a comparable ambient vertical stress level, Klotz (2000) recorded values of q_b between 3.5 MPa and 8 MPa in loose and dense DBS, suggesting higher values of N_q than measured during this research. However, direct comparison with the Klotz (2000) data is difficult, since 50 kPa ambient vertical stress is associated with approximate embedment depths of only 1.5 and 3 pile diameters in Klotz's 100-g and 200-g centrifuge tests respectively. Also, a finer fraction of DBS was used (Figure 4.9).

5.2.3 Variation with soil type

As would be expected, significantly higher base resistance is measured in LBS compared to DBS. At a pile tip depth of 100 mm, the base resistance in tests of comparable relative density differs by a factor of 6-8. Comparison is difficult at greater depths due to likely influence of the bottom boundary of the chamber on the LBS results.

5.2.4 Influence of pile size

Tests DJW-02 and DJW-08 allow the influence of pile size on base resistance to be examined. The tests were conducted in DBS at initial relative densities of 44% and 46% respectively. Test DJW-08 used a model pile of breadth 16.1 mm; half the size used in all other tests.

However, it should be noted that halving the pile breadth also has the effect of doubling the chamber width- pile breadth ratio. Therefore, the difference between tests DJW-02 and DJW-08 potentially derives from an absolute scale effect (of pile size) and a boundary effect.

The steady state base resistance measured on the smaller pile (DJW-08) was 1.82 MPa. This value is 15% lower than that recorded during test DJW-02. An initial conclusion

would be that a size effect opposite to that observed by Chow (1997) is evident. Reduced pile size appears to lead to reduced base resistance.

However, examination of the displacement data recorded during these tests indicates that the end wall of the chamber is within the zone of deformation created by the pile, thus restricting penetration. This observation is discussed in Section 5.6.5.2. Therefore, it is likely that the difference in base resistance between tests DJW-02 and DJW-08 is wholly or partly due to a boundary effect.

5.3 CHAMBER BOUNDARY STRESS

The vertical stress acting on the base of the chamber directly below the approaching pile was measured using the load cell shown in Figure 4.4. The electrical connections to this tranducer were damaged during test DJW-02, and a new transducer was only available from test DJW-04. The new transducer was damaged during test DJW-06, but was repaired for test DJW-07.

Figure 5.3 shows the variation in chamber base stress, $\sigma_{v,chamber}$, with pile tip depth. The total depth of sand in each case was 750 mm. It should be noted that the initial value on each curve (i.e. pile tip depth = 0 mm) indicates the proportion of the 100 kPa maximum surcharge pressure which is recorded as reaching at the base of the chamber.

In each case, the vertical stress recorded after surcharging was in the range 50-75 kPa. Back calculation of the side friction following Appendix 3 suggests a value of β less than 0.05. This appears to be a promising observation. The stress variation with depth through the chamber is less variable than might be expected.

However, a value of β less than 0.05 is lower than would be expected, based on δ_{sg} = 11° as measured during interface shear box tests, and implies a value of K_0= 0.25 (Figure 4.7). Two explanations are possible. Horizontal expansion of the chamber could lead to a value of earth pressure coefficient lower than K_0. Only minimal lateral strain is required to reach active conditions.

Alternatively, the chamber base load cell could be over-registering the vertical stress. This could occur if the stress cell is stiffer than quoted by the manufacturer, leading to a larger CAF than discussed in Section 4.3.6. Over-registration could also occur if the load cell was slightly proud of the chamber base plate during testing, or if the chamber base plate was not firmly seated in the bottom of the chamber prior to surcharging.

It is therefore appropriate to treat the measurements of chamber base stress during pile installation with caution noting that the initial values appear to be slightly high.

Even if the measurements from the chamber base load cell are treated as only qualitative, it is clear that the chamber base 'feels' the approaching pile as soon as installation begins. Increasing stress is recorded at the base of the chamber even during the early stages of penetration.

In spite of this clear influence of the pile on the stress at the chamber base, this interaction appears to have had negligible influence on the pile base resistance during the DBS tests, as discussed in Section 5.2.1. Some influence is evident during the LBS tests.

5.4 OVERVIEW OF PHOTOGRAPHIC DATA

The process of converting raw digital images into measurements of displacement in object-space is shown in Figures 3.6 and 3.29. The calculation of strains from displacements is discussed in Appendix 1.

Additional stages specific to this experiment include the removal of wild vectors created when PIV patches move behind control markers and the translation of the reference frame origin to the final position of the pile tip. The removal of wild vectors was carried out by manual interrogation of the raw PIV data.

The following stages of analysis will be introduced in the subsequent Sections:

- Soil displacement during surcharging
- Soil displacement during pile installation

- Soil strain paths during pile installation
- Streamlines of soil flow
- Soil strain post-installation (i.e. as would be the case prior to loading of pile)
- Soil strain rates during installation (i.e. indicative of the strain induced by an increment of penetration)
- Soil movement adjacent to pile shaft

Images were taken at pile tip displacement increments of approximately 1 mm. Two typical images are shown in Figure 5.4a. During PIV analysis, the field of view was divided into approximately 2000 PIV patches, of dimensions 30 × 30 pixels (Figures 5.4b, 5.4c). These patches have a nominal size equal to 4 × 4 mm, or 4-7 particle diameters, as demonstrated by the superposition of a PIV patch over a close-up photograph of Fraction B LBS soil grains (Figure 5.4d).

This small patch size leads to a displacement measurement point separation equal to only a few grain diameters. The displacement field is therefore being sampled at a spatial interval within which continuum behaviour is expected to break down. It is not conceivable that a smooth spatial displacement field would be measured from such a fine distribution of measurement points. In the same way, a smooth stress-strain curve would not be expected from a triaxial test of dimensions 4 × 4 mm. This point is discussed further in Section 5.6.3.

5.5 SOIL DISPLACEMENT DURING SURCHARGING

Figure 5.5a shows the displacement vectors recorded during application of the surcharge load as viewed in window 4 (mid depth of the chamber). The downwards movement is constant across the width of the chamber. This is despite no surcharge being applied over the central 40 mm of the chamber to allow access to the sand surface for installation of the pile.

The mean downward vector component from each row is plotted against distance below the soil surface in Figure 5.5b. The resulting straight line directed towards zero

displacement at the box base suggests that the influence of the applied surcharge stretches to the base of the chamber.

The gradients of the settlement curves shown in Figure5.5b indicate vertical strains of 0.4% and 0.08% during surcharging of tests DJW-02 and DJW-04 respectively at chamber mid-height.

The measured vertical strain of 0.4% in DBS corresponds to a change in relative density after surcharging and prior to pile installation of less than 1%. The equivalent value for LBS is smaller. Since this represents a small correction, and one that cannot be confirmed over the full height of the sample, all analysis will be referred to the initial sample density *prior* to surcharging.

5.6 SOIL DISPLACEMENT DURING PILE INSTALLATION

5.6.1 Instantaneous velocity fields

The most straightforward illustration of the mechanism of penetration is provided by an instantaneous velocity field around the pile tip. Figure 5.6 shows examples for DBS and LBS. In each case the pile tip is located at the origin, and is of breadth 32.2 mm. These velocity fields consist of approximately 1000 individual vectors, calculated from images taken at a pile tip embedment of 300 mm, and between which the pile was displaced 2 mm. The most striking feature is the cone of soil below the pile tip which is moving with the pile. This cone extends further downwards in DBS than LBS.

Figures 5.7a and 5.7b offer a closer view of the velocity field around the pile tip. These fields are generated using smaller PIV patches than Figure 5.6, and have been superimposed on the corresponding initial images. The fit between the images and the object-space displacement vectors can only be nominal due to image distortion.

The velocity field consists of three general zones. Directly below the pile tip is a zone of rigid or near-rigid soil which is translating with the pile. Below this zone, and extending upwards under a line at approximately 45° from the vertical is a zone of soil

which is translating radially away from the pile. Above this zone, is a region of soil in which the velocity is relatively low.

This sharp variation in velocity with inclination from the vertical is in direct contrast to a cavity expansion model for penetration, in which all components are assumed to vary only with the radial coordinate.

The lighter soil colour in the superimposed photographs indicates that particle breakage has occurred in the zone of soil below the pile. Figure 5.7c offers a better view of this zone of crushed soil. This image was captured during test DJW-01 by placing the digital camera directly against the chamber window. The field of view is only 60 mm wide, therefore does not include sufficient control points to allow image calibration. Therefore, the superimposed coordinates are only nominal, and were deduced by linear scaling. Figure 5.7c shows more clearly the extent of the zone of broken soil below the tip of the pile.

5.6.2 Soil element trajectories during pile installation

Observation of the full trajectory of soil elements during installation of the model pile offers a better insight into the penetration mechanism than can be provided by an instantaneous velocity field.

Figure 5.8 shows the displacement trajectories of a selection of the soil elements tracked through tests DJW-02 and DJW-04, to allow comparison of the behaviour in DBS and LBS. For clarity, not all elements are shown. On Figure 5.8a, every third element is plotted, and on Figure 5.7b every second element is shown. The coordinate origin is located on the centreline of the pile and level of the pile tip at the end of installation.

In contrast to the instantaneous vector fields presented previously, the element trajectories illustrate the curvature of the element paths during installation. As the pile approaches, the movement is generally downwards, with the soil trajectories curving towards the horizontal as the pile passes. In the case of LBS, the final part of the element trajectory is upwards. Greater net downward movement and less net lateral movement is observed in DBS compared to LBS.

Figure 5.9 shows in more detail the movement of a single soil element in DBS and LBS. A notable feature in both cases is the 'tail' at the end of the trajectory. After the pile tip has passed the soil element (i.e. $h > 0$), the direction of movement reverses, and the soil relaxes back towards the pile shaft. The displacement steps at the end of the trajectory indicate that this inwards relaxation reduces as the pile tip becomes more distant. This 'tail' in the displacement trajectory is examined more closely in connection with friction fatigue and the use of driving shoes in Section 5.12.

The smoothness of the trajectory is indicative of the precision of the measurement system. Random noise of ≈10 μm is evident between displacement steps at the end of the trajectory, corresponding to a measurement precision over the 200 mm field of view of $1/20000^{th}$. This is in agreement with the PIV measurement precision deduced in Chapter 3.

5.6.3 Steady state deformation

Figure 5.10a shows the displacement trajectories of a single column of soil elements from tests DJW-02 and DJW-04. It is notable that the trajectories show no systematic variation with depth. In the case of test DJW-02, base resistance, q_b , is constant (within 5%) between depths of 100 mm and 450 mm, so it would be expected that the deformation pattern viewed through window 4 would also remain constant with depth. During test DJW-04, q_b varied between 15 MPa and 18 MPa as the pile passed through window 4, so some variation in the deformation pattern might be expected.

In Figure 5.10b, the displacement trajectories are converted into displacement ratios, defined as the net horizontal movement, Δx, and net vertical movement, Δz, divided by the pile half-breadth, $B/2$, during installation. These demonstrate more clearly than Figure 5.10a the steadiness of the deformation pattern. There is no trend for $2\Delta x/B$ or $2\Delta z/B$ to increase or decrease with depth.

A steady state penetration mechanism and a constant base resistance are both observed during these tests. Also, the penetration requires only slightly greater base resistance than is measured during axisymmetric calibration chamber testing conducted by others

using the same sand (Section 5.2.2). Therefore, it can be assumed that the penetration mechanism present during pile installation in axisymmetry, or indeed in the field, is similar to that observed during this testing.

Returning to Figure 5.10b, some random variation in displacement ratio of approximately ±0.02 is evident. This is equivalent to a displacement of ±200 μm, which is less than half of the mean LBS and DBS particle diameters, and is larger than the random error present in the displacement measurement system.

Random noise of this magnitude is to be expected, considering that the PIV patch size is equivalent to 4-7 particle diameters. It is highly conceivable that whilst being displaced by 55 mm (>125 particle diameters) during installation of the pile, as shown in Figure 5.9, adjacent groups of 4-7 particles may become separated from their neighbours by half of a particle diameter. The assumption of continuum behaviour would be expected to break down when measuring displacement at intervals of 4 mm, as noted in Section 5.4.

5.6.4 Combination of patch columns to increase zone of observation

The steady state deformation pattern evident in Figure 5.10 allows analysis of the photographic data to be extended. The viewing window only allows a vertical extent of 160 mm (5*B*) to be simultaneously observed. However, by combining the displacement data during installation found from all soil elements originally located within a single vertical column, the penetration mechanism can be observed over a greater vertical extent.

This technique can be illustrated by considering the range of values of vertical soil location relative to the pile tip that is visible. The vertical position of a soil element relative to the pile tip is defined as *h*. Prior to pile installation, the soil elements visible in window 4 vary in vertical position from $h = -8B$ to $h = -13B$ (in the case of the wide pile, $B = 32.2$ mm).

At any given instant during pile installation, the displacement trajectories shown in Figure 5.8 provide data over a 5*B* variation in *h*. However, throughout the entire test, for a given soil element, *h* varies by 12*B* (assuming a final installed depth of 400 mm).

The steady state deformation pattern shown in Figure 5.8 shows that displacement trajectories for a given value of *h* will be the same, independent of the original depth of the soil element. Therefore, all trajectories from a single soil column can be combined to provide the deformation pattern over a greater vertical extent below the pile tip. Since multiple soil elements are observed at the same value of *h*, at different stages of the test, the mean displacement trajectory is used.

This transformation is equivalent to describing every soil element trajectory using a reference frame with the origin located at the tip of the pile (on the centreline). The coordinate axes then consists of the horizontal offset from the centreline, *x*, and the vertical distance above the tip of the pile, *h* (*h* is positive upwards). In subsequent figures (Figure 5.11 and onwards), these quantities are normalised by *B*/2, the half-breadth of the pile, to allow test DJW-08 (using a narrow pile) to be compared to the remaining tests.

When the PIV mesh is established prior to pile installation, a soil element at the top of window 4 on the pile centreline has coordinates (0, ≈ 7.5*B*). A soil element at the bottom of window 4 has coordinates (0, 13*B*). Since a steady state deformation pattern is observed, the slight displacement between *h*= 7.5*B* and *h*= 13*B* has a negligible contribution to the entire displacement trajectory.

To make clear the distinction between *x*-*y* plots of raw displacement data (as shown in Figure 5.5-5.10), and *x*-*h* plots which have been assembled from the raw data in the column-wise manner described above, all *x*-*h* plots have been presented as mirror images with the pile on the left hand side. This mode of presentation has the added benefit of making the *x*-axis positive in the left-to-right direction.

5.6.5 Net soil displacement during pile installation

5.6.5.1 Definition

The net soil displacement during pile installation is defined as the soil element displacement between the start of the test and the moment at which the element is level with the pile tip (h= 0). Net soil displacement is expressed as the horizontal displacement ratio, $2\Delta x/B$ and the vertical displacement ratio, $2\Delta z/B$.

Figure 5.11 shows the variation in horizontal and vertical displacement ratio with initial offset from the pile centreline, $2x_0/B$ for tests DJW-02 to DJW-08. During test DJW-01 the camera was alternated between 'near' and 'far' fields of view in order to obtain the data used for Figure 5.7. Therefore a complete sequence of images was not gathered, and the overall displacement ratios cannot be calculated.

Figure 5.11 includes data from both window 4, through which the pile can be observed, and window 3, through which the far field behaviour (x_0= 6.5B- 12B) can be seen. However, the difficulty in evenly illuminating both windows simultaneously prevented displacement data from the full range of offsets visible in window 3 being gathered.

5.6.5.2 Influence of chamber end wall

It is immediately evident from Figure 5.11 that the end wall of the chamber influenced the displacement field around the pile. All curves for horizontal displacement ratio tend towards zero at $2x_0/B \approx 31$, which corresponds to the end wall position. The exception is test DJW-08, using a narrow pile. In this case, the end wall is located at $2x_0/B$ = 62 and, again, this is the position towards which horizontal displacement tends to zero..

As discussed in Section 4.3.1.1, the chamber - pile size ratio was determined based on previously reported experience of axisymmetric calibration chamber tests. These results demonstrate that the difference between axisymmetric and plane strain geometry requires a much more conservative chamber - pile size ratio to be adopted if the displacement field around the pile is to be entirely uninfluenced by the chamber boundaries.

The horizontal displacement ratio close to the pile shaft during test DJW-08 converges towards the data from tests conducted using the larger pile. This suggests that although the far field behaviour is influenced by the end wall, the near field behaviour is less so.

In the near field, significant differences in displacement ratio exist between each test, and it can be assumed that the influence on the penetration mechanism of soil type and density are preserved, despite the far field influence of the end wall.

5.6.5.3 Influence of soil type

The curves of horizontal displacement ratio shown in Figure 5.11 divide clearly by soil type. As might be expected, the zone of horizontal deformation is concentrated closer to the pile shaft in compressible DBS compared to LBS. The slope of the horizontal displacement ratio with offset from the pile centreline indicates the horizontal compression. For LBS, this slope is approximately constant with offset, whereas for DBS the slope is much higher close to the pile ($1.5 < 2x_0/B < 5$).

Symmetry requires that $2\Delta x/B = 1$ for $2x_0/B = 0$. Most curves of horizontal displacement ratio converge towards $2\Delta x/B = 0.8$ at $2x_0/B = 1$, irrespective of soil type. Closer to the pile ($2x_0/B < 1$), no further data is available since tracking of the soil through the high strain zone, as visible in Figure 5.7, was not reliable.

Therefore, in the very near field ($2x_0/B < 1.5$), significant horizontal compression must be present for both sand types. If a linear horizontal strain is assumed for the range $0 < 2x_0/B < 1$, the two conditions noted in the previous paragraph imply a horizontal compression of 20% within this zone. The strain distribution very close to the shaft is explored in more detail in Section 5.11.

The vertical displacement ratio is also influenced by soil type. Figure 5.11 indicates that the DBS is pushed downwards almost twice as far as the LBS. For both soils, the zone of downwards displacement is concentrated closely around the pile shaft, whereas the horizontal displacement decays steadily with offset.

5.6.5.4 Influence of soil density

No clear influence of soil density on vertical displacement ratio is evident. All curves overly each other. In the case of LBS, the horizontal displacement ratio for tests DJW-04 and DJW-05 is approximately equal, with a slightly higher concentration of horizontal deformation closer to the shaft in the case of the looser sample. In DBS no clear trend can be deduced. The initial relative density increases sequentially between tests DJW-02, DJW-03 and DJW-06, and corresponding increases in base resistance are recorded. However, no clear trend in the variation of displacement ratio with initial offset is shown.

5.6.6 Net soil rotation during pile installation

The strain calculation procedure described in Appendix 1 allows the decomposition of deformation into strain (or stretch) and rotation. For each test, a network of triangular elements was constructed from the mesh of soil elements tracked by PIV. The procedure described in Appendix 1 was used to calculated both strains and rotations throughout he installation procedure. These values were combined on a column-wise basis as described in Section 5.6.4, to allow a larger spatial distribution of each quantity to be plotted than is simultaneously visible.

Figure 5.12 shows the variation of net soil rotation with distance from the pile shaft for each test. The zone of very high rotation (> 20°) close to the pile ($2x_0/B < 2$) justifies the use of a finite rotation strain calculation approach.

This observed rotation may have a significant influence on the directional variation of post-installation stiffness. DBS has a highly anisotropic fabric, due to the presence of flat platey particles. Post-installation, the plane of low stiffness, parallel to these plates and originally oriented horizontally, lies at an angle.

A clear difference is evident between the tests in DBS and LBS. The rigid body rotation measured in DBS is approximately twice that measured in LBS at a comparable initial offset.

5.7 SOIL STRAIN PATHS DURING PILE INSTALLATION

5.7.1 Mode of presentation

The soil element trajectories presented in Figure 5.8 are used to find the strain paths experienced during installation, following the calculation procedure described in Appendix 1. In order to present the evolution of strain within a soil element as it flows towards and beyond the pile tip, the style of plot depicted in Figure 5.13 has been used.

The position of the soil element is described by the h-coordinate, normalised by $B/2$. The strain quantities included on the plot are the cumulative horizontal and vertical strain, defined within the reference frame of the soil element. Also shown are the maximum and minimum principal strains, denoted by ε_I and ε_{II}. The out-of-plane principal strain of zero is always intermediate in these results. These strain quantities are calculated as natural (or logarithmic) strains, following Equations A1.15- A1.19.

The evolution of these strain quantities can be regarded as the projection of a Mohr's circle of strain along the shear strain axis (Figure 5.13). This projection allows the general development of the direct vertical and horizontal strains to be observed on the same plot. In addition, the maximum shear strain is indicated by the width of the envelope created by ε_I and ε_{II}. The horizontal and vertical planes are principal if the arcs of ε_v and ε_h coincide with ε_I and ε_{II}. Where ε_v and ε_h cross, the shear strain on the horizontal and vertical planes is equal to the maximum shear strain.

It should be noted that for very high values of natural strain, as observed in the very near field, the usual construction of a Mohr's circle does not apply. For example, the mean value of the principal strains will not equal the mean value of the vertical and horizontal strains, as is the case for an engineering strain (or small strain) formulation.

Figures 5.14- 5.17 shows strain paths for tests DJW-02, 06, 04 and 05 respectively, allowing both sand types to be compared at two initial densities. Strain paths from 6 different initial offsets are shown, corresponding approximately to $2x_0/B$= 1, 2, 3, 4, 6

and 10. These six positions are divided into three zones of behaviour- ‘very near’, ‘near’ and ‘far’ field- and discussed separately.

The variation of rigid body rotation with $2h/B$ for each initial offset is also shown in Figures 5.14- 5.17.

The volumetric strain paths are shown separately on Figures 5.18- 5.19. The strain paths for each initial offset are superimposed on the same figure. Throughout this analysis volumetric strain is defined in the conventional manner as the change in volume divided by the original volume, and is expressed as a percentage. The volumetric strain paths for the ‘very near’, ‘near’ and ‘far’ fields are discussed together in Section 5.7.5.

5.7.2 Very near field behaviour ($2x_0/B< 2$)

The very near field behaviour is indicated by the strain paths of soil elements originally located at $2x_0/B= 1$ and $2x_0/B= 2$. These strain paths are shown on the upper left two plots of Figures 5.13- 5.16.

These strain paths reach values of natural direct strains greater than 50% in compression and 200% in extension, which correspond to engineering direct strains of 65% and 86% respectively. These strain levels are beyond the range of conventional laboratory element testing, and conventional constitutive models for soil are rarely applied to such large deformation behaviour.

The shape of the strain path in the near field is similar for all four tests. Key characteristics are the sharp increase in horizontal extension close to the pile tip, and the more gradual increase in vertical compression. For $2h/B< -5$, the principal strain directions are approximately vertical and horizontal, as would be expected by symmetry, since the soil element is almost directly below the pile.

A reversal of the vertical strain direction occurs at $2h/B\approx -3$, followed by a reversal in the horizontal strain direction at $2h/B\approx -1$. There follows a phase of horizontal compression and vertical extension, accompanied by significant rotation. The maximum shear strain remains approximately constant for $2h/B> -2$. On passing the pile tip, the

soil elements remain in horizontal extension relative to their initial state, albeit having rotated by as much as 45°.

Whilst the general shape of the strain paths in DBS and LBS are alike, the strain levels for a given value of $2h/B$ are 30%- 50% higher in DBS.

5.7.3 Near field behaviour ($3< 2x_0/B< 6$)

The near field behaviour is indicated by the strain paths of soil elements originally located at $2x_0/B$= 3, 4 and 6. Once again, similar trends are observed in DBS and LBS. Within this range of offset the absolute values of strain are of comparable magnitude in both sands.

Compared to the very near field, the change in direction of strain rate occurs earlier, and at the same point in both the horizontal and vertical directions. This is followed by sufficient strain as to exceed the initial cycle. Both the horizontal and vertical strain paths return to and cross the strain axis. The final state is one of horizontal compression and vertical extension.

Shear strain continues to accumulate even after the reversal of horizontal and vertical strain direction. The point at which horizontal and vertical strain are equal (and close to zero) corresponds closely with the point of maximum shear strain (i.e. maximum principal strain difference). Some reduction in principal strain difference is evident between h= -3 and h= 0.

5.7.4 Far field behaviour ($2x_0/B\approx 10$)

The far field behaviour is indicated by the strain paths of soil elements originally located at $2x_0/B\approx$ 10. At this large offset from the pile shaft, the general strain path differs slightly between DBS and LBS. In DBS the trend of initial horizontal extension followed by compression seen in the near field is again observed. In contrast, zero or minimal horizontal extension is observed in LBS, and the horizontal strain increases monotonically in compression. Also, the absolute strain levels in DBS are typically 50% lower than in LBS. This continues the previous observation that the deformation is localised closer to the pile tip in DBS than LBS.

As the soil passes the pile tip, in LBS the horizontal and vertical strains are almost principal. In DBS, the horizontal and vertical strains are closer to being principal than in the near field, but significant shear strain remains on the vertical and horizontal planes. In both sands, the final strain state is one of horizontal compression.

5.7.5 Volumetric strain paths

Figures 5.18 and 5.19 show the volumetric strain paths in DBS and LBS respectively. In DBS gradual compression is observed for $2h/B < -4$. Greater compression is observed in the near field than in the far field. Immediately below the pile tip ($-4 < 2h/B < -1$), dilation is evident in the very near field ($2x_0/B < 2$), followed by further compression as the soil element moves around the pile shoulder ($-1 < 2h/B < 1$). The dilation is not sufficient to overcome the initial compression, and a net reduction in volume is measured over the entire strain path.

In LBS the far field volumetric behaviour is similar to DBS. Gradual compression is observed as the soil flows past the pile. A net compressive strain of 1-3% is recorded over the entire strain path. In the very near field, greater dilation is observed than in DBS. This dilation is sufficient to create a net *increase* in volume over the strain path for $2x_0/B = 0.97$ in test DJW-04. A similar trend of dilation in the very near field is evident during test DJW-05, although the strain path is not complete since the test was halted prematurely.

The end points of the volumetric strain paths indicate the horizontal variation in density adjacent to the pile shaft. In DBS, despite the dilation around the pile shoulder, there is a continual decrease in density with increasing offset. In LBS, the strong dilation in the near field creates a zone of soil close to the shaft that is less dense than the more distant soil.

In the interface layer adjacent to the pile shaft ($2x_0/B < 1$) high compression and particle breakage is observed (Figure 5.7). Unfortunately, this zone extends only a few millimetres beyond the pile shaft, and therefore contains only limited PIV data. The local zone of shearing around the pile tip contains sliding zones of thickness less than

the width of a single PIV patch. Furthermore, the changes in PIV patch texture and colour associated with this shearing and breakage hamper the matching procedure. These difficulties prevent reliable strain paths being obtained within this zone of interface shearing.

Section 5.11 discusses other evidence of the volume change behaviour within the zone $2x/B < 2$. The observation of dilation and loosening in the very near field is discussed further in Section 5.11.5.

5.8 STREAMLINES OF SOIL FLOW

5.8.1 Strain reversal points

The changes in strain direction described in Section 5.7 are best illustrated by superposition onto the streamlines of soil flow. The locations of the maxima and minima of ε_v and ε_h are plotted on Figure 5.20. These points coincide in the far field, yielding two distinct zone of deformation. Below the pile and within a region bounded by a line inclined downwards at approximately 55° from the horizontal is a zone of soil that is undergoing vertical compression and horizontal extension. Above this region the soil is experiencing horizontal compression and vertical extension.

In the very near field the maxima and minima of ε_v and ε_h do not coincide, and a short phase of both vertical and horizontal compression is evident.

5.8.2 Qualitative comparison with analytical solutions

The general shape of the strain paths shown in Figures 5.14- 5.17 matches qualitatively with predictions based on the Strain Path Method (SPM) proposed by Baligh (1985). Most published SPM solutions are limited to undrained penetration in axisymmetry. Therefore, the volumetric behaviour associated with sand is not captured. Also, the reduction in strain level with offset differs from the results in this research due to the plane strain boundary conditions. However, the SPM captures the general trend of a gently increasing vertical and horizontal strain rate, followed by a sharp reversal as soil flows around the pile shoulder (Figure 5.21).

In contrast, cavity expansion methods predict each strain quantity to increase monotonically as the pile approaches (or the cavity is expanded). Within the zone directly below the pile, this simple approach is valid. However, a cavity expansion method cannot capture the strain history of the soil above the strain reversal lines shown on Figure 5.20.

5.9 SOIL STRAIN POST-INSTALLATION (PRE-LOADING)

5.9.1 Spatial distribution of strain

The data presented within Section 5.7 demonstrates the complete strain path experienced by a soil element from the initial state through to, and beyond, the passage of the pile tip. This data can be assembled as the spatial distribution of strain around the pile at any given instant during steady state penetration. This spatial distribution of strain represents the strain within the soil surrounding the pile after installation.

This spatial distribution of strain also represents the initial conditions prior to application of the working load to the pile if the strain associated with removal of the installation force and during any interim creep period is ignored. This assumption is of minor significance. The pile tip rebound during unloading of a field pile might typically be equal to 1 or 2 mm. This would induce strains in the surrounding soil approximately equal to a reverse excursion along the strain paths in Figure 5.14-5.19 by a distance equal to $2\Delta h/B = 0.1$. The installation-induced strains depicted in Figures 5.14- 5.19 are very large compared to such a reverse excursion.

The spatial distribution of installation-induced strains is key to understanding the behaviour of a displacement pile under working load. A bored pile can be “wished-in place” and analysed, based on the assumption that installation-induced strains are small and negligible. In contrast, the strain paths shown previously indicate that condition of the soil surrounding a displacement pile is strongly influenced by the installation procedure.

The stiffness of soil is strongly strain level dependent. Furthermore, this stiffness is dependent on whether the direction in which the soil is being loaded has changed. Therefore, any attempt to quantify the stiffness of a pile from integration of the stiffness contributions provided by the deforming soil around the pile requires knowledge of the strain level and strain history of that soil.

Figures 5.22- 5.26 show the spatial distribution of strain surrounding the base of the pile in tests DJW-02, 04, 05, 06 and 08. These are the tests for which strain paths were previously presented. In addition, the strain distribution from test DJW-08 is shown, to allow the influence of the chamber - pile size ratio to be examined.

5.9.2 Contour plot production

The contours shown on Figure 5.22-5.26 are not evenly spaced. There are very high strain gradients close to the pile. For clarity the contour separation varies from 0.5% in the far field to 25% in the near field. There are generally sufficient labels on each plot to allow every contour to be correctly identified. In addition, Table 5.1 shows the contour sequence used in each type of plot.

The contour plots were produced using algorithms within Matlab. The underlying data for each test is in the form presented in Section 5.7, and consists of 35-40 columns of soil elements (only 6 of these columns were presented in Section 5.7). Delaunay triangulation was used by Matlab to combine these columns of data into 2-dimensional surfaces in $2x/B$ vs. $2h/B$ space. The contouring algorithm requires an evenly-spaced grid of data points. This evenly-spaced grid of points was constructed by linear interpolation within the Delaunay triangles and was finer than the underlying data. By interpolating the underlying data onto a finer grid, the contouring process does not introduce any smoothing. This contouring routine represents the underlying data more accurately than the use of a ‘weighted neighbour’ algorithm, or a sparse evenly-spaced grid.

Contour plot	*Contour sequence (%, compression positive)*
Horizontal strain	-150, -100, -75, -50, -40, -30, -25, -20, -15, -10, -8, -6, -5, -4, -3, -2.5, -2, -1.5, -1, -0.5, 0, 0.5, 1, 1.5, 2, 2.5, 3, 4, 5, 6, 8
Vertical strain	-10, -8, -6, -5, -4, -3, -2.5, -2, -1.5, -1, -0.5, 0, 0.5, 1, 1.5, 2,

	2.5, 3, 4, 5, 6, 8, 10, 15, 20, 25, 30, 40, 50
Maximum shear strain	0, 0.5, 1, 1.5, 2, 2.5, 3, 3.5, 4, 5, 6, 7, 8, 9, 10, 12, 14, 16, 20, 25, 30, 40, 50, 75, 100, 150
Volumetric strain	-30, -20, -16, -12, -10, -8, -6, -5, -4, -3.5, -3, -2.5, -2, -1.5, -1, -0.5, 0, 0.5, 1, 1.5, 2, 2.5, 3, 3.5, 4, 5, 6, 8, 10, 12, 16, 20, 30

Table 5.1 Contour sequence used to show the post-installation distribution of strain

The resulting contour plots cover a zone extending from the pile tip downwards to $2h/B$= -20. This represents a greater extent than can be viewed at a single instant in window 4, by using the columnar combination scheme described in Section 5.6.4.

5.9.3 Distribution of vertical and horizontal strain

The contour plots shown in Figures 5.22-5.26 offer an alternative view of the strain paths shown in Figures 5.14-5.19. Bulbs of horizontal and vertical strain extend below and to the side of the pile. In both cases, the strain level adjacent to the pile is lower than below. If installation is considered as the upward flow of soil past a stationary pile, the strain reversal can be easily pictured as the soil flowing into and out from these bulbs of strain. The bulb of horizontal strain has a wider extent than the bulb of vertical strain.

The upper extent of the bulbs of vertical and horizontal strain is bounded by the contour of zero strain. Above this contour, the initial strain probe has been entirely reversed, and the soil is now straining for the first time in the opposite sense to the original probe. The contour of zero vertical strain is aligned at approximately 35° degrees downwards from the horizontal in DBS, and at 40° downwards in LBS. The contour of zero horizontal strain is inclined slightly steeper, at 45° downwards, in both sands.

In Figure 5.22, an anomalous vertical band of approximately 0.5% horizontal strain is located at $2x/B$= 9. This is due to wild vectors that were not detected during the data processing stage. By examining the raw images, these wild vectors can be attributed to the edge of a sheet of overhead transparency, on which the control markers were printed. An erroneous under-estimation of the horizontal displacement of some soil elements by ≈ 40 μm occurred when these elements became ‘stuck’ on the OHT edge. The resulting false data can be ignored.

Comparison of Figures 5.22 and 5.26 allows the influence of the chamber - pile size ratio to be examined. There is good agreement between both the shape and the absolute values of the contours of strain around each pile. The end wall boundary effect appears to have had negligible influence on the kinematic behaviour close to the pile.

5.9.4 Distribution of maximum shear strain

In contrast to the bulb-shaped distributions of vertical and horizontal strain, the zone of maximum shear strain does not significantly reduce in width as the soil flows past the pile tip. The high shear strain induced as the soil flows to the 55° strain reversal points (Figure 5.20) is maintained as the soil moves past the pile.

5.9.5 Distribution of volumetric strain

Figures 5.22- 5.26 reveal differing volumetric behaviour in DBS and LBS. In DBS, the zone of compression extends far below the pile. A similar distribution of volumetric strain is recorded in the loose and dense models. Adjacent to the pile shaft ($2h/B$= 1), decreasing compression with increasing offset is apparent. This observation is consistent with the gentle decrease in net horizontal displacement ratio with increasing offset shown in Figure 5.11.

In LBS, a zone of net dilation is evident around the pile shoulder. Adjacent to the pile shaft ($2h/B$= 1), a contour of zero volumetric strain is found at an offset of $2x/B$= 1.5 in test DJW-04. Closer to the pile shaft is a zone of net dilation. Further from the pile, volumetric compression is observed. The maximum volumetric strain is 2.5%, and occurs at an offset of $2x/B$= 4.

The variation of volumetric strain with offset from the pile shaft is discussed further in Section 5.11.5, after observations of the volume change in the interface layer immediately adjacent to the pile have been presented.

5.10 SOIL STRAIN RATE DURING LOADING

As discussed in Section 5.9.1, the post-installation spatial distribution of strain can provide an indication of the stiffness of each zone of soil surrounding the base of the

pile, noting that stiffness is a strong function of strain level. However, if the stiffness contributions from each zone of deforming soil are to be combined to deduce the base stiffness of the pile, a further quantity is required. This quantity is the spatial distribution of strain rate during loading.

The spatial distribution of strain rate describes the mechanism of penetration over a small increment of pile settlement. As a simple analogy, the post-installation distribution of strain could be used to reduce the zone of deforming soil into a set of springs of varying stiffness, noting that stiffness is a strong function of strain level. However, the spatial distribution of strain rate is then required in order to establish by how much each of these springs are compressed or extended during an increment of penetration.

Firstly, a clarification of the definition of strain rate is required. Two different strain rates can be derived. The gradient of the strain paths in Figures 5.14-5.19 indicates the strain rate, where rate refers to the upwards velocity of the *soil relative to the pile tip*. This is the strain rate of a soil element flowing with an upwards velocity component of $2\Delta h/B$. Suitable units would be $\%B/\Delta h$. Since this rate is defined as the spatial gradient relative to the pile tip, it is equal to the gradient of the contour surfaces in Figures 5.22- 5.26 parallel to the streamlines of soil flow.

However, this strain rate is not applicable to an estimation of the soil deformation during an increment of loading. Instead, consider a small increment of pile tip settlement. The base resistance required to induce this increment of settlement depends on the stiffness and strain increment distribution within the deforming soil. In the limit of an infinitely small increment of settlement, base resistance can be recast as depending on the stiffness and strain rate distribution, where rate refers to the rate with respect to *absolute movement of the pile tip* (not movement relative to the soil). This strain rate with respect to pile settlement is defined using units of $\%B/\Delta s$, where Δs refers to a small increment of pile settlement.

The distinction between spatial strain rate and strain rate with respect to pile settlement is subtle. A significant difference exists only in zones of soil for which the streamlines deviate significantly from an upwards velocity component relative to the pile equal to the absolute downwards velocity of the pile tip. In these zones, a downwards movement of the pile of $\Delta s = B$ does not necessarily coincide with an upwards movement of the soil relative to the pile of $\Delta h = B$. Similarly, on the strain paths in Figures 5.14-5.19, a downwards movement of the pile of $\Delta s = B$ does not correspond to a movement along each strain path of $\Delta h = B$ by each soil element.

Since the spatial distribution of strain rate is derived by differentiation, it is inevitably more susceptible to noise than the post-installation strain distribution. However, the contours shown in Figures 5.27-5.30 show clearly the two zones of opposite strain rate. Table 5.2 shows the contour sequence used in these figures. The strain reversal lines of Figure 5.20 are evident as contours of zero horizontal and vertical strain rate inclined at approximately 55° downward from the vertical. Zones of negative horizontal strain rate and positive vertical strain rate are seen below these lines, with the strain rate reversed above them. The strain rate magnitude is calculated using updated (i.e. post-installation) reference lengths.

Contour plot	*Contour sequence (%B/Δs, compression positive)*
Horizontal strain, vertical strain, Maximum shear strain rate	20 -15 -10 -7.5 -5 -2.5 0 2.5 5 7.5 10 15 20 30 50 100 200

Table 5.2 Contours used to show spatial distribution of strain rate with pile settlement

5.11 SOIL COMPRESSION DIRECTLY BELOW PILE

5.11.1 Observation of a 'nose cone'

It is noted in Section 5.9.5 that the strain history of the soil within the interface zone ($2x_0/B < 2$) cannot be reliably captured by PIV. In Section 5.6.5.3, the net horizontal displacement ratio in the very near field is discussed. Close inspection of Figure 5.11 within the offset range $2x_0/B < 2$ allows the likely volumetric strain within the very near field to be estimated, assuming that the mode of deformation is horizontal compression. The measured net horizontal displacement ratio of $2\Delta x/B = 0.8$ for $2x_0/B = 1$ implies of

mean volumetric strain of 20% within the zone $2x_f/B < 1.8$. This would suggest that a very dense zone of soil is present very close to the pile ($2x_f/B < 1.8$). This region is within the loose zone found in the range $3 < 2x_f/B < 2$ and discussed in Section 5.10. Evidence for the existence of this dense zone is discussed below.

A highly compressed zone of soil below the pile tip- hereafter referred to as a 'nose cone'- is clearly visible during all tests on both DBS and LBS (Figure 5.31a, 5.7c). These zones are not rigidly translating with the pile. Instead, by assembling the image sequence as an animation centred on the pile tip, a more complex behaviour is seen. Zones of soil are observed to slide out from the compressed zone and flow around the shaft of the pile. A central core of the nose cone is stationary relative to the pile tip, but the shoulders of the zone are not (Figure 5.31b).

5.11.2 Sampling of nose cone

The nose cone from test DJW-03 was sampled during the test post-mortem. The sample had cohesion, and could be described as a weak rock (Figure 5.31c). The density of the sample was calculated by weighing, and then immersing the sample in water after tightly sealing it in cling film. The density was measured as 17.63 kN/m^3, which indicates a specific volume of 1.53. This is equivalent to a volumetric compressive strain during the test of 32%. The stress-volume path of soil entering the nose cone is sketched on p'-v axes in Figure 5.31e. The mean pressure, p', is assumed to equal q_b. However, it appears that the soil state lies below the conventional CSL established by Klotz (2000), albeit for a different initial grading of DBS. A triaxial compression test at a similar mean pressure would be expected to result in less contraction, with the final state lying on the CSL. In the case of pile installation, the strain level is higher than is achieved during triaxial testing. This could contribute to additional volume reduction. Luzzani & Coop (2002) used ring shear testing of DBS to attain a higher shear strain than can be achieved during triaxial testing and also observed continued volume reduction with increasing shear strain.

5.11.3 Index properties of reconstituted nose cone soil

The compressive strain on entering the nose cone may be reversed as the soil slips out from the nose cone and around the shaft of the pile. However, the soil is significantly

broken. The possible increase in volume as the soil leaves the high stress zone below the pile tip and undergoes shear strain at low stress adjacent to the shaft was investigated as follows.

The nose cone from test DJW-03 was broken up by gentle shaking. The maximum voids ratio of the reconstituted soil particles was measured by a series of quick tilt tests. The lowest density achievable by these tests was 15.15 kN/m^3, which corresponds to a specific volume of 1.78. This value is significantly lower than both the maximum and minimum specific volumes of virgin DBS, and is marked on Figure 5.31e. This specific volume represents an upper limit on dilation of the broken soil. Only minimal volume recovery can occur as soil exits the nose cone. Even if the soil recovered to the minimum achievable density, a net volume compression of 21% would remain.

Full recovery to a specific volume of 1.78 would not occur since the soil adjacent to the pile remains under load. An alternative stress-volume path would be to assume that the soil moves to a critical state. However, the CSL shown on Figure 5.31e offers no *p'-v* state at a stress level lower than q_b yet at a density attainable by the broken soil. A new CSL must apply. The actual volumetric strain within the zone of soil adjacent to the shaft must lie between the value within the nose cone (32%) and the minimum attainable by the reconstituted soil (21%). Therefore, the CSL for this heavily over-consolidated nose cone sand lies below the CSL for normally-consolidated sand, in *p'-v* space.

Irrecoverable volume reduction was also observed for the LBS. The soil from the nose cone of test DJW-04 was sampled in a disturbed state. A series of quick tilt tests revealed a maximum specific volume of 1.61. This compares to 1.80 for the virgin LBS, and represents an irrecoverable volumetric strain of 10.5%. As with DBS, the actual volumetric strain adjacent to the pile must lie between this value, and the (unknown) strain within the nose cone.

5.11.4 Particle breakage

The particle breakage evident in Figures 5.7c (DBS) and 5.31a (LBS) demonstrates that the soil emerging from the nose cone and passing along the shaft has a very different

grain size distribution compared to the virgin soil. It is conventionally accepted that significant particle breakage occurs in the carbonate sand, but the evidence of particle breakage in silica sand is perhaps more surprising. After a triaxial test on silica sand to a high stress level, limited particle breakage is observed. However, in addition to a high stress level, the flow of soil around a pile tip creates very high shear strains. These provide additional opportunity for particle breakage.

Vesic & Clough (1968) compared the grading curves of Chattahoochee River silica sand before testing, after isotropic compression to 62.1 MPa, and after compression and shearing at a cell pressure of 62.1 MPa (Figure 5.32). Breakage during a deformation event can be quantified by the area swept through by the changing PSD curve. On this basis, Figure 5.32 shows that for shearing at 62.1 MPa, approximately equal breakage is associated with the isotropic compression stage as with the shearing stage at constant cell pressure. At 20.7 MPa, breakage due to the shearing stage is approximately 3 times greater than due to the compression stage. The breakage contribution due to shear strain is likely to be even larger in the case of flow around a pile tip since the strain levels revealed in Section 5.7 are an order of magnitude higher than were attained in Vesic & Clough's triaxial apparatus.

Triaxial tests on DBS by Coop (1990) confirmed the influence of shear strain on particle breakage. The D_{50} size of DBS after shearing to failure was found to be lower than after isotropic compression to the same stress level. Ring shear tests by Luzzani & Coop (2002) on fine LBS at 100 kPa normal stress revealed continuing breakage with strain level, even at a low normal stress of 100 kPa.

5.11.5 Volumetric behaviour close to pile tip

Section 5.11.3 demonstrated that the soil flowing around the pile tip suffers significant irrecoverable volume contraction (> 10%). In contrast, Figures 5.18 and 5.19 show that dilation occurs slightly further from the pile tip. These two modes of volumetric behaviour are compared in Figure 5.33, by considering the volume changes that are associated with the stress levels and shear strain encountered close to the pile tip.

Two streamlines of soil flow are shown on Figure 5.33. Soil that flows through the nose cone and forms the interface layer adjacent to the pile shaft follows streamline ABC. Soil in the very near field, for which PIV data is shown in Figures 5.18- 5.19, follows streamline DEFG. A zone of high stress corresponding to the photoelastic observations of Allersma (1988a) is shown below the pile tip.

Very high stress and very high shear strain are encountered along streamline AB, resulting in volume compression and significant particle breakage, as evident in photographs of the pile tip (Figure 5.7). This volume change is irrecoverable due to particle breakage, as demonstrated by the index tests described in Section 5.11.3. Therefore, as the soil progresses along the streamline BC significant volume compression remains, creating a net increase in density.

Along streamline DE, high stress and high shear strain are encountered. This causes contraction and some particle breakage. On leaving the zone of high stress, the soil is now heavily over-consolidated. Also, further shear strain is required for the soil to pass around the pile shoulder. Figures 5.27- 5.30 show that the shear strain rate remains high within this zone, even though the photoelastic analysis shows the stress level has dropped.

Conventional critical state theory predicts that this over-consolidated soil will dilate when sheared along streamline EF. Such dilation is seen in Figures 5.18- 5.19. The slight volume compression along DE is more recoverable than the gross compression and particle breakage along AB.

However, subsequent to this dilation, contraction is observed as the sand flows along streamline FG (see Figures 5.18- 5.19). The shear strain rate remains high, as shown on Figures 5.27- 5.30, and it could be assumed that changes in mean stress are now negligible (compared to the previous drop in stress near point E). Conventional critical state theory would predict that shearing in these conditions would take place at constant volume. Instead, contraction is observed.

Perhaps critical state theory is not appropriate at such high strain levels. Continued shearing of carbonate sand to higher strain levels than are found in normal element testing shows that a constant volume condition is not reached. Instead, continued contraction is observed (Luzzani & Coop, 2002). Also, the major principal stress direction may rotate from vertical towards horizontal along streamline FG. Hollow cylinder tests on sand show that changes of principal stress direction cause contraction even if the stress level remains constant (Symes *et al.*, 1988).

The volumetric strain at the end of streamlines ABC and DEFG allows the variation of density with offset from the pile shaft to be deduced. This variation is shown schematically at the top of Figure 5.33. Adjacent to the pile shaft, the soil has become denser, following the irrecoverable volume compression discussed in Section 5.11.3. In DBS, the density decreases progressively away from the pile shaft. In LBS, Figures 5.18- 5.19 indicate that this progressive decrease in density is interrupted by a local loose zone in the very near field.

Loose zones soil close to model piles have previously been reported by Chong (1988), Allersma (1988) and Robinsky & Morrison (1964). However, the displacement measurement techniques used during these tests had insufficient resolution to differentiate between the interface layer and soil slightly more distant from the pile. This research has revealed a clear distinction between the behaviour of the two zones.

5.12 BEHAVIOUR ABOVE PILE TIP

5.12.1 Additional PIV meshes

An interesting feature of the displacement trajectories shown in Figure 5.8 is the ‘tail’, indicating movement of the soil towards the pile shaft after the tip has passed. A more detailed investigation of this behaviour was conducted using additional PIV meshes that were created in the zone of soil adjacent to the shaft and beyond the pile tip ($h > 0$). These meshes were used to observe the deformation within the soil after passage of the pile tip. Since the soil close to the pile centreline undergoes only minimal deformation beyond the pile tip, the PIV mesh could extend close to the pile. The closest column of

PIV patches was located 4 mm from the pile shaft. Data is presented from tests DJW-02, DJW-04 and DJW-06, representing DBS, LBS, and the use of a pile shoe, respectively.

5.12.2 Soil flow around pile shoe

The pile shoe used in test DJW-06 creates the largest trajectory 'tail', as the soil relaxes towards the pile to fill the gap behind the overhang of the pile shoe. Figure 5.34a shows the trajectories of deformation as the pile passes. This PIV run analysed the image sequence in reverse. The PIV mesh was established in the final image of the test. The displacement of the mesh was tracked through the reversed image sequence, in which the pile moves upwards through the soil and past the PIV mesh.

An enlarged view of the soil flow close to the pile shaft is shown in Figure 5.34b. The soil immediately adjacent to the pile is observed to move inward by a distance equal to the 4 mm overhang, filling the void behind the shoe. A reduced inward movement is recorded in the far field.

5.12.3 Horizontal strain adjacent to pile shaft

The purpose of a driving shoe is to relieve the horizontal stress acting on the pile shaft, easing installation. This stress reduction occurs as the soil adjacent to the pile unloads in horizontal extension. The displacement trajectories in Figure 5.34a are used to calculated the variation in horizontal extension strain with offset from the pile centreline. The gauge length is defined at $h = 0$. Figure 5.35a shows the variation of horizontal strain with offset for four values of h.

The unloading strain is concentrated in a zone close to the pile shaft ($2h/B < 5$). An initial large increment of unloading strain (shown on Figure 5.35a, labelled $2h/B = 2.72$) is recorded before $h = 1.36B$. The rate of unloading decreases with h thereafter. These two phases of unloading correspond to two mechanisms.

The initial large increment of unloading strain is associated with the flow of soil around the pile tip, and past the triangular zone of soil trapped behind the overhang (visible in Figure 5.34c). The second stage of unloading occurs as the soil flows along the smooth

shaft of the pile. The displacement trajectories show that the soil moves towards the pile shaft. The strain data recorded as the pile penetrates further (shown on Figure 5.35a, labelled 2*h/B*= 3.74, 4.82 & 5.89) shows that this inward movement leads to an accumulation of horizontal extension close to the pile shaft. Negligible vertical strain is recorded. These kinematic conditions can only be satisfied if the interface zone closer than 4 mm from the pile shaft is contracting. This contraction is discussed further in Section 5.12.6.

5.12.4 Stress relief from pile shoe

The unloading strain recorded behind the pile shoe is greater than 4%. If the relaxation of soil towards the pile is considered analogous to a translating retaining wall, this strain level would be sufficient to mobilise limiting active conditions. A larger overhang would not be expected to provide greater stress relief, or a further reduction in shaft friction.

5.12.5 Soil flow adjacent to straight pile

PIV analysis of the soil adjacent to the pile in tests DJW-02 and DJW-04 was also conducted. Figure 5.36 shows the tip of the pile entering the field of view during test DJW-02, with a row of PIV patches established adjacent to the pile shaft. Comparison with a subsequent image taken after 80mm (2.5*B*) of further penetration allows the intervening soil movement to be measured. These vectors of displacement reveal that the soil is moving towards the pile shaft (Figure 5.36). The greatest vector (250 μm, 1.9 pixels) was measured at the patch closest to the pile (located 4 mm from the shaft). To eliminate the possibility that this observation was due to a non-vertical alignment of the pile, a set of patches on the opposite side of the pile were tracked. Similar vectors were obtained.

The horizontal strain profiles deduced from the displacement vectors measured adjacent to the pile during tests DJW-02 and DJW-04 are shown in Figure 5.35b. Even though no pile shoe is used, the soil adjacent to the pile unloads in horizontal extension as the pile advances.

Close up photographs of the interface zone in DBS and LBS are shown in Figure 5.37. The closest displacement vector is located 4 mm from the pile shaft. The contracting interface zone between this point and the pile shaft is characterised by a zone of high particle breakage. Photographs of virgin DBS and LBS are shown for comparison.

5.12.6 A contractile zone of interface shearing

Conventional theory does not predict this zone of contraction close to the pile-soil interface. This soil within this zone is heavily over-consolidated, having passed through the highly stressed zone close to the pile tip. CPT friction sleeve measurements in sand typically show that the stress level behind the shoulder of a cone is 0.5-2% of the cone resistance, q_c (Lunne *et al.*, 1997). This suggests an over-consolidation ratio within the interface shearing zone of 50-200. Heavily over-consolidated sands dilate when sheared to intermediate strain levels in element testing. However, the level of shear strain within the interface zone adjacent to pile is much higher.

There exists only limited data of the volumetric behaviour of sand in a shear zone over very large slip displacements to compare with the observed behaviour. Luzzani & Coop (2002) measured continuing contraction of DBS when sheared in the ring shear apparatus beyond a nominal shear strain of 800%. This trend is compatible with the contractile behaviour observed adjacent to the pile.

Figure 5.38 summarises the mechanism of behaviour adjacent to the model pile. This mechanism links the kinematic observations to friction fatigue close to the pile tip. The zone of soil immediately adjacent to the pile (Zone B in Figure 5.38) contracts with continued shearing at the pile-soil interface. The soil more distant from the pile shaft (Zone A) is modelled as a stiff spring. This spring is fixed in the far field and exerts horizontal stress on the pile shaft. As Zone B contracts, this spring unloads, relieving the shaft friction on the pile.

5.12.7 A micromechanical hypothesis

From a micromechanical point of view, the contraction of the interface zone could be explained as follows. The hypothesised mechanism is equally applicable to the continuing contraction observed during ring shear testing by Luzzani & Coop (2002)

Volume reduction within the interface zone is permitted if the particles can repack in a more efficient manner, or if particles can migrate away from the zone. The close-up photographs in Figure 5.37 show that the fine particle within the interface zone are significantly smaller than the void spaces in the zone slightly more distant from the pile. This disparity between void size and particle size offers the possibility of internal erosion, or migration of fine particles without disturbing the load-carrying skeleton of larger particles. A possible mechanism of contraction is for fine particles to migrate outwards with continued shearing of the interface zone. This migration of particles reduces the amount of material within the interface zone, permitting the remaining particles to repack in a more dense state.

Further breakage of the particles within the interface zone may also occur with continued shearing. Breakage and subsequent repacking offers a second mechanism for volume reduction.

This migration of fine particles away from the shear zone might be more accentuated if the pile were oriented horizontally. If gravity is acting perpendicular to the shear zone, broken particles would have a greater tendency to fall away from the zone of shearing. The shear band in Luzzani & Coop's ring shear apparatus is oriented in the horizontal plane.

This possibility for migration of broken particles away from a shear band has implications for constitutive models in which a critical state of constant volume shearing is achieved when volume changes due to particle breakage and rearrangement balance (e.g. Baharom & Stallebrass, 1998).

The above mechanism can only be described as a hypothesis. No evidence yet exists for the redistribution of fine particles away from a shear zone with continued slip.

5.12.8 Horizontal unloading and friction fatigue

The soil adjacent to both the straight pile, and behind a pile shoe, is observed to relax inward, undergoing horizontal extension. This movement is permitted by volume

reduction in the interface zone. An estimate of the resulting reduction in horizontal stress acting on the pile shaft due to this inwards relaxation can be made by considering the one-dimensional unloading stiffness of the soil.

It is assumed that the one-dimensional unloading stiffness, κ_0, is approximately equal to the isotropic unloading stiffness, κ, in the Cam clay model. Since κ_0 is equal to the slope of the unloading curve in v- log σ'_h space, the unloading strain close to the pile shown in Figure 5.35b can be related to the decrease in σ'_h. Coop (1990) quotes a value of κ= 0.0075 for DBS. If it is assumed that the specific volume just outside the interface shearing zone during test DJW-02 is 2.0, then the measured one-dimensional unloading strain of 0.6% (Figure 5.35b) corresponds to a *fivefold* reduction in horizontal effective stress.

Therefore, although the horizontal movements are small and the contraction of the interface zone is only a fraction of the original D_{50} size of the soil, the loss of shaft friction is very significant. This result uses a very simplified model to relate the observed kinematics to the likely stress distribution. However, the magnitude of the stress change acting on the pile shaft is very large. A more realistic model is unlikely to eliminate this dramatic loss of horizontal stress.

5.12.9 Axisymmetric horizontal unloading

The plane strain conditions used during this test series lead to one-dimensional horizontal unloading as the interface zone contracts. In the case of a tubular pile, interface contraction permits horizontal unloading in an axisymmetric fashion. The process of interface shearing that leads to contraction is not likely to be influenced by the geometry of the interface. The slight curvature of a segment of tubular pile wall compared to the plane strain probe used during this testing is not expected to influence the magnitude of inward displacement.

Therefore, an alternative calculation of the horizontal stress relief can be made using a cavity contraction model and applying the same inward displacement. Equation 5.1

relates inward displacement, Δr, to the change in cavity stress, $\Delta\sigma_c$, during contraction of a cavity of radius R in an elastic material of shear stiffness G.

$$\Delta\sigma_c = \frac{2G\Delta r}{R} \tag{5.1}$$

Selection of an appropriate value of G should account for the small strain level and the high degree of over-consolidation. Jovocic & Coop (1997) measured values of G_0 in the range 300-1000 MPa during isotropic unloading of DBS from 5 MPa to 100 kPa. If the inward displacement of 250 μm measured during test DJW-02 is applied to a 1 m diameter field pile, the resulting reduction in horizontal stress is 300-1000 kPa. This reduction in horizontal stress is comparable in magnitude to measurements of friction fatigue recorded on field piles, and would represent the loss of a large fraction of local shaft friction.

A related issue concerns the use of segmental instrumented piles. The above calculation, although approximate and idealised, demonstrates that the high unloading stiffness of sand can lead to a significant loss of horizontal stress during cavity contraction. A contraction of the interface zone is analogous to a small reduction in diameter along the pile length. If the connected segments of an instrumented pile differ slightly in diameter or are non-concentric, a large change in horizontal stress can result. The above calculation recast for a 0.1 m diameter pile with a circumferential step of 20 μm (0.02 mm) predicts a change in cavity stress of 120- 400 kPa.

Coop & Wroth (1990) raise a similar point for the case if instrumented piles in clay, following a series of tests in which protuberances at segment connections were suspected of influencing the distribution of shaft friction. They warn that the fabrication tolerances of model piles may influence the stresses measured upon them.

5.12.10 The influence of installation method on friction fatigue

These tests revealed contraction of the interface zone with monotonic shearing at the pile-soil interface. Monotonic shearing is representative of the mechanism operative during press-in pile installation. Conventional dynamic pile installation methods

involve cyclic shearing at the pile-soil interface. Each hammer blow applies a cycle of displacement at the pile interface.

The mechanism of interface contraction leading to friction fatigue will be more significant under cyclic loading, compared to monotonic loading. It is widely reported from interface element testing that cycles of shear displacement lead to greater volume contraction than monotonic shearing (Dietz, 2000; Tabucanon *et al.*, 1995; Al-Douri & Poulos, 1991).

This link between cyclic shear displacment and reduced shaft friction is supported by Poulos *et al.* (1988). They note that the mean shaft friction measured in small-scale model pile tests after a given number of cycles decreases with increasing cyclic amplitude. Also, Dolwin *et al.* (1988) report a reduction in mean shaft friction with number of blows (and therefore displacement cycles) required for pile installation.

Back analysis of recent field data from long offshore piles supports this hypothesis. The Jardine & Chow (1996) design method was derived from experience using a jacked instrumented pile, and calibrated against a database of piles with mean length 16.4 m. This design method significantly underpredicts the rate of friction fatigue along the EURIPEDES test pile (Figure 2.15a). This pile was driven with a blowcount of 120-150 per 0.25 m close to the target depth. Although the total number of blows for installation is not available, the expected total blowcount used for the design of the instrumentation was 7000 (Zuidberg & Vergobbi, 1996).

Tomlinson (2001) compares the Jardine & Chow model for shaft friction distribution with data from 44.2 m long driven piles at Jamuna Bridge. This data is shown in Figure 2.15b. Tomlinson's design curve based on Jardine & Chow (1996) is labelled 'IC Method'. The rate of decay of local shaft friction is underestimated by the IC Method, leading to a non-conservative prediction of capacity.

The evidence described above draws attention to the influence of installation method on friction fatigue. The mechanism of interface contraction leading to relaxation of horizontal stress underlies the differing distribution of shaft friction on driven and

jacked piles. A pile of given geometry will suffer reduced friction fatigue if installed by monotonic jacking compared to driving.

5.13 SUMMARY: GENERALISED MECHANISM

The results presented in this Chapter provide more detailed experimental evidence of the penetration mechanism of a displacement pile than has previously existed. The distribution of strain surrounding a pile after installation can be summarised by the generalised zones of deformation shown in Figure 5.39.

The penetration mechanism can be recast as the deformation induced during an increment of pile settlement under working load (Figure 5.40). This is based on the assumption that the mechanism of steady penetration is comparable to that induced during subsequent loading. This incremental view of penetration indicates the deformation field appropriate to a settlement analysis of the pile under working load.

The mechanism of penetration observed in this research applies to plane strain conditions. In axisymmetry, the general pattern will be similar, although concentrated closer to the pile. Although the boundary conditions applied during this model testing are different to most field scenarios, they are well defined. Therefore, numerical or analytical approaches to field problems should be verifiable against this data.

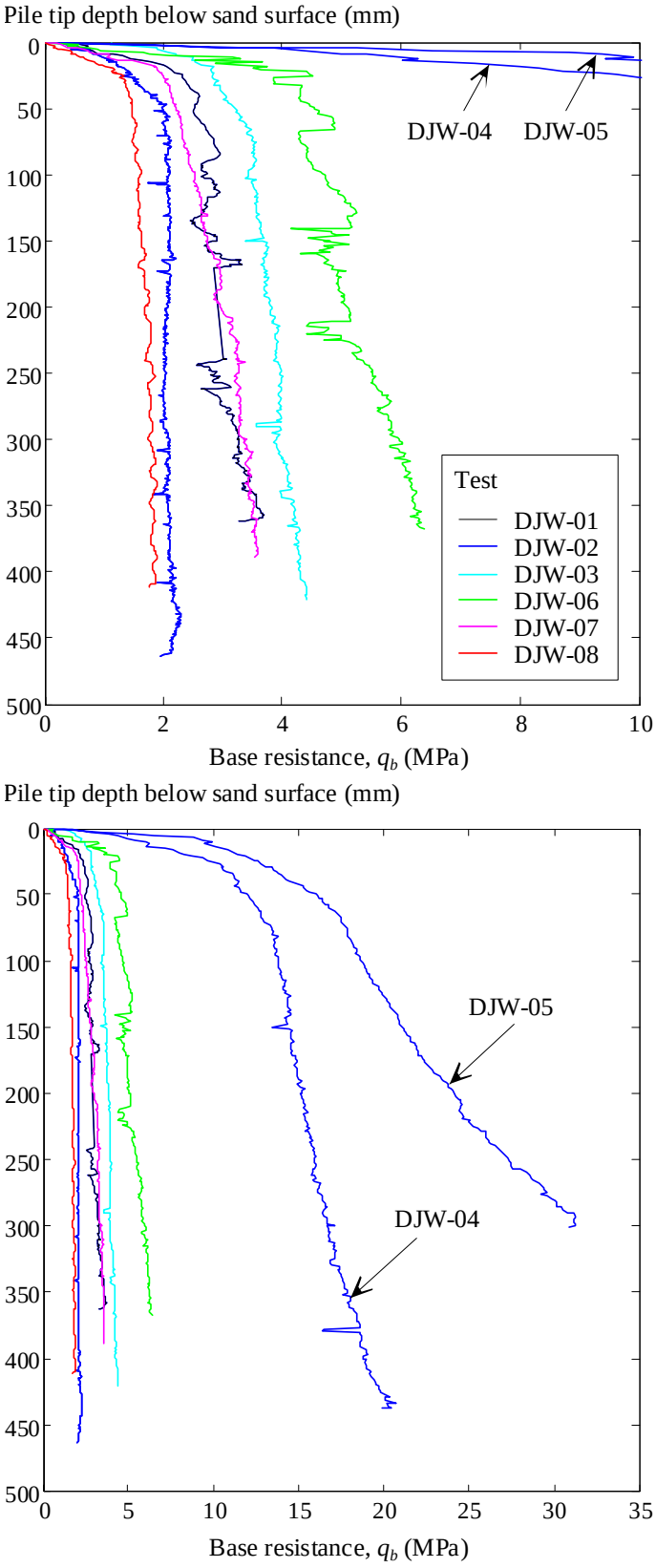

Figure 5.1 Base resistance, q_b, vs. pile tip depth during installation

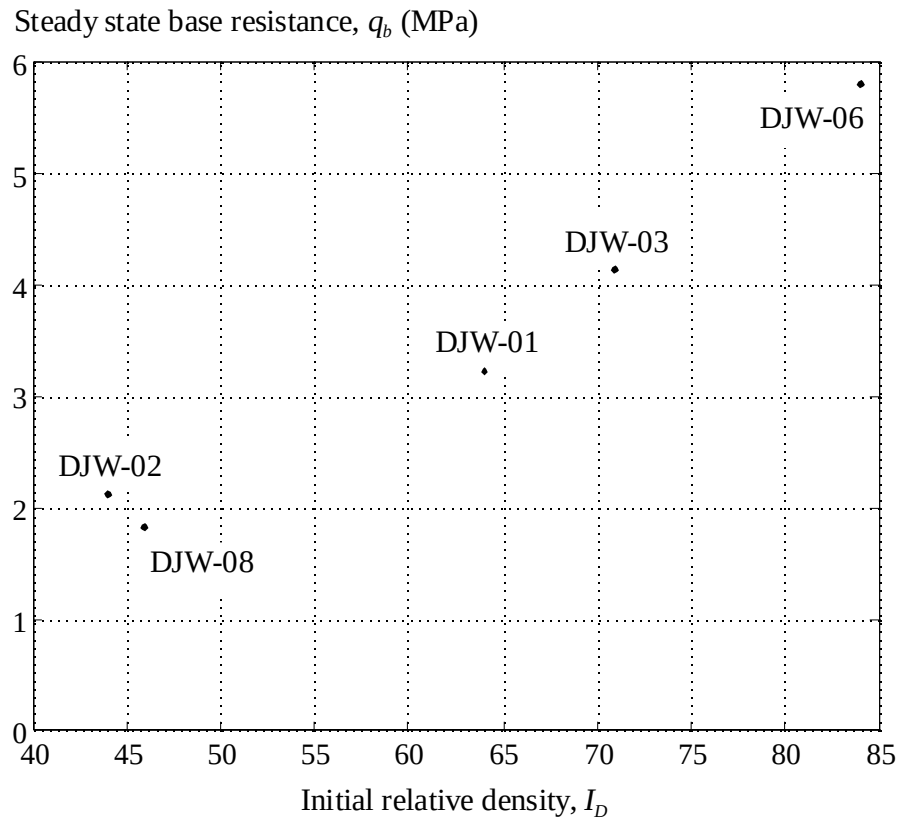

Figure 5.2 Variation of steady state base resistance with relative density

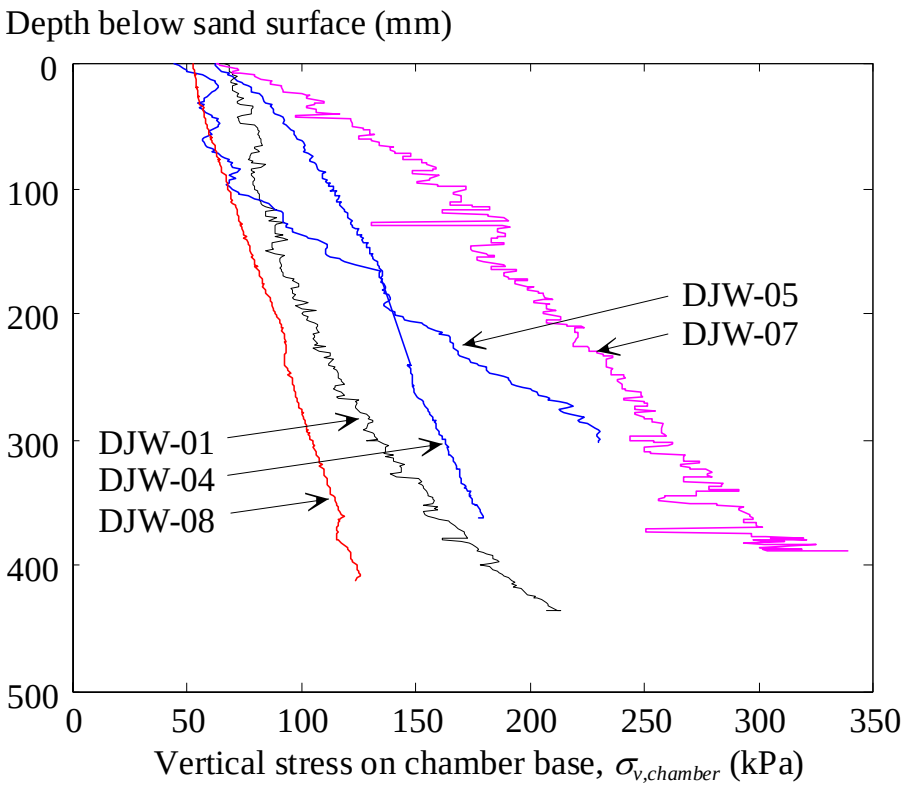

Figure 5.3 Vertical stress measured at chamber base during pile installation

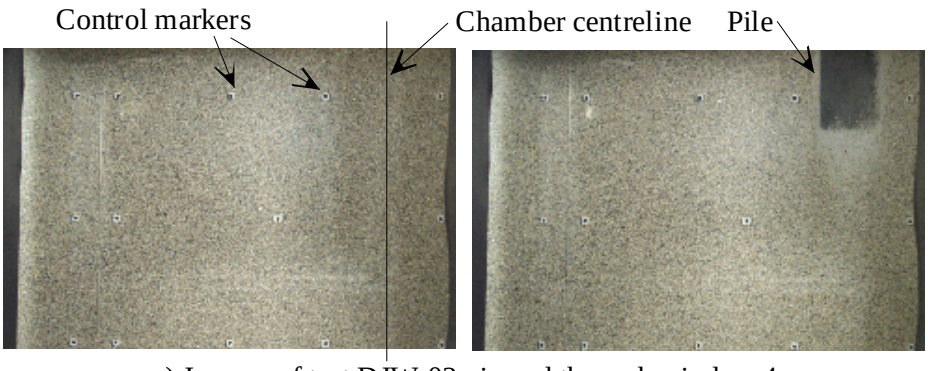

a) Images of test DJW-02 viewed through window 4

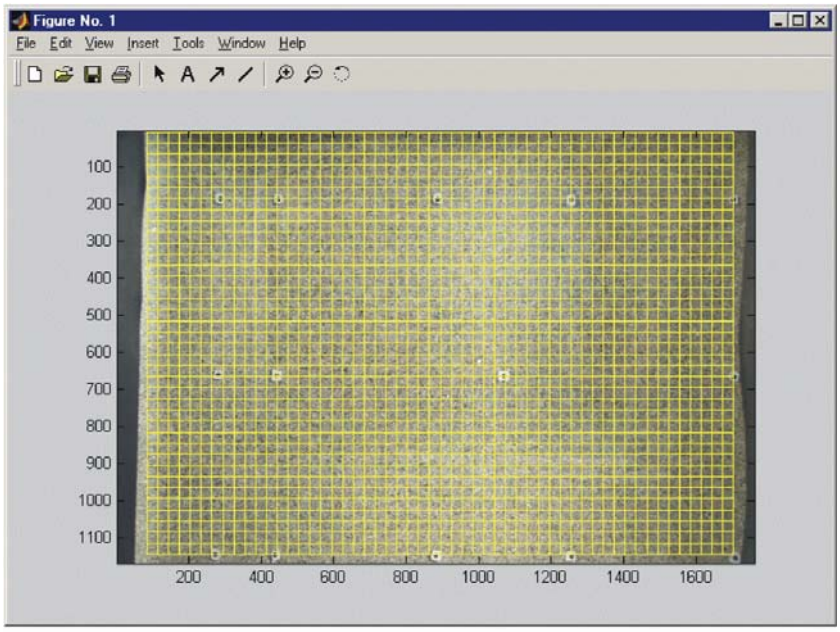

b) Mesh of 2000 PIV patches overlying initial image

30 pixels, ≈4 mm
≈4-7 D_{50} of virgin
DBS and LBS sand

c) Single PIV patch

d) PIV patch compared
to close-up photograph

Figure 5.4 Typical PIV mesh

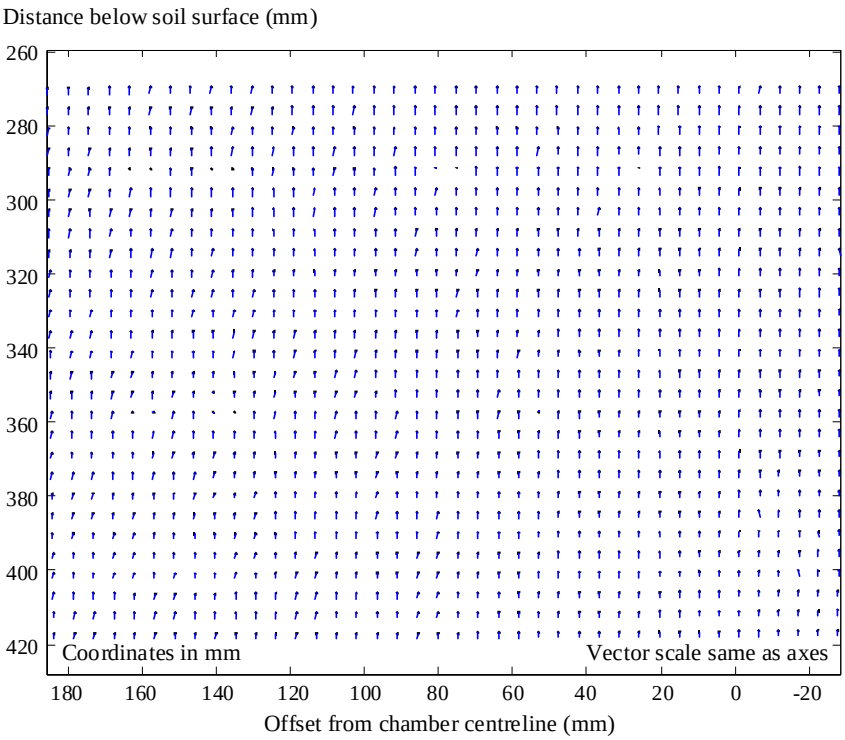

a) Displacement vectors recorded during surcharging to 100 kPa and unloading to 50 kPa (DJW-02, DBS)

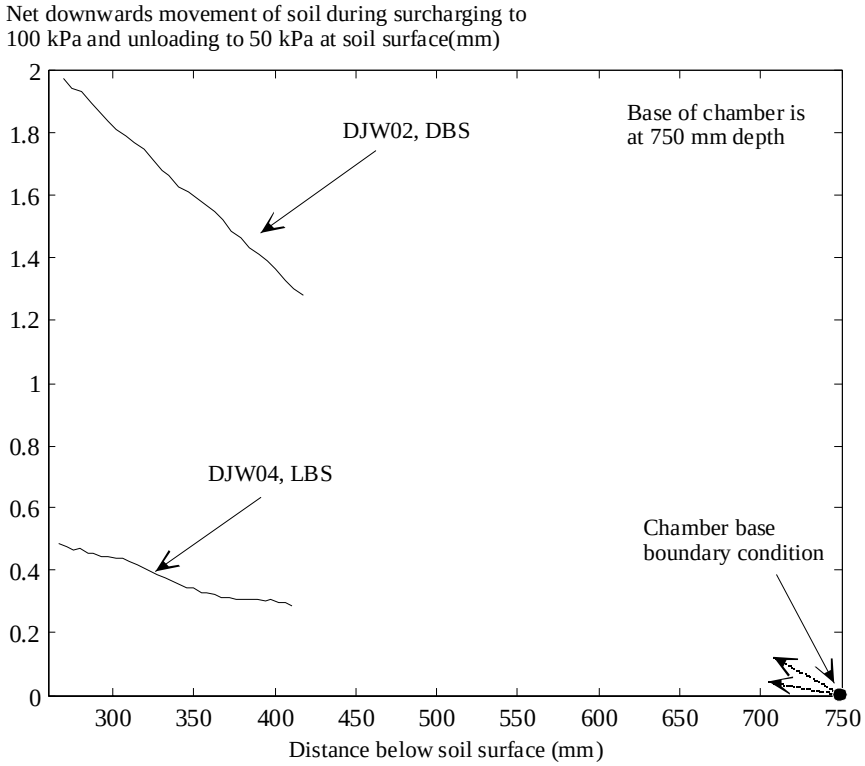

b) Variation of settlement during surcharging with distance below soil surface (viewed in window 4)

Figure 5.5 Downwards displacement of soil during application of surcharge pressure

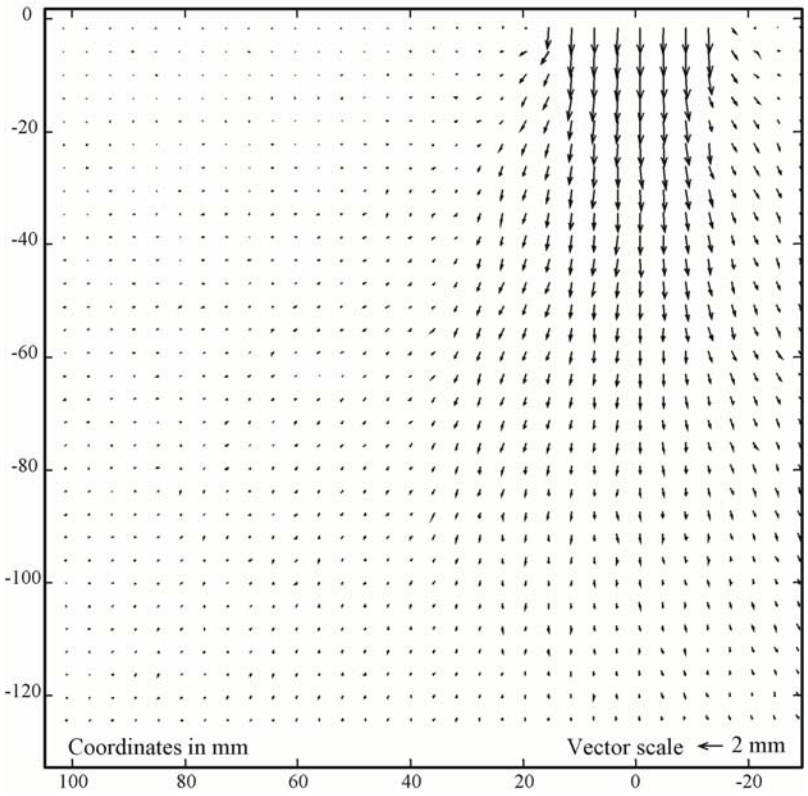

a) DJW-02, DBS

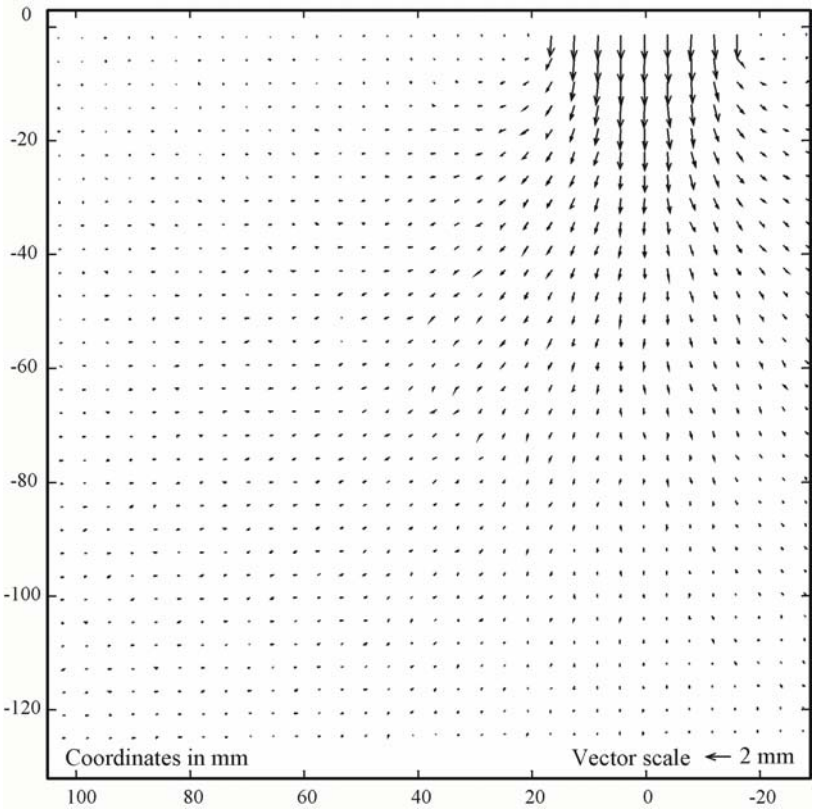

a) DJW-04, LBS

Figure 5.6 Instantaneous velocity fields around the advancing pile

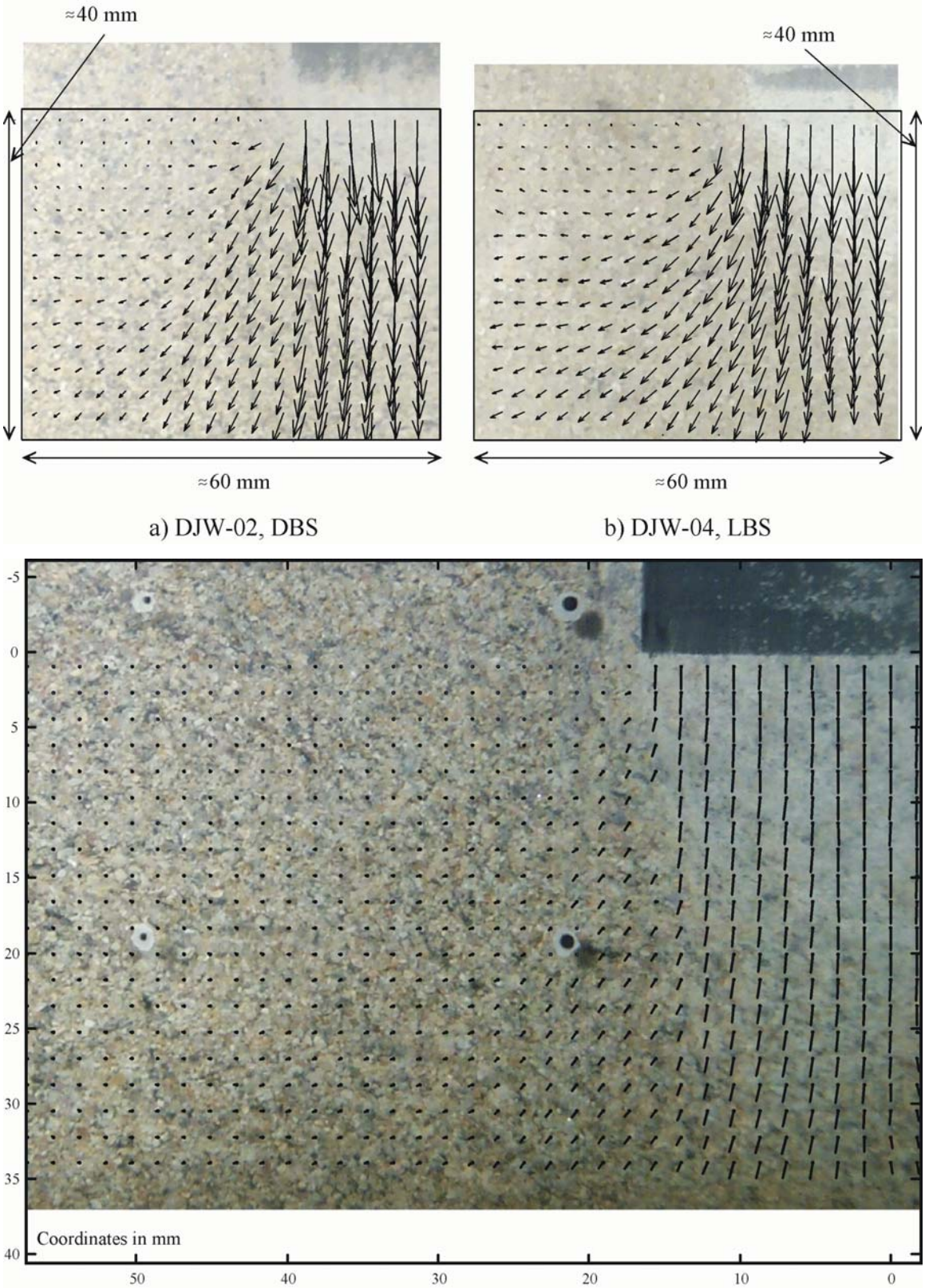

c) DJW-01, close-up view

Figure 5.7 Instantaneous velocity fields close to advancing pile (nominal fitting with photos ignoring image distortion)

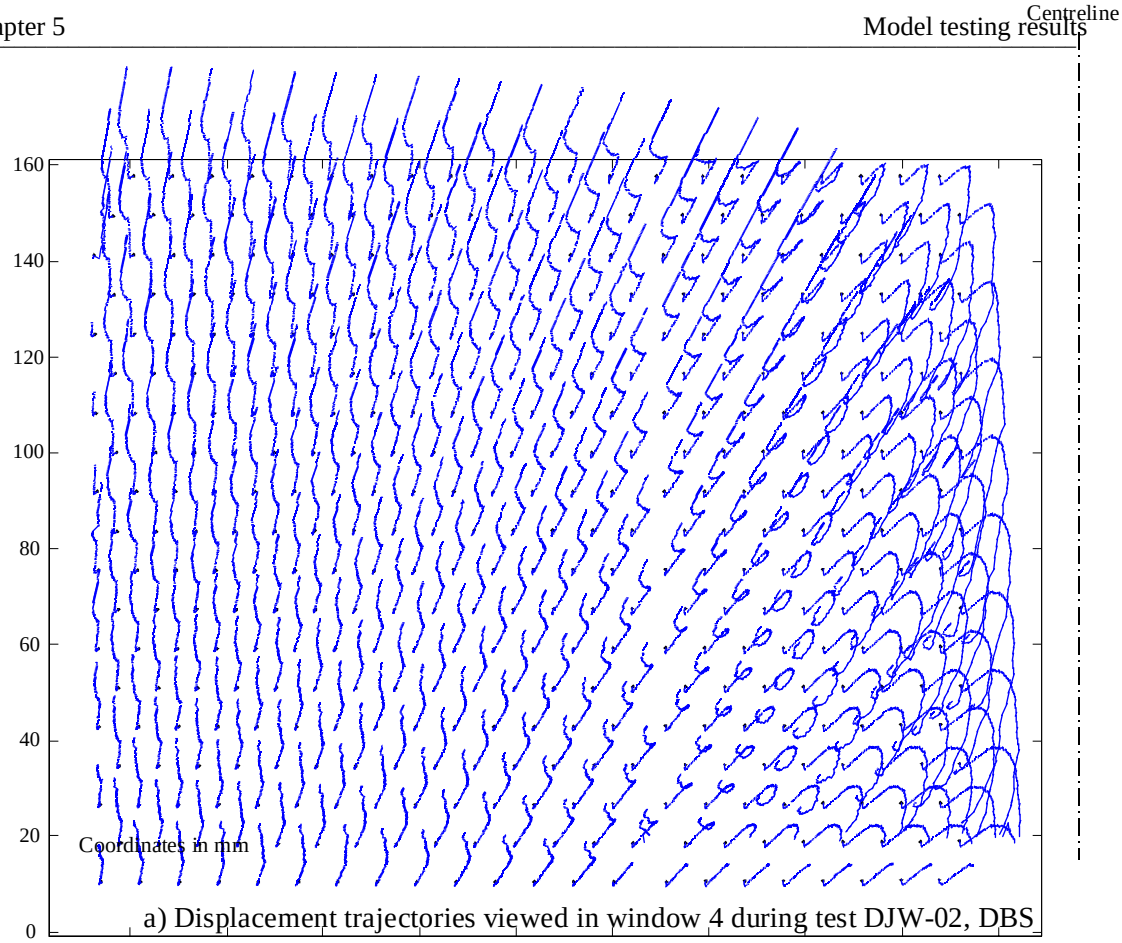

a) Displacement trajectories viewed in window 4 during test DJW-02, DBS

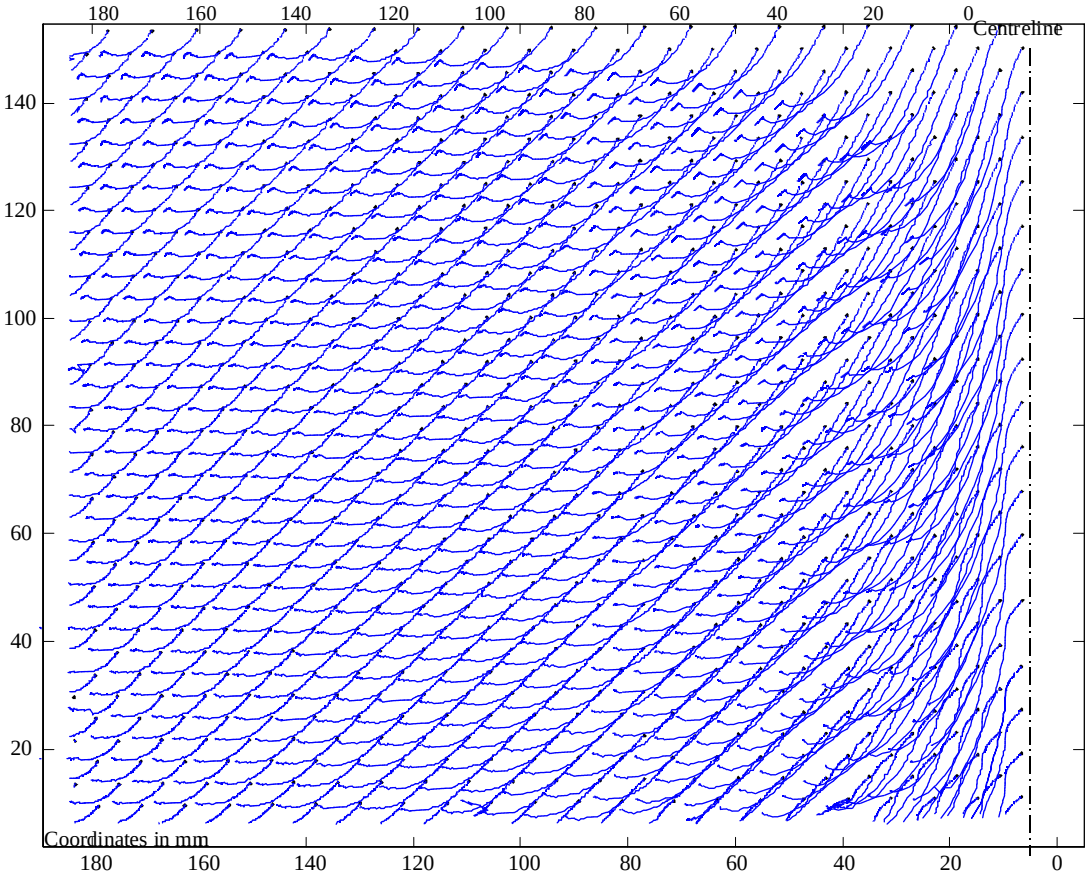

b) Displacement trajectories viewed in window 4 during test DJW-04, LBS

Figure 5.8 Soil element trajectories during pile installation: entire field of view

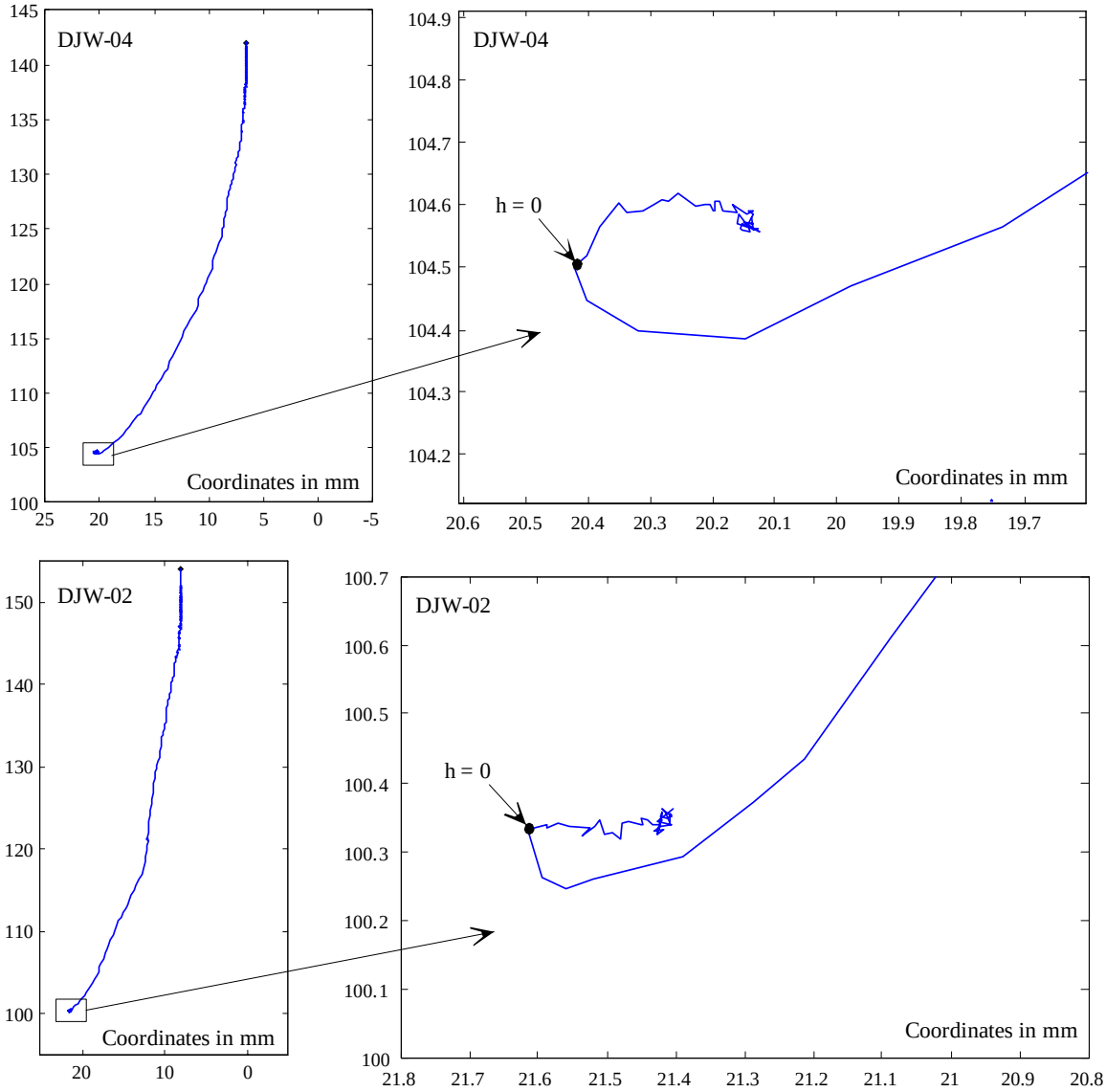

Figure 5.9 Soil element trajectories during pile installation: single soil elements

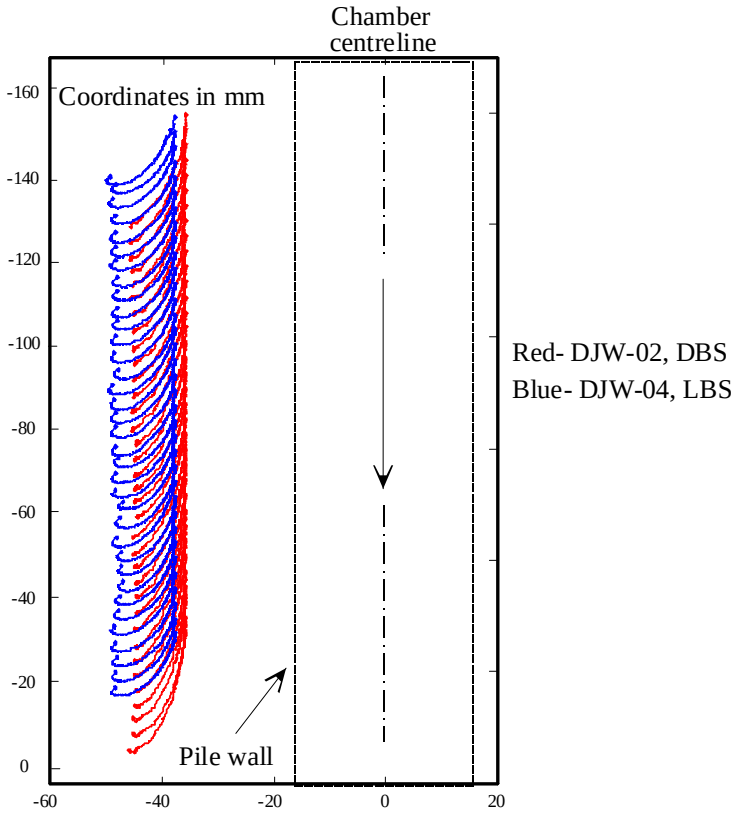

a) Displacement trajectories of a single column of soil elements

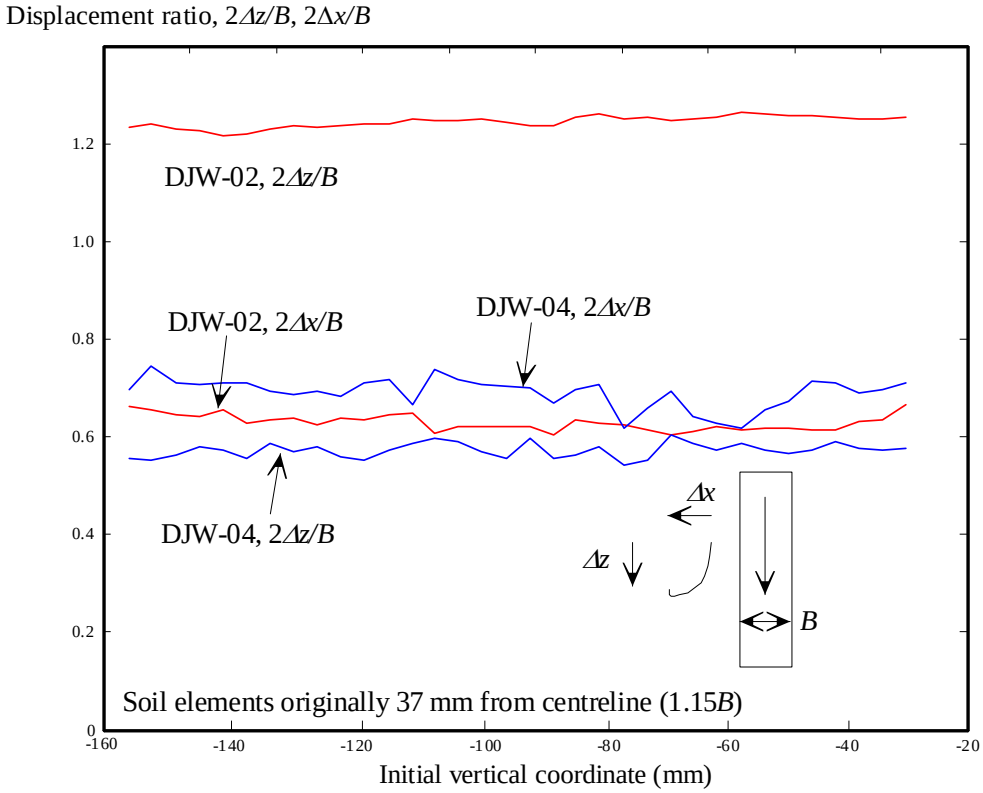

b) Displacement ratios of a single column of soil elements

Figure 5.10 Steady state deformation

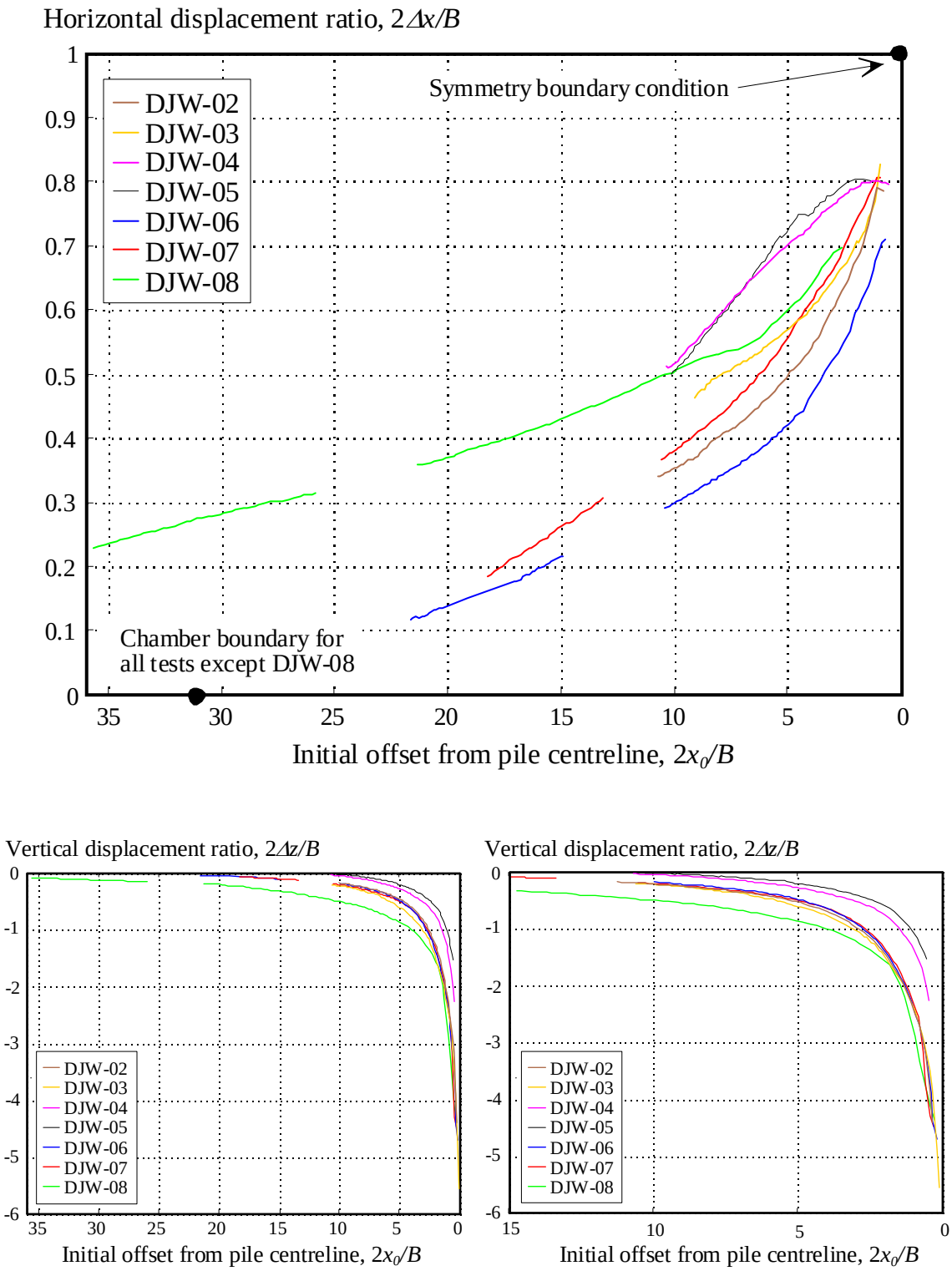

Figure 5.11 Horizontal and vertical displacement during pile installation

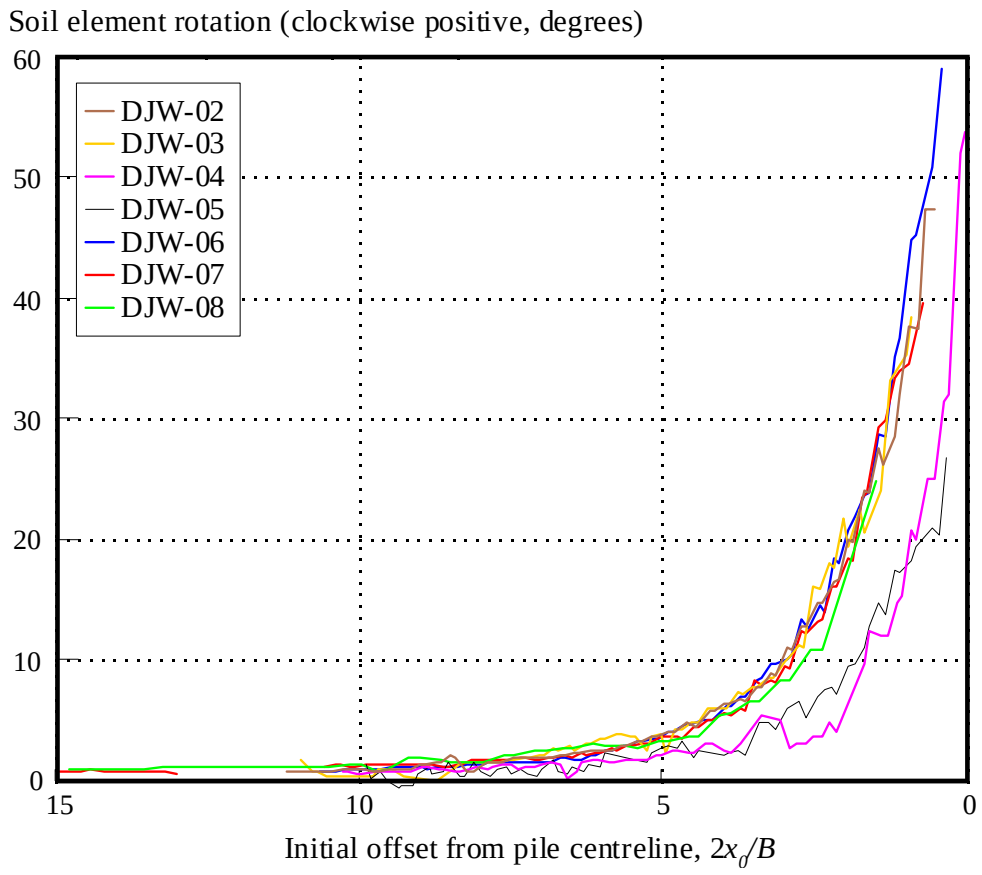

Figure 5.12 Soil element rotation during pile installation

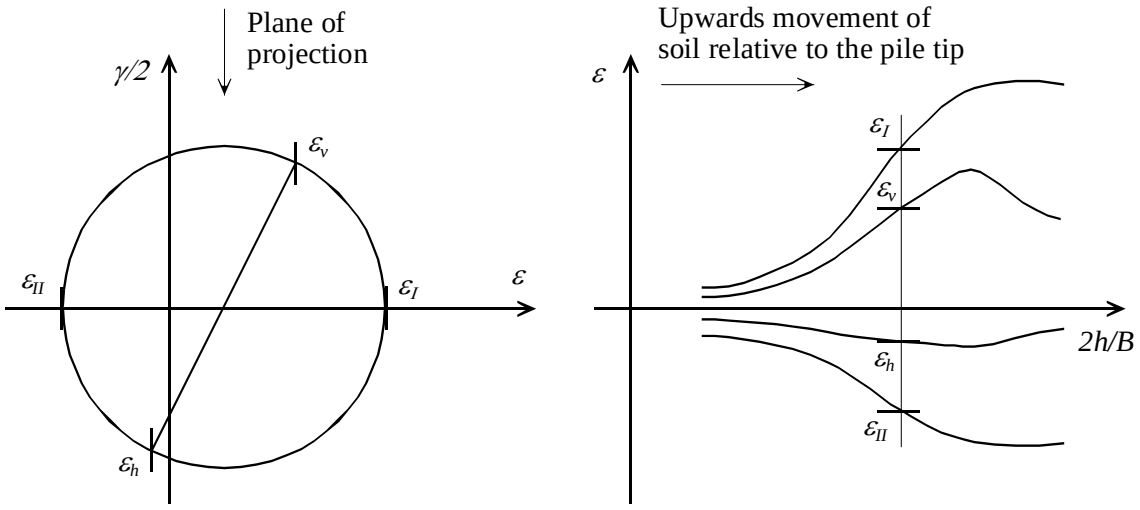

Figure 5.13 Illustration of strain path by evolving Mohr's circle of strain

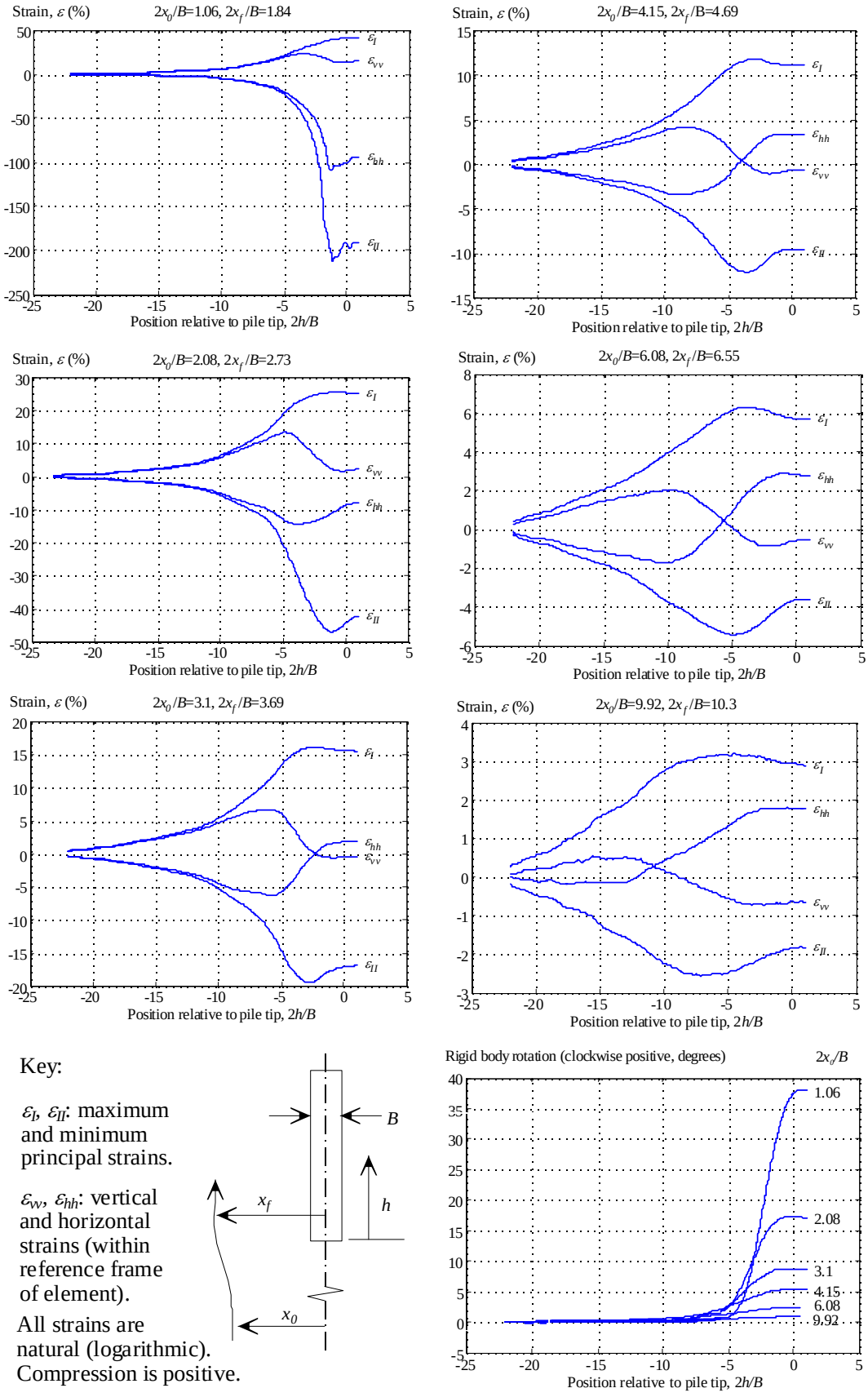

Figure 5.14 Strain and rotation paths during pile installation: DJW-02, DBS

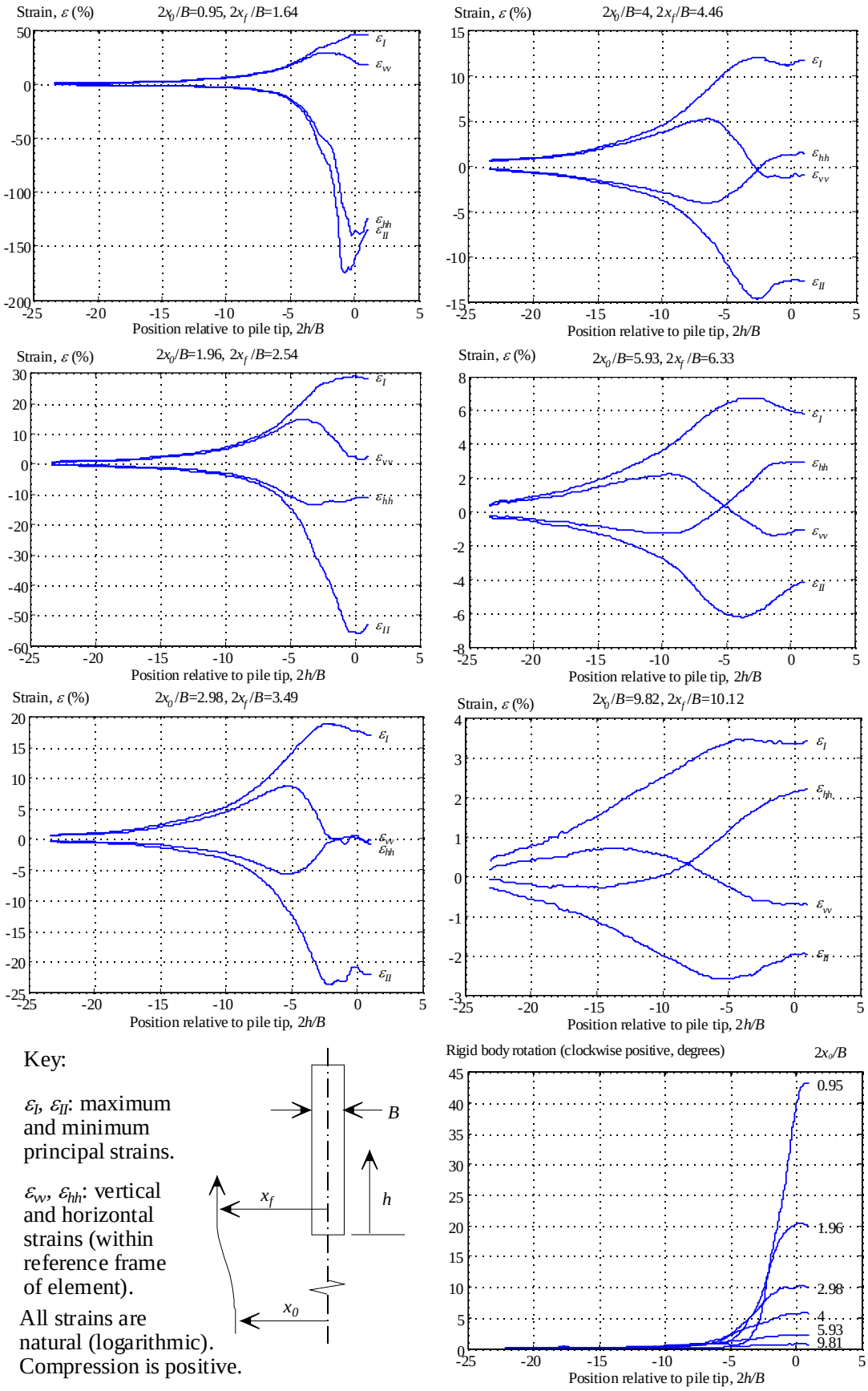

Figure 5.15 Strain and rotation paths during pile installation: DJW-06, DBS

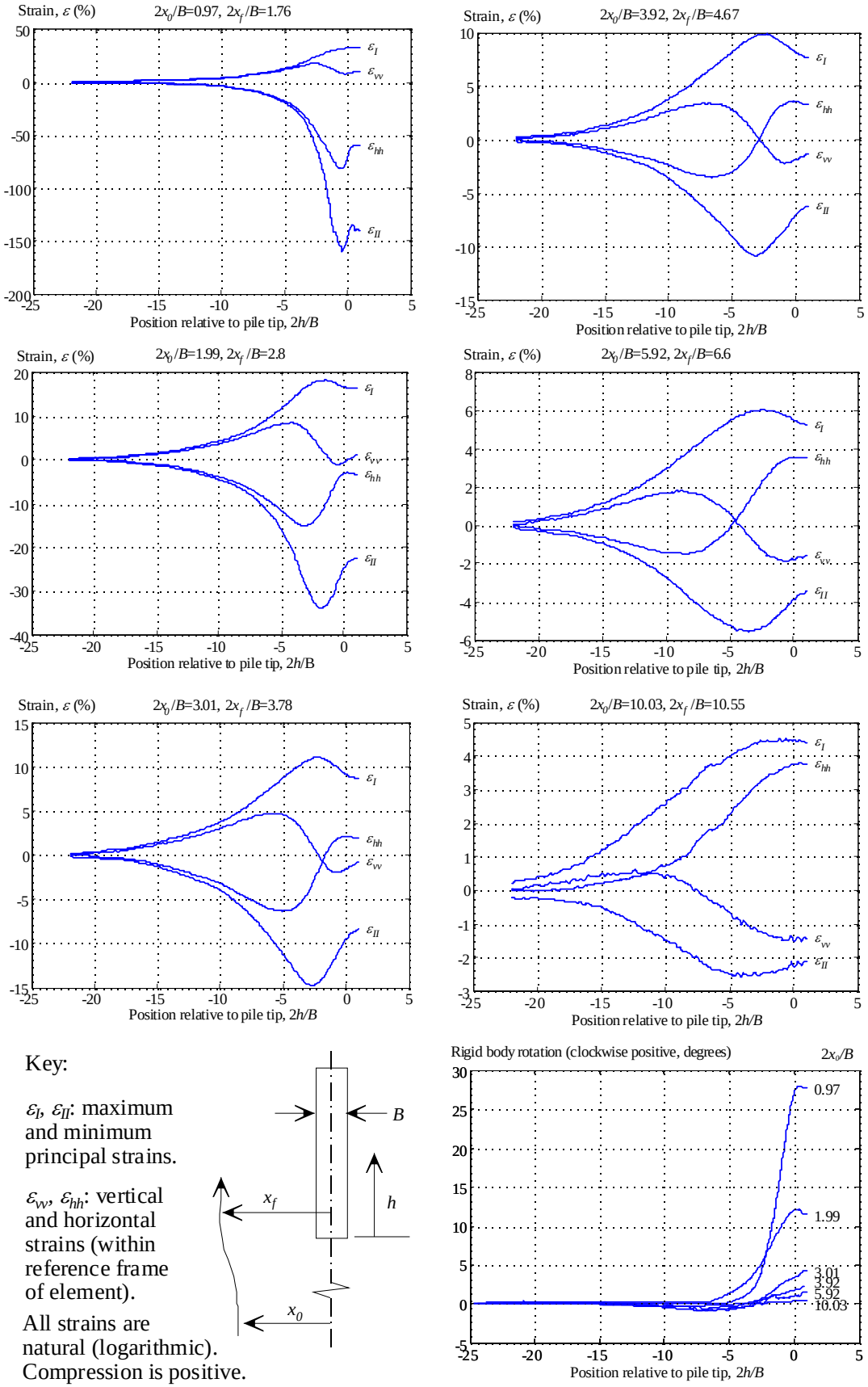

Figure 5.16 Strain and rotation paths during pile installation: DJW-04, LBS

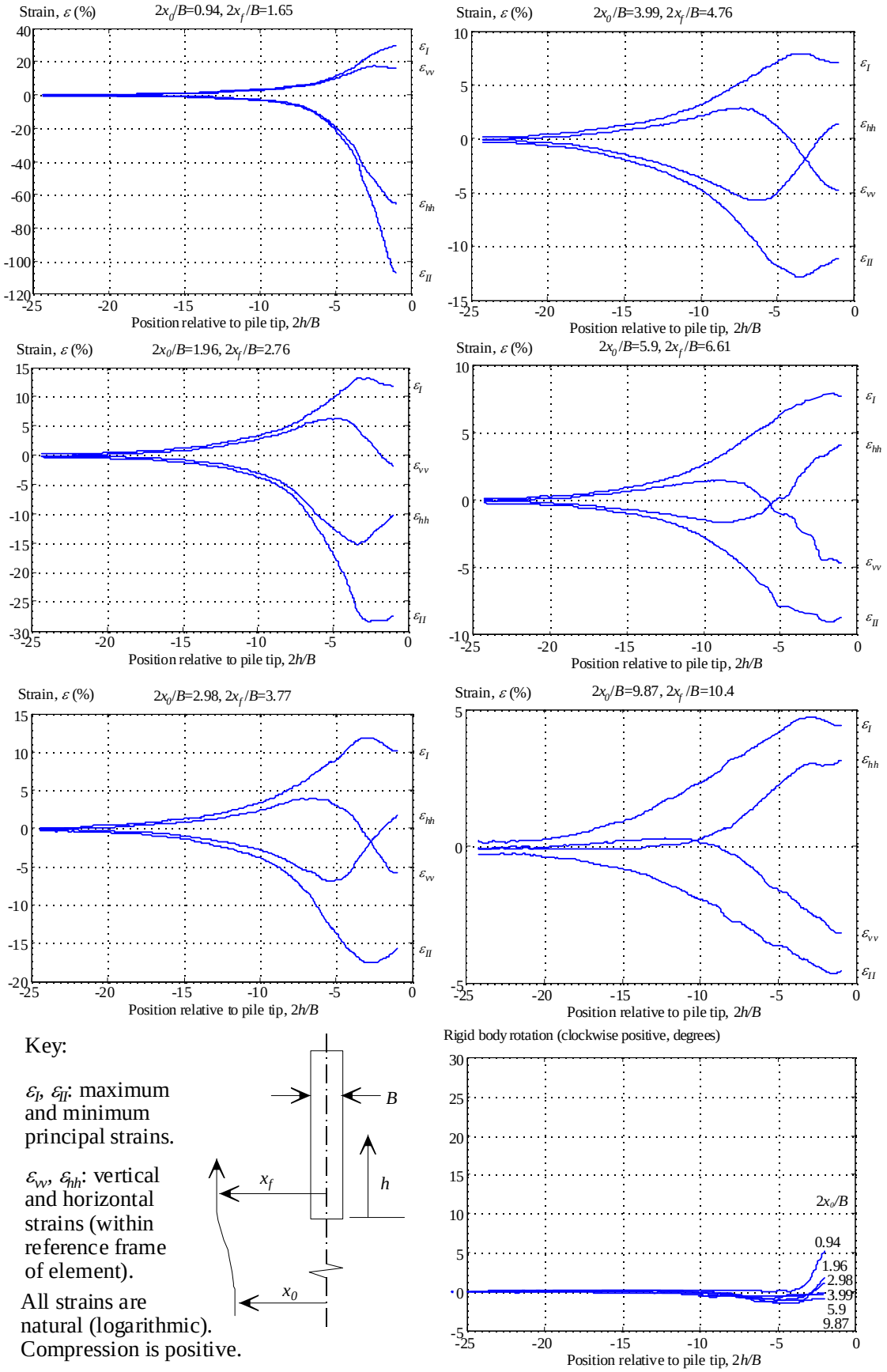

Figure 5.17 Strain and rotation paths during pile installation: DJW-05, LBS

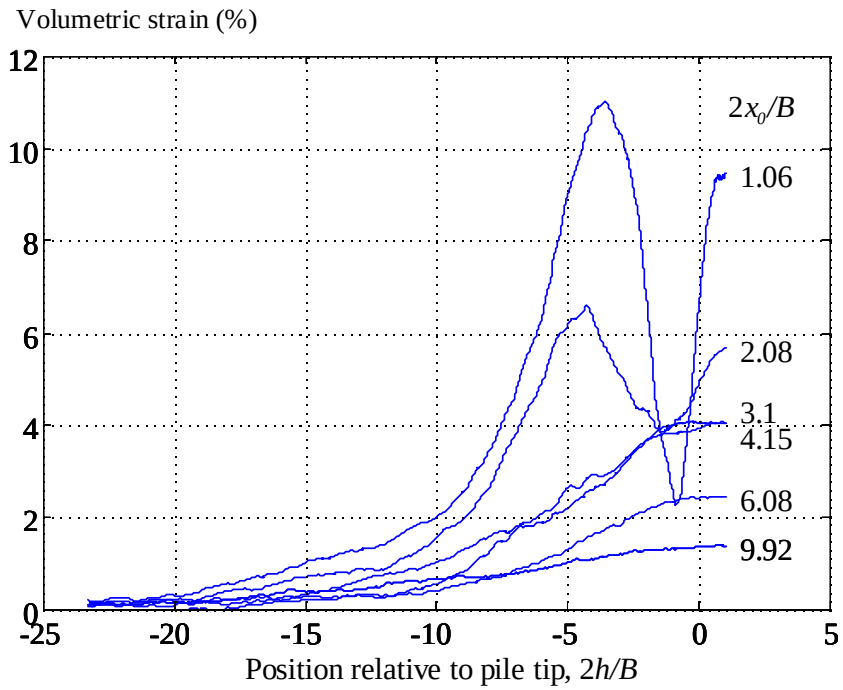

a) DJW-02, DBS

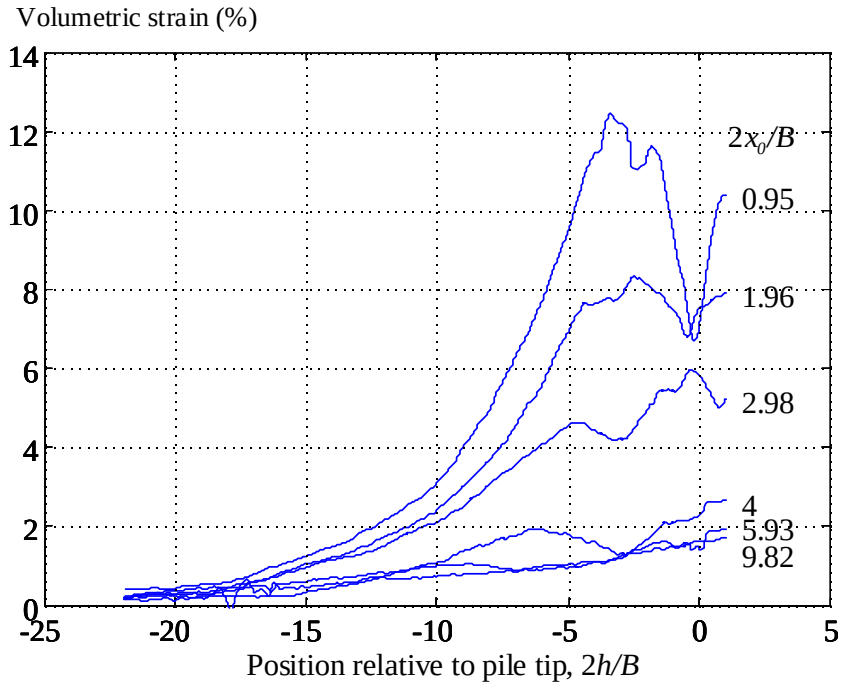

b) DJW-06, DBS

Figure 5.18 Volumetric strain paths: DBS

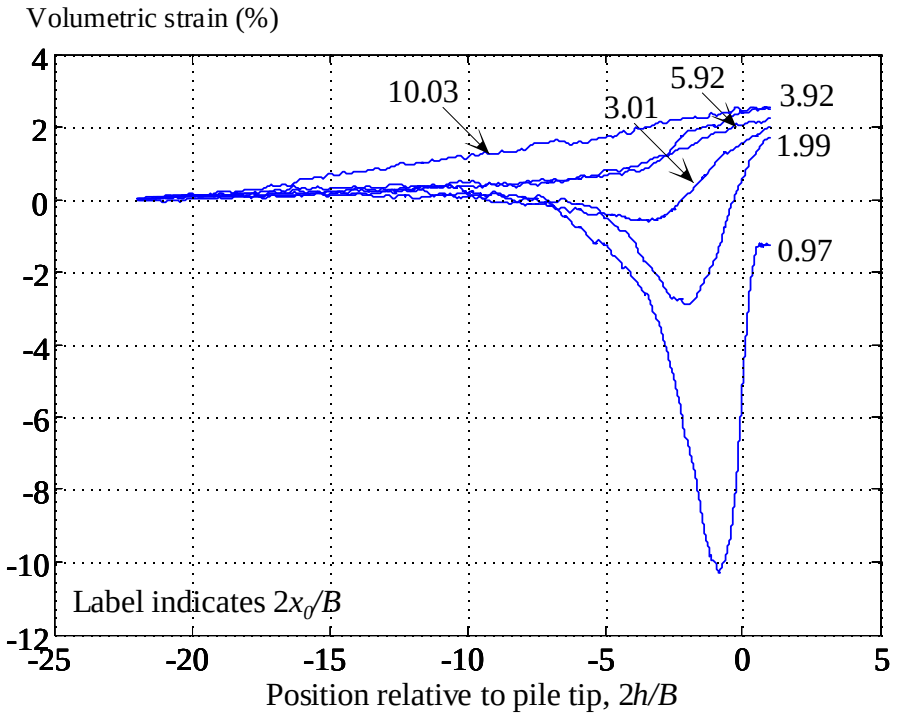

a) DJW-04, LBS

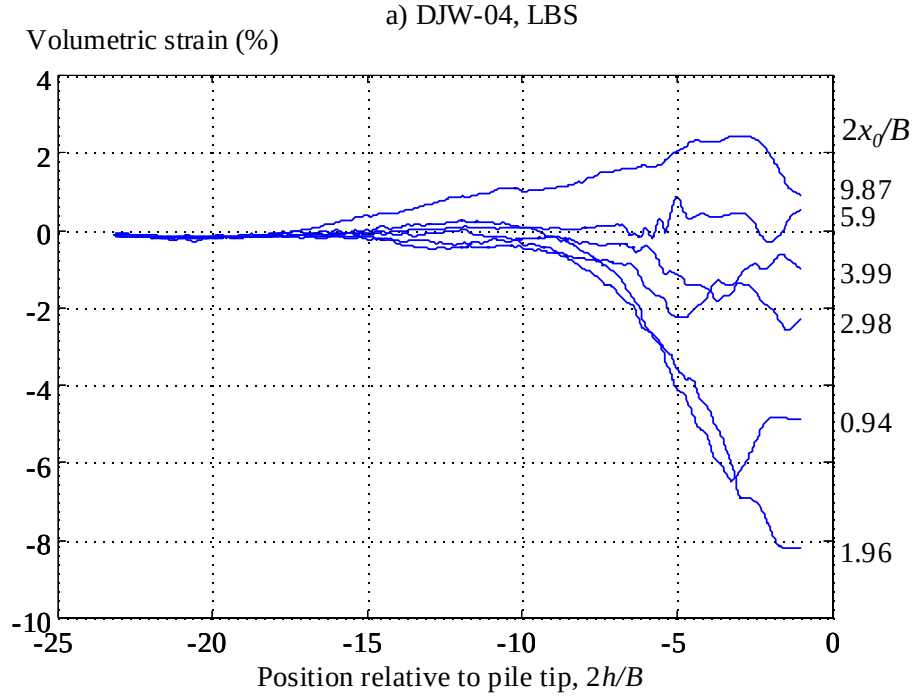

b) DJW-05, LBS

Figure 5.19 Volumetric strain paths: LBS

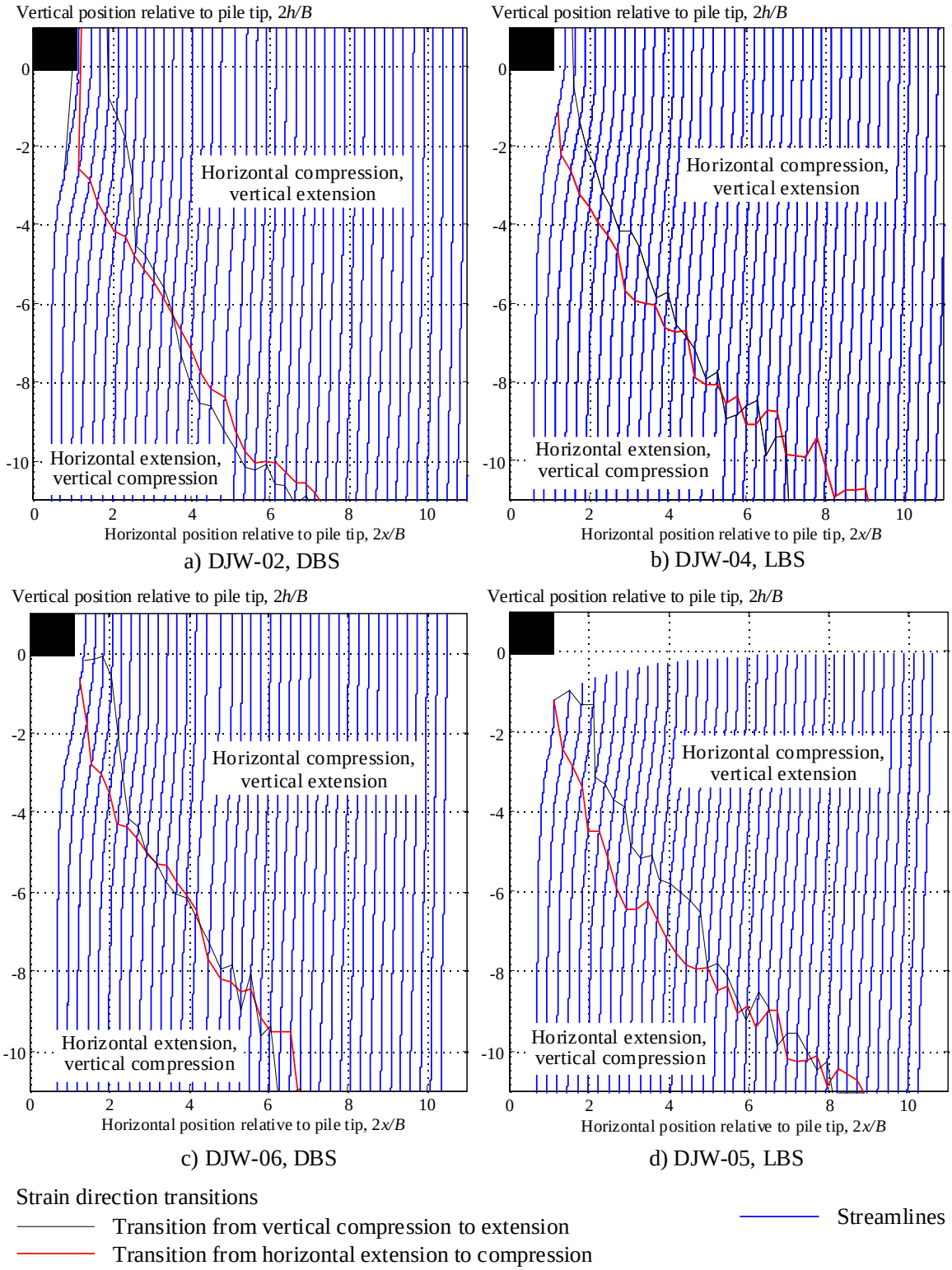

Figure 5.20 Streamlines of soil flow and strain rate reversal points

E1: Vertical strain

E1= ε_{zz}

E2: Cylindrical expansion strain

E2= $(\varepsilon_{rr}-\varepsilon_{\theta\theta}) / 1.732$

E3: Simple shear strain

E3= $2\varepsilon_{rz} / 1.732$

Axisymmetric 'simple pile'

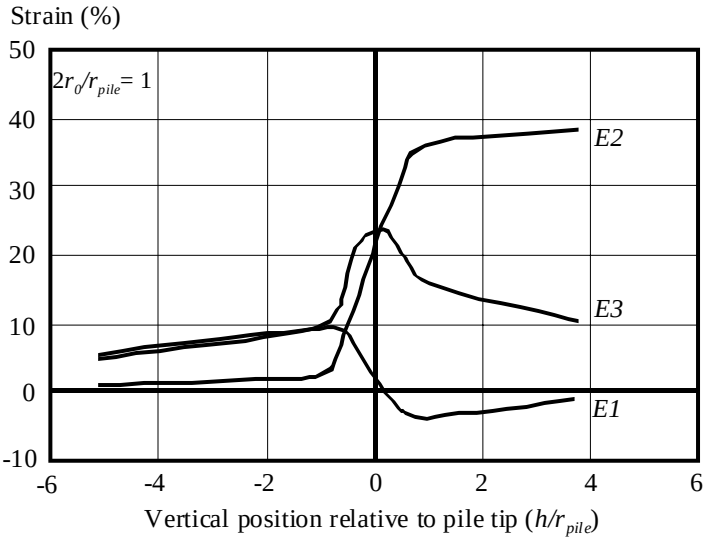

a) Strain paths around a 'simple pile' (from data published by Baligh, 1985)

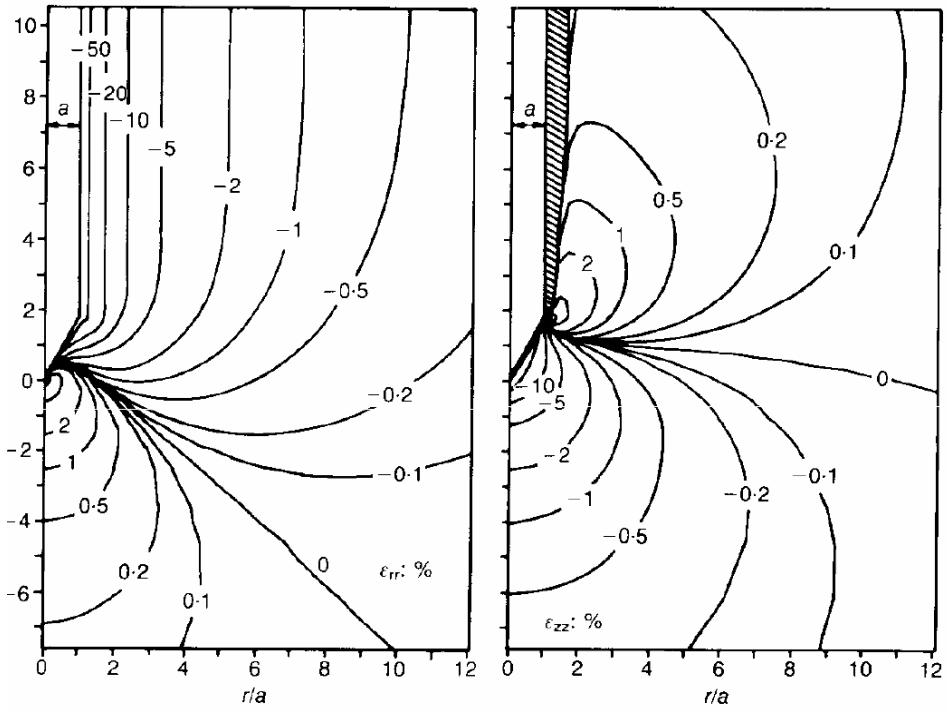

b) Radial and vertical strain contours around a 60° cone (Teh & Houlsby, 1991) (tension positive)

Figure 5.21 Predictions from the Strain Path Method

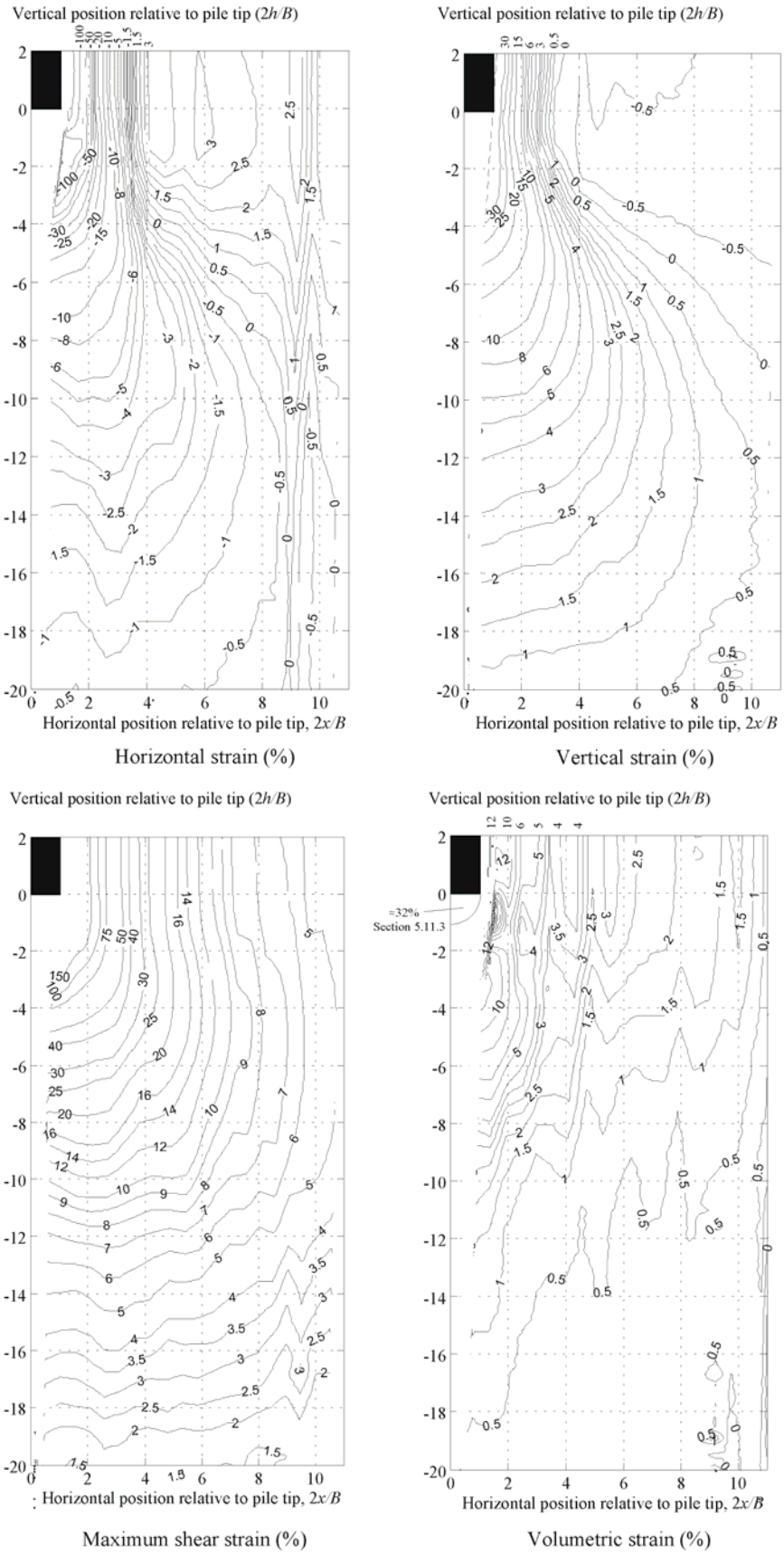

Figure 5.22 Post-installation strain distribution: DJW-02, DBS

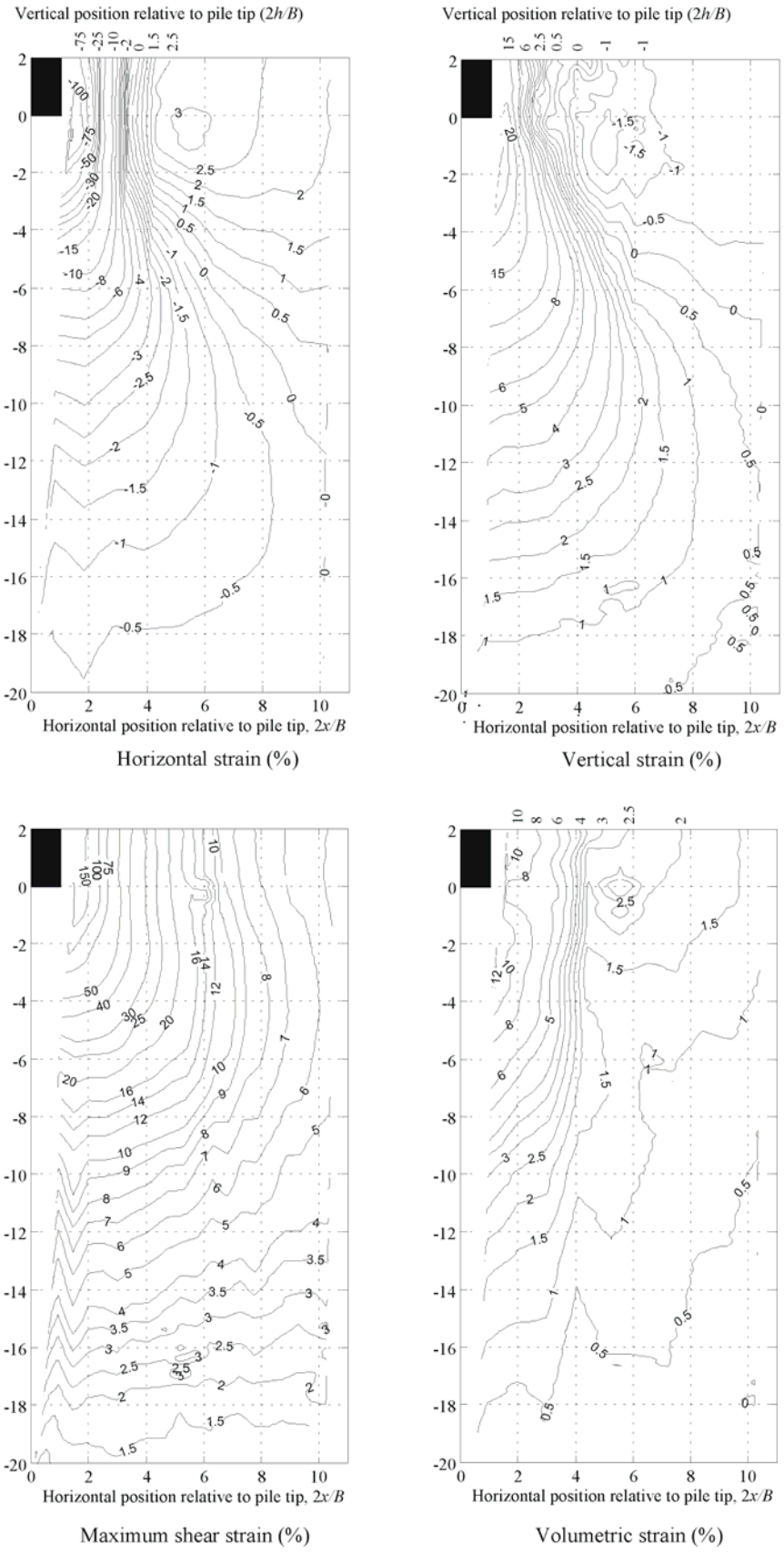

Figure 5.23 Post-installation strain distribution: DJW-06, DBS

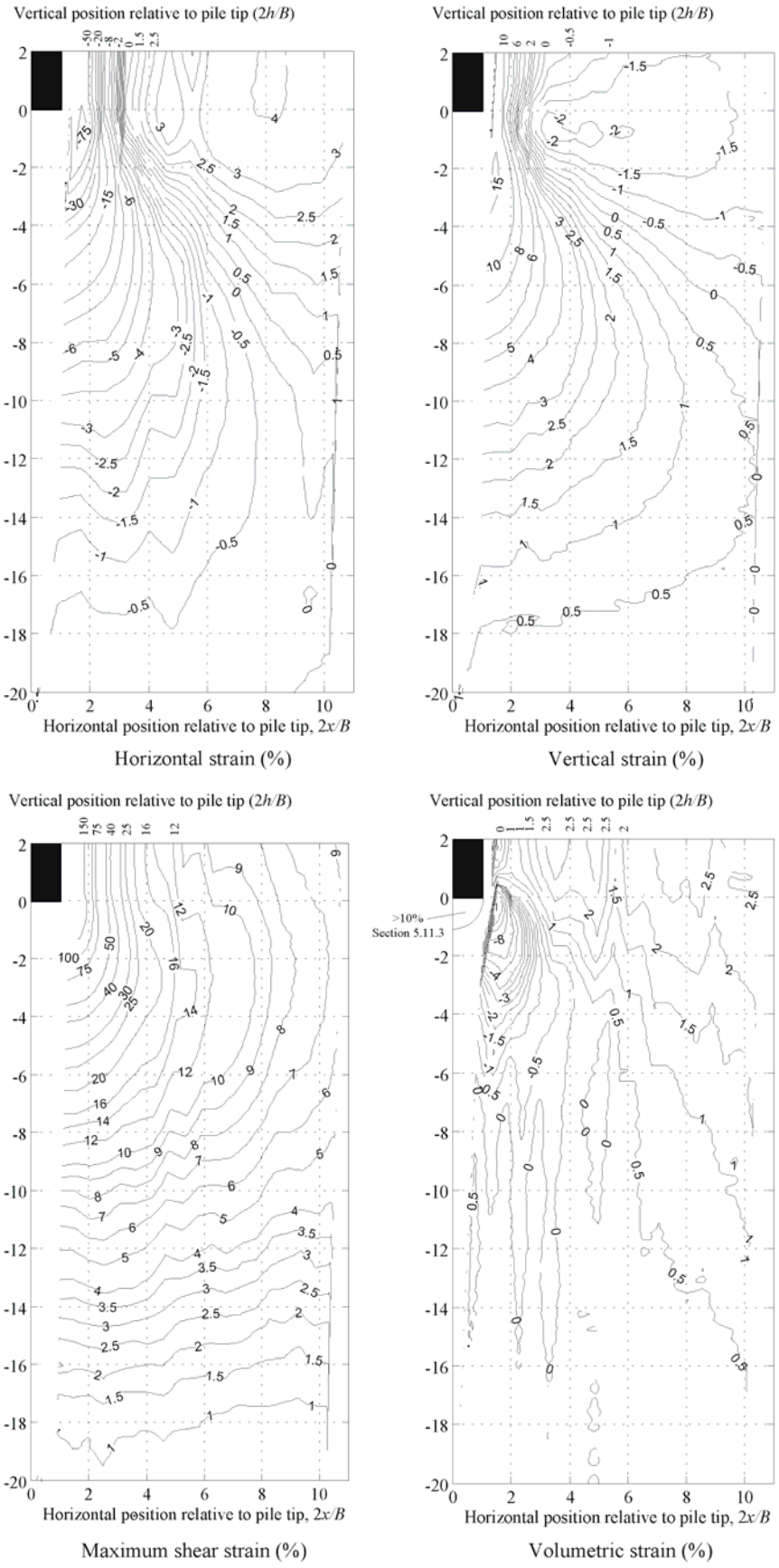

Figure 5.24 Post-installation strain distribution: DJW-04 , LBS

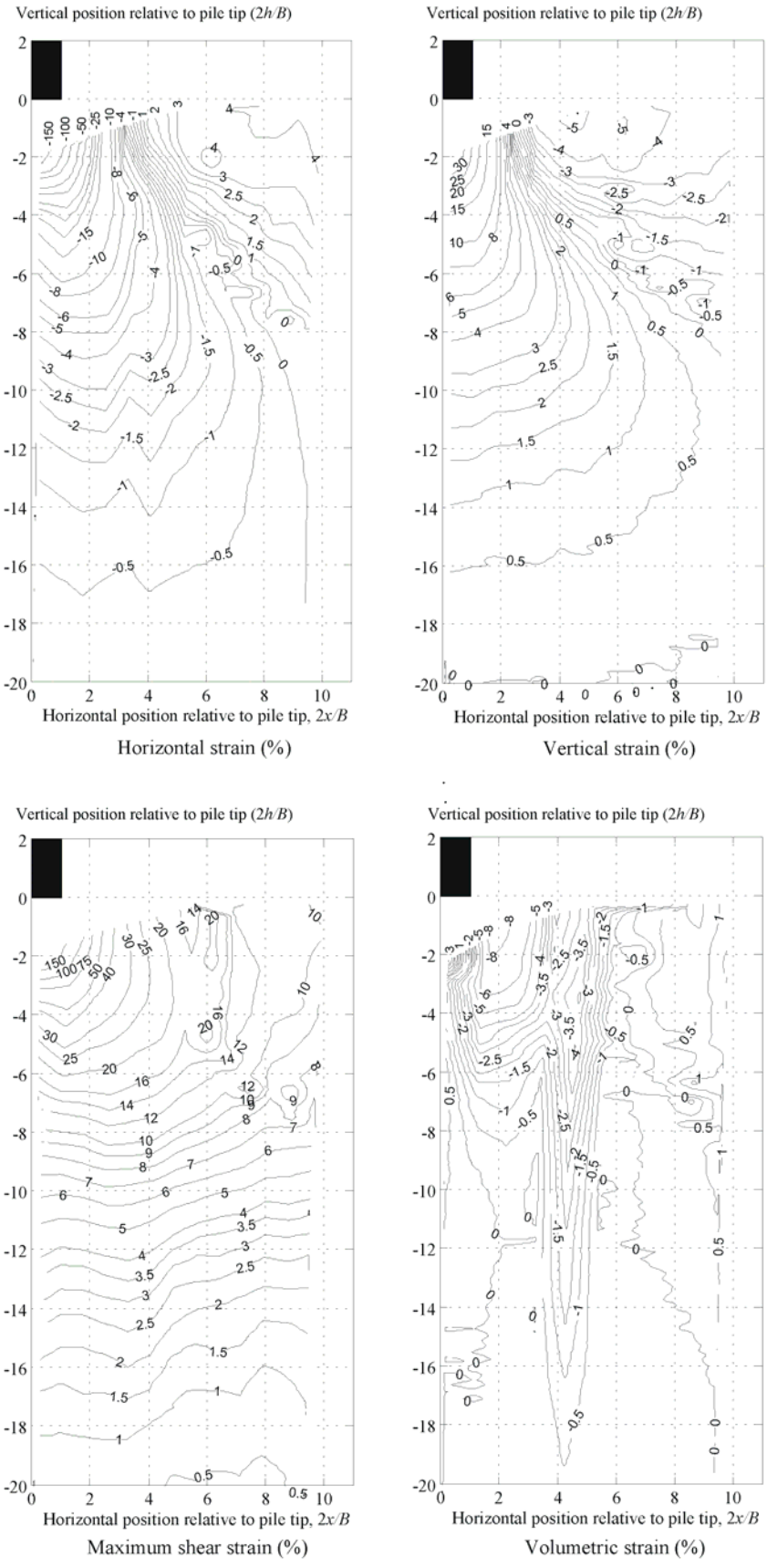

Figure 5.25 Post-installation strain distribution: DJW-05, LBS

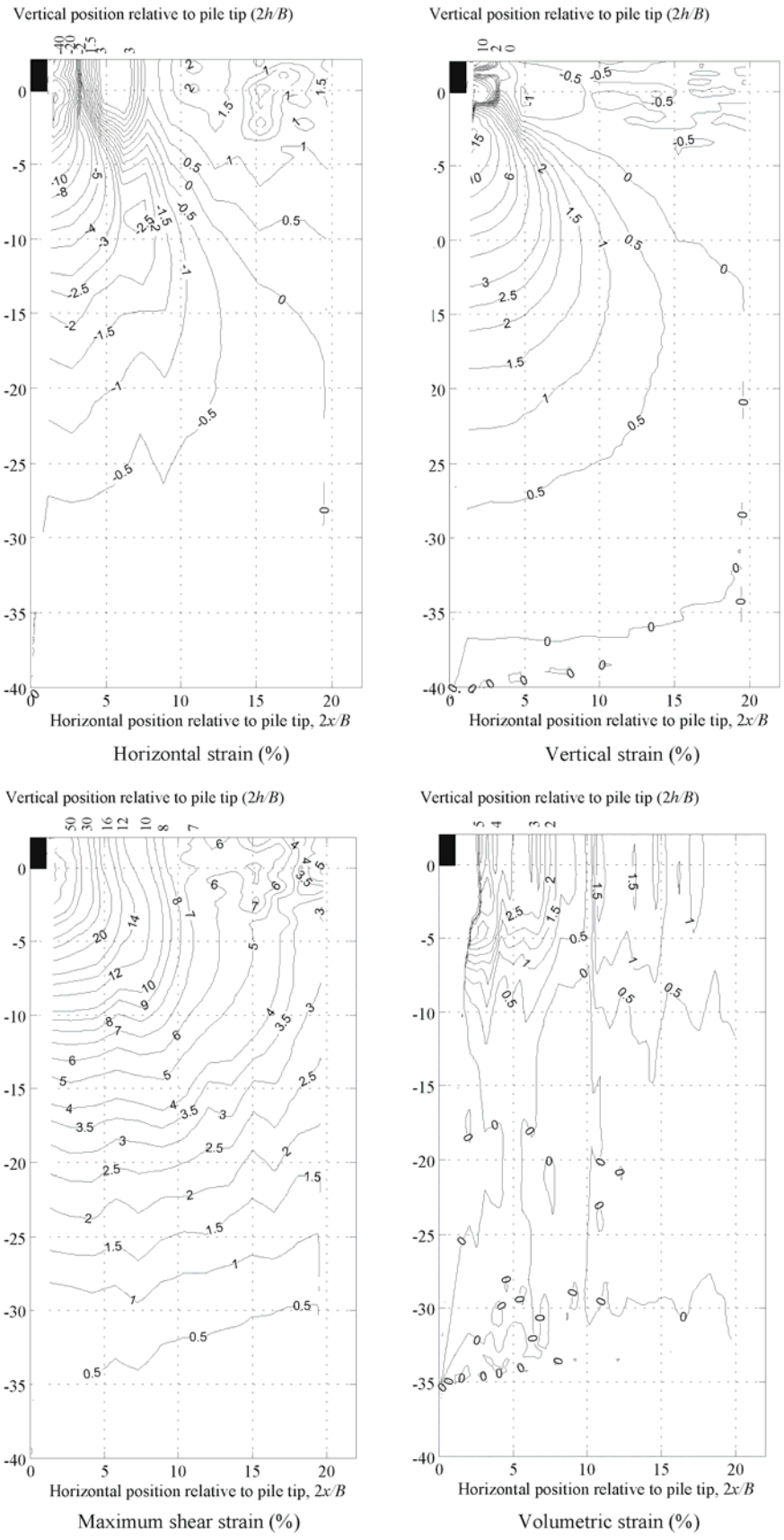

Figure 5.26 Post-installation strain distribution: DJW-08, DBS

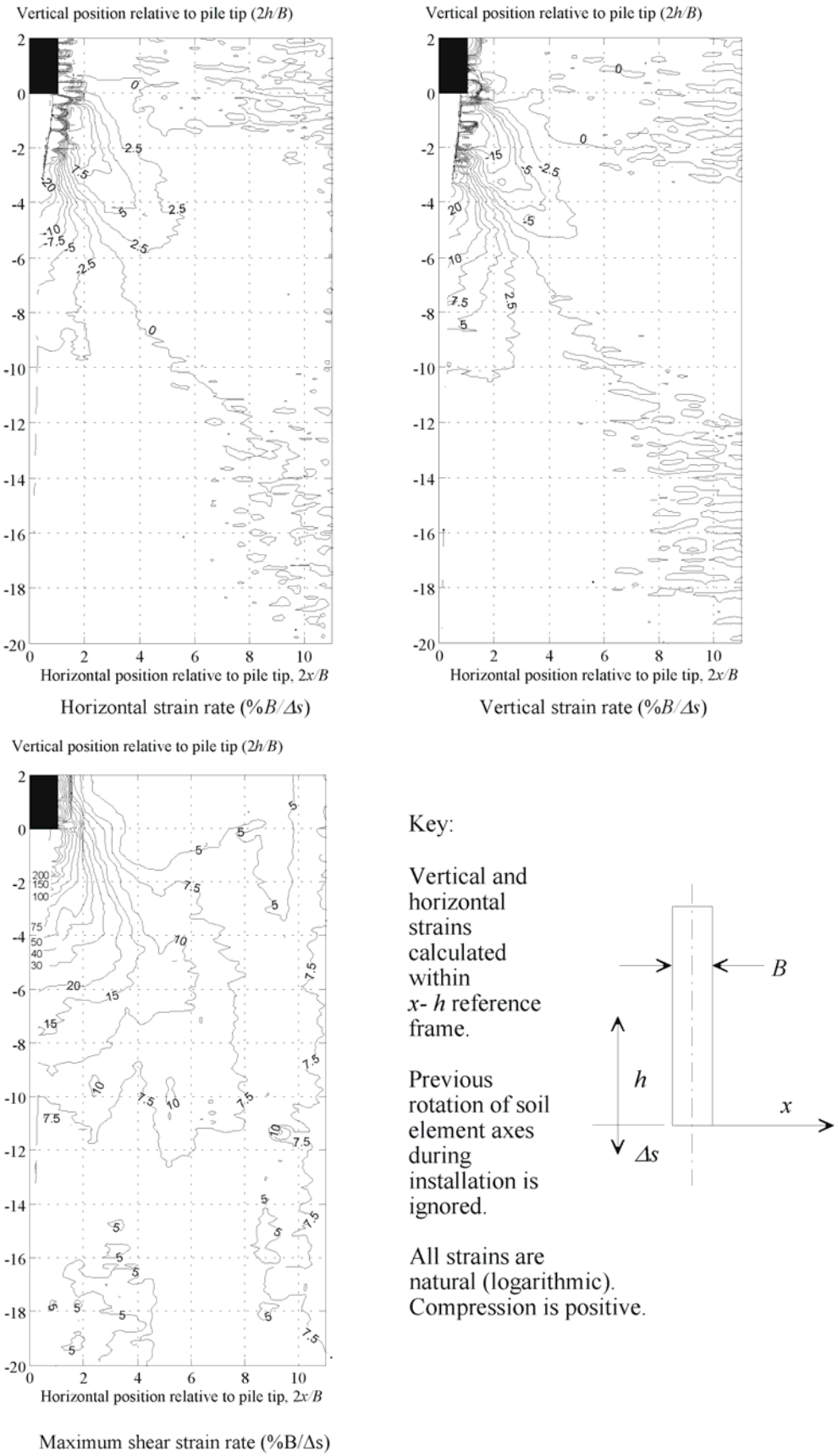

Figure 5.27 Spatial distribution of strain rate with pile settlement: DJW-02, DBS

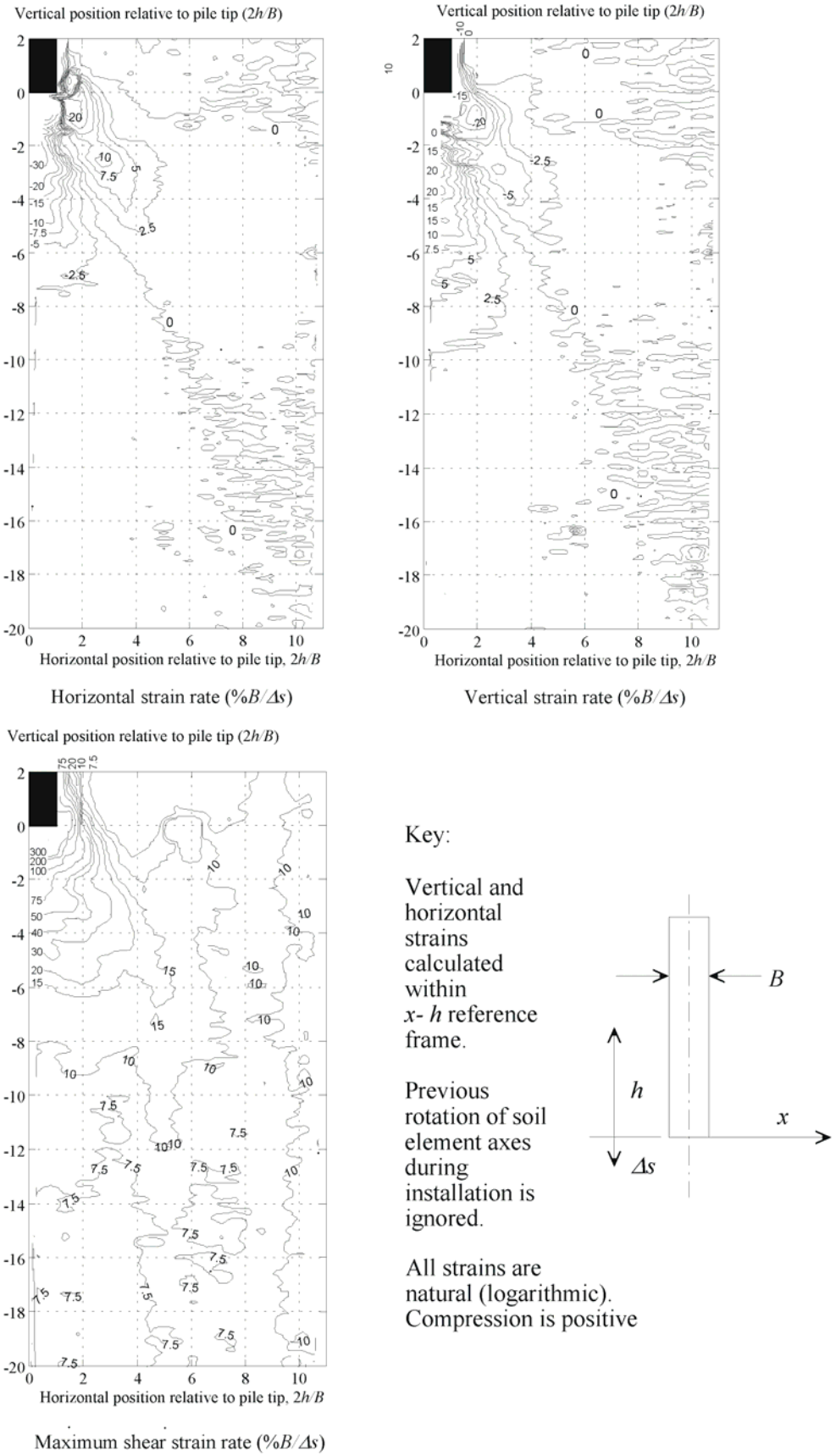

Figure 5.28 Spatial distribution of strain rate with pile settlement: DJW-06, DBS

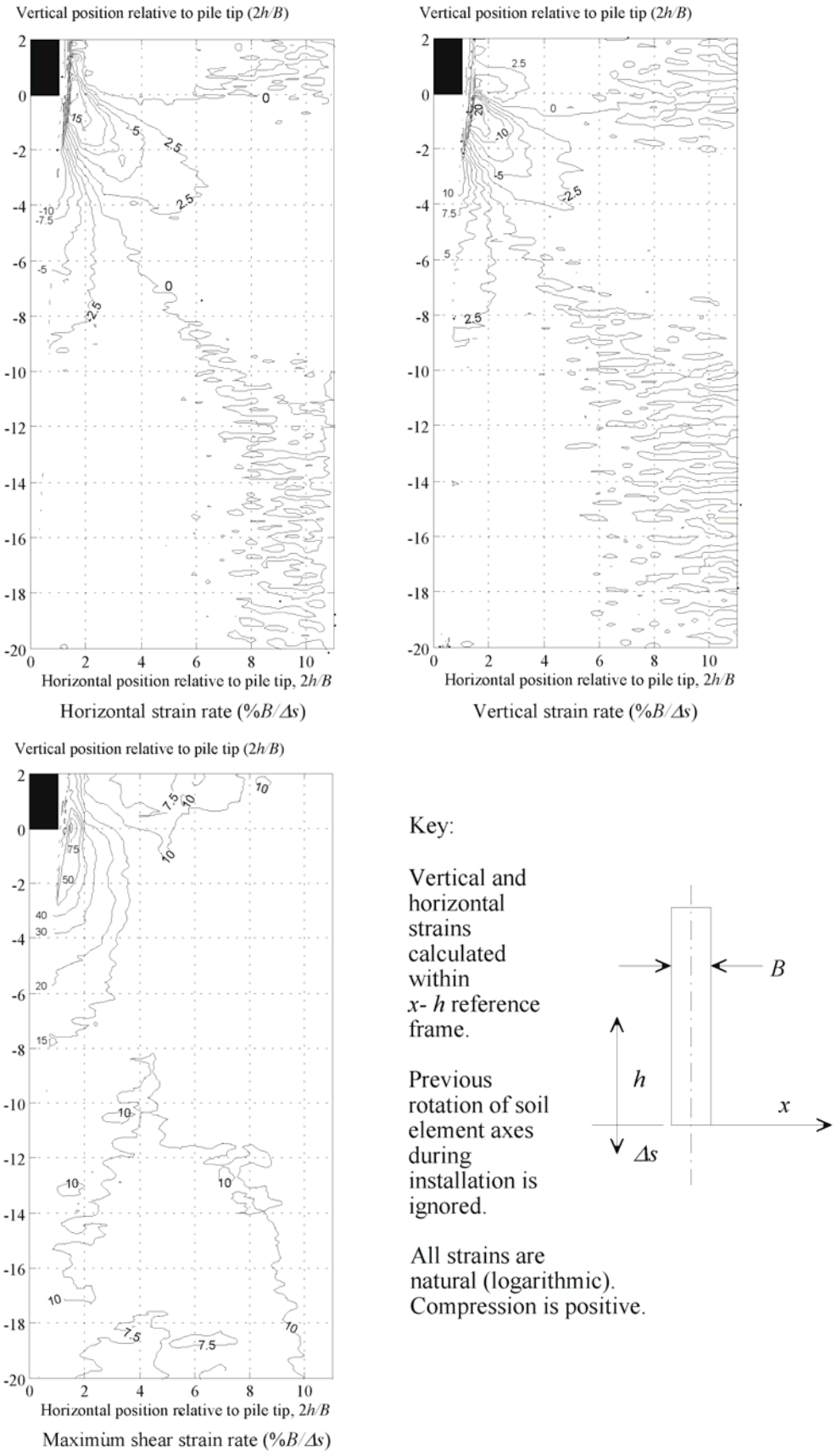

Figure 5.29 Spatial distribution of strain rate with pile settlement: DJW-04, LBS

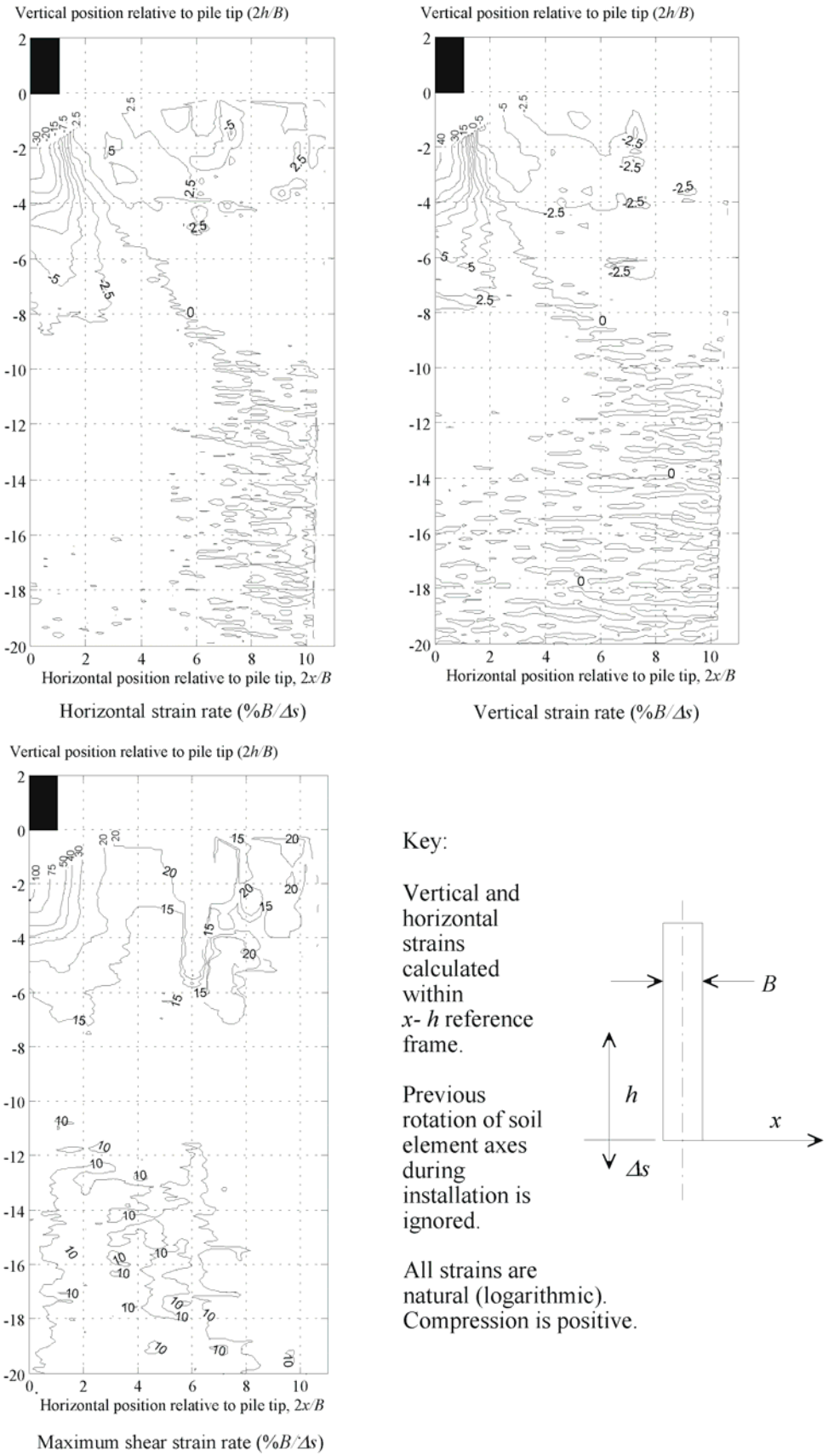

Figure 5.30 Spatial distribution of strain rate with pile settlement: DJW-05, LBS

a) 'Nose cone' of soil beneath pile tip

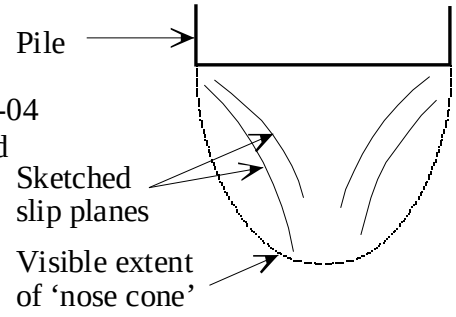

b) Slip planes observed within 'nose cone'

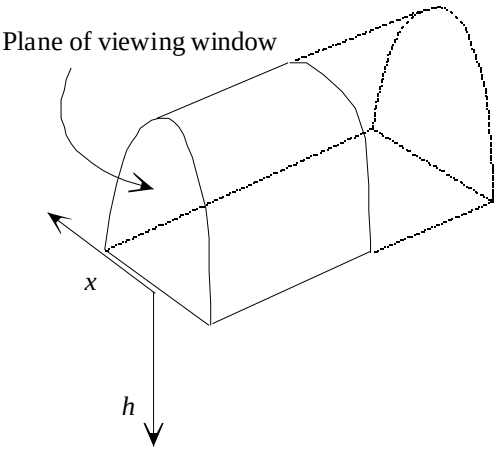

c) Cone of soil recovered from beneath tip of pile (Test DJW-03, DBS)

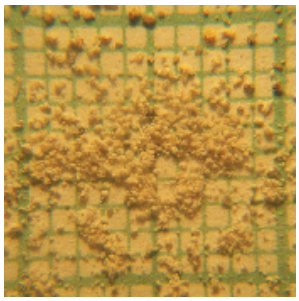

Grains recovered from beneath pile tip

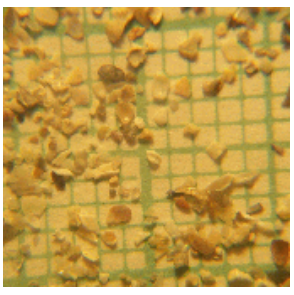

Virgin DBS

d) Comparative photographs of virgin DBS and grains recovered from soil cone

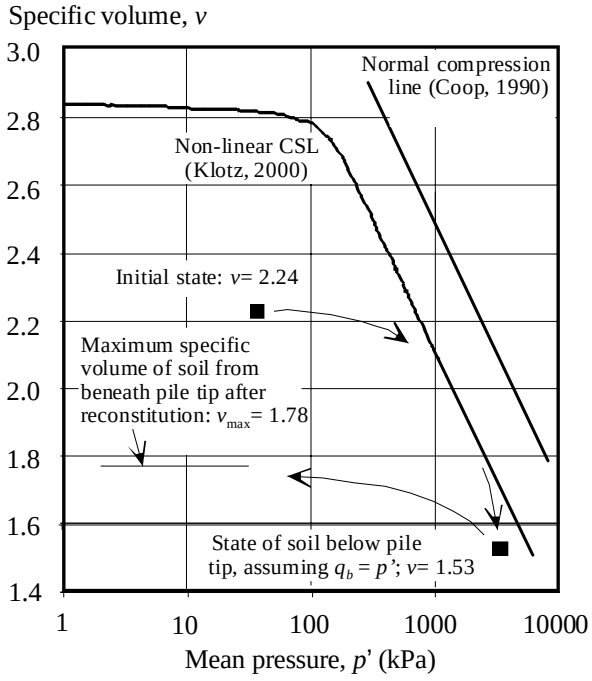

e) Stress-volume paths of soil beneath pile tip during test DJW-03

Figure 5.31 Post-mortem sampling and photography of cone of soil below pile tip

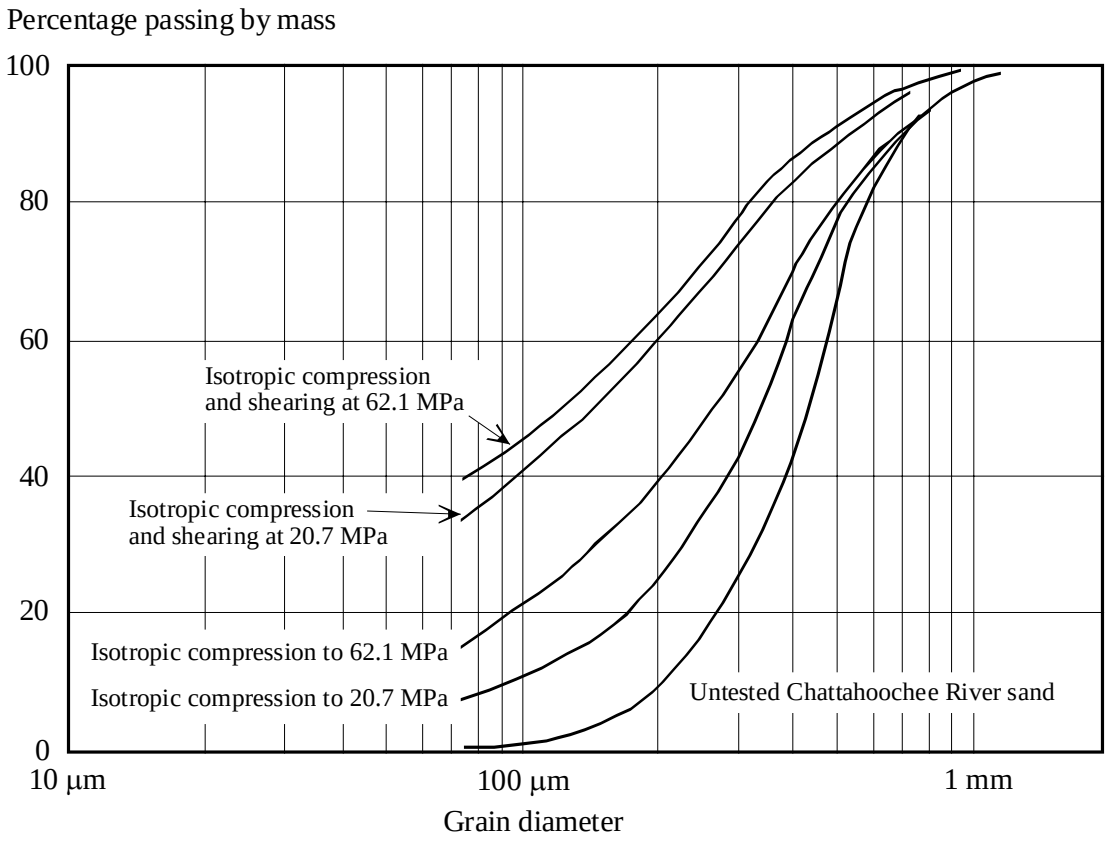

Figure 5.32 Particle breakage due to compression and shearing
(after Vesic & Clough, 1968)

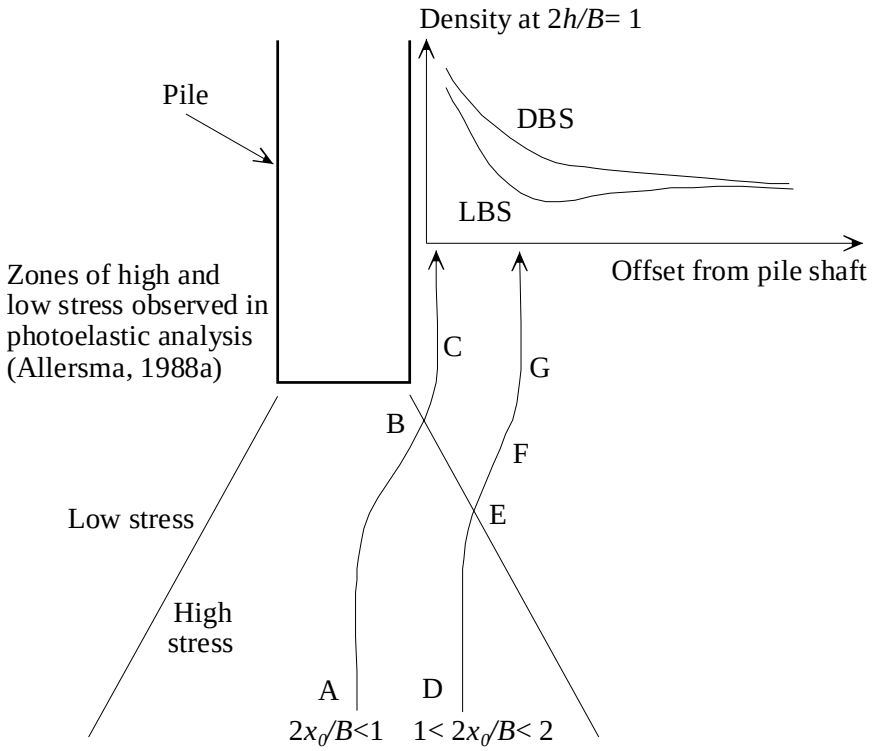

Volumetric behaviour in interface zone, along streamline ABC:

AB: Very high stress, shear strain

↳ Contraction, significant particle breakage

BC: Low stress, high OCR, shear strain

↳ No dilation- previous volume loss is irrecoverable.
Reduction in v_{max} is >10 % (Section 5.11.3, Figure 5.31e)

Volumetric behaviour in very near field, along streamline DEFG:

DE: High stress, shear strain

↳ Contraction, some particle breakage

EF: Low stress, high OCR, shear strain

↳ Dilation (to critical state)

FG: Low stress, high OCR, further shear strain

↳ Contraction (Section 5.9.5, Figures 5.18, 5.19)

Figure 5.33 Volumetric behaviour close to pile tip

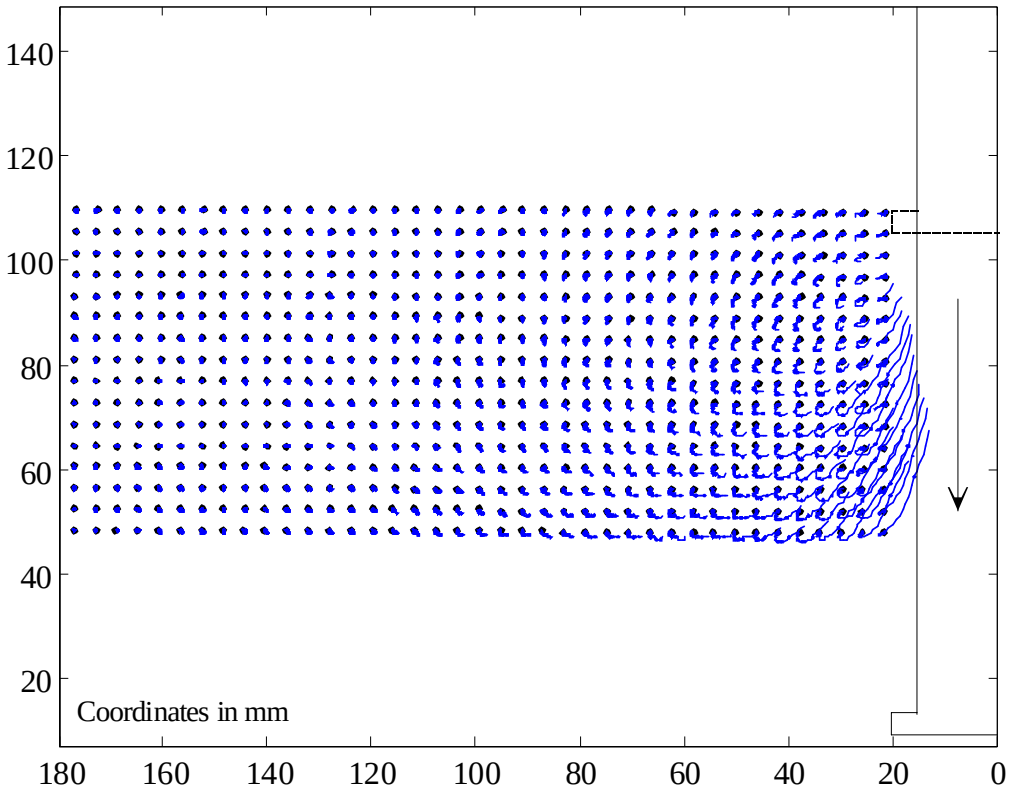

a) Trajectories of soil flow around pile shoe

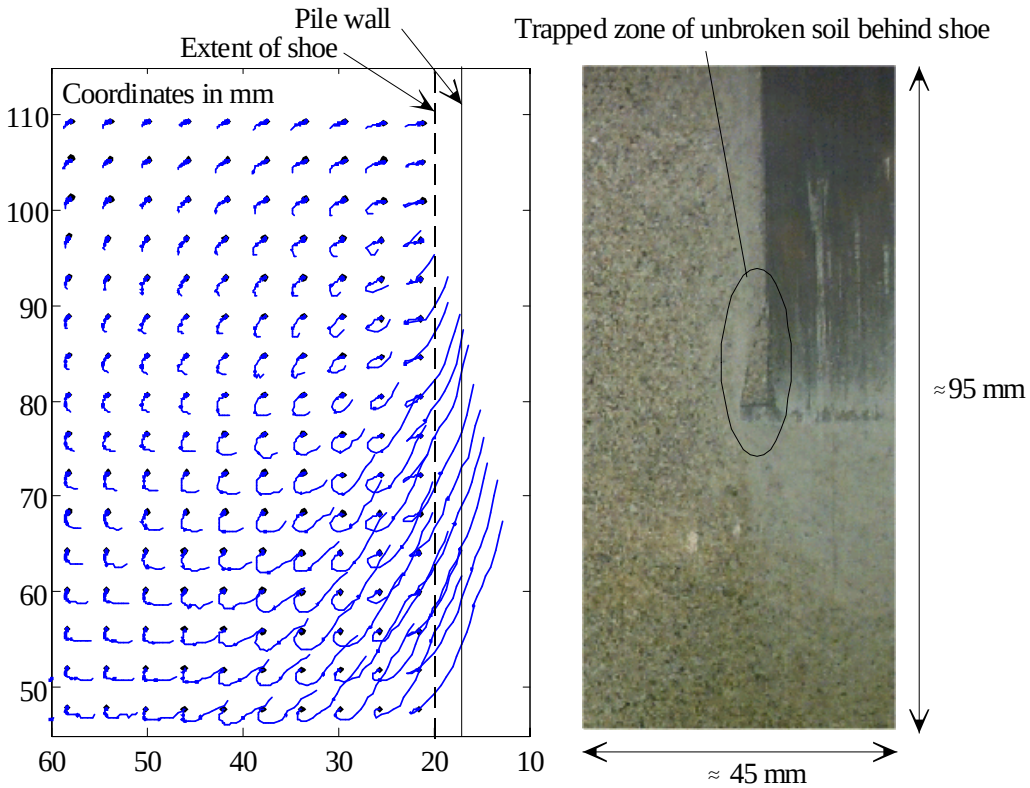

b) Soil flow close to pile shoe c) Image close to pile shoe

Figure 5.34 Soil flow around pile shoe

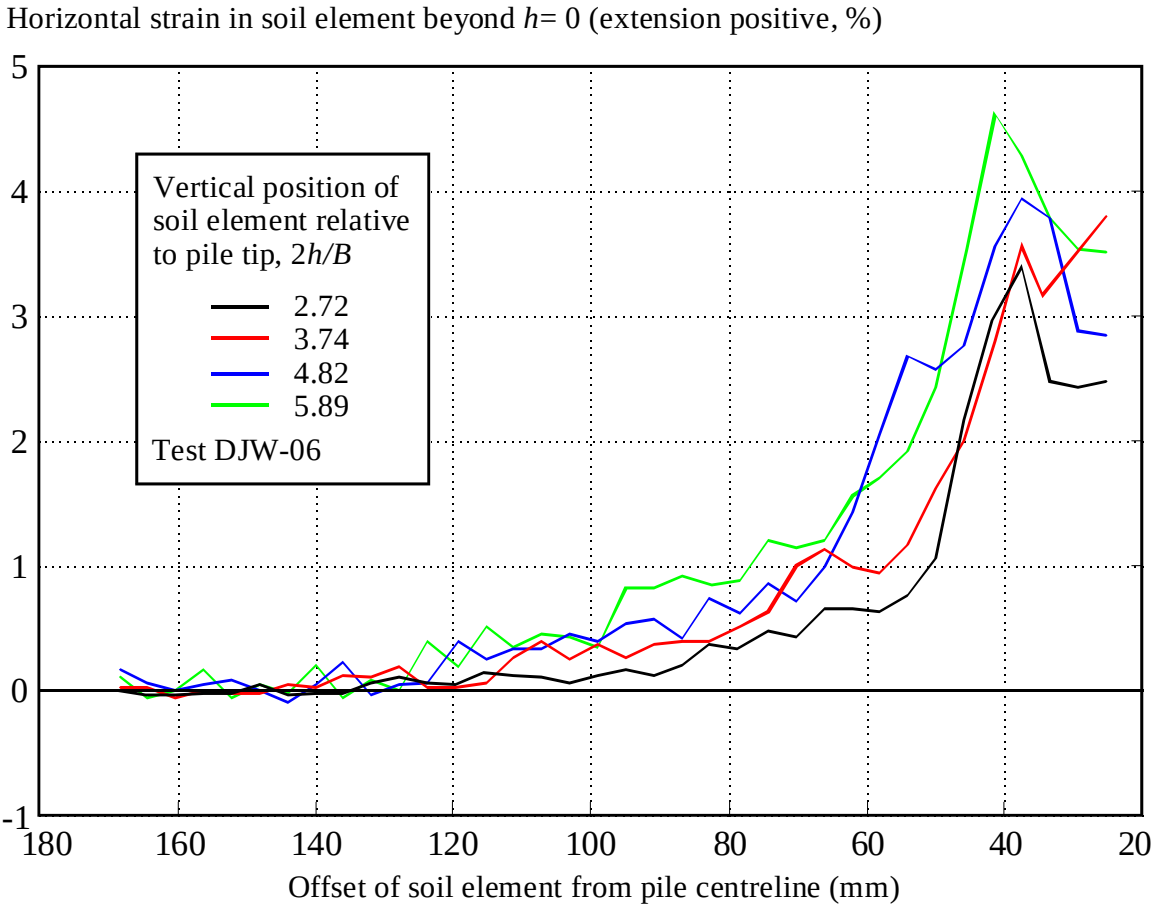

a) Test DJW-06: progressive horizontal unloading around a pile shoe

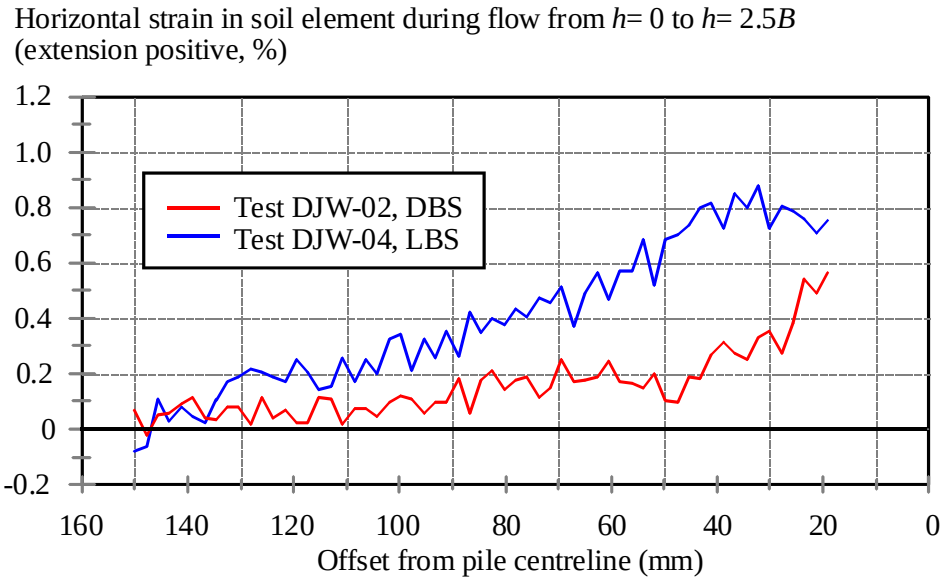

b) Tests DJW-02 and DJW-04: horizontal unloading along a straight pile shaft

Figure 5.35 Horizontal unloading along the pile shaft: friction fatigue

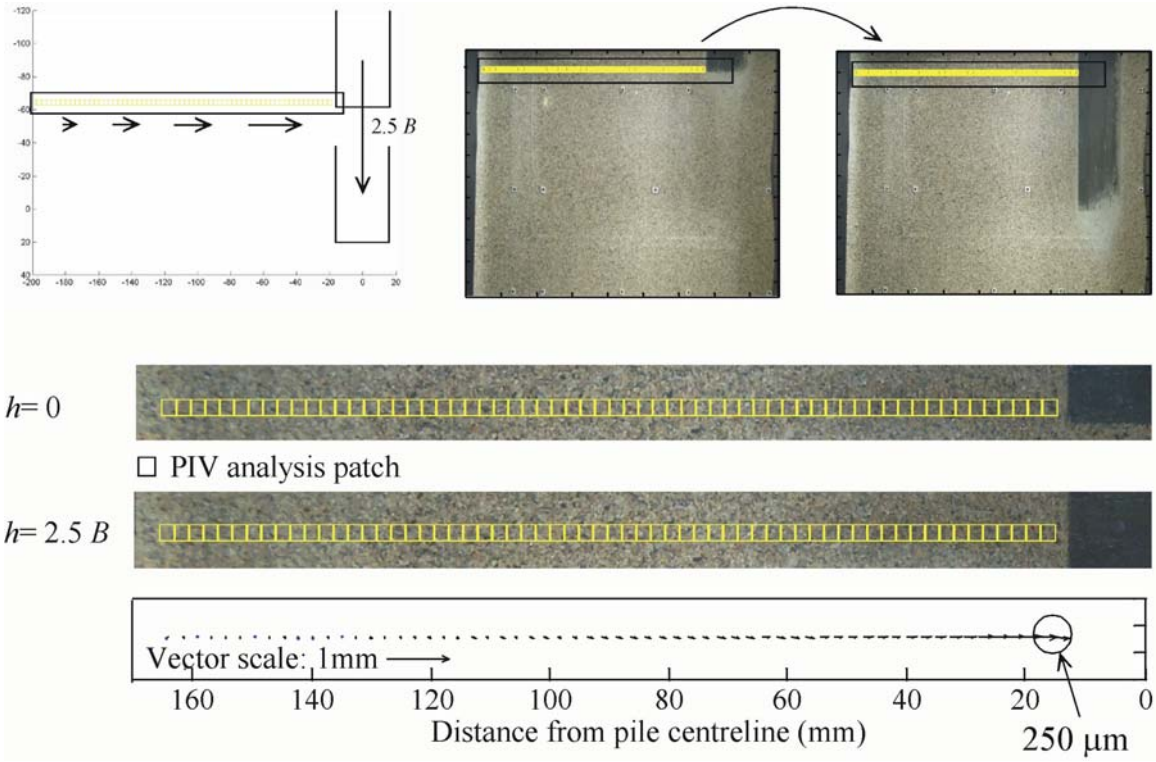

Figure 5.36 Soil movement adjacent to straight pile: DJW-02

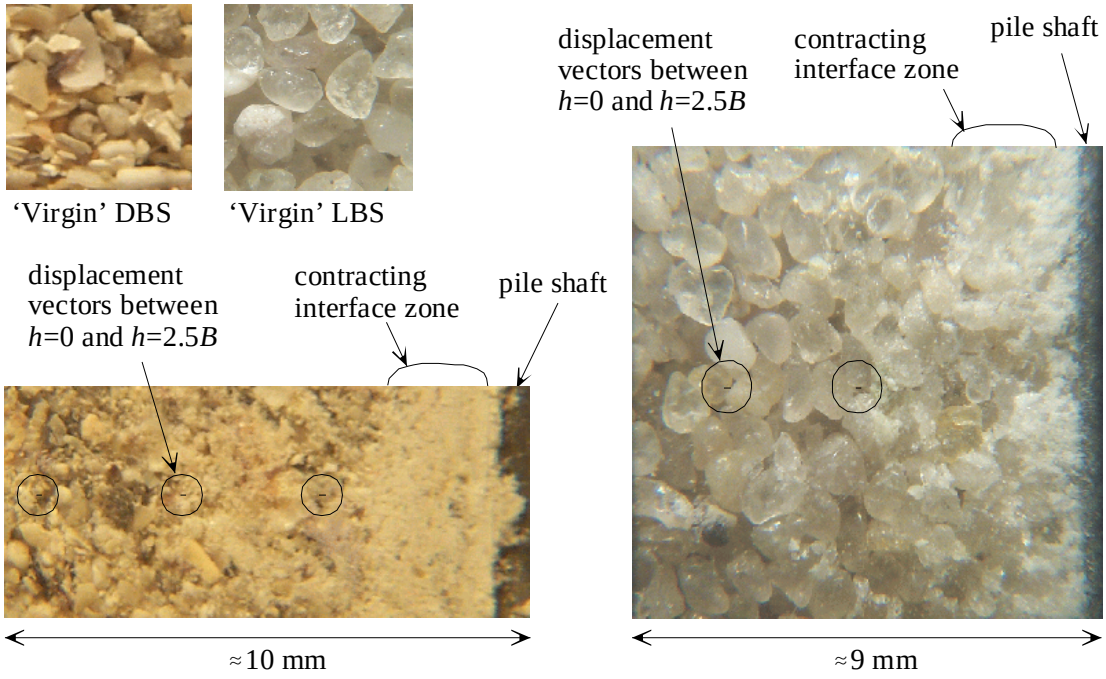

a) DJW-02, DBS b) DJW-04, LBS

Figure 5.37 Photography of interface shearing zone

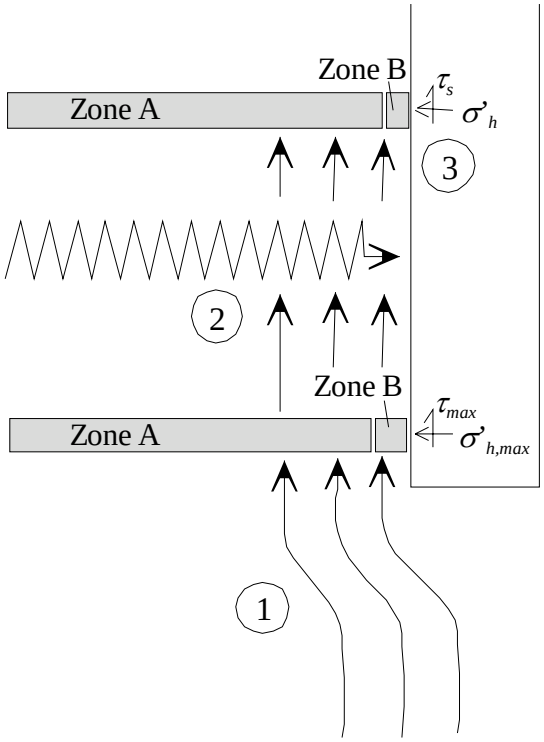

1 Horizontal compression as soil flows around the pile tip leads to high σ'_h, and τ_{max}

2 As the soil flows upwards relative to the pile shaft, shearing at the pile-soil interface leads to volume reduction in zone B.

3 This volume reduction causes unloading in horizontal extension of zone A. Hence, a reduction in σ'_h, and τ_s

Figure 5.38 The kinematics of friction fatigue close to the pile tip

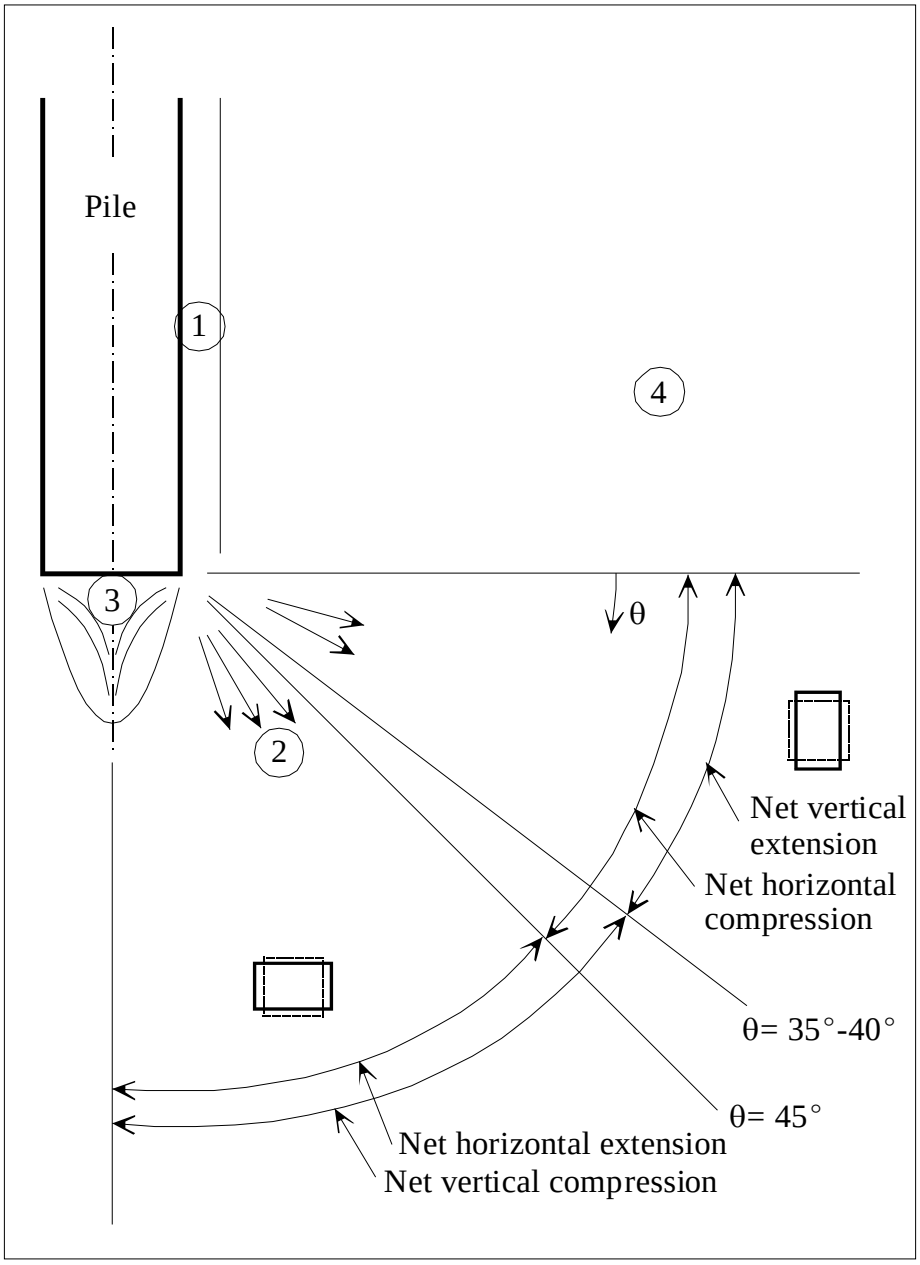

(1) Very dense zone. Significant particle breakage. Slight contraction with increasing pile penetration

(2) Very high shear strain reducing with distance from pile shoulder, constant with θ

(3) 'Nose cone' of very dense soil. Significant breakage. Not rigid. Soil flows through nose cone and around shoulder

(4) Slight densification, decreasing with offset from shaft. Horizontal extension with increasing pile penetration

Figure 5.39 Generalised pattern of strain after pile installation

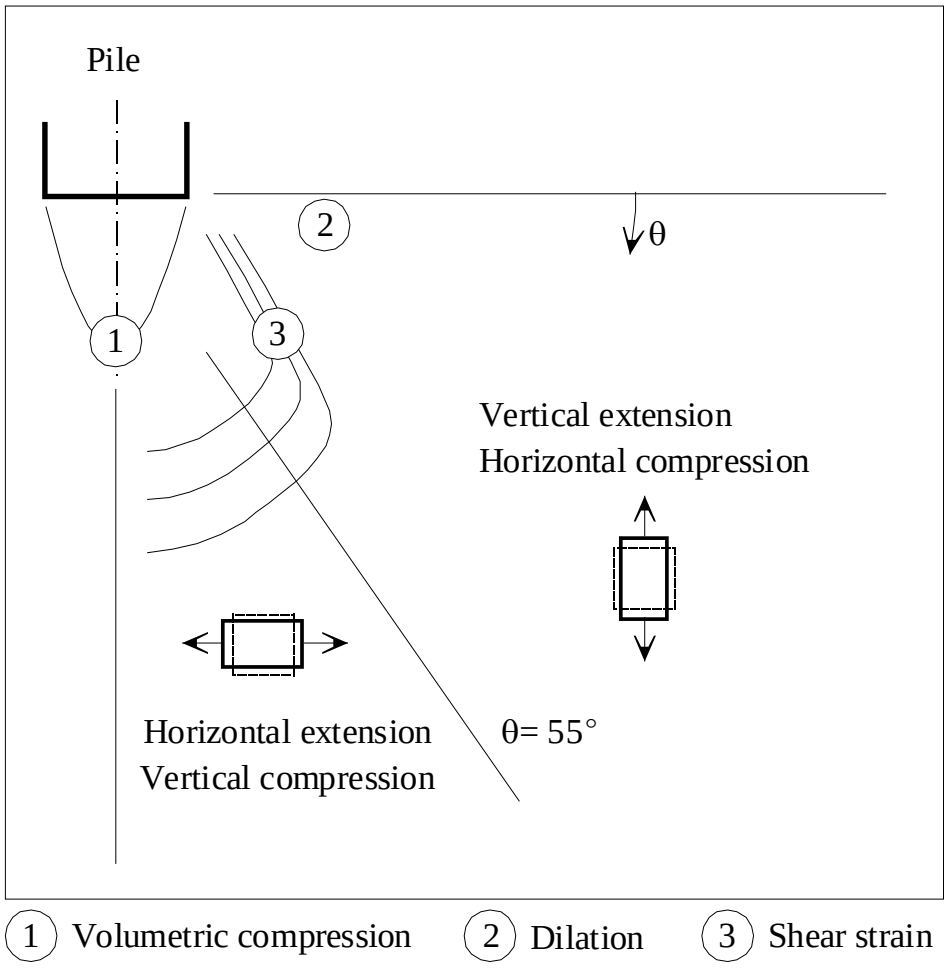

Figure 5.40 Generalised pattern of strain during an increment of penetration

CHAPTER 6

FIELD TESTING

6.1 INTRODUCTION

The results of four series of field tests are presented in this Chapter (Table 6.1). The first series of instrumented pile tests were conducted to observe the development of a soil plug during press-in installation and measure the stresses in the internal soil column. A description of these field tests leads to a discussion on the origin and relative magnitudes of internal and external shaft friction.

A framework based on vertical arching theory is demonstrated to show good correlation with field measurements of friction inside tubular piles. The theory is extended to include external shaft friction, and vertical arching is shown to influence the distribution of shaft friction both inside and outside a tubular pile.

Equations for predicting the influence of plugging on jacking force and hence selecting an appropriate machine type are described. Three further series of field tests are conducted to examine techniques for optimising the use of press-in pilers and improving the long-term performance of pressed-in pile foundations, utilising the influence of vertical arching.

Test identities	*Location*	*Associated publication or data report*
1999/1-3	Takasu, Kochi, Japan	White *et al.* (2000)
2000/1-3	Takasu, Kochi, Japan	Finlay *et al.* (2001)
2001/1-3	Akaoka, Kochi, Japan	Zhao *et al.* (2001)
No.1 –No. 4	Shinagawa, Tokyo, Japan	Jibanshikenjo Co. Ltd. (2001)

Table 6.1 Field testing programme

6.2 PLUGGING OF TUBULAR PILES

A common observation within the literature is that the plugging behaviour of tubular piles is not satisfactorily captured by existing design guidelines (Brucy *et al.*, 1991; Hight *et al.*, 1996; Randolph *et al.*, 1994; De Nicola & Randolph, 1997).

An open-ended tubular pile can penetrate the ground in an unplugged or a plugged manner. During unplugged penetration, the pile moves downwards relative to the internal soil column, in the manner of a sampler tube (Figure 6.1a). Penetration is resisted by shaft friction on the inside (Q_{si}) and outside (Q_{so}) of the pile and by base resistance on the annulus of pile wall (Q_w) (Equation 6.1). During plugged penetration the internal soil column is dragged downwards (Figure 6.1b), and the pile assumes the characteristics of a closed-ended pile (Paikowsky *et al.*, 1989). Thereafter, penetration is resisted by shaft friction on the outside of the shaft (Q_{so}) and by base resistance on the pile wall (Q_w) and the soil plug (Q_p) (Equation 6.2).

$$Q_{unplugged} = Q_{so} + Q_{si} + Q_w \tag{6.1}$$

$$Q_{plugged} = Q_{so} + Q_w + Q_p - W_p \tag{6.2}$$

When a tubular pile is being installed by jacking, (or is being loaded to failure- these events are analogous), penetration will occur by whichever mechanism offers least resistance (Raines *et al.*, 1992). If the shaft friction on the inside of the pile (Q_{si}) (plus the weight of the soil column) is greater than the base resistance of the soil column (Q_p), the pile will penetrate in a plugged manner. Hence, when predicting the jacking force,

the profiles of both unplugged and plugged penetration resistance with depth should be estimated. The mechanism that offers least resistance will govern the jacking force.

6.3 THE PREDICTION OF INTERNAL SHAFT FRICTION

When selecting a press-in pile driver, or predicting ultimate capacity, a continuous profile of pile capacity (or driving load) from the ground surface to the installed depth is calculated. The driving load of a tubular pile is the sum of the shaft friction and the base resistance and is the lower of $Q_{unplugged}$ and $Q_{plugged}$ (Equations 6.1 and 6.2) (ignoring the weight of the pile). In order to illustrate the relative magnitude of the components of resistance, a simple analysis is presented below, for a 800 mm diameter tubular pile with 15mm wall thickness, installed at a hypothetical site consisting of uniform medium dense sand (Figure 6.2). The profile with depth of each component of these loads is calculated below.

As dicussed in Chapter 2, conventional design practice is to predict base resistance (Q_w, Q_p) using a correlation with either friction angle and relative density (API RP2a, 1993; Fleming *et al.*, 1992; Berezantzev *et al.*, 1961), CPT resistance (Bustamante & Gianeselli, 1982; Jardine & Chow, 1996) or through a cavity expansion analysis (Randolph *et al.*, 1994). In this example, the variation of base resistance with depth is illustrated using the simple correlation with CPT resistance using the reduction factor ($0.5 - 0.25 \log (2\ r_p/D_{CPT})$) proposed for open-ended tubular piles by Jardine & Chow (1996). r_p is pile radius, and D_{CPT} is the diameter of a standard cone penetrometer, equal to 35.7mm.

Local shaft friction at failure, τ_s, is governed by the Coulomb equation (Equation 6.3) (Lehane, 1993). To find the total external shaft friction, (Q_{so}), Equation 6.3 is integrated over the pile surface area (Equation 6.4). It is often assumed that the earth pressure coefficient, K, and pile-soil angle of friction, δ, remain constant along the length of the pile (Fleming *et al.*, 1992; API RP2a, 1993) with limiting values of τ_s applying. Appropriate values from the API RP2a are used in this example ($K = 0.8$, $\delta = 25°$).

Recent methods for predicting the capacity of driven piles (Toolan *et al.*, 1990; Lings, 1997; Randolph *et al.*, 1994; Jardine & Chow, 1996) make some account for 'friction fatigue', to describe a progressive decrease local shaft friction at a given soil horizon as the pile penetrates further. This effect can be attributed to compaction of the soil under the high cyclic loading caused by driving (De Nicola & Randolph, 1997). There is evidence that friction fatigue is less significant when the pile is installed by jacking (Chow, 1997; De Nicola & Randolph, 1997; Miller & Lutenegger, 1997), and it has been ignored in this analysis. Section 6.4 addresses the validity of this simplification.

$$\tau_s = \sigma'_h \tan\delta = K\sigma'_v \tan\delta \tag{6.3}$$

$$Q_{so} = \int 2\tau_s \pi r_p \, dz \tag{6.4}$$

Internal shaft friction, Q_{si}, is the most difficult component of pile capacity to evaluate; the literature contains little guidance, and little field data exists. API RP2a (1993) assumes that the internal and external shaft friction profiles are equal. However, since the soil column is dragged downwards on all sides, vertical arching occurs, and internal shaft friction exceeds external shaft friction. This is analogous to the arching within silos first described by Janssen (1894). Equilibrium analysis of a horizontal slice of soil shows that vertical stress increases exponentially with depth (Equations 6.5 and 6.6) (Figure 6.2) (Randolph, 1985).

$$\frac{d\sigma'_v}{dz} = \gamma' + \frac{2K\sigma'_v \tan\delta}{r_p} \tag{6.5}$$

$$\sigma'_v = \frac{\gamma' r_p \left(e^{2Kh_{plug} \tan\delta / r_p} - 1\right)}{2K \tan\delta} \tag{6.6}$$

The total internal shaft friction can be found by integrating Equation 6.5 over the height of the soil column, h_{plug}, (Equation 6.6), and considering the overall equilibrium of the column (Equation 6.7):

$$Q_{si} = \sigma'_v \pi r_p^2 - W_p = \frac{\gamma' \pi r_p^3 \left(e^{2Kh_{plug} \tan\delta / r_p} - 1 \right)}{2K \tan\delta} - \gamma' h_{plug} \pi r_p^2 \qquad (6.7)$$

This analysis adopts the following recommended design variables for medium dense sand; K = 0.8 (API RP2a, 1993; De Nicola & Randolph, 1997) and δ = 25° (API RP2a 1993). Figure 6.3 shows the sharp increase in internal shaft friction and hence jacking force, as the length of the soil column increases during unplugged penetration. At the transition to plugged penetration, the soil column will 'lock up' and remain approximately of length, h_{crit}.

Beyond the transition to plugged penetration, the jacking force increases gradually with $Q_{plugged}$. Minimal further slippage of the soil plug may occur in order to maintain sufficient internal shaft friction to balance the increase in Q_p.

The sharply diverging curves of $Q_{plugged}$ and $Q_{unplugged}$ indicate the importance of considering both failure modes during ultimate load prediction. At an embedment of 0.5 m less than h_{crit}, $Q_{plugged}$ is 2.5 times greater than $Q_{unplugged}$. In contrast, 0.5 m deeper than h_{crit}, $Q_{unplugged}$ is 3 times greater than $Q_{plugged}$.

The key feature of Figure 6.3 is the exponential increase in internal shaft friction with depth. The exponential term contains K and tan δ, and scales with γ'. Whereas many accepted methods exist for predicting external shaft friction and base resistance, the physical processes which govern the plugging mechanism during driving and subsequent static loading are poorly understood (De Nicola & Randolph, 1997). Consequently, selection of the correct values for these crucial exponential parameters remains a significant source of uncertainty.

6.4 FIELDWORK: SUMMER 1999

6.4.1 Site description

Two tubular test piles were installed at the Takasu Research Centre in Kochi on the island of Shikoku, Japan, referred to as tests 1999/1 and 1999/2. The stratigraphy

consists of made ground overlying silt and sand (Figure 6.4). The results of laboratory testing of each strata are shown in Table 6.2. CPT data has been used to estimate a profile of relative density following Jamiolkowski *et al.* (1985).

Stratum	*Soil type*	D_{10} *(mm)*	D_{50} *(mm)*	*Submerged unit weight* (kN/m^3)
A	Made ground	-	-	9.82
B	Silt	-	-	9.54
C	Sand & gravel	0.22	1	9.63
D	Silty sand	0.047	0.18	9.23
E	Sand	0.18	0.3	8.95

Table 6.2: Soil properties at Takasu test site

Since Test 1999/1 took place soon after heavy rainfall, the groundwater table was located 0.75 m below ground level. During Test 1999/2, this had reverted to 2 m below ground level.

6.4.2 Pile and piler description

The dimensions of the two test piles are shown in Table 6.3. A specially modified press-in piler was used to install the test piles. Continuous calculation of jacking force was achieved by measurement of the oil pressure in the hydraulic rams. Embedded depth was measured using a displacement potentiometer attached to the head of the pile. The level of the soil column within the pile was measured using a displacement potentiometer attached to a weighted follower within the pile.

Test pile	*Diameter* D_{outer} *(mm)*	*Wall thickness,* t (mm^2)	*Wall area,* A_{wall} (mm^2)	*Plug area,* A_{plug} (mm^2)
1999/1	318.5	6.9	9731	72918
1999/2	162.5	5.0	5450	18265

Table 6.3: Dimensions of Takasu test piles

The piles were installed in a series of 700 mm strokes at a rate of approximately 50 mm/sec. A pause of 15 seconds between strokes occurred whilst the rams of the press-in piler were retracted.

6.4.3 Pile instrumentation

The aim of these tests was to investigate the phenomenon of plugging, and shed light on the distribution of stress within the plug. Internal shaft friction is governed by the horizontal stress on the pile wall, as well as the pile/soil interface angle of friction. Previous pile tests using closed-end tubular piles have measured horizontal stress using delicate total pressure cells embedded in the pile wall (eg. Coop, 1987; Chow, 1997).

However, since external shaft friction (and hence horizontal stress) is very much lower than internal shaft friction, a differential pressure is created across the wall of a tubular pile. This differential pressure is balanced by hoop stress within the pile wall (Figure 6.5, Equation 6.8). This hoop stress is much larger than the horizontal stress within the soil. Consequently it is preferable to use instrumentation that infers the horizontal stress from the hoop stress taking advantage of the increased signal size.

$$\sigma_{hi} = \frac{2F + \sigma_{ho} D'_o L}{D_i L} \tag{6.8}$$

Each test pile was split longitudinally and the two sections were re-assembled using strain-gauged bolts at 300 mm intervals (Figure 6.6). Whereas the detection of horizontal stress using a total pressure cell requires careful manufacture of the device and consideration of cell action effects, instrumented bolts are relatively cheap and quick to manufacture.

Since the purpose of the instrumented bolts is to quantify the horizontal stress acting on the *inside* of the pile, the component of hoop stress induced by horizontal stress acting on the *outside* of the pile must be deducted. This correction can only be carried out by estimating external shaft friction using a prediction method. The reliability of such a correction depends on the magnitude of the local external shaft friction being only a small fraction of the local internal shaft friction. Whether this is the case is investigated below by comparing the likely external shaft friction with the internal shaft friction predicted by Equations 6.3 and 6.6.

6.5 THE PREDICTION OF EXTERNAL SHAFT FRICTION

6.5.1 Typical assumed profiles of external shaft friction

The shaft friction profile predicted by the API (1993) method for the test pile at 7 m depth at Takasu is shown in Figure 6.7. This analysis predicts local shaft friction, τ_s, to increase linearly with in situ vertical stress; i.e. linearly with depth within each stratum. This approach assumes that the vertical stress acting on a soil element adjacent to the pile is equal to the in situ vertical stress, $\sigma'_{vo} = \gamma' z$. The mobilization of shaft friction is not considered to change the vertical stress profile.

This assumption is analogous to the approach adopted by Randolph and Wroth (1979) when analysing pile settlement, in which the main mode of deformation is shearing of concentric cylinders (Cooke, 1974; Frank, 1975). This approach derives from consideration of the free body diagram shown in Figure 6.8. Only stresses additional to the in situ vertical stress are shown. The vertical equilibrium of this element shows that:

$$\frac{\partial(r\tau)}{\partial r} + r\frac{\partial \sigma_v}{\partial z} = 0 \qquad (6.9)$$

When analyzing settlement at low loads, it is assumed that the shear stress mobilized at the pile shaft is much greater than the increase in vertical stress (Randolph, 1977). Thus Equation 6.9 can be reduced to:

$$\frac{\partial(r\tau)}{\partial r} = 0 \qquad (6.10)$$

This simplification implies that shaft friction does not increase the local vertical stress. Instead, shaft friction is carried by decreasing shear stress on circumferential surfaces. This assumption may be justified in settlement analysis as follows. Settlement analysis is concerned with the shaft friction that is mobilized at working loads; well below the limiting shaft friction governed by Equation 6.3. At this level of deformation, shaft friction is governed by stiffness of the surrounding soil, rather than the strength. No

direct link is assumed between vertical effective stress and shaft friction. Although an increase in vertical stress caused by a non-zero $\partial\sigma_v/\partial z$ term in Equation 6.9 will lead to a change in soil stiffness, this effect is not as strong as the direct link between shaft friction and normal stress shown in Equation 6.3.

6.5.2 External shaft friction: the governing parameters

6.5.2.1 Recent observations

Recent field and centrifuge test data indicates that, in contrast to the API assumption, shaft friction does not increase linearly with depth (De Nicola, 1996; Chow, 1997; Bruno, 1999) (e.g. Figure 6.9). Instead, there is a trend for local shaft friction to increase sharply close to the pile tip. For design purposes, this feature can be captured by an empirical rule using a weak exponential or power curve (Jardine & Chow, 1996; Randolph *et al.*, 1994). This increase in τ_s with depth, and close to the pile tip, must be due to changes in the parameters which govern friction at the interface. Equation 6.3 shows these parameters to be K, tan δ and the vertical effective stress acting locally adjacent to the pile, σ'_v. The following sections discuss the variation of each parameter with depth.

6.5.2.2 The variation of σ'_v with depth

When concerned with ultimate failure, the simplification between Equations 6.9 and 6.10 can be criticized. When shaft friction is fully mobilized the shear stress on the free body shown in Figure 6.8 close to the pile shaft is of comparable magnitude to the vertical effective stress, since it is assumed to be caused by the vertical stress multiplied by suitable values of K and tan δ (Equation 6.3). With a direct link between vertical effective stress and local shaft friction, correct modelling of shaft friction transfer between shear stress on circumferential planes on the base of the free body is required.

The forces on the free body shown in Figure 6.8 cannot be solved without recourse to a constitutive model. The results presented in Chapter 5 highlight the difficulties in modelling the failure of soil adjacent to a pile shaft; the stress and strain histories, coupled with the changes in soil fabric during pile installation preclude any

straightforward constitutive model. Instead, it is proposed that the vertical load transfer can be modelled in the following manner.

The general free body diagram in Figure 6.8 is redrawn as an element of soil immediately adjacent to the pile of finite size (Figure 6.10). The radial extent of this element, r_o, is defined as $\alpha\, r_p$ ($\alpha > 1$). The upwards shear stress acting on the outer face of the element is defined as a small fraction, λ, of the local shaft friction, τ_s. Since α is close to unity, σ_v is assumed not to vary radially. Vertical equilibrium of this element produces the following relationship:

$$\frac{d\sigma_v}{dz} = \frac{2\eta\tau}{r_p} \tag{6.11}$$

Where

$$\eta = \frac{1-\lambda\alpha}{\alpha^2 - 1} \tag{6.12}$$

Equation 6.11 represents an approximation of the vertical load transfer function described in Equation 6.9. The two new parameters, α and λ, can be combined into η, which describes the proportion of shaft friction transferred as shear on circumferential planes and vertical stress. As η tends to zero, the load transfer function reduces to the simplification of Equation 6.10, with shaft friction carried entirely by shear stress. Vertical stresses remain geostatic.

As η increases, the proportion of load transferred as vertical stress increases. The variation in ratio of shear and vertical load transfer with η is depicted in Figure 6.11. For various values of η, the ratio of upward shear force on the outer circumference, F_{outer}, to downward shaft friction on the inner face, F_{inner}, is plotted against α. This relationship has the simple form:

$$\frac{F_{outer}}{F_{inner}} = \alpha\lambda = 1 - \eta(\alpha^2 - 1) \tag{6.13}$$

Combining Equation 6.11 with Equation 6.3 and integrating allows a profile of vertical stress with depth to be calculated (Equation 6.14).

$$\frac{\sigma_{v2}}{\sigma_{v1}} = e^{2\eta K \tan\delta z / r_p} \tag{6.14}$$

However, this solution cannot satisfy the free field boundary condition $\sigma_v = 0$ *at* $z = 0$. With no vertical stress at the free surface, and hence no shaft friction, the exponent cannot evolve. Self weight is needed, leading to a revised equilibrium equation for the free body shown in Figure 6.10 (Equation 6.15):

$$\frac{d\sigma_v}{dz} = \frac{2\eta\tau_s}{r_p} + \gamma' \tag{6.15}$$

It was noted above that when η tends to zero, shaft friction is carried entirely by shear stress as assumed in Equation 6.10. Equation 6.15 demonstrates the corollary that when η tends to zero, vertical stress evolves geostatically, with $\sigma'_v = \gamma' z$.

Integration of Equation 6.15 from the free ground surface produces Equation 6.16.

$$\sigma'_v = \frac{\gamma' r_p \left(e^{2\eta K z \tan\delta / r_p} - 1\right)}{2\eta K \tan\delta} \tag{6.16}$$

6.5.2.3 Arching: clarification of the phenomenon

Equation 6.16 has the exponential form of Equation 6.6, and represents the vertical arching analogous to that found within silos. The difference is that the development of vertical stress with depth outside a pile is attenuated by the load transfer coefficient η. Equation 6.16 reduces to the internal arching condition for $\eta = 1$, corresponding to $\lambda = 0$ at $\alpha = \sqrt{2}$ (Equation 6.12). This illustrates the similarity between these analyses of

internal and external arching. $\lambda = 0$ at $\alpha = \sqrt{2}$ implies that no shear load is transferred beyond $r = \sqrt{2}\ r_p$, and shaft friction increases the vertical stress on an area of soil π $((\sqrt{2})^2 - 1)\ r_p$; i.e. an area equal to the internal area of the pile.

At this point, some clarification of 'arching' in piles and silos can be made. The term 'arching' was first used by Janssen (1894) to describe the exponential evolution of vertical stresses inside silos. A more general definition for vertical arching could be any cases where the interaction between shear forces (which are proportional to vertical stress) and vertical stress leads to a stress profile which varies exponentially with depth, deviating above (if friction acts downwards on the soil) or below (if friction acts upwards) the geostatic profile. This clumsy statement can be summarized by stating that vertical arching occurs in a soil body which is loaded such that its vertical equilibrium is described by an equation of this form:

$$\frac{d\sigma_v}{dz} = A_1\sigma_v + A_2 \qquad (6.17)$$

This vertical arching relationship is deduced purely from consideration of the vertical equilibrium of a loaded soil mass. This is different to cases of arching which are attributed to grain size effects or differential stiffnesses in, for example, trap door experiments or around stiff inclusions in sand (e.g. Standing 1997).

The exponential component of the behaviour will scale with A_1. In the case of internal shaft friction, A_1 is large and positive; in the case of silos it is large and negative. In the case of external shaft friction it is small and positive. Factor A_2 governs the underlying geostatic stress profile, and is equal to γ'.

6.5.2.4 Profiles of external shaft friction with vertical arching

To plot shaft friction versus depth for a uniform soil, Equation 6.16 can be simplified to:

$$\tau_s = \frac{\gamma' r_p \left(e^{2\eta K z \tan\delta / r_p} - 1\right)}{2\eta} \qquad (6.18)$$

Integration of Equation 6.18 produces an expression for total external shaft friction (Equation 6.19).

$$Q_s = \frac{\pi\gamma' r_p^2}{\eta}\left[\frac{r_p\left(e^{2\eta KL\tan\delta/r_p}-1\right)}{2\eta K\tan\delta} - L\right] \qquad (6.19)$$

Example curves for typical values of r_p, K, γ' and tan δ are shown in Figure 6.12 to demonstrate the influence of α on shaft friction profile. These curves replicate the gentle exponential increase in local shaft friction which has been adopted by recent design methods (Randolph *et al.*, 1994; Jardine & Chow, 1996). Values of η in the range 0.01-0.04 provide a shaft friction profile which reaches typical field values of $\beta_{max} = \tau_s / \sigma_{vo}$ of 0.5-2 close to the pile tip (Toolan *et al.*, 1990). This range of η indicate a load transfer distribution of $F_{outer} / F_{inner} > 85\%$ at $r = 2r_p$; in other words, less than 15% of the shaft friction needs to be transferred into vertical stress on an annulus of radius 2 r_p surrounding the pile to create the exponential profile shaft friction observed in the field. In other words, even if the vertical shear transfer phenomenon is small, it could be responsible for the typical field profiles shown in Figure 6.9.

Figure 6.12 demonstrates that by varying K tan δ and η, both the maximum value of shaft friction and the rate of increase with depth (or decay with distance from the pile tip) can be adjusted. K tan δ governs the initial slope of the shaft friction profile, with η controlling the sharpness of the exponential increase.

The shaft friction profiles shown in Figure 6.12 have the same general form as the shaft friction distribution proposed by Randolph *et al.* (1994). The differences are as follows:

- The Randolph *et al.* approach has three degrees of freedom: β_{max}, β_{min} and decay rate μ. This proposed approach has two: β (= K tan δ) and load transfer coefficient η.

- The Randolph *et al.* approach considers local shaft friction to decrease from some maximum value at the pile base due to a reduction in earth pressure coefficient, K; i.e. K is a function of $(L\text{-}z)/r_p$. This proposed approach considers local shaft friction to increase away from the free ground surface due to vertical load transfer and arching.

It can be argued that the proposed approach is more appropriate for the top of the pile, where the influence of the ground surface is likely to be greater than the pile tip. Conversely the Randolph approach is more appropriate close to the pile tip, where the assumption of constant $K \tan \delta$ with depth breaks down. Evidence for changes in K and $\tan \delta$ with depth are discussed in the following sections.

6.5.2.5 The variation of K with depth

The observation of soil movement towards the pile shaft described in Chapter 5 confirms that significant changes in earth pressure coefficient, K, occur close to the pile tip. The soil horizon adjacent to the pile shaft was observed to move inwards, unloading in horizontal extension, as the first few diameters of the pile were jacked past. This horizontal unloading was permitted by volume reduction within the interface layer adjacent to the pile shaft.

The sand adjacent to the shaft is heavily over-consolidated having passed through the zone of high stress adjacent to the pile tip. Consequently the relatively small measured unloading strain leads to a large reduction in horizontal stress acting on the pile shaft. The horizontal unloading is along a κ-line, and is hence very stiff. However, the rate of horizontal movement with increasing pile penetration tended towards zero over the 400 mm of shearing observed in the calibration chamber. Noting that the boundary conditions for shearing at a pile-soil interface are analogous to an interface shear box test, this observation matches with the observed tendency for a constant volume condition to be approached at high displacements. These observations suggest that at a given soil horizon, a significant decrease in K will occur as the pile tip moves past, but a limiting value will be reached. This suggests that K is a weak function of $(L\text{-}z)/r_p$ for high values of this variable.

As stated above, during calibration chamber testing, the rate of horizontal unloading with continued pile penetration decayed towards zero. This limiting behaviour corresponds to a state at which volume reduction in the interface zone adjacent to the pile has ceased even with continued penetration. Beyond this point, further changes in K will not occur.

Is this feasible, considering the kinematics of this process highlighted in Chapter 5? In Section 5.1.2.7, the diffusion of fine particles from the interface layer into the far field was hypothesized as a potential mechanism for the unexpected *contraction* of the overconsolidated (i.e. conventionally thought of as *dilatant*) soil adjacent to the pile.

The 'source' within this diffusion process is the zone of broken grains close to the pile interface which is created as the soil flows past the pile tip. Grain breakage may cease as the pile tip becomes more distant since the confining stress is significantly lower than at the pile tip; the particles may now be strong enough to avoid breakage. As a result, the rate of material movement away from the interface will decay towards zero, preventing further contraction, and reduction in K.

Other mechanisms for volume reduction in the near field beside the diffusion of fine particles are grain rearrangement and breakage in the interface layer. A limit to these processes can also be envisaged. Grain breakage has been discussed in the previous paragraph. If breakage is eliminated, critical state theory suggests that volume reduction of the unbreakable particles will also cease after sufficient rearrangement has occurred for a critical voids ratio to be reached.

The above discussion has concentrated on the smooth installation process associated with pile jacking, as modelled during the calibration chamber testing. Additional changes in K will be associated with dynamic installation. The two-way cycling of shear stress and Poisson strain expansion and contraction at the pile-soil interface will lead to contraction of the interface layer and a reduction in normal stress. Once again this is analogous to observations from CNS interface testing (Tabucanon *et al.*, 1995).

In conclusion, due to variations in K close to the pile tip, a better match with field and centrifuge data may be achieved if K is expressed as a function of distance from the pile tip in Equation 6.15. The function may be especially complex if the influence of a dynamic installation method, and the resulting two-way cycling, rotation of principal stress direction and associated contraction are included.

6.5.2.6 The variation of tan δ with depth

The final variable in Equation 6.3 is the coefficient of pile soil friction, tan δ. Interface shear box tests indicate that this friction coefficient is influenced by soil type, particle size and surface roughness (Kishida & Uesegi, 1987; Jardine *et al.*, 1993; Dietz, 2000). Normalised roughness, R_n is often used to combine the influence of particle size and surface roughness into a single dimensionless quantity (Uesegi & Kishida, 1986) (Equation 6.20). Alternatively, the ratio R_a/D_{50} uses a more mathematically rigorous definition of roughness, where R_a is the arithmetic-mean absolute deviation of the surface profile from the mean level. Figure 6.14 shows various definitions of surface roughness. Note that R_{max} in Uesegi & Kishida's nomenclature is denoted R_t by Dietz.

For typical surface preparations, R_{max} is 6-10 times larger than R_a (Dietz, 2000). Figure 6.13 shows the variation of tan δ with normalised roughness found from interface shear box testing (Paikowsky *et al.*, 1995). Very large displacements can be required to mobilize a constant value of tan δ (Cavalieri, 2000). This effect is attributed to a progressive reduction in particle size and hence normalized roughness, due to particle breakage at the interface.

$$R_n = \frac{R_{\max}}{D_{50}} \qquad (6.20)$$

R_n: Normalised roughness

R_{max}: Surface roughness described by peak-to-trough height; see Figure 6.14

In the case of displacement piles, the link between particle size and tan δ is complicated by the change in grading of the sand close to the pile that occurs during installation. The

high stress and strain mobilized as the soil flows close to the pile tip leads to large changes in grading curve. In their analysis of model pile tests in the centrifuge, Klotz & Coop (2001) note that higher base resistance (and hence higher particle breakage and higher normalized roughness on the pile shaft) correlates well with lower interface friction (Figure 6.15). However, they note that field piles are rougher than those used in the centrifuge. As a result field piles have a higher normalised roughness. Klotz & Coop argue that this value may be out of the range for which small changes in D_{50} will influence tan δ.

Typical values of normalised pile roughness for the coarse sands during the laboratory testing in Chapter 5 are shown in Table 6.4. An attempt was made to measure the grading of the interface layer close to the model pile used during the calibration chamber testing described in Chapter 5. Small samples were vacuumed from the interface zone, approximately 1 mm wide, adjacent to the model pile. These samples were passed through an Accusizer 780 Single Particle Optical Sizing machine (Figure 6.16). Due to the large particle sizes used, a non-standard intake nozzle was fitted. This led to a small change in the calibration curve. Therefore, these results are not correctly calibrated and may contain a small error in particle size. This error applies to all four sets of data. Therefore, although the absolute values may be in error, some comparison between these sets of data can be made. At the time of writing, the manufacturers have not developed a new calibration.

The Accusizer data suggests that the D_{50} size of the Dog's Bay sand in the 1 mm interface zone is 4.5 times lower than the virgin sand, whilst the D_{50} size of the LB Fraction B sand is reduced by a factor of 1.4 (Figure 6.16). It should be noted that these values are likely to be strongly dependent on the exact width of sampling zone.

To illustrate the variation in tan δ induced by particle breakage, Figure 6.17a uses Paikowsky's correlation to predict coefficient of friction, tan δ, from normalised roughness. Figure 6.17 illustrates the same variation with R_a/D_{50}, assuming $R_a = R_{max}/8$, as is reported typical by Dietz (2000). Although ignoring the differences in soil type

between Table 6.4 and the interface shear box tests, Figures 6.17 demonstrates that particle breakage during installation can significantly alter tan δ.

	Mean particle size, D_{50} (μm)	*Range of R_n for full-scale pile*[1]	*Range of R_n for model pile* [2]
Surface roughness, R_{max}		10 μm - 40 μm	1 μm - 2 μm
Leighton Buzzard Fraction B sand (LBS)	920	0.0125 - 0.0435	0.00125 – 0.0025
Dog's Bay sand (DBS)	580	0.0172 - 0.0690	0.0018 – 0.0034
DBS after element test [1]	130	0.0769 - 0.308	0.00769 – 0.0154
LBS after model pile test [2]	130	0.0769 - 0.308	0.00769 – 0.0154
DBS after model pile test [3]	610	0.0164 - 0.0656	0.00164 - 0.00328

Table 6.4. Typical normalised roughness of full scale and model piles

Notes: [1] Kishida *et al.* (1986), Lehane *et al.* (1993)
[2] Bruno (1999), Klotz (2000)
[3] Coop (1990). Dog's Bay sand, drained TX compression and shearing 10 MPa
[4] Test DJW-06, approximate measurement using Accusizer 780, Figure 6.16
[5] Test DJW-05, approximate measurement using Accusizer 780, Figure 6.16

In conclusion, changes in tan δ with depth are associated with changes in particle size and in the case of layered soils, particle type. Two processes will cause the relevant particle size to differ from the in situ value. Firstly, particle breakage will occur in the zone of high stress surrounding the pile tip. Since this amount of breakage is directly related to the intensity of the stress field around the pile tip, any variation in q_b with depth will be reflected in the profile of breakage with depth. Secondly, sorting, diffusion, and further breakage may occur in the interface zone as the pile shaft passes. If the interface has a normalised roughness typically within the range 0.02-0.7, the processes of particle breakage (or 'polishing' of the interface) described above can lead to further changes in tan δ (Paikowsky *et al.*, 1995).

In contrast to the comments of Klotz & Coop (2001), Figure 6.17 suggests that the interface friction angle of field piles is more likely to be influenced by particle breakage than model piles. Particle breakage increases the normalised roughness of an interface. In the case of field scale piles, this breakage pushes the normalised roughness of the interface up through the transition zone observed by Paikowsky *et al.* (1995) and Dietz (2000), with an associated change in angle of interface friction.

However, the interface roughness of a typical model pile lies below the transition zone, and only reaches the lower part of the transition zone when particle breakage is considered.

6.5.3 Relative magnitudes of internal and external shaft friction

Section 6.5.2 discussed the relative influence on shaft friction of:

1) Variation in σ'_v with depth
2) Variation in K with depth
3) Variation in tan δ with depth

It is argued that all three will have an influence during installation and in the short term. In particular, 1) will govern behaviour close to the ground surface; 2) will be important close to the pile tip, and 3) should be considered carefully in the case of pile interfaces with normalised roughness in the range 0.02-0.7. In the long term, set-up is known to significantly influence K (Section 2.3.4.7).

It is the purpose of this Section to highlight the relative magnitudes of internal and external shaft friction, $\tau_{s,outer} / \tau_{s,inner}$, on tubular piles during installation and in the short term. It is argued as follows that the uncertainty in the prediction of K and tan δ discussed in Section 6.4.2 has little influence on this ratio:

- Consider two soil elements which lie on either side of the wall of a tubular pile (Figure 6.18)
- The stress and strain paths experienced as the pile tip approached would have been identical, leading to similar values of K, σ_v and tan δ as the soil element passed around the tip of the pile (point A to point B in Figure 6.18).
- Subsequent changes in K and tan δ are due to a process described kinematically by volume reduction and particle breakage in the zone of intense shearing at the pile-soil interface. If it is assumed that this process is governed by the

kinematics of interface shearing, similar changes in K and tan δ can be expected on both the inside and outside of the pile.

Consequently, a comparison between internal and external shaft friction can be made by examining only the differing profiles of σ_v with depth, assigning equal values to K and tan δ on both the inside and outside of the pile shaft (Equation 6.21). This is achieved by combining Equations 6.3, 6.6 and 6.16.

$$\frac{\tau_{s,outer}}{\tau_{s,inner}} = \frac{\left(e^{2\eta Kz\tan\delta / r_p} - 1\right)}{\eta\left(e^{2Kz\tan\delta / r_p} - 1\right)} \qquad (6.21)$$

Figure 6.19 shows the variation in $\tau_{s,outer}$ / $\tau_{s,inner}$ for the typical values of K tan δ and η shown in Figure 6.12. For K tan δ = 0.35 and typical values of η, it is evident that beyond a depth of around 10 pile radii, the magnitude of $\tau_{s,outer}$, and hence the contribution of $\sigma'_{h,outer}$ to the hoop stress in the pile is negligible. This critical depth corresponds to 1.5 m in the tests reported in this Chapter.

Hence, at depth, the hoop stress induced in the pile wall is almost entirely due to the internal horizontal stress, $\sigma'_{h,inner}$. Throughout all subsequent analysis, the minor correction for external horizontal stress depicted in Equation 6.8 has been carried out assuming external shaft friction varies as predicted by API RP2a (Figure 6.7). Although this approach ignores external arching, the absolute value of local shaft friction is very low over the pile length for which $\sigma_{v,outer}$ / $\sigma_{v,inner}$ is not negligible. Pore pressures are assumed to be hydrostatic.

6.6 MEASUREMENTS OF JACKING FORCE AND PLUGGING

Figure 6.20 shows the measured profiles of jacking force and soil column length with embedded depth. Measurement of soil column length failed at 5 m depth during test 1999/2; the test was repeated using an uninstrumented pile to obtain profile 1999/3.

The jacking force follows the trend of the CPT data by increasing at depths of 2.3 m and 5.5 m. At the end of each 700 mm press-in stroke, a small drop (5-20%) in jacking force can be detected. This could be attributed to pore pressure dissipation whilst the rams are retracted between strokes.

Whereas the hypothetical example shown in Figure 6.3 predicted a single transition from unplugged to plugged penetration, the field data shows that multiple transitions can occur in layered soil. After an initial period of unplugged penetration, the soil column becomes sufficiently long to form a plug at approximately 0.8 m depth (transition A on Figure 6.20). Penetration continues in a plugged manner (with a brief period of slippage during Test 1999/1 between 1.4 and 1.7 m) until the hard layer at 2.3 m depth is reached (transition B).

Upon reaching a hard layer, plugged resistance (Equation 6.2) increases sharply since base resistance follows the CPT profile. In contrast, unplugged resistance (Equation 6.1) is less influenced by a hard layer. Hence, the 'easiest' failure mechanism reverts to unplugged penetration. This causes the soil column to increase in length, accompanied by an exponential increase in internal shaft friction. At approximately 2.7 m depth this increase in internal shaft friction causes the lower bound failure load to revert back to plugged penetration (transition C). On reaching the sand layer at 5.2 m depth, penetration again becomes unplugged due to the sharp increase in Q_b (transition D).

The series of transitions between each penetration mechanism shown in Figure 6.20 follow the pattern predicted by the inequality derived from Equations 6.1 and 6.2 (Equation 6.22) since Q_{si} increases with depth, and Q_b increases in hard layers.

$$\text{If} \quad Q_{si} + W_p > Q_b \quad \text{plugging will occur.} \tag{6.22}$$

It is notable that the changes in penetration mechanism are not accompanied by a noticeable change in jacking force. This is contrary to the conception of plugging held by many operators of press-in pilers, and indeed elsewhere in the literature. It is thought by operators that plugging is 'bad', because it leads to high jacking resistance, and is

blamed for refusal in hard soils. In design, there is often a desire to ensure that a plug forms, in order that the pile can be designed with base resistance across the full cross-section.

In fact, any transition from unplugged to plugged penetration (eg. A and C in Figure 6.20) is not a source of inconvenient 'extra' resistance as felt by operators, or a reassurance as desired by designers. It is quite the opposite; plugging introduces a mode of penetration which avoids resisting the sharply increasing internal shaft friction which would otherwise require greater jacking force to overcome.

In contrast, any transition from plugged to unplugged penetration (e.g. B and D in Figure 6.20) on reaching a hard layer is indicative of a stratum in which a close-ended pile (which cannot penetrate in an unplugged fashion) would be stronger.

When predicting the jacking force required to install a tubular pile, evaluation of the lowest failure load according to Equations 6.1 and 6.2 allows the possibility of plugging to be included in the rational manner described above, with correct inclusion of the exponential internal shaft friction.

6.7 MEASUREMENTS OF STRESS IN THE SOIL COLUMN

The output from the instrumented bolts is converted to internal horizontal stress, σ_{hi}, according to the calculation method shown in Equations 6.8. Figure 6.21 shows the variation of horizontal stress with embedded depth at each bolt location. The quantity h/r_p indicates the distance of each bolt from the pile tip, h, normalised by pile radius, r_p.

The similarity between the profiles of horizontal stress with the variation of soil column length with depth is notable. Changes in soil column length (i.e. periods of unplugged penetration in Figure 6.20) are associated with large increases in horizontal stress at a given bolt location. These profiles of horizontal stress are converted to plug force, $Q_{si} + W_p$, by integration over the length of the pile (Figure 6.22).

The measured curves of plug force closely match design predictions found using arching theory (Equation 6.7) with input parameters, K and tan δ, chosen as proposed by De Nicola & Randolph (1997). These guidelines are derived from centrifuge test data of jacked model piles, and link relative density, I_D, to earth pressure coefficient K. The correlation with these full-scale results is remarkable, particularly since the exponential function is very sensitive to the input parameters.

The analysis of dynamically-installed piles often assumes that a pile plug consists of a 'wedged' and 'unwedged' zone (Murff *et al.*, 1990; Randolph *et al.*, 1991). The 'unwedged' zone is considered not to mobilise shaft friction and act only as surcharge on the lower 'wedged' zone. The physical explanation for this phenomenon is that the cyclic loading created during installation will loosen the top of the soil column. Since press-in installation is monotonic, this loosening will not occur. The soil column is acted on by downward shear stress throughout installation. The design predictions shown on Figure 6.22 consider that the entire plug is 'wedged'.

If further research confirms that arching theory provides a robust technique for predicting internal shaft friction (Equation 6.7), this will provide a valuable technique for estimating the capacity of pressed-in piles. Reliance on empirical methods for prediction of plugging can be eliminated.

6.8 OPTIMIZATION OF THE CONSTRUCTION PROCESS

6.8.1 Sensitivity of plug capacity

The exponential build-up of internal horizontal stress observed during these field tests and predicted by arching theory indicates the sensitivity of internal shaft friction (Q_{si}) to the governing parameters K, tan δ and γ' in Equation 6.7. Hence, the proposition above that Equation 6.7 may offer a useful prediction tool for designers and better machine selection could be considered fanciful. A 10% uncertainty (typical in geotechnical parameter selection) in K or tan δ leads to a two order-of-magnitude difference in Q_{si} at a typical deep embedment with a plug length equal to the embedded depth (h/r_p = 50).

However, these obstacles to improving prediction represent significant opportunities for improving performance. The above paragraph could be recast as stating that only small changes in the operative geotechnical parameters are needed to bring about significant changes (improvements) in performance (capacity). This section discusses how the phenomenon of vertical arching of internal shaft friction can be exploited to improve the driveability and performance of pressed-in piles.

Firstly, how can driveability be improved? The field data shows that internal shaft friction accounts for more than 60% of the jacking force of Test 1999/1 beyond depths of 3 m. A construction procedure which reduces any of the controlling variables, K, tan δ or γ', could dramatically reduce the required jacking force. For laterally loaded piles, this decrease in axial capacity is not critical. If the adjustment can be recovered, axially loaded piles of significantly greater capacity than the strength of the press-in piler could also be installed. Two possible variations in the construction technique are discussed in Sections 6.8.2 and 6.8.3 below.

Secondly, how can performance be improved? If arching can be 'switched on' after pile installation, as the working load is applied to the pile, the design axial capacity of the pile can be greater than the jacking force used during installation. Section 6.4 discusses a technique for achieving this, supported by field data.

6.8.2 The use of a driving shoe to reduce K

6.8.2.1 Mechanism for the reduction in *K*

The use of a driving shoe can provide relief of internal horizontal stress by reducing the earth pressure coefficient, K (De Nicola & Randolph, 1997). Field tests have indicated that dynamic driving resistance can be significantly reduced through the use of a driving shoe (Raines *et al.*, 1992).

The physical mechanism by which K is reduced is hypothesised in Figure 6.23. As an element of soil passes through the shoe, the large decrease in horizontal confinement

causes a reduction in horizontal stress. The vertical stress remains high, governed by the internal shaft friction of the upper part of the soil column.

Consequently, the minimum value of K can be approximated by the active failure criterion (Equation 6.23). This assumes that the horizontal unloading mobilises sufficient strain for the failure envelope to be reached, and that horizontal and vertical stresses are principal. In the case of the field data presented above, this unloading to K_a would represent a maximum reduction of K from 0.8 to 0.35 in the dense sand stratum. The actual minimum value of K, denoted $K_{minimum}$, will be slightly higher than K_a since interface shear stress on the pile shaft prevents horizontal and vertical stresses remaining principal. A more complex expression for this case, which requires an estimate of the interface friction angle, is given in Equation 6.24 (Randolph, 1985).

$$K_a = \frac{(1-\sin\phi)}{(1+\sin\phi)} \tag{6.23}$$

$$K_{minimum} = \frac{\sin\phi\left[\sin(\Delta-\phi)\right]}{\tan\delta\left[1+\sin\phi\cos(\Delta-\phi)\right]} \qquad \text{where} \qquad \sin\Delta = \frac{\sin\delta}{\sin\phi} \tag{6.24}$$

This reduction in K leads to a dramatic reduction of internal shaft friction. This change is best illustrated by plotting the stress at the base of the soil column due to internal shaft friction and the weight of the soil, $(Q_{si}+W_p)/A_p$, against depth (Figure 6.24).

If $(Q_{si}+W_p)/A_p$ is lower than base resistance, q_b, an unplugged mechanism will form the lower bound failure load, plugging will be avoided, unplugged penetration will occur, and jacking force will be reduced. On Figure 6.24, a typical base resistance, q_b, in dense sand of 20 MPa has been highlighted. Following the same procedure as shown on Figure 6.3, the minimum failure load has been highlighted in colour, for cases of K = 0.4 and K = 0.8 .

For the case of K being reduced from 0.8 to 0.4 by the use of a driving shoe, Figure 6.24 indicates that the required jacking force to reach a depth of 15.6 m would be the same as that required to reach a depth of 8.4 m without a driving shoe.

6.8.2.2 Finlay *et al.* (2001) fieldwork

Recent field tests carried out by T. Finlay and Y. Zhao under the supervision of the Author have demonstrated the use of driving shoes to reduce shaft friction. Finlay *et al.* (2001) report a sequence of three field tests conducted at the Takasu test site during Summer 2000. A double-skinned tubular pile was instrumented in a manner that allowed separate measurement of total internal and external shaft friction. The dimensions of the test pile are shown in table 6.5. The piles were installed into the bottom of a 1.5m deep pit excavated through the variable made ground. Three tests were conducted;

- Test 2000/1: No driving shoe
- Test 2000/2: External driving shoe (Figure 6.25a)
- Test 2000/3: Internal driving shoe (Figure 6.25b).

The total external shaft friction, Q_{so}, during installation is shown in Figure 6.26. Q_{so} is dependent on the external embedded surface area, the angle of friction between the pile and the soil and the effective horizontal stress acting on the pile. The area of the pile in contact with the soil and the soil-pile angle of friction are equal for a given embedded depth, so any difference in external shaft friction between these three tests is due to differences in the horizontal effective stress acting on the pile.

	Outside diameter, D_{outer} *(mm)*	*Wall thickness, t, (mm)*	*Wall area,* A_{wall} *(mm^2)*	*Length (m)*
Outer skin	318.5	10.3	9973	10
Inner skin	267.4	6.6	5408	8

Table 6.5. Dimensions of double-skinned instrumented test pile

It can be seen from Figure 6.27 that the external driving shoe leads to a significant reduction in external shaft friction especially at large depths. The driving shoe was successful in reducing the effective horizontal stress acting on the pile by a factor of 4. Note that the use of an internal driving shoe has no influence on external shaft friction. The close agreement between the profiles of Q_{so} for no shoe and an internal shoe indicate the reliability of this data.

Whilst external shaft friction acts on the entire embedded depth of the pile, internal shaft friction acts only of the lower section of the inside surface which is in contact with the internal soil column (or plug). Extending the statements made in Section 6.2, it can be stated that internal shaft friction is a function of pile-soil friction angle, the horizontal effective stress profile along the soil column and the length of the internal soil column. An internal driving shoe will alter both the horizontal stress distribution along the internal soil column, and also its length.

Figure 6.27 shows that a significant reduction in internal shaft friction is achieved by using an internal driving shoe. Beyond a depth of 5 m (corresponding to a plug length greater than 2 m), significant internal shaft friction is mobilised and the influence of the internal driving shoe is clearly evident. For a given embedded depth, internal shaft friction is generally reduced by a factor of 3. The profile of Q_{si} when using an external driving shoe appears anomalous. The sharp drop to a negative value at 6 m depth suggests that the axial strain gauge at the bottom of the inner sleeve became damaged or debonded. Beyond 6 m depth the readings fluctuate, and are considered unreliable.

Despite reducing shaft friction by factors of 3 and 4 respectively, the internal and external driving shoes did not lead to a significant reduction in jacking force. This is because the reduction in shaft friction was partially balanced by an increase in base resistance created by the additional cross-sectional area of the driving shoes.

The instrumented double-skin pile used in this test series has a disproportionate base/shaft area ratio and was only installed to a shallow embedment. Consequently, shaft resistance comprised a smaller proportion of the total resistance than would be expected if the pile had a more typical geometry. Furthermore, following the success of this test series, it was hypothesised that the undesirable increase in base resistance could be reduced if a smaller driving shoe flange was used whilst still obtaining the desired stress relief along the pile shaft. This hypothesis was tested by the fieldwork conducted by Y. Zhao, G Yetginer and D. Rockhill under the supervision of the Author during Summer 2001.

6.8.2.3 Zhao *et al.* (2001) fieldwork

The Summer 2001 field testing took place at Akaoka test site, 10 miles east of Kochi, Japan. At the time of writing, only limited site investigation data was available. Figure 6.28 shows the CPT profile at the test site. The soil conditions are similar to the Takasu test site, with hard layers of dense sand at 2.5-3 m depth and beyond 7 m depth. Two test installations using the same design of double-skinned tubular pile as the Summer 2000 testing were carried out (Table 6.5). A new inner driving shoe with an overhang of only 6.6 mm (reduced from 15 mm) was fabricated.

Profiles of jacking force against depth for Test 2001/1 (no driving shoe) and Test 2001/2 (inner driving shoe) are shown in Figure 6.29. The use of a 6.6 mm inner driving shoe led to a 20-40% reduction in jacking force in the layer of dense sand beyond 6 m depth. This demonstrates the successful use of an inner driving shoe to reduce both inner shaft friction and also overall jacking force.

By linking the horizontal unloading as soil passes through a driving shoe to swelling along a κ-line, it can be shown that driving shoes much smaller than 6.6 mm may provide sufficient stress relief to reach active conditions. Coop & Lee (1993) demonstrate that the behaviour of sand at elevated stress levels, as found close to a pile tip, fits within the framework of Critical State Soil Mechanics and present appropriate Cam clay parameters for various sands. The construction shown in Figure 6.30 suggests that a driving shoe overhang of >0.6% of the pile radius may induce sufficient horizontal extension to reduce the horizontal effective stress to the active condition. In the case of the tubular pile used during the Summer 2001 test series, this represents a shoe overhang of less than 2 mm.

6.8.3 The use of water injection to reduce γ'

A drawback of reducing jacking force by using a shoe is that the reduction in capacity is difficult to recover. An alternative method to ease driving is to inject water close to the base of the soil column creating excess positive pore pressure. The jets should be positioned such that the water tends to flow up the soil column creating partial liquefaction of the soil within the pile, but with minimal loss of strength in the

surrounding soil. Pore pressure that is greater than hydrostatic reduces the effective weight of the soil, with a consequent reduction of internal shaft friction.

Figure 6.31 demonstrates how a variation in γ' could reduce internal shaft friction and jacking force. The soil column need not be fully liquefied to create a reduction in jacking force. However, unlike K and tan δ, γ' is not within the exponential term of internal shaft friction (Equation 6.7). As a result, the reduction in jacking force is proportional to the reduction in buoyant unit weight. This is of little benefit in attenuating the sharp exponential increase in internal shaft friction with depth unless full liquefaction is achieved. In this case, zero internal shaft friction is developed.

Examination of Figure 6.31 shows that 90% liquefaction would only permit an extra 2 m penetration before the minimum failure load returns to the value that would have existed without jetting.

However, water jetting is known to be effective in reducing jacking force, so a second mechanism may be operating. Water jetting creates both high pore pressure and also volumetric flow through the soil skeleton. Transport of fine particles away from the pile tip will lead to compression of the soil in this zone. This will lead to a reduction in base resistance. Consequently, jetting may have two influences on Figure 6.31; a reduction in both internal shaft friction and base resistance.

Following installation, the pore pressures will return to hydrostatic and the lost internal shaft friction will become available. However, a reduction in base resistance due to internal erosion is unlikely to return.

Field testing is required to confirm this long-term influence of jetting on both shaft and base resistance. Whilst some short-term reduction in shaft friction is predicted by arching theory (Figure 6.31), the observed reduction in jacking force associated with water jetting may be linked to internal erosion, and hence be irrecoverable.

6.8.4 A construction process which allows arching to be 'switched on'

The key observation from the Summer 2000 field testing is that internal shaft friction is significantly larger than external shaft friction and evolves exponentially with depth. A pile surface which is geometrically arranged such that the friction acting upon it is governed by arching theory is an efficient method of obtaining axial capacity, but is less attractive from the point of view of driveability. Ideally, installation should be without arching, yet arching should be available to resist working loads. These apparently contradictory demands can be satisfied by the construction sequence shown in Figure 6.32.

This novel foundation solution is based on the observation that the cross-section of an H-pile is 'open', in the sense that no body of soil is fully enclosed in the manner of a tubular pile. Equilibrium analysis of an element of soil within the pan of an H-pile (element A or B in Figure 6.32) shows that downward friction on the soil body during installation of a single H-pile, τ_s, can be resisted by upwards shear stress, $\lambda\tau_s$, in the soil between the tips of the flanges (Figure 6.33).

As with Figure 6.10, the vertical equilibrium of this element, and hence the variation of vertical stress and shaft friction with depth cannot be solved because λ is unknown. However it can be assumed that some proportion of the downward shaft friction will be carried by shear stress on 'circumferential' planes in the soil, and a small proportion will be resisted by an increase in vertical stress with depth. A weak exponential evolution of shaft friction will result, although this exponent is likely to be larger than proposed for external shaft friction on tubular piles since downward shaft friction acts on 3 sides of the element in Figure 6.33, and on only one side of Figure 6.10.

The equilibrium of the soil element in Figure 6.33 can be contrasted with the equilibrium of the square soil column between two adjacent H-piles that are being simultaneously loaded (Figure 6.34). The equilibrium of this soil element (Equation 6.25) only differs from the case of tubular piles (Equation 6.5) due to the differing geometry of squares and circles. Integration of Equation 6.25 leads to expressions for the vertical stress profile within the square column of soil (Equation

6.26) and the 'internal shaft friction' of two adjacent H-piles (Equation 6.27) with a plug length h_{plug}.

$$\frac{d\sigma'_v}{dz} = \gamma' + \frac{4K\sigma'_v \tan\delta}{B} \tag{6.25}$$

$$\sigma'_v = \frac{\gamma' B\left(e^{4Kh_{plug}\tan\delta/B} - 1\right)}{4K\tan\delta} \tag{6.26}$$

$$Q_{si} = \sigma'_v B^2 - W_p = \frac{\gamma' B^3\left(e^{4Kh_{plug}\tan\delta/B} - 1\right)}{4K\tan\delta} - \gamma' h_{plug} B^2 \tag{6.27}$$

The difference between the jacking force required to install individual H-piles and the capacity of the completed pile wall is illustrated in Figure 6.35 by sketching the approximate profile of each component of resistance. The components of resistance during installation are summed to give the installation force, $Q_{installation}$. The shaft friction profile in the pile pan during installation is governed by weak vertical arching (derived by considering the equilibrium of the element shown in Figure 6.32), leading to a gentle increase in $Q_{s,pan}$ with depth.

However, during loading of the completed pile wall, the pan of the pile has become a closed box section. Therefore, high vertical arching is generated. The profile of vertical stress with depth is now governed by the equilibrium of the element shown in Figure 6.33, leading to high internal shaft friction, Q_{si}, predicted by Equation 6.27. In this case, the unplugged penetration resistance is likely to exceed the plugged penetration resistance (i.e. $Q_{si} + W_P > Q_p$) due to the strong exponent in Equation 6.27. Therefore the capacity of the completed foundation is governed by $Q_{plugged}$ (Equation 6.2).

A simple calculation for the gain in capacity between installation and group loading for a 16 m long H-pile embedded 1 m into a dense bearing stratum is shown in Table 6.6. A basic prediction based on the API method combined with Equation 6.27 suggests that the pile wall would exhibit a group efficiency defined as $Q_{group\ load} / Q_{installation}$ of 1.75.

This figure is subject to significant uncertainty and probably overestimates group efficiency since $Q_{s,pan}$ during installation is likely to be higher than the API method predicts due to the confinement and hence arching within the pan (Figure 6.33).

Input parameters	
H-pile dimensions: Depth = 16m	400 x 400 x 13 x 21mm
Wall area, A_{wall}	22000 mm^2
Pan area, A_{plug}	138000 mm^2
Pan perimeter	1490 mm
Unit weight, γ'	8 kN/m^3
Earth pressure coefficient, K	0.8
Pile-soil friction angle, δ	25°
Cone resistance, q_c	20 MPa
Base resistance, $q_b = q_c/2$	10 MPa
Mean shaft friction without arching, $\left[\tau_s = K\sigma'_v \tan\delta\right]_{mean}$	24 kPa

Components of pile capacity	
At installation to final depth:	
$Q_{wall} = q_b \; x \; A_{wall}$	220 kN
$Q_{s,flanges} = \tau_{s,mean} \; x \; A_{flanges}$	307 kN
$Q_{s,pan\ (no\ arching)} = \tau_{s,mean} \; x \; A_{pan}$	572 kN
$Q_{installation}$ =	1099 kN
Capacity under group load[1]:	
$Q_{wall}+Q_{plug} = q_b \; x \; (A_{wall}+A_{pan})$	1600 kN
$Q_{s,flanges} = \tau_{s,mean} \; x \; A_{flanges}$	307 kN
$Q_{group\ load}$ =	1907 kN

[1]Plugged failure mechanism is lower bound under group load since $Q_{s,pan\ (arching)} = 2.84 \times 10^{25}$ kN! (Equation 6.25)

Table 6.6 Estimated group efficiency of an H-pile wall in typical ground conditions

6.8.5 Fieldwork: Shinagawa, Tokyo

6.8.5.1 Test scheme

A series of load tests on 20 m long H-piles carried out at Shinagawa, Tokyo, are used to illustrate the possibilities of a construction process which allows vertical arching to be 'switched on'. The site lies 1 km east of the Shinagawa subway station in Tokyo. The ground conditions consist of layers of fill, silt and sand and gravel overlying mudstone (Figure 6.36a). The construction of a large office block on the site was proposed by Giken Seisakusho Ltd. A foundation consisting of a wall of adjacent H-piles in a circular caisson arrangement was considered. The use of adjacent H-piles is suited to press-in installation since these can be easily installed using the 'self-walking' facility of the press-in piler.

The possibility of enhanced performance through arching was not previously considered. Prior to the testing, discussions between the Author and Giken led to the adoption of a scheme that allowed the capacity of a single pile to be compared to that of a pair, and three adjacent piles.

6.8.5.2 Test piles

A row of 400 mm × 400 mm H-piles were installed using a Giken Seisakusho HP-150 press-in piler. The row consisted of shallow piles, terminating above the mudstone bearing stratum. Interspersed with these shallow piles, and protruding down into the bearing stratum, were the test piles (Figure 6.36b). The test piles were instrumented with strain gauges at 6 locations along their length, to allow the load distribution to be estimated.

The HP-150 piler was fitted with a pre-augering attachment which is drilled into the soil ahead of the advancing wall prior to installation of each H-pile. The auger is used only to loosen the soil. No material is removed from the ground.

6.8.5.3 Load tests

A total of four load tests were carried out (Table 6.8). Test nos. 1, 3 and 4 were on piles installed into the bearing stratum. Test no. 1 consisted of a single pile. Test nos. 3 and 4 consisted of two and three adjacent piles respectively (Figure 6.36a). These pile groups were loaded concurrently via a metal loading plate. Test no. 2 used a single pile installed to only 15.5 m depth.

Three load tests were carried out by Jibanshikenjo Co. Ltd. of Sumida-ku, Tokyo between 14 and 20 days after installation of the test piles (Jibanshikenjo Co. Ltd, 2001). The load test procedure followed the code of the Japanese Geotechnical Society with regard to holding periods and loading increments. Reaction force was provided by tensile loading of two walls of 15 m deep sheet piles located 2 m distant on either side of the H-pile row. The HP-150 piler is shown in Figure 6.36c and the load test set-up is shown in Figures 6.36d-e.

	Test no. 1	*Test no. 2*	*Test no. 3*	*Test no. 4*
Number of piles	1	1	2	3
Pile tip depth (m)	20	15.5	20	20
Load increments (kN)	200	200	400	600
Reload loops at: (kN)	600,1200	600,1200,1800	1200,2400,3600	1800,3600 5400,7200

Table 6.7 Shinagawa load test programme

6.8.5.4 Force measurements during installation

The strain gauges were monitored during installation of the 6 test piles (Figure 6.37). The mean final installation load was 869 kN, with a standard deviation of 95 kN (COV = 0.11). Noting that the profiles of shaft friction implied by Figure 6.37 are slightly erratic, it is possible that some strain gauge damage may have occurred during installation. Furthermore, the strain gauge readings were zeroed after installation prior to load testing, erasing any residual stress measurements. Therefore, subsequent readings are likely to underestimate base resistance and overestimate shaft friction on the upper part of the pile.

6.8.5.5 Load test results

Figure 6.38 shows the load-displacement curves, and load distribution for the three tests. The load distribution is calculated from the change in strain gauge reading during load testing and therefore do not include residual stress. Two failure criteria have been selected; *B*/20 and *B*/10 pile head settlement, where *B* is the width of a single pile, 400 mm (Table 6.8). Two key observations are apparent and are discussed below:

- Ultimate capacity is greater than press-in installation force
- The capacity of each pile within a row is greater than a single pile: there is a positive ‘group effect’

6.8.5.6 Ultimate capacity compared to installation force

Comparison of Figures 6.37 and 6.38 reveals that the ultimate capacity of the single piles (Test nos. 1, 2) was significantly greater than the jacking force during installation. The single piles showed a ‘set-up’ over the 14-20 day period since installation of 28-41%. This ‘set-up’ could be attributed to pore pressure dissipation, creep, or the increase in stress on the pile shaft due to subsequent installation of the other piles.

Comparison of Figures 6.37 and 6.38 suggests that the additional capacity arises from shaft friction. However, it should be noted that any base resistance transmitted up through a soil plug which is rigidly attached within the pan of an H-pile will appear as shaft friction within the strain gauge readings.

Test	*No. 1*	*No. 2*	*No. 3*	*No. 4*
Installation load(s), $Q_{install}$ (kN) Mean value = 869 kN	780	939	844, 1012	804, 810, 962
Load at *B*/20 (kN)	1030	1200	3000	4450
Load at *B*/10 (kN)	1070	1320	3300	5100
'Set-up' ratio at *B*/20	1.32	1.28	-	-
'Set-up' ratio at *B*/10	1.37	1.41	-	-
Group efficiency, ζ_{group}, at *B*/20	-	-	1.45	1.44
Group efficiency, ζ_{group}, at *B*/10			1.54	1.59
Combined group and 'set-up' ratio at *B*/20, $\zeta_{group,setup}$			1.62	1.73
Combined group and 'set-up' ratio at *B*/10, $\zeta_{group,setup}$			1.78	1.98

Table 6.8 Shinagawa load tests results

6.8.5.7 Group efficiency, ζ_{group}

A group efficiency factor, ζ_{group}, can be defined using Equation 6.28, where Q_{single} and Q^n_{wall} are the capacity of a single pile and a wall of *n* piles respectively and *n* is equal to the number of the piles in the group. This formula is widely used, with the notation Q_{group} instead of Q_{wall} for the analysis of 2-dimensional pile groups. The calculation of ζ_{group} allows the beneficial or detrimental effect of nearby piles on the capacity of a single pile to be quantified. Vesic (1969) and Fleming *et al.* (1992) present data of ζ_{group} for pile spacing ratios in the range 2-10 diameters. An H-pile wall can be considered as a 1-dimensional pile group with an effective spacing ratio of 1.

$$\zeta_{group} = \frac{Q^n_{wall}}{nQ_{single}} \tag{6.28}$$

In this case, it is clear that the presence of adjacent piles has a beneficial effect on capacity. Positive group efficiencies in the range 1.44-1.68 are recorded for Test nos. 3 and 4. If the 'set-up' component of capacity is included, this positive efficiency increases to 1.62-1.98 (Equation 6.29, Table 6.8).

$$\zeta_{group,set-up} = \frac{Q^n_{wall}}{nQ_{install}} \tag{6.29}$$

This method of evaluating group efficiency does not lend itself to extrapolation to rows of H-piles of greater length. The shaft or base area is not proportional to the number of piles, *n*, unless the failure mechanism is assumed to be unplugged. If this is the case, however, some of the shaft is facing into a pan of soil rather than the free field. A different capacity is therefore expected for each form of shaft area geometry.

6.8.5.8 Wall efficiency, ζ_{wall}

An alternative indication of the group effect could be found by comparing the capacity of walls of different length, instead of comparing the capacity of a wall with that of a single pile. Figure 6.39 demonstrates that a wall of H-piles can be subdivided into two types of element: an 'end of wall' element and a 'box' element. The 'end of wall' element will mobilise shaft capacity with only weak vertical arching according to the mechanism shown in Figure 6.33. The resulting capacity if defined as Q_{end}. The 'box' element will mobilise shaft capacity within the box section according to the mechanism shown in Figure 6.34. Plugging may occur if the internal shaft capacity exceeds the base resistance on the soil column. The resulting capacity is defined as Q_{box}.

The additional capacity obtained by increasing the length of a wall by one pile is equal to Q_{box}. Therefore, the best measurement of the efficiency of the geometric arrangement is the ratio between the contribution of an additional pile and the capacity of a single pile. This ratio is defined as ζ_{wall} (Equation 6.30).

$$\zeta_{wall} = \frac{Q_{wall}^{n+1} - Q_{wall}^{n}}{Q_{single}} \qquad (6.30)$$

Noting from Figure 6.39 that $Q_{end} = Q_{single}$, and $Q_{wall}^{n+1} - Q_{wall}^{n} = Q_{box}$, the capacity of a wall containing *n* piles can be related to the capacity of a single pile using Equation 6.31. Comparison of Equations 6.28 and 6.31 shows that high values of *n*, for which the influence of the wall end diminishes, $\zeta_{wall} = \zeta_{group}$. Table 6.10 contains values of ζ_{wall} found from comparison of Test nos. 1, 3 and 4.

$$Q_{wall}^{n} = \left[1 + (n-1)\zeta_{wall}\right] Q_{single} \quad (6.31)$$

	Test nos. 1 & 3	*Test nos. 3 & 4*
Wall efficiency at B/20, ζ_{wall}	1.91	1.41
Wall efficiency at B/10, ζ_{wall}	2.08	1.68
Wall efficiency and 'set-up' ratio at *B*/20, $\zeta_{wall,set\text{-}up}$	2.27	1.67
Wall efficiency and 'set-up' ratio at *B*/10, $\zeta_{wall,set\text{-}up}$	2.57	2.07

Table 6.9 Wall efficiency, ζ_{wall} of Shinagawa test piles

The contribution of set-up to the wall efficiency can be included in Equation 6.30 by substituting the mean installation force of the component piles, $Q_{install}$ for Q_{single}, to evaluate $\zeta_{wall,set\text{-}up}$ (Equation 6.32, Table 6.10). These values indicate that in the case of these tests, the contribution of a single pile to the capacity of the wall is 2.07-2.57 times greater than the force required to install the pile.

$$\zeta_{wall,set-up} = \frac{Q_{wall}^{n+1} - Q_{wall}^{n}}{Q_{install}} \quad (6.32)$$

6.8.5.9 Comparison with other measurements of group efficiency

These positive group effects are in contrast to predictions using conventional theory. Firstly, it would be expected that a single pile in a wall of H-piles would have lower shaft capacity when loaded simultaneously with its neighbour since the area of the failure surface is reduced. Conventional theory would apply shaft friction to the perimeter of the H-pile wall. This perimeter has a length less than the sum of the perimeter of the individual piles.

Secondly, it is usually expected that the efficiency of a pile group with a low spacing ratio is close to or less than unity. Laboratory test data has suggested that a positive group effect occurs at spacing ratios of 2-6 due to compaction and stress-increases during group installation. However, this effect appeared to reduce to unity at a spacing ratio of 1, as used in these field tests (Vesic, 1969). Also, an efficiency of *less* than

unity is predicted by considering the superposition of elastic settlement troughs or the interaction of neighbouring stress fields (Fleming *et al.*, 1992).

Some insight into the source of the additional capacity observed at Shinagawa is provided by the distribution of shaft friction during load testing. Figure 6.40 shows the mobilisation of shaft friction between each strain gauge location. Although these results are polluted by some residual stress, there is clearly a concentration of shear stress on the lower part of each pile wall. In contrast, the single pile shows only a gentle increase in shaft friction with depth. This concentration of shear stress close to the pile tip is indicative of the mobilisation of plug capacity. This does not imply that a plug forms, only that a sharp increase in shaft friction with depth is occurring, which supports the arching hypothesis described in Section 6.8.4.1.

6.8.5.10 Implications for the design of H-pile wall foundations

This data shows that the strength of a H-pile wall is considerably greater than the sum of the jacking forces required for installation. Vertical arching within the soil column created following the installation of adjacent H-piles offers a significant increase in capacity. Also, the contribution of time-induced 'set-up' to the increased capacity has been measured. These increases in capacity exceed the reduction associated with the reduced foundation surface area.

These results demonstrate the possibility of using a relatively small (150 tonne) capacity press-in piler to construct large caisson foundations capable of supporting heavy structures. The range of values shown in Table 6.9 suggests that when designing to a failure criterion of $B/10$ settlement, a value of $\zeta_{wall,setup} = 2.0$ might be appropriate.

A proposed foundation design utilising the 'self-walking' capability of a press-in piler is a circular ring of H-piles. This would be of similar geometry to a caisson foundation. A modified version of Equation 6.31 would be required to analyse a ring of H-piles since this geometric arrangement contains no 'end' elements, and n 'box' elements (Equation 6.33).

$$Q_{wall}^{n} = n\zeta_{wall}\ Q_{single} \qquad (6.33)$$

Using Equation 6.33, the capacity of a caisson foundation consisting of a 20 m diameter circle of 157 no. 400 x 400 mm H-piles at the Shinagawa site installed to the same depth of the test piles could be tentatively predicted as 336 MN at a foundation settlement of *B*/10 (40 mm). This prediction is from short term load test data (14-20 days from pile installation). Further testing is required to confirm the applicability of this wall efficiency factor to longer H-pile walls.

6.8.5.11 Implications for design of an excavated H-pile caisson

It was proposed by Giken Seisakusho that the volume within the ring of H-piles could be exploited as a basement car park (Figure 6.36f). Excavation to a depth of 15 m would allow an 'Eco-park' automatic car parking facility to be installed within the ring foundation. This excavation would reduce the capacity of the foundation by removing shaft friction on the upper inside of the H-pile ring and possibly leading to stress relief and loss of shaft friction on the outside of the ring due to inward deformation.

An estimation of the capacity that would remain can be made by considering the load recorded at strain gauge level 4, located 3.5 m above the pile tip, during the load tests. It should be noted that these gauges are likely to underpredict the base capacity and shear transfer onto the lower part of the H-piles since residual stresses have been ignored. This data can only be considered as an estimate of the capacity after excavation, since the excavation may have the effect of lowering the ambient stress close to the pile tip, reducing the base capacity.

Table 6.10 shows the load recorded at strain gauge level 4 at head settlements of *B*/20 and *B*/10. Values of wall efficiency, $\zeta_{wall,3.5m}$, have been evaluated. In all cases, the extra capacity on the lower 3.5 m of the pile provided by an extra pile exceeded the mean installation force (869 kN).

The increased wall efficiency at a settlement of *B*/10 compared with *B*/20 supports the hypothesis that the improved capacity originates from mobilisation of the plug since

base response is less stiff than shaft response. Also, a higher wall efficiency is recorded at 3.5 m from the pile tip (Table 6.10) compared to the pile head (Table 6.9).

	Test no. 1	*Test no. 3*	*Test no. 4*
Force 3.5 m from pile tip at *B*/20 (kN)	415	1500	2520
Force 3.5 m from pile tip at *B*/10 (kN)	450	1750	3000
Extra capacity on lower 3.5 m at *B*/20 (kN)	1085	1020	
Extra capacity on lower 3.5 m at *B*/10 (kN)	1300	1250	
Wall efficiency, $\zeta_{wall,3.5m}$ at *B*/20	2.61	2.45	
Wall efficiency, $\zeta_{wall,3.5m}$ at *B*/10	2.89	2.78	

Table 6.10 Wall efficiency of lower 3.5 m of test piles

Following Equation 6.33, modified to consider only the lower 3.5 m of the pile wall, the capacity of a 20 m diameter, 20 m deep, H-pile caisson foundation at the Shinagawa site excavated to a depth of 15 m could be tentatively predicted as 200 MN at a foundation settlement of *B*/10 (40 mm). This prediction is from the short term load test data (14-20 days after pile installation, 450 kN). The foundation is constructed from 157 400 × 400 mm H-piles, each with a wall efficiency, $\zeta_{wall,3.5m}$, taken as the mean of the two values in Table 6.10.

These results indicate that a novel foundation comprising of a ring of adjacent H-piles installed in sequence offers both an efficient construction process and a high pile capacity though vertical arching.

6.9 CONCLUSIONS

The novel installation technique used by press-in pile drivers allows construction to proceed without the environmental problems associated with dynamic pile installation methods. However, the deployment of press-in pile drivers is currently limited to sites where the static load capacity of the machine is above the maximum expected resistance.

Predicting this resistance remains particularly problematic when installing tubular piles. Conventional design methods ignore internal shaft friction, or use an empirical

correlation to determine the critical failure mode; plugged, or unplugged. A more robust analysis technique is to evaluate driving load as the lowest of the plugged and unplugged failure loads.

Field tests reported in this chapter indicate that internal shaft friction is well predicted by vertical arching theory. Design values of K derived from centrifuge test data (De Nicola & Randolph, 1997) closely fit the field results.

Since arching evolves according to an exponential relationship, a large reduction in internal shaft friction can be achieved through only a small change in the governing parameters, K, $\tan\delta$ and γ'. Novel construction techniques that take advantage of this phenomenon allow the driveability and performance of jacked piles to be optimised.

The use of a driving shoe is proposed as a technique for permanently reducing internal shaft friction by decreasing the horizontal earth pressure coefficient within the internal soil column. Field tests that demonstrate the effectiveness of this technique are reported. An initial series of field tests using a 15 mm driving shoe produced a 3-4 times reduction in internal and external shaft friction. However, overall jacking force was not reduced since the additional cross-sectional area of the driving shoe lead to an increase in base resistance. A further series of field tests conducted with a 6.6 mm driving shoe were more successful, exhibiting a 20-40% reduction in overall jacking force.

Water injection is proposed as a technique of temporarily reducing the buoyant weight of the soil within the pile, leading to a reduction of internal shaft friction during installation. This loss of friction due to high pore water pressure would be recoverable after installation. However, it should be noted that a proportion of the reduction in jacking force generated by water jetting may be due to internal erosion, and will not be recovered by the return of pore pressures to hydrostatic.

The evaluation of vertical stress within a tubular pile by arching theory implies that the downward friction acting on the soil column leads to an increase in vertical effective stress. This implication has been extended to external shaft friction. However, upward

shear stress can act on circumferential planes around a pile to balance the downward action of the shaft friction. Consequently, the vertical arching effect is weaker. It has been demonstrated that a weak arching function leads to a profile of local shaft friction with depth which matches typical field profiles. This analysis contrasts with previous prediction methods by linking the variation in local shaft friction to a variation in vertical effective stress, rather than a variation in horizontal earth pressure coefficient

The evaluation of shaft friction using arching theory is not only applicable to tubular piles. Analysis of the shaft friction within the pan of adjacent H-piles has been presented. The formation of an enclosed soil column of square cross-section, rather than circular, between adjacent H-piles also leads to arching and large shaft friction. This arching develops only when both piles are loaded, creating downdrag on all four sides of the soil column. Field data from load testing at the Shinagawa test site in Tokyo confirmed this positive group effect.

Consequently, arching and the resulting shaft friction can be ‘switched on’ by loading adjacent H-piles piles simultaneously. Loading only one of the adjacent piles leads to a lower capacity. This phenomenon allows H-pile walls constructed by the press-in method to exhibit a greater capacity under a working load than was evident during their installation. The strength of the completed foundation is greater than the sum of its parts.

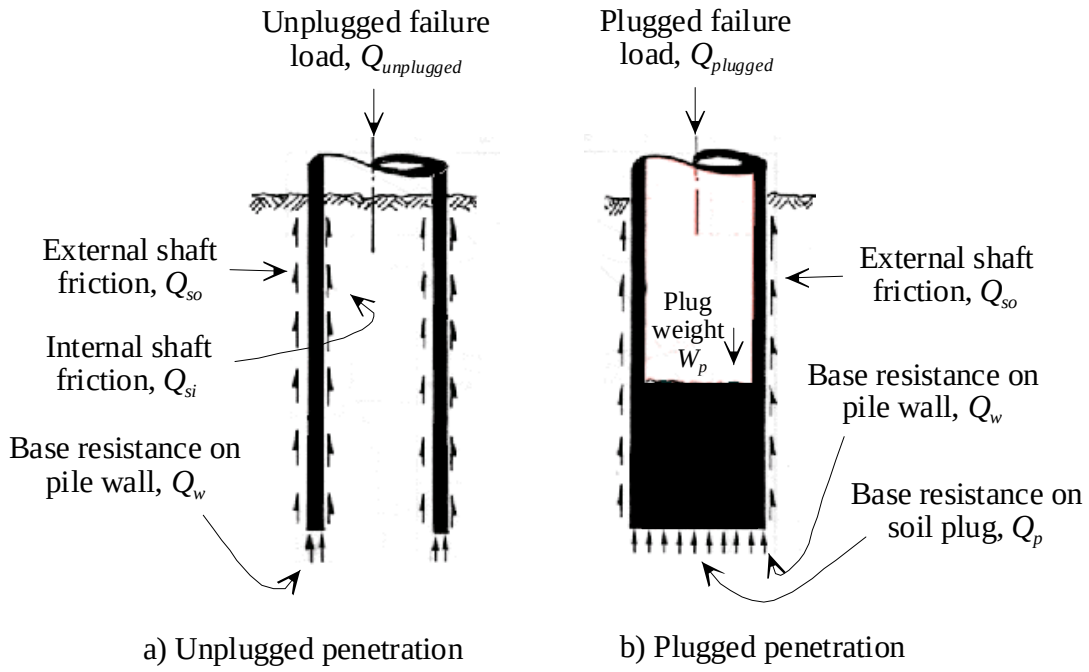

Figure 6.1 Modes of penetration for tubular piles

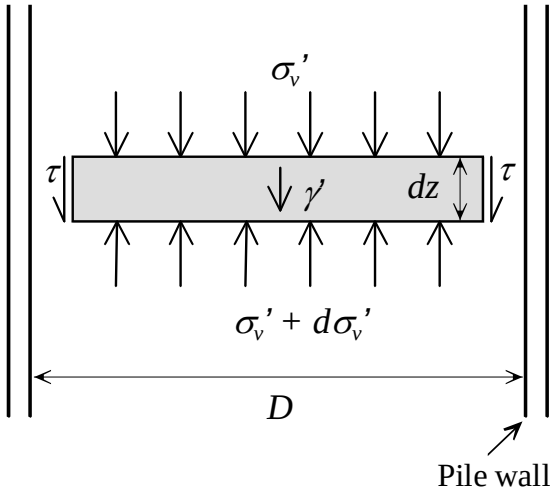

Figure 6.2 Equilibrium of a slice of soil within a tubular pile

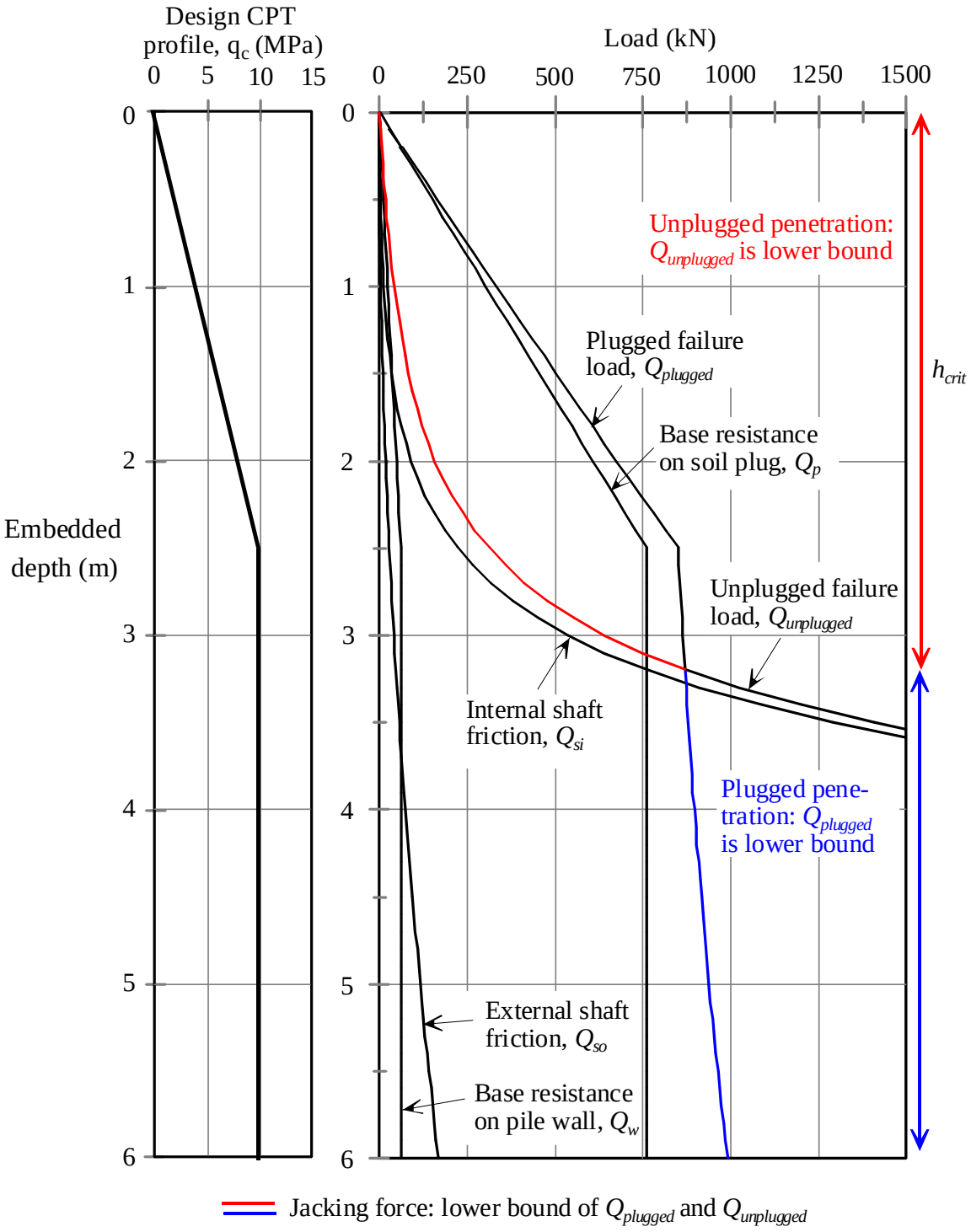

Figure 6.3 Predicted driving load vs. embedded length at a typical site

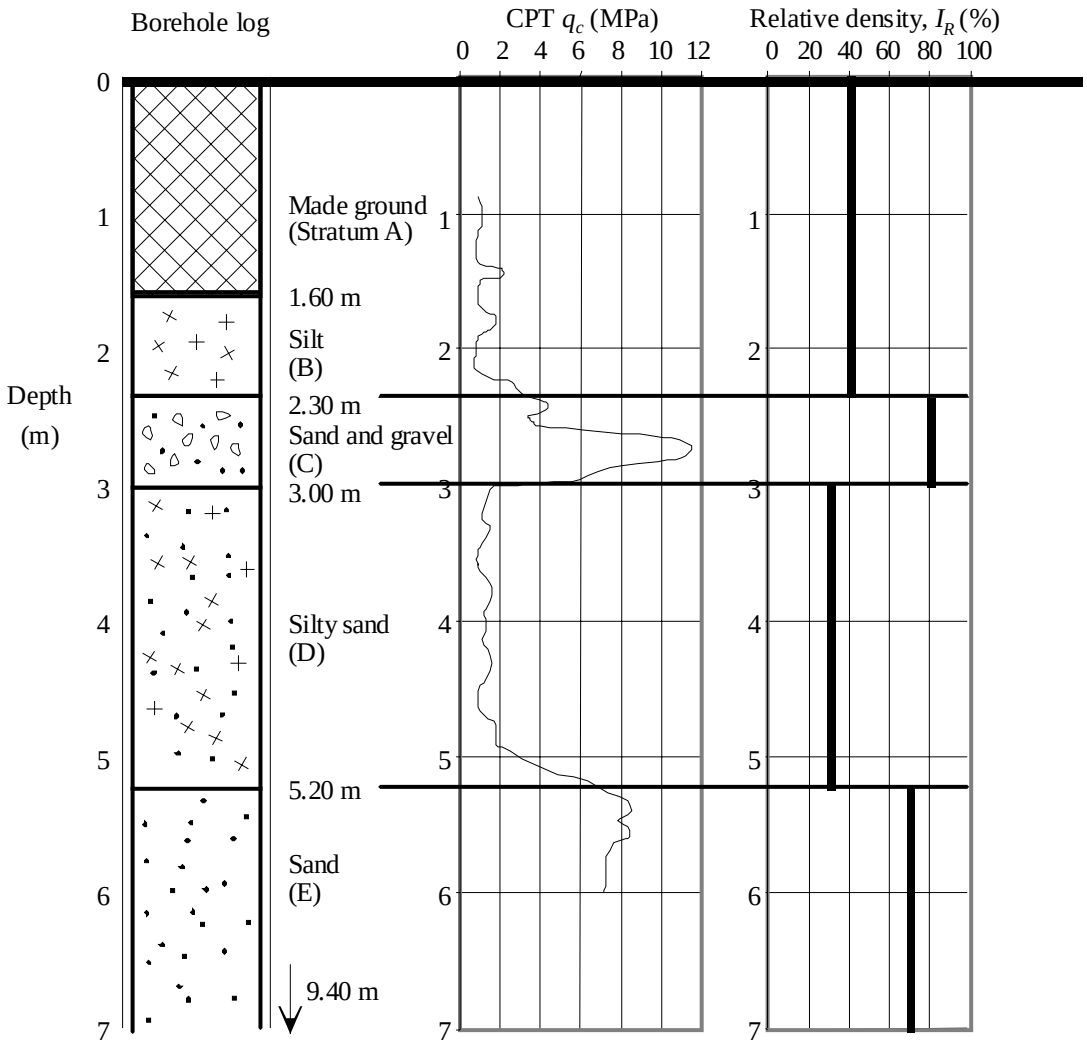

Figure 6.4 Takasu site stratigraphy and CPT profile

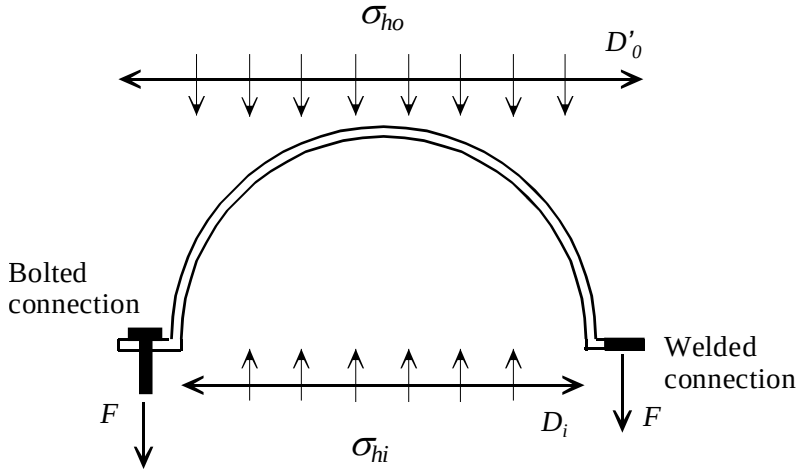

Force F measured by instrumented bolt

L = longitudinal bolt separation

Figure 6.5 Calculation of internal horizontal stress from bolt force

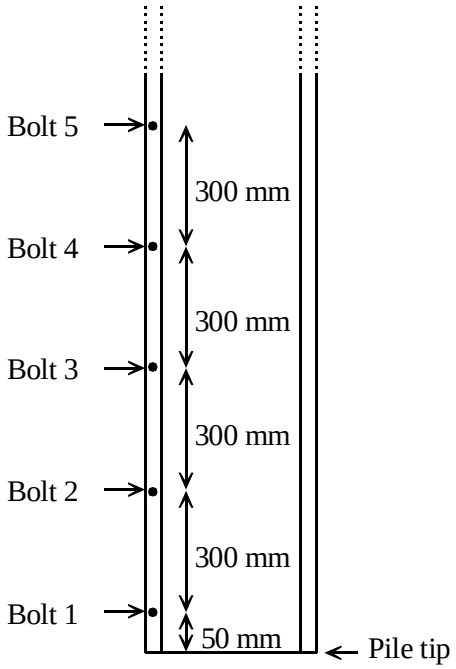

Figure 6.6 Tests 1999/1 and 1999/2: location of instrumented bolts

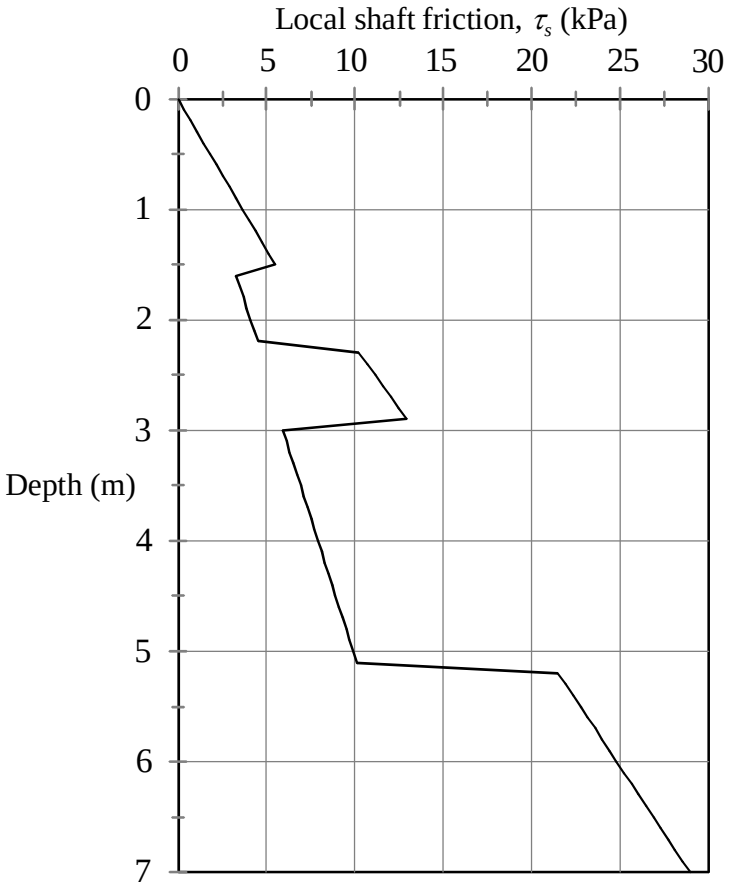

Figure 6.7 Local shaft friction predicted by API (1993) method for test pile at Takasu

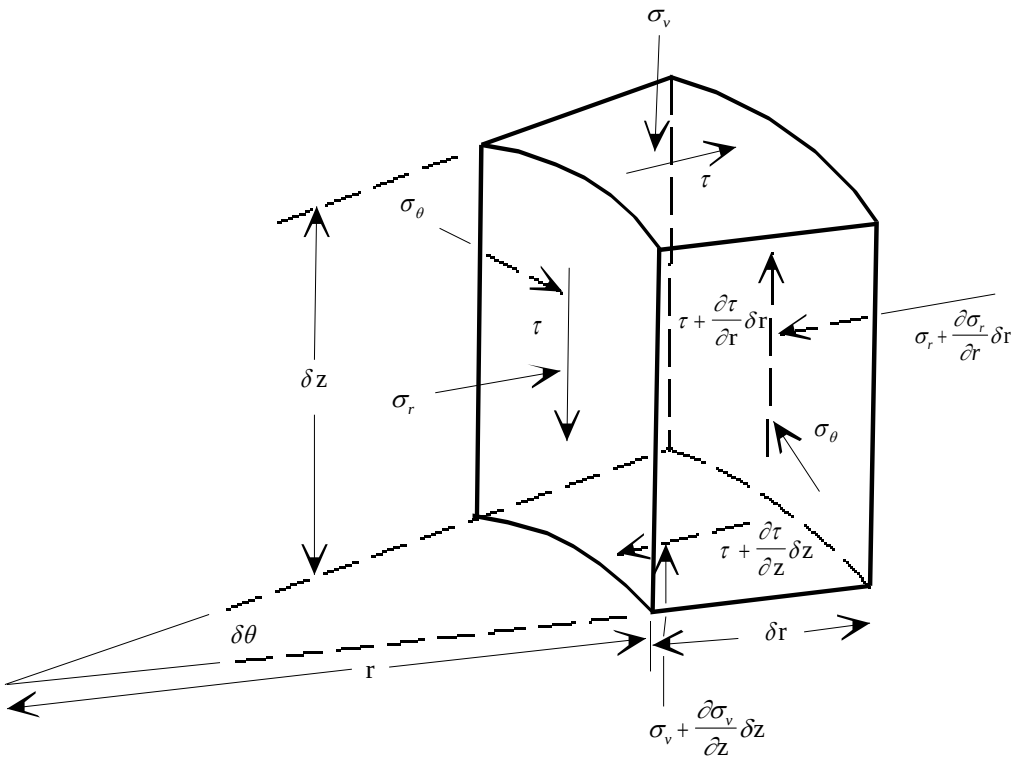

Figure 6.8 Free body diagram of soil element close to pile shaft

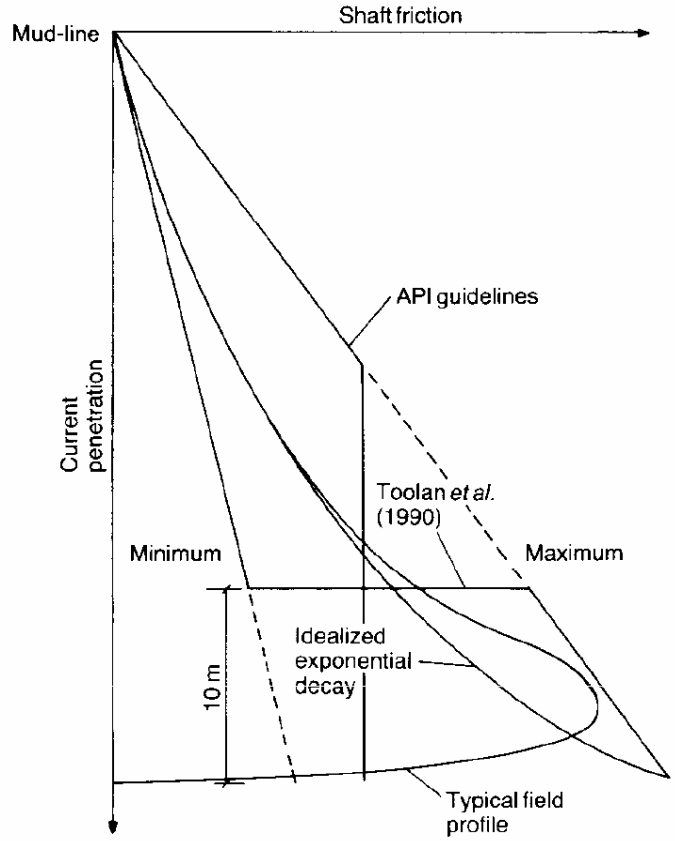

Figure 6.9 Typical profiles of shaft friction with depth (Randolph et al, 1994)

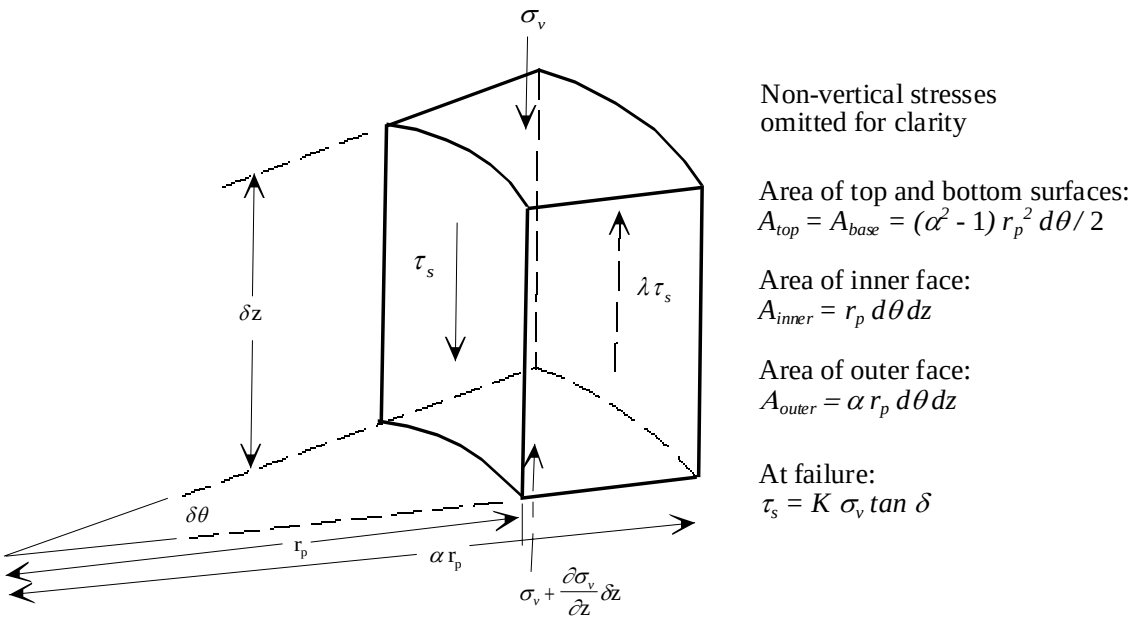

Figure 6.10 Simplified vertical equilibrium of soil element close to pile shaft

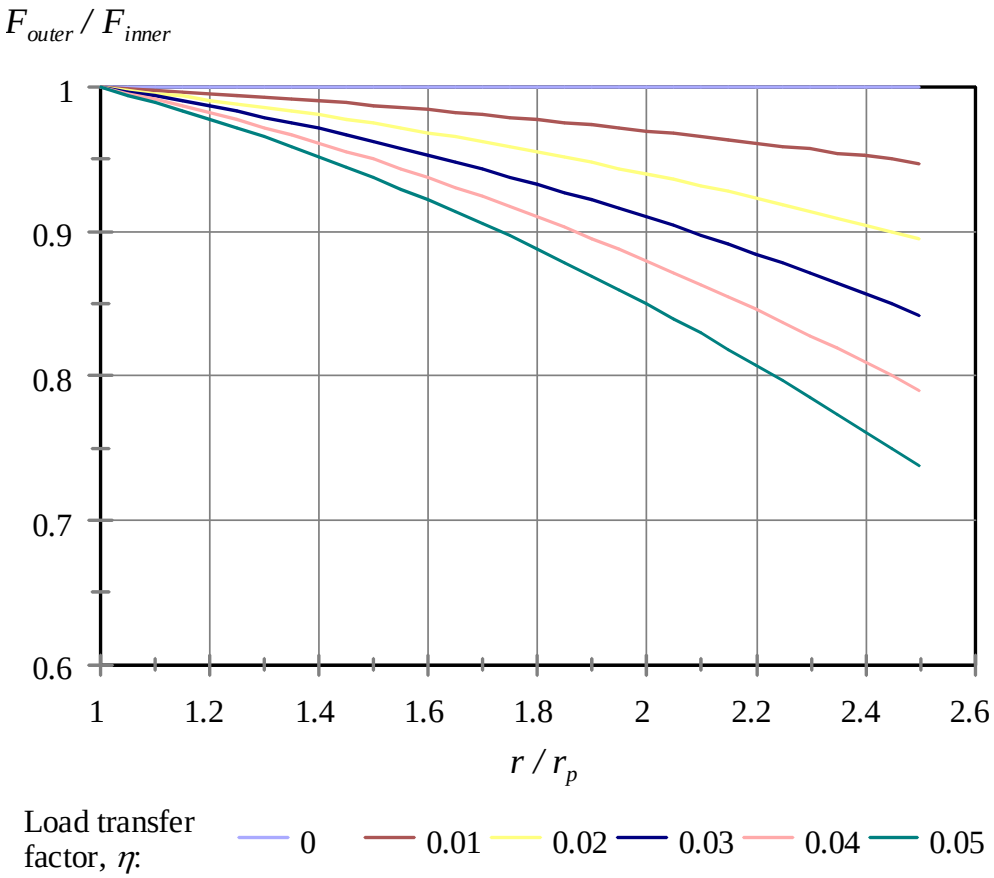

Figure 6.11 Influence of η on load transfer at pile wall

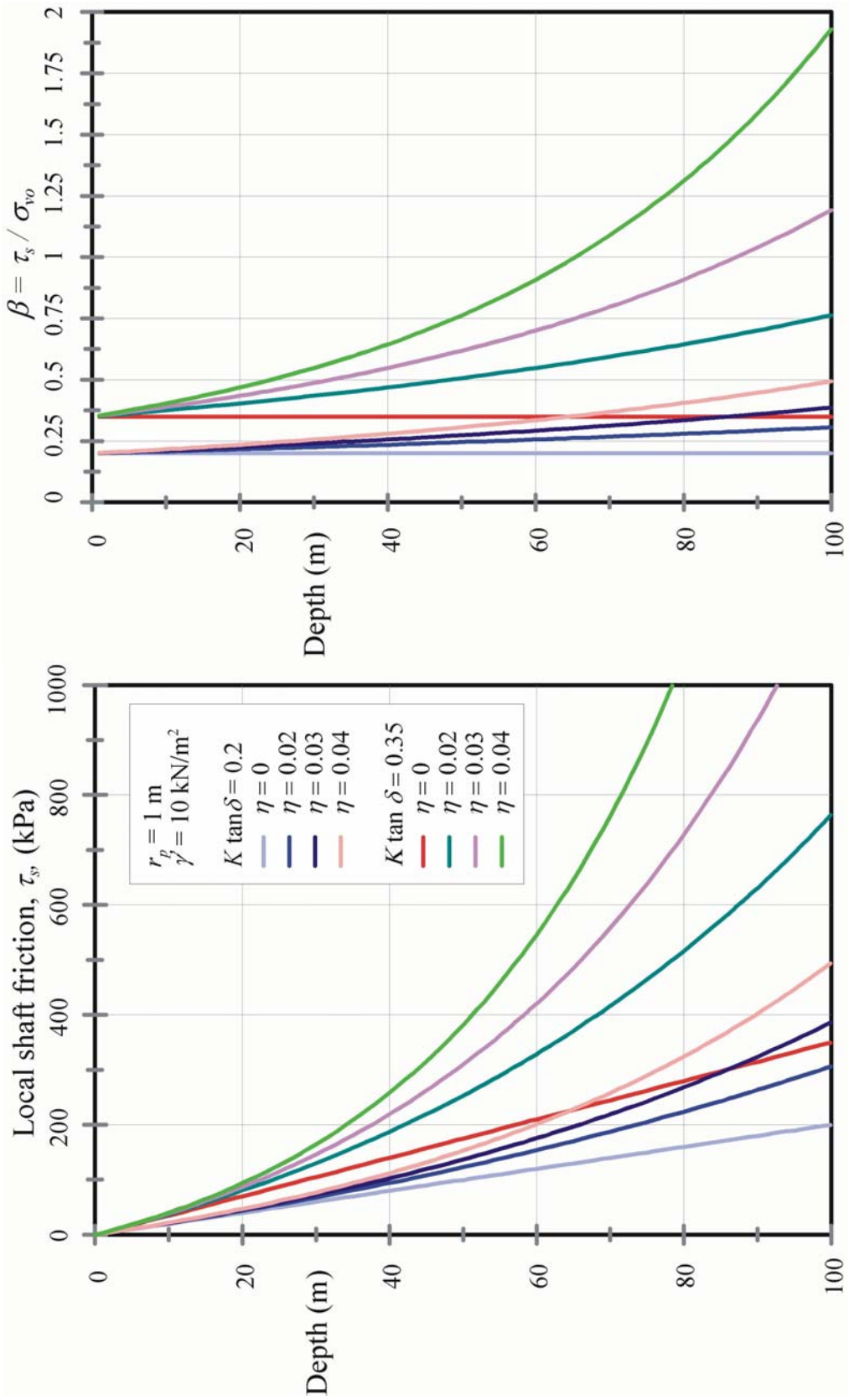

Figure 6.12 Influence of load transfer factor, θ, on shaft friction profile

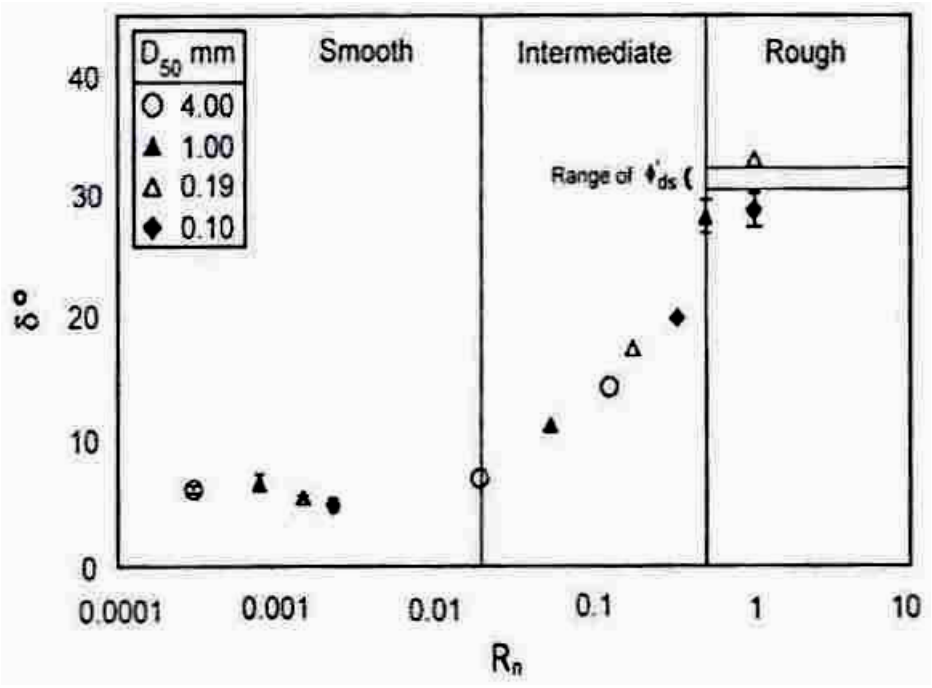

Figure 6.13 Variation of interface friction angle, δ, with normalized roughness, R_n (Paikowsky, 1995)

Amplitude roughness parameters			
R_a	the roughness average, the most universally recognised roughness measure that relates to the arithmetic-mean absolute deviation of the profile from the centre line	$R_a = \frac{1}{L}\int_0^L \lvert f(x)\rvert dx$	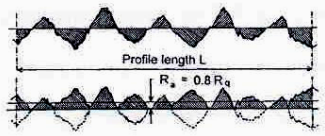
R_q	the root mean square parameter corresponding to R_a. With a Gaussian height distribution, R_q is approximately equal to 0.8R_a	$R_a = \sqrt{\frac{1}{L}\int_0^L f^2(x)dx}$	
R_t	the vertical height between the highest and the lowest points on the profile		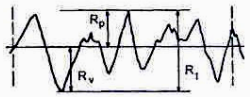
R_p	the highest point of the profile above the mean line		
R_v	the lowest point on the profile below the mean line		
R_{sk}	the skewness of a profile, measures the symmetry of the profile about the mean line, defined with reference to the amplitude distribution curve	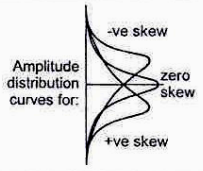	Derivation of the amplitude distribution curve: 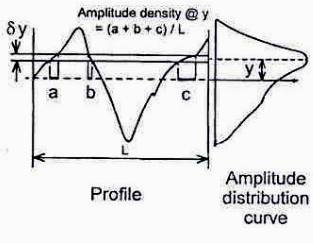
R_{ku}	the kurtosis of the distribution, measures the sharpness of a profile with spikey surfaces having higher kurtosis values than bumpy surfaces, defined with reference to the amplitude distribution curve	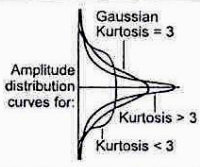	

Figure 6.14 Definition of surface roughness parameters (Dietz, 2000)

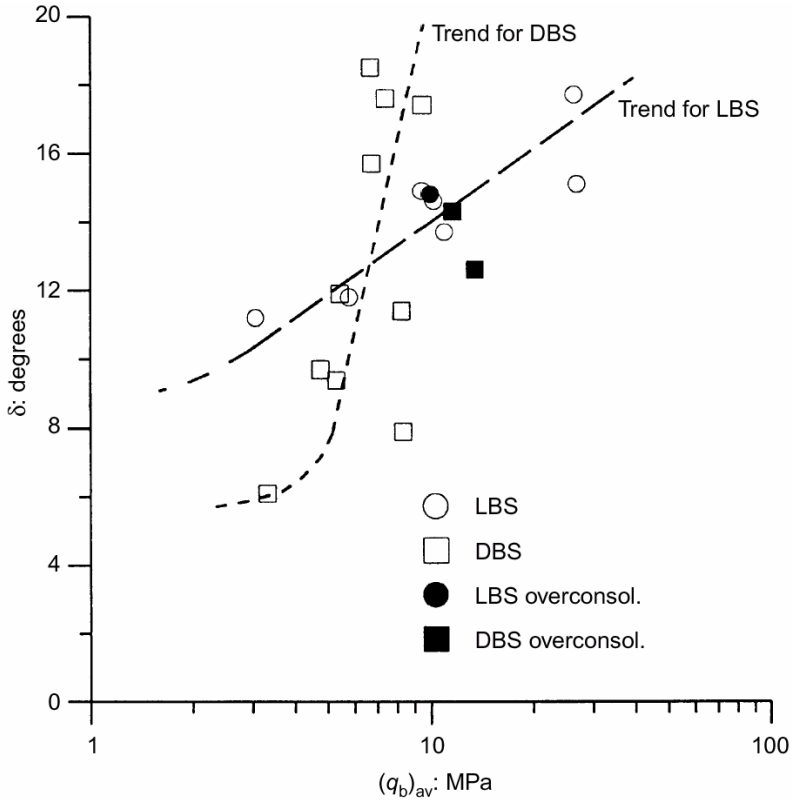

Figure 6.15 Interaction between base resistance and interface friction (Klotz & Coop, 2001)

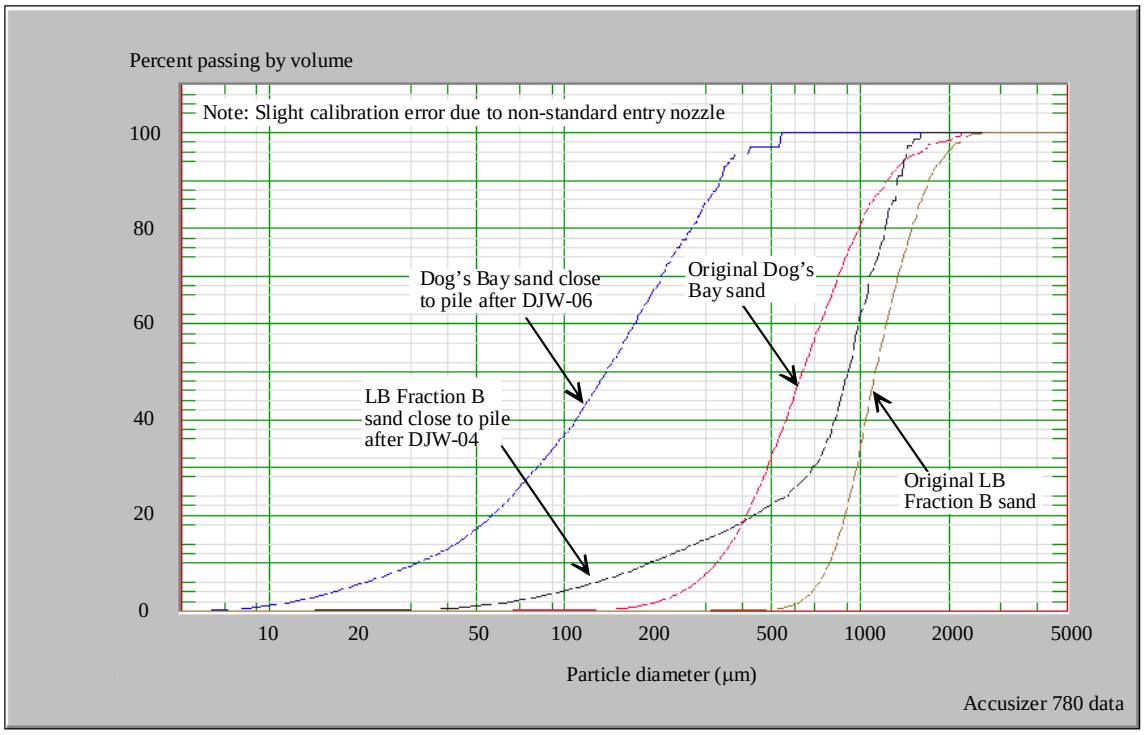

Figure 6.16 Approximate measurements of particle size change during pile installation

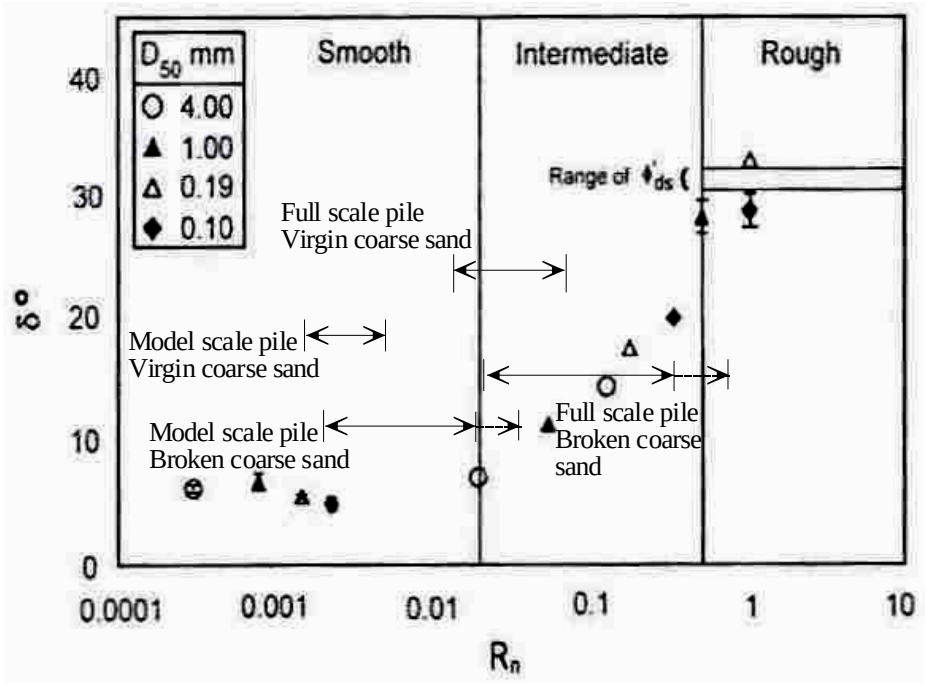

Likely range with improved sampling of thin interface layer

a) Paikowsky *et al.* (1995)

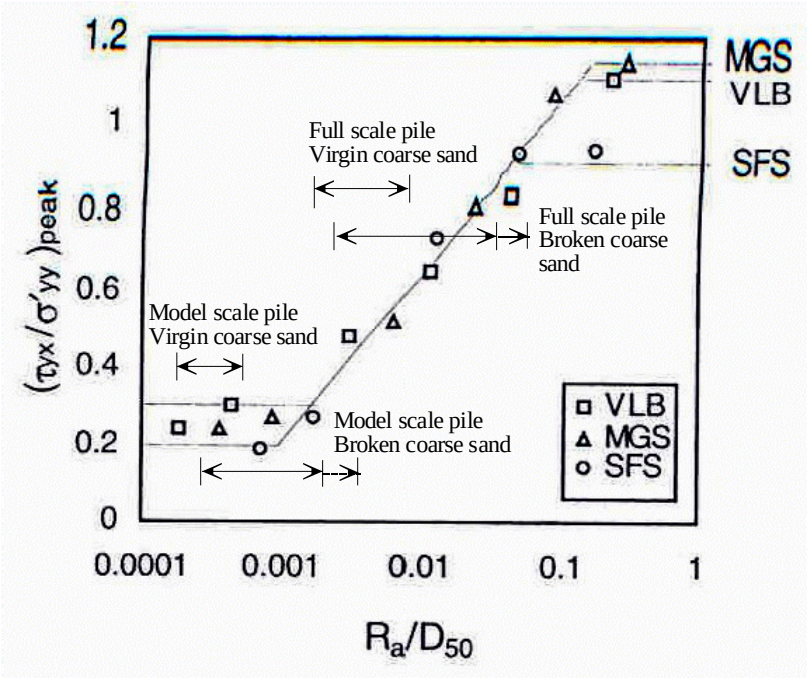

b) Dietz (2000)

Figure 6.17 Typical values of normalized pile roughness plotted against interface angle of friction following Paikowsky *et al.* (1995) and Dietz (2000)

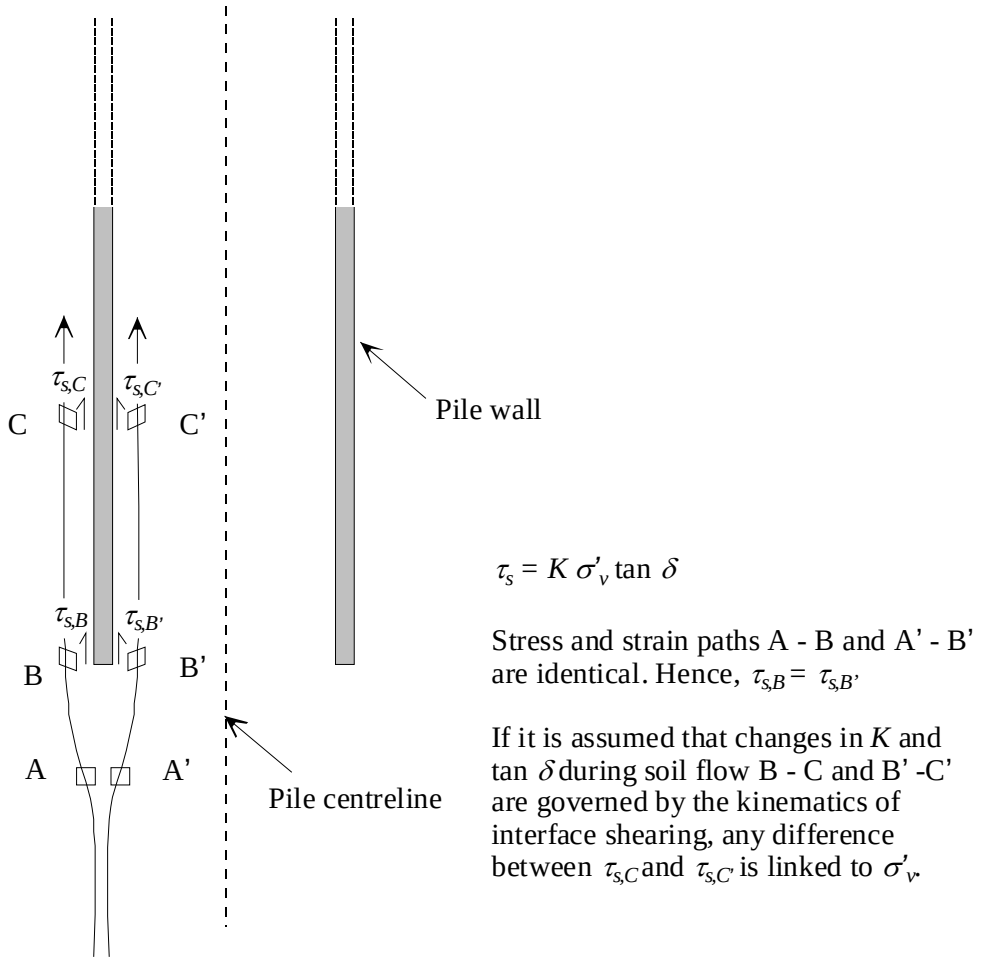

Figure 6.18 Comparison between internal and external shaft friction.

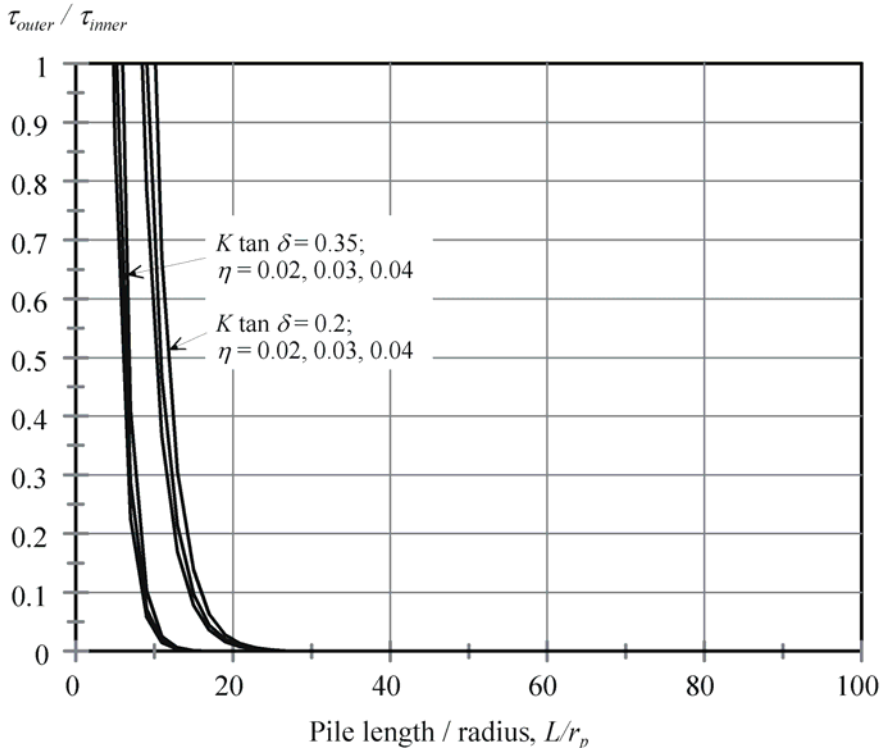

Figure 6.19 Relative magnitude of inner and outer local shaft friction with depth

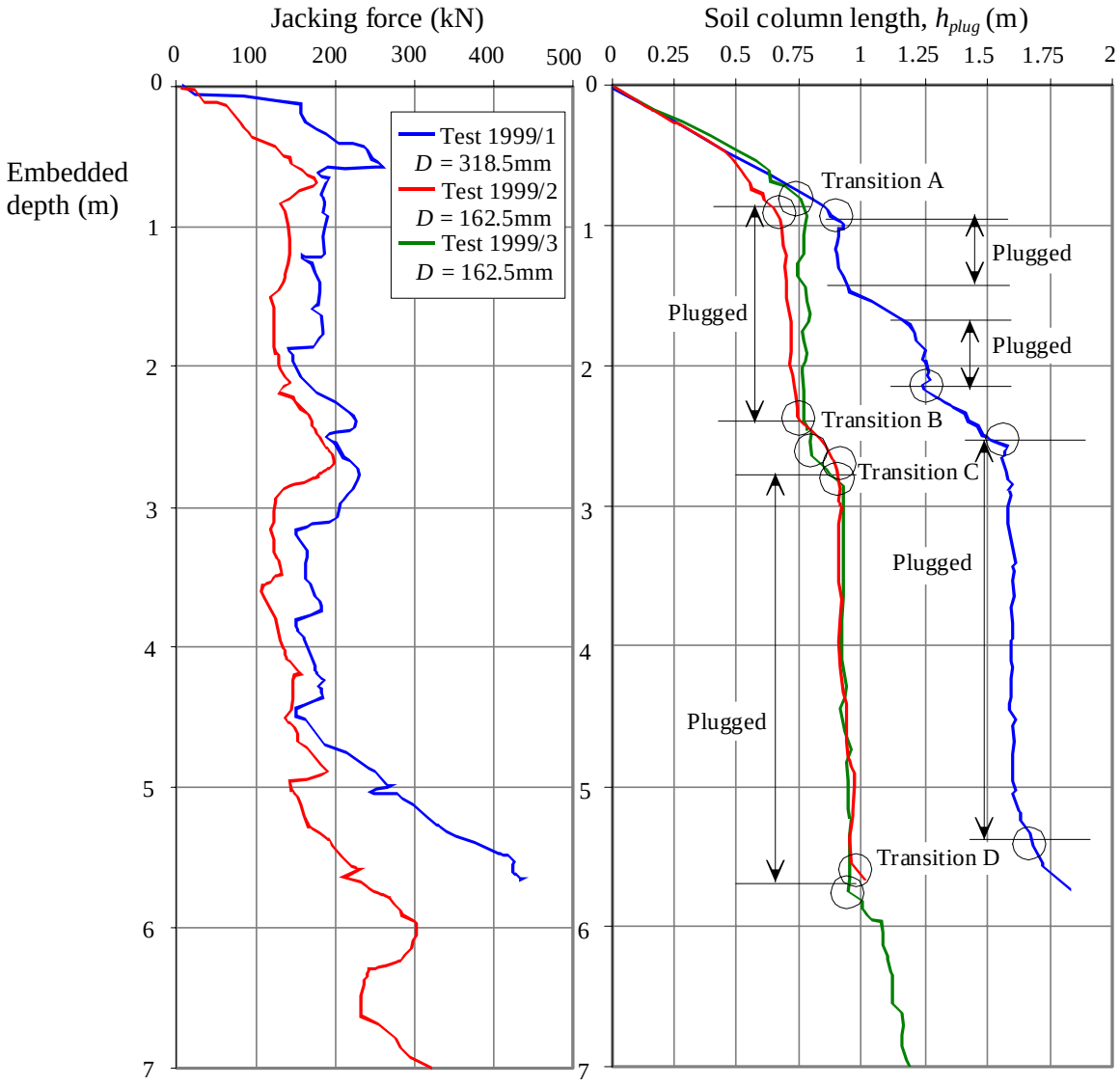

Figure 6.20 Tests 1999/1-3: Jacking force and soil column length vs. embedded depth

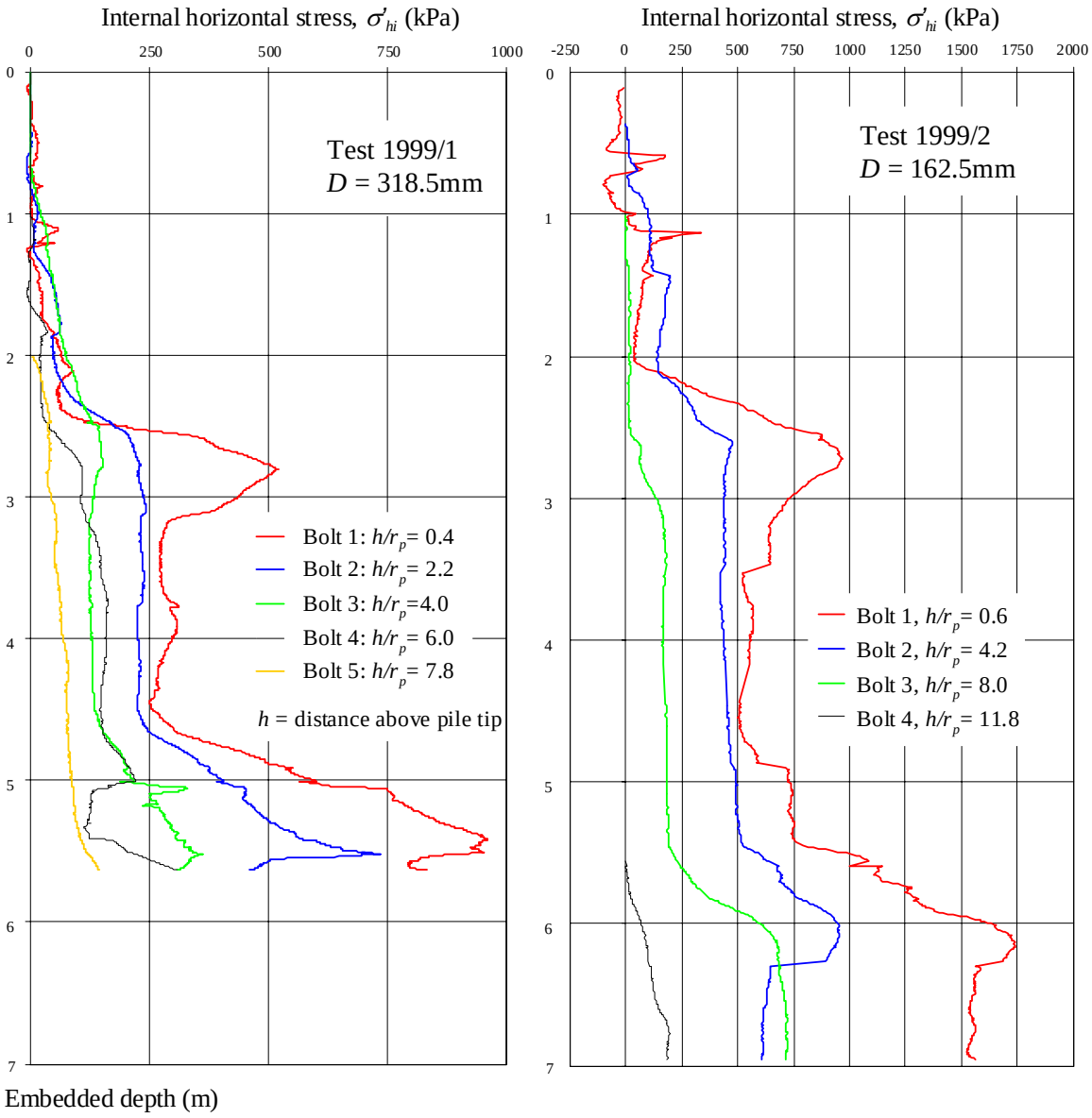

Figure 6.21 Tests 1999/1-1999/2: Variation of internal horizontal stress, σ'_{hi} with embedded depth

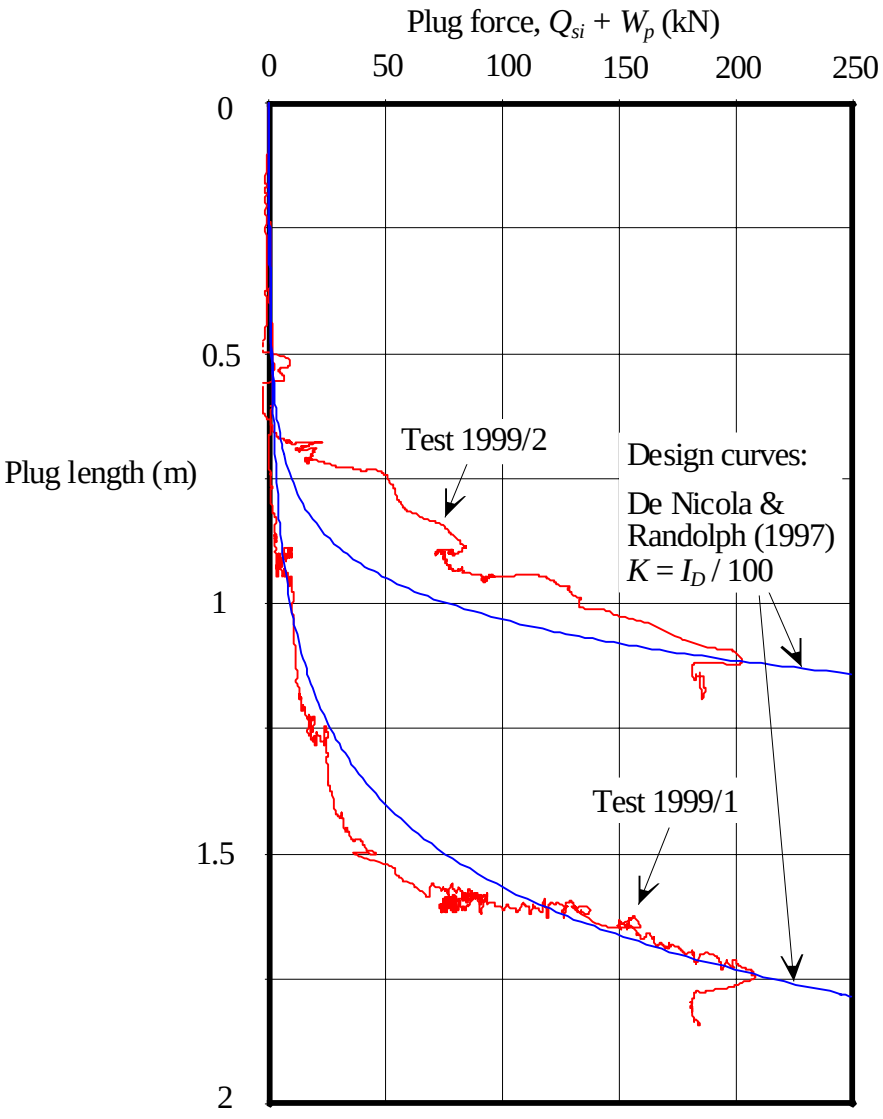

Figure 6.22 Variation of plug force (Q_{si} + W_p) with plug length

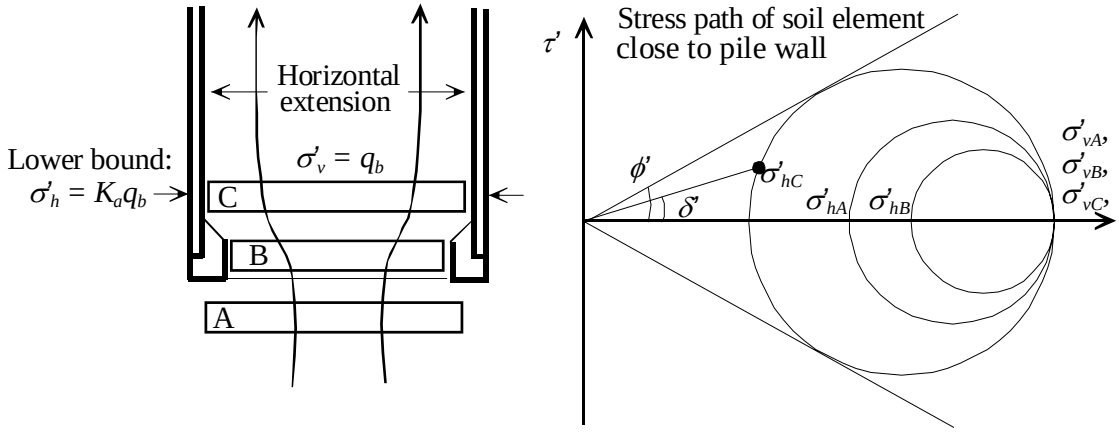

Figure 6.23 Hypothesised stress path at pile tip due to driving shoe

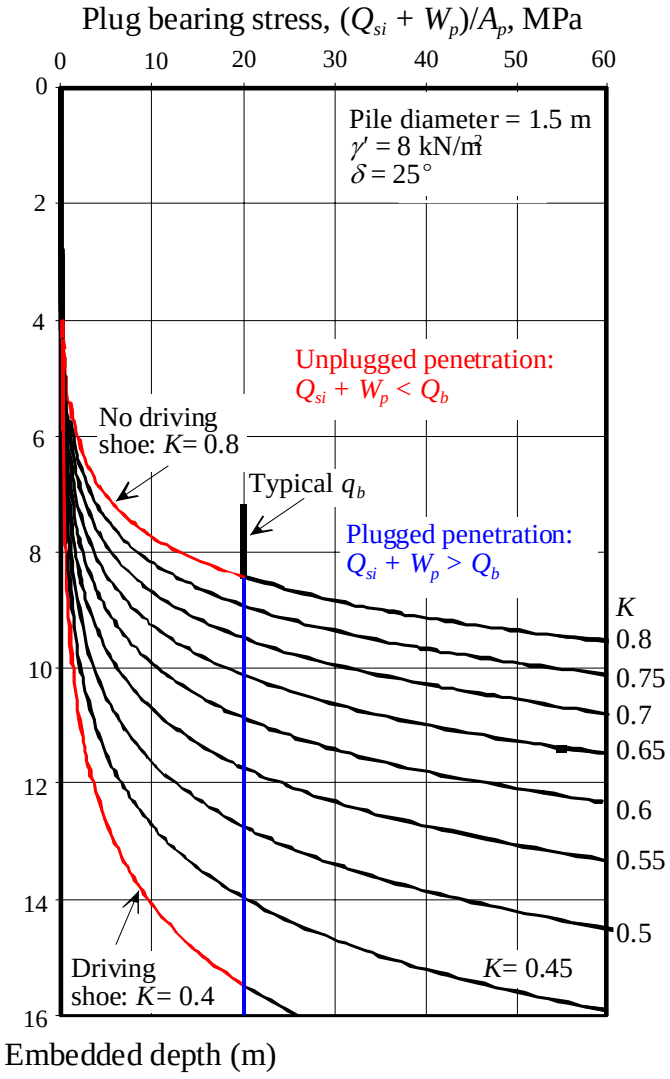

Figure 6.24 Effect of reducing K on plug force

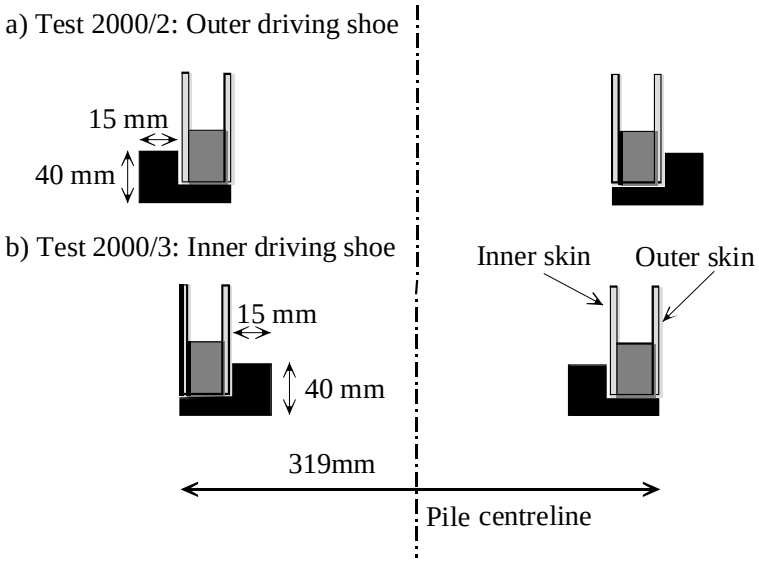

Figure 6.25 Driving shoes used during Summer 2000 fieldwork

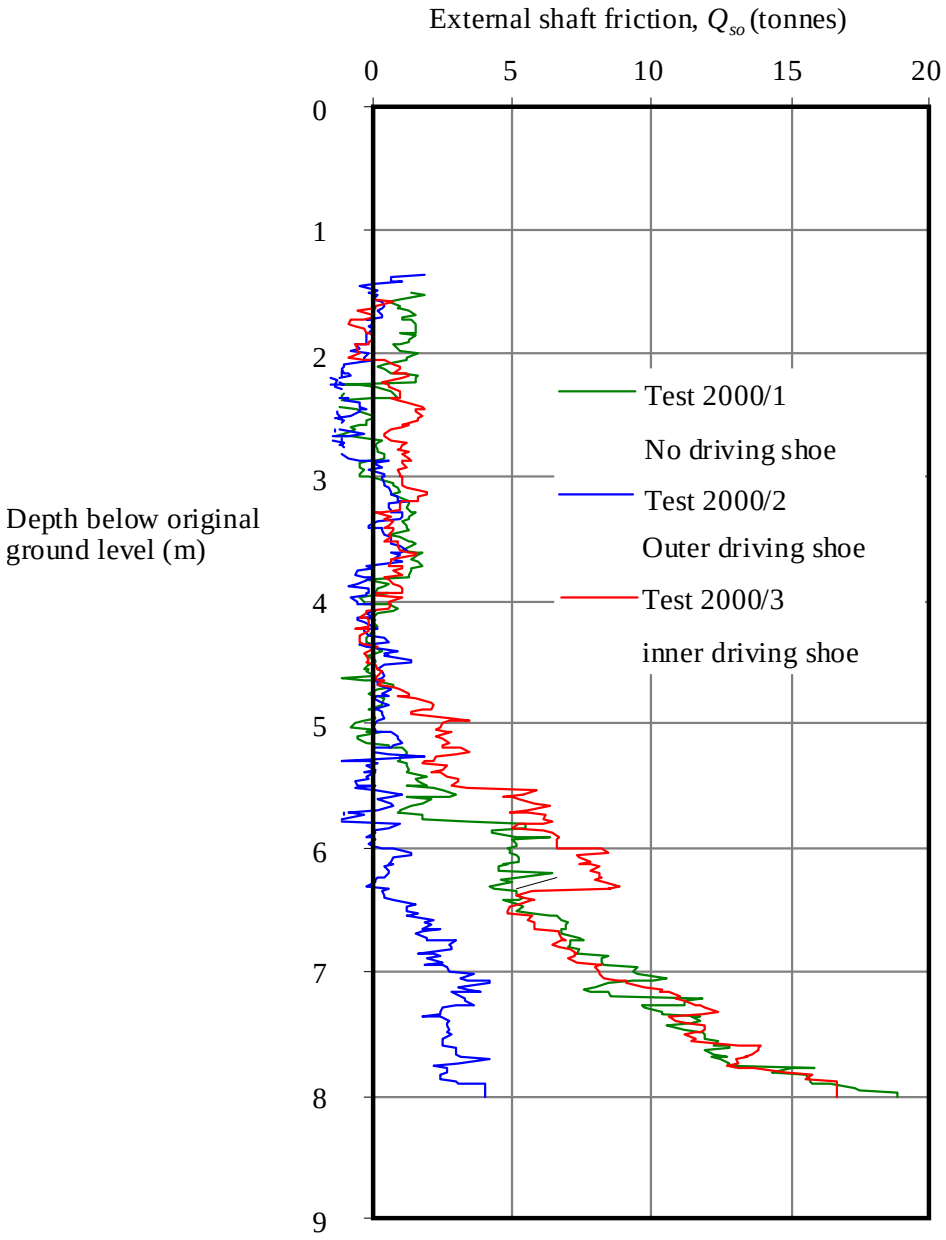

Figure 6.26 Tests 2000/1-3: Total external shaft friction vs embedded depth

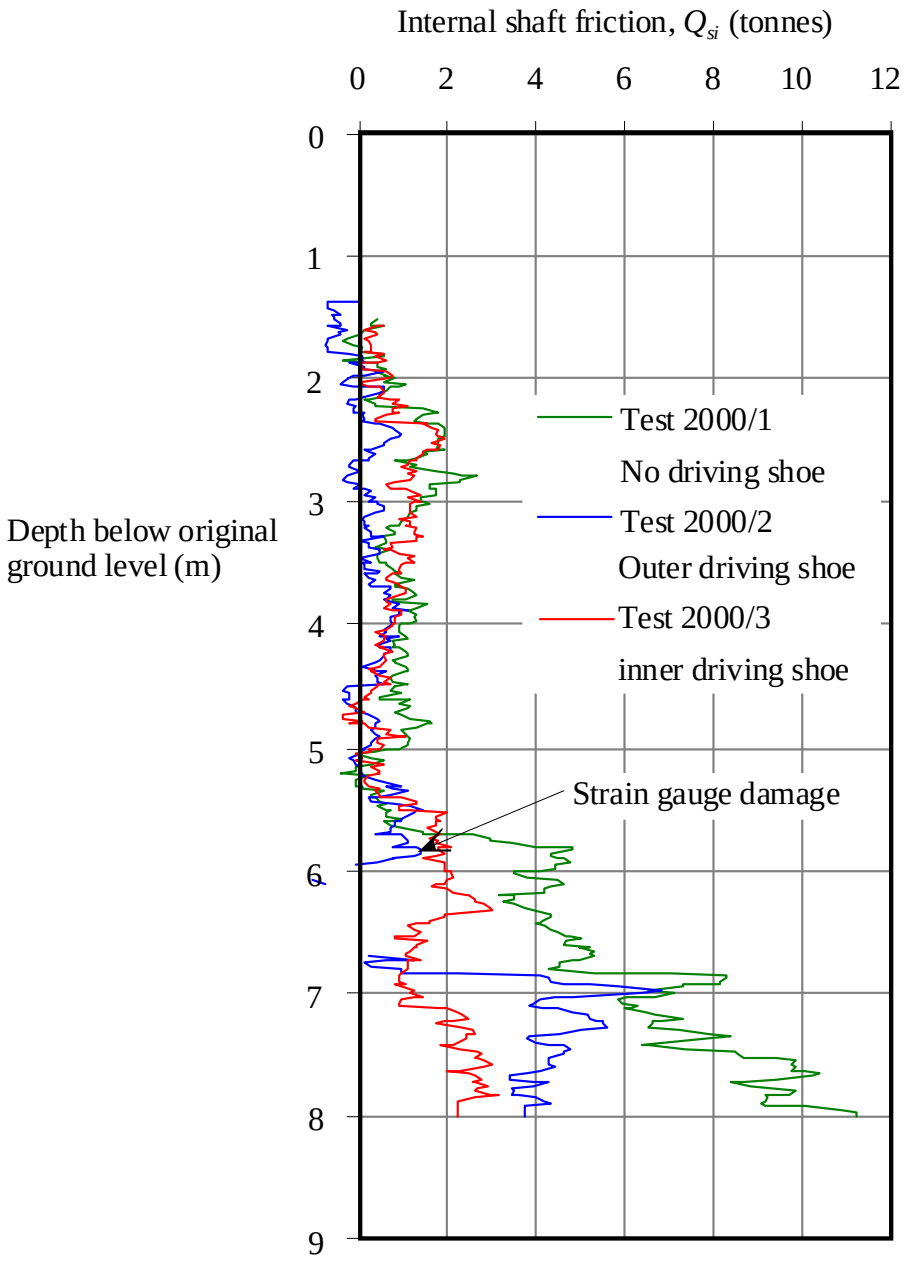

Figure 6.27 Tests 2000/1-3: Total internal shaft friction vs embedded depth

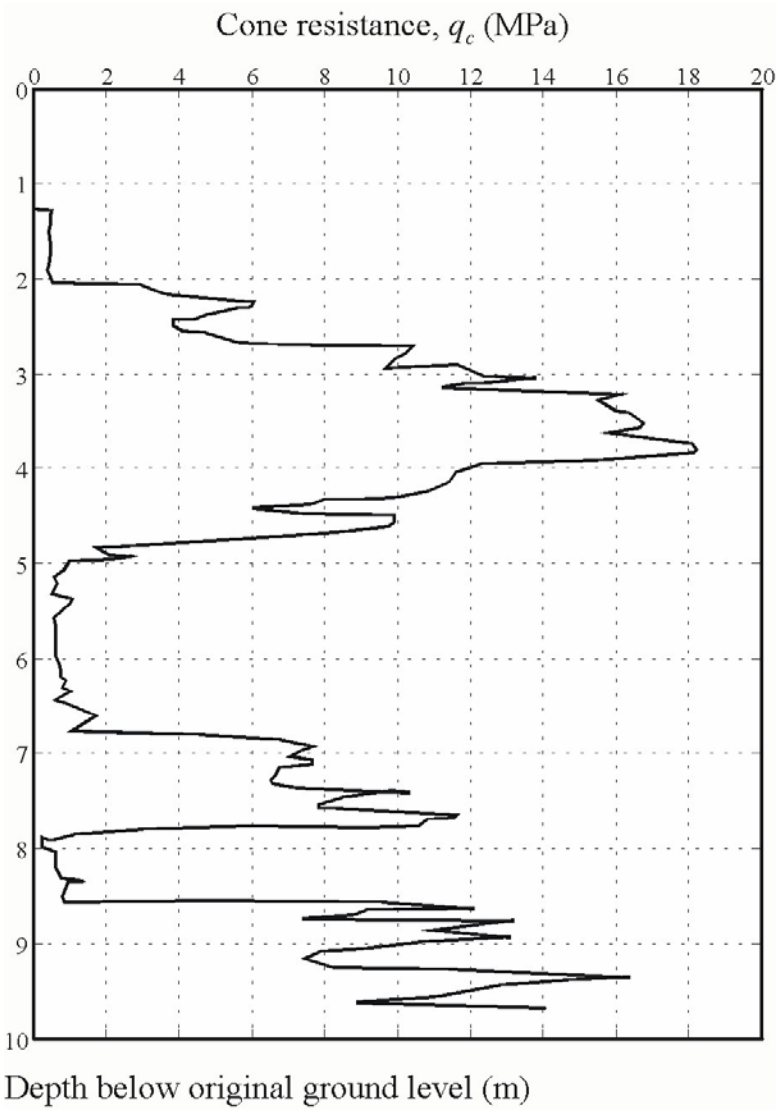

Figure 6.28 CPT profile at the Akaoka test site

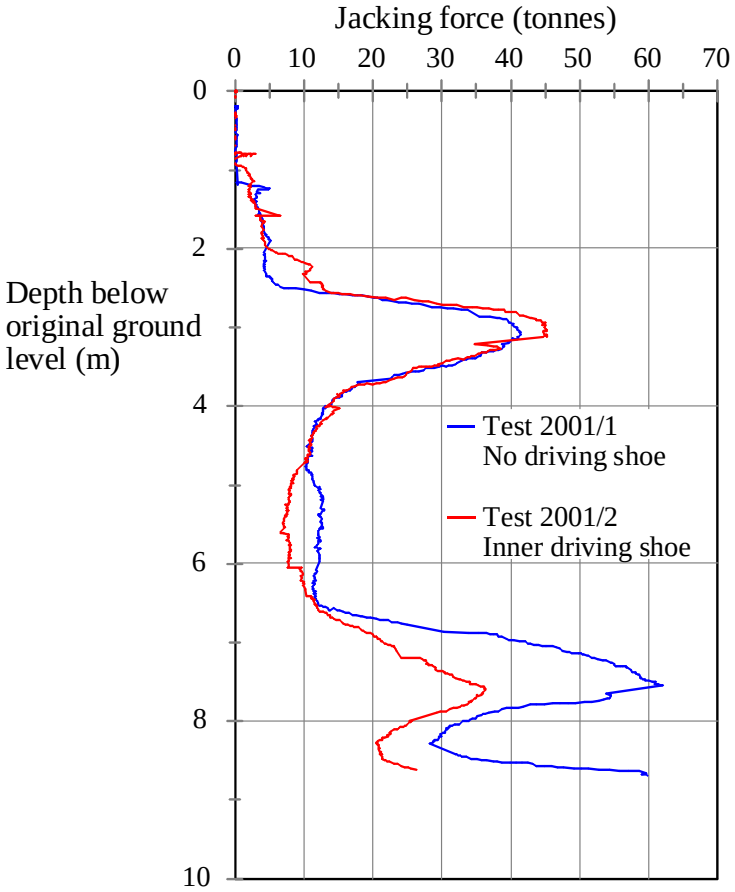

Figure 6.29 Jacking force with and without an inner driving shoe at Akaoka test site

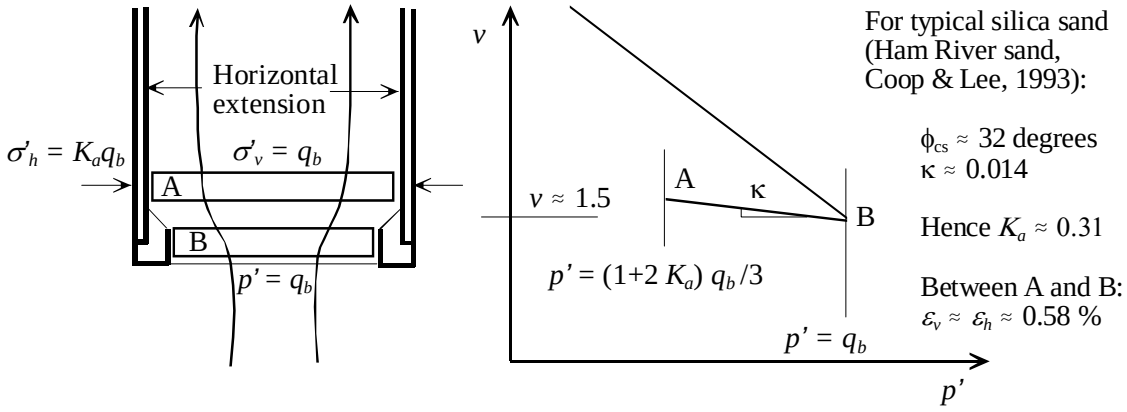

Figure 6.30 Horizontal unloading around a pile shoe

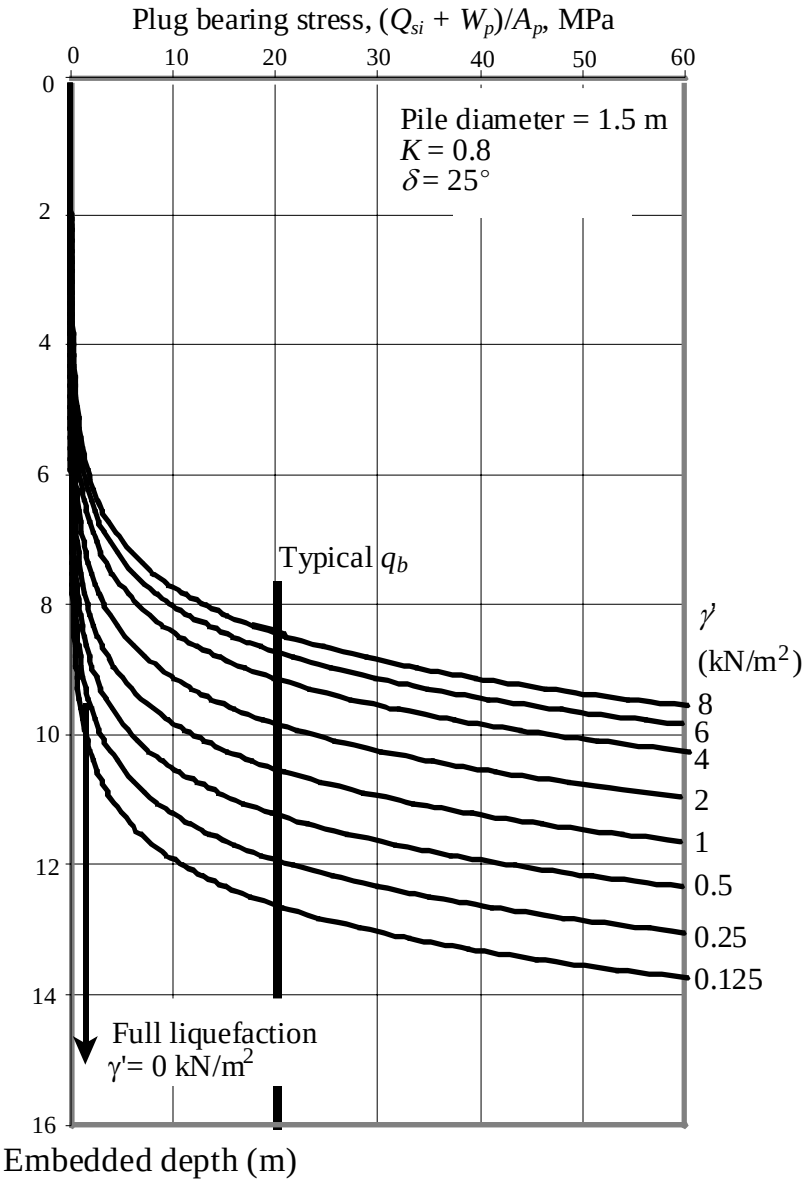

Figure 6.31 Effect of reducing γ' on plug force

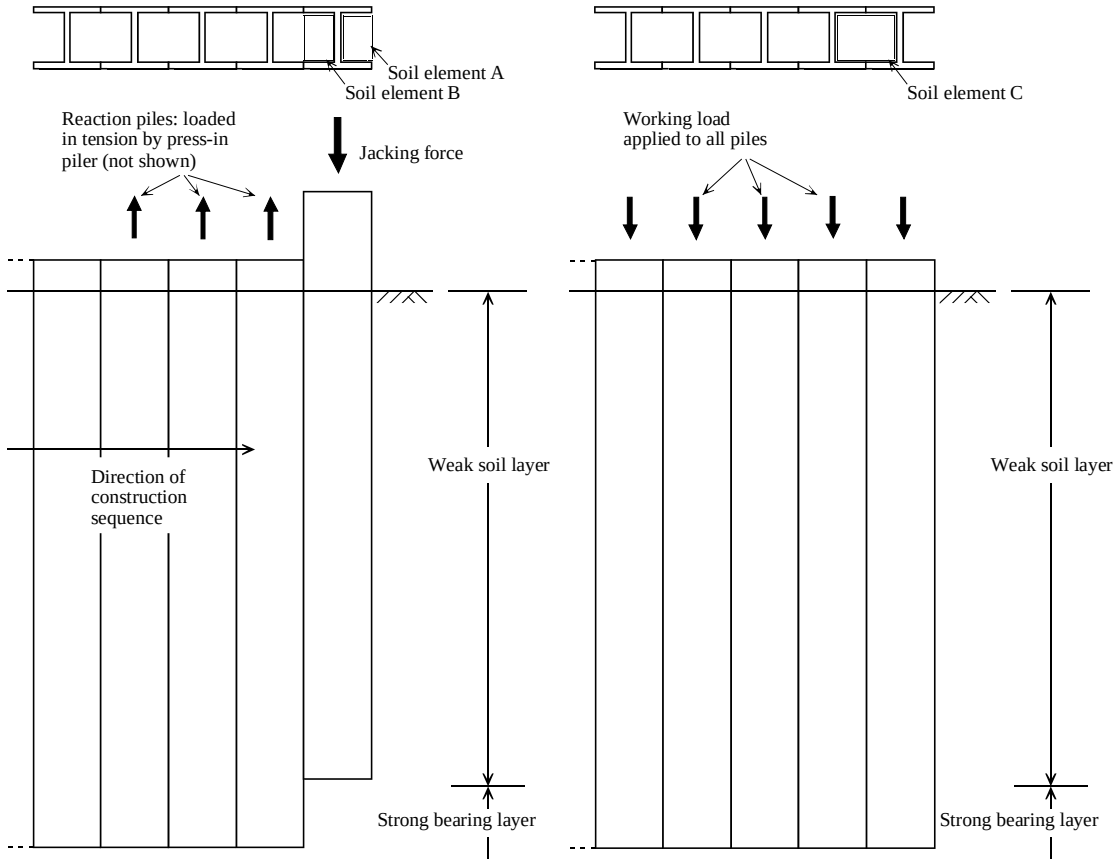

Figure 6.32 A construction sequence which allows arching to be ‘switched on’

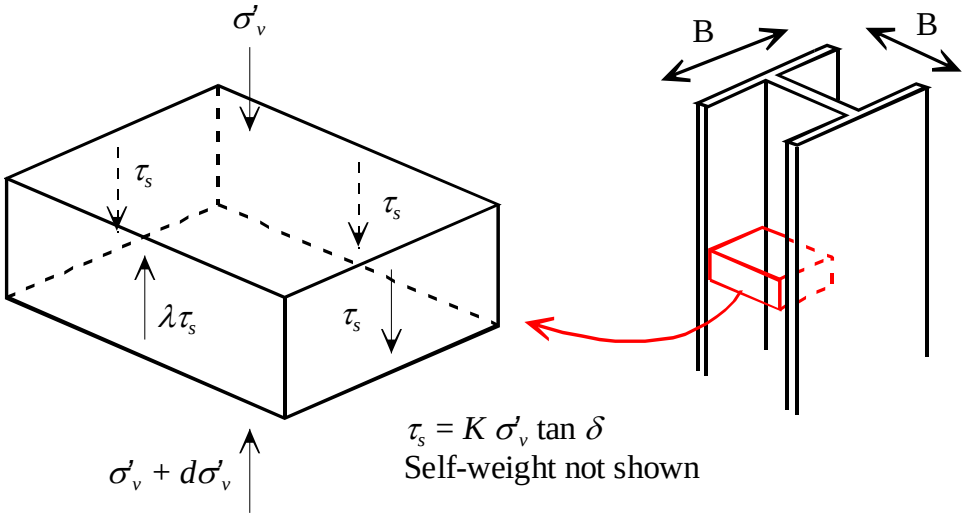

Figure 6.33 Equilibrium of a soil element in the pan of a single H-pile during installation

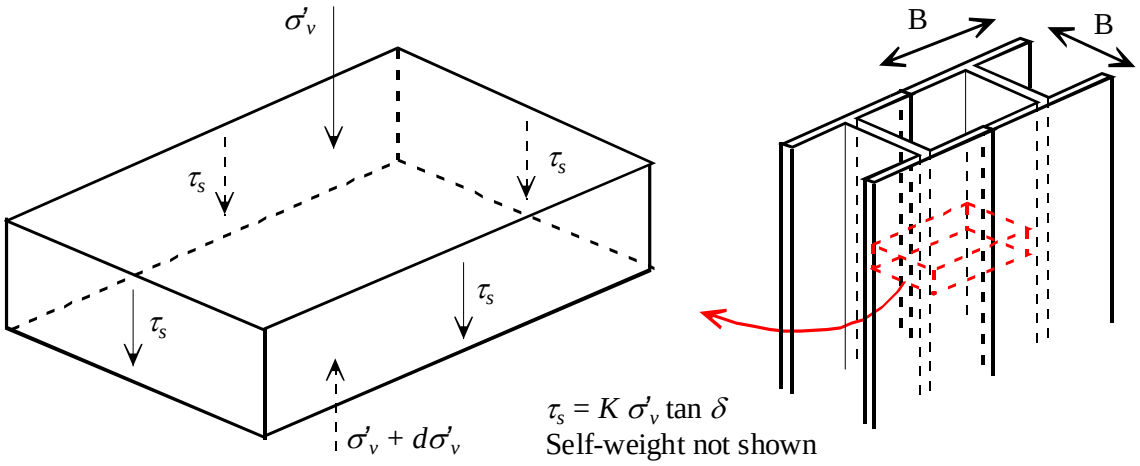

Figure 6.34 Equilibrium of a soil element between two adjacent H-piles under working load

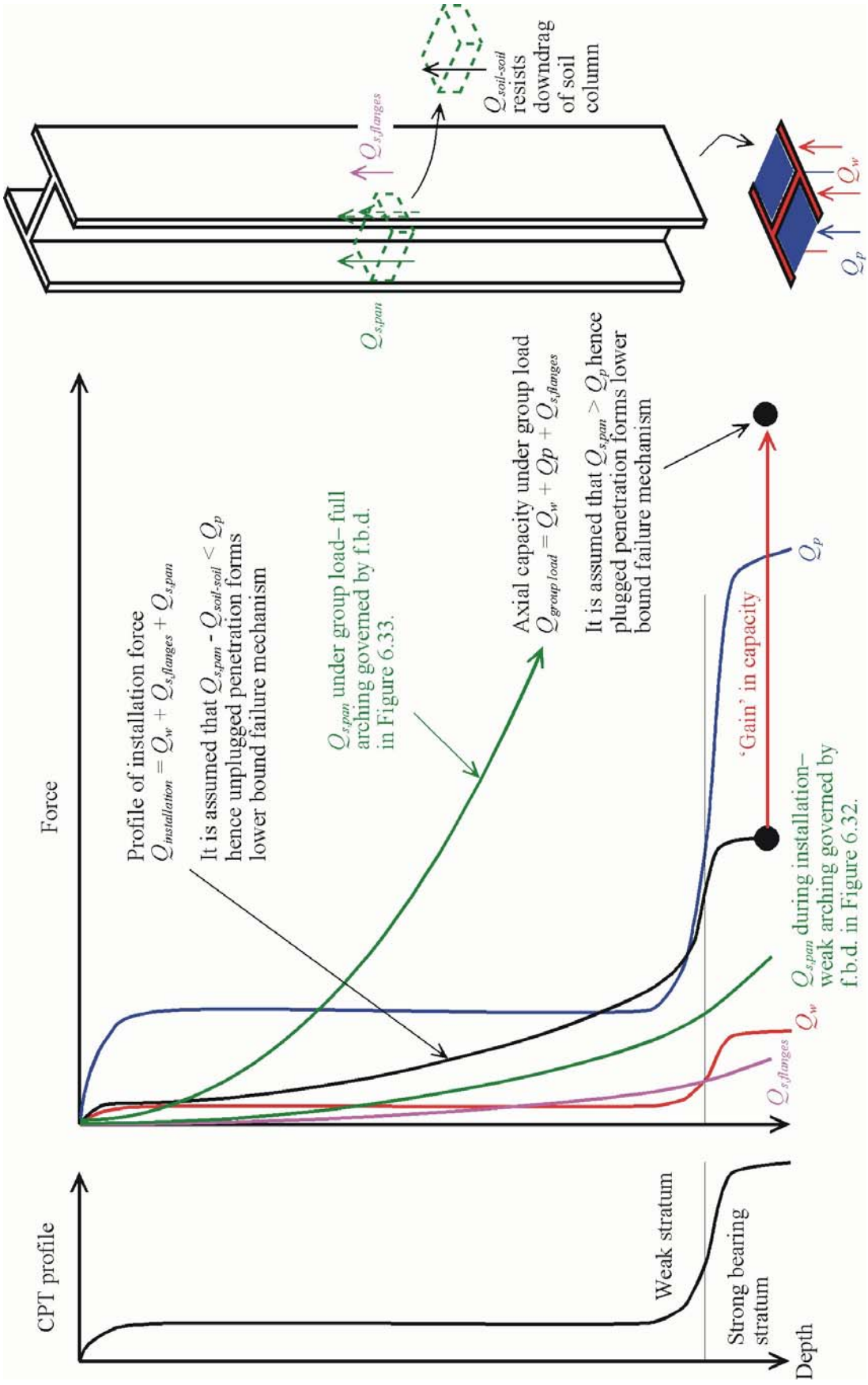

Figure 6.35 'Switching on' arching after installation to improve performance

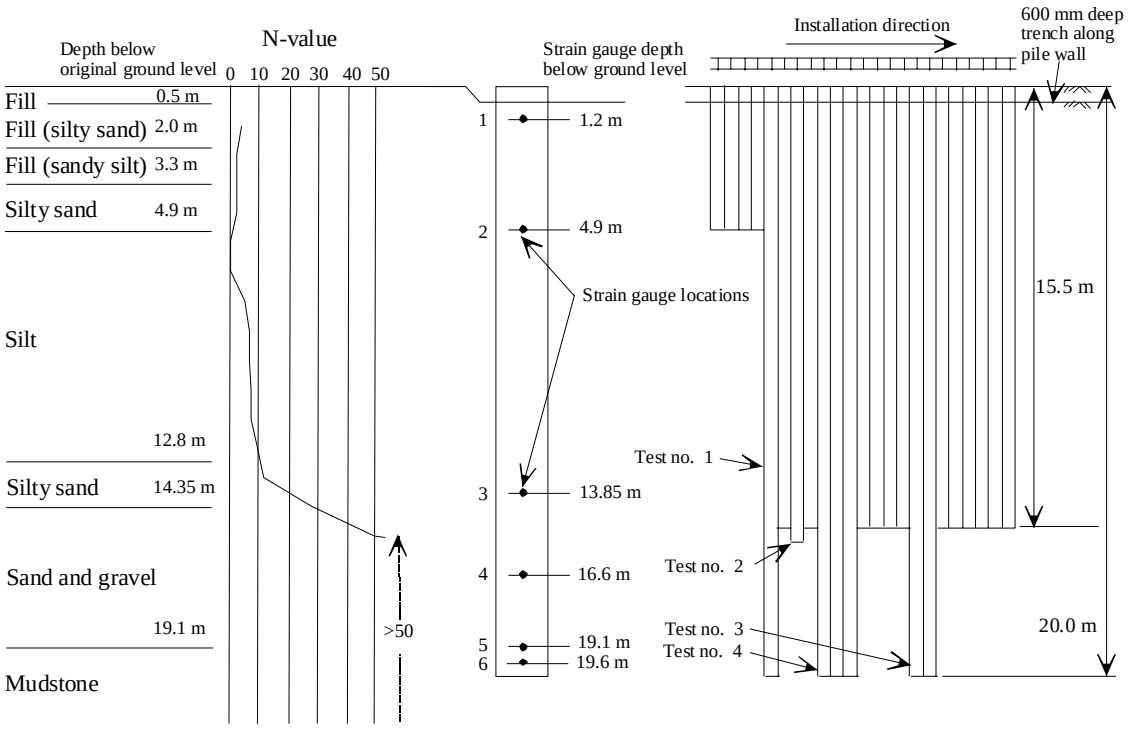

a) Borehole log and SPT data b) General arrangement of test and reaction piles

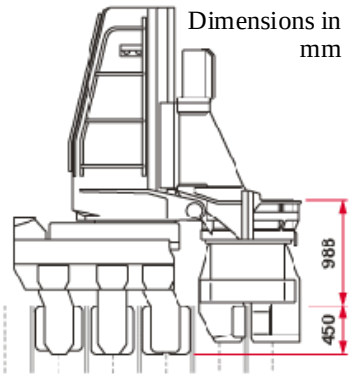

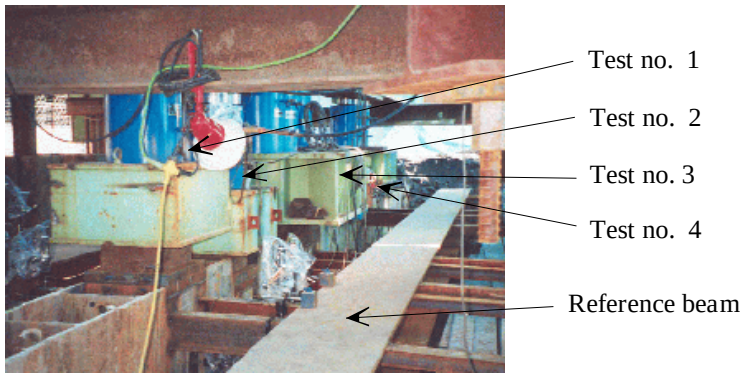

c) HP-150 press-in piler d) Load test arrangement

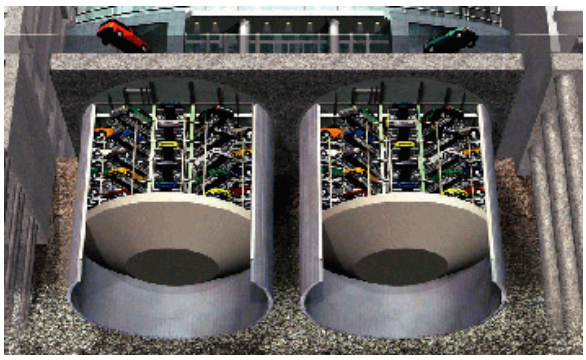

e) Aerial view of load test arrangement f) Proposed foundation design: excavated H-pile caisson

Figure 6.36 Shinagawa loading test arrangement

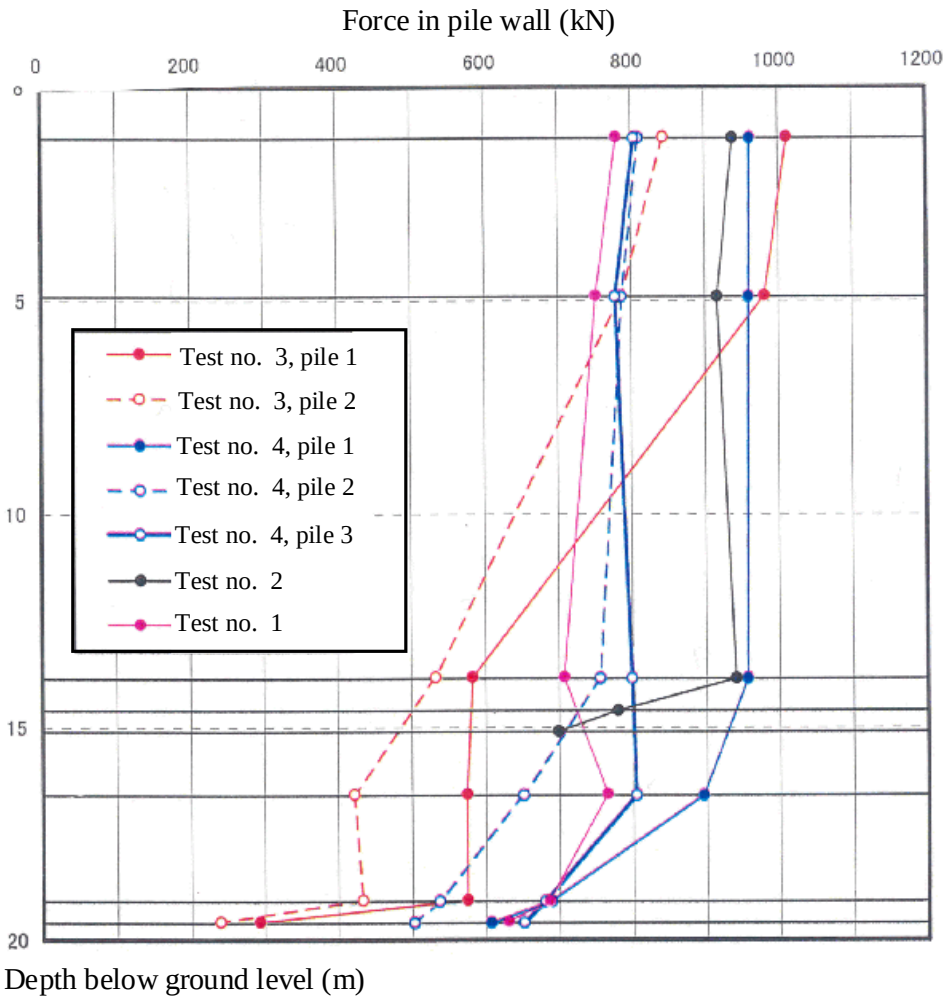

Figure 6.37 Load distribution in Shinagawa test piles at installation to final depth

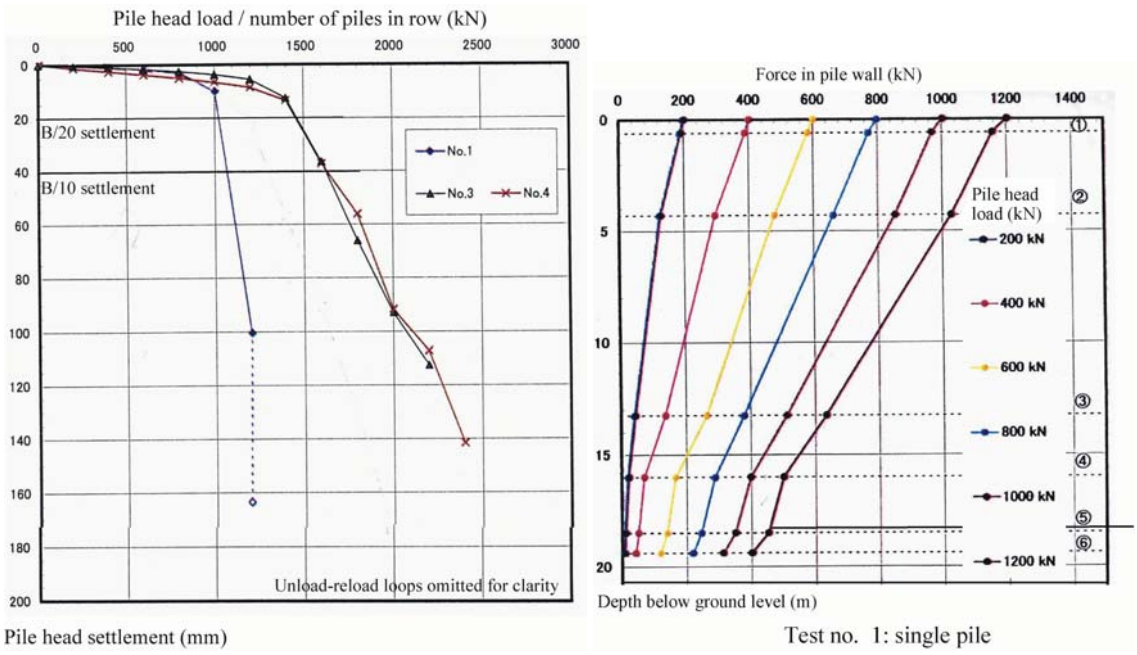

Figure 6.38 Load-displacement and load distribution curves for Shinagawa load tests

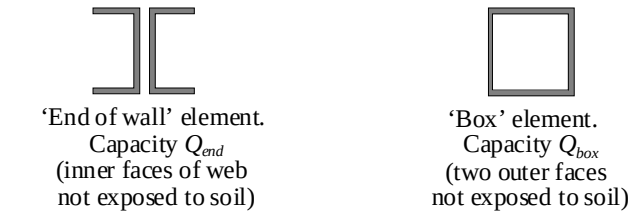

Elementary blocks

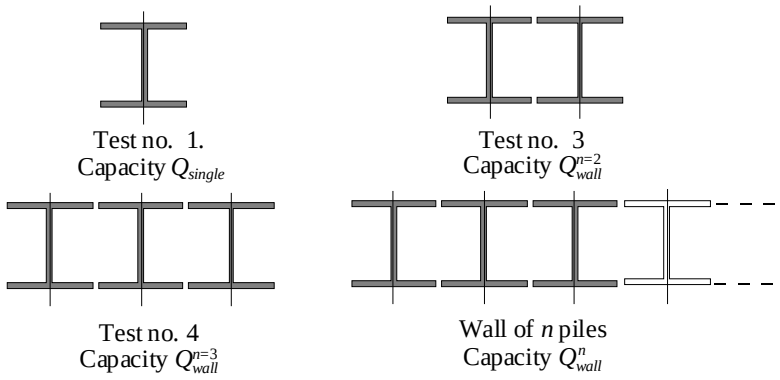

Cross-sections of load tests and wall of n piles

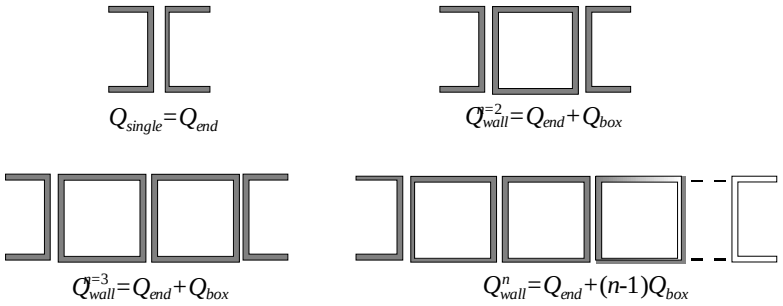

Decomposition of each load test and a
wall of n piles into elementary blocks

Figure 6.39 Decomposition of H-pile wall into 'end' and box' elements

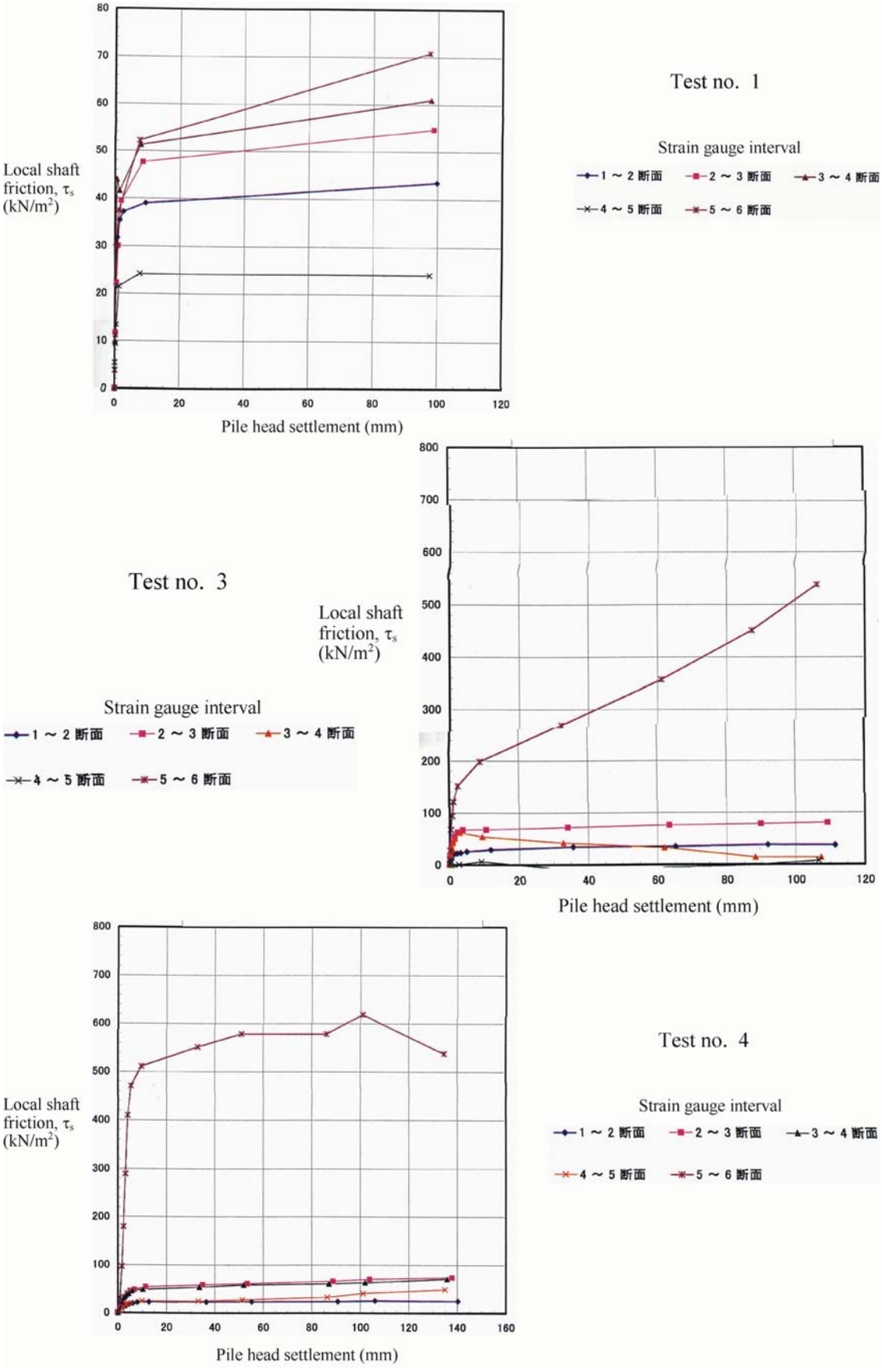

Figure 6.40 Shaft friction mobilisation during Shinagawa load tests

CHAPTER 7

CONCLUSIONS AND FURTHER RESEARCH

7.1 INTRODUCTION

Interim conclusions have been presented throughout this dissertation. To avoid repetition, this Chapter presents only the main conclusions from each phase of research. These conclusions are followed by some discussion of future research that could build upon this work.

7.2 DEFORMATION MEASUREMENT TECHNOLOGY

A new system for the measurement of soil deformation in geotechnical physical modelling has been developed. This system combines techniques of digital photography, Particle Image Velocimetry (PIV) and close range photogrammetry. The need for target markers within the observed soil is eliminated by using PIV to track the texture of the soil itself. The conversion of image-space data to object-space coordinates is carried out using principles of close range photogrammetry. This conversion overcomes the errors inherent in previous systems that assume a constant image scale. In addition, such image calibration allows apparent displacement due to camera movement to be separated from actual displacement.

A series of validation experiments were conducted to evaluate the performance of the new system. The precision and accuracy of the resulting displacement measurements was found to significantly exceed the current state-of-the-art. This improved

performance is achieved alongside an order-of-magnitude increase in the number of measurement points that can be established within the observed soil.

The resulting deformation data is of sufficient quality to allow both strain fields and strain paths of individual soil elements to be quantified. To resolve the large deformations present during pile installation, a strain algorithm that includes polar decomposition of strain and rotation has been implemented.

7.3 GROUND MOVEMENTS DURING PILE INSTALLATION

A plane strain calibration chamber was constructed to allow the installation of a displacement pile to be modelled at the correct stress level, whilst permitting the resulting ground movements to be observed. A series of 8 tests is reported. Model piles were installed into carbonate and silica sand at dense and loose initial states. The influence of pile breadth and the use of a driving shoe was investigated.

A steady state penetration mechanism was reached, during which the pattern of soil displacement around the advancing pile did not vary with depth. A constant value of base resistance with depth was encountered in carbonate sand. A gentle increase in base resistance was encountered in silica sand, probably due to the influence of the approaching chamber base boundary.

The observed pattern of displacement was used to deduce strain paths during pile penetration, and the distribution of strain around the installed pile. Although the boundary conditions applied during this plane strain model testing are different to most field scenarios, they are well defined. Therefore, numerical or analytical approaches to field problems should be verifiable against this data.

A key feature of the near and far field strain paths was a reversal of strain direction as the soil passes out from the zone of high stress beneath the pile. This general shape of strain path is as predicted by the Strain Path Method (SPM). However, complex volumetric behaviour is observed in the near field, which is beyond the scope of SPM analysis.

A study of the soil fabric close to the pile tip and along the pile shaft revealed dramatic changes in particle size distribution. Reconstitution of the broken soil indicated significant irrecoverable volume changes. The resulting large reduction in maximum void ratio indicates that the broken soil might be considered as a new material. Also, the relative roughness of the pile-soil interface, when considering the changes in particle size caused by pile installation, is higher than if calculated using the virgin particle size distribution.

Contraction of the zone of soil immediately adjacent to the pile shaft is observed with continued penetration. The inward displacement permitted during this contraction is of the order of a single grain diameter. This movement permits horizontal extension within the soil adjacent to the pile and hence relief of lateral stress acting on the pile. Although this inward movement is only small, the reload stiffness of the heavily over-consolidated soil is very high, leading to a significant reduction in lateral stress. This mechanism provides an explanation for the distribution of shaft friction close to the pile tip.

7.4 THE BEHAVIOUR OF PRESSED-IN PILES

A review of current literature highlighted the distribution of local shaft friction as a key source of uncertainty relating to the behaviour of displacement piles in sand.

Two models to describe the variation of local shaft friction along a pile shaft have been presented. Firstly, the calibration chamber testing revealed contraction of the interface zone leading to relief of lateral stress, as described in Section 7.3. The resulting local shaft friction at a given soil horizon is therefore a function of distance behind the pile tip; this phenomenon is often referred as friction fatigue. This mechanism of behaviour is imitated by element testing in interface shear apparatus. Existing data within the literature suggests that cyclic loading, as induced during dynamic pile installation, leads to greater contraction and thus increased friction fatigue compared to monotonic shearing. Recently published pile load test data supports this hypothesis.

Secondly, a theoretical analysis for the shaft friction distribution along a pile has been developed. This analysis combines the equilibrium of a circumferential element adjacent to the pile shaft with an empirical estimation of the vertical load transfer. This vertical arching solution predicts a gentle exponential increase in local shaft friction with depth, which is in agreement with field observations. This analysis contrasts with previous prediction methods by linking the variation in local shaft friction to a variation in vertical effective stress, rather than a variation in horizontal earth pressure coefficient

Four series of field tests are reported. The first test series examines the plugging behaviour of tubular piles. It is shown that internal shaft friction is well predicted by vertical arching theory, if the entire plug length is considered to be active. This is in contrast to dynamically-installed piles, for which the construction process can lead to loosening of the upper part of the plug. Therefore, large settlements are required before the internal shaft friction on the upper section can be mobilised.

7.5 THE CONSTRUCTION OF PRESSED-IN PILES

Since vertical arching evolves according to an exponential relationship, a large reduction in internal shaft friction can be achieved through only a small change in the governing parameters. Whilst this sensitivity hampers design, it aids optimisation of the construction process for ease of driving.

The second and third series of field tests explored techniques for improving the driveability of pressed-in piles. It was demonstrated that the use of a driving shoe with a relatively small overhang can reduce the jacking force required for installation.

The final test series, conducted at Shinagawa, Tokyo, examined the possibility of ‘switching on’ the high internal shaft friction created by vertical arching through a novel geometry of foundation. A wall of adjacent steel H-piles was installed and load tests conducted on individual piles and on rows of two and three. The results revealed a high positive group effect as predicted by vertical arching theory and in contrast to conventional pile analysis.

As a result of internal shaft friction governed by vertical arching, H-pile walls constructed by the press-in method to exhibit a greater capacity under a working load than was evident during their installation. The strength of the completed foundation is greater than the sum of its parts.

The Shinagawa tests demonstrate that a ring of H-piles installed by the press-in method offers a very efficient and economic foundation solution. High capacity is gained through the mobilisation of vertical arching after installation. Low environmental disturbance is created by during the construction process. Minimal space is required by the small press-in piler.

7.6 FURTHER RESEARCH

7.6.1 Improved measurement of deformations in geotechnical testing

The use of PIV analysis to measure deformation has a wide variety of possible applications. The system developed during this research has already been applied to centrifuge modelling (Take, 2002) and element testing (De Jong et al, 2003). The improved precision and increased number of measurement points permit pre-failure deformations and localisation to be investigated. The technique could in future be applied to dynamic phenomena, through the use of high-speed photography.

7.6.2 The prediction of foundation behaviour: base resistance

Prediction of the ultimate base resistance and base stiffness of displacement piles has previously been hampered by the unknown nature of the penetration mechanism. This research has revealed the actual strain path during pile installation. In addition, the base resistance required to maintain this steady penetration mechanism has been measured.

The measured displacement field and resulting base resistance are linked by the constitutive behaviour of the sand. The question remains- which aspects of the constitutive behaviour govern? This question could be addressed by an analysis in the form of a work approach in which a stress field around the pile is assumed, and the energy dissipation along the streamlines of soil flow is calculated. A parametric study

could be conducted in which the parameters of an appropriate constitutive model are varied until the work equation is satisfied. In particular, the relative contribution of shear and volumetric stiffness could be established.

The result of this research would be an improved understanding of the constitutive properties that govern base resistance. Site characterisation for pile design could then concentrate on establishing these properties reliably. This work approach is proposed since the strain range encountered during pile installation is not amenable to full numerical analysis (i.e. FEM).

Existing analytical solutions for pile base resistance (e.g. cavity expansion methods, Strain Path Methods) can be verified against the measured strain paths. Previously, these techniques have been verified only by comparison of predicted and measured values of base resistance. A more thorough validation can be made by comparing the strain paths measured in this research with those implicit in the analytical solution.

However, whether such research is worthwhile remains in doubt. The stress and strain ranges encountered during soil flow around the pile tip are beyond those achievable within conventional element testing apparatus. Also, no constitutive model can easily capture the compression and particle breakage in the interface layer. Therefore, even if an analytical solution or numerical model for ultimate base capacity can be validated, it may remain impractical to obtain the relevant input parameters from element testing.

It may prove easier to improve the prediction of load-settlement behaviour, rather than ultimate capacity. Current models offer scope for improvement. For example, Lehane & Randolph (2002) present a simple method for estimating the load-settlement behaviour of a tubular pile by idealising the strain immediately below the pile as one-dimensional vertical compression. Stiffness values along this strain path are found from oedometer testing and used to predict pile base stiffness.

However, in this work, the strain path below the pile tip was found not to be one-dimensional. Instead, significant horizontal extension accompanies the vertical

compression beneath the pile tip. Improved prediction using this, or other methods, may be possible if a more representative strain path is chosen to deduce values of stiffness.

7.6.3 The prediction of foundation behaviour: shaft resistance

7.6.3.1 Installation effects

The interface contraction mechanism observed during the calibration chamber testing is linked to the distribution of shaft friction close to a pile tip. This mechanism supports limited field observations that cyclic loading during pile installation leads to reduced shaft friction. The corollary to this observation is that pressed-in piles may offer greater shaft friction than dynamically-installed piles; i.e. current design methods may be over-conservative. If this is confirmed, refinements of current design methods could lead to cost savings. Due to the uncertainty associated with the scaling of installation effects on shaft friction, comparative tests should be conducted at field scale. Tests in which identical piles are installed at the same site by different installation methods would be valuable.

The monotonic installation procedure of a pressed-in pile is comparable to that of a suction caisson. Therefore, the use of offshore pile design methods to estimate the friction on suction caissons may also prove over-conservative. Opportunities may exist for improved design efficiency if this over-conservatism can be confirmed and eliminated.

7.6.3.2 Time effects

The review of current literature presented in Chapter 2 showed that time effects have a strong influence on the capacity of displacement piles in sand. This phenomenon is known as ‘set-up’. There is scope for improved prediction if set-up can be estimated. Improved performance will result if set-up can be *accelerated*. Currently, the mechanism by which set-up occurs is not understood, providing no cues for techniques by which set-up could be accelerated. The creep, ageing and stress distribution within the sand around a pile shaft require investigation. The strain paths revealed in this research represent the initial conditions for the development of set-up.

Element tests in which these strain paths are replicated (within the constraints of the triaxial apparatus) will be reported by Bowman (2002). Her research aims to replicate the creep and aging associated with set-up. Further research could aim to establish the post-installation stress distribution around the pile shaft, and the potential for stress redistribution leading to an increase in radial stress. The interface contraction mechanism observed in this work indicates that the initial stress distribution prior to set-up will be representative of cylindrical cavity collapse towards the pile shaft.

7.6.4 The use of pressed-in piles for large foundation structures

This research has demonstrated that foundation structures with high axial capacity can be constructed using a small and relatively weak press-in piler. A novel foundation geometry that allows the mobilisation of high internal shaft friction due to vertical arching under working load, but not during installation, offers significant opportunities for improved design efficiency.

The geometric possibilities for 'switching on' the additional arching capacity are worthy of further investigation. This research could be conducted in a relatively inexpensive fashion at model scale since the primary concern is the difference in capacity between single piles and pile walls or groups, not the absolute value.

APPENDIX 1

STRAIN CALCULATION PROCEDURE

A1.1 INTRODUCTION

The measurement technique described in Chapter 3 produces a grid of object-space displacement vectors, denoted u,v in this appendix, for each image pair. In order to calculate strain, the grid of displacement measurement points is divided into a network of constant strain triangle elements (Figure A1.1). The centroid of each triangular element is a strain measurement point, with the strain components and element rotation calculated according to the procedure described below.

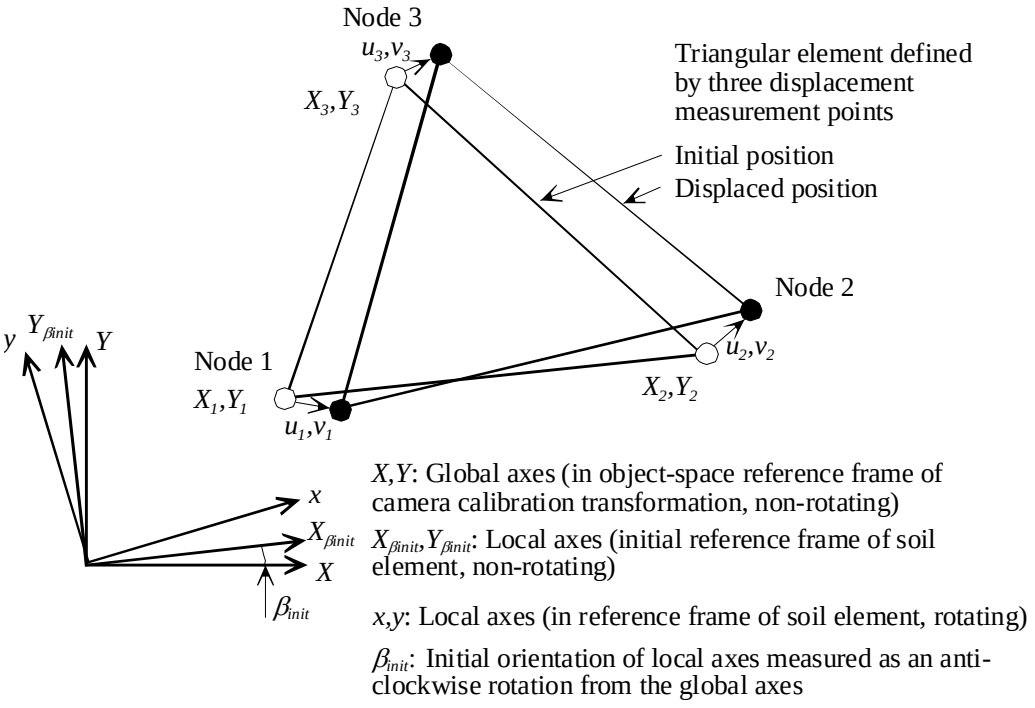

Figure A1.1 Constant strain triangle and reference frames

A1.2 DEFORMATION GRADIENT MATRIX, F

The movement of each marker during a single displacement increment is used to construct the displacement gradient matrix, *L*, using shape functions (Zienkiewicz, 1967) (Equation A1.1).

$$L = \begin{bmatrix} \frac{\partial u}{\partial X} & \frac{\partial u}{\partial Y} \\ \frac{\partial v}{\partial X} & \frac{\partial v}{\partial Y} \end{bmatrix} \tag{A1.1}$$

The displacement gradient matrix is converted to the deformation gradient matrix, *F*, using equation A1.2, where *I* is the identity matrix.

$$F = \begin{bmatrix} \frac{\partial x}{\partial X} & \frac{\partial x}{\partial Y} \\ \frac{\partial y}{\partial X} & \frac{\partial y}{\partial Y} \end{bmatrix} = L + I \tag{A1.2}$$

The deformation gradient matrix represents the transformation of a vector from undeformed coordinates, *x,y* to deformed coordinates, *x',y'* (Equation A1.3, Figure A1.2).

$$\begin{pmatrix} x' \\ y' \end{pmatrix} = F \begin{pmatrix} x \\ y \end{pmatrix} \tag{A1.3}$$

Where a deformation process consists of a series of incremental deformations, multiplication of the deformation gradient matrix of each deformation increment produces the total deformation. Hence, the total deformation of a soil element after n displacement steps is found using Equation A1.4, where L^n is the displacement gradient matrix for step *n*.

$$F^n = \left(L^n + I\right) F^{n-1} \tag{A1.4}$$

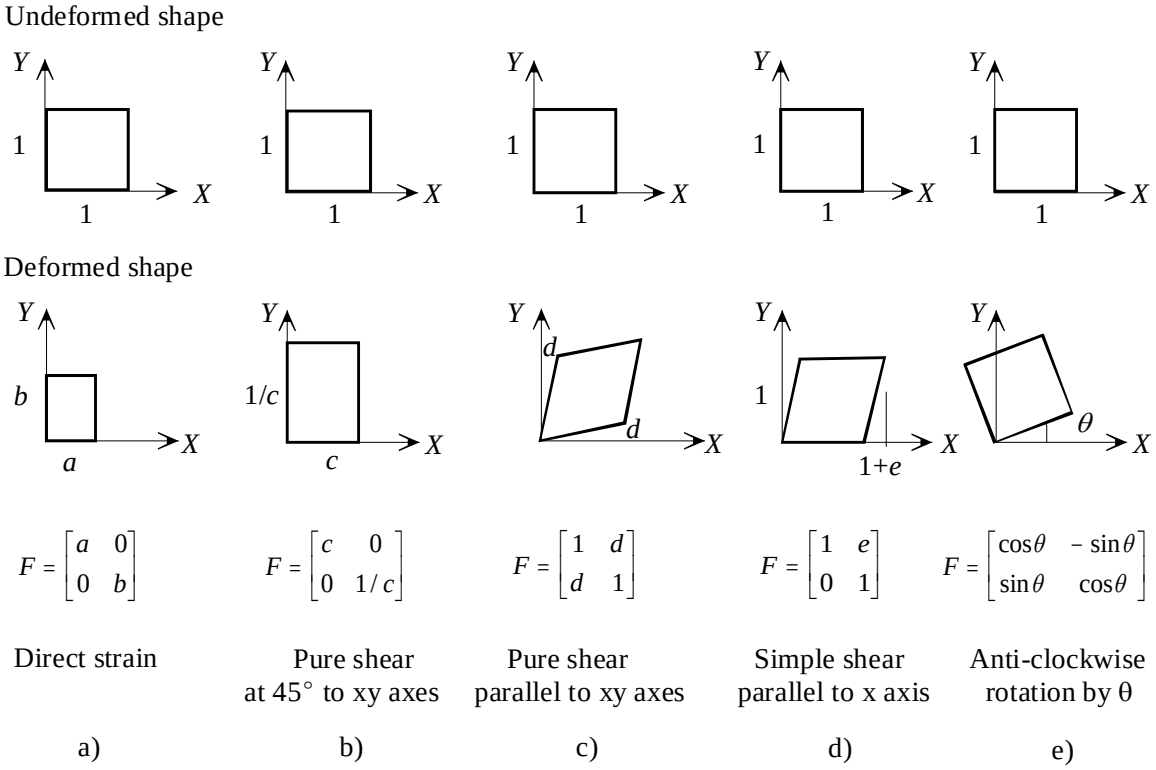

Figure A1.2 Elementary deformation gradient matrices

Polar decomposition allows the deformation gradient matrix to be divided into strain and rotation components, in order that individual components of deformation can be extracted. This process is known as polar decomposition (Chadwick, 1976). The symmetric part of F is the stretch matrix, U, representing strain, with the anti-symmetric part, R, containing rotation (Belytschko *et al*, 2000). Since R is anti-symmetric, $R^T R = I$, allowing F to be decomposed as shown in Equations A1.5-6.

$$U = \left(F^T F\right)^{1/2} \tag{A1.5}$$

$$R = FU^{-1} \tag{A1.6}$$

The rotation matrix, R, has the form shown in Figure A1.2e, allowing the rigid body rotation, θ, during the deformation described by F to be found.

A1.3 STRAIN QUANTITIES

A1.3.1 Engineering strain

The Biot strain tensor, E^{Biot}, is found from the stretch matrix, U, using Equation A1.7. The diagonal elements of E^{Biot} represent the elongation (change in length divided by original length) of line elements originally oriented with the x and y axes; i.e. engineering linear strain (Equations A1.8-A1.9). The sum of the off-diagonal elements is equal to the engineering shear strain on the xy plane, γ_{xy} (Equation A1.10). The eigenvalues of E^{Biot} are equal to the principal engineering strains, $\varepsilon_{eng,I}$, $\varepsilon_{eng,II}$, with the eigenvectors indicating the inclination of the principal strain directions to the xy axes.

$$E^{Biot} = U - I \tag{A1.7}$$

$$\varepsilon_{eng,xx} = E^{Biot}{}_{11} \tag{A1.8}$$

$$\varepsilon_{eng,yy} = E^{Biot}{}_{22} \tag{A1.9}$$

$$\gamma_{xy} = E^{Biot}{}_{12} + E^{Biot}{}_{21} \tag{A1.10}$$

Volumetric strain, Δ, is found directly from the element coordinates. Angle of dilation, ψ, over an increment of deformation is found using Equation A1.8, but cannot be defined for increments over which volumetric strain is greater than maximum shear strain (Equation A1.11).

$$\psi_{inc} = \sin^{-1}\left(\frac{-\Delta_{inc}}{\gamma_{\max,inc}}\right) = \sin^{-1}\left(\frac{-\Delta_{inc}}{|\varepsilon_I - \varepsilon_{II}|}\right) \tag{A1.11}$$

A1.3.2 Green-Lagrange strain

The Green-Lagrange strain tensor, E^{Green}, which is widely used in finite deformation analysis, is found using Equation A1.12. Green strain is defined as $(s^2/s_0^2 - 1)/2$ where s is the current length of a line element, and s_0 the original length. The diagonal elements of E^{Green} are equal to the Green strain in line elements originally oriented with the x and y axes (Equations A1.13-A1.14).

$$E^{Green} = \tfrac{1}{2}\left(F^T F - I\right) \quad \text{(A1.12)}$$

$$\varepsilon_{Green,xx} = E^{Green}{}_{11} \quad \text{(A1.13)}$$

$$\varepsilon_{Green,yy} = E^{Green}{}_{22} \quad \text{(A1.14)}$$

A1.3.3 Natural (logarithmic) strain

Natural (logarithmic) strain is defined is defined as the natural logarithm of the current length divided by the original length of a line element. The natural strains in the *x* and *y* directions are found by taking the logarithm of the diagonal elements of *U* (Equations A1.15-A1.16).

$$\varepsilon_{\log,xx} = \log_e(U_{11}) \quad \text{(A1.15)}$$

$$\varepsilon_{\log,yy} = \log_e(U_{22}) \quad \text{(A1.16)}$$

The engineering principal strain quantities can be converted to natural strain using Equations A1.17 and A1.18. To complete the set of natural strain quantities, maximum natural shear strain is defined as the difference between the natural principal strains (Equation A1.19). At a direct strain of 10%, the difference between natural and engineering direct strain quantities is less than 0.5%. If the principal direct engineering strains are ±10%, the maximum engineering and natural shear strains differ by less than 1%.

$$\varepsilon_{\log,I} = \log_e(1+\varepsilon_{eng,I}) \quad \text{(A1.17)}$$

$$\varepsilon_{\log,II} = \log_e(1+\varepsilon_{eng,II}) \quad \text{(A1.18)}$$

$$\gamma_{\log,\max} = \varepsilon_{\log,I} - \varepsilon_{\log,II} \quad \text{(A1.19)}$$

APPENDIX 2

RANDOM WALK SUMMATION

If PIV analysis is conducted through a series of images in which the test patch is updated between each image pair, then the random errors during each displacement step must be summed through the image series. These errors form a 'random walk'. The calculation below demonstrates that if the random error during a single step is equal to ρ, then the random error after n steps is equal to $\sqrt{n}\,\rho$.

Consider a random sequence of error vectors, with mean value zero (Equation A2.1).

$$\begin{bmatrix}\Delta x_1\\ \Delta y_1\end{bmatrix},\begin{bmatrix}\Delta x_2\\ \Delta y_2\end{bmatrix},\begin{bmatrix}\Delta x_3\\ \Delta y_3\end{bmatrix},\begin{bmatrix}\Delta x_4\\ \Delta y_4\end{bmatrix},\begin{bmatrix}\Delta x_5\\ \Delta y_5\end{bmatrix}.....\begin{bmatrix}\Delta x_n\\ \Delta y_n\end{bmatrix} \qquad \text{(A2.1)}$$

The standard error of these steps, $\underline{\rho}$, is divided into orthogonal components defined according to Equation A2.2.

$$\underline{\rho}=\begin{bmatrix}\rho_x\\ \rho_y\end{bmatrix} \quad \text{where} \quad \rho_x=\left(\frac{1}{n}\sum_{i=1}^{n}\Delta x_i^{\,2}\right)^{\frac{1}{2}} \quad \rho_y=\left(\frac{1}{n}\sum_{i=1}^{n}\Delta y_i^{\,2}\right)^{\frac{1}{2}} \qquad \text{(A2.2)}$$

A random walk denoted by summation of the vectors is denoted $\underline{R}$ (Equation A2.3).

$$\underline{R}=\begin{bmatrix}\Delta x_1\\ \Delta y_1\end{bmatrix}+\begin{bmatrix}\Delta x_2\\ \Delta y_2\end{bmatrix}+\begin{bmatrix}\Delta x_3\\ \Delta y_3\end{bmatrix}+\begin{bmatrix}\Delta x_4\\ \Delta y_4\end{bmatrix}+\begin{bmatrix}\Delta x_5\\ \Delta y_5\end{bmatrix}.....\begin{bmatrix}\Delta x_n\\ \Delta y_n\end{bmatrix} \qquad \text{(A2.3)}$$

The length of $\underline{R}$ is equal to the straight-line distance from the origin to the end of the random walk (Equation A2.4). This length is different to the distance covered during the random walk.

$$|\underline{R}| = \sqrt{(\Delta x_1 + \Delta x_2 + \Delta x_3 + \Delta x_4 + \Delta x_5 ..... \Delta x_n)^2 + \left(\Delta y_1^{\,2} + \Delta y_2^{\,2} + \Delta y_3^{\,2} + \Delta y_4^{\,2} + \Delta y_5^{\,2} ..... \Delta y_n\right)^2}$$

$$|\underline{R}| = \sqrt{\Delta x_1^{\,2} + \Delta x_2^{\,2} + \Delta x_3^{\,2} + \Delta x_4^{\,2} + \Delta x_5^{\,2} ..... \Delta x_n^{\,2} + 2\Delta x_1 \Delta x_2 + 2\Delta x_1 \Delta x_3 + 2\Delta x_1 \Delta x_4 .....}$$

(A2.4)

However, since the error vectors are randomly distributed around zero, the cross terms in Equation A2.4 cancel out. The length of vector R can be simplified to equation A2.5.

$$|\underline{R}| = \sqrt{\Delta x_1^{\,2} + \Delta x_2^{\,2} + \Delta x_3^{\,2} + \Delta x_4^{\,2} + \Delta x_5^{\,2} ..... \Delta x_n^{\,2} + \Delta y_1^{\,2} + \Delta y_2^{\,2} + \Delta y_3^{\,2} + \Delta y_4^{\,2} + \Delta y_5^{\,2} ..... \Delta y_n^{\,2}}$$

(A2.5)

Equation A2.5 can be simplified using Equation A2.2 to produce the final result:

$$|\underline{R}| = \sqrt{\sum_{i=1}^{n} \Delta x_i^{\,2} + \sum_{i=1}^{n} \Delta y_i^{\,2}} = \sqrt{n\rho_x^{\,2} + n\rho_y^{\,2}} = \sqrt{n}\,|\underline{\rho}|$$

(A2.6)

APPENDIX 3

CALCULATION OF WALL FRICTION

A3.1 INTRODUCTION

Section 4.3.7 discusses the influence of wall friction on the variation of vertical stress with depth in the calibration chamber. The following calculation is used to relate the geometry of the chamber and the interface friction at the boundaries to the profile of vertical stress. Since all tests were conducted dry, all stresses are effective.

Vertical equilibrium of a horizontal slice of soil during an increase of vertical load is governed by Equation A3.1, where upwards shear stress is created by friction against the side and end walls (Equations A3.2-A3.3). The interface friction angles of sand on steel and glass are denoted by δ_{ss} and δ_{sg} respectively.

$$\gamma dz = d\sigma_v + \frac{2\left(\tau_g L_g + \tau_s L_s\right)dz}{L_g L_s} \tag{A3.1}$$

$$\tau_s = K_0 \sigma_v \tan\delta_{ss} = \beta_s \sigma_v \tag{A3.2}$$

$$\tau_g = K_0 \sigma_v \tan\delta_{sg} = \beta_g \sigma_v \tag{A3.3}$$

Equation A3.1 can be simplified by the substitution shown in Equation A3.4, leading to the integration shown in Equation A3.5.

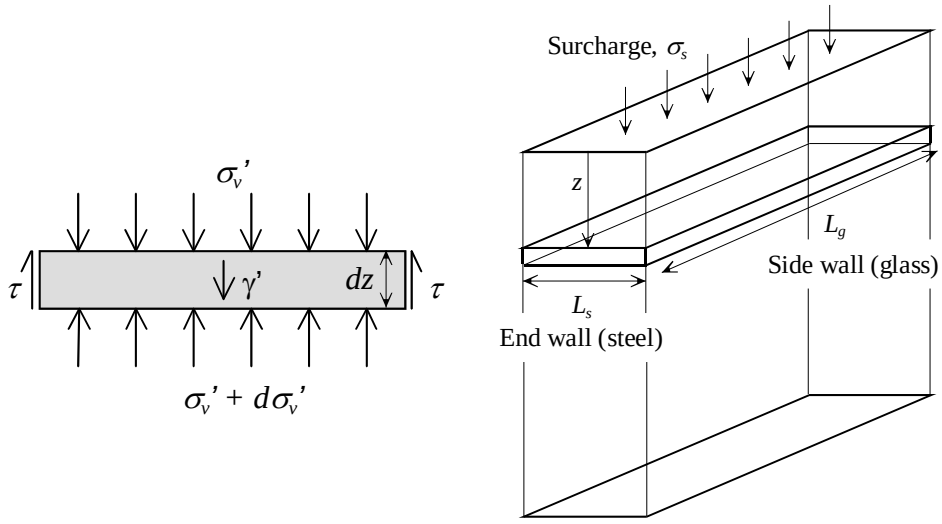

Figure A3.1 Vertical equilibrium of horizontal slice of soil

$$A = \frac{2K_0\left(L_s \tan\delta_{ss} + L_g \tan\delta_{sg}\right)}{L_s L_g} \tag{A3.4}$$

$$\int_0^z dz = \int_{\sigma_s}^{\sigma_v} \frac{d\sigma_v}{\gamma - A\sigma_v} \tag{A3.5}$$

Integration by substitution, applying a boundary condition of the surcharge pressure at the top surface, leads to Equation A3.6. During unloading after pre-compression, the direction of the shear stress is reversed between the ground surface ($z = 0$) and the depth at which the stress remains unchanged. The vertical stress profiles resulting from various values of interface friction during pre-compression to 100 kPa and unloading to 50 kPa are shown in Figures 4.6-4.7.

$$\sigma_v = \frac{\gamma}{A} + \left(\sigma_s - \frac{\gamma}{A}\right)e^{-Az} \tag{A3.6}$$

APPENDIX 4

CALIBRATION CHAMBER TEST PROCEDURE

The following sequence of events describes the preparation, execution and post-mortem of a typical calibration chamber test.

A4.1 Chamber assembly

- Start with rear assembly laid horizontal
- Affix rear glass sheet to inside of rear face
- Install false chamber base and total stress cell
- Place front glass sheet into chamber supported by polystyrene spacers
- Affix control points onto front glass sheet
- Lower front assembly onto rear assembly
- Bolt front and rear assemblies together
- Lift chamber upright and mount onto trolley

A4.2 Model preparation

- Mount sand pourer onto chamber and connect compressed air supply
- Pour model. Check density at intervals.
- Remove sand pourer
- Vacuum sand surface level
- Install surcharge bags and chamber lid
- Mount actuator and reaction frame on chamber
- Retract actuator, connect pile and pile cap
- Mount camera support frame and cameras

A4.3 Test

– Start data acquisition system and image capture software
– Slowly increase surcharge pressure from 0 kPa to 100 kPa
– After 10 minutes, slowly decrease surcharge pressure from 100 kPa to 50 kPa
– Start actuator (typical velocity 1 mm/min)
– Stop actuator when pile tip reaches required penetration depth
– After 5 minutes, reduce surcharge pressure from 50 kPa to 0 kPa
– Stop data acquisition system and image capture software

A4.4 Post-mortem

– Disconnect pile from pile cap, and retract actuator
– Remove actuator and reaction frame
– Lift chamber from trolley and rotate to horizontal
– Remove front assembly
– Take post-mortem photographs of soil fabric close to pile
– Remove front glass sheet
– Vacuum sand samples from grid of points close to pile
– Empty chamber of remaining sand

REFERENCES

Abdel-Aziz Y.I. & Karara H.M. 1971. Direct linear transformation into object space coordinates in close-range photogrammetry. Proc. Symposium on close-range Photogrammetry, Urbana, Illinois. 1:18

Adrian R.J. 1991. Particle imaging techniques for experimental fluid mechanics. Annual review of fluid mechanics 23:261-304

Ahmad A. & Chandler J.H. 1999. Photogrammetric capabilities of the Kodak DC40, DCS420 and DCS460 digital cameras. Photogrammetric Record 16(94):601-615

Airey D.W., Randolph M.F. & Hyden A.M. 1988. The strength and stiffness of two calcareous sands. Proc. Int. Conference on Calcareous Sediments. Perth, Australia, 1:43-50.

Al-Douri R.H. & Poulos H.G. 1991. Static and direct shear tests on carbonate sands. ASTM Geotechnical Testing Journal. 15(2):138-157

Allersma H.G.B. 1988a. Photoelastic investigation of the stress distribution during penetration. Proc. 2nd European Symposium on Penetration Testing. Amsterdam. 411-418

Allersma H.G.B. 1988b. Optical analysis of stress and strain around the tip of a penetrating probe. Proc. International Symposium on Penetration Testing, (2): 615-620

Allersma H.G.B., Stuit H.G. & Holscher P. 1994. Using image processing in soil mechanics. Proc. 12th International Conference on Soil Mechanics and Foundation Engineering, New Delhi 1341-1344

American Petroleum Institute (API) (1993) RP2A: Recommended practice of planning, designing and constructing fixed offshore platforms- working stress design, 20th edition, Washington 59-61

Andrawes K.Z. & Butterfield R. 1973. The measurement of planar displacements of sand grains. Géotechnique 23(5):571-576.

Angemeer J., Carlson E. & Klick J.J. 1973. Techniques and results of offshore pile load testing in calcareous soils. Proc. 5th Offshore Technology Conference, Houston 2:677-692

Arthur J.R.F. & Roscoe K.H. 1965. An examination of edge effects in plane strain model earth pressure tests. Proceedings 6th International Conference on Soil Mechanics 2:363-368.

Askegaard V. 1961. Measurement of pressure between a rigid wall and a compressible medium by means of pressure cell. Acta Polytechnica Scandanavica. Civil Engineering & Building Construction Series. No. 11. Copenhagen: Technical University of Denmark.

Åstedt B., Weiner L. & Holm G. 1992. Increase in bearing capacity with time for friction piles in silt and sand. Proc. Nordic Geotechnical Meeting. 411-416.

Axelsson G. 2002. A conceptual model of set-up for driven piles in non-cohesive soil. International Deep Foundations Congress, Orlando, FL. ASCE Geotechnical Special Publication 116:64-79

Baharom B. & Stallebrass S.E. 1998. A constitutive model combining the microscopic and macroscopic behaviour of sands in shear and volumetric deformation. Proc. 4th International Conference on Numerical Methods in Geotechnical Engineering, Udine.

Baldi G., Bellotti R., Ghionna V., Jamiolkowski M. & Pasqualini E. 1983. Design parameters for sands from CPT. Proc..European Symposium on Penetration Testing, Amsterdam. (2):425-432

Baldi G., Bellotti R., Ghionna V.N., Jamiolkowski M., Lo Presti D.C.F. 1989. Modulus of sands from CPT's and DMT's. Proc.12th International Conference on Soil Mechanics & Foundation Engineering, Rio de Janeiro, August 1989. (1):165-170

Baligh M.M. 1976. Cavity expansion in sands with curved envelopes. ASCE Journal of Geotechnical Engineering 112(GT11):1131-1146

Baligh M.M. 1985 Strain path method. ASCE Journal of Geotechnical Engineering 111(9):1108-1136

BCP Committee 1971. Field tests on piles in sand. Soils and Foundations. 11(2):29-49

Belytschko E. Liu W.K. & Moran B. 2000. Non-linear finite elements for continua and structures. Wiley & Sons, Chichester, UK.

Begemann H.K. 1977. Soil mechanics aspects of pile foundations. Foundation buildings research SBR, Samson, Alphen a/d/ Rijn (Netherlands) 44-65

Been K. & Jefferies M.G. 1985. A state parameter for sands. Géotechnique 35(2):99-112.

Been K., Jefferies M.G., Crooks J.H.A. & Rothenburg L. 1987. Cone penetration test in sands, 2: General inference of state. Géotechnique 37(3):285-299

Berezantzev V.C., Kristoforov V. & Golubkov V. 1961. Load-bearing capacity and deformation of piled foundations Proc. 5th Int. Conf. Soil Mechanics & Foundation Engineering, Paris 2:11-12

Beringen F.L., Windle D. & Van Hooydonk W.R. 1979. Results of loading tests on driven piles in sand. Proc. Conference on Recent Developments in the Design and Construction of Piles. ICE, London 213-225

Biddle A.R. 1996. Validation tests on vertical load capacity prediction methods for steel bearing piles. Document RT552. Steel Construction Institute. Ascot, UK.

Biddle A.R. 1997. Steel Bearing Piles Guide. Steel Construction Institute. Ascot, UK.

Bolton M.D. 1984. Strength and dilatancy of sands. Cambridge University Engineering Dept. Technical Report. CUED/D-Soils TR152

Bolton M.D. 1986. Strength and dilatancy of sands. Géotechnique 36(1):65-78

Bolton M.D., Gui M.W., Garnier J., Corte J.F., Bagge G., Laue J., Renzi R. 1999. Centrifuge cone penetration tests in sand. Géotechnique 49(4):543-552

Bond A.J. & Jardine R.J. 1991. Effects of installing displacement piles in a high OCR clay. Géotechnique. 41(3):341-363

Bond A.J., Hight D.W. & Jardine R.J. 1997. Design of piles in sand in the UK sector of the North Sea. Report OTH-94-457, prepared by GCG for the Health & Safety Executive, London

Borghi X., White D.J., Bolton M.D. & Springman S.M. 2001. Empirical pile design based on CPT results: an explanation for the reduction of unit base resistance between CPTs and piles. Proc. 5th Int. Conf. on Deep Foundation Practice, Singapore. 125-132

Bowman E.T., Soga K. & Drummond W. 2001. Particle shape characterisation using Fourier descriptor analysis. Géotechnique 51(6):545-554

Bowman E.T. 2002. Ageing and creep of dense granular materials. University of Cambridge PhD dissertation (in preparation).

Bransby P.L. 1968. Stress and strain in sand caused by rotation of a model wall. Cambridge University PhD dissertation.

Bransby P.L. & Milligan G.W.E. 1975. Soil deformations near cantilever sheet pile walls. Géotechnique 25(2):175-195.

Briaud, J.L. & Tucker L.M. 1988. Measured and predicted axial response of 98 piles. ASCE Journal of Geotechnical Engineering 114(9):984-1001

Briaud J-L, Tucker L.M. & Ng E. 1989. Axially loaded 5 pile group and a single pile in sand. Proc. 12th International Conference on Soil Mechanics and Foundations Engineering, Rio de Janeiro. (2):1121-1124

Brinch Hansen J. 1961. A general formula for bearing capacity. Bulletin no. 11, Danish Geotechnical Institute

Brinch Hansen J. 1970. A revised and extended formula for bearing capacity. Bulletin no. 28, Danish Geotechnical Institute. 5-11.

BS1377:1990. British standard methods of tests for soils for civil engineering purposes. British Standards Institute.

Brucy F., Meunier J. & Nauroy J-F (1991) Behaviour of a pile plug in sandy soils during and after driving Proceedings of the Offshore Technology Conference, Houston, Texas, OTC6514:145-154

Bruno, D. 1999. Dynamic and static load testing of driven piles in sand. PhD dissertation, University of Western Australia.

Bruno D. & Randolph M.F. 1999. Dynamic and static load testing of model piles driven into dense sand. ASCE. Journal of Geotechnical and Geoenvironmental Engineering 125(11):988-998

Budhu M. 1979. Simple shear deformation of sands. University of Cambridge PhD dissertation.

Bustamante M. & Gianaselli L. (1982) Pile bearing capacity by means of static penetrometer CPT. Proc. .2nd European Symposium on Penetration Testing, Amsterdam, 493-500

Butterfield R., Harkness R.M. & Andrawes K.Z. 1970. A stereo-photogrammetric method for measuring displacement fields. Géotechnique 20(3):308-314.

Carter J.P., Booker J.R. & Yeung S.K. 1986. Cavity expansion in cohesive frictional soils. Géotechnique 36(3):349-353.

Cavalieri A. 2000. The interface friction behaviour of sands. MEng dissertation, University of Trento, Italy.

Chadwick P. 1976. Continuum mechanics: concise theory and problems. George Allen & Unwin Ltd, London.

Chen J., Robson S., Cooper M.A.R. & Taylor R.N. 1996. An evaluation of three different image capture methods for measurement and analysis of deformation within a geotechnical centrifuge International archives of photogrammetry and remote sensing vol. XXX1, part B5, 70-75, Vienna

Chin J.T. & Poulos H.G. 1996. Tests on model jacked piles in calcareous sand. ASTM Geotechnical Testing Journal 19(2):164-180

Chong F. 1988. Density changes of sand on cone penetration resistance. Proc. 1st Symposium on Penetration Testing, ISOPT-1, Balkema, Rotterdam. (2):707-714

Chow F.C. 1997. Investigations into the behaviour of displacement piles for offshore foundations. PhD dissertation, University of London (Imperial College)

Chow F.C., Jardine R.J., Brucy F. & Nauroy J.F. 1998. Effects of time on capacity of pipe piles in dense marine sand. ASCE Journal of Geotechnical & Geoenvironmental Engineering 124(3):265-276

Clayton C.R.I. & Bica A.V.D. 1993. The design of diaphragm-type boundary total stress cells. Géotechnique. 43(4):523-535.

Clayton C.R.I. & Bica A.V.D. 1995. Discussion on: The design of diaphragm-type boundary total stress cells. Géotechnique. 45(2):349-351.

Cohen S. & Frydman S. 2002. Hydraulic gradient models of driven piles in sand. Proc. International Conference on Physical Modelling in Geotechnics. St John, Newfoundland. pub. Balkema.

Cooley J.W. & Tukey J.W. 1965. An algorithm for machine calculation of complex Fourier series. Mathematics of Computation. 19:297-301.

Cooke R.W. 1974. The settlement of friction pile foundations. Proc. Conference on Tall Buildings, Kuala Lumpur.

Coop M.R. 1987. The axial capacity of driven piles in clay. DPhil dissertation, University of Oxford

Coop, M.R. 1990. The mechanics of uncemented carbonate sands. Géotechnique 40(4): 607-626.

Coop M.R. & Wroth C.P. 1990. Discussion: Field studies of an instrumented model pile in clay. Géotechnique 40(4):669-672

Coop M. R. & Lee I.K. 1993 . The behaviour of granular soils at elevated stresses. Predictive Soil Mechanics: Proc. of the Wroth Memorial Symposium, 186-198. Eds. Houlsby G.T. & Schofield A. N.

Coop M.R. 1999. The role of high pressure testing in geotechnical research. Proc. Geotechnics in the New Millenium Symposium, Imperial College

Coop M.R. 2001. The influence of particle breakage and state on the behaviour of sands. Proc. 2nd International Workshop on Soil Crushability. Yamaguchi University.

Cousens T.W. 1975. The gravity flow of bulk solids in bunkers. PhD first year report. Cambridge University Engineering Department.

Coyle H.M. & Castello R.R. 1981. New design correlations for piles in sand. ASCE Journal of Geotechnical Engineering. 197(GT7) 965-985

Craig R.F. 1997. Soil Mechanics (6th edition) Spon Press; ISBN: 0419224505

Davidson J.L., Mortensen R.A. & Barreiro D. 1981. Deformations in sand around a cone penetrometer tip. Proc. 10th International Conference on Soil Mechanics and Foundation Engineering (2):467-470

DeJong J., Randolph M.F., & White D.J. 2003. Interface load transfer degradation during cyclic loading: a micromechanical investigation. Accepted for publication at the Third International Conference on Pre-failure Deformation of Geomaterials, Lyon, France

De Beer E.E. 1945. Etudes des fondations sur pilotis et des fondations directes. Annales des Travaux Publics de Belgique (46):1-78.

De Beer E.E. 1984. Different behaviour of bored and driven piles. Proc. 6th Int. Conf. Soil Mechanics & Foundation Engineering. Budapest. 307-318

De Nicola A. 1996. The performance of pipe piles in sand. PhD dissertation, University of Western Australia.

De Nicola A. & Randolph M.F. 1993. Tensile and compressive shaft capacity of piles in sand. ASCE. Journal of Geotechnical Engineering 119(12): 1952-1973

De Nicola A. & Randolph M.F. 1997. The plugging behaviour of driven and jacked piles in sand. Géotechnique 47(4):841-856

De Nicola A. & Randolph M.F. 1999. Centrifuge modelling of pipe piles in sand under axial loads. Géotechnique 49(3):295-318

De Ruiter J. & Beringen F.L. 1979. Pile foundations for large North Sea structures. Marine Geotechnology 3(3):267-314

Dietz M.S. 2000. Developing an holistic understanding of interface friction using sand within the direct shear apparatus. PhD dissertation, University of Bristol.

Dolwin J., Khorshid M.S. & Van Goudoever P. 1988. Evaluation of driven pile capacities- methods and results. Proc. International Conference on Engineering for Calcareous Sediments, Perth, Australia. (2):409-428

Eslami A. & Fellenius B.H. 1997. Pile capacity estimated from CPT data- six methods compared. Proc. 14th International Conference on Soil Mechanics & Geotechnical Engineering, Hamburg. (1):91-94

Ethrog U. 1994. Strain measurement by digital image processing. Proc. 10th Conf. Recent Advances in Experimental Mechanics. Balkema, Rotterdam. 411-415.

Eurocode 7: geotechnical design. Part 1: general rules (together with United Kingdom National Application Document). British Standards Institution DD ENV 1997-1

Evans K.M. 1987. A model study of the end bearing capacity of piles in layered calcareous soils. Oxford University D.Phil dissertation.

Fellenius B.H. & Altaee, A.A. 1995. Critical depth: how it came into being and why it does not exist. Geotechnical Engineering, Proc. Institution of Civil Engineers. 113(2):107-111

Festag G. & Katzenbach R. 2001. Material behaviour of dry sand under cyclic loading. Proc. 15th International Conference on Soil Mechanics and Geotechnical Engineering, Istanbul, (1):87-90.

Finlay T.C.R., White D.J., Bolton M.D. & Nagayama T. 2001. Press-in Piling: The installation of instrumented steel tubular piles with and without driving shoes. Proceedings of the 5th International Conference on Deep Foundation Practice, Singapore 199-208

Fioravante V. Jamiolkowski M. & Pedron S. 1994. Modelling the behaviour of piles in sand subjected to axial load, Proc. Centrifuge ’94, Balkema, Rotterdam 455-460

Fleming W. G. K., Weltman A. J., Randolph M. F. & Elson W. K. 1992. Piling Engineering Blackie (Halsted Press), Glasgow

Foray P., Genevois J.M., Labanieh S., Goulois A 1989. Effet de la mise en place sur la capacite portante des pieux dans les sables. Proc. 12th International Conference on Soil Mechanics and Foundation Engineering, Rio de Janeiro. 913-914

Foray P. Balachowski L & Colliat J.L. 1996. Effect of overconsolidation of dense sands on the bearing capacity of driven piles. Proc. 49th Canadian Geotechnical Conference, Newfoundland.

Frank R. 1975. Etude theoretique du comportement des pieux sous charge verticale. Rapport to recherché no. 46, Laboratoire Central des Ponts et Chausees.

Garnier J., Chambon P., Ranaivoson D., Charrier J. & Mathurin R. 1991. Computer image processing for displacements measurement. Proceedings of Centrifuge '91, Balkema, Rotterdam 543-550.

Gerber E. 1929. Untersuchungen uber die Druck-verteilung im Oertlick Belasteten Sand. Dissertation Technische Hochschule, Zurich

Ghionna V.N., Jamiolkowski M., Lancellotta R., Pedroni S. 1993. Base capacity of bored piles in sands from in situ tests. Proc. International Geotechnical Seminar on Deep Foundations on Bored and Auger Piles. Ghent, Belgium. Balkema, Rotterdam. 67-74

Gibson R.E & Anderson W.F. 1961. In situ measurement of soil properties with the pressuremeter. Civil Engineering and Public Works Review 56:615-618

Gill D.R. 1999. Experimental and theoretical investigations of pile and penetrometer installation in clay. PhD dissertation. Trinity College, Dublin.

Gill D.R. & Lehane B.M. 2001. An optical technique for investigating soil displacement patterns. ASTM Geotechnical Testing Journal. 24(3): 324-329

Golightly C.R. & Hyde A.F.L. 1988. Some fundamental properties of carbonate soils. Proc. International Conference on Calcareous Sediments, Perth, Australia. (1):69-78

Golightly C.R. 1989. Engineering properties of carbonate sands. Bradford University PhD dissertation.

Golightly C.R. & Nauroy J-F. 1990. End bearing capacity of piles in calcareous sands. Proc. Offshore Technology Conference, Houston, Texas. 345-355

Goodman J.W. 1968. Introduction to Fourier optics. McGraw-Hill, New York. pp297.

Grant R.J. 1998. Movements around a tunnel in two-layer ground City University, London, PhD dissertation

Ground Engineering. 1999. "Uncertainty principle". November 1999, 32-34. EMAP publications.

Gunn M.J. 1993. The prediction of surface settlement profiles due to tunnelling. In Predictive Soil Mechanics; Proceedings of the Wroth Memorial Symposium, ed. Houlsby G.T. & Schofield A.N. 304-316. Thomas Telford, London.

Gurtowski T.M. & Wu M-J. 1984. Compression load tests on concrete piles in alluvium. Proc. Symposium on Analysis and Design of Pile Foundations, ASCE, San Francisco. 138-153

Heerema E.P. 1980. Predicting pile driveability: heather as an illustration of the friction fatigue theory. Ground Engineering 13(Apr):15-37

Heikkila J. & Silven O. 1996. Calibration procedure for short focal length off-the-shelf CCD cameras. Proc. 13th International Conference on Pattern Recognition. Vienna, Austria, 166-170.

Heikkila J. & Silven O. 1997. A four-step camera calibration procedure with implicit image correction. IEEE Computer Society Conference on Computer Vision and Pattern Recognition (CVPR'97), San Juan, Puerto Rico.

Heikkila J. MATLAB camera calibration toolbox, version 2.1b. University of Oulu, Finland.

Hight D.W., Lawrence D.M., Farquhar G.B., Milligan G.W.E., Gue S.S. & Potts D. M. 1996. Evidence for scale effects in the end bearing capacity of open-ended piles in sand Proc. Offshore Technology Conference, Houston OTC7975: 181-192

Hight D.W. 1999. Geotechnics in the new millennium: laboratory testing. Proc. Geotechnics in the New Millenium Symposium, Imperial College

Hossain M.K. & Braiud J-L. 1993. Improved soil characterisation for pipe piles in sand in API RP2A. Proc. 25th Offshore Technology Conference, Houston. OTC7193:637-654

Houlsby G.T. & Hitchman R. 1988. Calibration chamber tests of a cone penetrometer in sand. Géotechnique 38(1): 39-44.

Houlsby G.T., Evans K.M. & Sweeney M.A. 1988. End bearing capacity of model piles in layered carbonate soils. Proc. Int. Conference on Calcareous Sediments. Perth, Australia, 1:209-214.

James R.G. 1965. Stress and strain fields in sand. Cambridge University PhD dissertation

Jamiolkowski M., Ladd C. C., Germaine J. T., Lancellotta R. 1985. New developments in field and laboratory testing of soils Proc. 11th Conf. on Soil Mechanics & Foundation Engineering (1): 57-156

Jamiolkowski M., Ghionna V.N., Lancellotta R. & Pasqualini E. 1988. New correlations of penetration tests for design practice. Proc. 1st International symposium on penetration testing, 1, ISOPT-1, Orlando, March 1988 (1)263-296

Janssen H. A. 1894. Versuche uber getreidedruck in Silozollen, Aeitschrift, Verein Deutscher Ingenieure (39):1045-1049

Jardine R.J., Potts D.M., Fourie A.B. & Burland J.B. 1986. Studies of the influence of non-linear stress-strain characteristics in soil-stucture interaction. 36(3):377-396.

Jardine, R.J., Lehane, B.M. & Everton, S.J. 1992. Friction coefficients for piles in sands and silts. Vol. 28: Offshore Site Investigation and Foundation Behaviour, Soc. for Underwater Technology pp 661-677

Jardine R.J. & Chow F.C. 1996. New design methods for offshore piles MTD Publication 96/103, Marine Technology Directorate, London

Jardine R.J., Standing J.R., Jardine F.M., Bond A.J. & Parker E. 2001. A competition to assess the reliability of pile prediction methods. Proc. XVth Int. Conf. Soil Mechanics and Geotechnical Engineering., Istanbul, Vol. 2, Balkema, Rotterdam, 911-914.

Jibanshikenjo Co. Ltd. 2001. Minatominami-1 Cho-me construction project vertical load test report for Giken Seisakusho (in Japanese) pp89

Joer H., Bolton M.D. & Randolph M.F. 1999. Compression and crushing behaviour of calcareous soils. Proc. 2nd International Workshop on Soil Crushability. Eds. Hyodo M. and Nakata Y., Yamaguchi University, Japan

Jovicic V. & Coop M.R. 1997. Stiffness of coarse-grained soils at small strains. Géotechnique 47(3):545-561.

Kaufman G.H, Ennose A.E., Gale B. & Pugh D.J. 1980. An electro-optical readout system for analysis of speckle photographs. J. Phys. E. 13:579-584.

Keane R. & Adrian R.J. 1990. Optimisation of particle image velocimeters. Part I: double pulsed systems. Measurement Science and Technology (2):1202-1215.

Keane R., Adrian R.J. & Ford D.K. 1990. Single exposure double frame particle image velocimeters. In ICALEO '90: Optical methods in flow and particle diagnostics, Proc. of the SPIE. eds. Dibble R.W., Ketterle W., Fourguette D.C. 91-110.

Kerisel J. 1961. Fondations profondes en milieux sable: variation de la force portante limite en function de la densite, de la profondeur, du diameter et de la vitesse d'enforcement. Proc. 4th International Conference on Soil Mechanics & Foundation Engineering (2):73-83

Kerisel J. 1985. History of geotechnical engineering up until 1700. Proc. International conference on soil mechanics and foundation engineering, San Francisco, Golden Jubilee Volume.

Kishida, T, Fukuaya, T & Hanzawa, H. 1986. Development of the friction meter for evaluating the skin friction of a pile. Soils and foundations 26(1): 122-128.

Kishida, H. & Uesugi, M. 1987. Tests of the interface between sand and steel in the simple shear appara-tus. Géotechnique 37(1): 45-52.

Klotz E.U. 2000. Influence of state on the capacity of driven piles in sand. PhD dissertation, City University, London

Klotz E.U. & Coop M.R. 2001. An investigation of the effect of soil state on the capacity of driven piles in sands. Géotechnique 51(9): 733-751

Kodak. 2000. Personal communication with Technical Support, Kodak UK.

Kraft L.M. 1990. Computing axial pile capacity in sands for offshore conditions. Marine Geotechnology 9:61-72

Kreyszig E. 1999. Advanced Engineering Mathematics. 8th Edition. John Wiley and Sons (WIE); ISBN: 047133328X.

Kutter B.L. 1982. Centrifugal modelling of the response of clay embankments to earthquakes. Cambridge University PhD dissertation.

Landreth C.C. & Adrian R.J. 1989.Measurement and refinement of velocity data using high image density analysis in particle image velocimetry. In Applications of Laser Anemometry to Fluid Mechanics. ed. Adrian R., Asanuma T., Durao D., Durst F., Whitelaw J. 484-497. Springer-Verlag, Berlin pp535.

Last N. 1979. Cone penetration tests on samples of dry Hokksund sand in a rigid walled chamber. Norwegian Geotechnical Institute Report. NGI52108-8.

Lee S.Y. 1989. Centrifuge modelling of cone penetration testing in cohesionless soils. Cambridge University PhD dissertation.

Lee J.H. & Salgado R. 1999. Determination of pile base resistance in sands. ASCE. Journal of Geotechnical and Geoenvironmental Engineering 125(8):673-683

Lehane B.M. 1992. Experimental investigations of pile behaviour using instrumented field piles. PhD dissertation, Imperial College, University of London.

Lehane B.M., Jardine R.J, Bond A.J. & Frank R. 1993. Mechanisms of shaft friction in sand from instrumented pile tests. ASCE Journal of Geotechnical Engineering 119(GT1): 19-35.

Lehane B.M. & Randolph M.F. 2002. Evaluation of a minimum base resistance for driven pipe piles in siliceous sand. ASCE Journal of Geotechnical and Geoenvironmental Engineering 128(3):198-205

Leung C.F., Lee F.H. & Yet N.S. 1996. The role of particle breakage in pile creep in sand. Canadian Geotechnical Journal. 33(6):888-898

Leung C.F., Lee F.H. & Yet N.S. 2001. Centrifuge model study on pile subject to lapses during installation in sand. International Journal of Physical Modelling in Geotechnics. 1(1):47-58

Lings M. L. 1997. Predicting the shaft resistance of driven pre-formed piles in sand Proceedings of the Institution of Civil Engineers, Geotechnical Engineering 125(April):71-84

Lunne T., Robertson P.K. & Powell J.J.M. 1997. Cone penetration testing in geotechnical practice. Blackie, London.

Luzzani L. & Coop M.R. 2002. On the relationship between particle breakage and the critical state of sands. Accepted for publication in Soils and Foundations.

Mair R.J. 1979. Centrifugal modelling of tunnel construction in soft clay Cambridge University PhD dissertation

Mair, R.J. 1993. Developments in geotechnical engineering research: applications to tunnels and deep excavations. Unwin Memorial Lecture (1992), Proc. ICE, London, Vol 97 No.1, 27-41

Malhotra S. 2000. Axial load capacity of steel pipe piles in sand: a review of the API method. Proc. 25th International Conference of the Deep Foundations Institute, New York. 205-218

Mansur C.I. & Hunter A.H. 1970. Pile tests- Arkansas River project. J. Soil Mechanics and Foundations Division, ASCE 96(SM5):1545-1582

Mayne P.W. & Kulhawy F.H. 1991. Calibration chamber database and boundary effects correction for CPT data Proc. 1st International Symposium on Calibration Chamber Testing (ISOCCT1), 257-264.

Meigh A.C. 1987. Cone penetration testing - methods and interpretation. Construction Industry Research and Information Association (CIRIA) Ground Engineering Report pp147.

Mey R., Oteo C.S., Sanchez de Rio J. & Soriano A. 1985. Field testing on large driven piles. Proc. 11th International Conference on Soil Mechanics and Foundation Engineering, San Francisco. 3:1559-1564

Meyerhof G.G. 1953. An investigation for the foundations of a bridge on dense sand. Proc. 3rd International Conference on Soil Mechanics and Foundation Engineering. Zurich. 2:66-70

Meyerhof G.G. 1963. Some recent research on bearing capacity of foundations. Canadian Geotechnical Journal. 1:16-26.

Meyerhof G.G. 1976. Bearing capacity and settlement of pile foundations. ASCE Journal of Geotechnical Engineering. 102(GT3)197-228

Meyerhof G.G. 1983. Scale effects of ultimate capacity. ASCE Journal of Geotechnical Engineering. 109(6)797-806

Meynart R. 1983. Speckle velocimetry: an application of image analysis techniques to the measurement of instantaneous velocity fields in unsteady flow. ICIASF ’83 record, IEEE New York. 30-36.

Mikasa M. & Takada N. 1973. Significance of centrifugal model tests in soil mechanics. Proc. 8th International Conference on Soil Mechanics and Foundation Engineering, Moscow. 273-278

Miller G.A. & Lutenegger A.J. 1997. Influence of pile plugging on skin friction in overconsolidated clay. ASCE Journal of Geotechnical Engineering 123 (6) 525-533

Milligan G.W.E. 1974. The behaviour of rigid and flexible retaining walls in sand. Cambridge University PhD dissertation.

Mosher R.L. 1987. Comparison of axial capacity of vibratory driven piles to impact piles. USA WES Technical Report, ITL-877

Murff J.D., Raines R.D. & Randolph M.F. 1990. Soil plug behaviour of piles in sand. Procedings of the Offshore Technology Conference, Houston OTC6421: 25-32

Nauroy J.F. & Le Tirant P. 1983. Model tests of piles in calcareous sands. Proc. Conference on Geotechnical Practice in Offshore Engineering, Austin, Texas, ASCE 356-369.

O’Neill M.W. & Vipulanandan C. 1989. Laboratory evaluation of piles installed with vibratory drivers. NCHRP Report 316, National Cooperative Highway Research Program, TRB, Washington DC.

Obaidat M.T. & Attom M.F. 1996. Computer vision-based technique to measure displacement in selected soil tests. ASTM Geotechnical Testing Journal 21(1):31-37

Paikowsky S.G., Whitman R.V. & Baligh M.M. 1989. A new look at the phenomenon of offshore pile plugging. Marine Geotechnology (8) 213-230

Paikowsky, S.G., Player, C.M. & Connors, P.J. 1995. Dual interface apparatus for testing unrestricted friction of soil along solid surfaces. ASTM Geotechnical Testing Journal 18(2): 168-193

Parkin A.K. 1988. Calibration of cone penetrometers. Proc. International symposium on penetration testing, 1, ISOPT-1, Orlando, March 1988. (1):221-243

Parkin A.K. & Lunne T. 1982. Boundary effects in the laboratory calibration of a cone penetrometer for sand. Proc. 2nd European Symposium on Penetration Testing, Amsterdam (2):761-767.

Phillips R. 1991. Film Measurement Machine User Manual. Cambridge University Technical Report, CUED/D-Soils/TR 246.

Poulos H.G., Randolph M.F. & Semple R.M. 1988. Evaluation of pile friction from conductor tests. Proc. International Conference on Calcareous Sediments, Perth, Australia (2):599-605

Poulos H.G. 1989. Pile behaviour - theory and application. Géotechnique 39(3):365-415

Potts D.M. 1976. Behaviour of lined and unlined tunnels in sand. Cambridge University PhD dissertation.

Raines D.R., Ugaz O.G. & O'Neill M.W. 1992. Driving characteristics of open-toe piles in dense sand. ASCE Journal of Geotechnical Engineering 118(1): 72-88

Randolph M.F. 1977 A theoretical study of the performance of piles. PhD dissertation, University of Cambridge.

Randolph M.F. & Wroth C.P. 1979. Analysis of the vertical deformation of pile groups. Géotechnique 29(4): 423-439

Randolph M.F. & Wroth C.P. 1979. Analytical solution for the consolidation around a driven pile. International Journal for Numerical and Analytical Methods in Geomechanics (3)3: 217-229

Randolph M.F.1985. Capacity of piles driven into dense sand. Cambridge University Engineering Department Technical Report: CUED/D-SOILS/TR.171.

Randolph M.F. 1988. The axial capacity of deep foundations in calcareous soil. Proc. Int. Conference on Calcareous Sediments. Perth, Australia, 2:837-857.

Randolph M.F., Leong E.C., & Houlsby G.T. 1991. One-dimensional analysis of soil plugs in pipe piles Géotechnique 41(4): 587-598

Randolph M.F., Dolwin J. & Beck R. 1994. Design of driven piles in sand Géotechnique 44(3):427-448

Robertson P.K. & Campanella R.G. 1983. Interpretation of cone penetration tests. Part I: sand. Canadian Geotechnical Journal 20:718-733

Robinsky E.I. & Morrison C.F. 1964. Sand displacement and compaction around model friction piles. Canadian Geotechnical Journal. 1(2):81-93

Roscoe K.H., Arthur J.R.F & James R.G. 1963. The determination of strains in soils by an X-ray method Civil Engineering & Public Works Review, 58:873-876,1009-12

Saada A.S., Liang L., Figueroa J.L. & Cope C.T. 1999. Bifurcation and shear propagation in sands. Géotechnique 49(3):367-385.

Sagaseta C. & Whittle A.J. 2001. Prediction of ground movements due to pile driving in clay. ASCE Journal of Geotechnical & Environmental Engineering. 127(1):55-66.

Salgado R. 1995. Design of piles in sands based on CPT results. Proc. 10th Pan-American Conference on Soil Mechanics and Foundation Engineering, Guadalajara (3):1261-1274.

Salgado R., Mitchell J.K. & Jamiolkowski M. 1997. Cavity expansion and penetration resistance in sand. ASCE. Journal of Geotechnical and Geoenvironmental Engineering. 123(4):344-354

Sangrey D.A., Castro G., Poulos S.J. & France J.W. 1978. Cyclic loading of sands, silts & clays. Proc. Specialy Conference on Earthquake Engineering & Soil Dynamics. ASCE (2):836-851

Schmertmann J.H. 1976. An updated correlation between relative density and Fugro-type electric cone bearing. Report to US Army Corps of Engineers, WES Vicksburg.

Schmertmann J.H. 1978. Guidelines for cone penetration test: performance and design. US Dept. of Transport, Federal Highways Administration, Washington. FHWA-TS-78-209

Schmertmann J.H. 1991. The mechanical aging of soil. ASCE Journal of Geotechnical Engineering. 117(9):1288-1330.

Schnaid F. 1990. A study of the cone-pressurementer test in sand. Oxford University DPhil dissertation.

Sentenac P., Lynch R.J. & Bolton M.D. 2001. Measurement of the side-wall boundary effect in soil columns using fibre-optics sensing, International Journal of Physical Modelling in Geotechnics (4):35-41.

Sharma J.S. 1994. Behaviour of reinforced embankments on soft clay. University of Cambridge PhD Dissertation.

Simons N. & Menzies B. 2000. A short course in foundation engineering. Thomas Telford, London.

Simpson B., O'Riordan N.J. & Croft D.D. 1979. Computer model for the analysis of ground movements in London Clay. Géotechnique 29(2):149-175.

Skempton A.W., Yassin A.A. & Gibson R.E. 1953. Theorie de la force portante des pieux dans le sable. Annales de l'Institut Technique du Batiment et des Travaux Publics. 53-64.

Slama C.C. (ed.) 1980. Manual of photogrammetry, 4th edition. American Society of Photogrammetry.

Smith I.A.A. 1972. Stress and strain in a sand mass adjacent to a model wall. Cambridge University PhD dissertation.

Standing J.R. 1997. Studies of the interface resistance of soil nails. PhD dissertation. University of London (Imperial College), London

Stroud M.A. 1971. Sand at low stress levels in the Simple Shear Apparatus. Cambridge University PhD dissertation.

Symes M.J., Gens A. & Hight D.W. 1988. Drained principal stress rotation in saturated sand. Géotechnique 38(1):59-81

Tabucanon, J.T., Airey, D.W. & Poulos, H.G. 1995. Pile skin friction in sands from constant normal stiffness tests. ASTM Geotechnical Testing Journal 18(3): 350-364.

Take W.A. 2002. The influence of seasonal moisture cycles on clay slopes. University of Cambridge PhD dissertation (in preparation)

Tan F.S.C. 1990. Centrifuge and theoretical modelling of conical footings on sand. Cambridge University PhD dissertation.

Taylor R.N., Grant R.J., Robson S. & Kuwano J. 1998. An image analysis system for determining plane and 3-D displacements in soil models. Proceedings of Centrifuge '98, 73-78 pub. Balkema, Rotterdam.

Teh C.I. & Houlsby G.T. 1991. Analytical study of the cone penetration test in clay. Géotechnique 41(1):17-34

Te Kamp W.C. 1977. Sonderingen en funderingen op palen in zand (Static cone penetration testing and foundations on sand). Fugro sounding syposium, Utrecht, Oct 1977

Tejchman A. & Gwizdala K. 1979. Analysis of safety factors of bearing capacity for large diameter piles. Eur. Conf. on Soil Mechanics & Foundation Engineering (1):293-296

Tennekoon B.L. 1970. Stresses and strains induced by a strip footing on sand. Cambridge University PhD dissertation.

Terzaghi K. 1943. Theoretical soil mechanics. J. Wiley & Sons, New York

Terzaghi K. & Peck R.B. 1967. Soil mechanics in engineering practice. J Wiley & Sons, New York.

Thompson G.W.L. 1997. The applicability of the new Imperial College pile design method to calcareous sands. MSc dissertation, Imperial College, University of London.

Thompson G.W.L. & Jardine R.J. 1998. The applicability of the new Imperial College pile design method to calcareous sands. Proc. Conference on Offshore Site Investigation and Foundation Behaviour, Society for Underwater Technology. 383-400

Thorburn S. & McVicar R.S. 1970. Pile load tests to failure in the Clyde alluvium. Proc. Conference on the Behaviour of Piles. ICE, London 1-7

Tomlinson M.J. 2001. Foundation design and construction, 7th edition. Prentice Hall, Harlow, England

Toolan F.E., Lings M.L. & Mirza U.A. (1990) An appraisal of API RP2A recommendations for determining skin friction of piles in sand. Proc. 22nd Offshore Technology Conference, Houston, Texas. OTC6422 (4):33-42

Uesugi, M & Kishida, H. 1986. Influential factors of friction between steel and dry sands. Soils and foundations 26(2): 33-46 .

Vesic A.S. 1963. Bearing capacity of deep foundations in sand. National Academy of Sciences, National Research Council, Highway Research Record 39. 112-153.

Vesic A.S. & Clough G.W. 1968. Behaviour of granular materials under high stresses ASCE Journal of the Soil Mechanics and Foundations Division 94(SM3):661-688

Vesic A.S. 1969. Experiments with instrumented pile groups in sand. ASTM STP 444 177-222

Vesic A.S. 1970. Tests on instrumented piles, Ogeechee River site. ASCE Journal of the Soil Mechanics & Foundations Division. 96(SM2):561-584

Vesic A.S. 1972. Expansion of cavities in an infinite soil mass. ASCE Journal of the Soil Mechanics & Foundations Division. 98(SM3):265-290

Wersching S.N. 1987. The development of shaft friction and end bearing for piles in homogenous and layered soils. PhD dissertation, Polytechnic of South Wales.

White D.J., Sidhu H.K., Finlay T.C.R, Bolton M.D., Nagayama T. 2000. Press-in Piling: The influence of plugging on driveability. Proceedings of the 8th International Conference of the Deep Foundations Institute, New York. 299-310

White D.J., Take W.A, Bolton M.D. 2001a. Measuring soil deformation in geotechnical models using digital images and PIV analysis. Proc. 10th International Conference on Computer Methods and Advances in Geomechanics. Tucson, Arizona. 997-1002 pub. Balkema, Rotterdam

White D.J., Take W.A, Bolton M.D. & Munachen S.E. 2001b. A deformation measuring system for geotechnical testing based on digital imaging, close-range photogrammetry, and PIV image analysis. Proc. 15th International Conference on Soil

Mechanics and Geotechnical Engineering. Istanbul, Turkey. 539-542. pub. Balkema, Rotterdam

White D.J., Finlay T.C.R., Bolton M.D. & Bearss G. (2002) Press-in piling: Ground vibration and noise during pile installation. Proceedings of the International Deep Foundations Congress. Orlando, USA. ASCE Special Publication 116 pp363-371

Winterkorn, A.F. & Fang, S.Y. 1975. Foundation Engineering Handbook, Van Nostrand Reinhold Co. New York.

Yasufuku, N. & Hyde, A.F.L. 1995. Pile end-bearing capacity in crushable sands. Géotechnique 45(4): 663-676.

Yasufuku N., Ochiai H. & Ohno S. 2001. Pile end-bearing capacity of sand related to soil compressibility. Soils & Foundations. 41(4):59-71

Yen T-L, Lin H., Chin C-T & Wang R.F. 1989. Interpretation of instrumented driven steel pipe piles. Proc. Congress on Foundation Engineering, Current Principles & Practices, Illinois. ASCE 1293-1308

Yu H.S. 1990. Cavity expansion theory and its application to the analysis of pressuremeters. DPhil dissertation, University of Oxford.

Yu H.S. & Houlsby G.T. 1991. Finite cavity expansion in dilatant soils: loading analysis Géotechnique 41(2):173-183

Yu H.S., Schnaid F. & Collins I.F. 1996. Analysis of cone pressuremeter tests in sands. ASCE. Journal of Geotechnical Engineering 122(8):623-632

Zelikson. A. 1969. Geotechnical models using the hydraulic gradient similarity method. Géotechnique 19(4):495-508

Zeitlin J.G. & Paikowsky S. 1982. Discussion on Coyle H.M. & Castello R.R. 1981. New design correlations for piles in sand. ASCE Journal of Geotechnical Engineering. 198(GT11):1515-1518

Zhao Y., Yetginer A.G., & Rockhill D.J. 2001. Factual report on Summer 2001 field testing. Report to Giken Seisakusho Ltd.

Zienkiewicz O.C. 1967. The finite element method in structural and continuum mechanics. McGraw-Hill, London.

Zuidberg H.M. & Vergobbi P. 1996. EURIPEDES, load tests on large driven piles in dense silica sands. Proc. 28th Offshore Technology Conference, OTC 7977 193-206